MAGMATIC ENVIRONMENTS AND TIMESCALES:

EXPERIMENTAL STUDIES ON MARTIAN BASALT AND TERRESTRIAL DACITE

A DISSERTATION SUBMITTED TO THE GRADUATE DIVISION OF THE UNIVERSITY OF HAWAIʻI AT MĀNOA IN PARTIAL FULFILLMENT OF THE REQUIREMENTS FOR THE DEGREE OF

DOCTOR OF PHILOSOPHY

IN

GEOLOGY & GEOPHYSICS

DECEMBER 2017

By

Emily C. First

Dissertation Committee:

Julia Hammer, Chairperson
Bruce Houghton
Thomas Shea
Jeff Taylor
John Allen

Keywords: cooling rate, diffusion, equilibrium, experimental petrology, Fe-Ti oxides, kinetics, Mars, plagioclase, Quizapu, volcanology

Acknowledgments

In my time at UH, I have been supported by a NASA Mars Fundamental Research grant (NNX11AM29G) and an NSF-EAR grant (13-47887), both to Julia Hammer. I am grateful for additional financial support from the Fred. M. Bullard graduate fellowship, ARCS Honolulu, and two student research grants from GSA (Lipman Award and MGPV division award). For sample lending or collecting, thanks to NiPR (Tokyo) for the thin section of Y-980459, Paul Pohwat at NMNH for the Lake County labradorite sample, and Carrie Brugger-Schorr for the Quizapu pumice sample. Analytical expertise from Eric Hellebrand and Kazu Nagashima, sample preparation by JoAnn Sinton, machine work by Roy Tom, and valuable discussions with Przemek Dera, Paul Wessel, and Janet Becker are acknowledged. Tanis Leonhardi and Diamond Tachera were cheerful and excellent laboratory assistants and friends. Co-authors not affiliated with UH have also been instrumental in getting projects off the ground. Stefanie Brachfeld helped conceive the Mars work and taught me about magnetics. Philipp Ruprecht inspired the Quizapu study, as well as organized the once-in-a-lifetime experience of participating in a field campaign at Quizapu and the surrounding volcanoes. I appreciate his mentorship.

I am grateful to all of my committee members for their time and patience over the years, and for their encouragement. The field experiences that Bruce and Tom afforded me were both instructive and dream-fulfilling. Bruce's volcanology courses, and talking science and life in the field with Tom, have been highlights of my time at UH. Tom has been around through all the ups and downs of my grad school life, and I am grateful for his mentorship and friendship. Jeff's pearls of wisdom introduced me to planetary science, and his unfailingly kind and jovial nature (and appreciation for experimental work) always make me smile. His depth of knowledge about the Moon and Mars have been invaluable. John demonstrated that good teaching is found in engineering lecture halls, not just small graduate seminars, and I am grateful for his outside perspective on my research. Finally, I thank Julia for being the advisor and mentor that most students wish for but never have. Her exceptional scientific mind and aptitude for teaching are inspiring. She has taught me how to use power tools, flames, crushing pressures, and explosive gases to my advantage, and I have enjoyed our hours in the lab talking about the world and doing science together. She has always encouraged me to pursue new avenues of thought and has shown confidence in me, which is in large part why I gladly undertook the long road to a PhD.

Many other members of the Geology & Geophysics department have contributed in indirect ways to this work, and my geological education in general, including Mike Garcia, Clint Conrad, Steve Martel, Deb Eason, Rob Dunn, and Scott Rowland. I am particularly indebted to Eric Hellebrand, for his hours of microprobe expertise, his infinite patience in answering my never-ending questions, and his lessons on fine wine. I am grateful to know him. John Sinton also deserves special recognition, for sharing his vast knowledge of Hawaiian geology, and petrology in general, for taking an interest in my work, for regaling us with stories from "the good old days," for being a generous teacher and friend, and of course, for officiating at my Hawaii wedding. The administrative and support staff within G&G and SOEST have also been incredibly helpful during my time here, particularly Alison Houghton, Susan Van Gorder, Lily Shao, Leona Anthony, and Connie Tsui.

What would any grad student be without their cohort? My time here at UH has been immeasurably enhanced by my peers (or GGPeeps as we've been dubbed). From class field trip partners to officemates to beach buddies to science sisters and bunnies, I have so much to be grateful for. One person stands out of this super bunch: Maria Janebo. Moving across the world in 2011, I could never have imagined that the sweetest, smartest, most wonderful roommate and friend would be waiting for me. Deciding to share Apt. 501 together was one of the best decisions I have ever made. Penny Larin, David Trang, Sarah Crites, Sarah Glancy, Brett Walker, Carolyn Parcheta, Sam Howell, Marissa Cameron, Dana Brodie (Tree), Samantha Weaver (Isgett), Sam Mitchell, Kendra Lynn, and Val Finlayson, among others, have all kept me going and kept me sane, with their support, kindness, and goofiness over the years. Even with such a fantastic Hawaii family, I would not be here without the support of my own mom, dad, and brother. My father has been my scientific inspiration for as long as I can remember, and my mother is an absolute rock of support, with her hand-made cards and patience with late-night phone calls. My brother listens patiently and always makes me believe in myself, keeping me laughing and loved with the jokes and stories that are just for us.

And then there is Ben, my husband, partner, and ultimate supporter. My gratitude for him could fill another dissertation, with chapters on picking me up late at night, bringing me into his wonderful family, making me laugh, taking on my stress, and talking about science. I would not have gotten here without you. Thank you for being exactly who you are.

Abstract

Magmatic minerals and melts record the environmental conditions at which they equilibrate (fully or partially), via compositional and textural patterns related to time and the temperature, pressure, composition, and oxidation state of the magma. The quantification of these patterns can yield geothermometers, geobarometers, oxybarometers, and geospeedometers. These powerful petrological tools are paramount to interpreting the magmatic processes that occur in sub-volcanic plumbing systems over the life of a volcano, including shortly before eruptions, but they require extensive experimental calibration. This dissertation consists of four studies that determine system-specific indicators of magmatic processes, furthering experimental contributions to volcanology. First, experimental pyroxene textures are used as geospeedometers to derive cooling rates of the Yamato 980459 meteorite, which are consistent with eruption as a pāhoehoe flow on Mars. Second, phase equilibrium experiments on dacite from Volcán Quizapu, Chile reveal identical, tightly constrained, water-saturated storage conditions before both the 1846-7 effusive eruption and the 1932 Plinian eruption. Third, these same experiments are used to document the re-equilibration of hemoilmenite and titanomagnetite in natural melt, revealing that these minerals may not record magmatic temperature and oxygen fugacity as faithfully as previously thought. Fourth, a long-duration diffusion experiment shows that the diffusivity of Mg in labradorite is anisotropic and up to ~100 times faster than published values, likely due to the use of a natural, hydrous melt. Overall, the work herein highlights the importance of using complex, natural systems as the basis for experimental studies, to derive the most accurate quantifications of volcanic processes. The four studies presented demonstrate that the marriage of micro-scale textural and compositional parameters is a powerful means of elucidating the macro-scale magmatic history of volcanic systems.

Table of contents

Acknowledgments…….....iii

Abstract…….....v

List of tables…….....xiii

List of figures……..... xiv

List of key abbreviations and symbols…….....xvi

Chapter 1. Introduction……..1

1.1 VOLCANOLOGICAL STUDIES FROM MICRO- TO MACRO-SCALE…….....1

1.2 EXPERIMENTAL PETROLOGY FROM THE ARCHIVES……..3

1.3 STRUCTURE OF THE DISSERTATION……4

Chapter 2. Igneous cooling history of olivine-phyric shergottite Yamato 980459 constrained by dynamic crystallization experiments…….6

2.1 INTRODUCTION…….6

2.1.1 Suitability of Y-980459 for 1-atmosphere cooling experiments……8

2.2 METHODS……..10

2.2.1 Experimental methods……10

2.2.1.1 Preparatory experiments……...14

2.2.2 Electron microscopy……...16

2.2.3 Image analysis…….18

2.3. RESULTS……...19

2.3.1 Textures……...19

2.3.1.1 Descriptive……19

2.3.1.2 Surface area per unit volume measurements…….23

2.3.2 Phase compositions……24

2.4 DISCUSSION……..27

2.4.1 Controls on phase composition and mode……27

2.4.2 Interpreting population C……..30

2.4.3 Missing population B_n……31

2.4.4 Cristobalite……..32

2.4.5 Inferences from P-enrichment patterns in natural olivine…….32

2.4.6 Evaluation of experiments according to match criteria……..33

2.4.7 Comparison to previous work……...34

2.4.7.1 Application to NWA 5789……..34

2.4.8 Cooling model……..35

2.5 IMPLICATIONS……..37

2.5.1 Volcanological context……37

2.5.2 Emplacement on Mars: A typical sample of a typical flow? ……..38

Chapter 3. Experimental constraints on dacite magma storage beneath Volcán Quizapu, Chile…….40

3.1 INTRODUCTION……...40

3.1.1 Geologic background……..41

3.1.1.1 Regional setting…….41

3.1.1.2 Eruptions at Quizapu……42

3.1.2 Petrology of dacite end-member……43

3.1.2.1 Summary……43

3.1.2.2 Estimates of magma storage conditions……43

3.1.3 Aim of this contribution…….44

3.2 METHODS……..44

3.2.1 Starting materials and experimental strategy……..44

3.2.2 Attainment of equilibrium…….46

3.2.3 Electron microscopy……...49

3.2.3.1 Scanning electron microscopy……...49

3.2.3.2 Electron microprobe analyses……...49

3.3 RESULTS……....53

3.3.1 Natural materials……53

3.3.2 Experimental samples…….57

3.3.2.1 Amphibole……..58

3.3.2.2 Plagioclase…….61

3.3.2.3 Pyroxene……...…….62

3.3.2.4 Biotite…….63

3.3.2.5 Fe-Ti oxides……...63

3.3.2.6 Glass……..63

3.4 DISCUSSION……..66

3.4.1 Pre-eruptive storage conditions…….66

3.4.1.1 A brief note on some natural phases……..66

3.4.1.2 Phase assemblage……..66

3.4.1.3 Mineral compositions……69

3.4.1.3.1 Amphibole……..69

3.4.1.3.2 Plagioclase……..70

3.4.1.4 Glass compositions……70

3.4.2 Implications for thermobarometry……...72

3.4.2.1 Fe-Ti oxide equilibration……...72

3.4.2.2 Amphibole compositional variability…….74

3.4.3 Stability of hydrous phases……76

3.4.3.1 Amphibole……..76

3.4.3.2 Biotite……77

3.4.4 Reservoir geometry……78

3.4.5 Water undersaturation……...80

3.4.6 Quizapu: A typical arc dacite? ……82

3.5 IMPLICATIONS……84

3.5.1 The relevance of pre-eruptive storage conditions……84

3.5.2 Re-examining the eruptive styles at Quizapu……...86

3.6 CONCLUSIONS……91

Chapter 4. Re-equilibration of Fe-Ti oxides: Textural and compositional effects of a single-step reduction……93

4.1 INTRODUCTION……...……93

4.1.1 The appeal of Fe-Ti oxides……...……..93

4.1.2 Applications to natural samples……...…….95

4.1.3 Prior experimental work……...……96

4.1.3.1 Diffusion coefficients……...……..96

4.1.3.2 General re-equilibration……...……96

4.1.4 Objectives of this work……...……99

4.2 METHODS……...……...99

4.2.1 Starting materials……...……99

4.2.2 Experimental and analytical procedures……...……...99

4.2.3 Null hypothesis……...……...101

4.3 RESULTS……...……...101

4.3.1 Overview……...…….101

4.3.2 Hemoilmenite……...……..102

4.3.3 Titanomagnetite……...…….104

4.4 DISCUSSION……...…….105

4.4.1 Hemoilmenite re-equilibration……...…….105

4.4.2 Titanomagnetite re-equilibration……...…….107

4.5 IMPLICATIONS……...……109

Chapter 5. Mg diffusivity in labradorite at hydrous magmatic conditions……...113

5.1 INTRODUCTION……...……..113

5.1.1 Mg in plagioclase: A promising system with one big problem……..…114

5.1.2 An experimental approach with relevance to nature……....115

5.2 MATERIALS AND METHODS……...……117

5.2.1 Starting materials……...……...117

5.2.2 Experimental procedure....……..118

5.2.3 Analytical……...……119

5.2.3.1 Electron microprobe (EPMA) ……...……..119

5.2.3.2 Electron backscatter diffraction (EBSD) ……...…….120

5.2.3.3 Post-processing……...…….121

5.2.4 Computational……...……....121

5.2.4.1 One-dimensional diffusion profiles……...……...121

5.2.4.2 Three-dimensional diffusivity……...……124

5.3 RESULTS……...……...125

5.3.1 General description……...……....125

5.3.2 Diffusion modeling……...……..…..128

5.4 DISCUSSION……...…….....129

5.4.1 Part I: Computational models and assumptions……129

5.4.1.1 Comparison of model results……...129

5.4.1.2 Mg partitioning and assumption of interfacial equilibrium……131

5.4.1.3 Insights from crystal and profile irregularities……...137

5.4.1.3.1 Crack-enhanced diffusion…….137

5.4.1.3.2 Reprecipitation……..139

5.4.1.3.3 Extreme core loss……..139

5.4.2 Part II: Rapid, anisotropic diffusion……...140

5.4.2.1 Sectioning effects……141

5.4.2.2 Environmental variables……..142

5.4.2.2.1 Confining pressure……142

5.4.2.2.2 Oxygen fugacity……143

5.4.2.2.3 Hydrous melt…….144

5.4.2.3 Lattice structure……...145

5.4.3 Part III: Dissolution……..147

5.4.3.1 Low thermodynamic driving force……...149

5.4.3.2 Dependence on surface energy……151

5.4.3.3 The means to fast-path diffusion? ……...154

5.5 CONCLUSIONS……...…155

Chapter 6. Conclusions……..157

6.1 IMPACTS …….…….……...157

6.2 FUTURE DIRECTIONS……...159

6.2.1 Toward a deeper understanding of the Y-980459 flow and potential source regions…….159

6.2.2 Furthering the experimental approach at Volcán Quizapu……..160

6.2.3 In pursuit of accurate temperatures and timescales……..161

6.2.4 Advancing the utility of experimental petrology……162

Appendix A (Chapter 2)……...163

Appendix B (Chapter 3)……...228

Appendix C (Chapter 4)……...252

Appendix D (Chapter 5)……...262

References…….280

List of tables

Table 2.1 Bulk compositions of natural and experimental materials……16

Table 2.2 Experimental run information and selected results……...20

Table 3.1 Bulk composition of starting materials…….45

Table 3.2 Experimental run table……..47

Table 3.3. Average matrix glass compositions…….50

Table 5.1 Glass compositions…….117

Table 5.2 Profile orientations and model results……132

Table 5.3 D_{Mg}^{plag} predictions for An_{66} (900 °C, 125 MPa)……...141

List of figures

Figure 2.1 Backscatter electron (BSE) mosaic of Y-980459……..7
Figure 2.2 Experimental time-temperature paths…….....9
Figure 2.3 Comparison of natural and experimental sample, in BSE……...12
Figure 2.4 Olivine dendrite morphology…….....13
Figure 2.5 Phosphorous X-ray distribution maps of Y-980459 olivine…….....15
Figure 2.6 Textural summary of natural and experimental pyroxene crystals…….....22
Figure 2.7 Surface area per unit volume trends for two pyroxene populations…….....24
Figure 2.8 End-member pyroxene and olivine compositions…….....25
Figure 2.9 Al/Ti versus atomic Mg for natural and experimental pyroxene…….....26
Figure 2.10 Residual glass compositions…….....28
Figure 2.11 Cartoon of Y-980459 lava flow emplacement…….....36
Figure 3.1 Location of Volcán Quizapu……42
Figure 3.2 Transmitted light image of Quizapu lava VQ-06-06……...43
Figure 3.3 Total alkali-silica diagram of Quizapu starting materials……...53
Figure 3.4 Composition of natural Fe-Ti oxides……...54
Figure 3.5 Backscatter electron (BSE) images of Fe-Ti oxides in the starting materials…….55
Figure 3.6 Composition of amphibole in experiments and Quizapu lava…….56
Figure 3.7 BSE images of orthopyroxene in starting materials……57
Figure 3.8 BSE images of plagioclase microlites in the Quizapu lava…….58
Figure 3.9 P-T diagrams with EPMA subsets……...59
Figure 3.10 BSE images of amphibole crystals in the starting materials…….60
Figure 3.11 Plagioclase compositions in experimental run products……61
Figure 3.12 BSE images of experimentally-grown biotite……...62
Figure 3.13 Residual glass compositions for experiments at 835 °C……...64
Figure 3.14 Residual glass compositions for experiments at 125 MPa……65
Figure 3.15 Phase diagram for Quizapu dacite at water-saturated conditions…….68
Figure 3.16 Titanomagnetite compositions from experiments and starting materials……...…..73
Figure 3.17 Experimental amphibole crystal with calculated pressures……...75
Figure 3.18 Conductive cooling model of Quizapu reservoir……...79

Figure 3.19 Mole fraction H_2O in magmatic fluid…….....81
Figure 3.20 Comparison with other dacites……..83
Figure 4.1 BSE images of hemoilmenite……..98
Figure 4.2 BSE images of titanomagnetite…….100
Figure 4.3 Mg in hemoilmenite……...102
Figure 4.4 Major-element compositions…….103
Figure 4.5 Al and Mn in titanomagnetite……104
Figure 4.6 Predicted Fe-Ti oxide compositions……..108
Figure 4.7 Experimentally-produced Fe-Ti oxide compositions.....110
Figure 5.1 BSE images and pole figures of representative labradorite crystals…….125
Figure 5.2 Mg and anorthite variation……126
Figure 5.3 Major-element glass composition……..127
Figure 5.4 Histogram of rim and core values……..128
Figure 5.5 Model fits for representative labradorite crystals……..130
Figure 5.6 Variation of D_{Mg}^{plag} with orientation, in 2D…….133
Figure 5.7 Crystal h3.2 overview……136
Figure 5.8 Crystal C4.1 overview……...138
Figure 5.9 Crystal Bb.2 overview……...140
Figure 5.10 Ellipsoid fit to Model A data, in 3D……146
Figure 5.11 Equilibrium anorthite isopleths and driving forces…….148
Figure 5.12 Orientation of small D_{Mg}^{plag} vectors, in 3D……153

List of key abbreviations and symbols

Abbreviation/Symbol	Meaning
ΔG_a	Activation energy
Ab	Albite mole percent in feldspar
amph	Amphibole
α, β, γ	Angles between crystal axes
θa, θb, θc	Angles between transect and + crystal axes
An	Anorthite mole percent in feldspar
ap	Apatite
BSE	Backscatter electron (mode)
bt	Biotite
ΔG_c	Bulk free energy per mole upon crystallization
CCO	Carbon-carbon dioxide-carbon monoxide redox buffer
cr	Chrome spinel
erfc	Complementary error function
Φ	Crystal fraction (crystallinity)
DRE	Dense rock equivalent
D_{Mg}^{plag}	Diffusivity of Mg in plagioclase
EBSD	Electron backscatter diffraction
EBSP	Electron backscatter pattern
EPMA	Electron probe micro-analysis
EDS	Energy-dispersive spectroscopy
En	Enstatite mole percent in pyroxene
A_e, B_e, C_e	Experimental pyroxene populations
Fs	Ferrosilite mole percent in pyroxene
Fo	Forsterite mole percent in olivine
gl	Glass
gm	Groundmass
hm	Hematite
HT/LT	High/Low temperature series
ilm	Ilmenite
Fe-Ti ox	Iron-titanium oxide
IW	Iron-wüstite redox buffer

Mg#	Magnesium number
mt	Magnetite
m.i.	Melt inclusion
C_{Mg}^{x}	Mg concentration in plagioclase at x
δ	Misfit
V_m	Molar volume
X_{H2O}^{fluid}	Mole fraction of water in fluid
A_n, C_n	Natural pyroxene populations
NNO	Nickel-nickel oxide redox buffer
ol	Olivine
Y-980459	Olivine-phyric shergottite Yamato 980459
Or	Orthoclase mole percent in feldspar
opx	Orthopyroxene
fO_2	Oxygen fugacity
plag	Plagioclase
$K_{Mg}^{plag/liq}$	Plagioclase-melt Mg partition coefficient
RSD	Relative standard deviation
SEM	Scanning electron microscope
σ	Standard deviation *or* surface energy
sf	Sulfide
+ΔT	Superheating
$\mathbf{S}_v^P$	Surface area per unit volume
Y98*	Synthetic Y-980459 materials
N_L	Test line length
P_{total}	Total pressure
usp	Ulvöspinel
-ΔT	Undercooling
v	Vector direction
η	Viscosity
vol%	Volume percent
P_{H2O}	Water pressure
WDS	Wavelength-dispersive spectroscopy
wt%	Weight percent
Wo	Wollastonite mole percent in pyroxene

Chapter 1. Introduction

1.1 VOLCANOLOGICAL STUDIES FROM MICRO- TO MACRO-SCALE

The desire to decipher the mechanisms of volcanic eruptions and the magmatic processes associated with them stems from the societal benefit of that very understanding, as well as from a scientific curiosity. The task is complex, bringing together macro-scale observations of eruptions and volcanic deposits with micro-scale investigations of crystal, bubble, and melt populations. Processes of phase nucleation, growth, and diffusion, already complex in simple systems, must be quantified in natural magmas, and further, linked to observed and inferred eruptive behavior and sub-volcanic storage.

On a macro scale, it is possible to estimate or even measure directly the rates of some volcanic processes. For instance, the height of an eruption column scales with mass eruption rate (Sparks 1986; Wilson et al. 1978); the velocity of ballistic ejecta can be determined through high-speed imaging (Taddeucci et al. 2012); the inflation rate of pāhoehoe sheet flows can be measured directly, or by analyzing time-lapse footage (Hoblitt et al. 2012; Hon et al. 1993; Orr and Hoblitt 2008); the cooling rate of a lava flow can be measured at distance via infrared spectroscopy or thermal cameras (e.g., Coppola et al. 2007; Flynn and Mouginis-Mark 1992; Harris et al. 2007); even the rate of magma influx to a subvolcanic reservoir can be estimated almost as it occurs, by modeling geodetic data (e.g., Dvorak and Dzurisin 1997; Lu et al. 2005). But once an eruption is over, scientists are forced to reconstruct a dynamic, often prolonged event, with nothing but a frozen record of the end result. At that point, some macro-scale information is lost for good. Fall deposits can provide excellent insight into large-scale dynamics of explosive eruptions (Mastin et al. 2009; Pyle 1989), but only to the extent that deposits are accessible (e.g., not deeply buried, or fallen over the ocean, etc.). For effusive eruptions, later lava flows or lobes bury earlier ones, levees are formed and destroyed, and inflation blurs stratigraphic distinctions, making temporal reconstruction of events difficult. In any volcanic system, no substitute for real-time geophysical data has been found in post-eruption records. Magmatic processes that occur beyond the realm of sub-volcanic plumbing systems, in the deeper crust and mantle, are less accessible still.

Our understanding of magmatism and volcanism on planetary bodies is even more limited, because igneous processes are not only distant in time, but in space as well. A few

hundred kilograms of rocks from a tiny fraction of the lunar nearside represent the only planetary materials in human possession that were collected in situ, preserving spatial information (Lunar Sample Preliminary Examination Team 1 1969). Robotically acquired chemical analyses from multiple sites on Mars (e.g., Bish et al. 2013; McSween et al. 2006), complemented by the associated photographs and location data, are good resources given that sample return is not yet possible. Meteorites from Mars (McSween 2002), the Moon (Korotev 2005), asteroids such as Vesta (Ruzicka et al. 1997), and other parent bodies offer glimpses into the micro-scale features of the extraterrestrial settings from which they formed. Meteorites are an invaluable starting point and basis of comparison for laboratory research (e.g., Filiberto et al. 2010; McCoy and Lofgren 1999; Musselwhite et al. 2006). Remote sensing and high-resolution imagery provide insights about composition, mineralogy, planetary dynamics, and surface morphology over broad swaths of extraterrestrial bodies, and sometimes on the scale of meters (Keszthelyi et al. 2008; Lucey et al. 1995; Moore et al. 2016; Simons et al. 1997). These combined datasets have yielded estimates of the thickness of the lunar crust (Wieczorek et al. 2013), maps of the crustal dichotomy between the southern highlands and northern lowlands on Mars (Watters et al. 2007), evidence of tectonism and volcanism on Jovian satellites (Hoppa et al. 1999; McEwen et al. 1998), and many other extraterrestrial insights.

Whether studying planetary datasets or single eruptive deposits on Earth, the limitations of large-scale observations force scientists to pick up a magnifying glass, attempting to link the micro-scale world of bubbles and crystals to the macro-scale processes that created and modified them. Experimental studies are essential to establishing the relationships between various magmatic processes and their manifestations in erupted products. The ability of experiments to provide snapshots (petrology) or live records (analog) of dynamic processes at known pressures, temperatures, and system sizes and compositions, is the key to forging that link. The realm of these experiments ranges from scaled analog experiments of conduit processes and plume dynamics (e.g., Del Bello et al. 2015; Mader et al. 1997; Seyfried and Freundt 2000) to laser-simulated space weathering (e.g., Gillis-Davis et al. 2017; Yamada et al. 1999), to small-scale melting and crystallization of natural magmatic compositions in the laboratory (e.g., Hammer 2008; Rutherford et al. 1985; Walker et al. 1978). Findings from these types of experimental studies forge the macro-micro links required, for example, to interpret pumice textures in terms of conduit dynamics and eruption style; to give mineralogical meaning to spectral signatures of

planetary surfaces; and to derive magmatic environmental conditions, and changes thereof, from erupted mineral compositions and textures. The following section highlights the importance of experimental petrology in accessing systems otherwise out of reach (e.g., magmatic storage deep in the Earth; igneous processes on planetary bodies).

1.2 EXPERIMENTAL PETROLOGY FROM THE ARCHIVES

The groundbreaking work of Bowen (e.g., 1928) gave us not only the well-known plagioclase phase diagram, but laid the groundwork for our understanding of magmatic fractionation in general. The following decades saw equilibrium experimental work continue on simple mineral systems and natural silicic melts (e.g., Bowen and Tuttle 1949; Roy and Tuttle 1956), laying the scientific and technological groundwork for the volcanological phase equilibrium studies of today. The seminal experiments of Yoder and Tilley (1962) on mafic material yielded the basalt tetrahedron as a tool for interpreting basalts and their fractionation products. In the following decades, led by James Kirkpatrick, Colin Donaldson, and Gary Lofgren, among others, experimentalists heated and cooled mafic magmas and simple systems to explore crystal growth and nucleation, including the effects of superheating ($+\Delta T$), undercooling ($-\Delta T$), oxygen fugacity (fO_2), and cooling rate on phase appearance order, nucleation density, and crystal morphology and composition (e.g., Donaldson 1976, 1979; Donaldson et al. 1975; Gibb 1974; Kirkpatrick 1974; Kirkpatrick et al. 1979; Lofgren 1980, 1983; Usselman and Lofgren 1976; Walker et al. 1978). Adding to the growing body of experimental work, theoretical treatments of nucleation and growth were taken from materials science and applied to geological systems (Dowty 1980; Kirkpatrick 1975, 1981). Recent decades have seen the continuation of dynamic crystallization experiments, increasingly applied to extraterrestrial samples (e.g., McCoy and Lofgren 1999; Radomsky and Hewins 1990); experimental quantification of texture-kinetics relationships for olivine, plagioclase, amphibole, and other minerals (e.g., Brugger and Hammer 2010; Faure et al. 2003; Rutherford and Hill 1993); development of experimentally-calibrated geothermometers and barometers (e.g., Ghiorso and Sack 1995; Johnson and Rutherford 1989; Putirka et al. 1996; Waters and Lange 2015); and, led by the work of Malcolm Rutherford and colleagues, experimental phase equilibrium constraints on pre-eruptive magmatic storage conditions at intermediate volcanoes around the world (e.g., Hammer and Rutherford 2002; Rutherford et al. 1985; Scaillet and Evans 1999).

1.3 STRUCTURE OF THE DISSERTATION

The studies presented here are possible thanks to the decades of pioneering experimental work described above. The fundamental concepts of crystal nucleation, growth, and equilibration are used to root discussions in each of the dissertation projects outlined below, in which experimental petrology is applied to a variety of volcanic situations. Emphasis is placed on how the kinetics of mineral growth, destabilization, and diffusion controls the experimental outcomes.

The dissertation consists of six chapters: this introduction, four research projects (Chapters 2 through 5), and a concluding section. Chapter 2 tackles a planetary topic, describing how dynamic crystallization experiments over a range of cooling rates reproduce the mineral textures and compositions of a martian basalt, specifically the primitive olivine-phyric shergottite Yamato 980459. Residual glass compositions and quantitative textural parameters of different pyroxene populations vary consistently with cooling rate, allowing estimation of the pre- and syn-eruptive cooling rates of this particular lava on Mars. Findings are compared to terrestrial analogs and remote sensing observations, to draw conclusions about the eruption processes that created the rock. This chapter is published in *Meteoritics and Planetary Science*.

Chapters 3-5 are based in the terrestrial realm of intermediate arc volcanoes. Chapter 3 is an investigation of the pre-eruptive magmatic storage conditions at Volcán Quizapu, Chile. Beginning with natural materials from the volcano, static, water-saturated experiments were performed from 810-900 °C and 35-200 MPa. Resultant textures and phase compositions were compared to those of the starting materials. The key components that constrain the storage conditions are residual glass composition, plagioclase composition, and stability of the hydrous phases amphibole and biotite. Based on these parameters, the Quizapu dacite magma equilibrated at ~850 °C and ~125 MPa water pressure prior to eruption, although the magma could have been water undersaturated, with a maximum P_{total} ~190 MPa.

The Fe-Ti oxide minerals from these experiments record a step-wise reduction in fO_2 between the equilibrium state of the starting materials and the experimental conditions, providing material for an offshoot chapter discussing the Fe-Ti oxide re-equilibration process. This Chapter (4) discusses the variety of disequilibrium textures and compositions of hemoilmenite and titanomagnetite, along with the implications for Fe-Ti oxide thermometry and oxybarometry. It appears that the re-equilibration process is not linear, and that Fe-Ti oxide compositions may

change quickly in response to environmental changes, but that those compositions may not represent the equilibrium compositions for the new environment.

Chapter 5 focuses on an indicator of magmatic timescales – diffusion of Mg in plagioclase. This system abounds in arc volcanic systems and is gaining traction as a means of estimating timescales of magma interaction. Previous studies have not used natural magmatic conditions to determine the diffusivity of Mg in plagioclase, so this work tackles an experiment using plagioclase crystals in a natural, water-saturated melt at sub-volcanic temperature and pressure. The findings are complicated, revealing anisotropic Mg diffusivities that are 100+ times higher than any previously reported. Possible causes for the results include the presence of water, low-Mg natural melt, and dissolution-enhanced diffusion. The dissertation is concluded with a recap of the findings and implications of each project.

Chapter 2. Igneous cooling history of olivine-phyric shergottite Yamato 980459 constrained by dynamic crystallization experiments

Published as:

First, E. & Hammer, J. (2016). Igneous cooling history of olivine-phyric shergottite Yamato 980459 constrained by dynamic crystallization experiments. *Meteoritics & Planetary Science* **51**, 1233–1255.

Abstract - Dynamic crystallization experiments were performed on a liquid having the bulk composition of olivine-phyric shergottite Yamato 980459, to constrain the igneous thermal history of this meteorite. Key characteristics of the meteorite's mineralogy and texture, including several morphologically distinct olivine and pyroxene crystal populations and a glassy mesostasis devoid of plagioclase, were replicated upon cooling from 1435 to 909 °C at 1 atmosphere under reducing conditions. Three sequential cooling ramps are required to produce synthetic samples with textures and compositions matching Yamato 980459. Olivine phenocrysts formed at < 1 °C h^{-1}, presumably at depth in the martian crust. Pyroxene phenocrysts formed mainly at ~10 °C h^{-1}, consistent with crystallization within a lava flow at depths of 25-45 cm. Increased cooling rate (~100 °C h^{-1}) in a third stage suppressed formation of plagioclase and produced groundmass crystals, consistent with crystallization at lava flow depths of 5-7 cm. Although Y-980459 is unique among martian meteorites (i.e., preserving a primary glassy mesostasis), its emplacement did not require unique physical conditions. Rather, the second and third cooling stages may reflect cooling within the core of a pāhoehoe-like flow and subsequent breakout on the surface of Mars.

2.1 INTRODUCTION

The thermal history of a volcanic rock is closely linked with its emplacement mechanism on a planet's surface. For example, explosively erupted pyroclasts cool through the solidus about a million times faster than do lava lake interiors (Wright and Okamura 1977; Lloyd et al. 2013). Constraining the igneous cooling rates of martian meteorites is thus important to the interpretation of volcanic processes on Mars. Cooling rates of igneous rocks are estimated by a

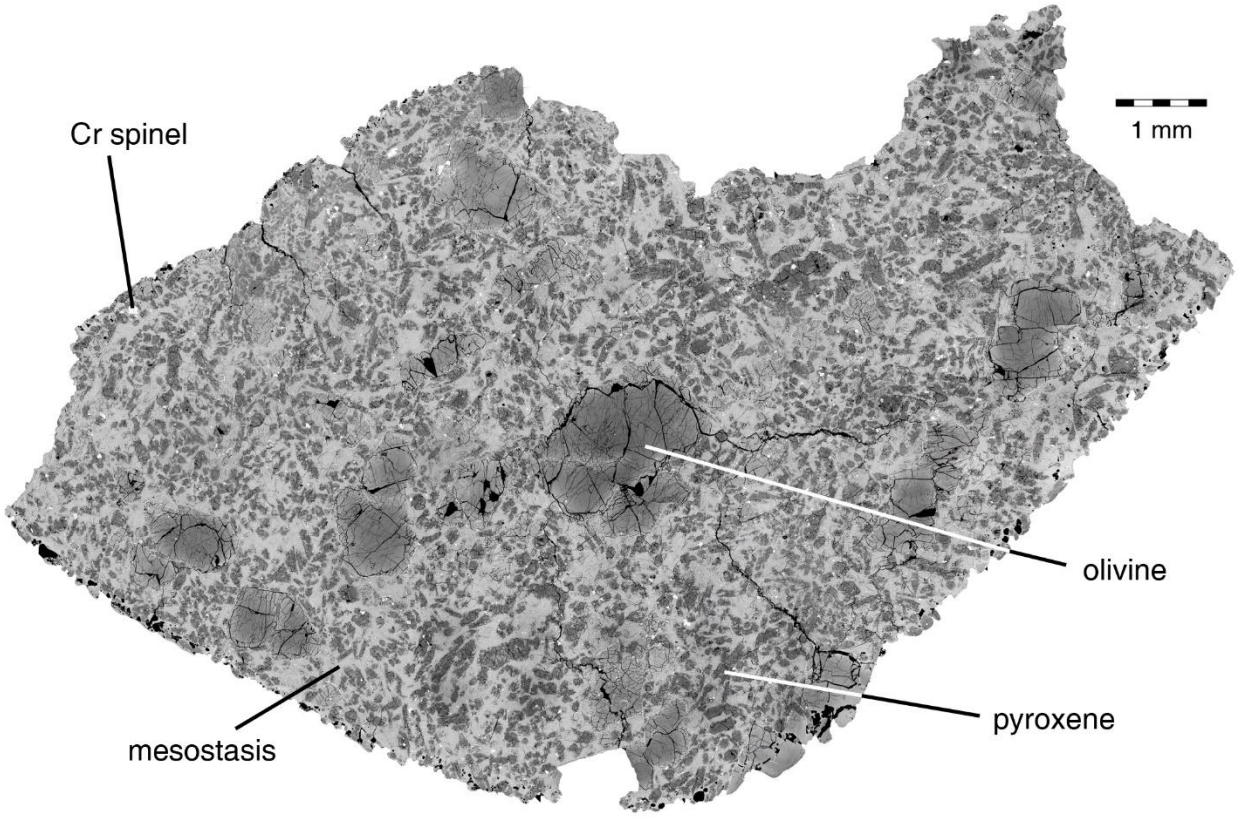

Figure 2.1. BSE mosaic image of Y-980459 thin section with key phases labeled. The light grey mesostasis hosts olivine and pyroxene dendrites and sulfide droplets, most of which are not visible at this magnification.

variety of means, both qualitative and quantitative, the most robust of which rely on experimentally calibrated data linking petrographic observables with known thermal history. Extant approaches are based on crystal morphology alone (e.g., Faure et al. 2003, 2007), crystal composition (e.g., Mollo et al. 2010), crystal composition and qualitative sample and crystal texture (e.g., McCoy and Lofgren 1999), quantitative crystal texture (e.g., Lentz and McSween 2005; Hammer 2009), and chemical diffusion rates (e.g., Miyamoto et al. 1986, 2009b). Estimations of cooling rate by comparison to experimental results from studies on unrelated materials are also common (e.g., McCoy et al. 1992 referencing Walker et al. 1978; Treiman and Sutton 1992 referencing Lofgren et al. 1974). Uncertainties are amplified when relevant experimental datasets (e.g., using similar whole rock compositions) are not available. Thus, experimental studies on specific compositions are necessary to interpret igneous cooling rates accurately.

The olivine-phyric shergottite Yamato 980459 (Y-980459; Figure 2.1) is proposed to have erupted as a thin lava flow (e.g., Greshake et al. 2004; Usui et al. 2008), based on the high cooling rates implied by its vitrophyric matrix. The range is quantified by Greshake et al. (2004) at 1450-1890 °C h^{-1} using textural comparisons with experimental studies on various bulk compositions (Donaldson 1976; Faure et al. 2003). Other studies consider crystal populations separately, arriving at cooling rates tailored to specific domains within the sample. For example, cooling rate estimates for phenocryst phases in Y-980459 range from 0.03 - 5 °C h^{-1} for olivine phenocrysts (Greshake et al. 2004; Mikouchi et al. 2004; Miyamoto et al. 2009a) and from 3 - 7 °C h^{-1} for pyroxene phenocrysts (Lentz and McSween 2005).

We performed dynamic crystallization experiments using the Y-980459 bulk composition as a starting material to evaluate critically whether these suggested cooling rates produce the crystal textures and compositional variations in the meteorite. Experimental time-temperature paths (Figure 2.2) were assessed for applicability to Y-980459 using a tiered set of match criteria, in order from most to least stringent: (1) phase assemblage (2) modal proportions (3) phenocryst texture (4) phase compositions (5) groundmass crystal texture. Olivine morphology, quantitative textural analyses of pyroxene populations, and compositional analysis of glass and crystalline phases guided our determination of cooling rates. We then compared these estimates to a lava flow cooling model to constrain the depth within a flow at which Y-980459 cooled.

2.1.1 Suitability of Y-980459 for 1-atmosphere cooling experiments

The whole rock composition, mineralogical, and textural characteristics of Y-980459 make it exceptionally well-suited for cooling rate evaluation via dynamic crystallization experiments. It lacks plagioclase/maskelynite and retains a primary glassy mesostasis, indicating final quenching on the surface of Mars. The bulk composition of Y-980459 is that of a magmatic liquid (Greshake et al. 2004; Ikeda 2004; Mikouchi et al. 2004; Musselwhite et al. 2006; Usui et al. 2008; Filiberto and Dasgupta 2011), obviating the need to calculate a liquid starting composition. Furthermore, constraints on the oxygen fugacity (fO_2) of the Y-980459 source are provided by valence-state dependent partitioning of vanadium between olivine phenocrysts and melt (Shearer et al. 2006). It is possible for fO_2 to change during transit to and on the surface of Mars, but such a shift would have profound effects on the mineralogy of the meteorite. For example, at significantly more oxidizing conditions, Fe-Ti oxides containing Fe^{3+} would appear

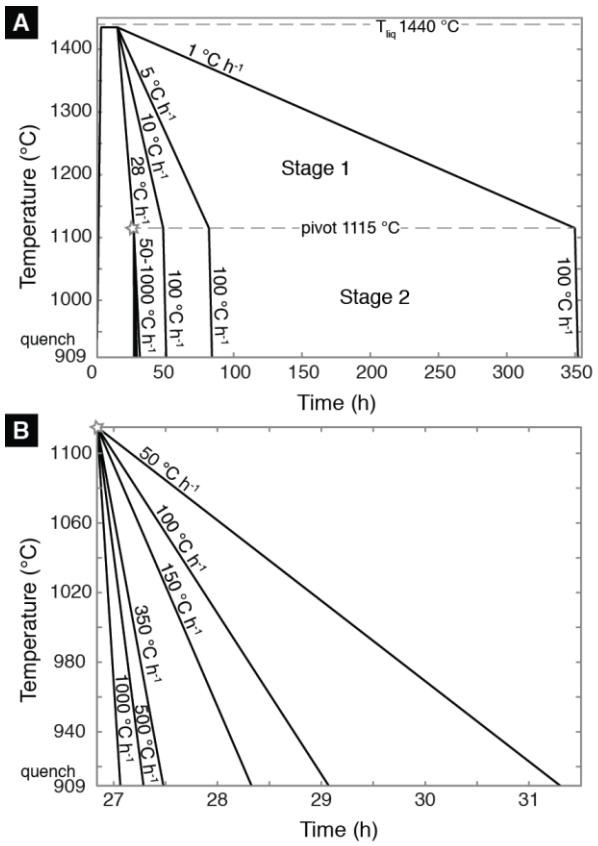

Figure 2.2. Time-temperature paths for experiments listed in Table 2. (A) Full experimental paths, emphasizing the HT series (Stage 2 = 100 °C h^{-1}). (B) Enlargement, beginning at starred pivot point in (A), showing Stage 2 paths for the LT series (Stage 1 = 28 °C h^{-1}). The 28, 100 °C h^{-1} path is part of both series. See Table 2 for experiment names and details.

(e.g., Hammer 2006; Balta et al. 2013) and at significantly more reducing conditions, Fe metal would become stable. Neither titanomagnetite, metal blebs, nor reaction textures consistent with destabilization of primary silicate phases are present in Y-980459. Lacking direct evidence that fO_2 changed in the magma during transit to the martian surface, for our experiments we adopt the ambient oxygen concentration corresponding to one log unit above the iron-wüstite redox buffer (IW+1) from Shearer et al. (2006).

The phase assemblage of the meteorite is relatively simple and well-documented (Greshake et al. 2004; Ikeda 2004; Mikouchi et al. 2004; Usui et al. 2008), providing a robust set of metrics for evaluating experimental run products: Nine to 26 vol% of the meteorite consists of normally zoned olivine mega-phenocrysts with cores up to $Fo_{85,}$ as well as smaller, more Fe-rich olivine phenocrysts (Figure 2.1, Figure 2.3A). Prismatic pyroxene phenocrysts (48-58 vol%) are composed of low-Ca pyroxene rimmed by high-Ca pyroxene (Figure 2.1, Figure 2.3A). The

glassy mesostasis (23-37 vol%) contains olivine dendrites (Figure 2.4A, Figure 2.4C), with feathery and baby swallowtail morphologies (Donaldson 1976; Faure et al. 2003), and chain-like pyroxene. Minor phases include chromium-rich spinel grains, generally euhedral in shape, which occur both as inclusions in phenocrysts and in the groundmass glass. Sulfide (Fe, S, Ni) droplets are present in the mesostasis. Lamellar phosphorus enrichments in Y-980459 olivine crystals are reported by Shearer et al. (2013) and in this study (Figure 2.5). Similar P enrichment patterns are recognized in an increasingly diverse set of olivine formation environments (e.g., Milman-Barris et al. 2008; Welsch et al. 2014; McCanta et al. 2016). The enrichments are spatially uncorrelated with major element compositional heterogeneity and have implications for initial crystal growth rate, as discussed below.

Phase equilibrium experiments performed at elevated pressure indicate that olivine is the liquidus phase of the Y-980459 composition up to 1.2-1.4 GPa (Musselwhite et al. 2006; Blinova and Herd 2009). The melt is multisaturated with olivine and low-Ca pyroxene at that pressure, suggesting this is the pressure at which Y-980459 melt equilibrated with a mantle mineral assemblage (Musselwhite et al. 2006; Blinova and Herd 2009). Furthermore, experimental olivine formed at ~1.2 GPa has a composition matching the most magnesian olivine (Fo_{84}-Fo_{86}) in the meteorite (Musselwhite et al. 2006), and thermobarometry (Lessel and Putirka 2015) supports the experimental results. The nominally anhydrous character of the shergottites in general, and Y-980459 in particular (e.g., Usui et al. 2012), has the consequence of imparting relative insensitivity of pressure to the magmatic phase relations. This factor, coupled with the ability to control fO_2 finely and maximize sample size, justify our 1-atmosphere investigation of crystallization dynamics in response to temperature change. With the understanding that absolute values of temperature scale upward with increasing pressure on the order of 20 °C per 100 MPa for a Y-980459 composition (Ghiorso and Sack 1995), the capability of our experiments to emulate crystallization processes occurring at depth in the martian crust or mantle is supported by similarities in the phase appearance sequence and in mineral compositions, as detailed herein.

2.2 METHODS

2.2.1 Experimental methods

Synthetic basalt with the composition of Y-980459 whole rock, hereafter termed Y98*, was created based on an S-free average of two published bulk analyses (Misawa 2003; Greshake et al. 2004; Table 2.1). Practical impediments to working with S include difficulty maintaining

fS_2, corrosion of the gas line supplying the furnace, and loss of S from the sample to holder materials. Given that S is a trace or minor element in this bulk composition (0.07-0.165 wt%; Table 2.1), its exclusion is unlikely to affect the phase assemblage (beyond the presence of a sulfide late in the crystallization sequence), silicate crystal morphologies, or liquid composition. Powdered oxide, carbonate, and phosphate reagents (SiO_2, TiO_2, Al_2O_3, Fe_2O_3, MgO, Cr_2O_3, NiO, $CaCO_3$, Na_2CO_3, K_2CO_3, $MnCO_3$, $CaHPO_4$) were hand ground under ethanol for 5 h. The resulting homogeneous mixture was conditioned for ≥ 6 h at 925 °C under a flowing H_2-CO_2 gas mixture. These gases imposed an fO_2 approximately one log unit above the iron-wüstite redox buffer (IW+1), corresponding to formation conditions inferred for Y-980459 (Shearer et al. 2006). This conditioning drove off carbon and imparted the appropriate ferric-ferrous ratio. Charges were prepared by mixing the conditioned starting material with a polyvinyl alcohol solution to form a bead, inserting an Fe-Pt wire loop, and drying the prepared beads in a 50-60 °C oven for ≥ 30 min.

The Pt wire loop method (Presnall and Brenner 1974; Donaldson et al. 1975) limits Fe loss from silicate melt to Pt container by minimizing the amount of Pt in contact with the sample. However, reducing conditions exacerbate Fe loss by stabilizing a greater mole fraction of Fe in the resulting FePt alloy (e.g., Kessel et al. 2001). Because our experiments were all run at reducing conditions (corresponding to the IW+1 buffer), we used Fe-alloyed Pt wire loops. Each 2-4 mm diameter Pt wire loop was pre-saturated with Fe by electroplating and annealing (Grove 1981). Electroplating was conducted in a 23-25 °C bath of 25 g $FeSO_4 \cdot 7H_2O$ dissolved in 100 mL tap water, with high-purity Fe foil serving as the anode (Figure S1). With currents of 45-50 mA, sufficient coating (approximately 20 wt% Fe pre-annealing) was achieved in 8-11 minutes per wire. Wires were then annealed in the gas mixing furnace at an fO_2 below the IW buffer for ≥ 3 h at 1500 °C, in order to ensure alloying of Fe and Pt metal. Post-annealing wire compositions of ~17-18 wt% Fe substantially reduced iron loss to the container, as evaluated by comparing the glasses fused on Pt and various FePt wires using energy dispersive spectrometry (EDS).

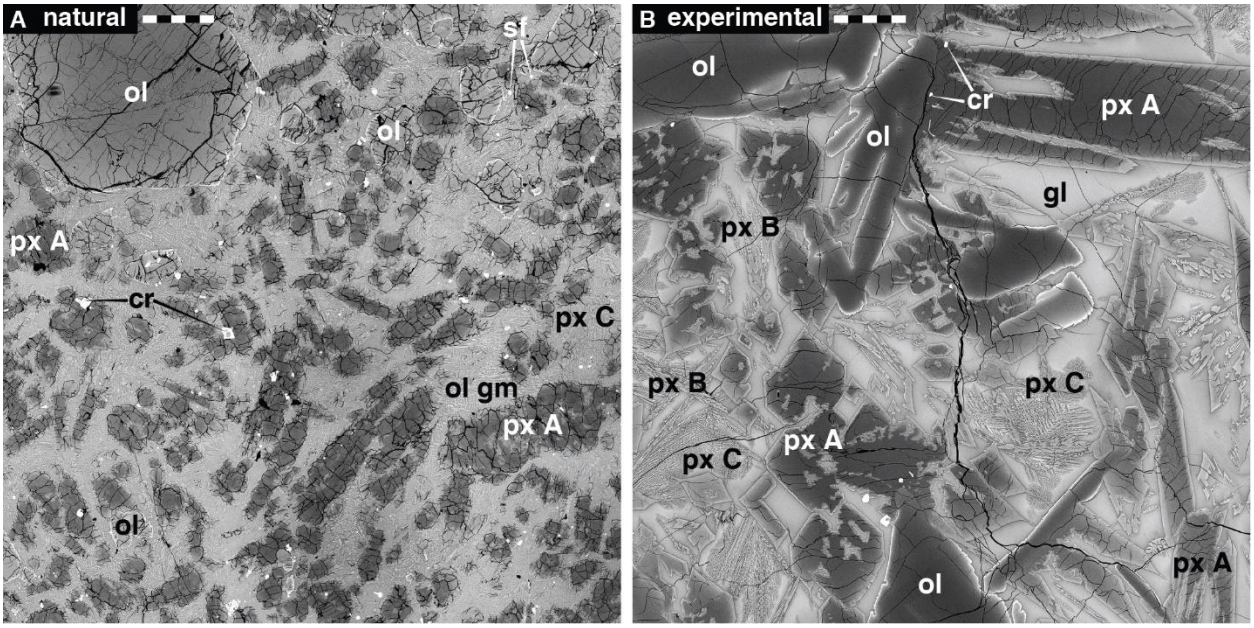

Figure 2.3. BSE 100x comparison of (A) meteorite and (B) experiment Y98*-f65. Scale bars are 250 μm. ol=olivine, ol gm=groundmass with olivine dendrites and glass, px A/B/C=pyroxene population A/B/C, cr=Cr-rich spinel, sf=sulfide, gl=glass.

Dynamic cooling experiments were conducted at atmospheric pressure in a DelTech gas mixing furnace at the University of Hawai‘i at Mānoa (UHM), using flowing H_2 and CO_2 gases to control the sample environment (Figure S2). Total linear gas flow rate was ~0.1 cm/s, consistent with methods in the experimental literature (e.g., O’Neill et al. 2003), and kept low to minimize loss of volatile elements Na and P from melt. Loss of Na was evaluated through quantitative analysis of matrix glass in experimental charges. P-loss was not quantified, but was evidently not so extreme as to prevent uptake in rapidly-grown olivine (Figure S3). Time-temperature paths were set with a programmable Eurotherm controller. The removable experimental apparatus (Figure S4) consisted of a double-bore alumina tube (“sample tube”) run through with two ~1 mm diameter Pt wires (“quench wires”). Adjacent to the sample tube was a zirconia-based SIRO2 C700+ solid electrolyte oxygen sensor (error ±0.02 to ±0.04 log units of pO_2 according to the manufacturer, Ceramic Oxide Fabricators), calibrated to the IW buffer, wrapped with an external Pt sensor wire. A four-bore alumina tube, inside the sensor tube, housed the Pt electrode and wire and a Pt-Rh S-type thermocouple (error ±2.3 to ±3.6 °C according to the manufacturer, Omega Engineering). The internal four-bore tube also provided the conduit for a regulated flow of pure air to ensure known oxygen concentration at the reference electrode. One or two half-inch SALI-type alumina fiber baffles just smaller than the

inner diameter of the furnace surrounded the sample and sensor tubes roughly one third of the way up the apparatus. These baffles served to ensure complete and timely mixing of the gases. Late in our study, the apparatus was modified to include a third, thinner quench wire to allow for two separate quenches per run (Figure S4).

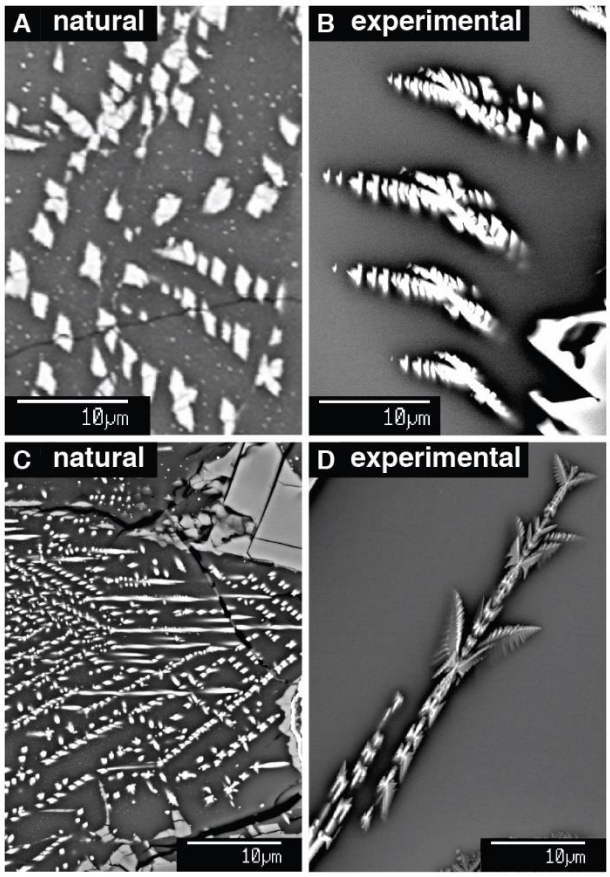

Figure 2.4. BSE images of olivine dendrites. (A) and (C) Y-980459; (B) experiment Y98*-f65; (D) experiment Y98*-f67. Note the morphological similarities between (A) and (B), (C) and (D). All images show dendritic crystals intersecting the section plane multiple times.

Wire loop experiments were conducted as either single- or multi-bead runs, often employing a Pt wire "chandelier" for up to four beads (Figure S4). The apparatus was inserted into the furnace at a hot-spot temperature of 938 °C, over approximately 6 min, to reduce the probability of thermal cracking of the sensor tube. A ramp rate of 3 °C min^{-1} was used to reach the desired starting temperature of the experiment. Oxygen fugacity was maintained at IW+1 ±0.1 log_{10} units over the course of each experiment. Larger excursions occurred for brief (< 1

min) periods. Below ~1050 °C, inefficient gas mixing caused some longer excursions in the reducing direction, mitigated by manually decreasing H_2 gas flow.

Samples were quenched into 100-200 mL of water by melting the quench wires with electric current (e.g., Edgar 1973). Because the water flask was attached to the furnace tube by a gas-tight seal (Figure S5), a closed system was maintained throughout the quench. Quench crystals were not observed in any charges. For double quench experiments, we quenched one sample earlier in the run and another at the end, obtaining a snapshot at an intermediate time point.

2.2.1.1 Preparatory experiments

More than fifty experiments were conducted to explore relevant experimental parameter space in reconnaissance fashion (Table S1). These runs, summarized below, helped to bracket mineral-in temperatures, establish pre-cooling dwell conditions, evaluate the use of one versus two cooling rates, determine cooling rates necessary for plagioclase suppression, and select the experimental quench temperature. Many of these early experiments used pure Pt wire and lost Fe from the sample to the wire. Although the compositions of olivine and pyroxene were likely affected, the plagioclase appearance temperature and the rates of crystal nucleation and growth are considered less sensitive. Beads suspended from Pt and FePt wires run with an identical two stage time-temperature path produced the same phase assemblage and texture (Figure S6).

Through a series of eight isothermal runs of ≥ 6 h each, the Y98* liquidus temperature was determined as 1440 ± 2 °C, with olivine as the liquidus phase. Two additional isothermal experiments bracketed the equilibrium plagioclase-in temperature between 1120 °C and 1133 °C (Figure S7). Super-liquidus treatments, intended to homogenize the starting material, resulted in unnatural textures upon cooling (single pyroxene crystal branching across the entire charge, Figure S8). Since the physical relevance of superheating is inferred to be minimal (e.g., Lofgren 1980; Hort et al. 1999), and the textures were markedly different from the material we wished to replicate, a pre-cooling dwell temperature of ~5 °C below the liquidus was implemented. Dwell periods of 12 and 24 h produced negligibly different outcomes (Figure S9), and the shorter time was adopted for subsequent runs. Single-rate cooling experiments, in which temperature was decreased from near the liquidus to 900-1000 °C at rates of 36, 72, and 320 °C h^{-1} failed to produce groundmass pyroxene, or produced barred pyroxene, or both (Figure S10). Single

constant-rate cooling was therefore unable to reproduce a key feature of Y-980459: at least two generations of morphologically distinct pyroxene crystals (as detailed below).

Two-stage cooling, utilizing two constant-rate cooling ramps changed at a pivot temperature, was explored next. A pivot temperature of 1115 °C, or 5 °C below the lower bracketing value for the equilibrium plagioclase-in temperature, was selected to separate the higher-temperature Stage 1 cooling from the lower-temperature Stage 2 cooling. This choice ensured that formation of feldspar was thermodynamically favored during the entire second stage of all experiments, and permitted evaluation of cooling-rate control on plagioclase nucleation behavior. A minimum Stage 2 cooling rate of 50 °C h^{-1} was adopted after observing plagioclase appearing in all runs at 36 °C h^{-1} and sporadically in runs with stage 2 cooling at 72 °C h^{-1}. Otherwise identical experiments quenched at 909 °C and 859 °C preserved no observable difference in texture (Figure S11); all subsequent experiments were quenched at 909 °C.

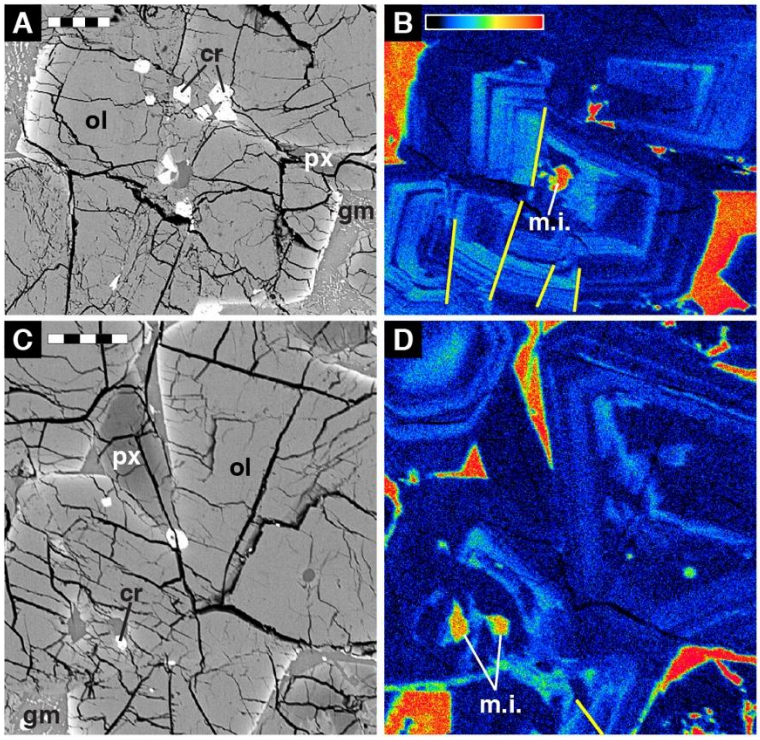

Figure 2.5. BSE images and phosphorus X-ray distribution maps from two smaller Y-980459 olivine crystals. (A) BSE image of crystal ol5; scale bar is 50 μm. (B) Phosphorus X-ray map of crystal ol5; scale as in (A); on qualitative color scale, red is high and blue is low. Yellow lines highlight offsets in phosphorus zoning attributed to cracks visible in BSE. We interpret these cracks to have formed post-crystallization as the result of shock. (C) BSE image of crystal ol8; scale bar is 50 μm. (D) Phosphorus X-ray map of crystal ol8; scale as in (C); color scale and yellow lines as in (B). ol=olivine, px=pyroxene, cr=Cr-rich spinel, gm=groundmass, m.i.=melt inclusion.

2.2.2 Electron microscopy

Every experimental charge was examined in backscattered electron (BSE) mode using the JEOL 5900 LV scanning electron microscope (SEM) in the W. M. Keck Cosmochemistry lab at UHM. Analytical conditions were 15 kV accelerating voltage and 12 mm working distance. For most runs, images at 100x magnification were collected over the entire charge and later stitched together to form a composite image of the bead. Additional images at higher magnification were taken at points of interest, and electron-dispersive spectrometry (EDS) was used to confirm phase identities.

Table 2.1. Bulk compositions in oxide wt%, *modified from Brachfeld et al. (2015)*.

	Y98* bulk	Y-980459 bulk		NWA 5789 bulk	
	Experimental glass[a]	Greshake et al. (2004)	Misawa (2004)[c]	Gross et al. (2010)	Irving et al. (2010)
SiO_2	49.84	49.4	48.70	49.24	48.57
TiO_2	0.58	0.48	0.54	0.48	0.45
Al_2O_3	5.92	6.0	5.27	5.65	5.33
Cr_2O_3	0.67	0.71	0.71	0.46	0.73
FeO	17.85[b]	15.8	17.53	16.61	17.56
MnO	0.47	0.43	0.52	0.47	0.45
MgO	18.34	18.1	19.64	17.74	19.15
NiO	n.a.	0.03	0.034	0.03	0.0267
CaO	6.69	7.2	6.37	6.48	6.53
Na_2O	0.14	0.80	0.48	0.43	0.69
K_2O	0.01	0.02	<0.02	0.02	0.02
P_2O_5	b.d	0.31	0.29	0.38	0.34
S	-	0.07	0.09	n.a.	n.a.
total	100.51	99.35	100.17	97.99	99.85

[a] Synthetic Y-98* composition determined from the average of five electron microprobe analyses of a glass bead (f46i, Table S1). Low concentrations of alkali oxides and P_2O_5 are attributed to volatilization during fusion.

[b] Y-98* FeO value is an interpolation based on an FePt wire composition of 20% Fe, pre-annealing.

[c] Published wt% Ni and wt% FeS have been converted to wt% NiO and wt% S, with appropriate adjustment to wt% FeO.

n.a.=not analyzed, b.d.=below detection limit

Experimental and natural phases were analyzed quantitatively using the JEOL Hyperprobe JXA-8500F electron microprobe at UHM, using Probe for EPMA software for all data output (e.g., Armstrong 1988; Donovan and Tingle 1996). Glass was analyzed over three sessions, with wavelength-dispersive spectrometry (WDS) spot analyses of Si (40-50 s on-peak counting time), Ti (30-50 s), Al (50-60 s), Cr (30-50 s), Fe (30 s), Mn (20-30 s), Mg (50 s), Ca (30 s), Ni (50 s, measured during one session only), Na (30 s, measured first), K (30-40 s), and P (30-50 s). High and low off-peak counting times were each half of on-peak times. For glass, an accelerating voltage of 15 kV and a beam current of 10 nA were used. The beam diameter was 10 μm, or ≥ 5 μm for smaller areas of glass. Basaltic glass standards VG-A99 USNM 113498/1 and VG-2 USNM 111240/52 (Jarosewich et al. 1980) were measured periodically to ensure measurement fidelity and check for drift. Calibration was based on these basaltic glass standards (Si, Al, Fe, Ca), sphene glass (Ti), Verma garnet or rhodonite (Mn), chromite USNM 117075 (Mg, Cr), NiO (Ni), Amelia albite (Na), orthoclase (K), and fluor-apatite USNM 104021 (P) standards. Background fits were linear for all elements. Phi-Rho-Z matrix corrections of Armstrong/Love Scott were applied. Detection limits and uncertainties were evaluated (Table S2).

WDS spot analyses of olivine and pyroxene were gathered over four sessions for Si (20-30 s on-peak counting time), Ti (30-40 s), Al (20-30 s), Cr (30-35 s), Fe (30-35 s), Mn (30-55 s), Mg (20-30 s), Ca (30-45 s), Ni (30-50 s), Na (20-30 s, measured first), K (25 s, measured for Y-980459 crystals only), and P (60-70 s, measured for Y-980459 crystals only). High and low off-peak counting times were each half of on-peak times. An accelerating voltage of 20 kV and a beam current of 20 nA were used for experimental crystals. Y-980459 olivine and pyroxene were measured with an accelerating voltage of 15 kV and a beam current of 25 nA (large crystals) or 15 nA (dendrites and rims). In all cases, beam diameter ranged from 10 μm (cores, large crystals) to focused (dendrites, rims). Springwater olivine USNM 2566 and Kakanui augite USNM122142 (Jarosewich et al. 1980) were measured periodically to ensure measurement fidelity and check for drift. Calibration was based on this olivine and pyroxene (Si, Al, Fe, Mg, Ca), sphene glass (Ti), chromite USNM 117075 (Cr), Verma garnet (Mn), NiO (Ni), Amelia albite (Na, Al), orthoclase (K), and fluor-apatite USNM 104021 (P, Ca) standards. Background fits were linear for Si, Fe, Mg, Ca, Ni, and Na, and exponential for Ti, Al, Cr, Mn, and P. Phi-Rho-Z matrix corrections of Armstrong/Love Scott were applied. Detection limits and uncertainties were

evaluated (Table S3, Table S4). High-resolution BSE images were collected at 15 kV accelerating voltage.

Phosphorus X-ray distribution maps for two olivine crystals in Y-980459 were acquired with a 15 kV accelerating voltage, 100 nA beam current, 40 ms dwell time, and 0.5 μm step size. Two PET(H) crystals collected P kα x-rays. Map dimensions are 500 x 450-600 pixels.

2.2.3 Image analysis

Point counts were made on composite BSE images, using at least 400 points per experimental charge and 916 points for the meteorite, employing the assumption that area fraction is equivalent to volume fraction when no fabric is present (Hilliard 1968). In the groundmass of Y-980459, areas of olivine versus pyroxene were distinguished in BSE images by the higher Z-contrast (i.e., greater Fe content) of the olivine dendrites in comparison with the pyroxene groundmass crystals. High magnification images (500-2000x) were used to obtain the average volume fraction of each groundmass phase in an area of mesostasis composed of that phase and glass. This ratio of crystal to glass was applied to the relevant points of the original low-magnification point count, for which groundmass crystals were unresolvable from glass. For experimental samples, the same method was applied to 2000x magnification images from each run to determine the pyroxene-glass ratio for regions containing fine-grained pyroxene.

The surface area per unit volume ($\mathbf{S}_v^P$) for pyroxene populations was determined using standard stereological image analysis techniques and detailed methodology of Hammer (2009). Measurements of $\mathbf{S}_v^P$ were used partly because they do not require knowledge of nucleation density. Metrics dependent on nucleation density (e.g., crystal size distribution) would provide less suitable characterizations of the crystal morphologies we studied, due to difficulty distinguishing branches of one crystal from another and the possibility of broken crystals in the natural sample. By using $\mathbf{S}_v^P$, texture was quantified in a way that is appropriate for both natural and experimental samples. The units of $\mathbf{S}_v^P$ are mm^2/mm^3, or simply mm^{-1}. Briefly, $\mathbf{S}_v^P$ of a phase is related to the number of intersections of that phase with a given length of test line (N_L) and the volume fraction of the phase (ϕ), as $\mathbf{S}_v^P = 2\ N_L / \phi$ (Underwood 1968). Circular test lines were digitally drawn on BSE images at 75-100x, 250-1000x, or 2000x, depending on population type (defined below). Intersections of crystal edges with the test line were marked using Photoshop and counted using Image J (Schneider et al. 2012). Volume fraction was determined by thresholding or point counting the image area inside each individual test circle. For statistical

purposes, we determined a sample size (n) for each test line, based on its length and the resolution of the image (included in the electronic Supplement). Test line length was also used to derive weighted averages, combining individual measurements in proportion to their spatial relevance.

2.3 RESULTS

The two-stage dynamic cooling experiments fall into two series, the HT (high temperature) series and the LT (low temperature) series (Figure 2.2), which explore the effects of initial cooling and lower-temperature cooling, respectively, on mineralogy and texture. In the HT series, the high-temperature (Stage 1) cooling rate varied from 28 °C h^{-1} to 1 °C h^{-1} and the lower temperature (Stage 2) cooling rate was held constant at 100 °C h^{-1}. In the LT series, Stage 1 was held constant at 28 °C h^{-1} and Stage 2 was varied from 1000 °C h^{-1} to 50 °C h^{-1}. For experiments discussed henceforth (Table 2), each run consisted of two sample beads run simultaneously on separate FePt alloy wire loops. No differences were observed between beads, unless otherwise noted, indicating general reproducibility of textural and compositional outcomes. An electronic Supplement contains full-bead BSE images of each run (Figure S12).

2.3.1 Textures

2.3.1.1 Descriptive

Every experimental sample contains all phases present in Y-980459, except sulfides (Table 2). Olivine phenocrysts in the LT series are large (1 mm range), have Fe-rich rims where in contact with glass, and exhibit skeletal morphologies. In the HT series, olivine phenocrysts are similar (Figure 2.3B), but the degree of infilling increases with decreasing Stage 1 cooling rate. Two beads (one each from Y98*-f57 and Y98*-f63) contain small polyhedral olivine grains (~100 μm), clustered at the base of the charge (Figure S13). However, no run products contain large, euhedral olivine grains resembling those in Y-980459.

Olivine dendrites or dendritic overgrowths formed in all runs in both series. Their morphologies are feathery, chain-like, or swallowtail in nature (Figure 2.4B, Figure 2.4D). Although these shapes are similar to those observed in the meteorite (Figure 2.4), the olivine dendrites in experiments are less volumetrically abundant than those in Y-980459.

Cr-rich spinel occurs throughout experimental samples and grains are especially prevalent on FePt wires. Spinel crystals from the HT series are euhedral, whereas some in the LT

Table 2.2. Experimental run information[a] and selected results.

	Sample Y98*-	Cooling rate (°C h^{-1})		Modal mineralogy (vol%)							Crystallinity (ϕ)		Surface area per unit volume (mm^{-1})		
		Stage 1	Stage 2	Olivine		Cr-spinel	Pyroxene			Glass	Point Count	K_2O	Pyroxene		
				Phenocryst	Dendrite		Pop A	Pop B	Pop C				Pop A	Pop B	Pop C
LT	f63	28	1000	19.8	tr.	0.4	36.3	0.8	3.0	39.6	0.60	0.59	95	1752	9178
	f56	28	500	29.7	tr.	tr.	30.1	0.8	3.4	36.0	0.64	0.58	89	1922	8649
	f67	28	350	20.7	tr.	tr.	38.1	2.7	7.5	31.0	0.69	0.69	65	1801	7123
	f57	28	150	18.2	tr.	tr.	37.1	10.7	1.0	33.1	0.67	0.51	89	1181	6672
	f64[b]	28	50	17.9	tr.	0.4	42.9	2.9	0.9	17.2	0.83	0.63	n.a.	n.a.	n.a.
LT&HT	f62	28	100	20.6	tr.	0.2	39.5	6.2	1.4	32.0	0.68	0.65	81	1295	5643
HT	f65	10	100	22.5	0.2	0.2	42.7	6.8	1.7	26.0	0.74	0.65	49	1169	6778
	f68	5	100	16.1	tr.	1.0	46.4	2.9	3.9	29.8	0.70	0.49	40	1882	5404
	f69	1	100	16.6	tr.	tr.	41.0	1.4	1.6	39.5	0.61	0.34	25	1657	5159
	f69[c]	1	100	1.7	tr.	0.7	39.2	0.7	2.8	53.5	0.47	0.26	n.a.	n.a.	n.a.
	Y-980459[d]	-	-	19.7	1.9	0.7	49.8	-	4.6	23.4	0.77	0.66	46	-	6477

[a] For all runs, an initial 12 h sub-liquidus dwell between 1428 and 1435 °C preceded cooling. All pivot temperatures between Stage 1 and Stage 2 were between 1111 and 1116 °C, below the equilibrium plagioclase-in temperature. All quench temperatures were 909 °C. For preparatory experiments, see Table S1.

[b] Y98*-f64 contains 17.9 vol% intergrown plagioclase and pyroxene.

[c] Y98*-f69 (bead ii) contains 1.4 vol% cristobalite.

[d] Y-980459 contains sulfides, though none fell on intersections for the point count.

tr.=trace, n.a.=not analyzed

series are skeletal. In HT runs < 28 °C h^{-1}, Cr-spinel crystals reach ~100 μm in diameter. This grain size is larger than all but one Cr-spinel crystal in Y-980459, in which most are 30-50 μm in diameter.

The experimental pyroxene crystals are qualitatively divided into three populations (A_e, B_e, and C_e), using criteria based on size, morphology, and atomic number contrast in BSE images (Figure S14). Population A_e (Figure 2.3B, Figure 2.6) consists of phenocrysts with Mg-rich cores and Ca- and Fe-rich rims, with some patchy zoning. These crystals are typically elongate and externally faceted, with numerous embayments and interior melt inclusions. Among the HT runs, more infilling occurs with decreasing Stage 1 cooling rate. Smaller crystals with faint to no zoning are nearly equant, with a combination of facets and sparse embayments. In the HT series, the abundance of population A_e peaks at 5 °C h^{-1}.

Population B_e (Figure 2.3B, Figure 2.6) consists of smaller crystals, generally chain-like, some of which branch off from phenocrysts. These chains are H-shaped or lantern-like (Bryan 1972; Donaldson 1976), occasionally occurring as isolated crosses. Population B_e is compositionally unzoned, with a similar or higher average atomic number than the rims of population A_e pyroxenes.

Population C_e (Figure 2.3B, Figure 2.6) comprises the smallest segments. These crystals are dendritic, finely branching or radiating, and are the most Fe rich. A glassy boundary layer typically separates phenocrysts from population C_e crystals. Populations B_e and C_e are absent from samples quenched at the end of Stage 1 (Figure S15), indicating that they formed during Stage 2. The abundances of both of these populations peak at intermediate cooling rates in both series.

Y-980459 contains two pyroxene populations, A_n and C_n, analogous to populations A_e and C_e. There is no population B_n in the meteorite (see Discussion). Population A_n is morphologically similar to population A_e (Figure 2.3A, Figure 2.6), but crystals tend to be smaller, with a higher number density. Population C_n (Figure 2.3A, Figure 2.6) comprises groundmass crystals that are elongate and micron-scale, similar to those in population C_e. However, C_n crystals cover a continuum of sizes and are chain-like, but blocky. They are infilled and segmented, with fewer branches than population C_e crystals.

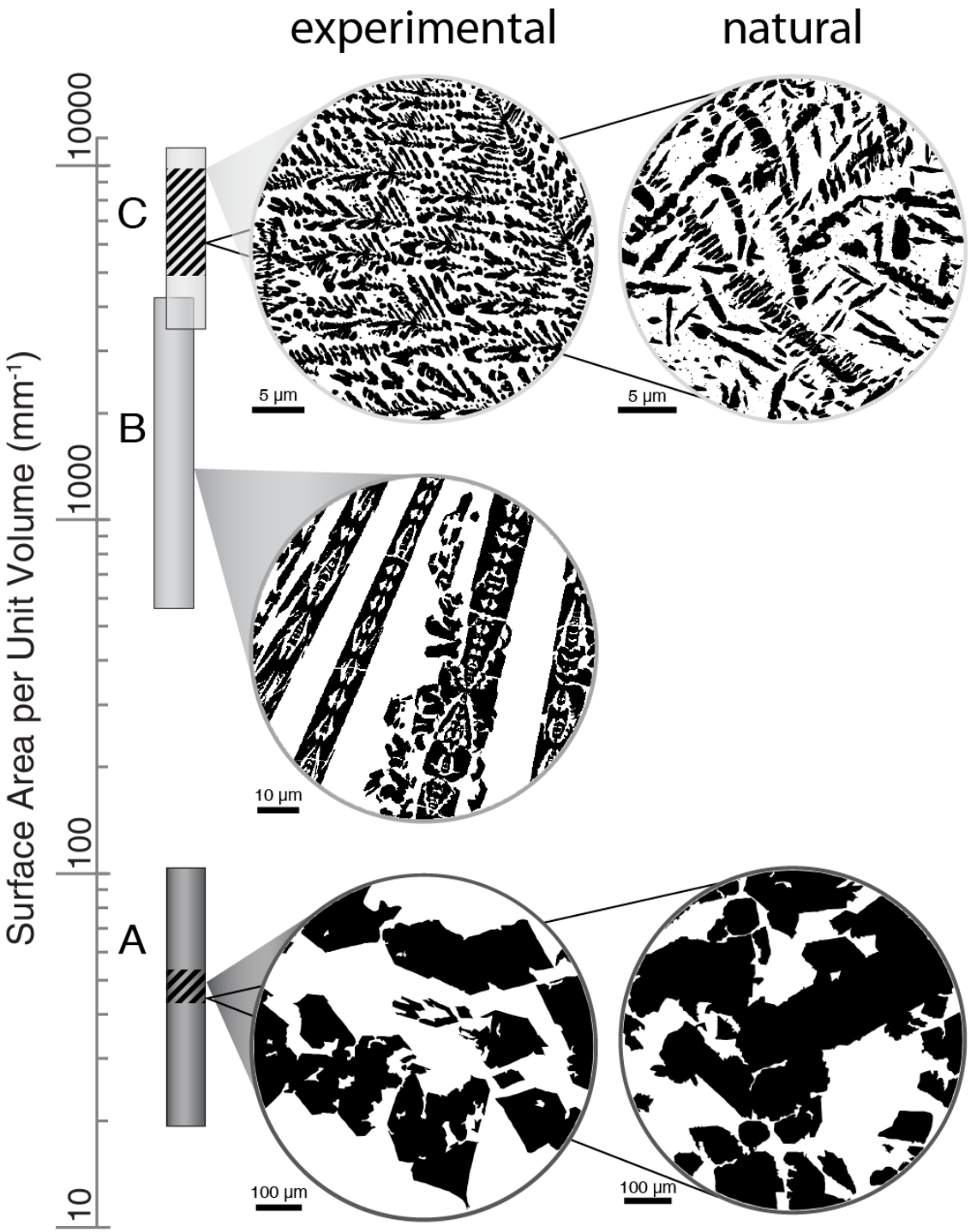

Figure 2.6. Summary of surface area per unit volume for experimental and natural pyroxene populations. Shaded vertical bars show experimental ranges exhibited by crystals of each of three populations, A, B, and C, described in the text. Ranges exhibited by meteorite crystal populations are indicated as subsets with diagonal striping. Binary images representative of each population in the experimental and natural samples are shown at right, with cones indicating the corresponding $\mathbf{S}_{\mathrm{v}}^{\mathrm{P}}$ value for each image.

Minerals not occurring in Y-980459 formed in two experiments. Plagioclase crystallized in Y98*-f64. Cristobalite (as determined by Raman spectroscopy and provided in the electronic Supplement) crystallized in one bead of Y98*-f69 (Figure S16). Paradoxically, the cristobalite-bearing bead has the lowest overall crystallinity ($\Phi = 0.47$) but highest glass SiO_2 content (55 wt%) of all beads analyzed. Cristobalite also appeared in an earlier run with the same T-t path (Y98*-f66, Table S1), indicating reproducibility. Cristobalite is not present in the bead quenched at the end of Stage 1 in run Y98*-f66 (Figure S15C), suggesting that it formed during Stage 2. The presence of this unexpected mineral hints at kinetic effects during the longest run, and is considered in the Discussion.

The overall crystallinity of the LT series increases linearly from $\Phi = 0.60$ to 0.68 as Stage 2 cooling rate decreases (Table 2), except for one anomalously crystalline run (Y98*-f67). This trend is consistent with slower low-temperature cooling allowing more time for crystal nucleation and growth. In the HT series (Table 2), crystallinity peaks at 10 °C h^{-1} ($\Phi = 0.74$), suggesting that the combined rates of nucleation and growth are maximized at intermediate cooling rates. Compared to the meteorite ($\Phi = 0.77$), experimental samples with the correct phase assemblage are less crystalline ($\Phi = 0.60$-0.74).

2.3.1.2 Surface area per unit volume measurements

The qualitative division of pyroxene crystals into populations is substantiated by calculated surface area per unit volume ($\mathbf{S}_v^P$; Figure 2.6, Table S5). Population ranges are distinct, with little overlap between populations B_e and C_e. In the LT series, the $\mathbf{S}_v^P$ of population A_e increases slightly with Stage 2 cooling rate (Table 2), although Y98*-f67 contradicts this trend, with a lower $\mathbf{S}_v^P$ than expected. (This run is also more crystalline, pointing to favorable nucleation and/or growth conditions.) In the HT series, the weighted average $\mathbf{S}_v^P$ of population A_e increases linearly with Stage 1 cooling rate (Figure 2.7A). Including the standard deviations of both A_n and A_e, the meteorite population overlaps the experimental $\mathbf{S}_v^P$ values between 5 and 16 °C h^{-1} (Figure 2.7A). The weighted average $\mathbf{S}_v^P$ of A_n (46 mm^{-1}) intersects the trend for the HT runs near Stage 1 = 10 °C h^{-1} (Figure 2.7A).

The $\mathbf{S}_v^P$ values of population B_e and C_e pyroxenes do not change coherently within the HT series (Table 2), suggesting formation during Stage 2. In the LT series, the weighted average $\mathbf{S}_v^P$ of population C_e consistently increases as Stage 2 cooling rate increases (Figure 2.7B).

Population C_n has a weighted average $\mathbf{S}_v^P$ of 6500 mm^{-1}, intersecting the LT experimental trend at a Stage 2 cooling rate near 150 °C h^{-1} (Figure 2.7B).

2.3.2 Phase Compositions

Pyroxene crystals from the LT and HT series span a large compositional range, from En_{80} to En_{11} (Figure 2.8). They evolve from magnesian to ferroan, and from low-Ca to higher-Ca. Population A_e crystals fall mainly at the high En end, and smaller crystals have lower

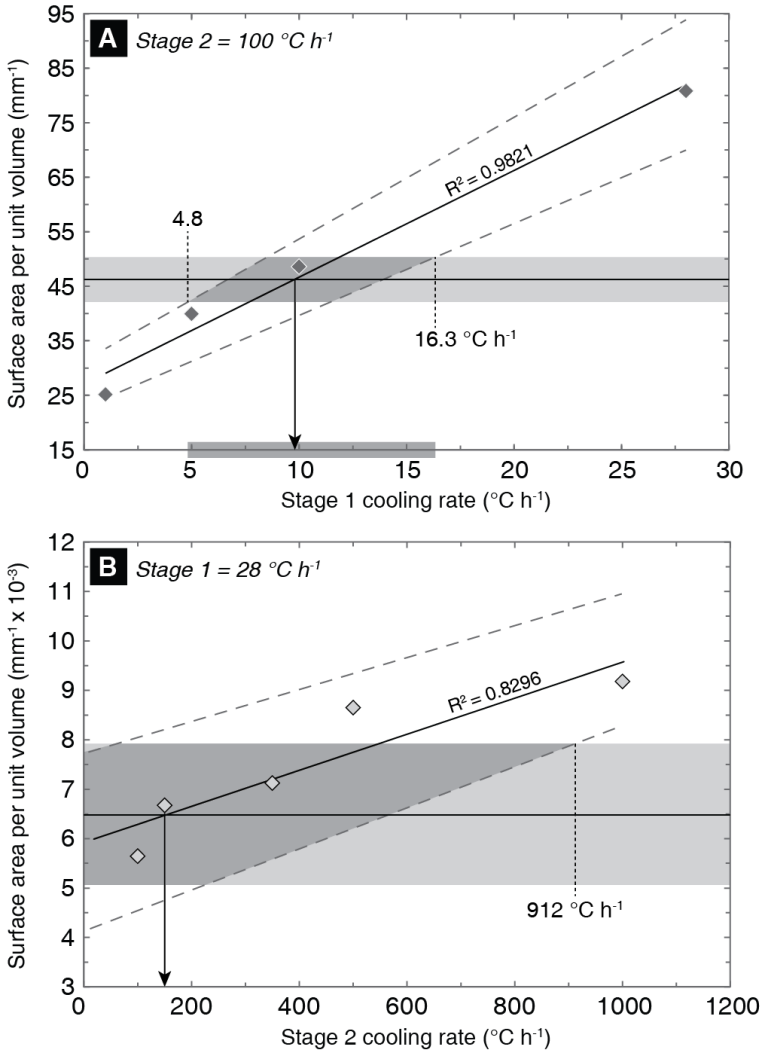

Figure 2.7. Surface area per unit volume of pyroxene populations. (A) population A; least-squares regression line fit to experimental (population A_e) weighted averages plotted as a thick line; least-squares fits to 1 σ variances plotted as dashed lines; meteorite (population A_n) weighted average plotted as horizontal black line, with 1 σ variance shown as shaded band. The intersection of this horizontal band with the region between the dashed lines represents the range of cooling rates possible for natural pyroxene population A, within error. (B) population C; lines and shading equivalent to those described in (A).

En contents. To a first order, this range is independent of cooling history, as demonstrated by the overlap within both the LT and HT series (Figure 2.9; Table S3). Experimental pyroxene crystals span approximately the same compositional range as Y-980459 pyroxene crystals (Figure 2.8).

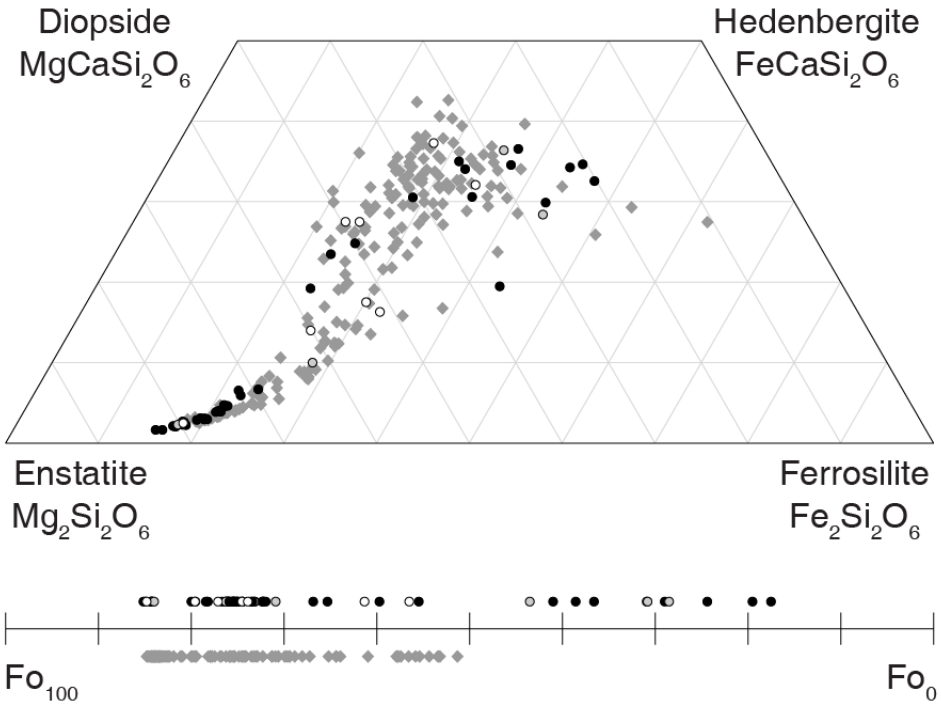

Figure 2.8. Pyroxene and olivine end-member compositions. Grey diamonds are experimental data points, and circles are Y-980459 data points. Meteorite data from this study (black), plus representative analyses from Greshake et al. (2004) (light grey), and Usui et al. (2008) (white).

In Y-980495 and both experimental series, pyroxene compositions cluster tightly at the high-MgO end of the spectrum, fanning out to larger scatter below 23 wt% MgO (Figure S17). This divergence point also corresponds to about 1.5 wt% Al_2O_3, 4 wt% CaO (Figure S17), and is reflected in the stoichiometric components (Figure 2.8). Pyroxene cores extend to slightly higher MgO contents in Y-980459 (maximum 31.71 wt% MgO) than in experiments (maximum 29.11 wt% MgO). Pyroxene crystals in Y-980459 contain less TiO_2 than those of experiments (Figure S17), consistent with the higher TiO_2 content of a subset of the meteorite Fe-Ti oxide crystals (Brachfeld et al. 2015). This low TiO_2 causes the Al/Ti trend in Y-980459 to be slightly higher than that defined by experiments (Figure 2.9). Mg-rich natural pyroxene analyses extend to much higher Al/Ti (Figure 2.9).

Pyroxene crystals in the meteorite extend to higher Na_2O contents than those in experiments (Table S3), as expected given the higher glass Na_2O in Y-980459 (Figure S18B).

Cr_2O_3 in meteorite pyroxene is ≤1.05 wt%, whereas in experiments many grains contain higher Cr_2O_3 (Table S3). Small differences in Cr-spinel abundance can explain this result. Indeed, pyroxene compositions in experiments with lower Cr-spinel abundance than Y-980459 (Table 2) extend to 1.7 wt% Cr_2O_3, whereas those with higher Cr-spinel abundance (Table 2) contain pyroxene more similar to the meteorite, reaching only 1.1 wt% Cr_2O_3. The differences noted above are minor. In general, compositional similarity between pyroxene in Y-980459 and the experimental set was achieved.

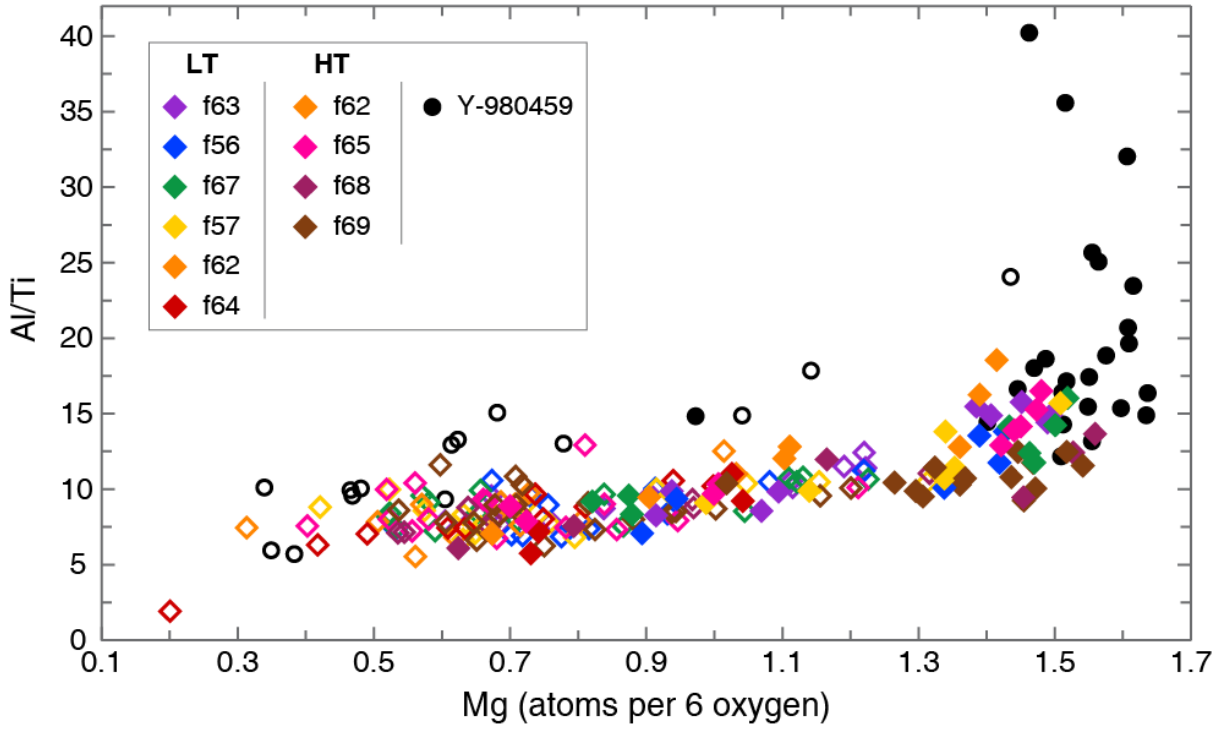

Figure 2.9. Pyroxene compositions, presented as Al/Ti ratio versus atomic Mg. Filled shapes represent cores; open shapes represent rims. Experimental analyses plotted as diamonds; Y-980459 plotted as circles. Error within symbol size.

The composition of experimental olivine is similarly uncorrelated with cooling history for both LT and HT runs. Olivine core compositions in experiments (37.86-44.78 wt% MgO) and Y-980459 (38.13-45.81 wt% MgO) largely overlap (Figure 2.8, Figure S19). One apparent mis-match is the lack of experimental rim or dendrite analyses more Fe-rich than Fo_{51}, compared with Y-980459 olivine as ferrous as Fo_{18} (Figure 2.8). Natural trends extend to higher FeO, MnO, and lower MgO, SiO_2 (Figure S19). Given the scarcity of olivine dendrites in experiments, and the difficulty of analyzing their sub-micron branches, the discrepancy is partly a sampling

bias. However, the high crystallinity of the meteorite ($\Phi = 0.77$) also suggests that the melt of Y-980459 would have had a lower MgO/FeO ratio at the time of dendrite formation, compared with experiments ($\Phi = 0.6$-0.74). This is supported by the meteorite's more evolved residual glass compositions (Fig 9).

Glass compositions in this study are more sensitive to experimental cooling history than crystal compositions. As Stage 2 cooling rate decreases, LT glasses are richer in Al_2O_3 (Figure 2.10A), but poorer in MgO and CaO (Figure 2.10B), consistent with increasing crystallinity (Table 2). Conversely, in the HT series, the two fastest cooling rates produced glasses with lower MgO and CaO than those of the two slowest cooling rate experiments (Figure 2.10C). This counterintuitive result is reflected in the crystallinity of the samples; the slowest-cooled experiment is the least crystalline (Table 2). The residual glass of Y-980459 is comparatively more evolved, in that it generally contains less MgO, less CaO, and more Al_2O_3 than experimental glasses (Figure 2.10). The experiment that comes closest to matching the 0.74 wt% MgO glass average for the meteorite is Y98*-f65 (1.97 wt% MgO). Y98*-f65 is also the closest match to the glass CaO and Al_2O_3 values in Y-980459. The glass in Y-980459 has higher average Na_2O and K_2O than any experimental glass (Figure S18), an inferred result of experimental Na loss during the initial high-temperature dwell (Table 2.1) and differences in crystallinity.

2.4 DISCUSSION

2.4.1 Controls on phase composition and mode

The experiment-meteorite overlap in olivine and pyroxene compositions provides evidence for broadly similar crystallization conditions. The reason for discrepancies in glass composition between Y-980459 and many experiments is therefore not immediately apparent. For example, taking the LT and HT series together, olivine and pyroxene reach similar maximum and minimum CaO and Al_2O_3 as their counterparts in the meteorite (Table S3, Table S4). However, glass in Y-980459 contains more Al_2O_3 and less CaO (on average) than experiments (Figure 2.10). Thus, it is the amount of each mineral composition that differs between the meteorite and experiments, not the presence or absence of a particular composition. Rather, glass compositions, modal analyses, and textural properties of each sample are better suited to preserving cooling history.

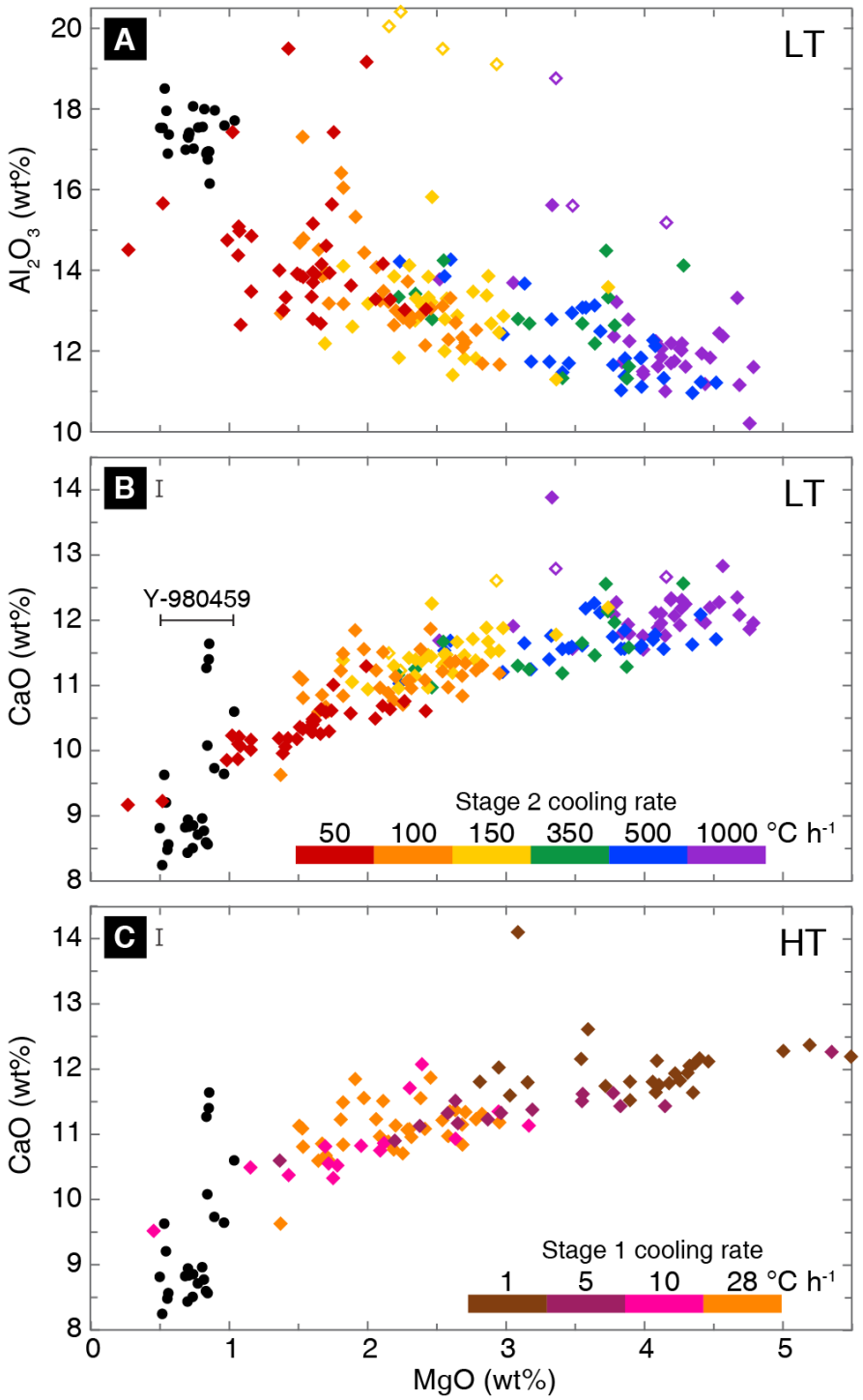

Figure 2.10. Glass compositions. Experimental data plotted as diamonds, meteorite plotted as black circles. Legend in (B) also applies to (A), and horizontal axis applies to all plots. (A) Al_2O_3 vs. MgO for the LT series. Open diamonds for Y98*-f57 and Y98*-f63 represent analyses of interstitial glass from areas of closely-packed olivine crystals, analogous to an intercumulus melt. (B) CaO vs. MgO for the LT series. (C) CaO vs. MgO for the HT series.

The tight-to-scattered trend in LT, HT, and natural pyroxene compositions (Figure 2.8) may be a hallmark of disequilibrium crystallization. Pyroxenes from several other shergottites

also exhibit greater heterogeneity at higher Fs and/or Wo contents (QUE 94201 and EETA 79001, Mikouchi et al. 1998; NWA 480, Barrat et al. 2002; NWA 5789, Gross et al. 2011; Tissint, Balta et al. 2015). Notably, the scattered analyses are made up largely of rims and non-phenocryst populations. In the present study, we interpret this pattern as an indication of greater melt inhomogeneity at the faster cooling rates (Stage 2) during which these pyroxene subsets formed. Rapid cooling places kinetic limitations on the ability of species to diffuse through the melt (Albarede and Bottinga 1972), creating a chemically inhomogeneous melt and corresponding inhomogeneous crystal population. Disequilibrium conditions appear to have affected the trace element compositions of even the pyroxene phenocrysts in Y-980459 (Usui et al. 2008), so with subsequent faster cooling, it is logical that the consequences of disequilibrium are more pronounced. Similar kinetic effects may have played a role in pyroxene crystallization for other shergottites, though the initial cause (rapid cooling, high undercooling, etc.) may vary.

In pyroxene analyses with less than ~1.6 Mg cations per six oxygens, the higher Al/Ti ratios in Y-980459 crystals compared with experimental crystals (Figure 2.9) are attributed to crystallization from a liquid slightly more depleted in Ti. The meteorite contains spinel grains with higher Ti contents than any in the experiments (Brachfeld et al. 2015), providing a mechanism whereby the natural liquid evolved with lower Ti. For the most Mg-rich meteorite pyroxene analyses, however, the Al/Ti ratio is highly variable and extends to values far too large for this explanation to be reasonable. These high values represent population A_n only and may reflect initial pyroxene crystallization at higher pressures, which would stabilize the jadeite component at the expense of the diopside and enstatite components (Putirka et al. 1996). This interpretation is in keeping with the positive Al_2O_3-Na_2O correlation present in Y-980459 pyroxene crystals (Table S3). A high-pressure interpretation is consistent with the Al/Ti pressure calibration reported in Nekvasil et al. (2004), but like Balta et al. (2015) we are cautious about placing numerical constraints on formation pressures of Y-980459 crystals based on experiments using an alkalic composition.

Kinetic effects may have influenced K_2O-based crystallinity calculations. For Y-980459, HT, and LT samples, the crystallinity calculated using glass K_2O content is consistently lower than point-counted crystallinity (Table 2). Thus, either perfect incompatibility is not an accurate assumption, or the full extent of glass heterogeneity was not captured by spot analyses. In Y-980459, K_2O was detected in 11 of 122 FeMg silicate analyses, at ≤ 0.04 wt%. Adding this K_2O

back to the melt does not reproduce the point counted crystallinity value, indicating that compatibility of K_2O cannot fully explain this discrepancy. Generally, we obtained analyses away from potential boundary layers, aiming for the largest and most homogeneous melt pockets. However, boundary layers around growing crystals are typically enriched in incompatible elements (e.g., Albarede and Bottinga 1972; Lasaga 1982). Milman-Baris et al. (2008) report K_2O enrichment of ~30% measured within 250 μm of olivine crystals in their experimental charges. Boundary layers are indeed visible in BSE images of Y-980459 and our experimental suite (Figure S20), and these unanalyzed regions could explain the apparent low glass K_2O content of samples. Additionally, olivine and pyroxene dendrites too small to measure grew rapidly and may have incorporated higher concentrations of normally incompatible elements from these boundary layers (e.g., Welsch et al. 2013), including K. Thus, we take point counts as the more accurate measure of sample crystallinity.

2.4.2 Interpreting population C

Population C crystals generally have a wide range of $\mathbf{S}_v^P$ values within a given sample, including individual measurements up to 1.5 times higher than the weighted average, in both Y-980459 and experiments. One explanation for these high values is that crystal growth typically begins rapidly in response to a perturbation in the degree of undercooling (e.g., Dowty 1980), such as an abrupt increase in cooling rate. Thus, some high $\mathbf{S}_v^P$ values would be expected at every Stage 2 cooling rate. However, following the perturbation, growth rapidly decays to a lower rate, shutting down dendritic growth. Slower cooling affords more time for crystals to infill and produce morphologies consistent with slow growth. Crystal populations with short growth windows may therefore capture both incipient and slightly more developed stages of crystallization. Thus, the brief growth interval of population C crystals promotes much greater variation in $\mathbf{S}_v^P$ (Figure 2.7B) than is seen for crystal populations grown over longer time periods. For example, population A grew for long enough that the quasi-steady state growth rate eclipsed any transient rapid growth initially following nucleation. Despite the variation in the data, the weighted average $\mathbf{S}_v^P$ of population C_e or C_n in each sample shows a clear dependence on cooling rate and is viewed as a viable constraint.

The nature of this smallest population also indicates minor discrepancies between Y-980459 and experiments. The highly branching and locally concentrated C_e pyroxenes (Figure 2.6) contrast with the blockier, evenly distributed C_n microlites (Figure 2.6). We examine two

explanations for these differences: flow-induced strain and higher pivot temperature, or a combination of these. These processes could also explain the scarcity of olivine dendrites in experiments.

First, flow is an important natural process not simulated in this study. Experimental work on basalt (Kouchi et al. 1986; Vona and Romano 2013) indicates a negative correlation between strain rate and nucleation incubation time. Essentially, flow promotes a greater nucleation density of microlites than does stagnation (up to 10x more; Kouchi et al. 1986). Field studies also invoke mechanical stirring as an explanation for the high crystallinity of particularly microlite-rich lavas (e.g., Macdonald 1953; Cashman et al. 1999; Hon et al. 2003). If Y-980459 crystallized while flowing, strain may have induced a greater nucleation density across the entire groundmass. This strain also could have broken apart fragile, branched crystals, scattering pieces of the crystals throughout the melt. These effects of flow may explain the presence of more individual groundmass crystals distributed throughout Y-980459, contrasted with the spatially restricted pockets of more branching crystals in experiments.

Second, the pivot temperature between the equivalent Stage 1 and Stage 2 cooling rates in the meteorite may have been different than that used in our experiments (1115 °C). We ascertained that a lower pivot temperature would likely result in plagioclase formation during Stage 1 (Figure S7). However, the upper bound is unconstrained. If Y-980459 began Stage 2 cooling at a higher temperature, the thermodynamic driving force for nucleation would be greater, because the undercooling would be larger. Thus, a combination of flow and higher pivot temperature may explain the more uniform spatial distribution and apparent higher nucleation density of the natural groundmass crystals.

2.4.3 Missing population B_n

The absence of a population B_n in Y-980459 is interpretable within the framework of nucleation and growth theory (Kirkpatrick 1981). The number density of population A_e is less than that of population A_n, and A_e crystals are generally larger. This indicates that during Stage 1 cooling, nucleation in experiments was somewhat inhibited relative to the natural magma. Thus, individual experimental crystals grew larger, as there was less surface area on which growth could occur. The initiation of rapid cooling (Stage 2) and relative scarcity of growth substrate promoted nucleation of two new experimental populations (B_e and C_e). Population A_e rims also grew, but evidently could not accommodate as much growth as population A_n. Thus, the

difference in A-population characteristics explains the presence of two additional populations in experiments, compared to one in the meteorite. If the volume fraction of population B_e is essentially that which would have grown on the rims of population A_e had there been more available outer surface area, the sum of the volume fractions of A_e and B_e (Φ_{A+B}) should be close to that of A_n ($\Phi = 0.50$). Indeed, $\Phi_{A+B} = 0.49\text{-}0.50$ for Y98*-f65 and Y98*-f68.

2.4.4 Cristobalite

The crystallization of cristobalite from a melt that has evolved only to a basaltic andesite composition is puzzling. In mafic rocks, if SiO_2 phases appear, they typically appear late in the crystallization sequence, as in basaltic shergottites Los Angeles (Rubin et al. 2000) and NWA 856 (Leroux and Cordier), and olivine-phyric shergottite NWA 5789 (Gross et al. 2011). Liquid immiscibility is another cited mechanism for silica saturation in mafic materials (e.g., lunar basalt 70017, Rutherford et al. 1974). However, Y98*-f69ii is only 47 vol% crystalline, and petrographic evidence for liquid immiscibility is absent. The appearance of cristobalite around the entire outer surface of the bead suggests a favorable condition at the melt-gas interface, though crystals also appear elsewhere in the sample. Extreme volatile depletion at this interface would increase silica activity in the melt and expand the cristobalite stability field (Mathieu et al. 2011). Indeed, compared to other experimental runs, Y98*-f69 glass is considerably poorer in Na_2O (Figure S18). However, for the given bulk composition (where Na is a minor element), Na_2O loss cannot increase SiO_2 activity enough to explain the presence of cristobalite (MELTS supplemental calculator, Ghiorso and Sack 1995). On a local scale, however, equilibrium thermodynamics cannot be assumed. Referencing a simple forsterite-silica binary phase diagram, if small areas of melt become enriched in silica, a local shift to the silica side of the eutectic could occur, resulting in cristobalite precipitation. The formation of this phase remains unclear, but it is likely attributable to local kinetic effects exacerbated by the abrupt hundredfold increase in cooling rate.

2.4.5 Inferences from P-enrichment patterns in natural olivine

Phosphorus distribution in the natural phenocrysts provides tantalizing evidence for diffusion-controlled early olivine growth in Y-980459 (Figure 2.5). As observed by Welsch et al. (2013), olivine crystals in magma reservoirs preserve a variety of morphologies indicating early diffusion-limited growth which may be overprinted by slower, interface-controlled growth; P-enrichment occurs at the highest growth rates (Milman-Barris et al. 2008; Weslch et al. 2014)

and thus the presence of both P-rich and P-poor areas in externally-faceted crystals preserves evidence of highly variable growth rate through time. The presence of P-rich lamellae in the Y-980459 olivine phenocrysts suggests that not all growth was slow, relative to the diffusivity of P in the melt. The skeletal shapes of experimental Y98* olivine crystals could represent an intermediate morphology experienced by Y-980459 olivine crystals between initial dendritic growth and final infilling (Welsch et al. 2014).

The preservation of melt inclusions near, but not within, phosphorus-rich zones is consistent with previous observations (Shearer et al. 2013) and the interpretation that they owe their existence to initially skeletal growth but were trapped during slow, near-equilibrium growth (Welsch et al. 2014). In their analysis of both transitional embayments and fully enclosed inclusions, Faure and Schiano (2005) demonstrate that the latter accurately preserve the far-field liquid composition at the time of entrapment precisely because slow growth is required to seal them off. However, this inference may not apply to the melt inclusions in Y-980459 olivine phenocrysts, because they are pervaded by cracks (Figure 2.5).

2.4.6 Evaluation of experiments according to match criteria

The relative success of experiments in reproducing features of Y-980459 can be evaluated according to the criteria outlined in the Introduction:

(1) *Phase assemblage:* All experimental runs, with the exception of Y98*-f64 and one bead of Y98*-f69, produced the meteorite phase assemblage of olivine + Cr-spinel + pyroxene + glass. The presence of plagioclase in Y98*-f64 provides a lower limit on natural Stage 2 cooling at 50 °C h^{-1}.

(2) *Modal proportions:* LT experimental products lacking plagioclase preserved significantly more glass than Y-980459, hinting that 28 °C h^{-1} is too fast for Stage 1 cooling. Among the LT runs, those with slower Stage 2 cooling are more crystalline, suggesting that natural cooling rates were closer to 100 °C h^{-1} than 1000 °C h^{-1}. The HT series contains the samples with crystallinity most similar to the meteorite (Y98*-f65 and Y98*-f68). These experiments also have similar mineral modes to Y-980459.

(3) *Phenocryst texture:* Quantitative analysis of pyroxene population A_e demonstrates that 10 °C h^{-1} is the best estimate for the Stage 1 cooling rate of population A_n. Though not a phenocryst phase, spinel morphology corroborates that 28 °C h^{-1} is too fast for Stage 1. The skeletal nature of experimental olivine phenocrysts, even during the slowest-cooled HT run,

suggests a cooling rate < 1°C h^{-1} for the final faceting of Y-980459 olivine phenocrysts. We refer to this stage of olivine phenocryst formation as Stage 0, since it is distinct from pyroxene phenocryst formation but was not constrained explicitly by experiments.

(4) *Phase compositions:* Stage 2 cooling rates of 50 °C h^{-1} and 100 °C h^{-1}, and Stage 1 cooling rates of 28 °C h^{-1} and 10 °C h^{-1}, produced residual glass compositions closest to those of Y-980459.

(5) *Groundmass crystal texture:* Quantitative analysis of pyroxene population C_e shows the best match to population C_n at cooling rates near 150 °C h^{-1}.

Although no single experiment exactly replicates all the characteristics of Y-980459, the run that is considered the best match to Y-980459 is Y98*-f65, cooled at Stage 1 = 10 °C h^{-1} and Stage 2 = 100 °C h^{-1}. In summary, experiments indicate that the initial cooling of Y-980459 must have been < 1°C h^{-1}, followed by at least two subsequent cooling stages in which cooling rate increased from ~10 °C h^{-1} to ~100 °C h^{-1}.

2.4.7 Comparison to previous work

The cooling rate estimates derived here specifically for magma of Y-980459 composition can be used to evaluate estimates from previous studies. Olivine phenocryst cooling rates < 1°C h^{-1} are in agreement with rates proposed by Miyamoto et al. 2009a (0.2 °C h^{-1}) and with the slow end of ranges proposed by Greshake et al. 2004 (0.5-2 °C h^{-1}) and Mikouchi et al. 2004 (0.03-5 °C h^{-1}). Pyroxene phenocryst cooling around 10 °C h^{-1} is higher than the range proposed by Lentz and McSween 2005 (3-7 °C h^{-1}), but if the entire 5-16 °C h^{-1} range in Figure 2.7A is considered, there is overlap. It is also probable that the cooling rate increase between Stage 0 and Stage 1 in nature was not as abrupt as that between Stage 1 and Stage 2. Thus, pyroxene phenocrysts may have experienced a range of increasing cooling rates (Greshake et al. 2004), with most crystallization occurring at cooling rates near 10°C h^{-1}. Finally, groundmass crystallization around 100 °C h^{-1} is more than ten times slower than the 1450-1890 °C h^{-1} range proposed by Greshake et al. (2004).

2.4.7.1 Application to NWA 5789

Olivine-phyric shergottite NWA 5789 is similar to Y-980459 in bulk composition (Table 2.1), phenocryst morphology, and phase compositions (Gross et al. 2011). Because of these similarities, the results of the present study are broadly applicable to NWA 5789. The euhedral olivine megacrysts in NWA 5789 likely formed under conditions similar to those inferred for Y-

980459, growing their final, faceted forms at cooling rates < 1°C h^{-1}. The morphology of pyroxene phenocrysts in NWA 5789 is qualitatively similar to that of population A_n in Y-980459 (Gross et al. 2011), hinting that crystallization occurred during cooling at ~10 °C h^{-1}. A refined estimate would require quantification of $\mathbf{S}_v^P$ for the NWA 5789 crystal populations, as we present herein for Y-980459. One key difference from Y-980459 is the presence of a holocrystalline, plagioclase-bearing mesostasis in NWA 5789. Based on the experimental dataset developed in this study, cooling of the NWA 5789 mesostasis probably occurred at < 50 °C h^{-1}. The presence of interstitial silica and merrillite (Gross et al. 2011), absent from Y-980459, also support slower cooling.

The putative crystallization history of NWA 5789 includes olivine megacryst and pyroxene core formation at up to 85 km depth, based partly on Al/Ti ratios in pyroxene (Gross et al. 2011). Later emplacement on or near the martian surface is suggested to produce the mesostasis texture (Gross et al. 2011). This sequence is nearly identical to the overall volcanic history previously suggested for Y-980459 (e.g., Greshake et al. 2004; Usui et al. 2008), which we refine below with constraints provided by quantitative textural analysis in consultation with the experimental data set.

2.4.8 Cooling model

We applied a numerical model of conductive lava flow cooling (Patrick et al. 2004) to Y-980459 crystallization in order to constrain the depths of crystallization using the derived cooling rates. Inputs specific to Mars or Y-980459 include lava density, martian surface temperature, and crystal fraction (Table S6). The model was run with two sets of starting parameters, corresponding to Stage 1 and Stage 2. In both cases, we constrained the depth below the flow top where Y-980459 could have crystallized. In this set-up, the crystallizing portion of interest is unaffected by cooling from the bottom surface of the flow.

Model calculations suggest that crystallization depths are 25-45 cm for A_n pyroxenes (with a depth of 32 cm corresponding to a cooling rate of ~10 °C h^{-1}) and 5-7 cm for groundmass crystals. These are corroborated by direct observations of lava flow temperatures at Kīlauea volcano. Thermocouple measurements from 20 cm deep in an actively inflating pāhoehoe flow indicate cooling rates around 20 °C h^{-1} over the crystallization interval (calculated from data in

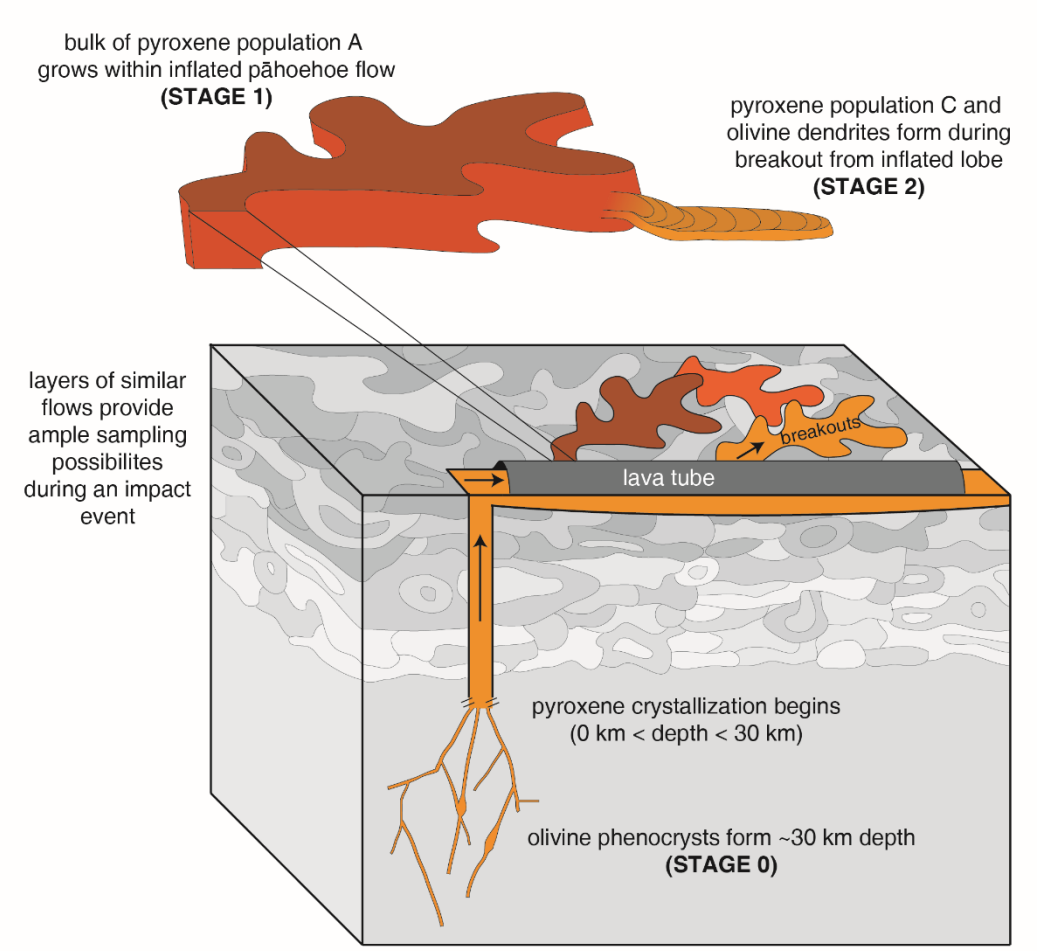

Figure 2.11. Schematic representation of the igneous cooling history of Y-980459, emphasizing the repetitive nature of a field of pāhoehoe-like flows. Estimate of ~30 km depth from Usui et al. (2012).

Hon et al. 1994); at 6 cm deep, cooling is around 85 °C h^{-1}. Thus, model depth estimates appear reasonable in light of relevant field data.

Remotely observed terrestrial pāhoehoe flows exhibit surface cooling rates of thousands of °C h^{-1} (e.g., Ball et al. 2008) to ≤ 900 °C h^{-1} (Flynn and Mouginis-Mark 1992). Modeled cooling rates agree with the higher end of these measurements, yet predict cooling rates >1450°C h^{-1} only within the upper 2 cm of the flow. This depth interval is smaller than the smallest length dimension of the Y-980459 meteorite (Misawa 2004). Therefore, the entirety of Y-980459 could not have cooled at rates >1450 °C h^{-1}. This model-based inference supports the experimental conclusion that groundmass crystallization was on the order of 100 °C h^{-1}, rather than 1000 °C h^{-1}.

2.5 IMPLICATIONS

2.5.1 Volcanological context

The igneous history of Y-980459 may be quite similar to that of a primitive terrestrial basalt. Melt inclusion CO_2 contents suggest that olivine phenocryst growth took place at ~30 km depth (Usui et al. 2012). Pyroxene phenocrysts may have begun crystallizing at depth, as suggested by Greshake et al. (2004) and consistent with geochemical evidence (Figure 2.9), but the cooling rates derived in this study (5-16 °C h^{-1}) imply that population A_n crystallized mainly in a surficial environment. Insulated lava tube systems cool too slowly (<1 °C h^{-1} using reasonable velocities; Ho and Cashman 1997; Thordarson and Self 1998), whereas lava in open channels cools too quickly (22-50 °C h^{-1}; Cashman et al. 1999). Rather, A_n crystals may have formed predominantly in an environment analogous to a pāhoehoe flow (Figure 2.11). For example, an inflating lobe on the order of decimeters thick may have crystallized population A_n. A subsequent break-out could produce cooling rates necessary for population C_n and olivine dendrites to form, then quench the residual melt.

A three-stage cooling model for Y-980459 was proposed by Usui et al. (2008). The recognized need for separate stages of olivine, pyroxene, and groundmass crystallization is in agreement with our findings. However, the suggestion that pyroxene phenocrysts formed dominantly before eruption is not consistent with cooling rates derived in this study. It has been previously suggested that Y-980459 represents a parcel of lava that cooled in a tumulus and later broke out (Lentz and McSween 2005). Our results agree with this scenario, while not specifically requiring a tumulus structure.

Breakouts from the interiors of ʻaʻā flows may manifest as pāhoehoe (Jurado-Chichay and Rowland 1995). It is also possible that population A_n crystallized in the upper few cm of a single thick flow. However, the presence of a pāhoehoe flow field composed of layered cooling units (Walker 1971) provides a vastly greater proportion of material matching the thermal history of Y-980459 compared with the single cooling unit scenario (Figure 2.11). Thus, Y-980459 may represent a relatively common terrestrial lava emplacement mechanism. Our interpretation of crystallization history (Figure 2.11) is consistent with previous work on Y-980459 (Greshake et al. 2004; Usui et al. 2008, 2012) and resolves likely lava flow emplacement conditions in greater detail. A similar volcanological history is broadly consistent with proposed thermal paths experienced by other olivine-phyric shergottites, including NWA 1068 (Barrat et al. 2002;

Filiberto et al. 2010), LAR 06319 (Filiberto et al. 2010; Balta et al. 2013), and NWA 5789 (Gross et al. 2011). To the extent that Y-980459 is a representative sample of its source area on the surface of Mars, our inference that it represents a pāhoehoe flow field connotes general relevance of this lava emplacement mechanism for the basaltic and olivine-phyric shergottite lavas.

2.5.2 Emplacement on Mars: A typical sample of a typical flow?

Most features of terrestrial effusive basaltic volcanism have been identified on Mars, including: stacked flows, flood lavas, thin (<1 m) flow margins, and inflated sheet flows (Keszthelyi et al. 2008). Of particular interest to the study of Y-980459 are the flood lavas, or long lava flows (e.g., Cashman et al. 1998; Keszthelyi et al. 2004), analogous to terrestrial flood basalts. Though these terrestrial counterparts were originally interpreted to require high effusion rates (Shaw and Swanson 1970), more recent works (see summary by Cashman et al. 1998) recognize inflation features and suggest that many flood basalts were emplaced at lower effusion rates (e.g., ~10-10^3 m^3 s^{-1}; Keszthelyi and Self 1998). There is growing evidence that some flood basalts are composed of compound, inflated pāhoehoe flows (Hon et al. 1994; Self et al. 1996; Vye-Brown et al. 2013). This particular emplacement mechanism encompasses cooling rates that could be relevant to Y-980459, from thicker, more insulated lobes to thin breakouts at the flow margin.

Flood lavas in the Cerberus plains illustrate the occurrence of such systems on Mars. The flows are > 1500 km long, exhibiting both inflated margins and "platy-ridged" morphology similar to those of the Laki Flow Field in Iceland (Keszthelyi et al. 2004). This terrestrial analogy suggests that the martian structures can be formed by pāhoehoe-like sheet flows, consistent with modeling that indicates a high thermal efficiency for platy-ridged flows (Keszthelyi et al. 2004). These pāhoehoe-like long flows may be thick overall, though individual lobes can be thin, in keeping with possible emplacement mechanisms for Y-980459.

In this sense (pāhoehoe lobe), model depths are in accord with previous inferences of a thin lava flow as the source of Y-980459. However, the flow field may be composed of many individual lobes stacked atop one another, resulting in a flow that is actually quite thick. Thus, we make the distinction between an anomalously thin flow and a fairly typical basaltic lava flow with thin individual cooling units. This type of flow is widespread on Earth (Self et al. 1998) and has been observed in remote sensing imagery from Mars (Keszthelyi et al. 2008; Hauber et al.

2009), making it a viable mechanism for the emplacement of Y-980459 and conceivably other shergottites.

Chapter 3. Experimental constraints on dacite magma storage beneath Volcán Quizapu, Chile

In preparation for publication as:

First, E., Hammer, J., & Ruprecht, P. (201-). Experimental constraints on dacite magma storage beneath Volcán Quizapu, Chile. *Journal of Volcanology and Geothermal Research*.

Abstract - We present water-saturated, phase equilibrium experiments on the end-member dacite magma from Volcán Quizapu, Chile, using as starting materials two nearly isochemical lava and pumice samples from the 1846-7 effusive eruption and the 1932 Plinian event. The main phase assemblage of An_{25-30} plagioclase + amphibole + orthopyroxene is stable at 850 ± 10 °C and 4.5-5 km depth, corresponding to ~125 MPa water pressure. Apatite and sulfide accessory phases are also stable at these conditions. At slightly higher water pressure, biotite joins the equilibrium assemblage. Because biotite is absent from all eruptive products at Quizapu, its stability field places a hard upper pressure limit on pre-eruptive storage conditions. This constrains water-saturated storage depths to a height of ~0.5 km, necessitating a sill-like reservoir. To more plausibly accommodate the 4-5 km^3 of material expelled during each eruption, we suggest that the Quizapu dacite magma may have been water undersaturated during equilibration, residing at a range of $P_{total} > P_{H2O}$. Constraints on amphibole stability from other experimental studies suggest that $X_{H2O}^{fluid} > 0.7$, limiting P_{total} to ≤ 188 MPa, or a depth of ≤ 7 km. Our experiments and observations additionally call into question the prevailing explanation for the effusive nature of the 1846-7 eruption. We suggest that a fissure geometry of the conduit, rather than pre-eruptive heating, allowed sufficient outgassing of the magma to preclude explosive eruption.

3.1 INTRODUCTION

Two major historic eruptions have issued from what is now known as Quizapu crater, a flank vent on Cerro Azul stratovolcano in the Andean Southern Volcanic Zone. Both eruptions emitted 4-5 km^3 of dacitic material of ~67 wt% SiO_2 (Hildreth and Drake 1992; Ruprecht et al. 2012). However, the eruption in 1846-7 consisted of lava effusion, whereas the eruption in 1932 was a Plinian event (Hildreth and Drake 1992). This dramatic difference in eruptive style has

already motivated a suite of studies (Fiege et al. 2017; Higgins et al. 2015; Ruprecht and Bachmann 2010; Ruprecht and Cooper 2012; Ruprecht et al. 2012). The present effort is focused on constraining the pre-eruptive storage conditions of the dacite magma(s). Because the dominant phase assemblage and phase compositions are identical for 1846-7 lava and 1932 pumice, our work applies to both eruptions, providing a robust baseline from which shortly pre- and syn-eruptive processes can be analyzed for the past eruptions and during future eruptive crises.

3.1.1 Geologic Background

3.1.1.1 Regional setting

Volcán Quizapu is located in the Maule region of Chile, roughly 300 km south of Santiago (Figure 3.1). The surrounding volcanic field is host to at least 12 Holocene vents and/or eruptive deposits, which range from basalt to rhyolite (Hildreth and Drake 1992). Cerro Azul itself is a composite cone with basal flows < 400 ka, whose eruptive products span nearly the entire compositional range of the volcanic field (Drake 1976; Hildreth and Drake 1992). Less than 10 km to the north is the edifice of Descabezado Grande, a similar-aged stratovolcano. Cerro Manantial Pelado to the northwest, the craters of La Resolana to the west, and Los Hornitos cinder cones to the south make up the prominent mafic centers in the field. The 150-300 ka Loma Seca Tuff forms a large plateau at the eastern end of the field, with the associated Calabozos caldera to the northeast (Grunder and Mahood 1988; Hildreth et al. 1984). Basement rocks of the 7 Ma Invernada pluton are exposed to the southeast (Drake 1976). There is some evidence for interconnectivity of volcanic centers in the region, perhaps associated with extensional stresses along the arc, expressed dominantly by the Liquiñe-Ofqui fault zone and associated splays (Cembrano and Lara 2009). In addition, 2-3 months after the Plinian eruption of Quizapu in 1932, a 600-m wide crater appeared on the north flank of Descabezado Grande (Fuenzalida 1942), essentially along an axis linking the stratovolcanoes and Quizapu vent. Although no juvenile material was expelled, ash plumes several kilometers high were visible sporadically for months (Hildreth and Drake 1992). Thus, despite the overwhelmingly dacitic nature of the eruptive products at Quizapu, the setting is rich with possibility for interactions between magmas that span the gamut of calc-alkaline compositions.

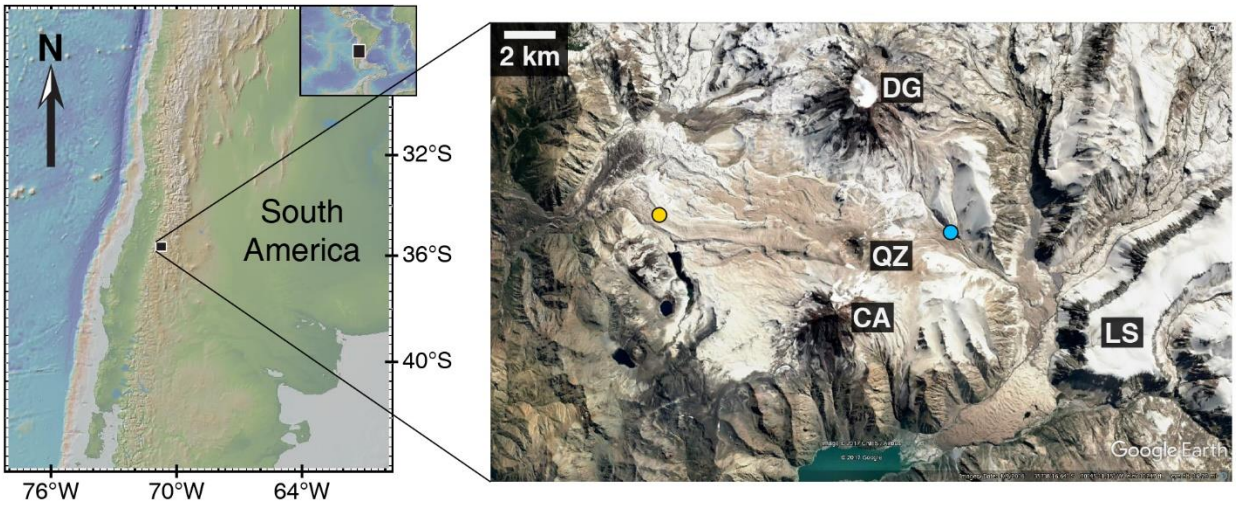

Figure 3.1. Location of Volcán Quizapu. Overview image at left modified from GeoMapApp; image at right from GoogleEarth. Blue point is where pumice sample was collected, yellow lava. Quizapu crater is to the left of QZ label. Note the similar crater on the north flank of Descabezado Grande. Multiple lobes of the 1846-7 lava flows are visible, mainly extending to the northwest, with one large lobe filling the valley to the southeast. Bright white is snow, and light tan is the 1932 pumice blanket. QZ = Quizapu, CA = Cerro Azul, DG = Descabezado Grande, LS = Loma Seca tuff.

3.1.1.2 Eruptions at Quizapu

Magma from the first, chiefly effusive, eruption at Quizapu (1846-1847) is thought to have interacted with a more mafic end-member. Lava flows range from homogeneous dacite to hybridized dacite-andesite mixtures. In many flow lobes, enclaves of andesite (~57 wt% SiO_2(Higgins et al. 2015) provide evidence for the involvement of more mafic material. Ruprecht and Bachmann (2010) postulate that this andesitic magma was volumetrically significant enough (10-45 vol% of most flow lobes) to both trigger the 1846 eruption and heat the main dacite body. In their analysis, this excess heat would have reduced the dacite viscosity enough to allow passive outgassing of volatiles.

Minor mafic scoria is also associated with the explosive 1932 eruption, but to a far lesser volumetric extent (< 5% of the deposit). This less evolved magma is only evident in three intervals in the fall deposit: an initial andesite scoria that passes via banded pumice to the dominant dacite, an intraplinian “brown band” of andesite and banded pumice, and a terminal basalt-andesite scoria layer (Hildreth and Drake 1992). Thus, limited magma interaction is evident in products from the Plinian eruption, but the mafic contribution was not significant enough to affect the overall dacite magma body in terms of composition or heat transfer (Ruprecht and Bachmann 2010).

3.1.2 Petrology of dacite end-member

3.1.2.1 Summary

Hildreth and Drake (1992) give a first overview of the Quizapu dacite petrology, expanded upon by Ruprecht et al. (2012). We briefly summarize here. End-member dacites from both the 1846-1847 and 1932 eruptions are indistinguishable in terms of phase assemblage and bulk composition (Table 3.1; Figure 3.2). They consist of ~15-20 vol% phenocrysts, mainly An_{25-40} plagioclase, with ~2 vol% each amphibole (dominantly magnesiohornblende) and orthopyroxene (En_{65-77}, $Wo_{<3}$). Subordinate clinopyroxene, titanomagnetite, ilmenite, apatite, and sulfide blebs each make up < 1 vol% of the material. Pumice clasts from 1932 lack microlites. Many 1846-1847 lavas contain plagioclase (and other) microlites, although their origin has been attributed to the andesitic recharge magma (Ruprecht and Bachmann 2010; Ruprecht et al. 2012).

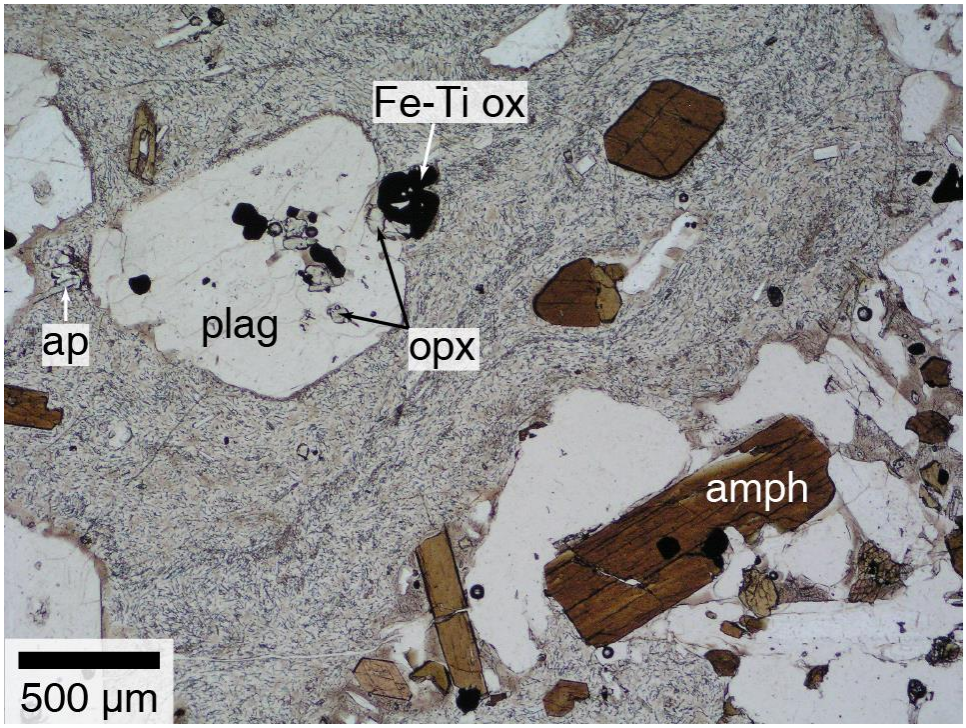

Figure 3.2. Transmitted light image of Quizapu lava VQ-06-06. The groundmass contains microlites and glass. amph = amphibole, ap = apatite, Fe-Ti ox = iron-titanium oxide (magnetite or ilmenite), opx = orthopyroxene, plag = plagioclase.

3.1.2.2 Estimates of magma storage conditions

Attempts have been made to link the above phase assemblage to a set of pre-eruptive magma storage conditions. Temperature and fO_2 estimates based on the compositions of Fe-Ti oxides or amphibole are broadly in agreement, converging around 835-885 °C and NNO+0.5 to

NNO+1 (Hildreth and Drake 1992; Ruprecht and Bachmann 2010; Ruprecht et al. 2012), although some Fe-Ti oxide pairs in the 1846-1847 end-member dacite yield temperatures up to 956 °C (Ruprecht et al. 2012). Probable storage pressures are currently based solely on amphibole barometry, and range from 120-180 MPa (Ruprecht et al. 2012). The water content of the magma is estimated at 3.5-5.5 wt% H_2O using amphibole compositions, or a slightly higher 4-6 wt% H_2O using plagioclase-liquid hygrometry (Ruprecht et al. 2012). These assessments of the magmatic environment beneath Quizapu delineate a general range of conditions that inform the initial placement of experiments in pressure-temperature space.

3.1.3 Aim of this contribution

Although the pressure, temperature, water, and fO_2 estimates derived from the natural Quizapu dacite phases are reasonable to a first order, laboratory experiments can help refine the nature of the pre-eruptive storage region. Published geothermometers and geobarometers have relatively large error bars (Putirka 2008), and some lack a thermodynamic basis (e.g., Ridolfi and Renzulli 2012). In performing calculations that are calibrated with experimental data, any deviation from the calibration set can induce significant errors in the results. For example, Quizapu amphibole crystals are more Cl-rich than any used to derive the chemometric equations of Ridolfi and Renzulli (2012). Because ambient magmatic conditions prior to eruption are the critical baseline from which all perturbations and syn-eruptive processes are evaluated, determining these conditions for the Quizapu system is essential. Driven by the absence of experimental data on the Quizapu dacite, and the possibility that it is not well-represented in thermobarometric calibration sets, we present a suite of water-saturated phase equilibrium experiments aimed at deducing the pre-eruptive storage conditions of the dacite magma prior to the 1846-1847 and 1932 eruptions.

3.2 METHODS

3.2.1 Starting materials and experimental strategy

All experiments were conducted at the University of Hawaii (Table 3.2). Two nearly isochemical samples were chosen to represent the end-member dacite from each eruption: lava VQ-06-06 from the 1846-7 eruption and pumice VQ-07-37 D from the 1932 eruption (Table 3.1). The starting materials were crushed and sieved to < 1.4 mm, and 0.2-0.3 g aliquots were loaded into 5 mm outer diameter Ag or $Ag_{70}Pd_{30}$ capsules. Enough deionized water was added to each capsule to exceed saturation (Moore et al. 1998), typically 5-10 wt% H_2O depending on

Table 3.1. Bulk composition of starting materials[a].

	VQ-06-06 lava	VQ-07-37 D pumice
SiO_2	65.89	66.41
TiO_2	0.56	0.54
Al_2O_3	15.62	15.5
FeO*	3.09	2.94
MnO	0.09	0.09
MgO	0.95	0.86
CaO	2.48	2.36
Na_2O	5.17	5.15
K_2O	3.19	3.28
P_2O_5	0.15	0.14
Total (dry)	97.2	97.3

a. Analyses from Ruprecht et al. (2012), Table 1

pressure. Chlorine was added to two experiments as HCl (Table 3.2). Capsules were crimped to a triple junction, then sealed using a Lampert PUK U4 tungsten inert gas impulse micro welder. In 15 experiments, secondary capsules of 4 mm outer diameter were filled with material from low-pressure experiments, crimped shut without welding, and placed inside the 5 mm capsule containing the initial starting material. These "reversal" experiments approached equilibrium from two directions, typically such that the original starting material crystallized to reach equilibrium, and the previously-run material melted. All experiments were conducted in Lindbergh/Blue M tube furnaces with Waspaloy vessels, using a cold-seal water-medium pressure line. Temperature was monitored with Omega K-type thermocouples (± 6.4 °C). Relative pressure changes were tracked with an Omega DP41-S strain gauge transducer (± 0.01 MPa), and absolute pressure was monitored with a Heise CM mechanical pressure gauge (± 0.5 MPa). Oxygen fugacity (fO_2) for most experiments was two log units below the Ni-NiO buffer (NNO-2), for reasons detailed below. Run duration varied from 7 to 14 days, and quenches were performed by air-cooling the vessel for ~15 seconds and then plunging it into a bucket of water, while pressurized. The samples are estimated to cool by 300 °C within 6 s (Brugger and Hammer 2010).

The experimental setup employed has a well-established intrinsic fO_2, set by the vessel, Ni filler rods, and pressurizing H_2O. Reported conditions range from NNO-0.3 (Muir et al. 2014) to NNO+1 ± 0.5 (Gardner et al. 1995a; Geschwind and Rutherford 1992). However, for most of

our runs, the water line at the University of Hawaii contained a small amount of polyethylene glycol (~5 mL per 100 mL H_2O) as a rust preventative. This substance precipitated undesired carbon-bearing compounds in the vessels, resulting in an fO_2 reduction inside sealed capsules via H_2 exchange (Eugster and Skippen 1967). A solid-state sensor composed of Ni, NiO, and MnO was run in identical sealed capsules for 7 days and analyzed by EDS, revealing that the ambient fO_2 was NNO-2.1 ± 0.2 (Taylor et al. 1992). This value corresponds exactly to the carbon-carbon monoxide-carbon dioxide buffer (CCO), as defined by (Jakobsson and Oskarsson 1994). After thoroughly flushing the line with pure H_2O and reaming out all carbon material from the vessels, another NiMnO solid-state sensor, along with a solid-state CoPd sensor, was run for 7 days. The results of this test revealed an fO_2 of NNO+0.2, and green NiO was present on the Ni rods at the end of the run.

Three experiments were run in the clean line, using new Waspaloy vessels. Each of these experiments replicated the temperature and pressure conditions of one of the experiments inadvertently run at NNO-2. Glass analyses of the NNO+0.2 experiments did not reveal any systematic differences from the NNO-2 experiments (Table 3.3). For example, in one case glass SiO_2 was higher in the more reducing run, in another it was lower, and in the third it was the same at both fO_2 conditions. This lack of systematic variation holds for every glass oxide measured. The Fe-Ti oxides in the three more oxidizing runs lack the disequilibrium features observed in NNO-2 experimental Fe-Ti oxides. However, neither Fe-Ti oxide minerals, glass FeO, TiO_2, nor MgO were used to determine pre-eruptive storage conditions. Previous experimental studies have concluded that the effect of fO_2 on phase stability of non-oxide minerals in intermediate to silicic magmas is minimal (e.g., Eggler and Burnham 1973; Riker et al. 2015; Spear 1981). Therefore, lower fO_2, while important for the stability of Fe-Ti oxide minerals and the composition of Fe-Mg silicates, does not inhibit the robust determination of pre-eruptive storage conditions for the Quizapu dacite. Calculations and conclusions use the NNO+0.2 data along with the NNO-2 suite.

3.2.2 Attainment of equilibrium

The experiments in this study are of the "partial equilibrium" type described by Pichavant et al. (2007), meaning that the expectation of equilibrium is limited to melt, phenocryst rims, and microlites. Total equilibrium experiments using a powdered bulk starting material would not yield appropriate results, because phenocrysts in arc magmas may have

Table 3.2. Experimental run table.

Run ID[a]	Starting Material[b]	Duration (h)	T (°C)	P (MPa)	Phases present[c]
1	lava	169	875	125	gl, plag, [amph], opx, Capx, [mt], [ilm], ap
4	lava	169	875	50	gl, plag, [amph], opx, Capx, [mt], [ilm], ap, gl
5	lava	213	875	35	gl, plag, [amph], opx, Capx, Fepx, [mt], [ilm], ap
6	lava	208	890	35	gl, plag, [amph], opx, Capx, [mt], [ilm], ap
7A	lava	188	850	100	gl, plag, [amph], opx, Capx, [mt], [ilm], ap, sf
7B	5	188	850	100	gl, plag, [amph], opx, Capx, [mt], [ilm], ap
8A	lava	189	875	100	gl, plag, [amph], opx, Capx, [mt], [ilm], ap
8B	5	189	875	100	gl, plag, [amph], opx, Capx, [mt], [ilm], ap
9A	lava	168	850	175	gl, plag, amph, opx, Capx, [mt], [ilm], ap, bt
9B	6	168	850	175	gl, plag, amph, opx, Capx, [mt], [ilm], ap, bt
10A	lava	168	875	175	gl, plag, amph, opx, Capx, Fepx, [mt], [ilm], ap, bt
10B	6	168	875	175	gl, plag, amph, opx, Capx, Fepx, [mt], [ilm], ap, bt
11A[d]	lava	243	875	50	gl, plag, [amph], opx, Capx, [mt], [ilm], ap
11B[d]	6	243	875	50	gl, plag, [amph], opx, Capx, [mt], [ilm], ap
12A	lava	193	875	75	gl, plag, [amph], opx, Capx, [mt], [ilm], ap
12B	6	193	875	75	gl, plag, [amph], opx, Capx, [mt], [ilm], ap
13	lava	169	890	50	gl, plag, [amph], opx, Capx, [mt], [ilm], ap, sf
14	lava	169	890	50	gl, plag, [amph], opx, Capx, [mt], [ilm], ap
15A	lava	214	835	150	gl, plag, amph, opx, Capx, [mt], [ilm], ap, bt
15B	13	214	835	150	gl, plag, amph, opx, Capx, [mt], [ilm], ap, bt
17A	lava	172	860	150	gl, plag, amph, opx, Capx, [mt], [ilm], ap
17B	13	172	860	150	gl, plag, amph, opx, Capx, [mt], [ilm], ap
18A	lava	171	875	150	gl, plag, amph, opx, Capx, [mt], [ilm], ap
18B	13	171	875	150	gl, plag, amph, opx, Capx, [mt], [ilm], ap
19A	lava	171	890	125	gl, plag, [amph], opx, Capx, [mt], [ilm], ap, sf
19B	13	171	890	125	gl, plag, [amph], opx, Capx, [mt], [ilm], ap
20A	lava	172	860	125	gl, plag, amph, opx, Capx, [mt], [ilm], ap
20B	14	172	860	125	gl, plag, amph, opx, Capx, [mt], [ilm], ap
21A	lava	193	850	125	gl, plag, amph, opx, Capx, [mt], [ilm], ap
21B	14	193	850	125	gl, plag, amph, opx, Capx, [mt], [ilm], ap
22A	lava	193	835	125	gl, plag, amph, opx, Capx, [mt], [ilm], ap, bt
22B	14	193	835	125	gl, plag, amph, opx, Capx, [mt], [ilm], ap, bt
23A[e]	lava	238	875	100	gl, plag, [amph], opx, Capx, [mt], [ilm], ap
23B[e]	14	238	875	100	gl, plag, [amph], opx, Capx, [mt], [ilm], ap
24A	pumice	341	850	150	gl, plag, amph, opx, Fepx, [mt], [ilm], ap, bt, sf
24B	lava	341	850	150	gl, plag, amph, opx, Capx, [mt], [ilm], ap, bt
25A	pumice	336	835	175	gl, plag, amph, opx, Fepx, [mt], [ilm], ap, bt
25B	lava	336	835	175	gl, plag, amph, opx, Capx, Fepx, [mt], [ilm], ap, bt
27	pumice	337	810	175	gl, plag, amph, [opx], Fepx, [mt], [ilm], ap, bt
28A	pumice	336	810	125	gl, plag, amph, [opx], Fepx, [mt], [ilm], ap, bt
28B	lava	336	810	125	gl, plag, amph, [opx], Fepx, [mt], [ilm], ap, bt

Table 3.2, *continued*.

29	pumice	337	810	150	gl, plag, amph, [opx], Fepx, [mt], [ilm], ap, bt
30A	pumice	168	890	175	gl, plag, amph, opx, Capx, Fepx, [mt], [ilm], ap
30B	lava	168	890	175	gl, plag, amph, opx, Capx, Fepx, [mt], [ilm], ap
31	pumice	336	810	200	gl, plag, amph, [opx], Fepx, [mt], [ilm], ap, bt
32	pumice	336	835	200	gl, plag, amph, [opx], Capx, Fepx, [mt], [ilm], ap, bt
33	pumice	261	850	200	gl, plag, amph, [opx], [mt], [ilm], ap, bt
34[f]	pumice	338	860	125	gl, plag, amph, opx, Capx, [mt], [ilm], ap
35[f]	pumice	338	835	150	gl, plag, amph, [opx], Capx, [mt], [ilm], ap, bt, sf
36[f]	pumice	338	810	175	gl, plag, amph, [opx], Capx, [mt], [ilm], ap, bt

a. Run ID B indicates secondary capsule within primary A capsule.

b. Numbers in the "Starting Material" column indicate the Run ID of previously-run material.

c. gl = glass, plag = plagioclase, amph = amphibole, opx = orthopyroxene, Capx = pyroxene richer in Ca than the opx, Fepx = pyroxene richer in Fe than the opx, mt = titanomagnetite, ilm = hemoilmenite, ap = apatite, sf = sulfide, bt = biotite, [brackets] indicate unstable phases

d. 0.34 wt% Cl added

e. 0.51 wt% Cl added

f. fO_2 = NNO+0.2

experienced a range of conditions prior to their residence in the pre-eruptive magma chamber. Thus, phenocrysts were intentionally left intact to prevent interaction of melt with crystal cores (Hammer 2008). Using a synthetic material necessitates either superheating, which affects phase textures and compositions (First and Hammer 2016), or risking that the material does not homogenize prior to experimentation. Given these constraints, natural starting material was used and partial equilibrium experiments were performed. Microprobe analyses were taken on rims, growth protuberances, and microlites – features likely to have been grown or modified during the experiments.

Durations of 7-14 days are in line with similar partial equilibrium experiments on moderately silicic magmas, for which partial equilibration was achieved (Costa et al. 2004; Hammer et al. 2002; Rutherford and Devine 1996). The homogeneity of experimental glass compositions is one measure of equilibrium. On average, glass analyses for individual experiments in this study have a relative standard deviation (RSD) of $\leq 1\%$ for SiO_2, Al_2O_3, and K_2O, and $\leq 6\%$ for other major elements, indicating good homogeneity. Comparison of forward and reverse experiments at various pressure-temperature conditions shows that they arrived at similar final states, in terms of phase presence and composition. Achieving a similar final state via these two different processes is a good indication that partial equilibrium was achieved (e.g., Médard and Grove 2008; Wyllie et al. 1981). Amphibole is an exception in some cases. After de-

stabilizing at low pressure, the experimental durations were not long enough in every case to recover cleanly faceted, un-rimmed amphibole phenocrysts, although further breakdown was avoided. Apparently, surmounting the energy barrier to resorb the breakdown rim and grow new amphibole simultaneously is difficult near equilibrium. Experiments run at the same conditions but with different starting materials (pumice versus lava) also arrived at similar final states. Experimental glass compositions display robust trends with temperature and pressure, even when averaged over all starting materials, further suggesting that a state of partial equilibrium was achieved in all runs. Thus, our experimental set closely approximates equilibrium for the conditions and durations applied, and results do not change with the choice of pumice versus lava starting material.

3.2.3 Electron microscopy

3.2.3.1 Scanning electron microscopy

Many experimental samples were examined using the JEOL 5900 LV scanning electron microscope (SEM) in the W. M. Keck Cosmochemistry lab at the University of Hawaii. Images were acquired in backscatter electron mode (BSE), and semi-quantitative spot analyses of mineral phases were obtained by electron-dispersive spectrometry, typically with an accelerating voltage of 15 keV.

3.2.3.2 Electron microprobe analyses

The starting materials and subsets of the experimental sample suite were imaged, and analyzed with wavelength-dispersive spectrometry, using the JEOL Hyperprobe JXA-8500F electron microprobe at the University of Hawaii. Glass, plagioclase, and amphibole analyses used a 15 keV accelerating voltage and a 10 nA beam current, whereas Fe-Ti oxides were analyzed with 20 keV and 25 nA. Probe for EPMA software, which applies the Armstrong/Love Scott algorithm for matrix corrections (Armstrong 1988), was used for raw data reduction and output. For all analyses, the takeoff angle was 40 degrees. High and low off-peak counting times were each half of the on-peak time. Background fits were linear for all elements in all phases, except for Cr in Fe-Ti oxides, which was exponential. Standards are published in (Jarosewich et al. 1980) or are in-house standards. On-peak counting times for glass analyses were 30 s (Fe,Mn), 35 s (Si, Ti, Na, K, P), 60 s (Ca), and 65 s (Al, Mg, Cl). Calibration standards were synthetic glass STG-72 (Si, Al, Fe, Mg), sphene glass (Ti), Verma garnet (Mn), fluor-apatite USNM 104021 (Ca, P), Amelia albite (Na), orthoclase OR-1 (K), and scapolite (Cl). Repeated

Table 3.3. Average matrix glass compositions (wt%) of starting materials and experimental products.

Sample	n	T (°C)	P (MPa)	SiO_2	σ [a]	TiO_2	σ	Al_2O_3	σ	FeO	σ	MnO	σ	MgO	σ	CaO	σ	Na_2O	σ	K_2O	σ	P_2O_5	σ	Cl	σ
pumice	11	-	-	71.56	16	0.34	03	15.18	11	1.67	07	0.07	02	0.34	01	1.11	02	5.43	18	4.08	05	0.05	01	0.17	02
lava	3	-	-	71.94	09	0.36	06	15.21	24	1.55	10	0.05	00	0.16	04	0.84	02	5.20	11	4.53	08	0.06	-	0.12	01
9A	10	850	175	71.01	44	0.29	02	15.67	24	2.01	11	0.06	01	0.30	01	1.39	07	5.24	08	3.89	03	0.06	02	0.09	01
9B	8	850	175	70.96	39	0.27	04	15.47	23	1.99	08	0.05	01	0.29	01	1.36	04	5.58	15	3.91	03	0.06	02	0.06	01
10A	10	875	175	69.90	75	0.38	03	16.07	48	2.32	10	0.07	02	0.44	01	1.75	13	5.26	15	3.67	04	0.06	02	0.09	01
10B	10	875	175	70.33	65	0.35	02	15.66	40	2.14	14	0.07	02	0.40	02	1.59	12	5.60	14	3.76	03	0.05	01	0.06	01
15A	9	835	150	71.58	22	0.23	02	15.55	18	1.88	08	0.06	01	0.23	01	1.21	03	5.11	12	4.03	03	0.06	01	0.09	01
15B	10	835	150	71.63	13	0.22	02	15.59	07	1.72	06	0.06	01	0.22	02	1.21	04	5.18	15	4.06	03	0.05	02	0.09	01
17A	10	860	150	70.06	19	0.34	02	16.21	10	2.14	05	0.08	03	0.39	02	1.65	03	5.26	07	3.73	13	0.07	01	0.10	01
17B	9	860	150	70.63	47	0.29	02	15.56	26	2.14	14	0.07	02	0.33	01	1.50	07	5.53	25	3.83	03	0.06	01	0.07	01
18A	9	875	150	70.62	49	0.37	03	15.64	36	2.33	07	0.07	01	0.42	02	1.59	08	5.13	12	3.68	05	0.07	01	0.10	01
18B	10	875	150	69.94	29	0.33	02	15.99	25	2.08	13	0.07	01	0.41	02	1.64	05	5.64	14	3.78	02	0.05	01	0.08	01
20A	10	860	125	71.21	21	0.32	02	15.23	09	1.93	11	0.06	01	0.30	02	1.21	03	5.53	10	4.09	04	0.05	01	0.09	01
20B	10	860	125	71.45	15	0.30	01	15.15	10	1.94	10	0.06	01	0.27	01	1.18	03	5.44	11	4.09	02	0.05	02	0.08	02
21A	10	850	125	71.52	16	0.25	02	15.49	07	1.87	09	0.07	02	0.24	01	1.17	03	5.12	09	4.12	03	0.06	02	0.10	01
21B	10	850	125	71.50	16	0.23	04	15.20	06	1.85	08	0.07	02	0.22	01	1.11	02	5.55	15	4.17	03	0.06	03	0.06	01
22A	7	835	125	72.19	18	0.23	04	15.20	05	1.75	10	0.06	02	0.19	01	0.97	04	4.98	08	4.29	04	0.06	02	0.10	01
22B	9	835	125	72.51	11	0.21	02	15.28	08	1.52	11	0.05	01	0.18	01	0.91	02	4.84	11	4.37	06	0.05	01	0.09	01
24A	2	850	150	72.15	37	0.28	01	14.97	16	1.67	06	0.06	-	0.24	00	1.06	01	5.38	07	4.13	04	0.06	-	0.04	01

Table 3.3, *continued*.

24B	10	850	150	71.46	50	0.23	02	15.28	23	1.91	11	0.07	02	0.26	01	1.21	07	5.46	12	4.01	05	0.05	02	0.08	02
25A	11	835	175	70.88	33	0.21	02	15.64	19	2.00	11	0.07	02	0.28	01	1.44	05	5.55	11	3.79	05	0.06	02	0.10	01
25B	10	835	175	71.37	68	0.22	03	15.52	14	1.90	06	0.06	01	0.26	01	1.35	04	5.27	76	3.89	04	0.06	02	0.10	01
27	10	810	175	72.38	14	0.14	03	14.95	08	1.68	12	0.06	01	0.14	01	0.99	03	5.44	09	4.09	04	0.04	00	0.10	02
28A	10	810	125	73.62	36	0.16	05	14.45	14	1.38	21	0.07	02	0.16	11	0.74	03	4.98	14	4.36	06	0.04	01	0.07	01
28B	10	810	125	73.73	16	0.16	02	14.31	19	1.32	05	0.06	01	0.13	02	0.76	06	4.98	17	4.43	05	0.05	02	0.07	02
29	10	810	150	72.47	18	0.15	03	14.80	08	1.65	06	0.06	02	0.14	01	0.97	03	5.43	08	4.20	03	0.05	01	0.11	01
30A	10	890	175	69.78	26	0.33	03	15.83	21	2.24	09	0.08	03	0.49	01	1.80	06	5.62	09	3.70	02	0.06	04	0.10	01
30B	10	890	175	68.99	101[b]	0.35	04	16.09	50	2.67	34	0.07	02	0.50	05	1.91	19	5.62	10	3.64	06	0.08	02	0.07	01
31	10	810	200	71.57	17	0.17	04	15.44	07	1.74	07	0.08	02	0.18	02	1.27	03	5.56	14	3.88	05	0.05	01	0.09	01
32	10	835	200	70.45	47	0.23	02	15.89	20	2.01	16	0.07	02	0.26	01	1.60	05	5.61	11	3.74	04	0.05	01	0.10	01
33	10	850	200	70.99	43	0.27	06	15.60	28	1.82	09	0.07	02	0.27	01	1.46	08	5.54	20	3.86	03	0.04	01	0.10	01
34	8	860	125	71.22	22	0.31	02	15.63	07	1.84	08	0.08	02	0.33	02	1.34	05	5.06	10	4.02	04	0.05	01	0.12	01
35	9	835	150	72.64	19	0.24	03	14.93	08	1.48	05	0.07	02	0.21	02	0.95	02	5.08	10	4.26	02	0.06	01	0.13	01
36	10	810	175	72.03	14	0.26	02	15.57	05	1.26	05	0.07	02	0.24	02	1.19	03	5.17	15	4.07	03	0.04	00	0.10	00
1σ of EPMA standard [c] n=130				0.28		0.03		0.11		0.07		0.02		0.02		0.03		0.07		0.05		0.02		0.01	

a. Numbers in the columns to the right of each oxide column indicate 1 σ variance after the decimal (i.e., "50" = 0.50 wt% variance)

b. σ =1.01 wt%

c. Standard STG72, in-house synthetic glass standard

analyses of STG-72 or STG-56 were used to assess and correct for analytical drift. The beam diameter was 15 μm where possible, and never < 5 μm. Given the instability of Na in hydrous glass under the electron beam, automated time-dependent intensity (TDI) corrections were applied to all unknowns by assessing Na count rates five times over the course of each spot analysis. Count rates always decreased with time under the beam, although larger beam diameters somewhat mitigated the effect, as the correction percentage ranged from 5-25% for 10 and 15 μm diameters, 10-35% for 7 μm diameter, and 15-50% for 5 μm diameter. TDI corrections were also applied to Si for analyses showing a clear positive trend in Si count rate with time, although the correction percentages were low, typically on the order of 0.5-1%.

For plagioclase analyses, on-peak counting times were 45 s (Si, Mg, Ca, Na, K) and 90 s (Al, Fe). Calibration standards were Lake County plagioclase USNM 115900 (Al, Ca, Na), andesine AC 362 (Si), Springwater olivine USNM 2566 (Fe, Mg), and orthoclase OR-1 (K). Repeated analyses of Lake County plagioclase were used to assess and correct for analytical drift. The beam diameter was typically 1 μm due to the small size of experimental microlites and rims. A 5 μm beam was used for standards. TDI corrections were applied to Na for most unknowns (i.e., those for which a clear negative trend in count rate with time was apparent).

Amphibole analyses measured Si, Ti, Al, Fe, Mn, Mg, Ca, Na, K, and Cl, all with 40 s on-peak counting times. Calibration standards were UCLA diopside (Si, Mg, Ca), sphene glass (Ti), Verma garnet (Al, Fe, Mn), Amelia albite (Na), orthoclase OR-1 (K), and scapolite (Cl). Repeated analyses of diopside USNM 117733 were used to assess and correct for analytical drift. The beam diameter ranged from 1-10 μm for unknowns, and 10 μm for standards. Amphibole formulas were calculated based on the standard formula $A_{0\text{-}1}B_2C_5T_8O_{22}(OH,F,Cl)_2$, using a 23(O) basis and assuming 2(OH, Cl, F) (Leake 1978). Two schemes were averaged to arrive at the final formulas prior to site assignment: sum to 13 cations excluding Ca, Na, and K; sum to 13 cations excluding Ca, Na, K, and Mn (Robinson et al. 1982). Water and F were calculated by difference, for site assignments only.

Analyses of Fe-Ti oxides had on-peak counting times of 30 s (Si, Al, Cr, Fe, Mn, V) and 65 s (Ti, Mg). Calibration standards were Verma garnet (Si, Mn), sphene glass (Ti), chromite USNM 117075 (Al, Cr, Mg), Minas Gerais magnetite USNM 114887 (Fe), and V_4O (V). Repeated analyses of both sphene glass and chromite USNM 117075 were used to assess and correct for analytical drift. Corrections were applied for the interference of Cr on Mn and of Ti

on V (Donovan et al. 1993), using interference standards Cr_2O_3 (Cr) and sphene glass (Ti). The beam diameter varied from focused to 5 μm, and 10 μm for standards. Analyses were re-calculated to account for Fe speciation, using the method of Droop (1987).

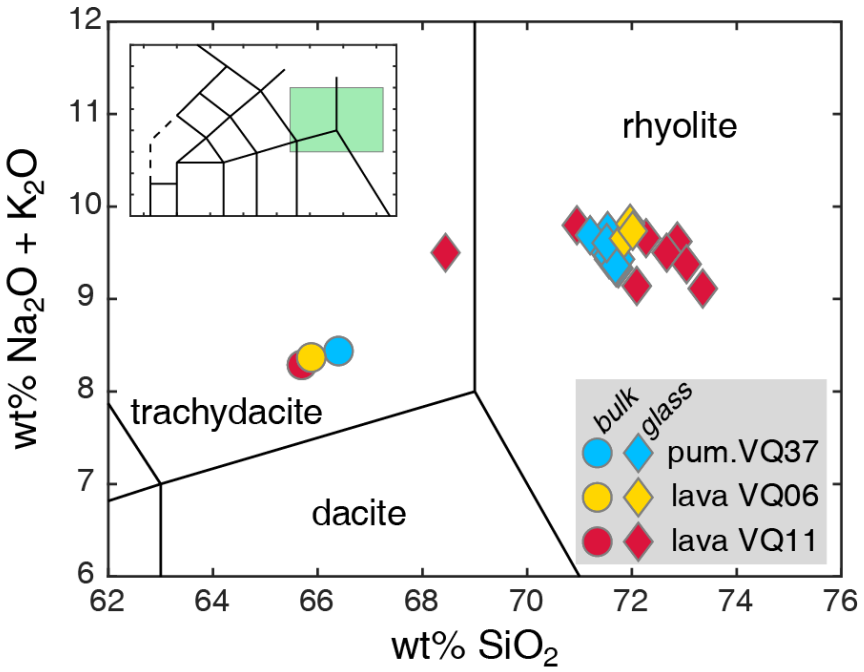

Figure 3.3. Total alkali-silica diagram of Quizapu starting materials (pumice VQ-07-37 D and lava VQ-06-06) and a nearly identical lava sample (VQ-06-11). Bulk analyses and VQ-06-11 glass from Ruprecht et al., 2012; other glass this study. The pumice glass analysis is the first glass geochemistry reported for a 1932 pumice.

3.3 RESULTS

3.3.1 Natural Materials

Extensive descriptions of the volcanic products from Quizapu are provided in Hildreth and Drake (1992), Ruprecht et al. (2012), and Higgins et al. (2015). Here, we briefly report additional observations from our study of the two starting materials, lava VQ-06-06 and pumice VQ-07-37 D. Glass and Fe-Ti oxides were analyzed by EPMA in both samples. Plagioclase microlites and amphibole phenocrysts were also analyzed in VQ-06-06.

Bulk compositions, though referred to as dacites, are slightly more alkalic, falling in the trachydacite field, while the residual glass of both the lava and pumice samples is rhyolitic (Figure 3.3). Fe-Ti oxides in both starting materials were analyzed, yielding compositions similar to those previously reported for the same samples (Ruprecht et al. 2012), though significantly lower in V and Mn (Figure 3.4c-d). Our analyses of ilmenite also have lower Mg# and higher Ti (Figure 3.4b). The Fe-Ti oxides in both starting materials average within error of each other

$Mt_{68}Usp_{32}$ for the spinel phase ("magnetite") and $Hm_{15}Ilm_{85}$ for the rhombohedral phase ("ilmenite"), using the end-member recalculation scheme of Buddington and Lindsley (1964). We report previously unrecognized zoning in both magnetite and ilmenite from VQ-06-06 (Figure 3.5). The zones are visible in backscatter with maximum contrast settings, but the compositional differences between them are far less than the overall range for the sample. This is illustrated with magnetite EPMA points 1-4 in Figures 3.4a and 3.5a, and ilmenite EPMA points 1-3 in Figures 3.4b and 3.5b. One magnetite in VQ-07-05 D displays fine-scale crosshatching (Figure 3.5c). In addition to magnetite and ilmenite, a nearly pure Fe-O phase with pervasive melt pockets is present in both the lava and the pumice (Figure 3.5d). This phase is completely

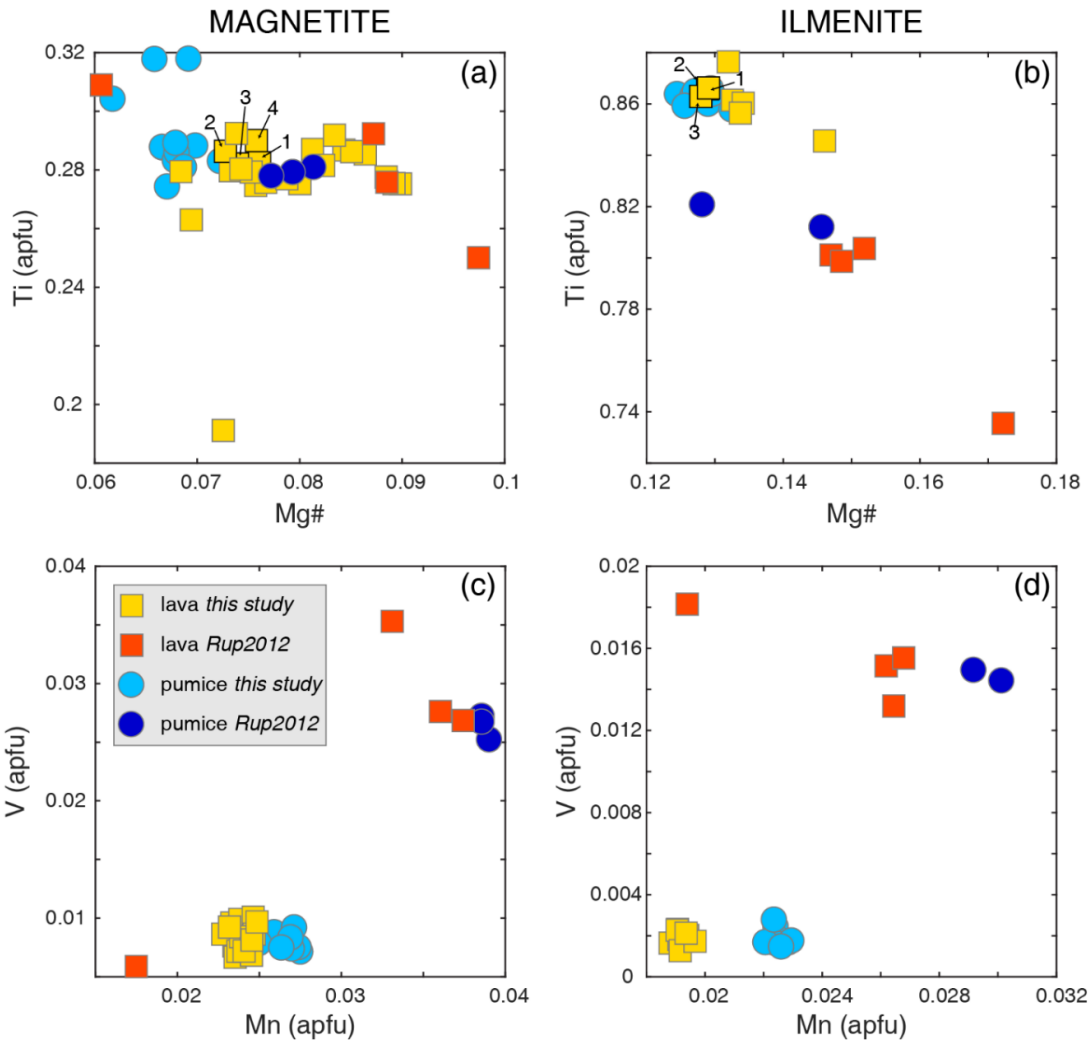

Figure 3.4. Composition of natural Fe-Ti oxides from this study and as reported in Ruprecht et al., 2012, for lava VQ-06-06 and pumice VQ-07-37 D. The apparent disagreements between the two studies are likely due to a lack of interference corrections in the EPMA data of Ruprecht et al. Thickly outlined and labeled squares correspond to the starred EPMA spot analyses in Figure 3.5. None are compositional outliers.

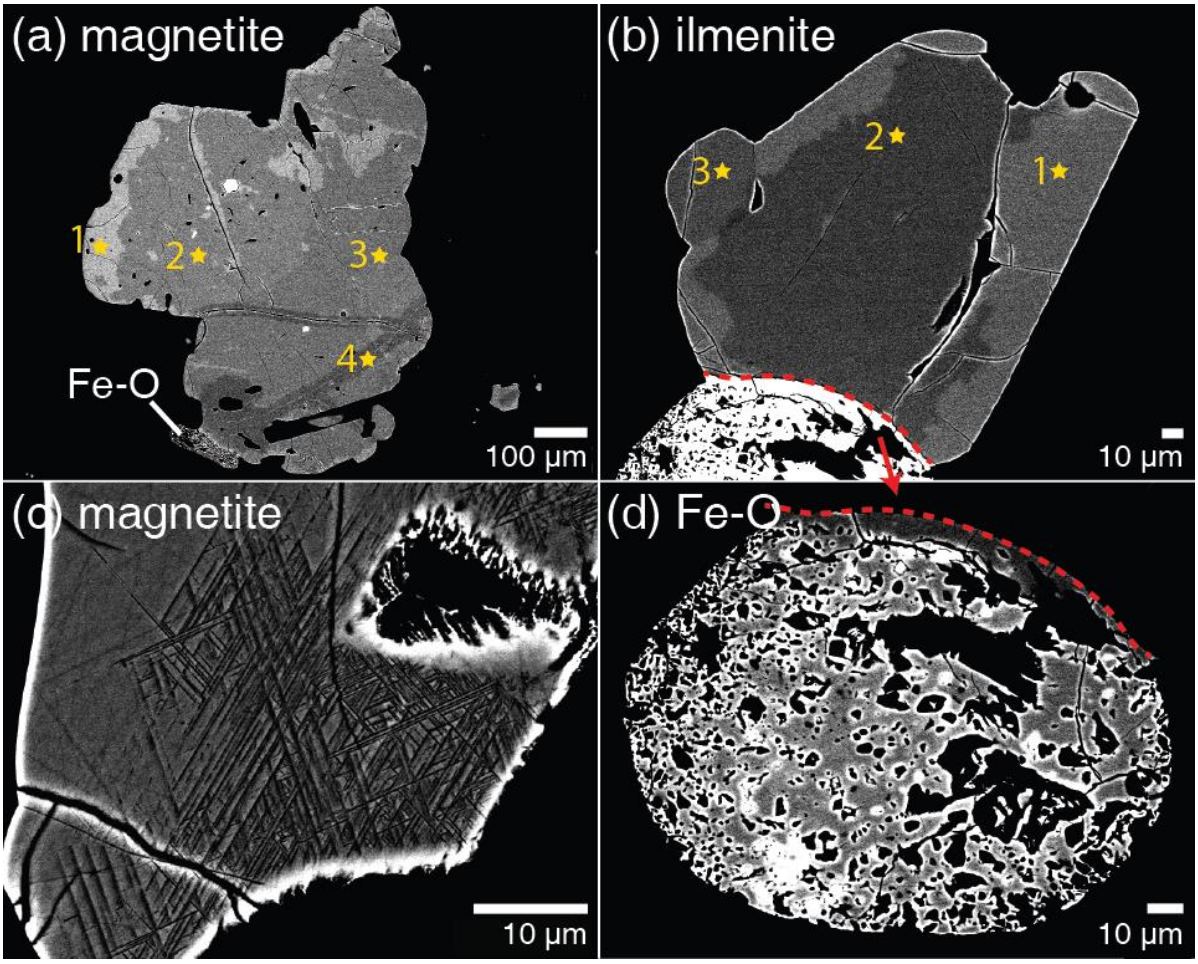

Figure 3.5. Backscatter electron (BSE) images of Fe-Ti oxides in the starting materials (lava a, b, d; pumice c). The zoning in (a) and (b) is visible only at maximum contrast, and EPMA analyses of the different zones do not yield appreciably different compositions (see Figure 3.4). The trellis feature in (c) is interpreted as rapid oxyexsolution during the 1932 eruption. The Fe-oxide in (d) is the same grain as the bright phase in (b). In (d), the main grain is a pure Fe-O phase (not hematite). The darker grey near the top of the grain is an area richer in Ti, and the bright white area in the southwest quadrant is an Fe-S phase.

opaque in transmitted light, with no hint of red, suggesting that it is not hematite. Our analyses of amphibole phenocrysts in VQ-06-06 and those of Ruprecht et al. (2012) show nearly complete overlap (Figure 3.6). In VQ-07-37 D, orthopyroxene is generally unzoned (Figure 3.7b), although irregular, non-concentric zoning is visible in one glomerocrystic grain (Figure 3.7a). Orthopyroxene in VQ-06-06 is subtly reversely zoned, with growth features evident on some BSE-darker rims (Figure 3.7c-d). Plagioclase microlites in VQ-06-06 are typically ~An20, though we report analyses as low as An18 and as high as An43. Compositional variations within single microlite crystals often show an hourglass morphology (Figure 3.8), and could represent sector zoning (e.g., Bryan 1972; Shea and Hammer 2013) or an infilled rapid growth morphology similar to the baby swallowtails in olivine (Faure et al. 2003).

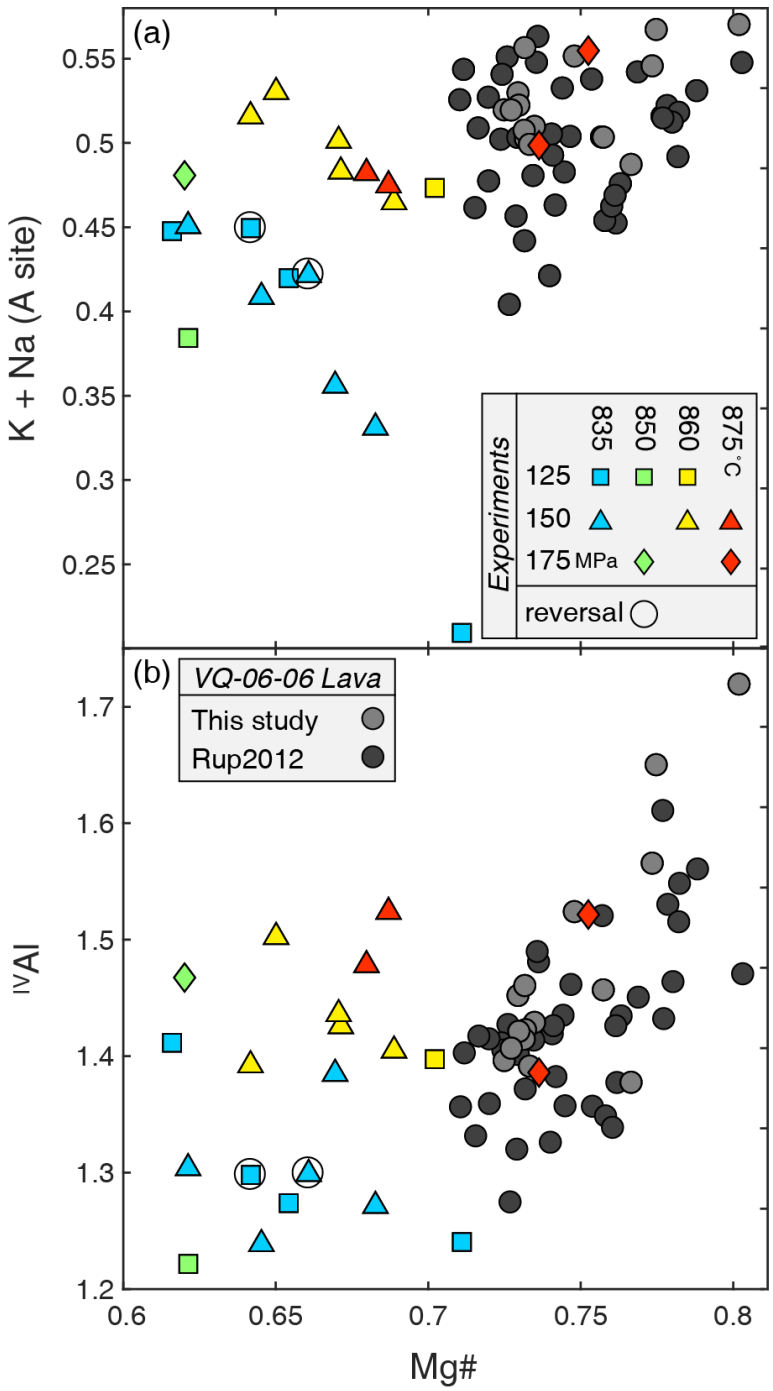

Figure 3.6. Composition of amphibole in experiments and Quizapu lava, for the subset of experiments analyzed (see Figure 3.9). The lower Mg# of experiments is a reflection of the relatively low fO_2 imposed. (a) Edenite exchange favors higher A site occupancy at higher temperature (b) Higher tetrahedral Al at higher temperature is the result of the same edenite exchange. Both (a) and (b) show that Fe-Mg exchange favors lower Mg# at higher temperature.

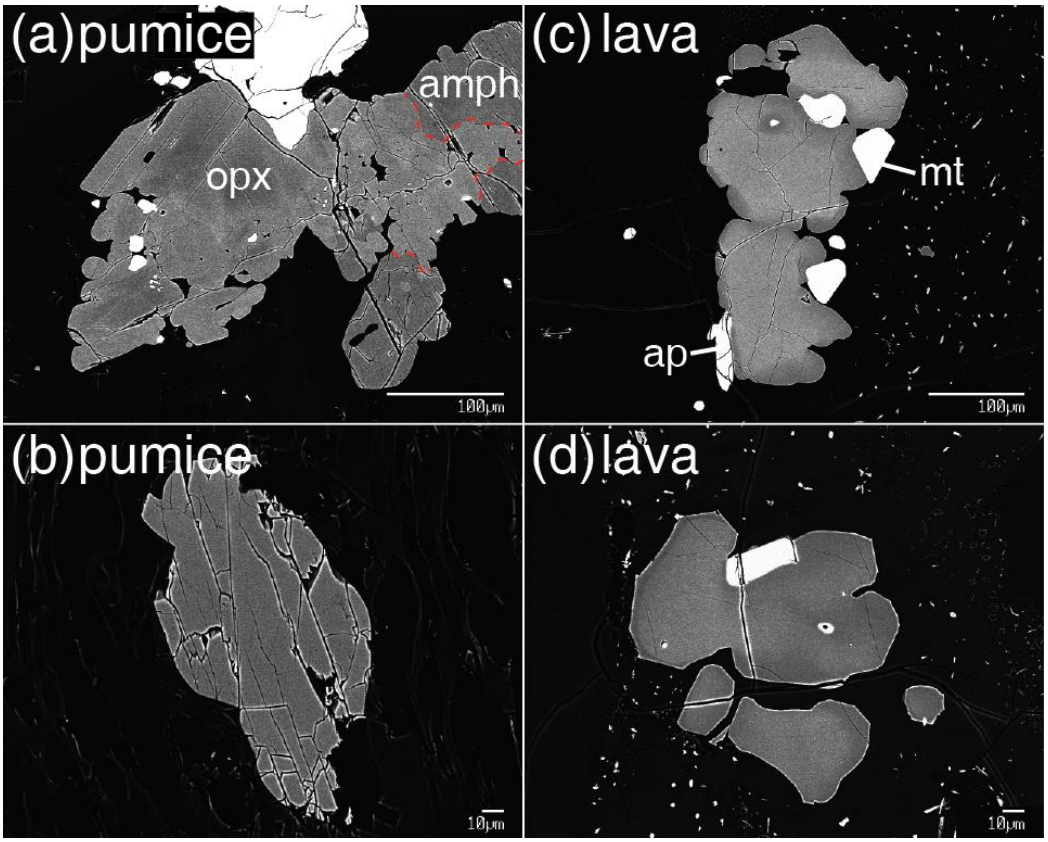

Figure 3.7. BSE images of orthopyroxene in starting materials. (a) Unevenly zoned orthopyroxene intergrown with amphibole in pumice, with the main grain boundaries marked in red. (b) Typical unzoned crystal in the Quizapu pumice. (c) Reverse zoning of orthopyroxene in the lava. (d) Ssubtle reverse zoning, and sharp growth faces on some edges. amph = amphibole, ap = apatite, mt = magnetite, opx = orthopyroxene.

3.3.2 Experimental Samples

Fifty-two successful experimental samples were produced at static P-T conditions, 49 at NNO-2 and three at NNO+0.2 (Table 3.2; Figure 3.9). All samples contain plagioclase, orthopyroxene, apatite, and glass. Ca-rich pyroxene is present in lesser abundance in most runs. Amphibole and Fe-Ti oxides are physically present in all samples, but not always as euhedral crystals. Sulfide grains were noted in several runs. Apatite is ubiquitous as an accessory phase, frequently displaying skeletal morphologies in the form of perfectly hexagonal outlines with a large central melt pocket. Many experiments at ≥ 125 MPa contain biotite, a phase not present in the starting materials. Microprobe spot compositional analyses were obtained on subsets of experimental samples, for plagioclase, amphibole, magnetite, ilmenite, and glass (Figure 3.9).

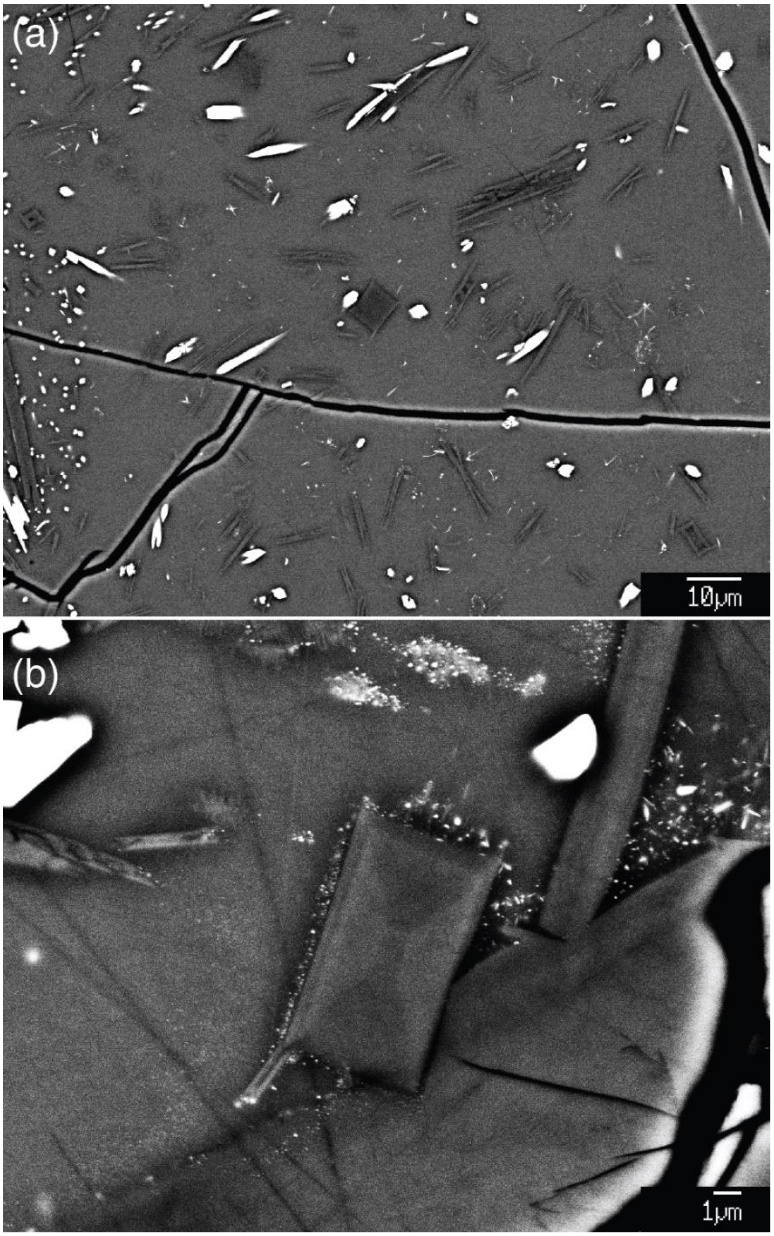

Figure 3.8. BSE images of plagioclase microlites (~An_{20}) in the Quizapu lava. (a) is a broad picture of their distribution and common morphologies, whereas (b) shows zoning within a single microlite, likely induced by differential growth rates in different sectors, or by rapid growth followed by slower infilling.

3.3.2.1 Amphibole

Above ~125 MPa, amphibole phenocrysts are euhedral and largely resemble those in the natural materials (Figure 3.10). Some phenocrysts are somewhat separated, typically along cleavages, though individual sections of the crystal are all euhedral (Figure 3.10c). At P < 125 MPa, amphibole crystals display diffuse breakdown rims composed mainly of pyroxene, with less abundant plagioclase (Figure 3.10f). Many rims contain apatite and/or BSE-bright needles

that may be Fe-Ti oxides, although they are too small for EDS or WDS identification. Breakdown rims are more pervasive with decreasing pressure. Amphibole is surrounding by breakdown rims at 100 MPa and 875 °C, regardless of whether additional Cl was added to the experimental charge. The amphibole-in curve steepens with temperature, suggesting a maximum thermal stability limit around 900 °C for this system. Some amphibole crystals are sector zoned (Figure 3.10e-f).

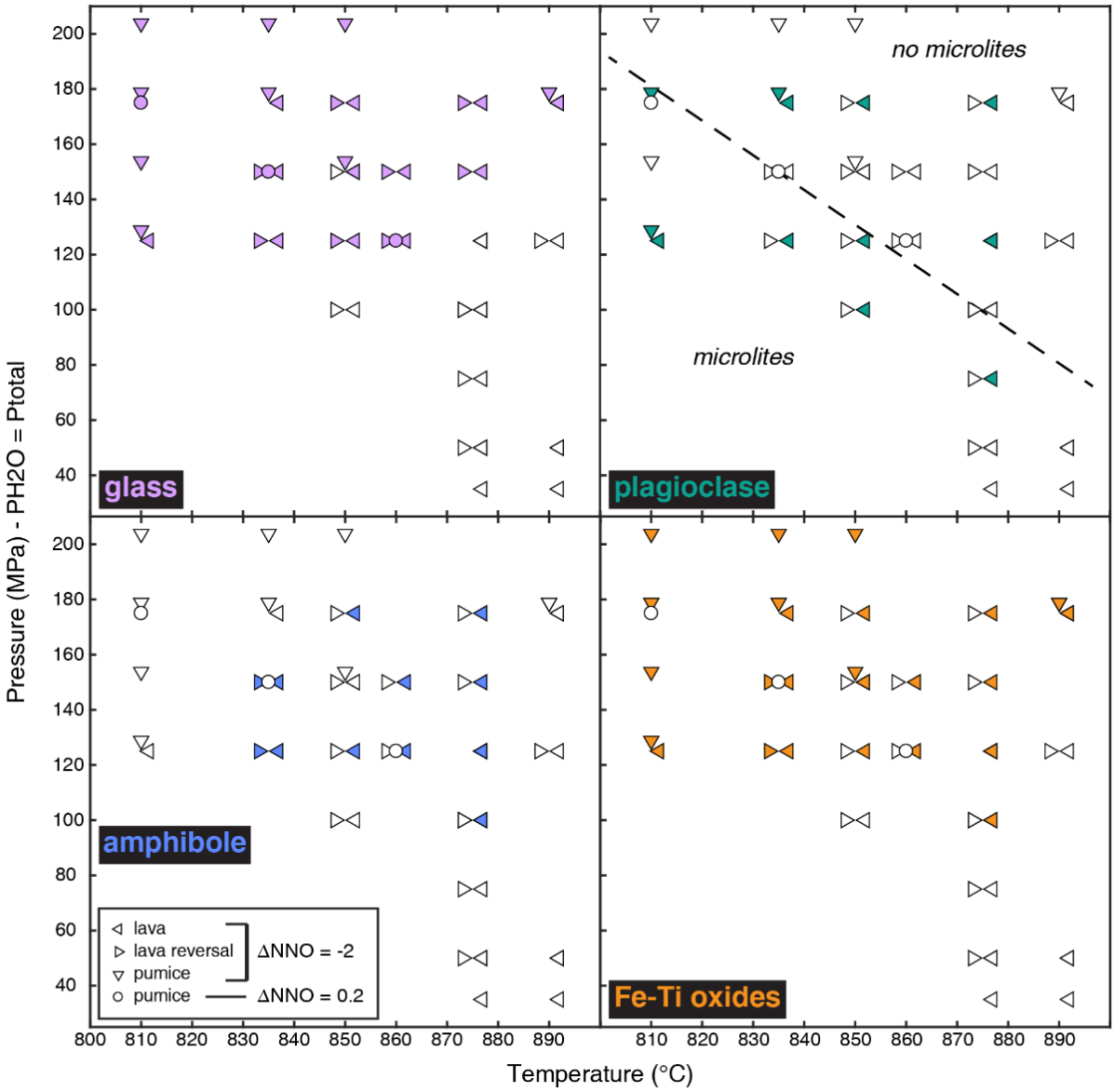

Figure 3.9. Pressure versus temperature diagrams showing the locations of experiments performed (all symbols), filled in based on the experiments for which EPMA analyses were collected for the labeled phase. Note the approximate demarcation of microlite-bearing versus microlite-free samples (see text discussion).

Amphibole crystals were analyzed by EPMA in 13 experimental samples that used lava VQ-06-06 as a starting material, including two reversal experiments, all at NNO-2.1 (Figure 3.9c). Experimental amphibole cores preserve the natural amphibole compositions, which themselves span a considerable range in major and minor elements (e.g., 7.6-11.1 wt% Al_2O_3; 0.48-0.71 wt% K_2O). Intra-crystalline compositional variation of experimental rims is of a similar magnitude as variation in the natural sample (e.g., Al_2O_3 RSD = 8% for VQ-06-06 and ≤ 8% for each experimental sample). Amphibole from reversal experiments has the same composition as that from the corresponding forward experiments (circled points, Figure 3.6). In terms of total abundance of a given element, compositions of BSE-visible rims on stable experimental amphibole crystals fall within the compositional range of VQ-06-06 for all but three elements: in most experimental rims, total Mg and Ca are both lower than in the natural lava, and total Fe is higher than in VQ-06-06. The high total Al in low-fO_2 amphibole discussed by Anderson and Smith (1995) is not observed in any experimental samples. However, the high total Fe and low Fe^{3+}/total Fe noted by those authors is in accord with our experimental findings.

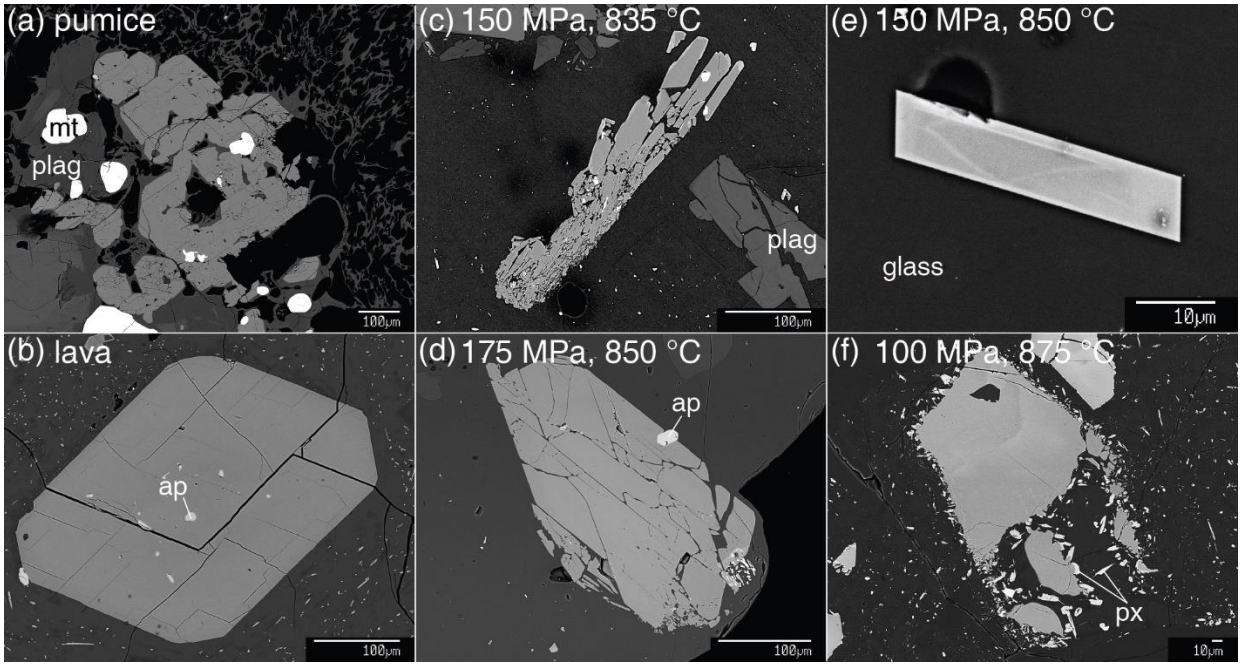

Figure 3.10. BSE images of amphibole crystals. (a-b) Starting materials (c-f) Experimental samples. Note the apparently unzoned, euhedral nature of the natural crystals. Experimental crystals in (c), (d), and (e) reside within the zone of amphibole stability, whereas that in (f) does not, as evidenced by the breakdown rim. Subtle sector zoning is visible in (e) and (f). In (f), zoning is interpreted to be inherited from the starting material. Crystals in (c) and (d) are also likely inherited from the starting material, but kept growing during experiments. The small crystal in (e) is interpreted to represent syn-experimental nucleation and growth. ap = apatite, mt = magnetite, plag = plagioclase, px = pyroxene.

Lower temperature experiments have lower occupancy of the A site, lower tetrahedral Al, and lower Mg#, defined as Mg/(Mg+Fe^{2+}) in the C site (Figure 3.6). Amphibole rims in the experiment run at 175 MPa, 875 °C (red diamonds in Figure 3.6) are very faint in BSE and match the natural amphibole composition. Two of the experiments analyzed contain amphibole with breakdown rims (P = 100 MPa). In these cases, there is no growth rim to analyze; WDS spots in all locations on these remnant amphibole grains reflect the natural input composition. No difference is noted in amphibole Cl content (average 0.05 wt%) between these two experiments, one of which contained added Cl as well as the usual H_2O.

3.3.2.2 Plagioclase

Plagioclase phenocrysts, with varied textures and compositional zoning, are inherited from the starting material. Whole crystals and fragments are both common. Rims, interpreted as new growth, occur in many experiments, though they are discontinuous and not present on every crystal within a given charge. Plagioclase microlites grew in experiments at lower P-T conditions (≤ 810 °C at 175 MPa to ≤ 890 °C at 75 MPa; Figure 3.9b). Plagioclase shows a range of compositions in each experimental sample, but there is a general trend of increasing anorthite content (An) with increasing T and P, reflected in both the average and minimum An of each sample (Figure 3.11).

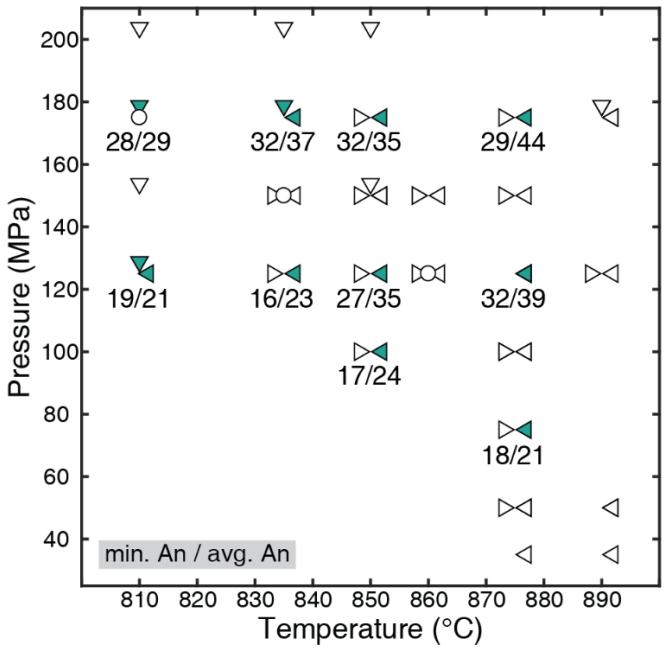

Figure 3.11. Plagioclase compositions in experimental run products. Filled symbols are those from which the analyses are taken. Symbol meanings as in Figure 3.9. Both minimum and average An content increase with increasing temperature or pressure, with the exception of the sample at 875 °C, 175 MPa.

3.3.2.3 Pyroxene

Iron-poor orthopyroxene occurs as unzoned crystals, typically globular in shape and variably rounded. Overgrowths of Fe-rich orthopyroxene occur on most of these crystals in the NNO-2 experiments, ranging from small tabs to fully encircling rims. More Ca-rich pyroxene is much less abundant, but occurs in most experiments as individual crystals, and rarely as part of an overgrowth. Pyroxene also occurs as uncommon, roughly concentrically zoned crystals that are generally Ca-rich, though some discrete zones may have less Ca. In the NNO+0.2 experiments, orthopyroxene has few to no overgrowths. At 175 MPa, 810 °C, orthopyroxene is unstable and surrounded by biotite. Smaller, euhedral crystals of Ca- and Al-rich pyroxene are present near some of these reaction sites.

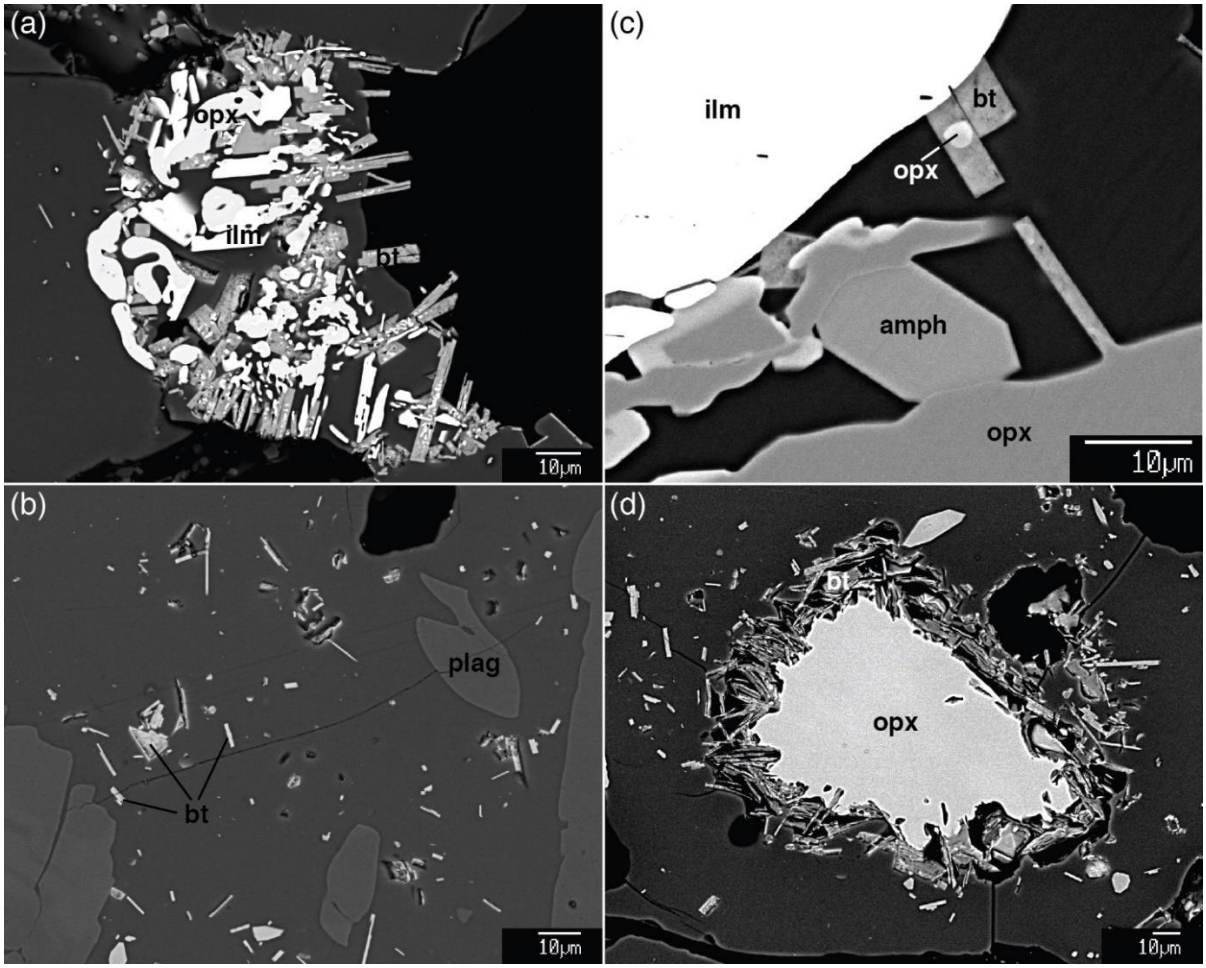

Figure 3.12. BSE images of experimentally-grown biotite. In (a), biotite is associated with rounded Fe-rich orthopyroxene and relict ilmenite. Biotite in (b) is scattered throughout the glassy groundmass, and its euhedral nature indicates that it formed individually from the melt, not as a reaction product. (c) highlights the biotite-orthopyroxene relationship, with biotite growing around and from orthopyroxene (and/or ilmenite). (d) shows a partially reacted orthopyroxene crystal rimmed by euhedral biotite laths. amph = amphibole, bt = biotite, ilm = ilmenite, opx = orthopyroxene, plag = plagioclase.

3.3.2.4 Biotite

Although never noted in the natural Quizapu materials, biotite formed at 12 experimental P-T combinations (Figure 3.12). The phase is stable on the high pressure, low temperature side of a curve passing near 125 MPa, 835 °C and 175 MPa, 875 °C. Biotite most typically occurs in association with the very Fe-rich pyroxene in/around magnetite rims, but also as a groundmass phase (i.e., small, faceted, individual crystals, widely separated by areas of glass) in experiments across much of the stability range. Some biotite crystals contain inclusions of Fe-rich pyroxene or grow directly around a larger swath of pyroxene. The vast majority of biotite crystals are euhedral and tabular, with a few triangular crystals present. In NNO+0.2 experiments, biotite presence or absence is the same as in NNO-2 experiments at the same pressure-temperature conditions. At the highest pressure NNO+0.2 experiment, biotite is more abundant than at the same pressure-temperature conditions at NNO-2, occurring largely as a reaction rim around orthopyroxene, but also in the groundmass.

3.3.2.5 Fe-Ti oxides

Fe-Ti oxides display disequilibrium textures in all experimental samples run at NNO-2. At NNO+0.2 (runs 34-36), magnetite and ilmenite grains are both euhedral and unzoned. In NNO-2 runs, cores of both magnetite and ilmenite preserve the starting composition, except in Mg and Mn. Rims do not vary coherently with temperature or pressure in most elements. The textures and compositions of the Fe-Ti oxide minerals are described in detail in Chapter 4.

3.3.2.6 Glass

Residual glass compositions across the experimental spectrum display tightly constrained trends with both temperature and pressure, for seven of the 11 elements analyzed (e.g., Figures 3.13-14). MnO, Na_2O, P_2O_5, and Cl contents do not change consistently in pressure-temperature space. Chlorine contents of experimental glasses are lower than in the starting material glasses at all pressures and temperatures. Glass SiO_2 and K_2O decrease with increasing experimental temperature or pressure, whereas Al_2O_3 and CaO increase with increasing temperature or pressure. Within these trends, variation in Al_2O_3 is greatest, and CaO and K_2O are more tightly constrained. Experiments at a narrow range of pressures and temperatures match the glass composition of Quizapu pumice (Figure 3.15).

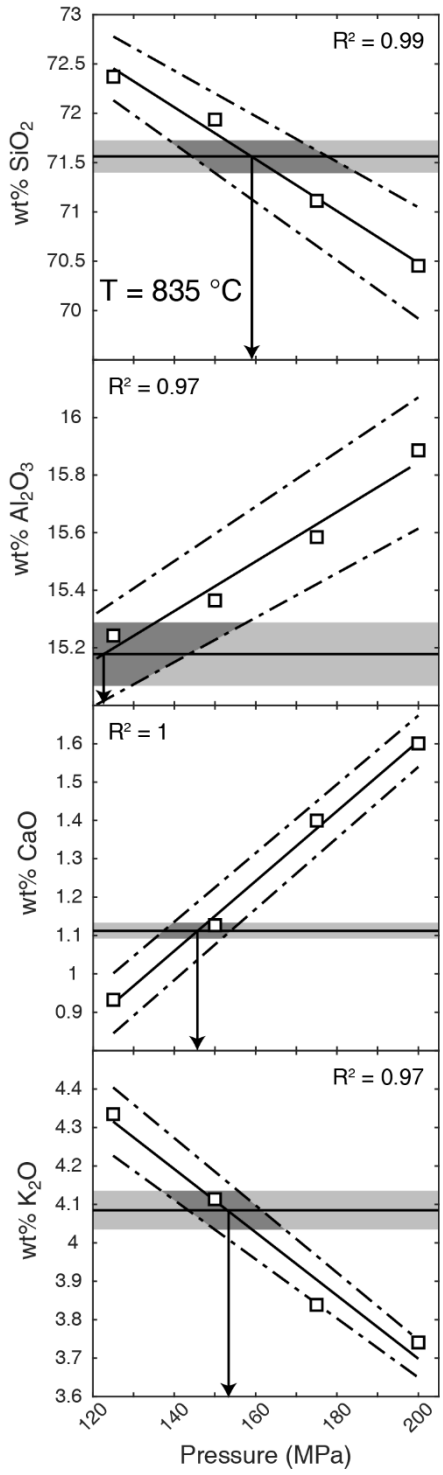

Figure 3.13. Residual glass compositions for experiments at 835 °C, at all pressures. Symbols are the average value of all experimental analyses at the given conditions. R-squared values refer to the solid line fit to experimental data points; dot-dashed lines are linear fits to 1 σ variance of the data. Horizontal solid line marks the Quizapu pumice glass composition, with 1 σ variance shown by the shaded band. The dark grey intersection of natural and experimental trends gives the pressure range over which the natural glass composition is matched. An arrow is shown marking the best fit pressure value for each oxide plot.

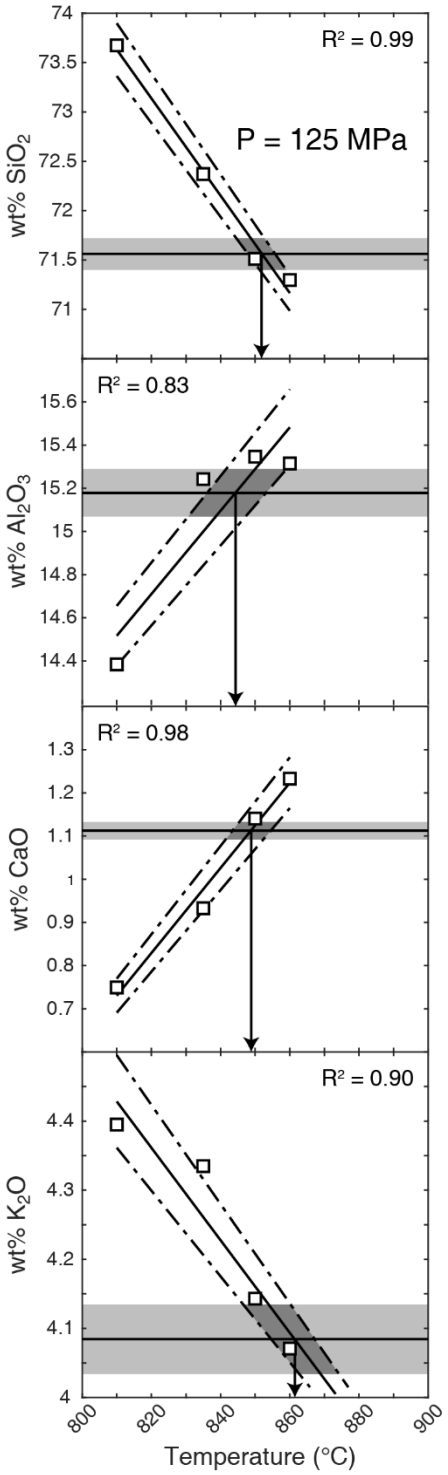

Figure 3.14. Residual glass compositions for experiments at 125 MPa, at all temperatures. Symbols and interpretations as in Figure 3.13. Arrows mark temperatures that result in experimental glass compositions closest to the natural pumice glass composition, for the given oxides.

3.4 DISCUSSION

3.4.1 Pre-eruptive storage conditions

The main objective of our experiments is to establish the pressure-temperature conditions at which the experimental materials reproduce well the natural phase assemblage and phase compositions. We focus on phenocryst phases and glass, but note that all experimental samples also contain apatite, and that sulfides occur in many, possibly all samples (we did not systematically search for them). Both accessory minerals are present in the natural materials, indicating a secondary measure of agreement between experimental samples and the natural materials.

3.4.1.1 A brief note on some natural phases

Although the low fO_2 of most experiments precludes a comparison of Fe-Ti oxides for the purposes of determining storage conditions at Quizapu, the textures and unzoned nature of Fe-Ti oxides in experiments run at NNO+0.2 suggest that this fO_2 is close to that at which the natural sample equilibrated. We consider the subtle zoning in Fe-Ti oxides from the lava (Figure 3.5a-b) to represent post-eruptive modification in the cooling lava flow that did not substantially alter the phase compositions (Figure 3.4a-b). The cross-hatched texture in one pumice magnetite (Figure 3.5c) likely represents rapid oxidation upon cooling exposed to atmospheric conditions (Lattard et al. 2012). Thus, these features are not expected in the experimental products, nor are they observed. In both the lava and pumice, the pure Fe-O phase displays signs of instability (extreme rounding, punctuated throughout with melt; Figure 3.5d), indicating that this phase was not part of the stable pre-eruptive assemblage.

Plagioclase microlites in the lava sample show a compositional range that supports growth directly from the dacite melt, rather than transfer from an andesitic recharge magma. We suspect that this interpretation applies to all Quizapu lava samples with plagioclase microlites. Thus, our use of a higher-crystallinity lava as a starting material does not reflect contamination from a more mafic magma, and phase equilibrium constraints derived from it should (and do) match those based on pumice starting material.

3.4.1.2 Phase assemblage

The major natural phase assemblage of plagioclase, amphibole, and orthopyroxene is present in most experiments from 835-875 °C, between 125 and 175 MPa. Amphibole is physically present in all experimental samples, but those that show amphibole resorption and/or

reaction rims are excluded, as these features are indicative of disequilibrium (e.g., Browne and Gardner 2006; De Angelis et al. 2015; Rutherford and Hill 1993). The additional presence of biotite excludes a large high-pressure, low-temperature section of the region of phase match, limiting potential storage conditions to the area between the biotite- and amphibole-in curves (Figure 3.15).

Because the biotite stability field may shrink at lower fO_2 (e.g., Costa et al. 2004; Rutherford 1969), biotite crystallization in NNO-2 experiments suggests that biotite would be present at higher fO_2 as well. This assertion is confirmed by two NNO+0.2 experiments (35 and 36) which contain biotite in greater abundance than in the corresponding NNO-2 experiments (27 and 15). At 860 °C and 125 MPa, neither the NNO+0.2 nor the NNO-2 experiments contain biotite. For the experiments at hand, it thus appears that higher fO_2 promotes a higher degree of biotite crystallization, but does not significantly affect the phase-in curve. Based on reaction textures of biotite replacing orthopyroxene (Figure 3.12d), it is likely that the biotite-in curve is related to the orthopyroxene-out curve, just as amphibole-in sometimes corresponds to clinopyroxene-out (e.g., Hammer et al. 2002). However, below 200 MPa and above 810 °C, orthopyroxene is stable in the NNO-2 experiments (Table 3.2). Due to the increased stability of orthopyroxene at low fO_2 (Costa et al. 2004), it is possible that the driving force for dissolution and/or reaction was low enough that these processes were not evident in the experimental samples. The irregular nature of stable orthopyroxene crystals in this system (Figure 3.7) makes it even more difficult to discern a small amount of dissolution. Spotting a biotite crystal is more straightforward, which explains the good agreement between NNO-2 and NNO+0.2 experiments in terms of biotite presence. We conclude that at the fO_2 of the natural Quizapu system (~NNO to NNO+1), the orthopyroxene-out curve is difficult to constrain, and likely falls near or coincident with the biotite-in curve, although the curvature may be slightly concave down, as in other systems (e.g., Costa et al. 2004; Muir et al. 2014).

Plagioclase is stable throughout the experimental interval, but the presence or absence of plagioclase microlites provides an independent constraint on magmatic storage conditions. For a plagioclase-bearing magma residing at equilibrium, there is no thermodynamic driving force for crystallization or resorption of the equilibrium plagioclase. At temperatures and pressures below the equilibrium plagioclase isopleth, an effective undercooling ($-\Delta T$) is induced, driving nucleation and growth of plagioclase. At temperatures and pressures above the equilibrium

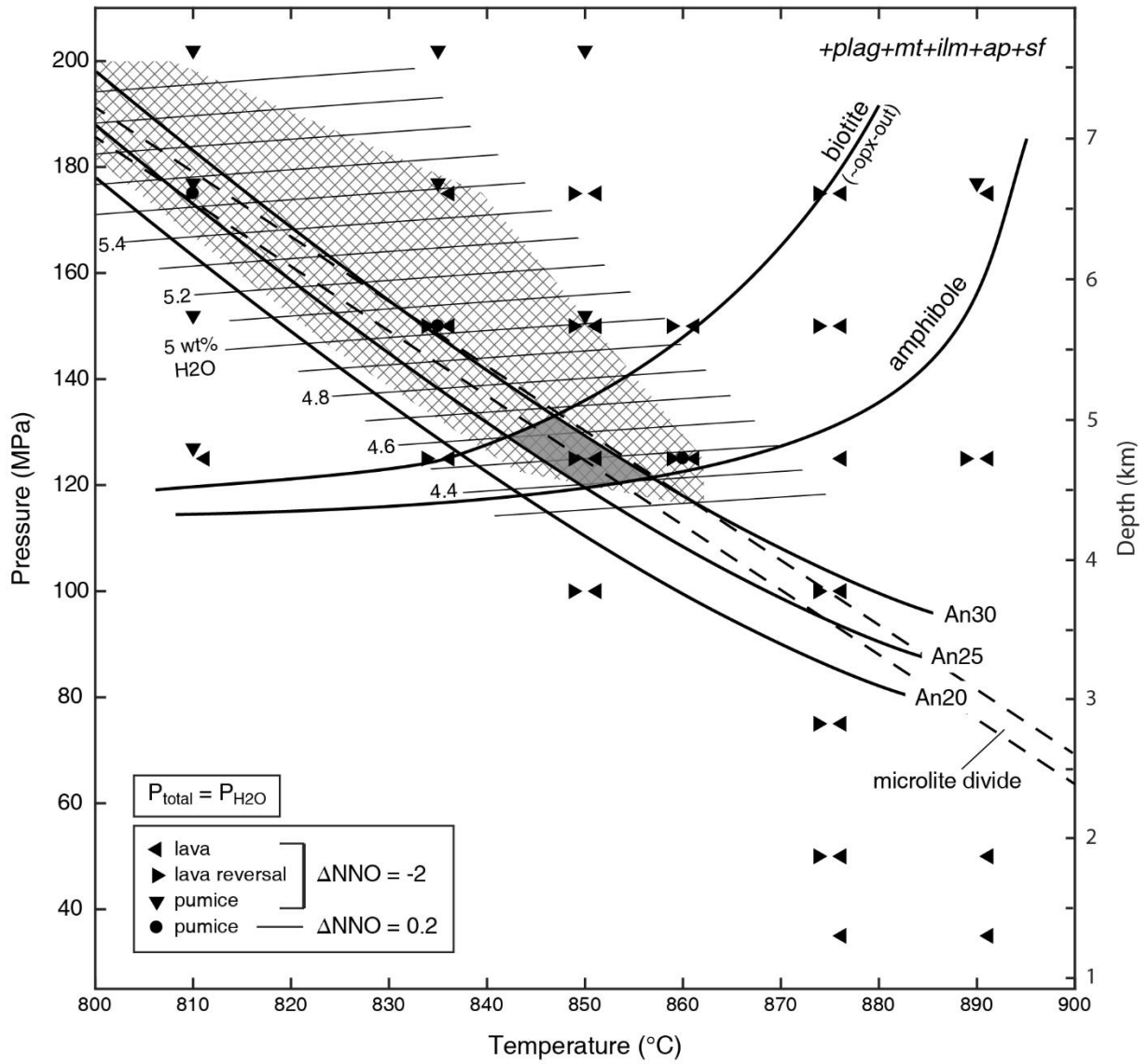

Figure 3.15. Phase diagram for Quizapu dacite at water-saturated conditions. Symbols indicate starting materials or conditions. Amphibole and biotite are stable above their respective curves. Cross-hatching indicates pressure-temperature conditions over which experimental glass compositions match Quizapu pumice glass composition. For clarity, glass match area was calculated only for expts with stable amphibole. Water solubility contours are based on this glass composition and the model of Zhang et al. (2007). Dashed double line represents the dividing line between microlite-bearing samples (below) and microlite-free samples (above). Shaded grey region represents the experimental estimate of long-term pre-eruptive storage conditions before both the 1846-7 and 1932 eruptions.

plagioclase isopleth, an effective superheating (+ΔT) is induced, driving resorption of plagioclase. Thus, crystallization of microlites is expected when experimental conditions are undercooled with respect to the storage conditions of the Quizapu dacite. Conversely, experiments that are superheated with respect to the natural equilibrium conditions should not crystallize plagioclase microlites. The band dividing microlite-bearing from microlite-free

experiments nearly parallels the plagioclase compositional isopleths and passes through the region between amphibole- and biotite- in curves at ~845-855 °C (Figure 3.15), pointing to equilibrium storage at or near these conditions.

3.4.1.3 Mineral compositions

3.4.1.3.1 Amphibole

The experimental fO_2 of NNO-2, lower than that estimated for Quizapu rocks (~NNO to NNO+1), is reflected in the total Fe and Mg content of amphibole rims. An overall higher abundance of Fe, coupled with a larger fraction of Fe^{2+}/total Fe reflects the availability of more Fe^{2+} in the melt relative to Quizapu lava, as expected for a lower fO_2 melt. Greater incorporation of Fe into the amphibole structure comes at the expense of Mg, which occupies the same lattice sites as Fe. This low-Mg signature is partially overprinted by the effect of increasing temperature, which correlates with increasing Mg# in Fe-Mg silicates. Thus, the better match to natural amphibole at higher temperature (Figure 3.6) implies that T ≥ 875 °C is too high for the natural amphibole crystals to have formed. At the higher fO_2 of the natural samples, the Mg# of crystallizing amphibole would be higher than the Mg# of amphibole crystallizing at the same temperature at lower fO_2. A match to natural Mg# at the low experimental fO_2 is thus a negative constraint, indicating that natural storage conditions were < 875 °C.

The low A-site occupancy and ^{IV}Al in lower temperature experiments (Figure 3.6) can be explained via the edenite exchange

$$^{IV}Si + {}^{A}[] = {}^{IV}Al + {}^{A}(Na + K) \qquad \text{eq 3.1}$$

where $^{A}[]$ indicates a vacancy in the A site. The right hand side of the equation is favored less at lower temperatures (e.g., Spear 1981). The edenite exchange is common in amphibole crystals, noted as a substitution mechanism in Quizapu amphibole as well as in other dacitic systems (e.g., Fish Canyon, Bachmann and Dungan 2002). Because there is no redox-sensitive Fe or Mg involved in the exchange above, it is a better test for compositional matching between natural and experimental amphibole. However, the range of natural amphibole compositions is wider in K+Na and ^{IV}Al space, making specific temperature comparisons difficult. Broadly, natural amphibole compositions have higher Na+K and ^{IV}Al than most 835 °C experimental amphibole crystals, but the natural compositions largely overlap those of the other three experimental temperatures. Recalling that the Mg# argument above reduces the Quizapu magma temperature

to < 875 °C, the components of the edenite exchange suggest that this open-ended constraint be narrowed to 835-875 °C, a range in good agreement with phase assemblage and plagioclase microlite considerations.

3.4.1.3.2 Plagioclase

Plagioclase compositions further constrain the pre-eruptive storage conditions, based on the experimental anorthite content. Given the lack of evidence for a significantly more evolved magma than the dacite which erupted in 1846-7 and 1932, we consider the most albitic plagioclase in natural samples to represent best the plagioclase in equilibrium with the main dacite body. Plagioclase crystals in rare clasts of rhyodacite pumice (69-70 wt% SiO_2; < 0.5 wt% of all 1932 ejecta;) are similar to those in the main dacite (Hildreth and Drake 1992). Over an extensive suite of Quizapu samples, from both 1846-7 and 1932, the most albitic plagioclase is consistently An_{25-30} (Ruprecht et al. 2012), so this range is taken to represent the stable plagioclase composition of the pre-eruptive magma chamber. In the same vein, the most albitic experimental plagioclase crystals are the least likely to have been inherited from crystal cores in the starting material that do not represent the magma of interest, and are the compositions we use to draw An isopleths. However, in experiments without microlites, identification of newly formed plagioclase is difficult. In several samples, a more anorthite-rich plagioclase was expected to form, due to higher P-T conditions, yet was not captured in the analyses. The analytical set likely includes plagioclase from the starting material that is not in equilibrium with the melt. Thus, we do not identify isopleths in the microlite-free region. The region where experimental isopleths of An_{25-30} coincide with the stable Quizapu phase assemblage represents the water-saturated pre-eruptive storage conditions (Figure 3.15).

3.4.1.4 Glass compositions

A magmatic melt is the single phase whose chemistry reflects the combination of mineral and volatile phases saturating, as well as their composition and abundance. Experimentally matching a natural quenched glass composition is regarded as a robust indicator of magmatic storage conditions and has been frequently applied to silicic systems (e.g., Hammer and Rutherford 2003; Costa et al. 2004; Larsen 2006). Four of the most abundant oxides in the experimental glasses were used to calculate an overall best match to the Quizapu pumice glass. Oxides with high abundances in the melt reduce the noise of localized variations, while

reflecting accurately the overall state of the system. Although both Na_2O and FeO^T have higher abundances than CaO, they were excluded due to volatility and fO_2 concerns, respectively. Thus, SiO_2 (~70 wt%), Al_2O_3 (~16 wt%), K_2O (~4 wt%), and CaO (~1.5 wt%) were used to arrive at the best fit temperature and pressure values. This set of oxides is robust in that it includes two compatible and two incompatible elements, in total comprising > 90 wt% of the melt.

For a set of pressures at a given temperature, and vice versa, the intersection of the experimental composition trend of a given oxide with the natural abundance of that oxide indicates a best estimate of the natural pressure or temperature. Thus, for every pressure and every temperature, there are four estimates, one based on each oxide (Figures 3.13-14). These four estimates are weighted according to three factors and combined to give the overall best match temperature at a given pressure, and vice versa. The three weighting factors are: logarithmic abundance in the pumice glass, RSD for pumice analyses, and coefficient of determination (R^2) for experimental data. In this way, oxides with higher abundance, tighter natural constraints, and more robust experimental trends are weighed more heavily. For the three conditions at which higher-fO_2 experiments were conducted (Table 3.2), glass data from those experiments were included in the calculations. Any shifts in temperature and pressure estimates compared to using only NNO-2 data were unsystematic and well within the 1σ uncertainty of the estimates. Thus, for the oxides used, fO_2 does not have a strong effect on residual glass composition.

The sets of best-match ranges based on constant temperature and constant pressure generally agree, indicating a match to the natural pumice glass in a narrow, negatively sloping region in pressure-temperature space (Figure 3.15). The area defined by these best match conditions includes an error envelope that takes into account the standard deviation of both the natural and experimental samples. This glass-based equilibrium storage estimate completely overlaps with the storage region estimated via phase assemblage and mineral compositional constraints. Water-saturated pre-eruptive storage of the Quizapu dacite is thus tightly constrained to 852 ± 10 °C at 127 ± 7 MPa (4.5-5 km deep). Given the experimental uncertainties, we take 850 °C and 125 MPa as the magmatic storage conditions.

3.4.2 Implications for thermobarometry

3.4.2.1 Fe-Ti oxide equilibration

Estimates of Quizapu end-member dacite temperatures from Fe-Ti oxides that meet the (Bacon and Hirschmann 1988) Mg/Mn equilibrium criteron range from 837-874 °C (Hildreth and Drake 1992), 870 °C (Ruprecht and Bachmann 2010), and 866-956 °C (Ruprecht et al. 2012). In VQ-06-06 and VQ-07-37 D, all analyzed magnetite grains could be in equilibrium with all analyzed ilmenite grains, within each sample. Only one touching Fe-Ti oxide pair was found in each sample, so these pairs and other non-touching pairs were used to obtain temperature and fO_2 estimates (after (Ghiorso and Evans 2008). For lava VQ-06-06, temperatures range from 831-858 °C, and fO_2 from NNO+0.3 to NNO+0.5. Published analyses of the same sample (Ruprecht et al. 2012) yield temperatures of 890-906 °C and fO_2 from NNO+0.6 to NNO+1.1. Published analyses of Quizapu dacite pumice Fe-Ti oxides (VQ-07-37 D and VQ-06-17) give 866-885 °C, NNO+0.7 (Ruprecht et al. 2012), whereas our analyses of VQ-07-37 D Fe-Ti oxides yield 835-866 °C, NNO +0.3. These discrepancies are only partly explained by uncertainty in the oxythermometer (about ± 30 °C).

One potential contributor to the temperature-fO_2 discrepancies are the much higher values of V and Mn in the (Ruprecht et al. 2012) analyses compared to our own (Figure 3.4). Given the additional calibration dedicated to correcting for interference of Ti on V and Cr on Mn in our EPMA analyses, we suspect that such corrections were not performed for the analyses of Ruprecht et al. (2012). The proximity of the Ti Kβ peak to the V Kα peak, and likewise Cr Kβ to Mn Kα, lead to overestimates of V and Mn concentrations if not properly accounted for. Based on substitution of the average V and Mn values from our study into the (Ruprecht et al. 2012) analyses, estimated temperatures could shift by -5 to +1 °C (Ghiorso and Evans 2008). Oxygen fugacity values remain unchanged to 0.01 log units lower. Although the shift in temperature emphasizes the importance of accounting for elemental interferences in EPMA analyses, it does not explain the larger discrepancies between studies.

The remainder of the differences are likely due to a combination of statistically-insufficient sample size and analytical error. Jolles and Lange (2017) find a broad temperature range (~50 °C) given by all ~5,000 possible Fe-Ti oxide pairs in a single pumice clast of Early Bishop Tuff rhyolite. Those authors conclude that even the relatively small analytical errors encountered with WDS spot analyses contribute to the wide range of T-fO_2 estimates from single

volcanic samples. The limited total number of analyses between this study and that of Ruprecht et al. (2012) (n = 7 for VQ-07-37 D; n = 17 for VQ-06-6) could therefore explain the temperature discrepancies observed.

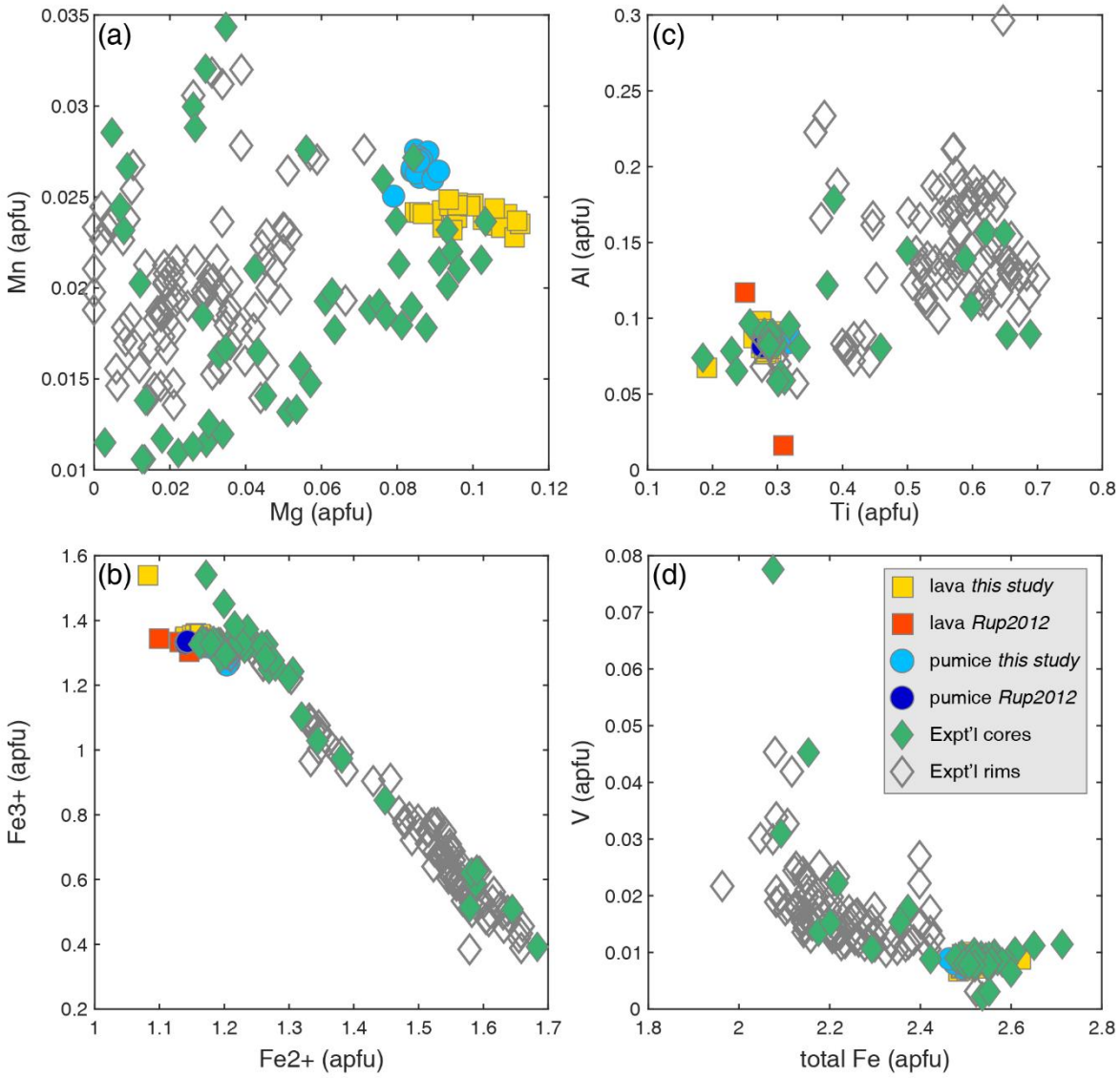

Figure 3.16. Titanomagnetite compositions from experiments and starting materials. Note the good separation between cores and rims in panels (b-d), with the exception of the 10 "core" points that probably represent rims in 3D (see text). In contrast, experimental cores record large compositional differences from the starting materials, in both Mn and Mg (a), despite the use of these two elements in particular to establish whether or not crystals have achieved equilibrium (Bacon and Hirschmann, 1988).

Other potential pitfalls of classic Fe-Ti oxide thermometry involve the core assumptions on which the method relies. The Bacon and Hirschmann (1988) Mg/Mn test for equilibrium of coexisting cubic and rhombohedral oxides is considered a requirement for, but not adequate

proof of, equilibration between the two phases. However, analyses of the cores of experimental magnetite grains suggest that Mg and Mn may equilibrate more quickly than other elements, making them poor indicators of overall equilibrium. In Figure 3.16b-d, 10 core analyses plot within the field of rim analyses, and the rest essentially overlap the composition of the starting materials. These 10 points could represent analyses that fell in an apparent core in 2D space, but were part of a rim in 3D. However, in Mn versus Mg space (Figure 3.16a), 40 of the 50 core analyses plot in the rim field, and only three of the remaining points truly overlap the compositions of the starting materials. This deviation of Mg and Mn from the starting compositions, even in apparently un-altered magnetite cores, strongly suggests that Mg and Mn diffuse more quickly than other major or minor elements in titanomagnetite, at least at low fO_2 (NNO-2). It is difficult to say whether this hypothesis agrees with studies of diffusion in titanomagnetite. Only some cations (e.g., Fe, Mn) have been explored over temperature and fO_2 space, yielding minima at intermediate fO_2 that shift with temperature and diffusion mechanism (Aggarwal and Dieckmann 2002). In general, Ti appears to diffuse slowly compared to Mn and Fe, but Fe-Ti interdiffusion rates span the gap (Van Orman and Crispin 2010 and references therein). No study on Mg diffusivity has yet been reported. Until such data are reported, we suggest that Mg will diffuse at a rate similar to Mn and tracer Fe, that is, faster than either tracer Ti or Fe-Ti interdiffusion.

The morphology of experimental ilmenite grains unfortunately does not allow for a parallel analysis. However, it is evident that even when Mg/Mn equilibrium is met, the criterion may reflect only the fastest-equilibrating elements, leaving open the possibility that elements which more strongly affect the oxythermometry (e.g., Fe, Ti) remain in disequilibrium, with the potential to give incorrect temperature and fO_2 estimates. By the same token, some analyses that fail the Mg/Mn test may reflect Fe-Ti oxides at the early stages of a re-equilibration event, frozen before Fe, Ti, and other elements deviated significantly from their previous equilibrium concentrations. These Fe-Ti oxides still have the potential to yield reasonable temperature and fO_2 estimates.

3.4.2.2 Amphibole compositional variability

The compositional scatter of both natural and experimental amphibole crystals, also noted in Quizapu samples by (Hildreth and Drake 1992), precludes their use as precise indicators of pre-eruptive storage conditions. This relatively large variation may reflect growth under (1)

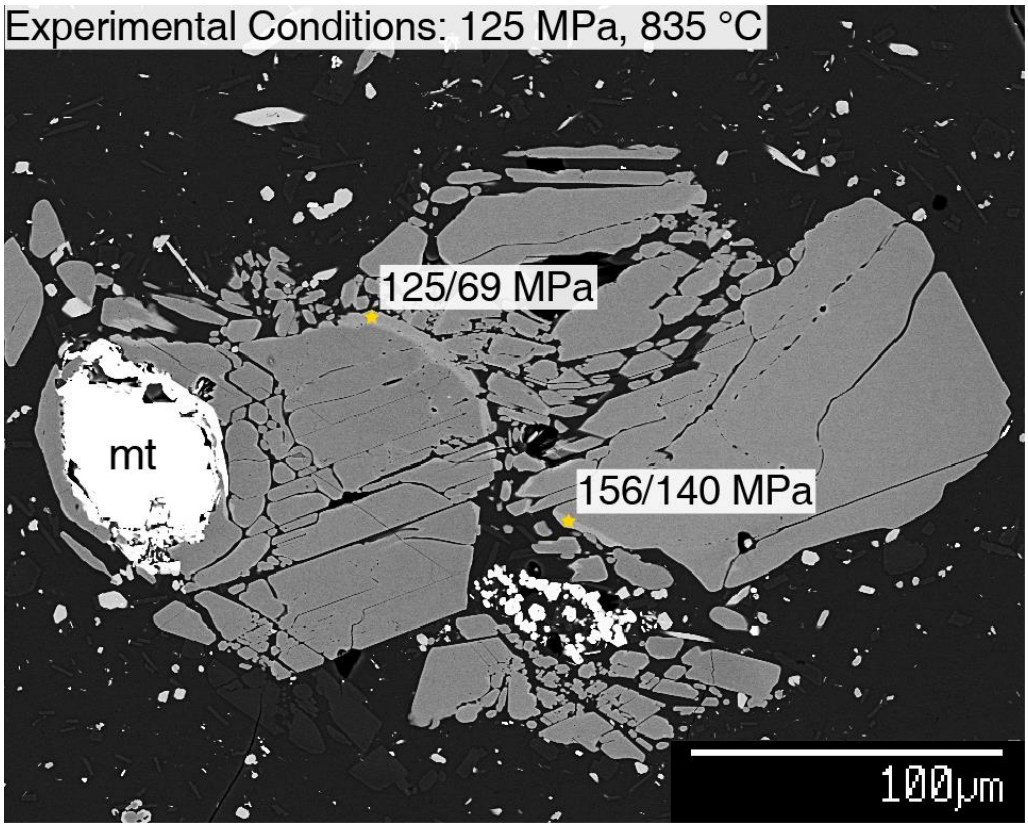

Figure 3.17. Experimental amphibole crystal (stable). Stars mark EPMA points on the rim, within 100 µm of each other. Pressures next to the points are calculated from the model of Ridolfi and Renzulli, 2012, eqn1b/eqn1c. Only one pressure returns the experimental pressure, and there is significant variation depending on the equation used. mt = magnetite.

variable conditions before entering the pre-eruptive storage region, with the implication that subsequent storage was not long enough to diffusively re-equilibrate the grains, or (2) it may be due to cryptic sector zoning. This type of partial disequilibrium, growth-induced zoning is prevalent in pyroxene crystals (Nakamura 1973; Welsch et al. 2016) and has been reported in both natural and experimental amphibole crystals (Mokhtari and Velde 1987; Shea and Hammer 2013). Sector zoning in clinopyroxene has even been shown to result in erroneous thermobarometry (Hammer et al. 2016). If the compositional variation of Quizapu amphibole is due to variable conditions (1), then thermobarometry may be accurate but may not reflect the magmatic storage conditions immediately pre-eruption. If compositional variation is due to sector zoning, then thermobarometry estimates cannot be trusted. We propose that sector zoning does exist in Quizapu amphibole crystals (e.g., Figure 3.10e-f), but that it may not always be evident in BSE images. For example, syn-experimental amphibole rims grown during the same experiment, even on the same crystal, can give vastly different pressures using equations 1b and

1c of (Ridolfi and Renzulli 2012) (Figure 3.17). Based on these observations, we urge caution when applying amphibole thermobarometry, as the values returned may not represent the magmatic conditions during the time period sought, or may not accurately reflect any intrinsic conditions.

3.4.3 Stability of hydrous phases

3.4.3.1 Amphibole

Experiments point to an amphibole thermal stability limit of ~900 °C at 200 MPa (Figure 3.15), similar to that determined for Mount St. Helens dacite (910±8 °C; Rutherford and Devine 2008), but slightly lower than for the Volcán San Pedro dacite (~925 °C; Costa et al. 2004). We find that the limiting melt H_2O content for amphibole stability in the Quizapu dacite is 4-4.5 wt% H_2O, in agreement with many other studies that find ~4 wt% H_2O as the minimum H_2O content for amphibole stability (Costa et al. 2004; Hammer et al. 2002; Ridolfi and Renzulli 2012; Riker et al. 2015). Conversely, a melt water content ≥ 4 wt% does not guarantee amphibole stability, which depends also on X_{H2O}^{fluid} (Riker et al. 2015). At conditions where amphibole is unstable, the breakdown rims are reminiscent of those formed in the experiments of Browne and Gardner (2006) at 60+ MPa. The more diffuse, less tightly-encircling reaction rims that characterize amphibole breakdown in our experiments may point to moderate undersaturation of amphibole (Browne and Gardner 2006).

The impetus for adding Cl to some experiments was to test the hypothesis that additional Cl would induce amphibole stability at pressures lower than those indicated by H_2O-only systems, because the amphibole thermobarometer of Ridolfi and Renzulli (2012) is not calibrated with crystals as Cl-rich as those from Quizapu; the calibration set includes crystals with a maximum of 560 ppm Cl, whereas Quizapu crystals reach up to 2200 ppm (Ruprecht et al. 2012). The more limited analyses in our own study have a maximum of 905 ppm Cl, with a mean of 686 ppm Cl, in line with the analyses of Hildreth and Drake (1992; mean 600-700 ppm Cl). Because halogens substitute for OH- in the amphibole crystal structure, the excess Cl beyond that included in the barometric calibration could serve to stabilize the phase at lower P_{H2O} than the range calculated for Quizapu on the basis of amphibole barometry (~120-180 MPa; (Ridolfi et al. 2010; Ruprecht et al. 2012). There is precedent for such a stabilizing effect, exemplified by studies on Mount St. Helens dacite that suggest high F content significantly decreases the low-

pressure stability limit of amphibole (Rutherford 2008; Rutherford and Devine 2008). However, the abundance of water in the fluid phase of our experimental suite (typically several wt% beyond saturation) likely scavenged Cl from the melt to a greater degree than it would have in nature, making the differences between pure-H_2O versus Cl-added runs difficult to assess. Even so, Cl in experimental amphibole rims reaches 895 ppm, significantly higher than the maximum Cl content in analyses used to calibrate the thermobarometer of Ridolfi and others (2012; 2010). Our experimental results indicate storage conditions on the low end of those calculated from Quizapu amphibole phenocrysts, and extending slightly lower (119-133 MPa). Given the error bars on the natural estimate (at least ±15 MPa), we do not view our results as inconsistent. We conclude that, in the Quizapu system, relatively high Cl contents do not significantly decrease the low-pressure stability limit of amphibole.

3.4.3.2 Biotite

The formation of biotite in many experimental samples (Figure 3.12), despite its absence from the natural materials, places a tight constraint on the maximum water pressure for the Quizapu magmas. Although biotite is frequently associated with unstable Fe-Ti oxide phases and orthopyroxene, we emphasize that it is also present as a groundmass phase. High fO_2 is known to reduce the thermal stability of biotite (McBirney 1993), but biotite occurs in two of the three experiments run at NNO+0.2. Although the lowest pressure, highest temperature experiment at NNO+0.2 does not contain biotite, the equivalent samples run at NNO-2 also lack biotite. Therefore, in the pressure-temperature region relevant to the Quizapu dacite, biotite presence or absence does not reflect oxidation state. In detail, biotite is more prominent in the higher fO_2 experiment at 175 MPa, 810 °C than it is in the lower fO_2 experiment at the same conditions, and it appears to be mainly associated with the breakdown of orthopyroxene (Figure 3.12d). This is consistent with experiments on dacite from nearby Volcán San Pedro, which show that orthopyroxene is stable at higher water contents under more reducing conditions (Costa et al. 2004). Other studies have noted a very limited region over which orthopyroxene and biotite are concurrently stable, suggesting that the orthopyroxene lower stability limit may be associated with biotite reaction (Dall'Agnol et al. 1999; Muir et al. 2014).

Experimental work on Volcán San Pedro (Costa et al. 2004), and Pinatubo (Scaillet and Evans 1999) show that the addition of sulfur can greatly expand the stability field of biotite. In

our experiments, no sulfur was added, although the presence of sulfides and a strong smell of sulfur upon opening capsules indicate that sulfur was present both in the melt and as a volatile species. Sulfur has not been measured in the Quizapu dacite, but a relatively high sulfur content could explain the ready appearance of biotite in our experiments compared with others (Costa et al. 2004; Scaillet and Evans 1999). The higher bulk K_2O content of Quizapu could also play a role in stabilizing biotite without invoking sulfur (3.2 wt% K_2O Quizapu (Ruprecht et al. 2012) versus 2.72 wt% San Pedro (Costa et al. 2004) and 1.67 wt% Pinatubo (Scaillet and Evans 1999).

The biotite stability curve for Mount Unzen dacite is similar to ours in that both have the same direction of curvature, and both become closer to the amphibole stability curve at lower temperature (Holtz 2005). However, both amphibole and biotite are apparently stable to much lower pressures in the Unzen dacite (Holtz 2005; Sato et al. 1999). One group attributes the low-pressure stability to the high K_2O/Na_2O ratio (=1.1) of the Unzen melt (Sato et al. 1999). In comparison, the K_2O/Na_2O ratio in Quizapu pumice glass is 0.75. Focused experimental studies of these somewhat exceptional examples of hydrous mineral stability (e.g., biotite at San Pedro, amphibole and biotite at Unzen) would greatly expand our understanding of the stability criteria and subsequent consequences of hydrous mineral crystallization in intermediate arc magmas.

3.4.4 Reservoir geometry

The depth range over which the water-saturated Quizapu assemblage is stable is narrow: 4.5-5 km deep at 850 °C (Figure 3.15). Given the homogeneity of erupted dacites, Ruprecht et al. (2012) suggest that dacitic melt was extracted from an andesitic mush and stored in an overlying reservoir. The 4-5 km^3 (DRE) of material erupted in each event at Quizapu suggests a minimum size for this magma reservoir. Strictly limiting the height of the storage region to 0.5 km from top to bottom, the reservoir geometry is sill-like, and the most equant dimensions that would produce a chamber of ~5 km^3 are 0.5 km x 3.2 km x 3.2 km. The thermal evolution of such a body can be approximated to a first order via one-dimensional conductive cooling in the z direction (Figure 3.18).

Assuming a wall rock temperature of 600 °C and a homogeneous magma temperature of 850 °C, the upper and lower 60 meters of the magma body at Quizapu would cool below the solidus temperature in the time between eruptions (85 years, Figure 3.18), reducing the chamber by ~1 km^3, to a total of 3.9 km^3. However, a further 40 m on both the top and bottom of the

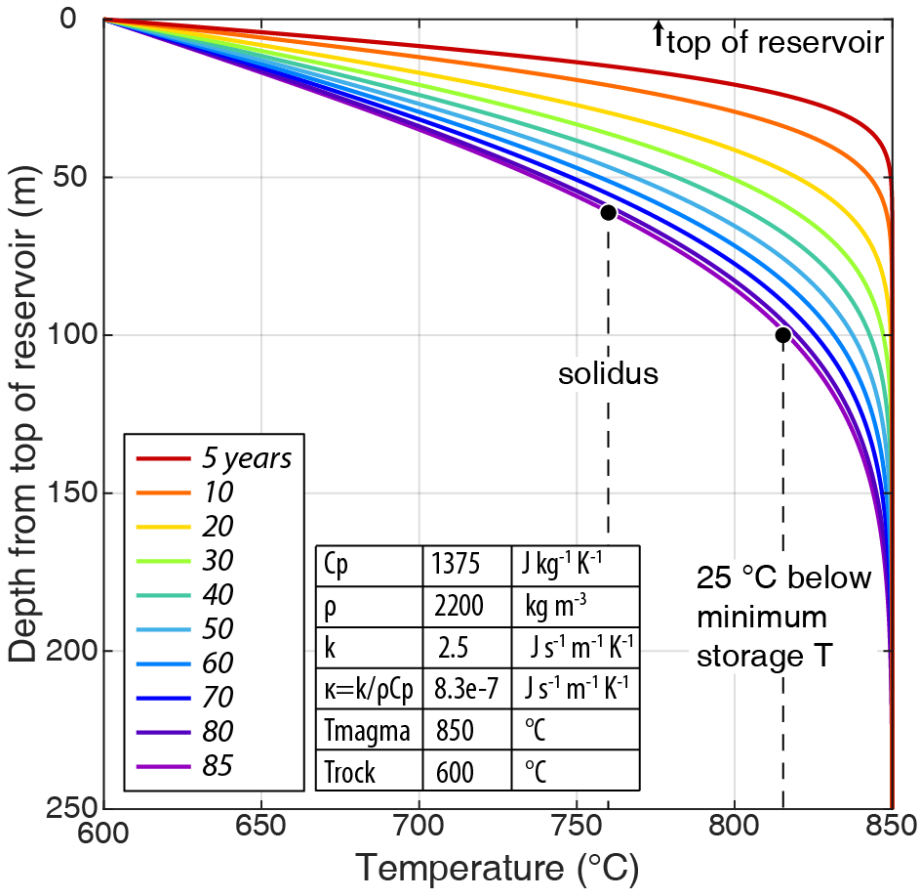

Figure 3.18. Simple conductive cooling model of Quizapu reservoir in the vertical direction (z), assuming a magma temperature of 850 °C and a wall rock temperature of 600 °C. Lateral (x-y) dimensions > 6 times larger allows cooling from the sides to be ignored. Cooling shown here would also occur from the bottom of the chamber at the same time. Isochrons are calculated using an error function fit to the diffusion equation, with input parameters as listed. Magma density and heat capacity from MELTS thermodynamic model for Quizapu bulk dacite at 850 °C (Gualda et al. 2012); magma conductivity and approximate solidus from (Annen 2009). After 85 years (the time between Quizapu eruptions), the top 61 meters of the reservoir would reach the solidus temperature, and the top 100 meters would cool to 25 °C or more below the minimum estimated equilibrium storage temperature (842-862 °C).

chamber would cool to a temperature more than 25 °C below the lower bound of experimentally-determined storage conditions (Figure 3.18). Thus, despite the potential eruptibility of this volume, only ≤ 3 km^3 could consist of the end-member dacite that constituted 95% of the erupted volume in 1932 (Hildreth and Drake 1992). One solution to this conundrum is to allow a larger initial magma chamber, at least 0.7 km high (~7 km^3, maintaining the x and y dimensions). After 85 years of conductive cooling, 5 km^3 of end-member dacite magma would still exist, given the same cooling considerations. Another possibility is that the pre-Plinian reservoir assembled only shortly before eruption, leaving little time for cooling. Even if this were the case, our calculation does not account for bubble volume. The passive outgassing in 1846-1847 could allow for this

simplification, and thus for a smaller magma reservoir, but the reservoir that fed the 1932 eruption would have to be larger, if a significant magmatic volatile phase (as opposed to e.g., deep magma influx) was the cause of overpressure and the initial driving force for the Plinian eruption.

The homogeneity of the erupted dacite (Hildreth and Drake 1992; Ruprecht et al. 2012) and the rapid ascent rates associated with Plinian eruptions (e.g., Rutherford 2008) preclude a scenario of continuous mush extraction to feed the eruption. A pre-existing, large-volume reservoir is necessitated. The maintenance of this reservoir was likely possible due to frequent influx of newly-extracted dacite, buffering the chamber and slowing its cooling, especially from the bottom. However, the height restriction of 0.5 km still applies for the region over which end-member dacite could have equilibrated. Increasing the dacite compositional range could expand storage depths and probable chamber dimensions, but the hard constraint of biotite absence is still limiting, as the mineral was not observed in any erupted material. The most plausible way to allow for a larger/taller magma reservoir is to invoke water undersaturation.

3.4.5 Water undersaturation

Water undersaturation would allow for a higher total pressure (P_{total}) at the same narrow range of P_{H2O} established here. To achieve water undersaturation while maintaining volatile saturation (a probable state for relatively shallow, silicic magmas; Johnson et al. 1994), additional volatile phase(s) like CO_2 must be available. The other key criterion that must be met is for biotite to remain excluded from the phase assemblage. The biotite crystal structure contains approximately twice as many volatile sites as amphibole, per given number of cations. For each 100 g of mineral crystallized, biotite requires ~8 g of structural water (OH groups), whereas amphibole requires only ~4 g of OH groups. Thus, an increase in total pressure without an increase in dissolved water content is not likely to result in biotite saturation.

Because phase assemblage and composition tends to respond more to changes in P_{H2O} than P_{total} (e.g., Hammer et al. 2002; Merzbacher and Eggler 1984; Muir et al. 2014; Riker et al. 2015) the Quizapu phase assemblage matched in this study could be maintained even at higher P_{total}. Riker et al. (2015) show that plagioclase An content decreases and crystallinity increases, with decreasing P_{total} at constant X_{H2O}^{fluid} or with decreasing X_{H2O}^{fluid} at constant P_{total}. A similar result for plagioclase composition is reported by Rutherford and Devine (1988). Thus, there should be

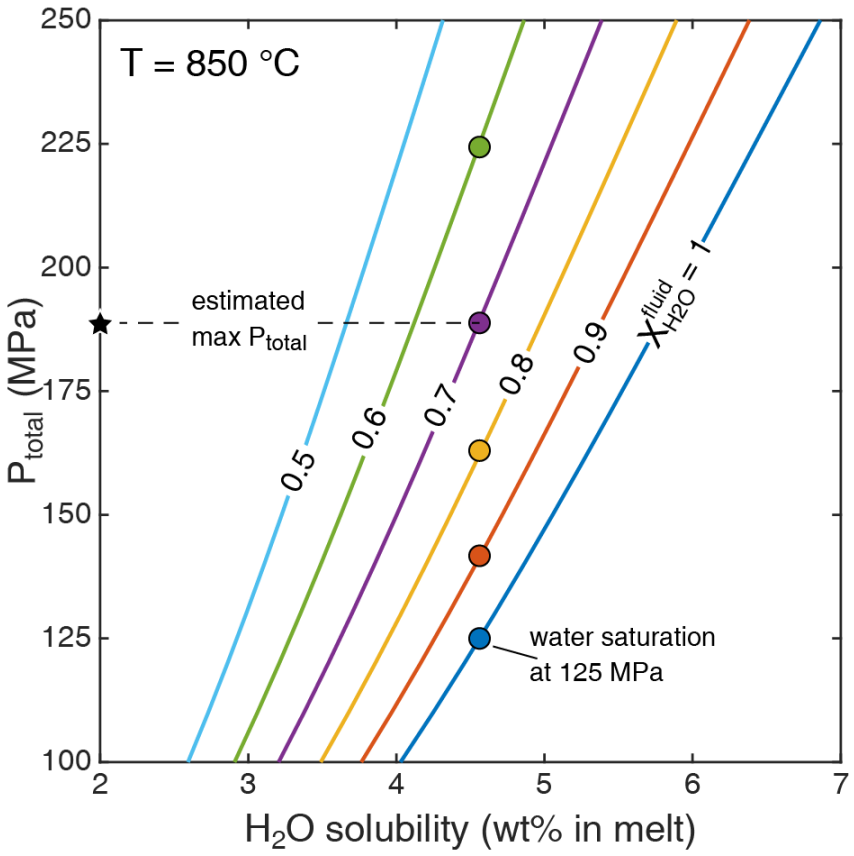

Figure 3.19. Isopleths of mole fraction H_2O in magmatic fluid, for Quizapu dacite glass (quenched melt) composition. Calculated using the solubility model of Moore et al. (1998). Each circle shows the total pressure at which the given melt water content occurs, assuming a mole fraction of H_2O in the fluid corresponding to the same-colored isopleth. Taking independent constraints on amphibole stability (Riker et al., 2015), it is likely that X^{fluid}_{H2O} is at least 0.7. Using this isopleth gives an estimate of maximum P_{total} at 188 MPa (star).

a suite of conditions that combine higher P_{total} and lower X^{fluid}_{H2O} to yield the plagioclase composition and crystallinity of the Quizapu dacite. This suite represents the pressure-fluid space where opposing driving forces balance each other (higher An/lower crystallinity at higher P_{total}; lower An/higher crystallinity at lower X^{fluid}_{H2O}).

Amphibole stability places a limit on the reduction of X^{fluid}_{H2O}, and by extension the maximum P_{total}. It has been proposed that hydrous amphibole stability is limited to pressures ≥ 125 MPa at water saturation (Johnson et al. 1994). For the Quizapu dacite melt, this corresponds to ~4.5 wt% H_2O in the melt at the storage temperature of 850 °C (Zhang et al. 2007). This melt water content is also that which best describes the estimated storage region, which is centered at 125 MPa. In addition, amphibole in a similar dacite at 885 °C is found to crystallize only at $X^{fluid}_{H2O} > 0.7$, even when melt H_2O content is held constant (Riker et al. 2015). An experimental

study of Mount St. Helens 1980 dacite finds a similar X_{H2O}^{fluid} criterion for amphibole stability, albeit at higher temperature (920 °C; Rutherford and Devine 1988). We apply this fluid compositional constraint to the Quizapu system in order to estimate a maximum P_{total}. On a plot of P_{total} versus wt% H_2O for the Quizapu pumice glass composition, the P_{total} at the intersection of 4.5 wt% H_2O and X_{H2O}^{fluid} = 0.7 represents the maximum total pressure, given the constraints above (Figure 3.19, star at 188 MPa). Allowing some leniency in the X_{H2O}^{fluid} stipulation would push this limit to higher pressure (e.g., 225 MPa for X_{H2O}^{fluid} = 0.6). But a secondary constraint from apatite, based on its stability only at high X_{H2O}^{fluid} in the experiments of Riker et al. (2015), suggests that $X_{H2O}^{fluid} \geq 0.9$, which would limit P_{total} to 142 MPa. In all cases, only values of P_{total} between that of water-saturated storage (125 MPa) and the maximum determined above (142+ MPa) are possible, with the true P_{total} determined by X_{H2O}^{fluid}.

3.4.6 Quizapu: A typical arc dacite?

Despite the volcano's unusual eruptive history, the magma that fed the Quizapu vent is not particularly remarkable. The storage conditions we determine (T = 850 °C, P_{H2O} = 125 MPa) place Quizapu in the middle of the range of other experimentally-determined arc dacite storage regions (Figure 3.20). It is colder than both the Mount St. Helens 1980 dacite (Rutherford et al. 1985) and the mixing-derived dacite erupted at Mount Unzen from 1991-1995 (Holtz 2005; Sato et al. 1999; Venezky and Rutherford 1999), but hotter than the Pinatubo 1991 climactic dacite (Rutherford and Devine 1996; Scaillet and Evans 1999). Storage of the dacite end-member of the intermediate magmas erupted at Novarupta in 1912 (Hammer et al. 2002) occurred at similar to slightly hotter temperatures. Quaternary dacites erupted at Cerro Uturuncu, Bolivia, were stored around 870 °C (Muir et al. 2014). Close to Quizapu, Volcan San Pedro erupted dacite estimated to have the same storage temperature, 850 °C (Costa et al. 2004).

The Quizapu dacite is also average in terms of its P_{H2O} and the possibility of water undersaturation (Figure 3.20). Novarupta dacite was stored at lower P_{H2O}, but may have been water undersaturated, with P_{total} closer to 110 MPa (Hammer et al. 2002). Mount Pinatubo dacite records protracted storage at P_{H2O} near 200 MPa, likely at water saturated or modestly undersaturated conditions (Rutherford and Devine 1996; Scaillet and Evans 1999). This storage was followed by 2-3 weeks at lower P_{H2O} (Hammer and Rutherford 2003). Saturation conditions are determined by the cause of this lowered P_{H2O}. If the decrease is due to physical ascent, then

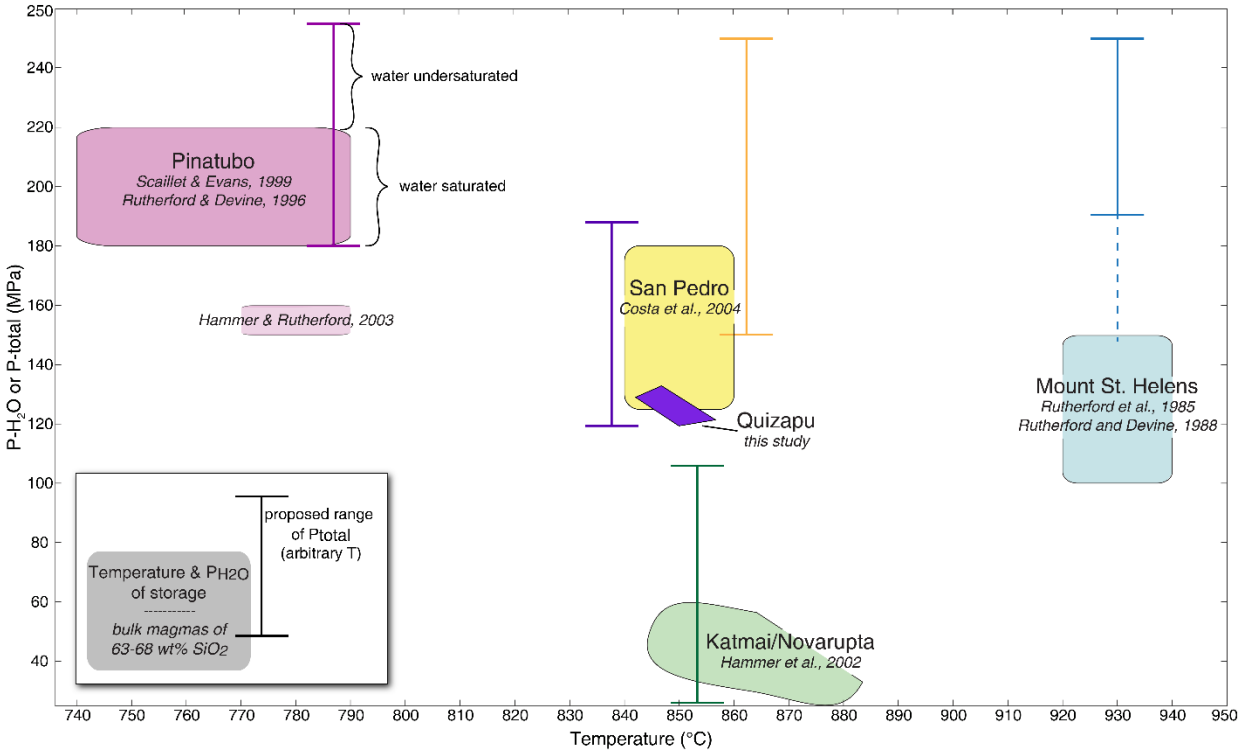

Figure 3.20. Comparison of Quizapu to several other arc dacites, in terms of pressure and temperature of equilibration, as determined by experimental studies. See text for discussion. Fields based on the studies listed in each box. Note that the P_{total} bars do not correspond to a preferred temperature; they are placed for visual convenience. At pressures over which shaded fields (P_{H2O}) and correspondingly colored brackets (P_{total}) overlap, water saturation is indicated. At pressures shown only by the brackets, water undersaturation is indicated (see labels for Pinatubo). The dashed line above the Mount St. Helens P_{H2O} field is to guide the eye up to Ptotal conditions – in this case, all conditions are water undersaturated. For studies that did not explicitly report P_{H2O}, we take the reported glass composition and melt water content to calculate P_{H2O}, using the Moore et al., 1998 solubility model.

water saturation is expected; if instead it is due to in situ volatile fluxing by a basaltic recharge magma, then water undersaturation is likely (Hammer and Rutherford 2003). The 1980 Mount St. Helens dacite was also stored near P_{H2O} = 125 MPa, but experiments demonstrate that it was significantly water-undersaturated (Rutherford and Devine 1988; Rutherford et al. 1985). San Pedro dacite overlaps the upper half of the P_{H2O} range determined for Quizapu. Its P_{total} is not well constrained, estimated between 150 and 250 MPa, allowing for the possibility of water saturated or undersaturated storage. Phase assemblage match criteria for Cerro Uturuncu dacite are met in both saturated and undersaturated experiments (Muir et al. 2014). Studies on Mount Unzen dacite also allow for variable interpretations, either concluding that the magma was water saturated during storage (Sato et al. 1999), or that the phase assemblage and compositions require variations in water content that include water undersaturation (Holtz 2005).

Determining the total equilibrium pressure of a given phase assemblage is a complicated task, belied by the large estimated ranges and uncertainties in the above studies. With the exception of Mount St. Helens, most systems do not have firm constraints on whether pre-eruptive storage was water saturated. Riker et al. (2015) elegantly demonstrate that changes in fluid composition and degassing path alone can produce the same compositional and textural variations as magma mixing, heating, and decompression. Thus, a next logical step in the study of the Quizapu dacite (and others) is to examine more closely its volatile species and degassing behavior.

3.5 IMPLICATIONS

3.5.1 The relevance of pre-eruptive storage conditions

We demonstrate above that, for the two studied eruptions, Quizapu is not unusual in terms of the pressure and temperature of its magma chamber. The volcano falls on a broad trend of negative correlation between P_{H2O} and temperature: i.e., hotter storage at lower P_{H2O} (Figure 3.20). Perhaps surprisingly, there is no contrast in storage conditions between the two disparate eruptions at Quizapu, and there is no correlation between pre-eruptive conditions and eruption style or intensity for other dacitic eruptions. The effusive eruptions of San Pedro and both eruptions of Quizapu fall directly between the 1991 climactic eruption of Pinatubo, (VEI 6; Newhall and Punongbayan 1996) and the explosive 1980 eruption of Mount St. Helens (VEI 5; Lipman and Mullineaux 1985) (Figure 3.20). Storage conditions for the 1991-1995 Mount Unzen dacite overlap the Pinatubo storage region, yet the Unzen eruption was largely effusive (Nakada et al. 1999). Novarupta falls off-trend and produced the largest eruption of the 20th century (VEI 6; Hildreth and Fierstein 2012). However, this dacite is the end-member of a continuum ranging from dacite to andesite, and was erupted alongside a large volume of rhyolite, so the dacite storage conditions alone do not encompass the entire pre-eruptive magma storage environment (Hammer and Rutherford 2002; Coombs and Gardner 2001). While a recent study finds pre-eruptive depths and water contents to be key controls on the eruption styles of some intermediate magmas (Andújar and Scaillet 2012), our experimental study, along with the volcanic systems discussed above, serves as a counterpoint to those conclusions, emphasizing that eruptive style was largely determined in the conduit, after storage.

Although the storage-conditions-as-eruptive-determinants theme does not apply to Quizapu and several other dacitic systems, we leave open the possibility that initial conditions

may play a larger role in modulating eruptive style in other systems (e.g., water content of phonolites from Vesuvius, Teide, and Erebus- Andújar and Scaillet 2012; superheating of Glass Mountain obsidian- Waters and Andrews 2016; water content of Soufrière Hills andesite- Thomas and Neuberg 2014). The Andújar and Scaillet work echoes a theme from "classical" volcanology, where the size and intensity of an intermediate-composition eruption is attributed to the volume of magma stored in the crust, the dissolved H_2O content, and tectonic setting (e.g., Bullard 1984; Schmincke 1973; Walker 1974). This view has given way to an emerging paradigm of eruption style governed in large part by events transpiring after magma departs the storage area, including degassing, outgassing, and the time-evolution of the conduit size and shape (e.g., Gonnermann and Manga 2012; Houghton et al. 2010; Loewen et al. 2017). What, then, is the utility of determining the temperature, pressure, and water content of a magma during static storage in a sub-volcanic chamber? Broadly, these parameters are required to define the initial state of the system, and represent the state from which all perturbations to the system are measured. Specifically, these parameters are necessary to calculate initial magma viscosity, to corroborate or improve geophysical models, to estimate ascent times or velocities, and to place initial constraints on magma mixing models. Some examples are highlighted below.

Magma viscosity, itself an important factor influencing eruptive style (e.g., Eichelberger 1995; Shea et al. 2017) is highly dependent on temperature and water content, both of which are constantly evolving. For example, addition of 2 wt% water to a rhyolite melt decreases viscosity by more than two orders of magnitude, and cooling of a basalt by 200 °C can decrease viscosity by a similar amount (Giordano et al. 2008). Viscosity is a key parameter in conduit flow models (e.g., Gonnerman and Manga 2012), making magmatic temperature and water content important variables to establish. Using the Conflow model (Mastin 2002), Ruprecht and Bachmann (2010) demonstrate that at 1000 °C, fragmentation of the Quizapu magma would be suppressed until ascending to within ~ 1 km of the surface, whereas fragmentation is predicted at 4 km depth with an input temperature of 870 °C (all other parameters equal; closed system degassing assumed). Clearly, the 1846-7 eruption involved open system degassing; the example is simply to illustrate the importance of temperature for modeling conduit processes in general. Ruprecht and Bachmann (2010) also contains a second key example of pre-eruptive temperature playing a defining role in dynamic calculations: heat transfer from recharge andesite to resident dacite is calculated using the equilibrium dacite storage temperature as a baseline. In a similar

consideration of storage conditions, Holtz (2005) use the experimentally-established equilibrium temperature and P_{H2O} for the mixed Unzen dacite to estimate the proportions of high- and low-temperature magmas that mixed to form the erupted dacite, as well as the water contents of each mixing end member.

Rutherford and Devine (1993) make use of Mount St. Helens pre-eruptive storage conditions to perform decompression experiments at relevant temperatures and confining pressures. These experiments are compared to naturally erupted material, using amphibole breakdown rim widths to establish magmatic ascent rates during the May 18 explosive eruption (> 66 m/h) and subsequent dome-forming eruptions (10-50 m/h). With ascent rates in hand, the experimentally-established storage depth of ~8 km is used to calculate the timescales of magma ascent from reservoir to surface in post-1980 lavas (6-10 days for one amphibole population, 8-25 days for another population, implying some mixing of freshly-derived and sluggish, older magma).

A final example of the utility of pre-eruptive storage conditions is exemplified by Cerro Uturuncu, Bolivia. For volcanoes with prolonged eruptive histories, phase equilibrium experiments can give us a sense of what a magmatic plumbing system looked like thousands of years ago. In the case of Cerro Uturuncu, this data is the only information available for comparison with present-day deformation indicated by geophysical data (1-2 cm uplift/year from a source 11-17 km deep; Sparks et al. 2008), thus elucidating the magmatic evolution of a newly re-awakened system. Phase equilibrium experiments reveal that pre-eruptive equilibration of dacite erupted for the past ~1 Ma occurred at 2-6 km depth, far too shallow to correspond to the modeled source of current deformation (Muir et al. 2014). These results indicate that either significant deepening of the magma system has occurred over the past ~270 ka (age of the last eruption at Uturuncu), or more likely, that the current deformation is not indicative of accumulation of magma in a reservoir poised for eruption, but rather represents a deeper input of more mafic material (Muir et al. 2014). In the following section, we use our own phase equilibrium experiments to gain insight into the eruptive dynamics in a system that is not simply restless, but still active: Quizapu itself.

3.5.2 Re-examining eruptive styles at Quizapu

By their nature, the static experiments presented herein are not designed to directly address the eruptive dynamics at Quizapu. Rather, they establish a robust starting point from

which future experiments and calculations regarding eruption processes at Quizapu can proceed. Nonetheless, the work herein does provide insights extending beyond the magma chamber. Analyses of experimental plagioclase microlites and amphibole phenocrysts, in combination with observations of natural lavas and pumice, permit re-consideration of the prevailing hypothesis regarding the cause of effusive eruption in 1846-7 at Quizapu (pre-eruptive heating; Ruprecht and Bachmann 2010).

Plagioclase microlites are present in some 1846-47 lava flow samples, but none of the 1932 pumices. Ruprecht et al. (2012) estimate the compositions of these microlites as moderately calcic using BSE images, and then assert that the microlites were transferred from the recharge andesite to the resident dacite magma prior to eruption. Both Ruprecht and Bachmann (2010) and Ruprecht et al. (2012) present this "microlite transfer" as evidence for heating of the dacite magma chamber shortly prior to the 1846-7 eruption. Our quantitative EPMA analyses of plagioclase microlites permit testing of this assertion. The microlites span a range of anorthite content up to ~An_{40}, but cluster near An_{20}. Experimental samples crystallized plagioclase microlites largely in the range An_{20}-An_{40}, strongly suggesting that the microlite population in the Quizapu dacite lava crystallized *in situ* and was not transferred to the dacite from a different magma. We conclude that even if heating occurred, microlite transfer did not.

This examination of microlites refutes the notion that the dacite lava is entirely glassy, and brings other inconsistencies to light regarding the pre- and syn-eruptive dynamics in 1846-7. The very heterogeneity of the dacite lava flows is intriguing. Some flow lobes consist mainly of end-member dacite, such as the one from which our starting material was collected (Figure 1), but others consist of up to 45% mafic material in the form of enclaves (Ruprecht and Bachmann 2010). Still others represent a more homogenized, hybrid mix of dacite and andesite. Overall, mafic material is estimated to compose 10-24 vol% of the flow field (Ruprecht and Bachmann 2010). Clearly, the macro-scale, visual evidence for the involvement of the hotter andesite magma is heterogeneous. Heat transfer is more rapid than mass transfer, however, meaning that magma which did not interact directly with the more mafic recharge may nonetheless have undergone a heating event. The end-member dacite lava used as one of our starting materials would represent this type of "heated only" magma, if the effusive eruption style was caused by heating.

However, we find no conclusive evidence that the end-member dacite, erupted as lava in 1846-7, underwent any heating. First, as stated above, it is not glassy, but rather does contain abundant plagioclase microlites. Limited exposures of the end-member dacite lava lobes do lack plagioclase microlites, and would accurately be described as "glassy." However, based on our own field observations, these parts are small and unrepresentative of the flow lobes as a whole (e.g., one glassy area extends for < 50 m along a flow lobe > 5 km long). Second, given the dacite composition, at 130 °C above the equilibrium storage temperature (980 °C), plagioclase is not stable at any pressure > 80 MPa, and even then, the composition of the crystals should be more calcic than that of the observed microlites until < 20 MPa (Waters and Lange 2015). If reheating took place at depth (i.e., in the magma chamber; Ruprecht and Bachmann 2010), then considerable resorption of plagioclase should be evident in the erupted dacite, either texturally (rounded corners on plagioclase relicts) or compositionally (higher Al_2O_3/MgO in the glass). Some plagioclase phenocrysts erupted in the 1846-7 lava flows do display melt channeling and/or sub- to anhedral outlines, features interpreted to represent resorption (Ruprecht et al. 2012). However, it is not clear if these crystals are present in all flow lobes, or only those which contain mafic enclaves and mingled dacites. In addition, similar internal morphological complexities and melt pockets in plagioclase have been attributed to growth effects by other authors (e.g., Tequila volcanic field; Frey and Lange 2011). Plagioclase texture and abundance thus are unreliable indicators of pre-eruptive heating. Certainly, the supposition of glassy, microlite-free dacite (e.g., Ruprecht et al. 2010) is generally incorrect for the Quizapu lavas.

Further evidence that heating was at best heterogeneous, or absent, comes from amphibole phenocrysts. Both non-rimmed, euhedral crystals (like those in the starting material) and crystals with breakdown rims are present in the 1846-7 flow field. Even ≤ 40 °C above the established storage temperature (experiments 1 and 19, Table 3.2), there is experimental evidence of amphibole breakdown after ≤ 7 days. An additional ~100 °C of heating, as proposed for the 1846-7 Quizapu eruption, would likely produce reaction rims tens of microns in width after only a few hours (De Angelis et al. 2015). Given the estimate of "days to weeks" between magma mixing and eruption (Ruprecht and Cooper 2012), it seems implausible that the euhedral amphibole phenocrysts in end-member dacite flow lobes were subject to heating.

The single piece of evidence that could reflect heating of the end-member dacite is the very subtle reverse zoning of some orthopyroxene phenocrysts in the lava (Figure 3.7c-d; visible

due to highly enhanced contrast). Patchy compositional variation, including in the sense of reverse zoning, is present in some orthopyroxene crystals from the 1932 eruption, although these may be glomerocrystic in origin (Figure 3.7a). Isolated orthopyroxene phenocrysts in the 1932 pumice are unzoned. Thus, the zoning of 1846-7 orthopyroxene crystals is different from that in most of the 1932 crystals. This may reflect a small and/or rapid shift in magmatic environment relative to the stable pre-eruptive conditions in 1846-7. Because more Mg-rich orthopyroxene would be stable at higher temperatures, reverse zoning does indicate a direction of change consistent with heating. However, the subtlety of zoning suggests a relatively small compositional change, likely to be inconsistent with heating by 130 °C.

Despite the clear involvement of andesite recharge in some parts of the flow field, there is a lack of convincing evidence that the end-member dacite was heated much beyond its equilibrium storage temperature in 1846-7. This conundrum raises additional questions that call for a more thorough investigation of the 1846-7 flow field, involving both field work and petrography.

(1) If heating of the dacite by up to 130 °C did occur (Ruprecht and Bachmann 2010), then why is the dacite not glassier overall? The simplest explanation is that heating was heterogeneous, and in fact affected some of the erupted material either very little or not at all. Another cause of variable glassiness could rest in the conduit dynamics of the eruption – perhaps shear heating along conduit margins suppressed microlite formation in a relatively small proportion of the magma. Small increases or decreases in ascent rate with time could also result in additional suppression or growth of microlites, respectively.

(2) If heating was the cause for effusive eruption, then how did multiple flow lobes with end-member dacite erupt with little to no evidence of the event? Again, we have made a strong case that, for the end-member dacite, the absence of evidence for heating means that heating was heterogeneous and had very little effect on some flow lobes. Yet, all lava erupted effusively, regardless of the evidence (or lack thereof) for heating by > 100 °C. We suggest, therefore, that heating was unlikely to have been the main influence on eruptive style.

(3) If heating was not the key difference between the effusive 1846-7 eruption and the explosive 1932 eruption, then what parameters controlled the eruptive styles? Answering this question definitively would take much more study, but some ideas can be put forth based on other silicic, effusive eruptions.

The near-identical nature of the 1846-7 and 1932 end-member dacites suggested from the start that pre-eruptive storage conditions did not influence eruptive style at Quizapu, and our experiments confirm this explicitly for temperature and pressure. Although we did not vary X_{H2O}^{fluid}, water-saturated conditions successfully reproduce the phase assemblage from both eruptions, and the presence of stable amphibole in both cases suggests that fluid content was not appreciably different in 1846-7 than in 1932, in direct contrast to the conclusions of Andújar and Scaillet (2012) that pre-eruptive volatile contents are the main control on eruptive style. The Quizapu examples do not preclude a pre-eruptive volatile control at other volcanoes, but for many systems, shallow ascent dynamics are found to play a larger role in controlling eruptive style (e.g., Eichelberger 1995; Adams 2006a, 2006b; Loewen et al. 2017).

To explain the effusive nature of the 1846-7 eruption, it is therefore necessary to turn toward processes within the sub-volcanic plumbing system, rather than the thermodynamics of magma storage. The 1846-7 magma may have outgassed prior to extrusion due to the formation of a permeable foam (Eichelberger et al. 1986), or more gradual gas loss due to strain-induced outgassing via permeable pathways (e.g., Caricchi et al. 2011) or melt fracturing (e.g., Cabrera et al. 2015; Gonnermann and Manga 2003). Slow ascent rate is necessary to allow for sufficient outgassing, by whichever means it occurs, and is evidenced by the duration of the Quizapu effusive eruption, which was ~100 times longer than the 1932 Plinian eruption, but expelled the same volume (DRE) of material. The key to allowing slow ascent, and thereby sufficient outgassing to preclude explosive eruption, may lie in the conduit size and geometry.

There is evidence that some silicic lava flows and domes erupt along fissures, at least initially, rather than issuing from central vents (e.g., Medicine Lake, Donnelly-Nolan et al. 2016), and Quizapu appears to follow this trend. Hildreth and Drake (1992) interpret the observations of eye witnesses and early post-eruption reports to indicate that the eruptive vent for the 1846-7 eruption was most likely a ~1 km long fissure, trending NNE. Fissures can accommodate high discharge rates at relatively slow ascent rates, compared to point source vents, where an equally high discharge rate would correspond to far more rapid ascent. A fissure geometry also provides greater surface area over which magma is in contact with wall rock or atmosphere, allowing outgassing at higher rates, which favors effusive eruption. Pre-existing fractures in the upper crust allow for easy fissure formation in certain locations, a critical element that allows the resultant eruption to have an effusive rather than explosive character, given the

same initial magma pressure (e.g., Yellowstone, Loewen et al. 2017). There is abundant evidence for pre-existing crustal structures in the Andes, from the Liquiñe–Ofqui fault zone with its major NW-SE trending faults, to compressional structures that strike roughly along-arc in a NNE direction and define many volcanic clusters (Cembrano and Lara 2009). Mafic volcanic centers, not expected given the 45-km thick crust, occur in the Southern Volcanic Zone due to facilitated magma ascent through crustal structures related to the Andean arc and even pre-Andean tectonic regimes (Salas et al. 2017). It is thus reasonable to expect some of these same or similar structures to influence the more prevalent, silicic volcanism in the region.

The hypothesized NNE-trending fissure vent at Quizapu would roughly align with the arc itself, and more locally, with the Cerro Azul-Descabezado Grande volcanic axis (Figure 1), making it consistent with the regional tectonic trends. The cessation of the 1846-7 eruption appears to have left non-erupted material to solidify in the vent, which is partially visible in the current crater wall (Hildreth and Drake 1992, their Figures 5-6). This massive, un-brecciated filling of the eruptive fissure would have forced magma to take a different path to the surface in 1932, and, lacking access to another easily-opened fissure, it discharged through a point source vent in a highly explosive eruption.

This explanation of the Quizapu eruptive style change is a new hypothesis, but one that deserves additional study. Further field work to establish the eruptive sequence of the extruded lava lobes is needed, as well as a dedicated effort to establish if any lavas came from vents not coincident with the current Quizapu crater, and if so, whether those sources were fissures, and how long they might have been. Additional petrologic work on each lava lobe should complement the field study, to map out the presence and intensity of indicators of pre-eruptive heating. Although we have discounted heating as the primary driver of eruptive style for the flow field in general, it may still have played a role in specific portions of the field, or at particular points in the temporal sequence of the eruption. Together, further field work and petrography can clarify the 1846-7 eruption dynamics at Quizapu.

3.5 CONCLUSIONS

The temperature-pressure conditions at which the Quizapu dacite equilibrated are robustly determined to be 850 °C and 125 MPa (4.75 km), based on stability of the major phase assemblage $An_{25\text{-}30}$ plagioclase + amphibole + orthopyroxene. These conditions apply to magmatic storage before both the 1846-7 and 1932 eruptions. The ease of biotite formation just

outside of the established pre-eruptive storage region leads to the hypothesis that the dacite may have equilibrated at slightly water-undersaturated conditions, likely at a $P_{total} \leq 188$ MPa. Our work paves the way for a deeper understanding of the Quizapu system in future studies. Focused topics that may prove to distinguish Quizapu from other arc dacites include (1) the intricacies of pre- and syn-eruptive degassing, including X_{H2O}^{fluid}, along with contributions of CO_2, S, and Cl; (2) the specific mechanisms that induce hydrous phase saturation versus breakdown, including halogen and S partitioning, and bulk composition; (3) further modeling and experimentation of heating and/or mixing of the dacite with andesitic recharge magma, including volatile exchange; (4) linked field and petrological studies of the 1846-7 flow field to address the heterogeneous nature of pre-eruptive heating and the possibility of shallow, ascent-driven controls on eruptive style. The experiments and natural observations addressed in our study suggest that the difference in eruptive styles between 1846-7 and 1932 was not dominantly related to the presence or absence of mafic recharge magma. Rather, slow ascent combined with an elongate conduit geometry (fissure) may have allowed for more outgassing in 1846-7 compared to 1932. The Quizapu system, which appears "simple" at first glance, remains only partially understood. The questions and directions discussed in sections 3.5-3.6 provide a path forward for future research that will further elucidate the magmatic and volcanic processes at this active volcano.

Chapter 4. Re-equilibration of Fe-Ti oxides: Textural and compositional effects of a single-step reduction

In preparation for publication as:

First, E. and Hammer, J. (201-) Re-equilibration of Fe-Ti oxides: Textural and compositional effects of a single-step reduction. *American Mineralogist*.

Abstract - Fe-Ti oxide minerals are regarded as the gold standard for recording faithfully magmatic temperature and oxygen fugacity (fO_2), and equilibrating quickly enough to record perturbations (e.g., magma mixing) shortly before eruption. However, the limited experimental work available hints at non-linear re-equilibration processes. Here, static experiments intended to determine the phase equilibrium relationships in an arc dacite are used to gain insight into the re-equilibration of hemoilmenite and titanomagnetite following a step-wise reduction in fO_2. Crystals that last equilibrated at ~NNO+0.5 are subjected to pressures from 100-200 MPa and temperatures from 810-890 °C, at a reduced fO_2 of NNO-2. After 7-14 days, nearly all Fe-Ti oxide grains display disequilibrium textures and compositions. In titanomagnetite, these are manifested as solid central regions surrounded by variably-thick lacework patterns of titanomagnetite and melt. Concentration gradients in Ti (higher near the rim) extend slightly into the solid cores, reflecting higher ulvöspinel activity at lower fO_2. In hemoilmenite, Fe-rich lamellae are exsolved and subsequently replaced by melt, resulting in crystals frozen at various stages of reaction, from slightly rounded with exsolutions to completely reacted but for a few small blebs. Some euhedral hemoilmenite (< 10 μm) crystallizes, with the same Ti-rich composition as the residual blebs. These grains are nearly pure ilmenite, a phase too Ti-rich even for the low fO_2 of the experiments. Clearly, Fe-Ti oxides may react to environmental perturbations within days, but their path to equilibrium is non-linear, seeming to overshoot before possibly moving back toward an equilibrium composition.

4.1 INTRODUCTION

4.1.1 The appeal of Fe-Ti oxides

Iron-titanium oxide minerals change composition predictably with temperature and oxygen fugacity (fO_2), and are thus lauded as reliable indicators of magmatic environmental

conditions. As temperature increases or as fO_2 decreases, the pure Fe components magnetite (Mt) and hematite (Hm) are preferentially replaced by the Ti-bearing components ulvöspinel (Usp) and ilmenite (Ilm), respectively (e.g., Andersen and Lindsley 1988; Buddington and Lindsley 1964; Ghiorso and Evans 2008; Ghiorso and Sack 1991; Spencer and Lindsley 1981). Minor components give more nuance to the thermometer-oxybarometer, but have a lesser effect on calculated temperature and fO_2. A key requirement for any application of this thermometer-oxybarometer is that the titanomagnetite and hemoilmenite compositions under consideration are in equilibrium with each other (Bacon and Hirschmann 1988). According to phase equilibrium and diffusion studies, titanomagnetite can change composition quickly at magmatic temperatures, developing diffusion rims ≥10 μm after ~1 day to ~3 weeks at temperatures of 800-900 °C (Devine et al. 2003; Freer and Hauptman 1978; Gardner et al. 1995b; Rutherford and Devine 2003; Venezky and Rutherford 1999). The fast re-equilibration rate is often cited to assert that the Fe-Ti oxide thermometer-oxybarometer can provide quantitative information about the duration, as well as temperature and fO_2, of magma mixing and heating processes that occur on the order of days to weeks before eruption.

Other petrologic indicators can access useful information about this key time frame, but they record different magmatic variables, or only duration. The thickness of amphibole breakdown rims can provide an estimate of magmatic ascent rates, or overall duration at low pressure or high temperature (e.g., Browne and Gardner 2006; Rutherford and Devine 2003; Rutherford and Hill 1993). Depending on the magnitude of perturbation from equilibrium, rim formation is appreciable within 2-10 days in Mount St. Helens dacite (Rutherford and Hill 1993), and within hours in high-silica andesite (De Angelis et al. 2015). However, this empirical tool requires calibration over a broader range of magmatic conditions and compositions to be a more widely applicable indicator of magmatic environments, and there is evidence that rims produced by heating and by decompression may be indistinguishable, complicating any quantification of magmatic conditions (De Angelis et al. 2015). Amphibole is also a potential thermobarometer (e.g., Johnson and Rutherford 1989; Ridolfi and Renzulli 2012), but reaction can take weeks before compositional changes are detected (Hammer and Rutherford 2003), leaving this tool unusable over the timescales in question. Diffusion modeling of Fe-Mg and other concentration gradients in olivine provides an estimate of the time between magmatic perturbation and eruption, which can be resolved over days to years, but the method requires a priori knowledge

of magmatic temperature and fO_2 (e.g., Costa and Chakraborty 2004; Hartley et al. 2016; Lynn et al. 2017). Diffusion of major and trace elements in plagioclase occurs too slowly to approach volcanic timescales (e.g., Giletti and Casserly 1994; Grove et al. 1984), with the possible exception of Mg (e.g., LaTourrette and Wasserburg 1998; Van Orman et al. 2014). In all cases, ambient magmatic conditions must again be known or assumed. Residual glass compositions can record magmatic fluctuations within weeks of eruption, if fast-growing or fast-equilibrating minerals dominate the assemblage (e.g., lower P_{H2O} prior to Pinatubo 1991 eruption evidenced by plagioclase-driven melt compositional changes (Hammer and Rutherford 2003). However, glass thermobarometry is highly system-dependent, and no externally-applicable calibrations have yet been proposed. Thus, Fe-Ti oxides have the potential to supply important information about late-stage processes in a magma's history that may otherwise go unrecorded.

4.1.2 Applications to natural samples

In cases where titanomagnetite and hemoilmenite are fully equilibrated (i.e., homogeneous in composition across entire crystals), these phases are thought to record static pre-eruptive storage conditions. For example, in the Bishop Tuff, a continuous range of temperatures, derived from Fe-Ti oxides across the stratigraphy, is invoked as evidence for the existence of a thermally zoned magma reservoir prior to eruption (Evans and Bachmann 2013; Evans et al. 2016; Hildreth and Wilson 2007). However, some magmatic systems preserve homogeneous Fe-Ti oxide crystals that yield temperature estimates outside the stability field of the main phase assemblage. This juxtaposition suggests that Fe-Ti oxides reflect late-stage fluctuations in temperature or fO_2 that are not recorded by the rest of the assemblage, but that occurred long enough before eruption for the Fe-Ti oxide grains to homogenize. This situation is invoked for a subset of Fe-Ti oxides in the dacite lava erupted at Volcán Quizapu, which yields temperatures up to 130 °C hotter than the equilibration temperature of the dacite (Ruprecht and Bachmann 2010; Ruprecht et al. 2012). This temperature difference was used to calculate the resultant viscosity decrease from putative heating by an influx of andesite, which is in turn implicated in producing the effusive eruption style (Ruprecht and Bachmann 2010). Fe-Ti oxides recording partial equilibration (i.e., preserving a concentration gradient) have also been used to glean information about magmatic events shortly before eruption, based on compositional differences between rims and cores. For example, Nakamura (1995) uses Ti zoning in titanomagnetite to calculate apparent pre-mixing (core) and post-mixing (rim) temperatures of

the Unzen 1991 dacite. The average temperature is applied to diffusion modeling of the Ti concentration gradients to estimate that mixing occurred no more than a few months before eruption. Likewise, temperatures derived from Fe-Ti oxides in Mount Rainier banded pumice are assumed to represent the post-mixing magma temperature (Venezky and Rutherford 1997). Subsequent diffusion modeling of Ti gradients in titanomagnetite is used to estimate mixing timescales of 4-5 days before eruption.

4.1.3 Prior experimental work

4.1.3.1 Diffusion coefficients

Despite its popularity and clear potential to elucidate magmatic processes, the Fe-Ti oxide system has yet to be explored experimentally in sufficient detail. The diffusivities of Fe, Ti, and minor species (e.g., Mn, Al) in (titano)magnetite depend on temperature and fO_2 in complex ways, possibly involving vacancy mechanisms at higher fO_2 and interstitial mechanisms at lower fO_2 (Aggarwal and Dieckmann 2002; Dieckmann et al. 1987). Increasing temperature may also favor diffusion via interstitial sites over vacancies (Dieckmann et al. 1987). The result is a suite of various diffusivity minima at different fO_2, which shift according to temperature (Van Orman and Crispin 2010). Fe-Ti interdiffusion is faster in titanomagnetite with higher Ti content, with similar complexities of diffusion mechanism (Aggarwal and Dieckmann 2002; Aragon et al. 1984; Freer and Hauptman 1978). Cation diffusivities (Mn, Mg, Co, Ni, Al, and others) in hemoilmenite at 1000 °C can be as fast as those of Fe in titanomagnetite at 1200 °C, but additional details are absent in the single abstract that reports diffusivities in hemoilmenite (Stenhouse et al. 2010).

4.1.3.2 General re-equilibration

Studies with a dedicated focus on Fe-Ti oxide equilibration are largely based in simple, synthetic Fe-Ti-O systems. This is the case for experiments used in the first calibration of the Fe-Ti oxide thermometer-oxybarometer (Buddington and Lindsley 1964), as well as hemoilmenite reduction experiments (Hammond and Taylor 1982), and experiments examining the magnetic properties of co-equilibrating titanomagnetite and hemoilmenite (Charilaou et al. 2011). The reduction experiments of Hammond and Taylor (1982), performed by weighing hemoilmenite during reduction in a flowing gas atmosphere, imply that hemoilmenite fully re-equilibrates within several hours at temperatures > 1000 °C and days at 900 °C, after a step reduction of 1-2 log units fO_2. A constant-rate cooling experiment from 1150-985 °C at 0.5 °C h^{-1} (~2 weeks)

resulted in hemoilmenite with the same equilibrium composition as that achieved in isothermal experiments (Hammond and Taylor 1982). Unfortunately for purposes of comparison, no images or compositional tables are provided. The same study addresses diffusion indirectly, estimating Fe-Ti interdiffusion based on the experimental grain dimensions, obtaining logD ≈ -11 to -12 m^2 s^{-1} at 900 °C. This value is roughly three orders of magnitude faster than Fe-Ti interdiffusion in titanomagnetite (Aragon et al. 1984; Freer and Hauptman 1978), but agrees with the conclusion of Stenhouse et al. (2010) that diffusion in hemoilmenite is comparatively fast.

The textural and chemical manifestations of re-equilibrating Fe-Ti oxides in natural magmatic melts have been studied experimentally, though generally as side notes in larger phase equilibrium studies. Nonetheless, these studies have refined our understanding of the effects of fO_2 and temperature on titanomagnetite composition, confirming predictions from simple-system experiments and thermodynamics, in natural andesite (Devine et al. 2003; Martel et al. 1999) and dacite (Evans and Scaillet 1997; Rutherford and Devine 1988). Whereas changes in titanomagnetite composition are evident in the above studies, hemoilmenite compositional changes are limited and have not been addressed systematically, nor have textural changes for either phase. One exception is the more detailed treatment by Venezky and Rutherford (1999), which examines changing titanomagnetite and hemoilmenite composition over time in natural dacite, based on step heating or cooling. They find that, in many cases, the rims of non-touching Fe-Ti oxides in the same sample are suitable for thermometry and return experimental temperatures (750-850 °C). However, in several experiments, calculated temperatures based on Fe-Ti oxide compositions after long run durations (9-13 days) are farther from the run temperature than those calculated based on Fe-Ti oxides held for shorter durations (5-6 days) at the same conditions. These anomalies bely the possibility that the new equilibrium composition can be "overshot" (i.e., that compositional changes may occur first in a direction that moves the crystal farther from equilibrium, before moving toward equilibrium). The rate of re-equilibration is enhanced by exsolution lamellae, which increase the surface area over which exchange reactions occur (Venezky and Rutherford 1999). Notably, 20 μm Ti-rich rims on titanomagnetite grains form ~2-20 times faster than predicted by Fe-Ti interdiffusion rates (< 10 days compared to 160 days at 775 °C (Freer and Hauptman 1978). Venezky and Rutherford also provide some textural details, reporting that at conditions more than 25 °C different from the original equilibration temperature, melt channels form in titanomagnetite. Finally, although diffusion is

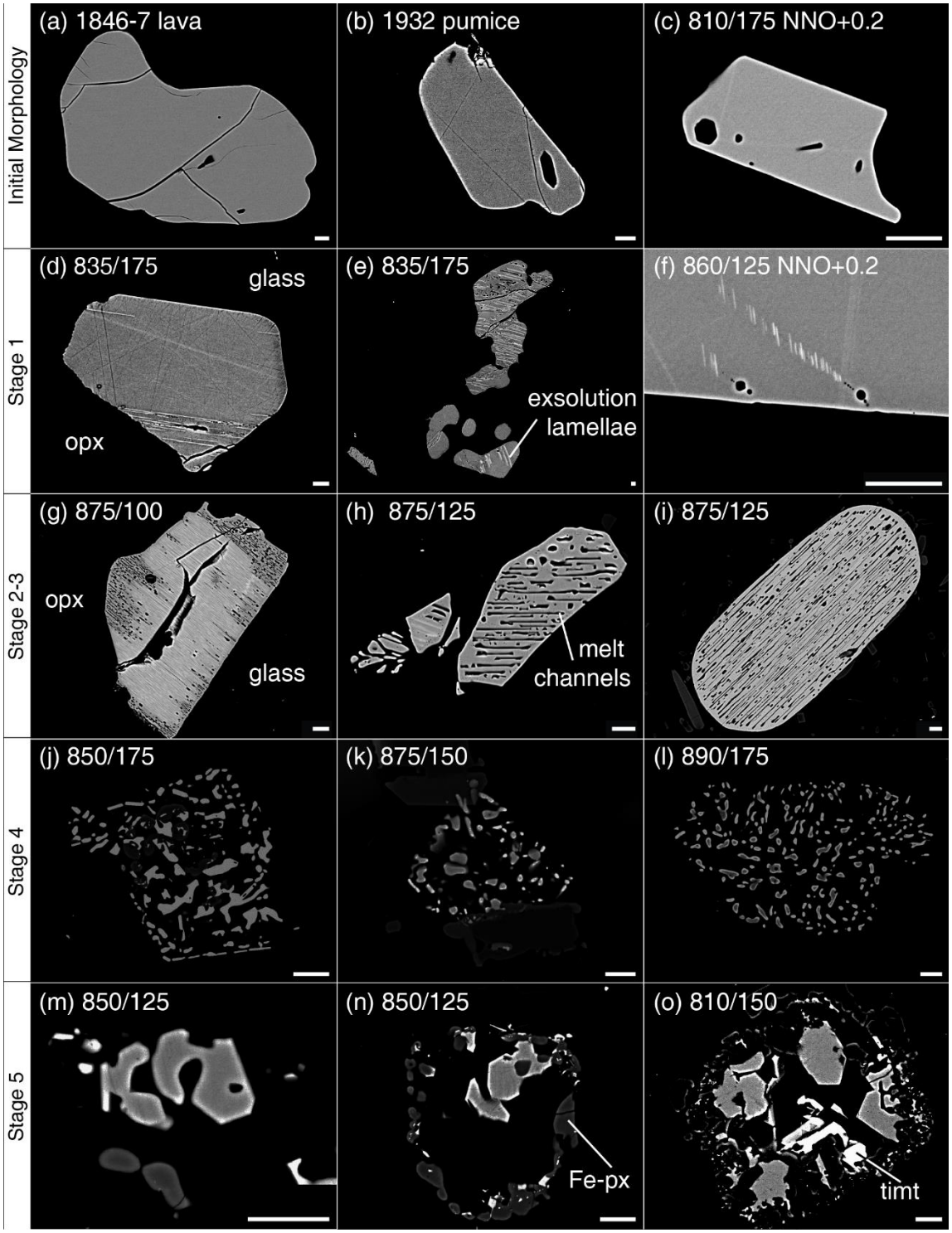

Figure 4.1. BSE images showing the hemoilmenite re-equilibration process described in the text. Each row shows three representative images of the stage at left. Experimental conditions are listed as T (°C)/P (MPa), with fO_2 = NNO-2 unless otherwise indicated. Note the absence of correlation of morphological stage with T or P. The medium grey phase in all images is hemoilmenite. (a) and (b) are from starting materials. The composition of residual blebs in (j)-(l) is approximately the same as that of the euhedral grains in (m)-(o), that is, ilmenite with almost no hematite component. Unless otherwise noted, black areas are glass. opx = orthopyroxene, Fe-px = Fe-rich orthopyroxene, timt = titanomagnetite. Scale bars are 10 μm.

enhanced at higher temperature, compositional changes occur more rapidly at lower temperature in the experiments of Venezky and Rutherford (1999), implying that re-equilibration is not a simple process based on diffusion alone (e.g., Frost 1991).

4.1.4 Objectives of this work

The studies above lay a stimulating groundwork for understanding the rates and mechanisms of Fe-Ti oxide re-equilibration in natural magmas. Here we describe the results of a step-change in fO_2 on the textures and compositions of titanomagnetite and hemoilmenite in contact with hydrous dacite at 810-890 °C, 100-200 MPa, and fO_2 near NNO-2. Each experiment is controlled at static pressure and temperature, and all are run at the same fO_2, which is approximately 2.5 log units more reducing than that of the starting material. This work (1) reveals longer-than-expected equilibration times, (2) elucidates a textural progression that hints at the dominant re-equilibration mechanisms, and (3) suggests a complex response to oxidation/reduction and heating/cooling perturbations. While far from a comprehensive treatment, our study refines gaps in the understanding of Fe-Ti oxide equilibration that may guide future studies.

4.2 METHODS

4.2.1 Starting Materials

Experiments were conducted using near-isochemical dacite lava and pumice (Table 3.1), from Volcán Quizapu, Chile, erupted in the 1846-7 effusive eruption and the 1932 Plinian eruption, respectively. In both starting materials, euhedral, homogeneous titanomagnetite and hemoilmenite are present (Figure 3.4-3.5). Zoning visible only at maximum contrast and rare oxyexsolution features are interpreted as syn- or post-eruptive modifications that do not concern the magmatic storage of the minerals (Figure 3.5). In both rocks, titanomagnetite has a composition of $Mt_{68}Usp_{32}$ and hemoilmenite has a composition of $Hm_{15}Ilm_{85}$. These Fe-Ti oxides indicate equilibration at an fO_2 of ~NNO to NNO+1 and a temperature of ~835-885 °C (Hildreth and Drake 1992; Ruprecht and Bachmann 2010; Ruprecht et al. 2012).

4.2.2 Experimental and analytical procedures

The experimental set is the same as that forms the basis of Chapter 3, and the reader is pointed to the methods therein for details. Briefly, we perform water-saturated, static experiments over 810-890 °C and 35-200 MPa, with durations ranging from 7-14 days (Table

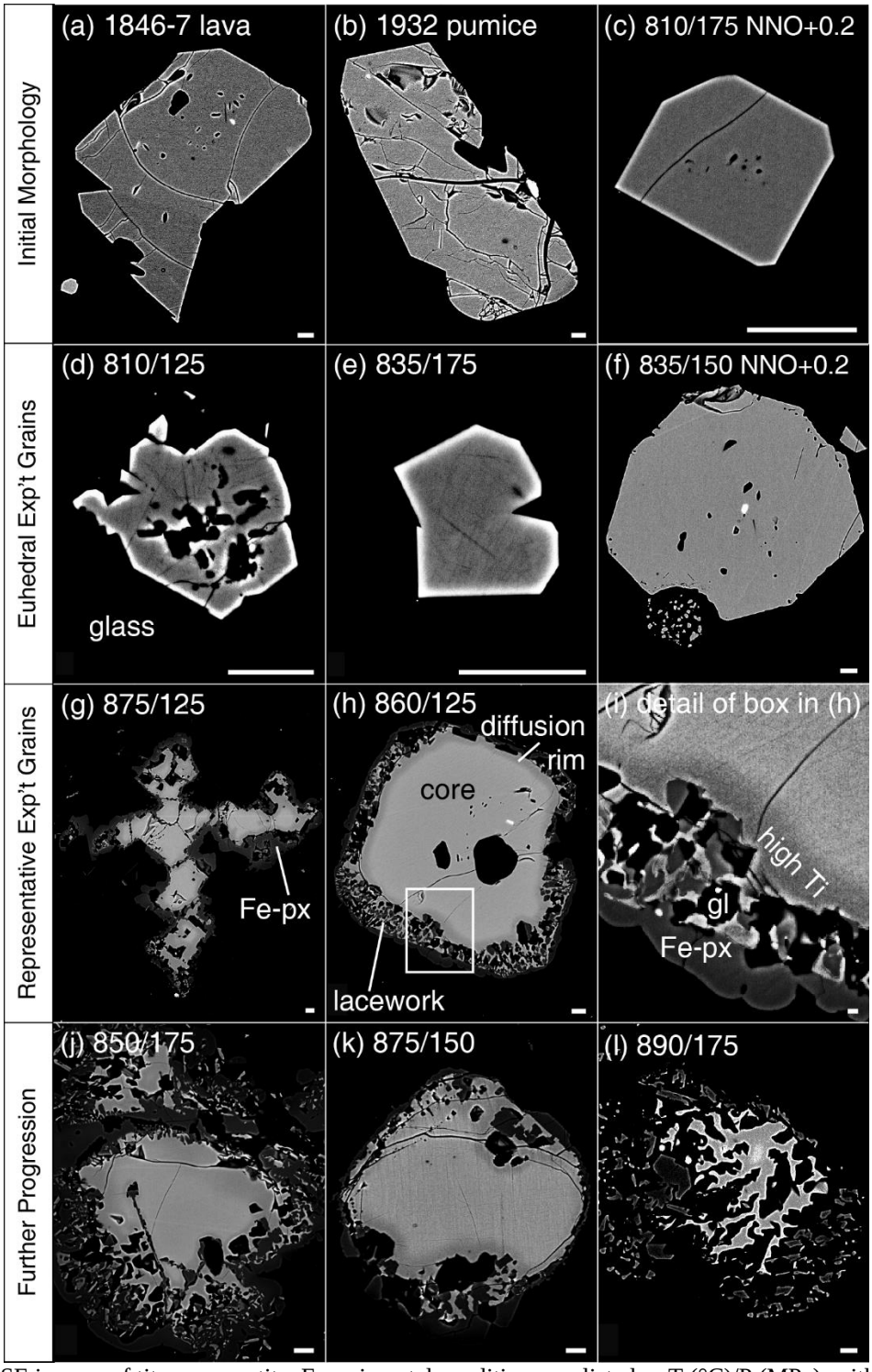

Figure 4.2. BSE images of titanomagnetite. Experimental conditions are listed as T (°C)/P (MPa), with fO_2 = NNO-2 unless otherwise indicated. Black areas are glass. Note the infilled, euhedral nature of crystals from NNO+0.2 runs (c and f). Atypical, small, euhedral crystals formed in some runs (d-e). Most crystals look like those in the bottom two rows. A blow-up of the box outlined in (h) is shown in (i), with contrast stretched differently for Fe-px and titanomagnetite to highlight the Ti diffusion rim. As for hemoilmenite, no T-P relationship with morphology is observed. We interpret (l) as an off-center cut through the lacework patterned edge of a larger grain. Fe-px = iron-rich orthopyroxene, gl = glass. Scale bars are 10 µm.

3.2). Most experiments are run at an fO_2 that is 2.1 log units below the Ni-NiO redox buffer (NNO-2.1), and three are run at NNO+0.2. Oxygen fugacity is determined with a precision of ~0.2 log units by solid state sensor assemblages (Ni-Mn-O and Co-Pd-O) run at experimental conditions (Taylor et al. 1992). Thus, a single step ΔfO_2 of 2-3 log units below initial equilibration was induced in experiments run at NNO-2.

Textures and qualitative compositions of all run products were documented with backscatter electron (BSE) imaging, on scales of < 10 to > 100 μm. In a subset of experiments, Fe-Ti oxides were analyzed by electron microprobe, using the JEOL Hyperprobe JXA-8500F at the University of Hawaii. All spot analyses had an accelerating voltage of 20 keV and a beam current of 25 nA. Images were acquired at lower currents. Beam diameter varied from focused to 5 μm. On-peak counting times were 30 s (Si, Al, Cr, Fe, Mn, V) and 65 s (Ti, Mg). Interferences on Mn and V peaks were corrected. Re-calculation to account for Fe^{3+} followed the method of Droop (1987). Standards and additional methods are detailed in Chapter 3.

4.2.3 Null hypothesis

If the 50-100 μm Fe-Ti oxides in our samples fully equilibrate within the experimental duration of 7-14 days, run products should contain euhedral titanomagnetite and hemoilmenite crystals, with no exsolution lamellae or melt channels. Their compositions should reflect Mg/Mn equilibrium (Bacon and Hirschmann 1988) and reproduce the experimental temperatures and fO_2 upon application of the thermometer-oxybarometer. If re-equilibration is a simple process that occurs mainly via Fe-Ti interdiffusion, then partial re-equilibration of the Fe-Ti oxides would manifest as smooth concentration gradients between the rims and cores of euhedral crystals.

4.3 RESULTS

4.3.1 Overview

Titanomagnetite (Figure 4.1) and hemoilmenite (Figure 4.2) display disequilibrium textures in all experimental samples run at NNO-2. Some samples also contain euhedral Fe-Ti oxide grains. The two Fe-Ti oxides are not chemically equilibrated in any low-fO_2 runs. At NNO+0.2 (runs 34-36), Fe-Ti oxide grains appear similar to those in the starting materials. For both titanomagnetite and hemoilmenite, there is no link between pressure, temperature, and texture, and only limited evidence for compositional dependence on temperature and pressure. Thus, the detailed results and subsequent discussion sections differentiate between experiments

at low and high fO_2, but not between experiments at different pressures and temperatures, except where explicitly noted.

4.3.2 Hemoilmenite

In experiments run at NNO-2, hemoilmenite occurs as euhedral to rounded grains with parallel exsolution lamellae of (titano?)magnetite (Figure 4.1g-i) as well as clusters of small (< 5 μm) anhedral blebs. Single, continuous lamellae can reach tens of microns in length. Melt channels, ranging from minor to pervasive, occur along and parallel to these lamellae. In the clusters, hemoilmenite grains are completely surrounded by melt (Figure 4.1j-l). Small, euhedral to subhedral hemoilmenite occurs in 15 experimental samples, run at 810-890 °C and 125-200 MPa (e.g., Figure 4.1m-o), although the other morhpologies described occur as well. Some of these smaller, euhedral grains occur inside a pyroxene halo, like those found around titanomagnetite grains, but with little to no titanomagnetite present (Figure 4.1n). Similar grains also appear in the lacework area around some titanomagnetite grains. In experiments run at NNO+0.2, hemoilmenite grains are generally euhedral (Figure 4.1c). Exsolution lamellae occur

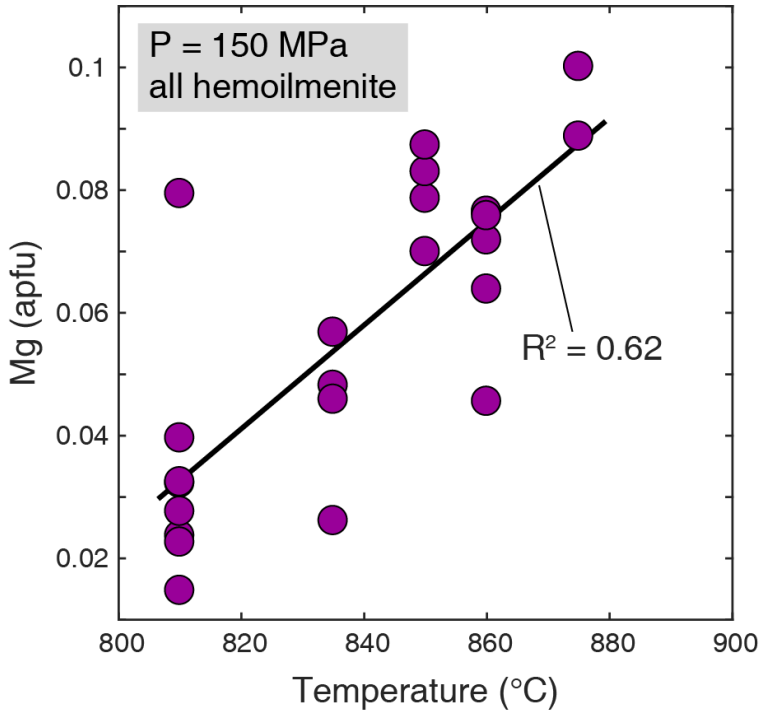

Figure 4.3. Mg composition of hemoilmenite (in atoms per formula unit) versus experimental run temperature, at 150 MPa. This plot represents the best composition-temperature trend for any element at any pressure, in the experimental hemoilmenite crystals, and yet the correlation displayed is still mediocre. No other elements vary systematically with temperature, and Mg variation is still less clear at other pressures. This lack of coherence in most elements is likely related to the "overshoot" of hemoilmenite during re-equilibration.

rarely and are all < 4 μm long, with sub-micron widths (Figure 4.1f). Similarly-small melt pockets are associated with the rim-ward extent of these sets of lamellae (Figure 4.1f).

Hemoilmenite compositions do not vary coherently with pressure, but a single element, Mg, broadly increases with temperature. The trend is most robust at 150 MPa (Figure 4.3). Small, euhedral hemoilmenite grains (Fig 4.1m-o) are higher in TiO_2 compared to larger grains, by 3-8 wt%, and their end-member composition verges on pure ilmenite, at $Hm_{0\text{-}6}Ilm_{94\text{-}100}$. These small, euhedral grains average 51.7 wt% TiO_2, whereas all other grains average 46.8 wt% TiO_2 (Figure 4.4a). Some BSE-darker regions of large ilmenite grains, as well as small, anhedral blebs, are as TiO_2-rich as the small, euhedral grains. The TiO_2-rich analyses do not consistently match the natural ilmenite compositions in any elements. Other analyses match in some elements at some conditions, but without clear trends. Almost all analyses of experimental ilmenite grains have higher Fe^{2+}/Fe^{3+} than ilmenite analyses in the lava or pumice, and lower Mg#, defined as $Mg/(Mg+Fe^{2+})$.

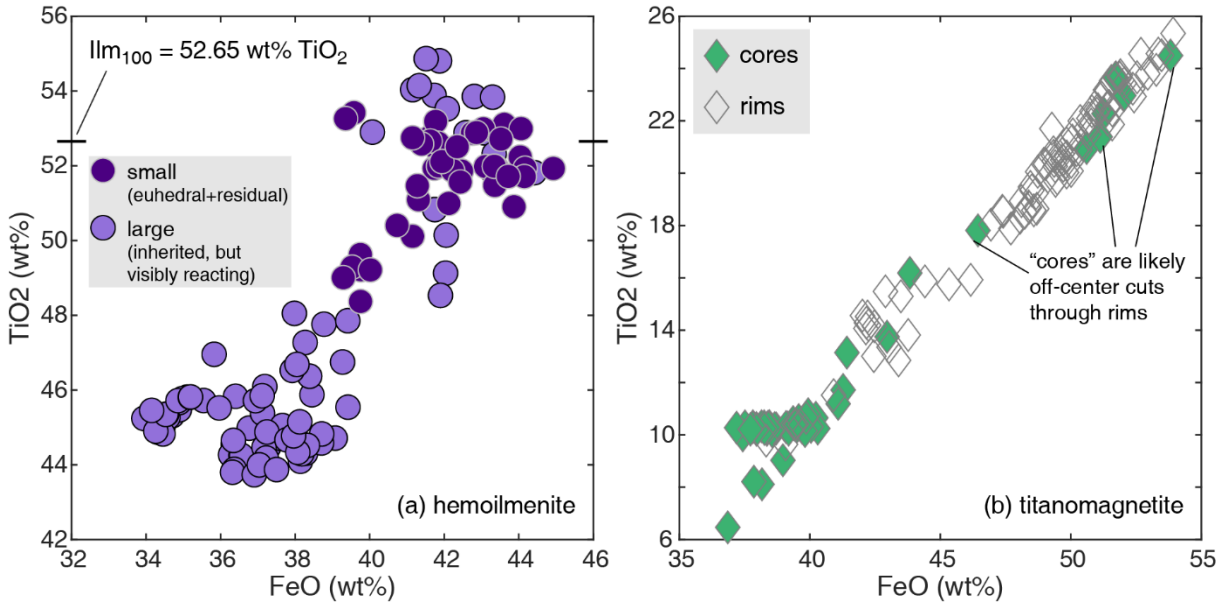

Figure 4.4. Major-element composition of (a) hemoilmenite, and (b) titanomagnetite crystals in all experimental samples. In (a), note that some analyses on large grains do extend to high TiO_2, representing areas that already lost Fe and would soon have become residual blebs (e.g., dark areas between closely-spaced lamellae in Figure 4.1g-i). However, no small grains overlap the low-TiO_2 field defined by the majority of large-grain analyses. The TiO_2 composition of Ilm100 is shown for reference. FeO would be 47.35 wt% in pure ilmenite. In (b), the ten core compositions that plot within the high-Ti, high-Fe field defined by most of the measured (diffusion) rims are interpreted as rims in 3D, appearing as cores due to sectioning far from the crystal center (e.g., Figure 4.2l).

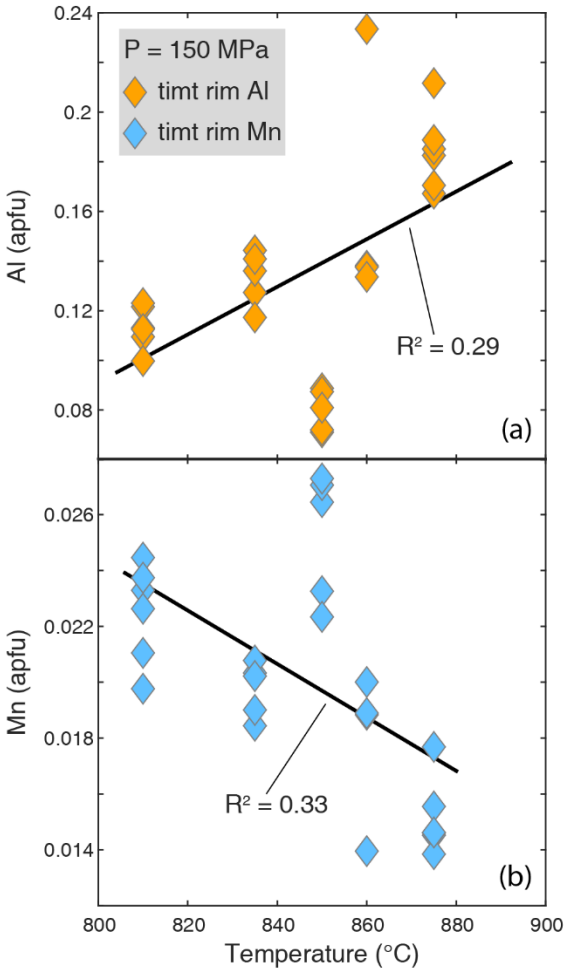

Figure 4.5. Temperature dependence of Mn and Al (atoms per formula unit) in experimental titanomagnetite crystals, at 150 MPa. As in Figure 4.3, these are visually the best correlations of any elements at any pressure, and even they are statistically unconvincing. This is likely due to complex re-equilibration processes in titanomagnetite that do not immediately yield an accurate reflection of the imposed conditions.

4.3.3 Titanomagnetite

The dominant morphology of titanomagnetite crystals at NNO-2 is a homogeneous, infilled central region surrounded by a Ti-rich diffusion rim that is broken up to varying degrees in a geometric (usually ~90°) lacework of melt and crystal (Figure 4.2g-l). Fe-rich orthopyroxene partially to completely surrounds the crystals and can be interspersed in the lacework rims. Apatite, amphibole, plagioclase, and hemoilmenite are also found in some of these halos, but pyroxene is by far the dominant phase. Run 25 (175 MPa, 835 °C) contains some small, euhedral titanomagnetite grains (Figure 4.2e). None of the titanomagnetite grains in run 28 (125 MPa, 810 °C) are surrounded by pyroxene; instead, they range from small, euhedral crystals on the edge of larger hemoilmenite grains to large, nearly euhedral grains with minor, discontinuous lacework

edges or centers (Figure 4.2d). In experiments at NNO+0.2, titanomagnetite grains are unzoned and euhedral (Figure 4.2c). They lack the lacework pattern, except in run 35 (150 MPa, 835 °C), where many titanomagnetite crystals display some dissolution in a similar, but more poorly developed, form (Figure 4.2f). In one instance, many small titanomagnetite grains are present next to a moderately embayed portion of a larger crystal (Figure 4.2f).

Experimental titanomagnetite cores preserve the starting compositions in all elements except for Mg and Mn (Figure 3.16). Concentration gradients at the rim contain more Ti, Al, V, and Fe^{2+} than these cores, but less Mn, Mg, Fe^{3+}, and total Fe. Titanomagnetite cores contain ~10 wt% TiO_2, whereas rims contain ~20 wt% TiO_2 (Figure 4.4b). At 810 °C and 125 MPa (run 28), rim compositions are closer matches to the natural titanomagnetite compositions, in all elements except Mn and Mg. This experiment contains no high-Ti titanomagnetite. Our analyses do not reveal robust trends with pressure or temperature at most conditions, but Al and Mn record some temperature sensitivity, most obviously at 150 MPa (Figure 4.5). The scatter of experimental data for a given temperature and pressure is larger than the scatter of the natural data, except in Cr. Most experimental analyses for a given pressure, temperature, and element have relative standard deviations (RSDs) > 10%, whereas analyses of the starting materials typically have RSD < 10%.

4.4 DISCUSSION

The complexities of texture and composition in the experimental Fe-Ti oxides at NNO-2 indicate that the titanomagnetite and hemoilmenite crystals, originally equilibrated at the natural fO_2 of ~NNO to NNO+1, did not fully re-equilibrate during the experiments. The experimental crystals are not described as euhedral, homogeneous, or lacking exsolution lamellae and melt channels. Thus, the null hypothesis that full re-equilibration will occur on the experimental timescale is soundly rejected. This unexpected result yields insight into the mechanisms and kinetics of Fe-Ti oxide re-equilibration.

4.4.1 Hemoilmenite re-equilibration

Various “snapshots” of hemoilmenite in experiments at all temperatures and pressures (Figure 4.1) lead us to propose that a hemoilmenite crystal placed in an environment more reducing than that at which it last equilibrated evolves in the following sequence: (1) Exsolution lamellae, likely of nearly pure magnetite, develop first near the edges of the grain and extend progressively farther into the core of the crystal; dissolution acts to round the crystal edges

(Figure 4.1d-f); (2) Melt channels form in situ, preferentially along/parallel to the magnetite lamellae, removing the most Fe-rich material; additional lamellae continue to exsolve (Figure 4.1g-i); (3) Melt channels merge lengthwise and begin to connect in the perpendicular dimension, further removing Fe-rich portions of the crystal (Figure 4.1g-i); (4) Only the most Ti-rich (Fe-poor) hemoilmenite remains, in small blobs that vaguely outline the solid grain that used to exist (Figure 4.1j-l); (5) New, faceted hemoilmenite that forms is similar in composition to these Ti-rich blebs, nearly devoid of hematite component (Figure 4.1m-o). We will refer to this phase as simply "ilmenite."

The presence of most, if not all, of steps (1)-(5) in single samples, without correlation with temperature or pressure, suggests that the progression depends more upon initial crystal size and local surroundings. Progress all the way to step (5) in most samples is evidence of the enhanced reaction rates allowed via the exsolution lamellae and melt channels, which increase surface area relative to volume (Venezky and Rutherford 1999). At NNO+0.2, the experimental fO_2 is less perturbed from the initial state, and progress toward re-equilibration does not extend beyond minute indicators of steps (1) and (2). Such sluggish kinetics are in accord with the small thermodynamic driving forces associated with small departures from equilibrium (e.g., Kondepudi and Prigogine 2014).

We interpret the compositional changes in hemoilmenite as a type of reverse oxyexsolution mechanism. Instead of classic oxyexsolution, wherein titanomagnetite exsolves ilmenite in response to an oxidation (Buddington and Lindsley 1964; Frost 1991; Venezky and Rutherford 1999), hemoilmenite exsolves magnetite in response to a reduction. This process apparently occurred in a reduction experiment of Buddington and Lindsley (1964), but no images or compositional details are provided. The reduction-exsolution reaction for our specific starting composition ($Hm_{15}Ilm_{85}$) can be expressed as

$$Fe^{2+}_{0.85}Fe^{3+}_{0.3}Ti_{0.85}O_3 \rightarrow 0.85Fe^{2+}TiO_3 + Fe^{2+}_{0.1}Fe^{3+}_{0.2}O_{0.4} + 0.025O_2 \qquad \text{eq 4.1}$$

hemoilmenite ilmenite magnetite

A similar equation is reported in Hammond and Taylor (1982) to describe the reduction of hemoilmenite, although their reaction includes hemoilmenite (albeit very Ti-rich) on the right-hand side of the equation, rather than pure ilmenite.

Interestingly, pure ilmenite is not thermodynamically stable at any temperature, for an fO_2 of NNO-2, and yet it is present in 11 runs. We project experimental Fe-Ti oxide compositions into their simple hematite-ilmenite (HmIlm) and magnetite-ulvöspinel (MtUsp) end-member components (Buddington and Lindsley 1964) in order to examine expected versus predicted outcomes, and thermodynamic stability. The intersections of hemoilmenite and titanomagnetite compositional isopleths in fO_2-temperature space indicates the temperature and fO_2 at which Fe-Ti oxides of those compositions are in equilibrium (Buddington and Lindsley 1964), their Fig. 5). For example, interpolating between the plotted isopleths, our experiments at 835 °C are expected to contain hemoilmenite with a composition of ~Hm_2Ilm_{98}, in equilibrium with titanomagnetite ~$Mt_{30}Usp_{70}$ (Figure 4.6). Similar or even higher Hm compositions are present, but most fall closer to pure ilmenite (Figure 4.7). The difference between Ilm_{98} and Ilm_{100} may seem trivial, but at the high-ilmenite end of the hemoilmenite solid solution, the temperature or fO_2 distance between successive isopleths is approximately five times larger than in the region near Ilm_{15}. Not just at 835 °C, but at every experimental temperature, true ilmenite is found. Thus, it seems that over the course of re-equilibration, hemoilmenite in our experiments "overshot" the new equilibrium, producing compositions predicted for fO_2 even lower than NNO-2. Longer experiments would be necessary to resolve whether the hemoilmenite crystals eventually correct back to the expected equilibrium composition. These interpretations recall the anomalous experiments of Venezky and Rutherford (1999), in which Fe-Ti oxide compositions appear to reflect a higher perturbation temperature than that to which they were subjected, but do begin to move toward equilibrium after longer durations.

4.4.2 Titanomagnetite re-equilibration

The mechanism(s) of titanomagnetite re-equilibration are more difficult to evaluate. Diffusion of Ti into the crystals is evident in the BSE-dark, Ti-rich rims that occur on all the experimental titanomagnetite crystals (Figure 4.2). It should be noted that these rims are not interpreted as new growth, but rather as diffusion fronts, due to the lack of growth features (e.g., facets, protrusions) and the smooth nature of the compositional zoning in BSE images. However, this interpretation could prove overly simplified, given the lacework melt patterns and the possibility of re-equilibration mechanisms other than diffusion. Rims extend inward beyond the limit of the lacework region, suggesting that diffusion is faster than dissolution. The presence of extremely Fe-rich orthopyroxene around and within the lacework indicates that, as with

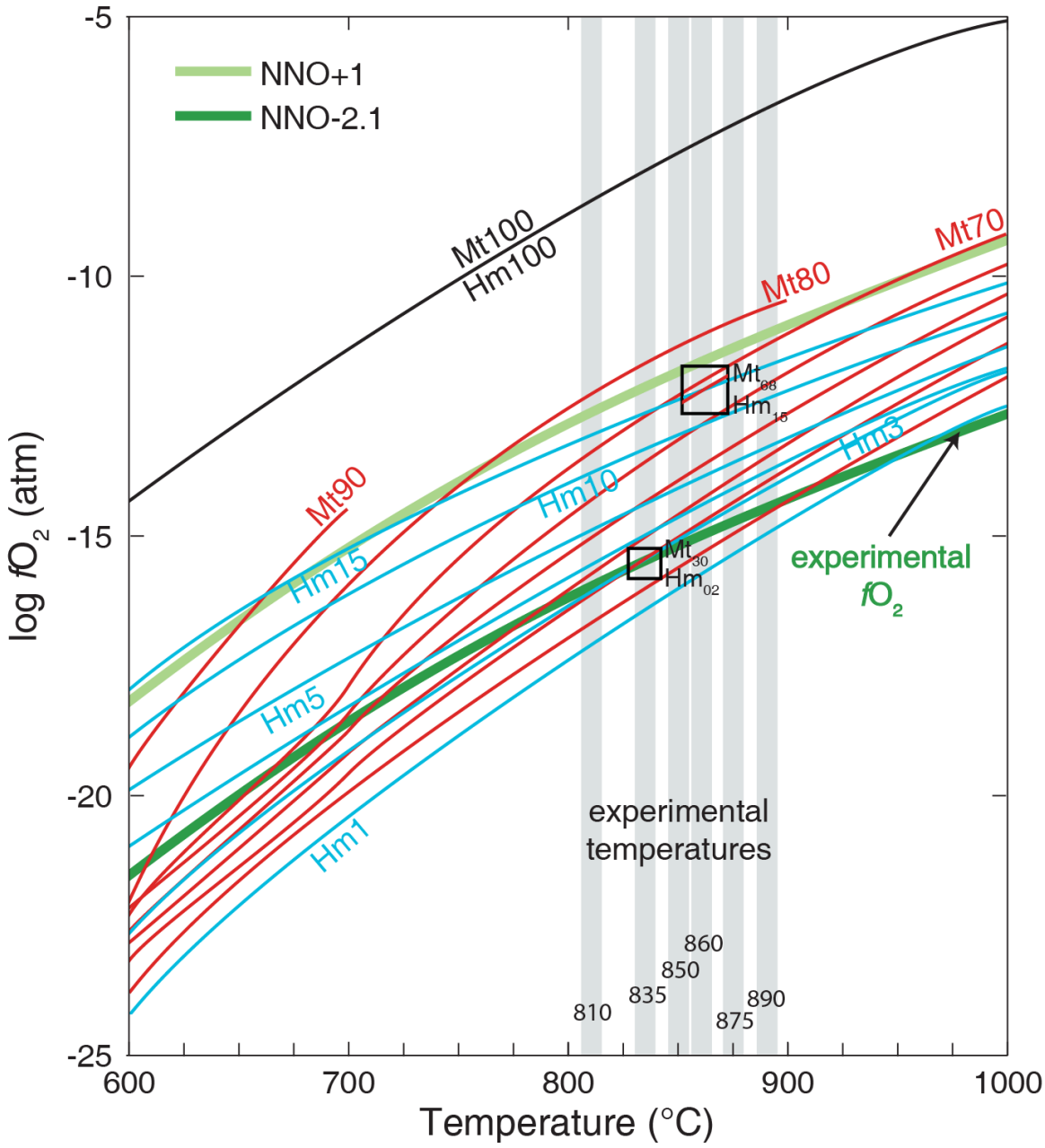

Figure 4.6. Compositional isopleths, re-drawn from Buddington and Lindsley Figure 5. Mt isopleths that are not labeled decrease in 10 mol% increments, with Mt20 as the lowest red curve. The upper black box marks the compositions of the titanomagnetite and hemoilmenite in the starting materials. The lower black box shows the expected equilibrium compositions for an experiment at 835 °C.

hemoilmenite, more Fe-rich material is preferentially removed. However, in this case much of the Fe is taken up by new growth of a crystalline silicate phase. Also in accord with hemoilmenite, the progress of dissolution and diffusion in titanomagnetite grains shows no trend with pressure or temperature. The presence of small, euhedral ilmenite grains at the periphery of

some of these unstable titanomagnetite grains suggests that the titanomagnetite itself is unstable, and that its components would recrystallize as ilmenite during a longer experiment. In one case, ilmenite occurs near the center of an Fe-rich orthopyroxene ring (Figure 4.1n), suggesting that titanomagnetite was once present but has fully dissolved. In general, though, titanomagnetite appears to have reacted to a lesser extent than hemoilmenite over the same duration, consistent with its lack of exsolution lamellae and melt channels. Time series experiments up to a month or longer would be needed to quantify fully the reaction kinetics of titanomagnetite.

The reaction between the input titanomagnetite ($Mt_{68}Usp_{32}$) and the surrounding melt, to produce Fe-rich pyroxene and the Usp-rich titanomagnetite observed in diffusion rims ($Mt_{40}Usp_{60}$), may proceed as follows:

$$Fe^{2+}_{1.32}Fe^{3+}_{1.36}Ti_{0.32}O_4 + 0.28TiO_2^{melt} + 0.28SiO_2^{melt} \rightarrow$$

titanomagnetite $Fe^{2+}_{1.6}Fe^{3+}_{0.8}Ti_{0.6}O_4 + Fe^{2+}_{0.28}Si_{0.28}O_{0.84} + 0.14O_2$

titanomagnetite ferrosilite eq 4.2

Although some of the final titanomagnetite compositions do fall in the range expected at NNO-2 and the experimental temperatures, many are compositions that would be expected at fO_2 slightly higher than NNO-2 (Figure 4.7). While hemoilmenite reacted beyond the equilibrium composition, titanomagnetite did not progress past the expected NNO-2 composition, and in many cases its composition reflects an intermediate state between the natural equilibrium conditions in the starting material and the experimental conditions. The mis-match of re-equilibration rates and/or mechanisms explains why most Fe-Ti oxide pairs in the experiments are not in Mg/Mn equilibrium (Bacon and Hirschmann 1988), precluding application of the Fe-Ti oxide thermometer-oxybarometer for these crystals and analogous crystals in natural volcanic systems.

4.5 IMPLICATIONS

The diffusion gradients in experimental titanomagnetite crystals clearly delineate reaction fronts, and yet, these rims are neither the equilibrium composition expected at the run conditions, nor are they in equilibrium with coexisting hemoilmenite. Hemoilmenite, even in the form of euhedral, syn-experimental crystals, is also not the expected equilibrium composition. Thus, evidence of reaction is present, but accurate thermal data cannot be obtained. The relatively large variation in magnetite rim compositions at a given temperature and pressure is further evidence that reequilibration has progressed variably and incompletely. Devine et al.

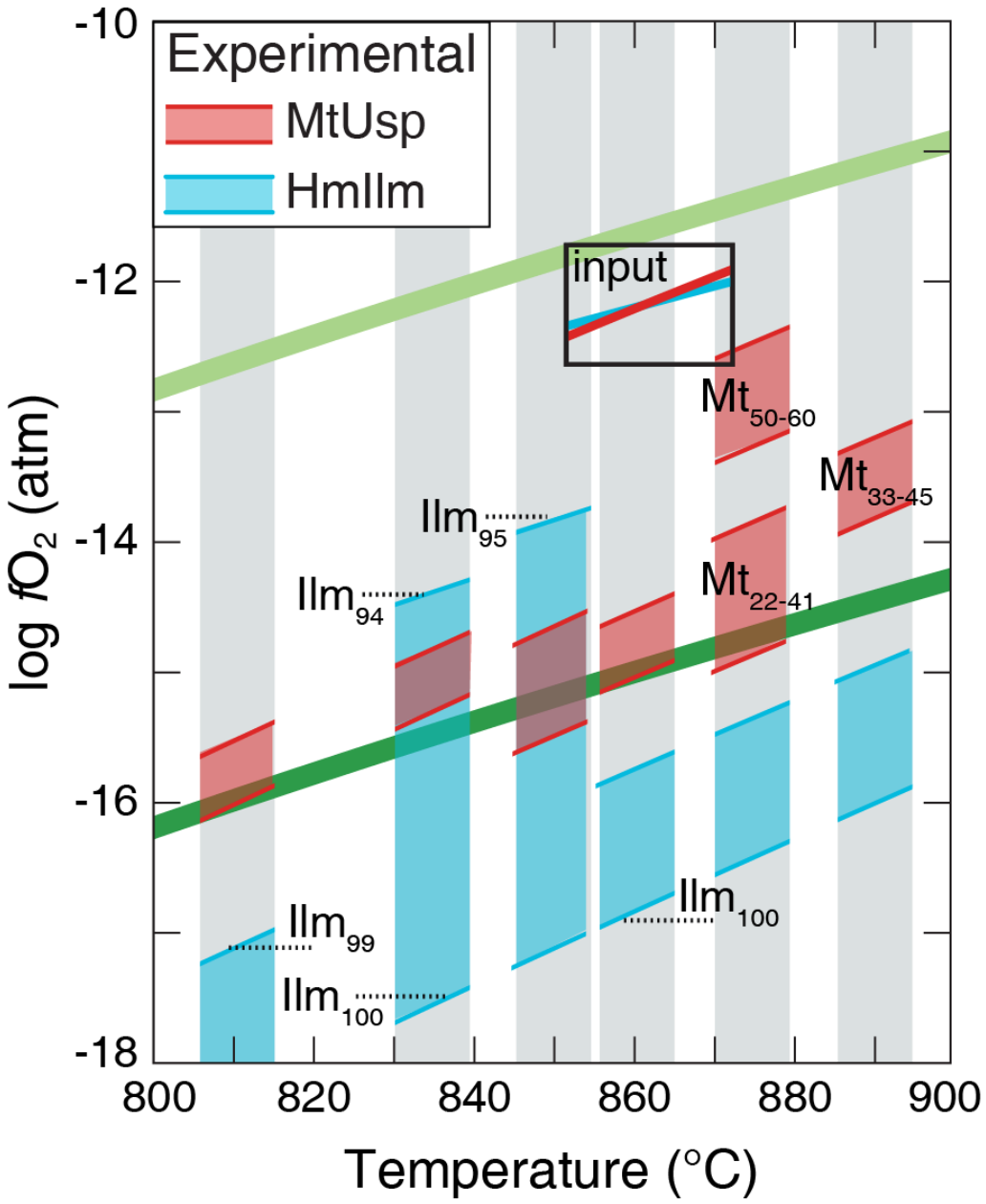

Figure 4.7. Close-up of relevant portion of Figure 4.6, showing actual experimental titanomagnetite and (hemo)ilmenite compositions. Note that in most instances, hemoilmenite compositions appear to reflect a lower fO_2 than that of the experiment (dark green line, NNO-2), whereas titanomagnetite compositions appear to reflect a higher fO_2.

(2003) report a similar failure of natural diffusion rims to yield reasonable temperature estimates for Soufrière Hills andesite. Even the seminal experiments of Venezky and Rutherford (1999) hint at complex re-equilibration processes that result in rapid compositional changes, but not necessarily rapid equilibration. Fe-Ti oxide compositions in some of their experiments yielded

temperatures close to the run temperature after a short period, but much farther from the run temperature after a longer duration. Thus, applied thermometry that assumes Fe-Ti oxides equilibrate by diffusion from the rim inward, yielding equilibrium compositions as they progress (Nakamura 1995), must be reexamined.

The rates of titanomagnetite reaction following a step-wise reduction are similar to those observed following a temperature perturbation. After 7-14 days, titanomagnetite diffusion rims in our study are ~10-20 μm wide at all temperatures, in general agreement with the formation of 10 μm long diffusion profiles in 3.5 days at 850°C in the experiments of (Venezky and Rutherford 1999). However, in contrast to that study, our rims could not be used for quantitative thermometry or oxybarometry. In general, the rapidity of Fe-Ti oxide re-equilibration appears to be overstated – the reaction rates we observe are not slow, but importantly, they do not result in equilibrium compositions, at least initially. The assumption that Fe-Ti oxide compositional changes occur only by diffusive re-equilibration, via simple rim-to-core concentration gradients, is an oversimplification. Diffusion surely plays a role in re-equilibration, but textural complexities (exsolution lamellae, lacework pattern, melt channels) expose additional surface area that could generate errors if not accounted for in modeling. Full equilibration of Fe-Ti oxides could require weeks to months in a typical silicic magma, depending on temperature, and we have shown that the compositions of partially re-equilibrated crystals are not necessarily accurate indicators of magmatic conditions. Thus, the use of Fe-Ti oxides as recorders of late-stage magmatic processes requires that either (1) the process is short with respect to the duration of sub-volcanic storage, but prolonged relative to the eruptive timescale, or (2) the system is hot enough that reactions occur more rapidly (e.g., mafic magmas), or (3) the Fe-Ti oxide crystals are small (e.g., $\leq$ 30 μm). We suggest that compositional analyses be combined with detailed textural analyses of re-equilibrating Fe-Ti oxides, to provide greater insight into the possible mechanisms of re-equilibration.

Finally, we draw attention to the fact that magma mixing is not required to generate Fe-Ti oxides with heterogeneous compositions and disequilibrium textures. A simple step change in fO_2 is enough to produce the textures and compositions in our experiments, which persist even after two weeks. In nature, reduction of a stored magma might occur with the influx of new magma from depth, as hot, mantle-derived magmas are likely to be reduced in comparison with resident magma. Future studies could aim to differentiate between the effects of temperature and

fO_2 on Fe-Ti oxide texture and re-equilibration mechanism, because both are likely to change in natural settings. Further exploration of partially-equilibrated crystals is needed, to resolve whether compositions are truly intermediate between initial and final equilibrium states, and if not, whether there is nonetheless a pattern to the compositional changes through time.

Chapter 5. Mg diffusivity in labradorite at hydrous magmatic conditions

In preparation for publication as:

First, E., Shea T., Hammer, J., Hellebrand, E., & Tachera, D. (201-). Mg diffusivity in labradorite at hydrous magmatic conditions. *American Mineralogist*.

Abstract - The diffusivity of Mg in plagioclase (D_{Mg}^{plag}) is a key parameter used increasingly as a geo-speedometer, but it is not well constrained. All published experimental values for D_{Mg}^{plag} were obtained under dry conditions with single, oriented crystals. Here, we present a novel experiment aimed at assessing the overall differences between these idealized setups and natural magmatic systems. The combined effects of hydrous melt, pressure, and fO_2 on D_{Mg}^{plag} at 900 ºC and 125 MPa are investigated, in a water-saturated experiment on An_{66} plagioclase run for 42 days. Some dissolution of the input labradorite occurred, but mass balance and thermodynamic arguments suggest that the overall driving force for dissolution was low, and that equilibrium was approached. Mg concentration profiles measured via electron microprobe are well fit by a simple 1-D diffusion model, which yields diffusivities that are anisotropic and up to 100+ times larger than any previously reported. The fast diffusion direction is approximately [-1 -3 1]. The presence of water, good interfacial contact due to melted surroundings, and potentially dissolution itself, may act to enhance Mg diffusion. Our work underscores the importance of examining diffusion in all directions, not just those of the crystallographic axes, and it suggests that D_{Mg}^{plag} may be higher in volcanic settings than previously thought.

5.1 INTRODUCTION

The influx of new magma to a volcanic system is a common precursor, and even trigger, for eruption. Evidence for mixing of influx magma with resident magma often takes the form of element zoning in igneous minerals, and diffusion modeling of these chemical gradients is a useful method for investigating the time between the onset of new magma input and volcanic eruption (e.g., Costa et al. 2010; Druitt et al. 2012; Gerlach and Grove 1982; Hartley et al. 2016; Moore et al. 2014; Shea et al. 2015a; Singer et al. 2016; Zellmer et al. 1999). Constraining these

timescales is important not only for our scientific understanding of magmatic plumbing systems, but also for a better grasp on the onset of eruptive hazards at volcanoes around the world.

As minerals grow, elements are incorporated in concentrations determined by an interplay of variables, including melt and mineral composition, oxygen fugacity (fO_2), temperature, and pressure. Environmental changes drive corresponding shifts in the equilibrium crystal compositions, reflected as step changes in element concentration. Though time, these sharp boundaries are dampened by diffusion, with the eventual result that the entire crystal has a homogeneous composition – that of equilibrium in the new environment. Crystals preserve no temporal information once they have fully equilibrated. Fortunately, in volcanic systems, diffusion is often arrested by eruption, before full equilibration is achieved. It is these partially equilibrated crystals, with their preserved gradients in concentration, that are essential for modeling the diffusivity of various elements. Concentration gradients may be fit by solutions to the diffusion equation (i.e., Fick's second law) to derive timescales of magma mixing (e.g., Costa et al. 2008). Parameters that must be known or assumed, in order to determine these timescales, include: temperature, initial concentrations at each growth step, and perhaps most importantly, the diffusivity of the relevant species in the crystal. The ideal minerals to model are those that are abundant in erupted materials, contain species that diffuse at a moderate rate, and for which predictive relationships between element concentration and other variables have been established.

5.1.1 Mg in plagioclase: A promising system with one big problem

Plagioclase has excellent potential for diffusion modeling: it is one of the most common mineral phases, and its major-element zoning (described by the end-member component anorthite, An_x) remains largely intact over volcanic timescales (Grove et al. 1984). Anorthite content therefore provides a fixed backdrop on which minor- and trace-element concentrations can be modeled. Magnesium (Mg) is a particularly appealing element to investigate, because its diffusivity is fast enough to record partial re-equilibration on laboratory timescales, yet slow enough to preserve a diffusion profile (Faak et al. 2013; LaTourrette and Wasserburg 1998; Van Orman et al. 2014). Moreover, its partitioning is dependent on anorthite content in a predictable way (Bindeman et al. 1998; Dohmen and Blundy 2014; Nielsen et al. 2017; Sun et al. 2017), making equilibrium Mg concentrations readily established. However, uncertainty in the key

parameter, the Mg diffusion coefficient in plagioclase (D_{Mg}^{plag}), hinders accurate timescale determination. Literature values span five orders of magnitude at a single temperature (Costa et al. 2003; Faak et al. 2013; Van Orman et al. 2014). This range exists, in part, because the compositional (i.e., An_x) dependence of D_{Mg}^{plag} remains in question: both a ~500x decrease in D_{Mg}^{plag} from An_{20} to An_{90} (Van Orman et al. 2014) and no An_x dependence whatsoever (Faak et al. 2013) have been reported. Moreover, the influence of pertinent magmatic variables (e.g., H_2O content, natural melt) has yet to be explored.

5.1.2 An experimental approach with relevance to nature

Currently available values for D_{Mg}^{plag} are derived from experimental setups that used oriented crystals in fluid- and melt-free surroundings at atmospheric pressure (Faak et al. 2013; LaTourrette and Wasserburg 1998; Van Orman et al. 2014). The initial work of LaTourrette and Wasserburg (1998) measured self-diffusion of Mg using polished, oriented crystals at atmospheric pressure and fO_2. The experiments of Faak et al. (2013) used polished crystals, cut into cubes, although they found no difference in D_{Mg}^{plag} between polished and unpolished sides, suggesting that sample preparation at the polishing level is not responsible for differences in D_{Mg}^{plag}. Their study also employed a more natural fO_2, between NNO and QFM. However, the surroundings consisted of diopside, diopside+SiO_2, and gabbro powders that sintered to the crystal surface but in most cases did not melt. The most recent study of D_{Mg}^{plag} used natural single crystals, oriented and polished, surrounded by powdered MgO, Al_2O_3, SiO_2, and plagioclase, all unmelted (Van Orman et al. 2014). These experiments were conducted in air, at atmospheric pressure.

The idealized experimental setups above provide several methodological advantages over natural systems. For example, the same crystal can be examined pre- and post-experimentation, to check for irregularities that formed syn-experimentally. Single crystals are useful in that compositional profiles can be acquired with exact knowledge of their position with respect to the crystal faces, in three dimensions. Complications of growth and dissolution are avoided by using diffusion couples or powdered surroundings. Finally, dry experiments allow for the use of 1-atmosphere furnaces, which in turn allow for precise atmospheric control over a wide range of fO_2. Unfortunately, these systems do not reflect processes occurring in natural

magmas. While idealized experiments are unquestionably useful for providing information about changes in D_{Mg}^{plag} and diffusion mechanisms with changes in single variables, the specific D_{Mg}^{plag} values thus obtained have questionable relevance to nature.

Spandler and O'Neill (2010) describe the benefits of conducting diffusion experiments using natural melts. One key point is that natural concentration levels of trace elements are present. This stipulation is important, because diffusion mechanisms may depend on the species concentration (Burgess and Cooper 2013; Spandler and O'Neill 2010). In addition, the presence of a natural melt ensures that the chemical potentials of both major and minor components are fixed at relevant levels (Spandler and O'Neill 2010). Thus, any interaction between the species of interest and the other elements present reflects natural associations that may play a role in the rate of diffusion. Finally, a natural silicate melt contacts the crystal surface fully and smoothly, ensuring that diffusivity is not hindered by poor contact of powder or enhanced by the formation of surface defects like those that may form in traditional diffusion couples (Spandler and O'Neill 2010). Melt-based surroundings also allow for the incorporation of water, which can affect diffusion coefficients.

Here, we aim to provide experimental constraints on D_{Mg}^{plag} using materials and conditions more relevant to volcanic systems, by surrounding natural plagioclase crystals with pressurized, water-saturated silicate melt at magmatic temperature. Temperature (e.g., Zhang 2010), confining pressure (e.g., Holzapfel et al. 2007), presence of volatile species (e.g., Kohlstedt and Mackwell 2008), composition of the mineral (e.g., Giletti and Casserly 1994), surrounding material (e.g., Faak et al. 2013), and fO_2 (e.g., Behrens et al. 1990) can all affect cation diffusion rates in igneous minerals, yet have not been adequately explored for Mg-in-plagioclase and many other systems. Although our experimental setup does not easily allow for the separation of these variables, it represents a significant step toward understanding how D_{Mg}^{plag} might differ between idealized solid-solid diffusion experiments and natural volcanic settings. If higher pressure, the presence of natural melt, and hydrous conditions have no influence on D_{Mg}^{plag}, then our experiment should recover the D_{Mg}^{plag} values obtained for dry plagioclase in isolation from a melt phase. Establishing a baseline of understanding at this broad level provides the

impetus and direction for future work addressing specific mechanisms of Mg diffusion in plagioclase.

As in previous D_{Mg}^{plag} studies, we consider the rate of chemical diffusion approximately the same as that of self-diffusion (LaTourrette and Wasserburg 1998; Van Orman et al. 2014), a reasonable assumption for low-concentration species (Van Orman et al. 2014; Zhang 2010). The measured D_{Mg}^{plag} can also be viewed as tracer diffusion (Zhang 2010). We determine D_{Mg}^{plag} values that differ appreciably from prior work, and we consider in detail the possible causes and consequences of this difference.

5.2 MATERIALS AND METHODS

5.2.1 Starting Materials

In an effort to closely mimic natural magmatic conditions, we used as a matrix material the glass fraction of a dacite pumice erupted at Volcán Quizapu, Chile in 1932 (sample VQ-07-37 D, Ruprecht *et al.* (2012). After crushing the pumice by hand, mineral-free pieces were individually picked under a high-magnification binocular microscope. This glass fraction was then crushed further with a mortar and pestle, to minimize free pore space, allowing more material to fit in the experimental capsule. The composition of the glass is rhyolite (Table 5.1), in equilibrium with cognate plagioclase of An_{25-30} (Chapter 3; (Hildreth and Drake 1992; Ruprecht et al. 2012).

Table 5.1. Glass compositions[a]

	Initial	**Final**[b]	**Δ%**[c]
SiO_2	71.74	71.77	+0.05
TiO_2	0.32	-	-
Al_2O_3	15.14	15.84	+4.6
FeO	1.67	-	-
MnO	0.07	-	-
MgO	0.34	-	-
CaO	1.11	1.68	+52
Na_2O	5.48	4.50	-18
K_2O	4.09	3.76	-7.9
P_2O_5	0.05	-	-
log η (Pa s)[d]	4.12	4.51	+145

a. Normalized to 100% anhydrous
b. Minor elements not measured
c. Δ% = 100*(Final-Initial)
d. Accounts for water saturation

Three single plagioclase crystals were obtained from the National Museum of Natural History, all somewhat broken: anorthite 122261, labradorite 135512-1, and andesine 105476. These samples are reported as standard-grade, homogeneous crystals of An_{93}, An_{66}, and An_{43}, respectively and are the same sample set used in a previous Mg diffusivity study (Van Orman et al. 2014). The three compositions are sufficiently different as to be easily distinguishable from one another within a single experimental charge, in backscatter electron (BSE) images. Each sample was gently broken into pieces that ranged from ~200 μm to 1 mm.

5.2.2 Experimental procedure

Natural dacite glass (0.16893 g) and aliquots of all three NMNH plagioclase samples (0.01275 g anorthite, 0.01173 g labradorite, 0.01241 g andesine) were combined in a 5-mm outer diameter $Ag_{70}Pd_{30}$ capsule. The system thus consisted of 17.9 wt% plagioclase – enough to ensure adequate sampling while maintaining large regions of melt between crystals. Given a water solubility of 4.4 wt% H_2O at the experimental conditions (Zhang et al. 2007), we added 6.9 wt% deionized water to ensure saturation. After crimping to a triple junction, the capsule was sealed using a Lampert PUK U4 tungsten inert gas impulse micro welder. The experiment was conducted at T = 900 °C and P = 125 MPa in the cold-seal water-medium pressure line at the University of Hawaii experimental petrology lab, using a Lindbergh/Blue M tube furnace and a Waspaloy vessel. Relative pressure changes were tracked with an Omega DP41-S strain gauge transducer (± 0.01 MPa), and absolute pressure was monitored with a Heise CM mechanical pressure gauge (± 0.5 MPa). Oxygen fugacity (fO_2) was two log units below the Ni-NiO buffer (NNO-2), as described in Chapter 3 Methods (page 46). The sample was brought to magmatic temperature (900 °C) over 40 minutes by inserting the pressurized vessel into the furnace and monitoring the vessel temperature adjacent to the capsule with an Omega K-type thermocouple (± 6.75 °C). Run duration was 1010.5 hours (~42 days).

Pressure was maintained at 125 ± 0.5 MPa by an electronically-controlled screw-jack mechanism (described in Brugger and Hammer (2010), until a short period (< 2 days) in the first fifth of the run in which mechanical failure caused a pressure decrease to 70 MPa. During the decompression, water solubility of the system decreased to 3.1 wt% (Zhang et al. 2007), or 1.3 wt% less than in the intended system, but water saturation was maintained, and the capsule did not rupture. After re-pressurizing to 125 MPa, the experiment was uninterrupted for the remaining 34 days of the experiment, and pressure was maintained manually. Temperature was

unaffected for the entire experimental duration. Such a pressure change is unlikely to have influenced D_{Mg}^{plag} (e.g., Holzapfel et al. 2007; Van Orman et al. 2001). However, the run product does preserve evidence of the pressure excursion, in the form of tabular overgrowths on ≤ 10% of the plagioclase crystals. The overgrowths are more albitic (An_{47}) than the labradorite or anorthite starting materials, but slightly less albitic than the andesine. On day 42, quench was performed by air-cooling the vessel for ~15 seconds and then plunging it into a bucket of water, while pressurized. Experimental products were mounted as individual pieces of plagioclase + glass in a 10-hole round plug for polishing and subsequent analysis. Traditional lapidary polishing down to 0.25 μm was followed by vibratory silica polishing, to provide a surface suitable for generation of electron backscatter diffraction patterns (EBSPs) and orientation indexing.

5.2.3 Analytical

5.2.3.1 Electron microprobe (EPMA)

Linear transects of spot compositional analyses of plagioclase were obtained using wavelength dispersive spectrometry on the JEOL Hyperprobe JXA-8500F electron microprobe at the University of Hawaii. For Mg, an accelerating voltage of 15 keV, a beam current of 40 nA, and a beam diameter of 2 μm were used. Spacing of transect points was typically 2.5-4 μm near crystal rims, and up to 10 μm in crystal cores. Mg concentrations were determined using the aggregate intensities option of the Probe for EPMA software (v. 10.9.9), combining the net count rates of three spectrometers (Donovan et al. 2011). Due to this constraint, major elements were not measured at the same time. Background positions (Table D1) were chosen after long-duration high-resolution scans of feldspar standards Lake County plagioclase (USNM 115900) and anorthite (USNM 137041) (Jarosewich et al. 1980), in order to avoid interferences from third-order peaks of Ca-kα and Ca-kβ. The third-order Ca-kα is well resolved from the Mg-kα peak (~1.9 mm) and its shoulder is indistinguishable from the background for the low-Mg anorthite. An exponential background calculation model was used based on the high-resolution wavescans. Unanalyzed major element concentrations were specified to ensure accurate ZAF correction. Count times were 120 s on the peak and 60 s on each background position (high and low). UCLA Diopside was used as the calibration standard, and the Lake County plagioclase standard permanently housed in the UH facility (USNM 115900) was repeatedly measured to

check for Mg drift. Using the same beam diameter and spacing as for transects, 84 measurements of standard Lake County plagioclase give an average of 0.082 wt% Mg, with $1\sigma = 0.001$ wt% Mg (Table D2).

The effects of beam current, beam size, and spot spacing were assessed using the Lake County plagioclase standard. At 100 nA, with 240 s peak count time, beam damage was significant, but precision was not much improved over that of 40 nA, 120 s (RSD = 0.58% vs. RSD = 0.78%). Larger spot sizes produced the most precise results, with extremes of RSD = 0.78% for 5 μm spots and RSD = 2.69% for 1 μm spots.

Major-element concentrations (Si, Al, Ca, Na, and K) were obtained for 3 transects directly adjacent and parallel to Mg transects, as well as for one transect in the surrounding glass. An accelerating voltage of 15keV and a beam current of 10 nA were used for these analyses. Count times were 30 s on peak for all five elements, and 15 s each on high and low off-peak positions. For the glass transect, an automatic time-dependent intensity correction was applied to account for sodium loss. Background was linear for all elements. Calibration was based on Lake County plagioclase (Jarosewich et al. 1980), and in-house standards Amelia albite and OR-1 orthoclase. Basalt glass A99 (USNM 113498/1) was measured repeatedly to monitor drift (Jarosewich et al. 1980). Two spots on low-An plagioclase rims were acquired during a glass measurement session that also had a 15 keV, 10 nA setup (see Chapter 3 Methods).

Transects were set up to be approximately perpendicular to the crystal rim from which they originated, and were taken as far away from crystal corners as possible, to avoid merging diffusion fronts (Costa and Chakraborty 2004; Shea et al. 2015b). Given the inherent difficulty in programming exactly perpendicular transects, small geometric corrections were applied post-analysis, to obtain the true perpendicular distance from the rim at each analytical point. It is these distances that are used for plotting and fitting the data.

5.2.3.2 Electron backscatter diffraction (EBSD)

Orientations of each plagioclase grain were determined via EBSD, using the JEOL 5900 LV scanning electron microscope (SEM) in the W. M. Keck Cosmochemistry lab at the University of Hawaii. The SEM is equipped with a Nordlys EBSD detector, and measurements were made through the CHANNEL 5 program suite. An accelerating voltage of 20 keV, stage tilt of 70°, and working distances of 15-23 mm were used. The match unit was anorthite with unit cell parameters a = 8.18 Å, b = 12.87 Å, c = 14.17 Å, $\alpha = 93.1°$, $\beta = 115.9°$, and $\gamma = 91.2°$ (Angel

et al. 1990). EBSPs were obtained on individual spots and at least one map (~1000 μm^2) for each grain. Each pattern was indexed using automated Kikuchi band detection algorithms, supplemented by manual band tracing as warranted. Crystal axis orientations were exported in equal angle, lower hemisphere pole figures. Because of the nature of the triclinic crystal system, in which the crystallographic axis designations *a*, *b*, and *c* are not symmetrically equivalent to *-a*, *-b*, and *-c*, the three axis locations marked on each pole figure are not always the positive axes, as the positive axes do not necessarily intersect the lower hemisphere. Points are labeled for clarity.

5.2.3.3 Post-processing

The orientation of each transect in the plane of section was determined by manually measuring its angle from vertical, on an oriented image. The direction of each transect was chosen to point down the diffusion gradient (i.e., from core to rim). This is a convention for the sake of consistency, and embeds the assumption that diffusion along a given orientation in the crystal lattice is the same moving toward or away from the crystal rim. Measured transect angles were plotted on the lower hemisphere pole figures, using Stereonet9 (Allmendinger et al. 2013; Cardozo and Allmendinger 2013). Angles between the crystal axes (α, β, γ) and between the transect and each positive axis (θa, θb, θc) were calculated using the built-in function in Stereonet9. Note that, even where negative axes are visible on the pole figure, the angles reported are always with respect to the positive axes. Although α, β, and γ angles are set by the match unit for each individually indexed point, some uncertainty is introduced in transferring the tight cloud of EBSD data points into Stereonet9. All α, β, and γ measured in Stereonet9 are ≤ 1° different from match unit data. Typical accuracy is within 0.5°.

Some EPMA transects have multiple segments that are not perfectly colinear, due to non-consecutive data collection. For these transects, the orientation reported is an average, if all segments contribute relatively equally to the sloping part of the diffusion profile. If one segment overwhelmingly contains the sloping part of the diffusion profile, its orientation is applied to the profile as a whole.

5.2.4 Computational

5.2.4.1 One-dimensional diffusion profiles

Concentration gradients in Mg are modeled in MATLAB using the complementary error function solution to the diffusion equation. This method solves the one-dimensional diffusion equation (Crank 1975; Fick 1855)

$$\frac{\partial C}{\partial t} = D\frac{\partial^2 C}{\partial x^2} \quad \text{eq 5.1}$$

and assumes that D is independent of concentration. We use a form of the solution appropriate for diffusive exchange between two phases, where the initial concentration in the phase of interest is uniform (e.g., Lasaga 1998; Zhang 2010). For the specific case of Mg in plagioclase, this solution is expressed as

$$C_{Mg}^{x} = C_{Mg}^{core} + \left(C_{Mg}^{rim} - C_{Mg}^{core}\right)\mathrm{erfc}\left(\frac{x}{2\sqrt{D_{Mg}^{plag} t}}\right) \quad \text{eq 5.2}$$

where C_{Mg}^{x} is the concentration of Mg in plagioclase at distance x from the crystal rim, C_{Mg}^{core} and C_{Mg}^{rim} are the concentration of Mg at the crystal core and rim, respectively, and t is time (e.g., Faak et al. 2013). The equation above is suitable for tracer or binary diffusion only, a condition met in our system, where Mg essentially exhibits tracer diffusion (see section 5.1.2). Furthermore, the form of the complementary error function solution is derived under the assumption that the phase in question can be approximated as a semi-infinite medium (e.g., Greenberg 1998, Lowrie 2007). We consider this assumption accurate, because all modeled crystals retain a plateau of initial Mg concentration, which acts as an infinite reservoir over the experimental timescale. The adhering melt also acts as a semi-infinite medium, as it comprises 82.1 wt% of the experimental charge and is found to be homogeneous (i.e., without compositional gradients at the crystal-melt interface; see 5.3 Results). Given the experimental duration, the best-fit D_{Mg}^{plag} is determined by minimizing the misfit between the EPMA data points and the complementary error function solution. A single misfit value for each modeled profile is calculated using the root mean square deviation as

$$\delta = \frac{1}{n}\sqrt{\sum_{x_0}^{x_n}(C_{Mg}^{meas}(x) - C_{Mg}^{model}(x)^2} \quad \text{eq 5.3}$$

where δ is the misfit, in units of wt% Mg, n is the number of EPMA analyses in the profile, $C_{Mg}^{meas}(x)$ is the measured Mg concentration, and $C_{Mg}^{model}(x)$ is the modeled Mg concentration, both at distance x from the crystal rim.

In the basic case (model A), three initial parameters are varied simultaneously to obtain the best solution: C_{Mg}^{core}, C_{Mg}^{rim}, and D_{Mg}^{plag}. Incorporating both rim and core values into the minimization algorithm eliminates the inherent bias of choosing those values by eye, a method commonly applied (e.g., Girona and Costa 2013). Typically, one million to three million

combinations of variables are tested for each profile, to arrive at the best fit solution. If the best fit is obtained using the upper or lower bound of any variable, additional simulations are run, until the true best fit is found. A range of possible D_{Mg}^{plag} values is established by setting the rim and core compositions as the best fit values, while allowing D_{Mg}^{plag} to vary. These low and high D_{Mg}^{plag} values are derived in two ways. The first method uses a misfit criterion to establish upper and lower bounds, deriving the solutions with misfit values 50% larger than the minimum misfit. The second method uses a discrepancy criterion, accepting solutions with the same or lower discrepancy as the best fit solution. Discrepancy is defined as the number of data points not fit by the model, within analytical error, and the basis of our method comes from the 1-D olivine diffusion model of (Girona and Costa 2013). Analytical error is taken as the relative percent error determined by the EPMA software, typically 1% relative, or ~0.001 wt% Mg. This is similar to the standard deviation of repeated analyses of Lake County standard plagioclase.

In a more complex set of simulations (models B and C), the EPMA concentration profile is allowed to shift in space away from the crystal rim location by up to 100 μm, as a first-order approximation of dissolution. These simulations also include an artificial core data point, whose x position can shift up to 100 μm core-ward from the last measured analysis. This additional "data" allows for the possibility that in some samples, the true core plateau (assumed to be 0.0823 wt% Mg based on repeated analyses of the Lake County standard plagioclase) is not reached by the EPMA profile, but would be if the profile extended further toward the crystal center. In model B, the core composition is allowed to vary, but this time only between 0.081 wt% Mg and 0.085 wt% Mg, bracketing the true core value. The value of D_{Mg}^{plag} can vary, but the rim composition is fixed as the best fit rim value from model A.

A third set of simulations (model C) is identical to model B except that the fixed rim Mg concentration is equal to the calculated equilibrium partitioning value of Mg in the experimental system (0.003 wt% Mg, (Sun et al. 2017). This criterion is the one most typically adopted in studies aimed at deriving timescales from natural diffusion profiles (e.g., Costa et al. 2010; Faak et al. 2014; Lynn et al. 2017; Ruprecht and Cooper 2012). A final set of simulations is run for only three profiles (model D). The setup is identical to that of model C, minus any allowances for the possibility that profiles were truncated by dissolution (i.e., the profile is fixed in space

relative to the observed crystal rim). For each profile in model B, model C, and model D, after a best-fit solution is determined by minimizing the misfit, two error assessments are undertaken, using the misfit and discrepancy criteria as described for model A.

5.2.4.2 Three-dimensional diffusivity

Diffusivity vectors (i.e., vectors pointing in the direction of the EPMA transect, with magnitude scaled to D_{Mg}^{plag} established by model A, B, or C) were plotted in 3-D space. Each transect's angles with respect to the crystallographic axes, derived from EBSD analysis, were transformed into Cartesian x-y-z triples describing the endpoint of each vector in space, assuming an origin at (0,0,0). The transformation is best visualized as a set of three right circular cones in space, with heights aligned to the *a*, *b*, and *c* crystallographic axes and apertures equal to twice θa, θb, and θc, respectively. The intersection of the bases of the three cones is the endpoint of the vector. Allowing each cone base to become a plane (perpendicular to the given axis) and solving for the intersection point of those planes gives the desired coordinates. The cone geometry is used to solve for each plane's distance from the origin. Further details and the relevant MATLAB code are provided in the Appendix, along with a shorter, purely mathematical transformation for comparison (Phillip First, personal communication). Both methods give identical vector endpoints. Crystallographic axis orientations were reproduced in the Cartesian system using a transposition of the transformation matrix (Prince 1994). Additional details are provided in the Appendix.

A subset of diffusivity vectors was fit by an ellipsoid to describe the directional variation of D_{Mg}^{plag}. Each vector was reflected symmetrically across the origin in order to create an origin-centered ellipsoid. The underlying assumption is that D_{Mg}^{plag} does not vary along the same orientation based on a positive or negative direction of travel (i.e., +/- crystal axes; Przemek Dera, personal communication). The fit ellipsoid was derived by finding the eigenvectors and eigenvalues of the covariance matrix of the set of Cartesian endpoints describing each vector. The eigenvectors are the principal components of the data set, giving the directions of the principal axes of the ellipsoid, and the eigenvalues provide the aspect ratio. Scaling factors were applied to the covariance matrix, in order to modulate the ellipsoid volume (while holding aspect ratio and axis orientation constant) until the best fit to the data points was achieved. Residuals between the data points and the fit ellipsoid are calculated as the vector difference between the

diffusivity vector and a point on the ellipsoid surface along the same vector direction – in essence, the difference in measured and predicted D_{Mg}^{plag}. An overall misfit of the fit ellipsoid to the data is calculated as

$$\delta = \frac{1}{n}\sqrt{\sum_{v_0}^{v_n}(D_{Mg}^{plag-pr}(v) - D_{Mg}^{plag-epsd}(v)^2} \qquad \text{eq 5.4}$$

where δ is the misfit, in units of diffusivity ($m^2\ s^{-1}$), and v is a given vector direction corresponding to one of the measured diffusivity vectors. $D_{Mg}^{plag-pr}$ is the diffusivity determined by 1-D modeling of the Mg concentration profile, and $D_{Mg}^{plag-epsd}$ is the diffusivity predicted by the ellipsoid fit, both in direction v.

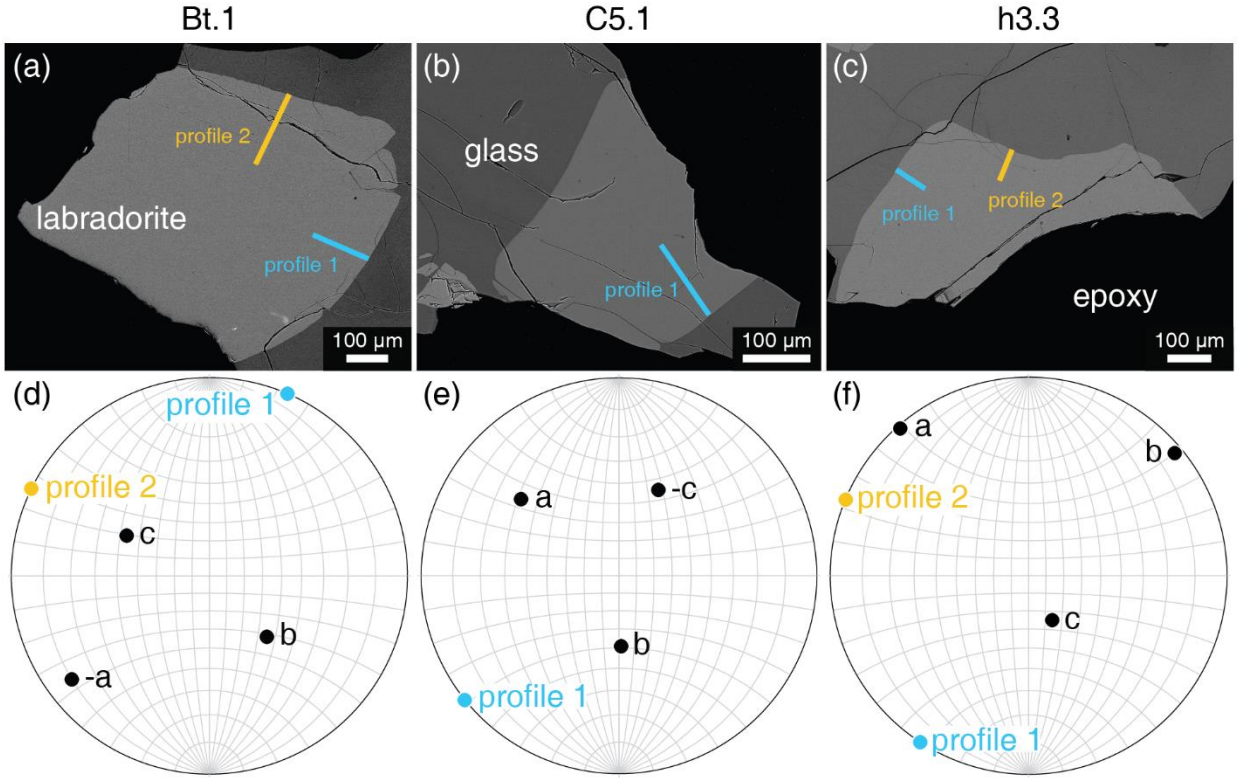

Figure 5.1. BSE images and pole figures for three representative labradorite crystals (Bt.1, C5.1, and h3.3). EPMA transects are marked in blue and orange. Glass is dark grey, and epoxy is black.

5.3 RESULTS

5.3.1 General description

Large (100s µm) crystals of labradorite, anorthite, and andesine are present in the run product, distinguishable from one another via BSE imaging and EDS spot analyses. Grains are unzoned in backscatter (Figure 5.1a-c), except for several anorthite crystals with parallel zones

of BSE-darker material, and one labradorite crystal with both parallel and "swirly" zones. This labradorite grain was not used for compositional analyses. Most crystals are rounded, with facets discernible in only a few cases. Discontinuous, lower-An rims are present on at least four crystals. Two EPMA spots yield a composition of An_{47} for these rims, which exhibit facets but have slightly rounded corners.

The post-experimental residual glass is lower in Na_2O and K_2O, but higher in Al_2O_3 and CaO, than the initial input glass (Table 5.1). The labradorite crystal fraction has an average

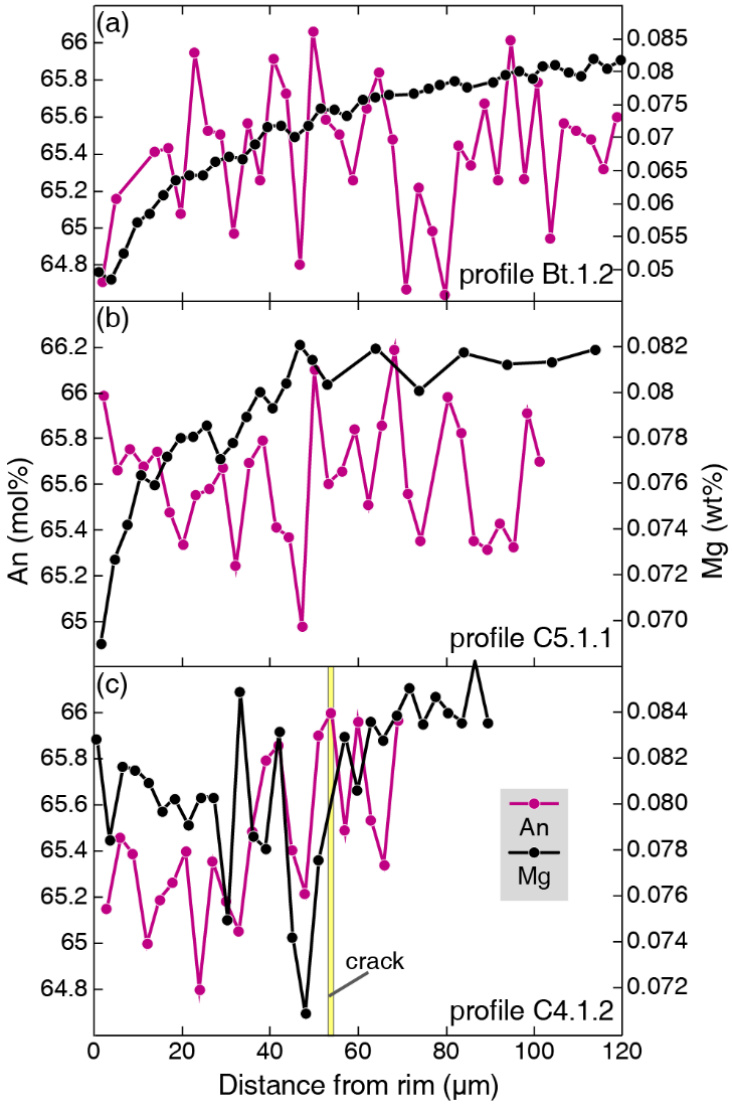

Figure 5.2. Comparison of An variation and Mg variation in three labradorite crystals. **(a)** and **(b)** are used in diffusion modeling, but **(c)** is not. Note the lack of correlation for (a) or (b), and the coarse correlation in (c). The range of An in panels (a) and (b) is < 2% relative, whereas the change in Mg is 40% relative in (a) and 15% relative in (b). Altogether, An content is relatively homogeneous, and Mg concentration profiles used in diffusion modeling are not simply the result of partitioning according to bulk plagioclase compositional zoning.

composition of $An_{65}Ab_{34}Or_1$, with a relative standard deviation of 0.5 mol% An. This composition is in good agreement with the NMNH description of An_{66}, which is also referenced in the study of Van Orman et al. (2014). However, a common "standard" composition for Lake County plagioclase is An_{68} (Jarosewich et al. 1980). The Mg content of the labradorite in experiments consistently peaks at 0.080-0.083 wt% Mg, in accord with repeated analyses of the Lake County plagioclase standard housed in the UH electron microprobe facility (0.082 ± 0.001 wt% Mg).

Twenty-five Mg transects were obtained on 16 labradorite crystals. Concentration profiles were also gathered on two anorthite crystals and one andesine crystal, but the Mg concentrations were too low (0.035 wt% and 0.02 wt%, respectively) to yield meaningful profiles. In 21 of the 25 profiles, Mg systematically decreases toward the crystal rim, either sharply (e.g., Figure 5.2b) or gradually (e.g., Figure 5.2a). The steepness of each profile lessens toward the core, where a concentration plateau is usually evident. The along-profile distance from the crystal rim to this core plateau varies from ~10 μm to ~130 μm. Of the 21 decreasing-Mg profiles, 18 were suitable for diffusion modeling. In several cases, additional decreases in Mg are superposed on the overall trend and are centered around visible cracks in the crystal.

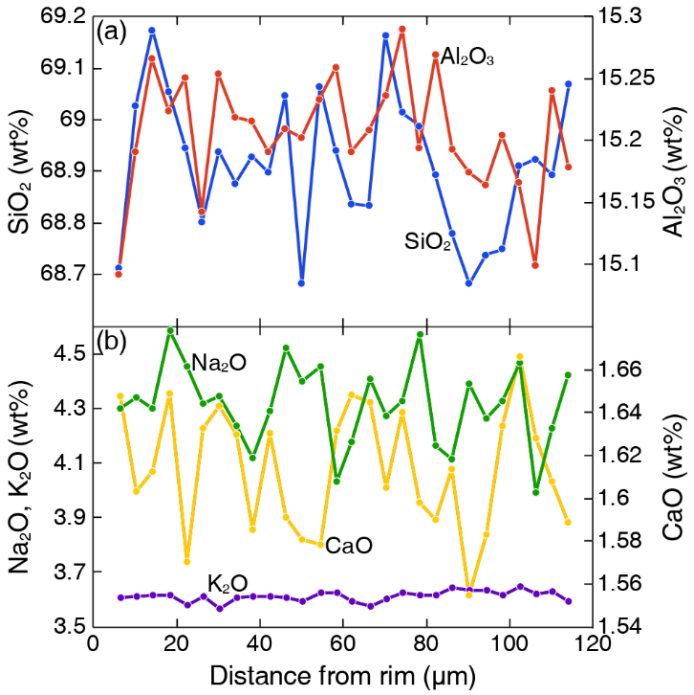

Figure 5.3. Major-element glass composition in a transect extending from the rim of crystal C5.1. No smooth compositional changes are visible with distance, indicating that no boundary layer is present. All five elements show variations of < 10% relative, over the 120 μm profile.

Major-element transects in three crystals show no consistent trends with distance from the crystal rim, with an absolute maximum variability of 1.4 mol% An. There is no obvious correlation of An content with Mg concentration in crystals for which Mg can be described by a simple diffusion model (e.g., Figure 5.2a-b). In rarer cases, where Mg varies unevenly and over a smaller range, a coarse correlation with An content is observed (Figure 5.2c). One major-element transect was continued into the adjacent glass for 114 μm. This transect revealed no compositional gradient in any analyzed element (Figure 5.3).

In naming crystals and profiles, the final number designates the profile. For example, Bt.1.2 indicates crystal Bt.1, profile 2. The crystal names are abbreviations relating to their positions on and within particular thin sections or grain mounts.

5.3.2 Diffusion modeling

Complementary error function modeling of the Mg profiles (Table 5.2) yields best fit rim values (model A) from 0.0506-0.0763 wt% Mg, with a prominent peak between 0.0685 and 0.0726 wt% Mg (Figure 5.4). Core values from model A span 0.0803-0.0834 wt% Mg without a clear modal value (Figure 5.4). For each model, best fit diffusivities span more than two orders of magnitude between lowest- and highest-D_{Mg}^{plag} profiles. Model A results give best fit D_{Mg}^{plag} values ranging from 8.7 x 10^{-19} m^2 s^{-1} to 2.8 x 10^{-16} m^2 s^{-1} (Figure 5.5). Model B results are

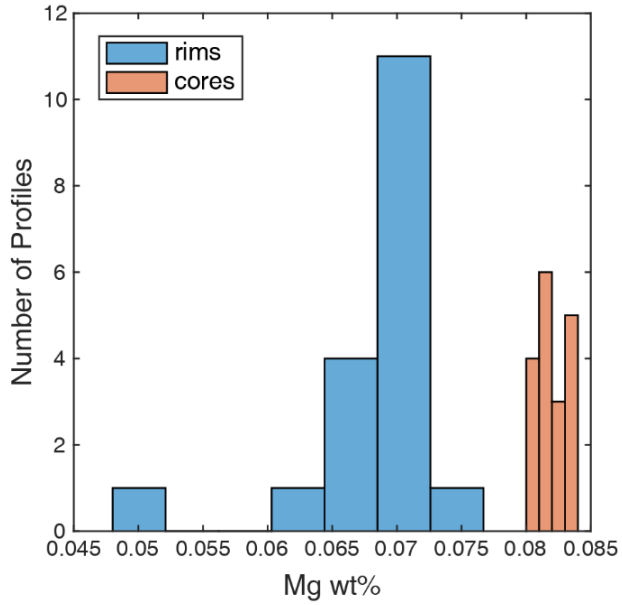

Figure 5.4. Best fit rim and core values for Mg concentration profiles, fit by model A. Note the much wider spread of rim values compared with the tightly constrained core values. Bin widths for rims are 0.0041 wt% Mg, and 0.001 wt% Mg for cores.

similar, with D_{Mg}^{plag} spanning 9.4 x 10^{-19} m^2 s^{-1} to 3.0 x 10^{-16} m^2 s^{-1}. Model C results yield D_{Mg}^{plag} values from 4.1 x 10^{-18} m^2 s^{-1} to 7.9 x 10^{-16} m^2 s^{-1}, more than twice as fast as either other model. Model D simulations result in far less good fits to the concentration data than do the other three models (misfit up to 670% relative, compared to model C). Predicted D_{Mg}^{plag} values are one to two orders of magnitude slower than those predicted by models A-C. An attempt to model diffusion on either side of a crack in profile h3.2.1 yields preliminary D_{Mg}^{plag} values of 5 x 10^{-18} m^2 s^{-1} and 1.6 x 10^{-17} m^2 s^{-1}.

For model sets A and B, the eight Mg profiles with values of D_{Mg}^{plag} > 1 x 10^{-17} m^2 s^{-1} show a marked correlation with orientation (Figure 5.6). The same set of profiles for model C corresponds to D_{Mg}^{plag} > 3 x 10^{-17} m^2 s^{-1}. The anisotropy is described by a diffusion ellipsoid, which has the lowest misfit for the set of D_{Mg}^{plag} vectors from model A, although model B results can be fit almost as well (Appendix D). The ellipsoid fit to model C vectors is significantly worse. The full triaxial ellipsoid description is not likely a better fit to the data than a prolate spheroid, but either shape represents an improvement in fit over a sphere. The direction of fastest diffusion, based on any of the model sets, is approximately [-1 -3 1], and the ratio of longest to smallest ellipsoid axes is 8:1.

5.4 DISCUSSION

The following discussion is divided into three parts. In Part I, we consider the derived results, including the relative ability of each model to describe the data, and the possible reasons for any differences. We also discuss the applicability of various assumptions in the modeling process. Part II considers the high D_{Mg}^{plag} values and the variability of D_{Mg}^{plag} in the context of theoretical and diffusion studies on plagioclase and other minerals. In Part III, we discuss the dissolution in experiments from a thermodynamic angle, and as a potential control on the mechanism of diffusion.

5.4.1 Part I: Computational models and assumptions

5.4.1.1 Comparison of model results

Models A and B yield similar diffusivity estimates, typically within 5% percent of each other, and with similar misfit values for a given profile (Figure 5.5). For profiles where the differences in diffusivity are larger between models A and B, the difference in misfits is not

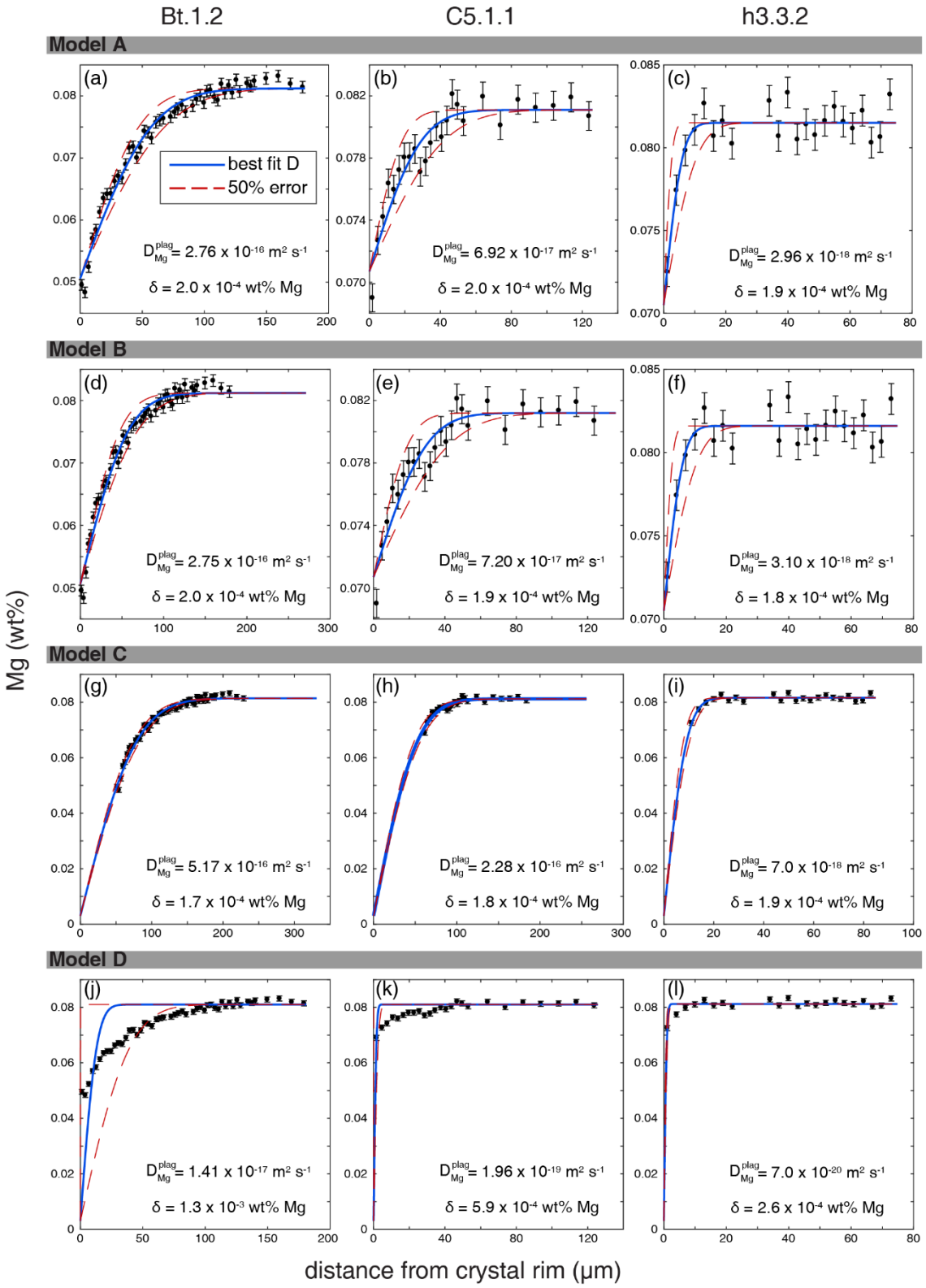

Figure 5.5. Model fits A-D for three representative crystals (the same crystals shown in Figure 5.1). Best fit D_{Mg}^{plag} and misfit are shown. High and low D_{Mg}^{plag} estimates in Appendix D.

necessarily larger as well. This suggests that the shapes of those profiles are fit well by a broad range of D_{Mg}^{plag}. The overall agreement between models A and B indicates that exact core plateau values and the distance to the core plateau do not strongly affect calculated D_{Mg}^{plag} values. Using rim values close to those measured by EPMA (best fits in model A), diffusion profiles are best fit without any simulated dissolution, a result not unexpected given that the rim value was derived using a dissolution-free model (model A).

When the rim value is set to the equilibrium partitioning value, however, allowing for dissolution creates a better fit to all profiles. Except for profile Bt.1.2, the faster diffusivities calculated via models A and B produce larger best fit dissolution distances. In terms of the overall description of the profiles, though, the misfits for model C are on par with those of models A and B – never more than 15% different, and typically within 5% relative. Thus, although model C is useful for examining if and how the concentration profiles might fit into larger profiles that are no longer measurable, it cannot be used to estimate the length scale of dissolution in the crystals.

Model D is perhaps more instructive. When forcing the rim Mg concentration to the calculated equilibrium value and the rim distance to the current, visible rim location, concentration profiles are fit considerably less well than with any other model. Based on the three profiles that were assessed with model D, the quality of fit worsens with increasing diffusivity. This outcome is both expected (profiles closer to vertical can better accommodate the low rim value) and counterintuitive (the high-diffusivity profile Bt.1.2 has the lowest rim Mg concentration, i.e., closest to the forced value for model D, yet it is poorly fit by the model). The model D fits might be explained by evolving melt composition, inadequate partitioning models, or faulty assumptions about crystal-melt equilibration rates. We explore each of these possibilities below.

5.4.1.2 Mg partitioning and assumption of interfacial equilibrium

The simplest explanation for the poor model D fits is that the model discounts the possibility of crystal dissolution. However, the models that do treat dissolution (B and C) are inherently simplified, in that dissolution is modeled as a single truncation that cuts off a portion of the concentration profile. Models of continuous dissolution, or rapid dissolution followed by

Table 5.2. Profile orientations and model results.

Profile	θa	θb	θc	n[a]	Model	D (m^2 s^{-1})	Rim (wt% Mg)[b]	Core (wt% Mg)	Dissolution (μm)	Extension (μm)	δ
						x 10^{17}					**x 10^{4}**
h3.1.1	66	29	116	30	A	28.4	0.0704	0.0834	-	-	1.93
					B	28.4	-	0.0834	0	100	1.87
					C	74.9	-	0.0834	100	100	1.93
Bt.1.2	63	48	140	49	A	27.6	0.0506	0.0812	-	-	2.00
					B	27.5	-	0.0812	0	90	1.96
					C	51.7	-	0.0814	50	100	1.69
					D	1.41	-	0.0810	-	0	13.1
h3.2.1	72	18	103	42	A	25.5	0.0632	0.0803	-	-	1.44
					B	29.7	-	0.0810	0	100	1.52
					C	79.1	-	0.0810	90	100	1.30
C5.1.1	78	68	46	25	A	6.92	0.0707	0.0811	-	-	2.01
					B	7.20	-	0.0812	0	10	1.94
					C	22.8	-	0.0812	60	70	1.78
					D	.0196	-	0.0810	-	0	5.93
Bb.1.1	44	134	95	25	A	4.46	0.0679	0.0831	-	-	2.11
					B	4.59	-	0.0832	0	0	2.04
					C	8.46	-	0.0830	30	10	1.92
Ab.1.1	114	146	95	86	A	1.94	0.0719	0.0826	-	-	1.00
					B	1.94	-	0.0826	0	0	0.993
					C	5.80	-	0.0826	30	0	0.983
Bt.1.1	149	73	92	41	A	1.56	0.0651	0.0833	-	-	1.75
					B	1.60	-	0.0834	0	0	1.71
					C	3.99	-	0.0834	20	0	1.71
h6.1.1	105	145	52	19	A	0.980	0.0706	0.0831	-	-	2.19
					B	0.940	-	0.0830	0	10	2.09
					C	2.88	-	0.0832	20	30	2.06
h3.3.1	106	163	77	25	A	0.930	0.0722	0.0817	-	-	1.35
					B	0.890	-	0.0816	0	0	1.30
					C	2.47	-	0.0816	20	0	1.33
C3.2.1	102	165	75	15	A	0.510	0.0705	0.0805	-	-	1.71
					B	0.610	-	0.0810	0	0	1.84
					C	2.41	-	0.0810	20	20	1.88
h1.2.2	11	81	122	27	A	0.496	0.0704	0.0817	-	-	1.90
					B	0.510	-	0.0818	0	0	1.84
					C	2.48	-	0.0818	20	0	1.87
C5.2.1	44	71	79	35	A	0.290	0.0700	0.0831	-	-	1.63
					B	0.460	-	0.0832	0	0	1.56
					C	0.740	-	0.0830	10	0	1.56
C3.1.1	68	26	114	34	A	0.356	0.0655	0.0807	-	-	1.69
					B	0.380	-	0.0810	0	0	1.70
					C	0.910	-	0.0810	10	0	1.71
C3.1.2	91	88	25	31	A	0.346	0.0662	0.0826	-	-	2.14
					B	0.350	-	0.0826	0	0	2.07
					C	0.920	-	0.0826	10	0	2.08
C3.4.1	100	78	23	26	A	0.305	0.0721	0.0824	-	-	1.82
					B	0.310	-	0.0824	0	0	1.75
					C	0.640	-	0.0824	10	0	1.78
h3.3.2	26	117	111	22	A	0.296	0.0705	0.0815	-	-	1.92
					B	0.310	-	0.0816	0	0	1.84
					C	0.700	-	0.0816	10	0	1.86
					D	0.007	-	0.0812	-	0	2.65
h1.2.1	73	85	171	17	A	0.087	0.0763	0.0813	-	-	1.51
					B	0.094	-	0.0814	0	0	1.43
					C	0.411	-	0.0814	10	0	1.44
h3.2.2	140	51	83	11	A	2.42	0.0685	0.0804	-	-	2.72
					B	2.90	-	0.0810	0	30	2.60
					C	6.90	-	0.0810	30	50	2.73
Bb.2.1	128	141	74	19	A	0.382	0.0526	0.0659	-	-	2.26
h1.1.1	63	90	52	20	A	3.50	0.0671	0.0796	-	-	1.62

a. Number of EPMA spot analyses included in the profile fit

b. All rims for model B are the same as for model A; all rims for models C and D are 0.003 wt% Mg

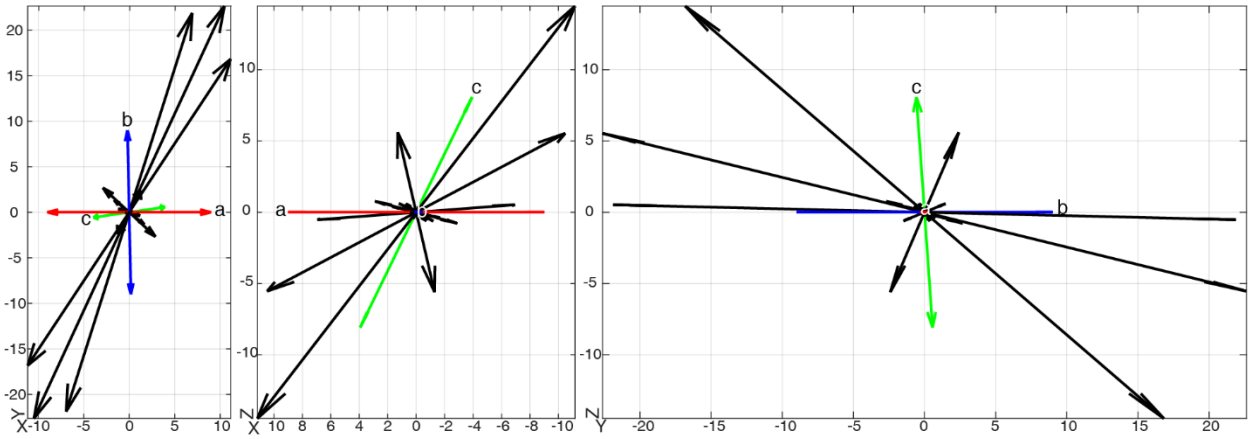

Figure 5.6. Variation of D with orientation, shown in XY, XZ, and YZ Cartesian planes. Black vectors represent EPMA transects. Each has been scaled by its model A diffusivity value and multiplied by 1 x 10^{17}, so that a diffusivity of 5 x 10^{-17} m^2 s^{-1} is represented by a vector with a magnitude of 5. Each data vector is continued across the origin.

diffusion, could potentially provide better results. At present, we consider alternative explanations for the model D fits, other than dissolution.

First, we examine the possibility that the melt Mg content used to calculate the equilibrium plagioclase Mg concentration is incorrect. The partitioning of Mg between plagioclase and melt is computed as

$$K_{Mg}^{plag/liq} = \frac{C_{Mg}^{plag}}{C_{Mg}^{liq}} \qquad \text{eq 5.5}$$

where $K_{Mg}^{plag/liq}$ is the equilibrium partition coefficient, and C_{Mg}^{plag} and C_{Mg}^{liq} are the concentrations of Mg in plagioclase and melt, respectively. Using $K_{Mg}^{plag/liq}$ from one of the available models (e.g., Sun et al. 2017), an equilibrium plagioclase Mg concentration is determined by multiplying this partition coefficient by the melt Mg concentration. If $K_{Mg}^{plag/liq}$ is fixed, then a higher melt Mg concentration is associated with a higher plagioclase Mg concentration. We compute the equilibrium plagioclase Mg content using the initial experimental glass composition (0.206 wt% Mg). However, the post-experimental glass composition is notably different. We have only major-element data for the post-experimental glass, and therefore cannot directly compute a final equilibrium Mg concentration for the labradorite. However, mass balance calculations suggest that the ending experimental melt was produced by dissolution of ≤ 5 wt% of the total plagioclase mass in the capsule. Using a conservative estimate of 5 wt% dissolution, assuming all input plagioclase contains as much Mg as the initial labradorite crystals, the post-

experimental glass would contain 0.205 wt% Mg, similar to the pre-experimental concentration. The only way that melt Mg concentration could be increased would be locally, in boundary layers adjacent to the dissolving crystal. Such concentration gradients are expected to form during "diffusive dissolution," in which the rate-limiting factor for dissolution is melt diffusivity (Liang 1999). However, melt concentration gradients are not visible in BSE images, and one EPMA transect in glass did not reveal a gradient in major elements near the adjacent crystal (Figure 5.3). Therefore, it is unlikely that melt near the crystal interface was significantly enriched in Mg, and we take C_{Mg}^{plag} calculated using the initial melt composition as an upper bound on the equilibrium labradorite Mg concentration for this experimental system.

Having eliminated the second most straightforward explanation of incorrect melt composition, a third interpretation that could explain the poor model D fits is that the predicted equilibrium C_{Mg}^{plag} is incorrect. Partitioning equations from multiple studies predict an equilibrium concentration of 0.0025-0.0030 wt% Mg for our experimental plagioclase (Bindeman et al. 1998; Nielsen et al. 2017; Sun et al. 2017), but none of those studies include calibration data from melts as Mg-poor as the rhyolitic melt used in this study (0.206 wt% Mg). Moreover, EPMA analyses of the rare An_{47} rims that formed during our experiment (likely due to decompression, see "Dissolution and growth") reveal Mg concentrations seven times higher than predicted by these equilibrium partitioning relationships. For An_{47} plagioclase in equilibrium with the initial melt, the predicted Mg concentration is 0.003-0.004 wt% (Bindeman et al. 1998; Nielsen et al. 2017; Sun et al. 2017). One EPMA analysis indicates a true concentration of 0.022 wt% Mg in these rims. Additional analyses were attempted, but unsuccessful, due to the small width of the rims. Even allowing for a build-up of Mg in the adjacent melt, a five- to six-fold increase in melt Mg concentration (to 1.1-1.3 wt%) is required to return accurate estimates of Mg in the An_{47} tabs (Bindeman et al. 1998; Nielsen et al. 2017; Sun et al. 2017). Considering the main crystals, a 17-fold or greater increase in melt Mg (to ≥ 3.5 wt%) is required to predict even the lowest near-rim Mg concentration. We consider such extreme enrichment implausible, as detailed above.

The limited extent of our data does not allow us to write a new predictive equation for Mg partitioning in plagioclase, but it supports the idea that the equilibrium partitioning relationships currently available are unlikely to represent our system accurately. We do not advocate that these predictive tools are generally at fault. For example, using its estimated parent

melt composition and temperature (3 wt% Mg, 1100 °C; (Stewart et al. 1966), the model of Sun et al. (2017) returns an initial Mg value for Lake County Labradorite of 0.085 wt%, close to our EPMA-determined 0.083 wt%. However, we conclude that further analysis of plagioclase in Mg-poor melts must be undertaken to assess partitioning behavior more accurately. Even were appropriate equilibrium values to be obtained, however, we question the validity of tying them to diffusion in the crystal interior.

A final assumption that may be at fault regarding the poor model D fits is that of instantaneous equilibrium at the crystal-melt interface. Although adopted in many treatments of diffusivity modeling (e.g., Dohmen et al. 2017; Lynn et al. 2017), and rigorously demonstrated in several cases (Liang 1999, 2003; Spandler and O'Neill 2010; Yu et al. 2016), achieving this equilibrium is inherently dependent on diffusion. It is most often assumed that interphase (grain boundary) diffusion allows equilibration over a timescale that is orders of magnitude shorter than that required via volume diffusion, and that this diffusive process controls the rim composition at crystal-melt interfaces (Zhang 2010). Elements in the melt itself typically diffuse orders of magnitude faster (Zhang et al. 2010). Taking this explanation as true, it still does not follow logically to anchor one end of a diffusive profile derived via volume diffusion to an interface concentration that is only achievable via a much faster mechanism. One or two microns away from the interface, as our profiles demonstrate, the Mg concentration is far greater than that predicted by equilibrium partitioning. There may exist a distance of < 1 μm over which the equilibrium Mg concentration jumps up to the concentration measured in the profile, but this steep gradient cannot be described by the diffusion equation (eq 5.2). Further reason to doubt the relevance of anchoring to an equilibrium concentration comes by examining rim compositions of the labradorite crystals. If the melt composition can be assumed to be relatively homogeneous around each crystal, then rim compositions in all directions should be similar. Instead, we see significant differences between crystals and within a single crystal (e.g., 0.0506-0.0651 wt% Mg for crystal Bt.1, model A). It appears that the speed of Mg diffusion and/or crystal dissolution affects how far the crystal rim can progress toward an equilibrium composition. Therefore, the assumption of instantaneous interfacial equilibrium is not always an accurate one.

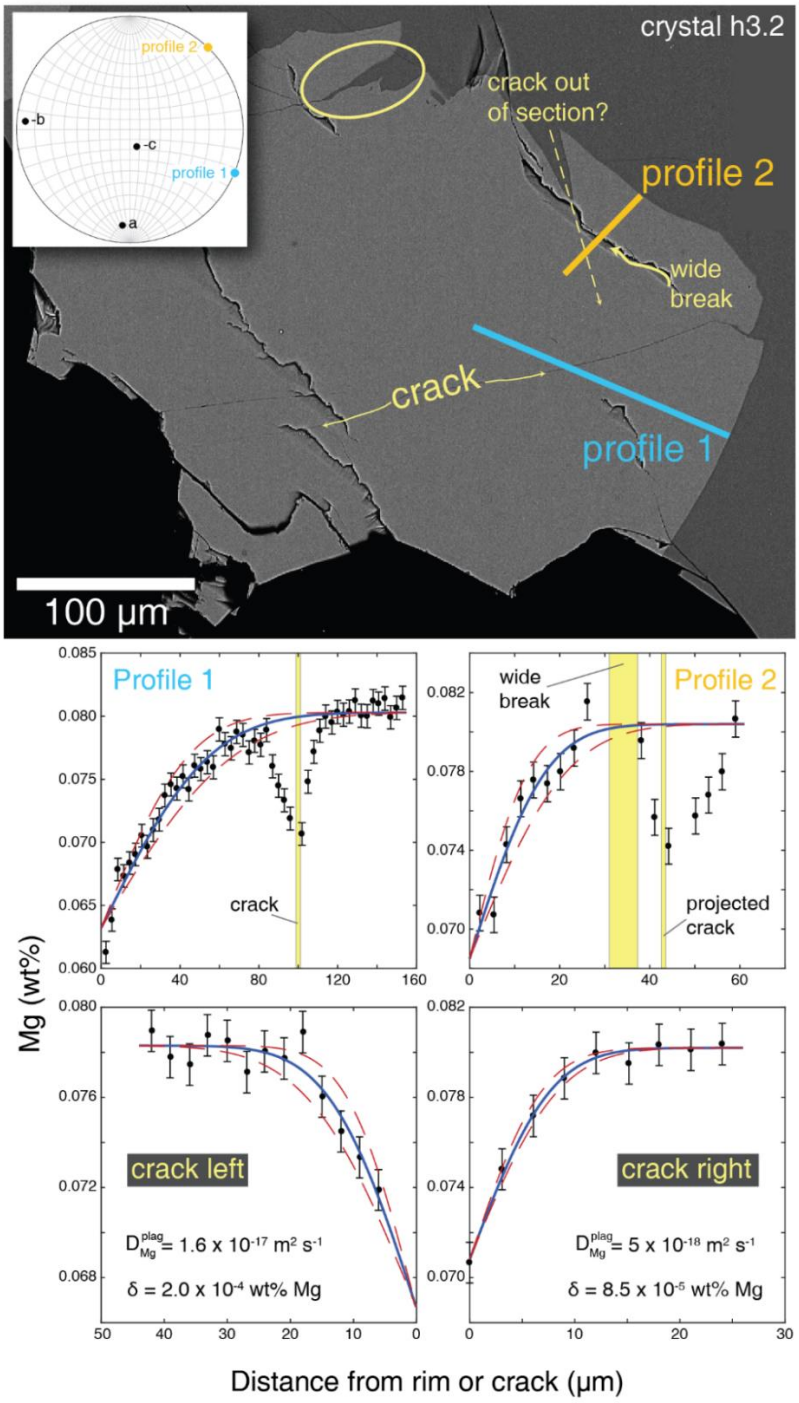

Figure 5.7. The effect of cracks on diffusion profiles in crystal h3.2. Profile 1 has a modeled D^{plag}_{Mg} of ~3 x 10^{-16} m^2s^{-1}, and Profile 2 has a much lower D^{plag}_{Mg} (~3 x 10^{-17} m^2s^{-1}). The crack across Profile 1 matches exactly with the downdrop in Mg, but in Profile 2 is offset. We interpret the downdrop in Profile 2 to reflect Mg diffusion toward a crack out of the plane of section, likely originating from the embayment noted on the BSE image. Diffusion modeling is also applied to the "v" in Profile 1, treating the tip of the "v" as the rim and points on the overarching diffusion profile as cores (bottom panels). This simple exercise reveals excellent fits, especially on the right side of the "v," and yields D^{plag}_{Mg} values that are higher than most in the literature (Table 5.3), but slower than the overarching profiles' values.

5.4.1.3 Insights from crystal and profile irregularities

5.4.1.3.1 Crack-enhanced diffusion

Where Mg concentration dips in a "v" shape, a crack is sometimes visible. In the clearest cases, these cracks appear to be melt-filled (BSE dark grey) rather than voids (BSE black), suggesting that they were features present during the high-temperature experiment and not polishing artifacts (Figure 5.7). However, thin melt-filled cracks are susceptible to damage during polishing (Figure 5.8), so if any part of the crack contains residual glass, it is likely that the entire length was melt-filled during the experiment. Alternatively, the crack present syn-experiment may plunge into or out of the visible section, but its presence weakens the surroundings, resulting in additional cracking during post-experimental sample preparation. The crystal-melt interface on either side of these cracks allows diffusion to proceed in a way analogous to that at the crystal rim. The complexities in this situation are greater, due to superposition on the overall rim-core profile and the proximity of the two crystal surfaces. However, a first attempt at estimating D_{Mg}^{plag} from a crack-induced diffusion profile within rim-core profile h3.2.1 gives an excellent fit to the data on one side of the crack, and a reasonable fit on the other side (Figure 5.7). The D_{Mg}^{plag} values are lower than that derived for the full rim-core profile (2.6×10^{-16} m^2 s^{-1}), but they are still larger than or comparable to literature predictions (Table 5.3). Because cracks fall anywhere along the rim-core profile, where original core concentrations could already be lowered, diffusivities calculated based on the Mg drawdown surrounding cracks are likely to be minimum estimates (Shea et al. 2015b).

Some core-rim Mg profiles display concentration decreases similar to those associated with cracks, but no crack is visible at the "v" location. Because An content is approximately constant in the labradorite crystals, and no greyscale changes are visible in BSE images at the "v" locations, these drawdowns are unlikely to be due to coupling of Mg and An. Instead, we hypothesize that melt-filled cracks are present, but out of the plane of section. For example, the "v" in profile h3.2.2 does not correspond to the wide, disrupted region clearly visible on the crystal surface. However, the projected extension of a prominent embayment that narrows into the crystal crosses the profile in approximately the location of the Mg drawdown (Figure 5.7). At the top of the same crystal, another embayment narrows into the crystal and visibly passes into a

thin, melt-filled crack. Thus, it is reasonable to suggest that the same pattern occurs at other embayments, though not necessarily visible within the plane of section.

Transect C4.1.1 is a complex Mg concentration profile, not suitable for diffusion modeling. There are no visible cracks along its length (Figure 5.8), but we suspect that cracks outside the plane of section are largely responsible for the complicated shape of the profile. The most prominent "v" is noted, and a schematic diffusion profile is shown to suggest what the overall rim-core profile fit may have looked like without interruptions. Similarly, a slightly out-of-section syn-experimental crack may explain the ~5 μm offset between the "v" and the visible crack in profile C4.1.2 (Figure 5.8). The "v" is reflected to a lesser extent in An content, so this particular instance may reflect small-scale complications of partitioning as well as crack-enhanced diffusion.

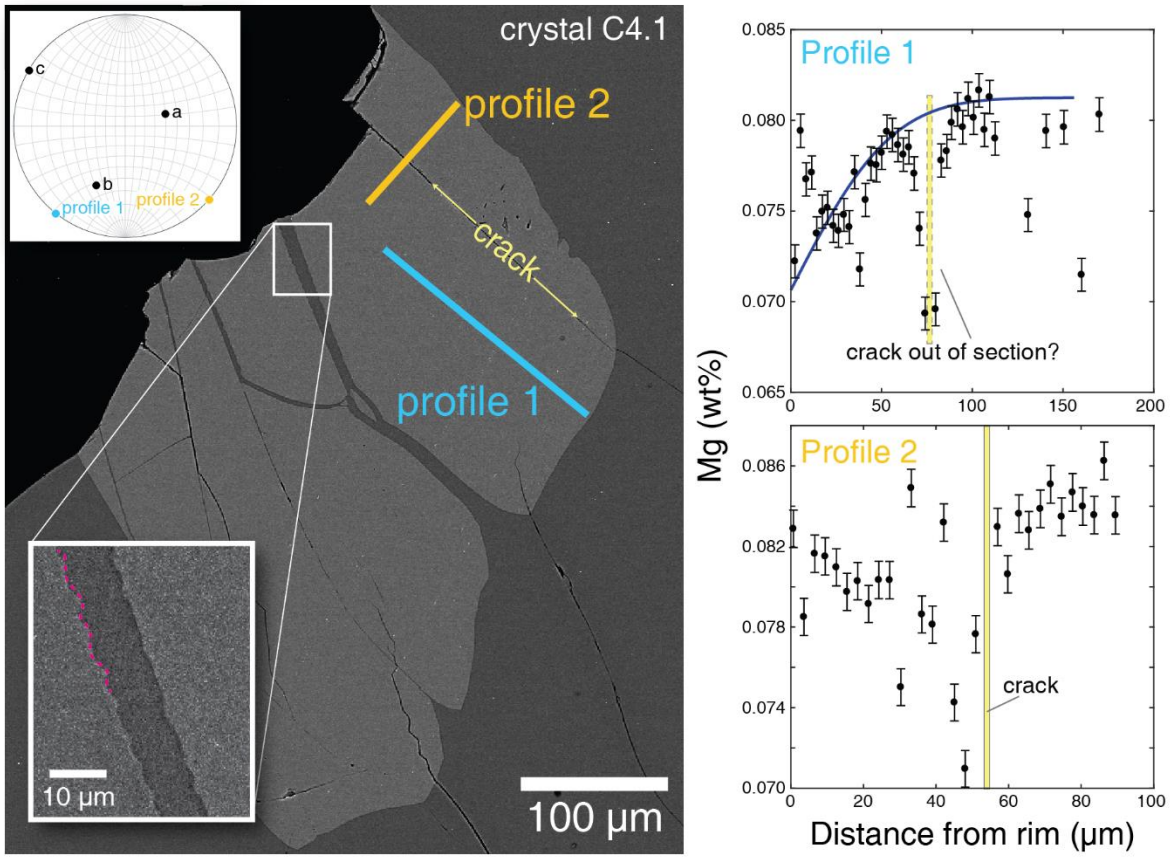

Figure 5.8. Crystal C4.1- an example of how cracks may affect Mg diffusion even when not visible in the section (Profile 1), or when their visible manifestation is slightly offset from the concentration "v" (Profile 2). Blue curve on Profile 1 plot illustrates what the diffusion path may have looked like were the crystal crack-free. Zoomed-in region of BSE image shows micro-scale instabilities interpreted to indicate crystal growth (reprecipitation); part of the crystal-melt boundary is outlined to highlight these subtle features.

It is evident from our observations that the presence of any melt within the body of a crystal can serve to enhance diffusion, by providing more surface area over which species can be exchanged between the two phases. In studies of natural crystals, this effect should be considered. In particular, we emphasize that cracks need not be visible within the plane of section in order to affect the concentration profiles measured.

5.4.1.3.2 Reprecipitation

A melt channel significantly larger than the cracks discussed above (10+ μm wide) is visible in one plagioclase crystal (C4.1). Along the edges of this feature, the labradorite surface undulates with an irregular wavelength of 5-10 μm (Figure 5.8 inset). No compositional difference is evident at or near these small amplitude (1-2 μm) peaks, but the pattern suggests instabilities consistent with crystal growth (Kirkpatrick 1975). If so, this crystal is the only one yet observed at which the process of dissolution is balanced to some extent by reprecipitation. If the magnitude of reprecipitation is a rough proxy for the magnitude of dissolution, then the overall amount of dissolution appears to have been small, consistent with a calculated dissolution of ≤ 5 wt% of the original plagioclase.

5.4.1.3.3 Extreme core loss

Transect Bb.2.1 was taken across the entire short dimension of an ~80 x 300 μm labradorite crystal (Figure 5.9). The concentration profile is fairly symmetrical, supporting the base assumption that diffusion along a given orientation axis is the same whether the net mass flux proceeds in the negative or positive crystal direction. The same concentration profile has a core plateau between 0.066 and 0.067 wt% Mg, indicating that diffusion proceeded quickly enough to decrease the initial Mg concentration significantly (~0.083 wt% Mg) even at the apparent crystal core. This drawdown was likely aided by the presence of a central crack, visible in BSE and evident in the V-shaped center of the concentration profile. The model A estimated D_{Mg}^{plag}, based on the left side of the profile and excluding the central "v," is ~3.8 x 10^{-18} m^2 s^{-1}. Due to the loss of the original core plateau, this value is a minimum. On the diffusivity ellipsoid, the Bb.2.1 profile orientation corresponds to a D_{Mg}^{plag} of 1 x 10^{-16} m^2 s^{-1}, which is 26 times faster than the apparent diffusivity given by model A. Thus, although the rim Mg concentration, in general, has a larger effect on model fits than does the core composition, extreme core loss could affect modeled diffusivities significantly, consistent with Shea et al. (2015b).

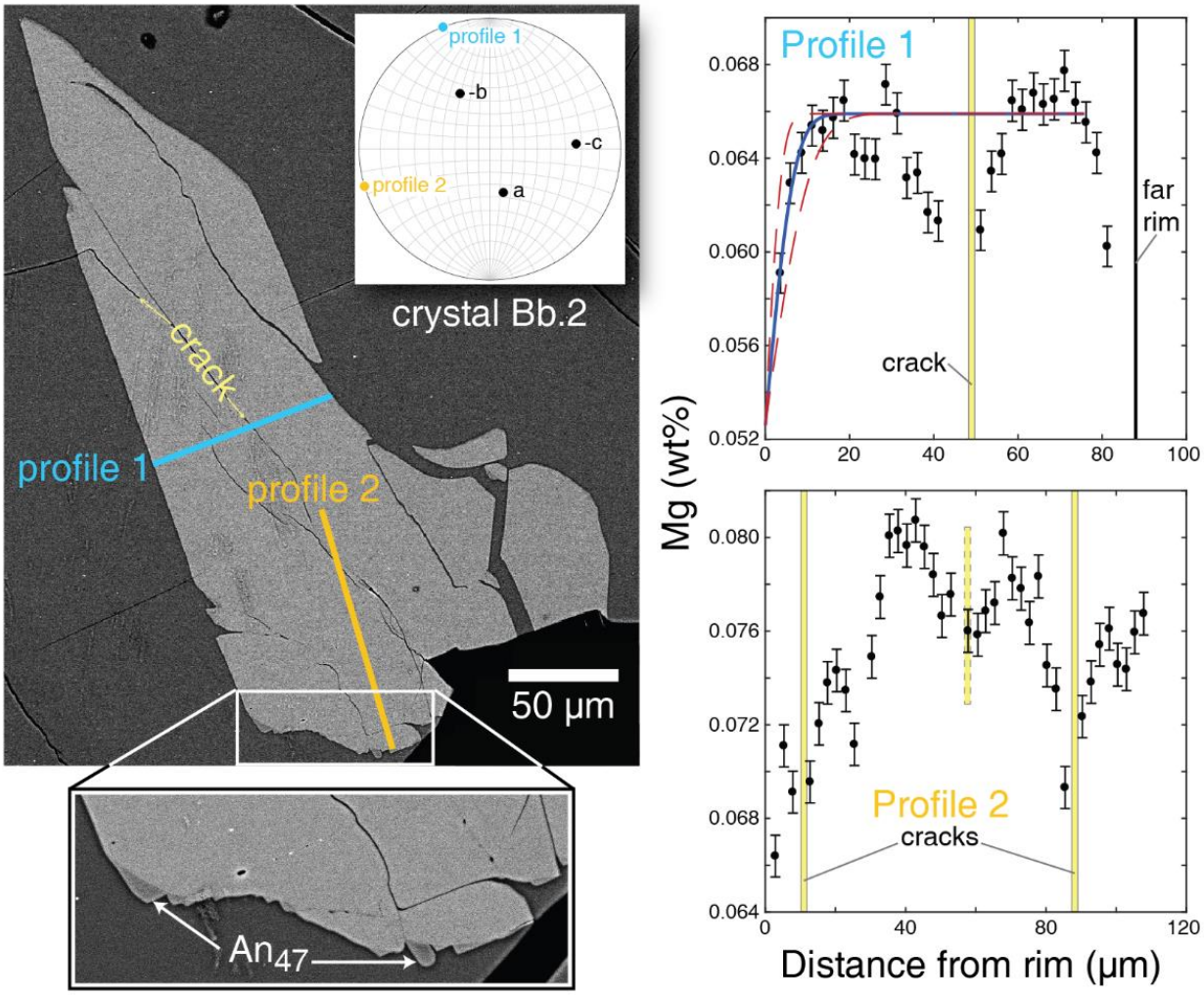

Figure 5.9. Crystal Bb.2 – a labradorite with very low Mg concentration at the apparent crystal core. If the crystal was small to begin with, this is due to diffusive re-equilibration reaching the center of the crystal; if the plane of section cuts into a large crystal near its edge, the low core Mg may be a sectioning effect only. In either case, the diffusivity derived from modeling the left part of Profile 1 would be a minimum. Both Profile 1 and Profile 2 show crack-enhanced diffusion. This crystal is one of the 4+ with low-An overgrowths. Note that the darker tab-like growths have facets, but are rounded at the corners.

5.4.2 Part II: Rapid, anisotropic diffusion

Setting aside the detailed complexities discussed above, three broad points arise from our results. First, dissolution of the input labradorite occurred. Second, the highest estimated D_{Mg}^{plag} values are 40-400 times larger than the literature predicts (Table 5.3; Costa et al. 2003; Faak et al. 2013; Van Orman et al. 2014). Third, an orientation dependence of diffusivity is suggested. Below, we evaluate the abilities of random sectioning, environmental factors, dissolution, and lattice structure to produce the high and variable Mg diffusivities indicated by our experiment.

Table 5.3. D_{Mg}^{plag} predictions for An_{66} (900 °C, 125 MPa)

Source	Equation	D (m^2 s^{-1})[a]
		x10^{17}
Costa et al., 2003	8	0.654
Faak et al., 2013	42	0.0642
Van Orman et al., 2014	4	0.203
This study high[b]	-	29.7
This study low[c]	-	0.087

a. An entry of "1" represents 1 x 10^{-17}

b. Models A and B only

c. Diffusivities < 1 x 10^{-17} may be compromised by dissolution

5.4.2.1 Sectioning effects

By nature of the experiment performed, the sample and crystals therein could not be oriented in any particular way prior to mounting and polishing. The resultant cuts through the labradorite crystals were thus random. In one sense, this random sectioning is an improvement over previous methods, providing access to D_{Mg}^{plag} information along directions other than those parallel to the crystallographic axes. However, the effects of using randomly-oriented, off-center sections to determine timescales, or equivalently diffusivities, are not straightforward and could contribute to inaccurate and/or widely varying estimates (Shea et al. 2015b). In addition, the fit of the 1-D diffusion model to the concentration profile is not an indication of the accuracy of the derived timescale or diffusivity (Costa and Chakraborty 2004; Liang 2003; Shea et al. 2015b), leaving questions about the reliability of such estimates.

Despite these uncertainties, there are several consistent patterns that allow us to consider our profiles in meaningful ways. Measuring concentration profiles perpendicular to crystal edges and away from crystal corners results in the best accuracy for a given cut (Costa and Chakraborty 2004; Shea et al. 2015b), so this is how we oriented every profile, to the extent possible on the given crystal. For simple zoning patterns in olivine, timescale retrieval is more accurate when observed core concentrations are used as initial concentrations, rather than the true maximum core concentration for the entire crystal (Shea et al. 2015b). This concept holds true for the Mg concentration profiles in this study and was the motivation for modeling core Mg values for each individual profile, rather than using one plateau value for all concentration profiles. With loss of true initial concentrations, at either core or rim, timescale estimates are

generally shorter than the true durations (Shea et al. 2015b). These findings agree with those of Liang (2003), who calculated that ignoring a moving boundary due to dissolution can result in timescale estimates that are only half of the true duration. In these studies, concentration profiles whose shapes are fit by a short timescale at a given diffusivity correspond in this work to a low diffusivity at a given timescale. Likewise, long timescale profiles at a given diffusivity are equivalent to higher diffusivity profiles for a given duration. Thus, absence of initial rim or core Mg compositions, whether due to dissolution (rim), or sectioning effects and/or rapid diffusion (core), should result in estimates of D_{Mg}^{plag} that are smaller than the true value. Given the evidence for dissolution in our experiment, and therefore loss of initial rim compositions, it would seem reasonable to conclude that any diffusivity obtained in our study is likely to be a minimum for that profile.

However, the loss of initial rim and/or core compositions is not the only factor at play. Neglecting 2-D flux can result in timescale overestimates up to three times greater than the true duration represented (Fe-Mg zoning in olivine, Costa and Chakraborty 2004), and likewise can result in overestimates of diffusivity. The third dimension, not accessible with traditional thin sections, also contributes to mass flux. This means that profiles appearing perpendicular to a crystal edge in 2-D may still be only "apparent" concentration profiles, as they are not necessarily perpendicular to the plane of the crystal face (Ganguly et al. 2000). However, simulated concentration profiles on random cuts do not yield timescales more than five times longer than the true duration, and the majority are within a factor of two (Fe-Mg zoning in olivine (Shea et al. 2015b). Because concentration is proportional to both $t^{-1/2}$ and $D^{-1/2}$ (e.g., eq 5.2), the same scaling can be assumed reasonably to apply to diffusivity estimates. By this evaluation, sectioning effects alone cannot explain the 100-fold range of D_{Mg}^{plag} values in our study, nor the highest D_{Mg}^{plag} values obtained from our models, which are 40+ times higher than published values.

5.4.2.2 Environmental variables

5.4.2.2.1 Confining pressure

In general, increasing confining pressure slows diffusion (Lasaga 1998), but the effect is relatively small over the range of pressures relevant to volcanic systems. For example, the diffusion of rare-earth elements in pyroxene slows down by a factor of only 1.1 over a 100 MPa

pressure interval (Van Orman et al. 2001). The effect of confining pressure on trace Mn in olivine is similarly minimal, slowing diffusion by less than 0.025 log units over 100 MPa (Holzapfel et al. 2007). Data are not available for the activation volume of Mg in plagioclase, but the activation volumes for H, Na, and K in plagioclase are small and positive (~5 cm^3 mol^{-1}; (Zhang et al. 2016), meaning the diffusivities of those species decrease slightly with increasing pressure. Whether pressure exerts a positive or negative influence on Mg diffusivity, however, the magnitude of the effect should be small. Given the experimental pressure of 125 MPa, we conclude that confining pressure alone would not alter D_{Mg}^{plag} outside the bounds of uncertainty, in comparison to the literature data obtained at atmospheric pressure (Faak et al. 2013; LaTourrette and Wasserburg 1998; Van Orman et al. 2014).

5.4.2.2.2 Oxygen fugacity

The low fO_2 of our experiment (NNO-2) compared to that typical of arc volcanic systems (~NNO) requires an evaluation of the potential effect of fO_2 on Mg diffusivity in plagioclase. For elements with multiple possible valence states (e.g., Fe^{2+}/Fe^{3+}), a decrease in fO_2 works to increase the ratio of the lower valence cations. Because these cations typically diffuse faster than their higher valence counterparts (due to weaker bonding (Zhang 2010), the fO_2 decrease typically serves to increase diffusivity of the variable-valence element in question. However, decreasing fO_2 also has the general effect of decreasing the density of vacancy defects associated with higher valence cations (Lasaga 1998; Zhang 2010), resulting in lower diffusivity for other elements (Dohmen and Chakraborty 2007). This joint effect of fO_2 is observed in plagioclase, where Fe diffusivity increases but Na diffusivity decreases as fO_2 is lowered (Behrens et al. 1990). Because Mg occurs only as a divalent cation, the relatively low fO_2 of the experiment should work to lower D_{Mg}^{plag}. However, our results show D_{Mg}^{plag} many times faster than previously predicted, suggesting that the fO_2 effect is not significant in comparison to other driving forces in the experiment. The study of Faak et al. (2013) is thus far the only one to vary fO_2 in any way, and there is no evident correlation between fO_2 and D_{Mg}^{plag}, although the variable was not explicitly examined and varied only from log fO_2 of -9 to -11, in this case equivalent to the range ~NNO to ~NNO-2. Our own experiment had a similar fO_2, but the overall experimental setup was different enough to preclude direct comparison. However, the D_{Mg}^{plag} values obtained

by Faak et al. (2013) are slower than those predicted by the study of Van Orman et al. (2014) for compositions with < 90 mol% An. The Van Orman et al. (2014) experiments were conducted in air, suggesting that fO_2 does affect Mg diffusion in plagioclase, in the direction expected for a single-valence-state element. Conversely, experiments reveal no difference in tracer diffusion of Sr in albite for air versus ~IW (Giletti and Casserly 1994). There is clearly more work to be done to understand fully the complex effects of fO_2 on trace element diffusion in plagioclase, but we are confident that a low fO_2 is not responsible for the high diffusivities obtained in our study.

5.4.2.2.3 Hydrous melt

One key difference between our study and prior works is the use of a natural rhyolitic melt containing water at saturation concentration. Although the specific effects vary from element to element and mineral to mineral, water in nominally anhydrous minerals generally weakens the overall mineral structure, which serves to enhance diffusion (Lasaga 1998; Zhang 2010). In olivine, diffusion experiments at ~0.3 GPa water pressure yield Fe-Mg interdiffusivities three times faster than do experiments at dry conditions, presumably due to vacancy formation associated with H+ incorporation (Kohlstedt and Mackwell 2008). In feldspar, the effect of water is variable. In the presence of an N_2-H_2O fluid phase, NaSi-CaAl interdiffusion in peristerite increases by a factor of 2.2 for every increase of $X_{H2O} = 0.1$ (Baschek and Johannes 1995). In the range An_{67}-An_{90}, NaSi-CaAl interdiffusion is similarly enhanced at hydrothermal conditions (Liu and Yund 1992). In contrast, diffusion coefficients of both Na and K are insensitive to ambient H_2O concentration (Behrens et al. 1990; Giletti and Shanahan 1997). The same insensitivity is observed for Sr, an element with the same charge and similar ionic radius as Mg^{2+} (Giletti 1991; Giletti and Casserly 1994). However, despite long-held assumptions, it is not an element's charge and ionic radius that predict diffusivity most accurately (Spandler and O'Neill 2010), so we do not necessarily expect Mg diffusivity to show the same dependencies as Sr diffusivity in plagioclase.

The diffusion of H+ in plagioclase is the same parallel and perpendicular to the b crystal axis, and is interpreted to occur by interdiffusion of H+ and Na+, facilitated via Frenkel defects (Johnson and Rossman 2013). Both of these conclusions would suggest that water is not responsible for Mg diffusional anisotropy, nor rapid Mg diffusion. However, the apparent isotropy of H+ diffusion could reflect unmeasured anisotropy, with principal diffusion directions

not related to the crystal axes, as we observe for Mg. If this scenario is true, then D_{Mg}^{plag} anisotropy may be linked to D_{H+}^{plag} anisotropy. Clearly, studies that measure H+ diffusion in additional orientations are needed to confirm or refute this hypothesis. As for diffusion mechanism, the linking of H+ to Na+ is based on similarities of activation energy and diffusion rates for the two species, not concurrent measurements or observations. We consider the possibility that, rather than the proposed interdiffusion mechanism, H+ incorporation is balanced by metal vacancies, as in olivine (Kohlstedt and Mackwell 2008). These vacancies would provide sites for Mg to jump through the crystal lattice. We acknowledge that the above arguments are hypothetical and require further study of both proton and Mg diffusion in plagioclase. For now, the possibility that melt water content is responsible for Mg diffusional anisotropy and/or overall high Mg diffusivity in our experiment remains a viable hypothesis.

The very presence of melt in our experiment, by nature of its perfect interface contact, could also have enhanced Mg diffusion out of the labradorite crystals compared to studies that used solid glass (LaTourrette and Wasserburg 1998) or powder (Faak et al. 2013; Van Orman et al. 2014). Because diffusion may depend on species concentration (Spandler and O'Neill 2010), the lower MgO content of our natural melt compared with the high MgO content of other surroundings (Faak et al. 2013; Van Orman et al. 2014) may have played a role in determining the diffusion mechanism and thereby diffusion coefficient of Mg in plagioclase.

5.4.2.3 Lattice structure

In previous studies, weak anisotropy of D_{Mg}^{plag} is observed. It is > 1 but < 3 times faster in the c direction than in the b direction for both anorthite (LaTourrette and Wasserburg 1998) and labradorite (Van Orman et al. 2014). A different study found no anisotropy of D_{Mg}^{plag} based on Mg concentration profiles in perpendicular directions within the same crystal; however, the crystallographic directions were not specified (Faak et al. 2013). Based on the ellipsoid data fit for model A, predicted D_{Mg}^{plag} in the c direction is the same as that in the b direction, within the misfit of the ellipsoid (1.0×10^{-16} m^2 s^{-1} versus 9.6×10^{-17} m^2 s^{-1}). At first glance, this result seems to agree with previous findings of little to no anisotropy of D_{Mg}^{plag}. However, anisotropy is clearly evident in our dataset. The key difference is that we report anisotropy that is not directed along crystal axes, and thus may have been present but unmeasured in studies which analyzed

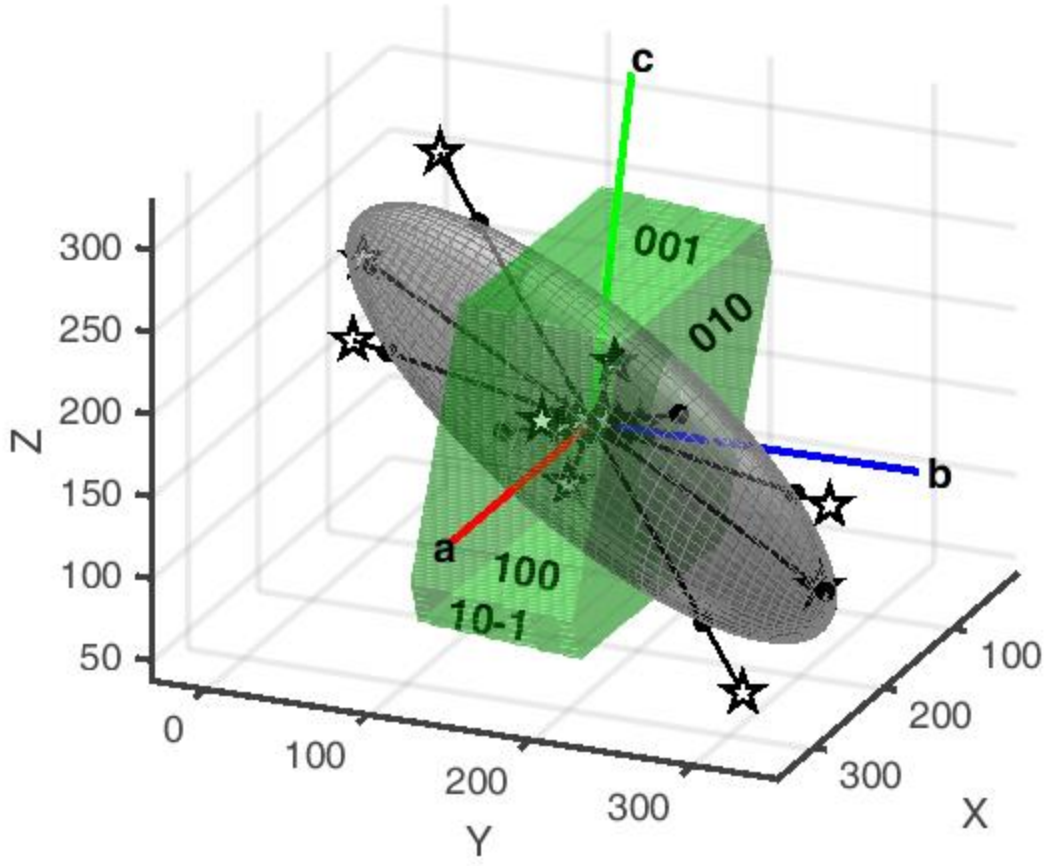

Figure 5.10. Ellipsoid fit to model A diffusivities for $D_{Mg}^{plag} > 1 \times 10^{-17}$ m^2 s^{-1}, with a simple model plagioclase crystal superimposed to show how the fast diffusion direction relates to common crystal faces. As in Figure 5.6, diffusivities were all scaled by 1×10^{17} in order to avoid roundoff errors during computation. Stars mark the end points of the data vectors that were fit by the ellipsoid. Solid black circles mark the points on the ellipsoid surface corresponding to each vector orientation. The difference between a star and the corresponding circle is the residual of the model-data fit.

concentration profiles solely along crystal axis directions. Anisotropy in D_{Mg}^{plag} that appears unrelated to crystal axis directions, reported here, is no more unexpected than would be isotropic diffusivity, given the triclinic structure of plagioclase. Indeed, the review of Zhang (2010) specifically notes that the principal axes of diffusion in a triclinic mineral will not necessarily be the same as the crystallographic axes, and this is what we observe.

The fast diffusion direction determined by our experiment corresponds approximately to the [-1 -3 1] crystal direction (Figure 5.10). This orientation is not related to plagioclase cleavage

directions or any common twin plane or exsolution orientation. However, the lattice structure of planes normal to [-1 -3 1] should be favorable to Mg transport between them. In olivine, divalent cations diffuse much faster parallel to the *c* axis, likely due to the chains of octahedral sites that parallel this axis (e.g., Ohashi and Finger 1974). It is not only vacancies on the metal sites, but also interstitial octahedral sites (i.e., those that are already unoccupied in the normal crystal structure), that may enhance diffusion along these chains (Spandler and O'Neill 2010). Lithium is also thought to diffuse via both vacancy and interstitial octahedral sites in olivine, along the same chains (Dohmen et al. 2010). In several accessory minerals (zircon, apatite, rutile, titanite), He may diffuse through the crystals via void space between lattice sites, and anisotropy in the cases of rutile and zircon is explained by larger void diameters in lattice planes perpendicular to the fast diffusion direction (Cherniak and Watson 2011). Because Mg is a divalent cation and thus likely to interact with the ionic crystal structure, its diffusion probably occurs via site vacancies and interstitial sites, rather than voids. However, the examples above reinforce the need to closely examine patterns in crystal structure for specific lattice orientations, in order to understand diffusional anisotropy.

5.4.3 Part III: Dissolution

At the water-saturated experimental conditions of 125 MPa and 900 °C, plagioclase in equilibrium with the starting glass has a composition of An_{96} (Figure 5.11). Because the plagioclase used in experiments was less calcic than the equilibrium plagioclase, by 30 mol% An, partial dissolution occurred (Tsuchiyama 1985). At temperatures ≤ 860 °C, the Lake County labradorite is more calcic than the plagioclase estimated to be in equilibrium with the experimental melt (Waters and Lange 2015). Thus, an experimental temperature ≤ 860 °C may have discouraged dissolution, but the trade-off would have been slower Mg diffusion, resulting in concentration profiles too short to be measured with the precision of the electron microprobe. A shorter experimental duration would result in the same problem. A more mafic glass composition would be in equilibrium with An_{66} plagioclase at the experimental temperature (Lange et al. 2009), but the liquid would be quite similar to the presumed melt from which the Lake County plagioclase crystals originally formed (Stewart et al. 1966), resulting in an Mg gradient in the crystal too small to be resolved accurately by EPMA. Clearly, studying diffusivity under natural conditions is not a straightforward challenge, but it is one that has the potential to yield a deeper understanding of diffusion, and by extension timescales, in volcanic systems.

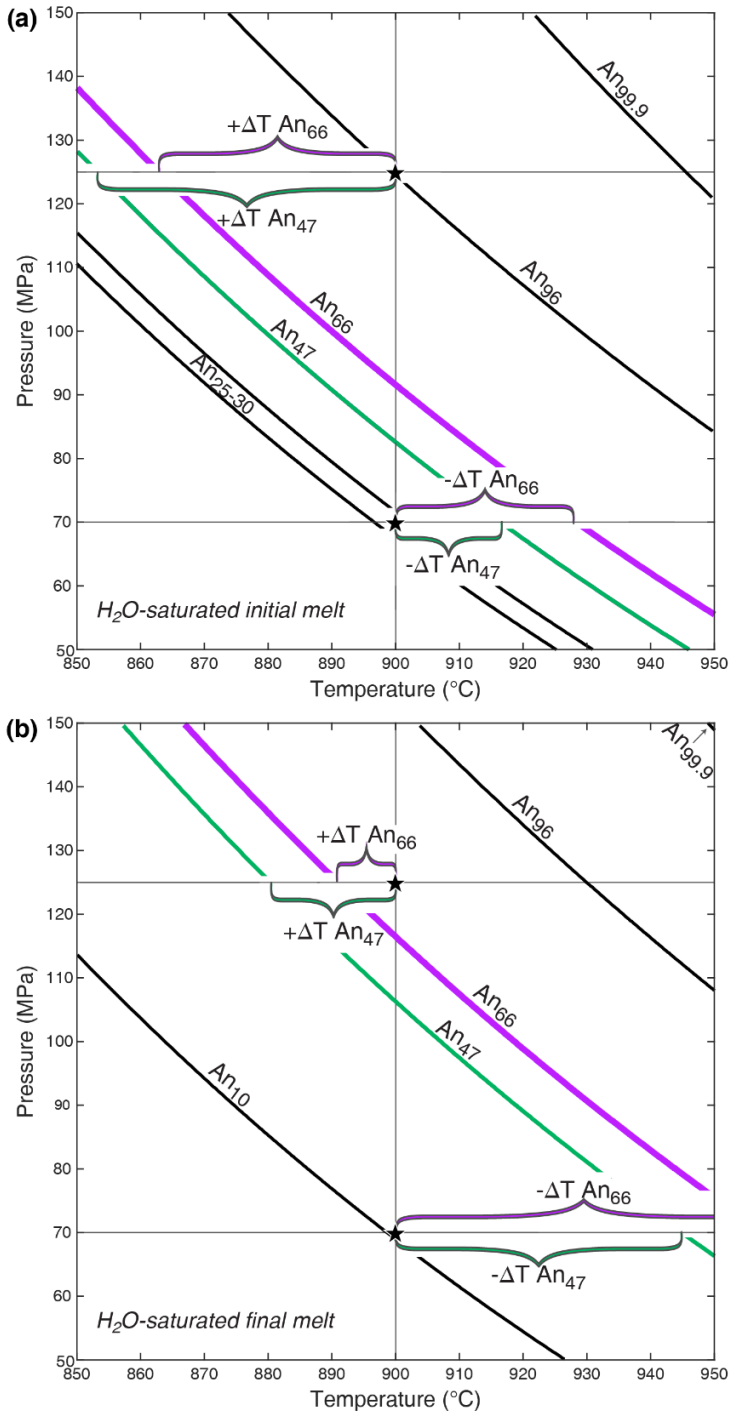

Figure 5.11. Equilibrium anorthite isopleths, calculated using the plagioclase-liquid hygrometer of Waters and Lange (2015) and the water solubility model of Zhang et al. (2007). Panel **(a)** shows equilibrium plagioclase compositions in contact with the starting melt composition **(b)** is as (a), but for the post-experimental melt composition. Relevant experimental conditions are marked by stars at 900 ºC and 125 MPa, along with the farthest extent of < 2-day decompression, at 70 MPa. Note the large decrease in superheating with respect to the An_{66} isopleth, between the start and end of the experiment. Also note that along the decompression path, the driving force for dissolution (+ΔT) turns to a driving force for crystallization (-ΔT), explaining the formation of An_{47} rims.

5.4.3.1 Low thermodynamic driving force

The lack of facets on most of our experimental crystals, and extensive rounding on some, are archetypal features of dissolution (e.g., Kuo and Kirkpatrick 1985; Tsuchiyama 1985). In addition, the post-experimental glass composition is well-reproduced by simulated dissolution of the input plagioclase. However, only ~5 wt% dissolution is predicted, consistent with the continued presence of crystals several hundreds of microns in diameter. Small (< 5 μm) An_{47} tabs that formed in the first week of the experiment are also preserved (Figure 5.9). Many of these tabs are rounded at corners, but retain distinct faces. Faces are also discernible on several labradorite crystals. Thus, while the evidence for dissolution is irrefutable, it is likely that the vast majority of crystal mass was preserved. Extrapolation of the Arrhenius relationship for GP4-Lab1 in Figure 9 of (Tsuchiyama 1985) predicts a dissolution distance of only 10 nm at 900 °C for rounded, unmantled labradorite in the system Ab-An-Di. Given that the extrapolation is large (350 °C) and the computed dissolution distance would be unresolvable in our study, we do not take this as a quantitative prediction. However, the comparison is supportive of generally slow dissolution at our experimental temperature. Changing melt composition (moving toward equilibrium with the dissolving plagioclase) would serve to decrease the driving force for dissolution even farther.

Additional evidence also points toward the driving force for labradorite dissolution in our study being small for the majority of the experimental time. In a slightly more viscous melt ($\log \eta = 4.72$ Pa s (Giordano et al. 2008) dissolving forsterite, Donaldson (1990) reports compositional gradients working to homogenize the melt 100-200 μm from the crystal-melt interface after 0.6 hours, and up to 400 μm into the melt after only three days. Given that the length scale of crystal-free melt in our experimental sample is typically < 1 mm, and that no compositional gradients are present, it is likely that equilibrium was approached during the first week of the experiment. The An_{47} tabs that grew shortly thereafter are well preserved, with dissolution suggested only by a subtle rounding of corners after 34 days at the experimental conditions. This failure to equilibrate with the surrounding melt is typical of plagioclase (Brugger and Hammer 2010) and supportive of a low driving force for dissolution in our experiment. We examine the thermodynamics in more detail below, making use of the plagioclase-liquid hygrometer (Waters and Lange 2015) to predict plagioclase compositions in equilibrium with the initial and final experimental melt.

In the initial melt at 900 °C and 125 MPa, the input An_{66} plagioclase is unstable relative to the predicted equilibrium plagioclase of An_{96}, experiencing an effective superheating ($+\Delta T$) of 36-37 °C (Figure 5.11a). The system could approach equilibrium by dissolution, reprecipitation, or diffusive exchange, but major element diffusive exchange is slow (e.g., Grove et al. 1984), so dissolution is likely to dominate. At 70 MPa and 900 °C, with the same initial melt composition, the equilibrium plagioclase is more albitic (An_{25-30}), so the system is undercooled ($-\Delta T$ = 17 °C with respect to the An_{47} tabs) and is expected to approach equilibrium by crystallization (Figure 5.11a). The same considerations apply to plagioclase in equilibrium with the final experimental melt composition, but the driving force for dissolution of at 125 MPa is greatly reduced ($+\Delta T$ = 8-9 °C with respect to An_{66}), and the driving force for crystallization at 70 MPa is enhanced ($-\Delta T$ = 45 °C with respect to An_{47}) (Figure 5.11b). Thus, by the time the experiment was quenched, the melt had come very close to or achieved equilibrium with the An_{66} labradorite, and the short decompression between 125 MPa and 70 MPa (see Methods) included conditions at which An_{47} is a stable plagioclase composition. Given the above argument that equilibrium was approached in roughly a week, it is likely that the final melt composition is that from which the An_{47} tabs formed. But note that any melt composition intermediate between initial and final would provide the required impetus for crystallization (Figure 5.11). Subsequently, the final melt provides a much lower driving force than did the initial melt, for dissolution of An_{66} and An_{47} at 125 MPa.

At near-equilibrium conditions, like those attained after ~one week in our experiment, crystal dissolution is likely to be limited by interface kinetics, rather than the diffusion rate of components in the surrounding melt. This situation is the “Regime II” dissolution described by Liang (2000). Because the labradorite in our experiment did equilibrate (or nearly so) with the melt, Regime II dissolution was likely at work during most of the experiment. However, at the very beginning, when the driving force was greatest (Figure 5.11), dissolution was probably faster, and limited by the diffusivity of plagioclase components in the initial melt. This diffusive dissolution is thought to prevail at high temperatures in silicate melt systems that are out of equilibrium (Liang 1999), and corresponds to “Regime I” of Liang (2000). A useful estimate is that Regime I controls dissolution when the rate of diffusion of a component in the melt is more than four to six orders of magnitude greater than the rate of diffusion of that component in the solid (Liang 2000). Based on experiments in granitoid melts, dry diffusivity of Mg in the melt is 1.0×10^{-16} m^2 s^{-1}, but adding 3.6 wt% H_2O increases that to 1.0×10^{-12} m^2 s^{-1} (Mungall et al.

1999; Zhang et al. 2010). Mungall et al. show that this four-orders-of-magnitude increase in diffusivity corresponds to an equivalent decrease in viscosity (i.e., log η = 8.93 Pa s to log η = 4.93 Pa s; (Giordano et al. 2008). Applying the relationship to Mg diffusivity in our experimental melt (log η = 4.12-4.51 Pa s; (Giordano et al. 2008) yields D_{Mg}^{melt} of 3.8-7.3 x 10^{-12} m^2 s^{-1}. This is approximately four orders of magnitude faster than the highest modeled D_{Mg}^{plag} from our study, and six to seven orders of magnitude faster than the lowest D_{Mg}^{plag}. Thus, Regime II (interface controlled) dissolution is predicted based on the difference of Mg diffusivity in the melt and crystal, in agreement with the thermodynamic considerations above. The importance of the plagioclase-melt interface geometry is reinforced by considering the effects of surface energy.

5.4.3.2 Dependence on surface energy

As the crystal input to our experiment consisted of mostly irregular fragments, the surfaces present at the start of the experiment would have had a wide variety of surface energies. The activation energy for crystal nucleation has a positive dependence on surface energy (σ), as summarized by equation (5) of Dowty (1980)

$$\Delta G_a = \frac{16\pi\sigma^3 V_m^2}{3\Delta G_c^2} \qquad \text{eq 5.6}$$

where ΔG_a is activation energy, V_m is molar volume, and ΔG_c is the bulk free energy change per mole, upon crystallization. A similar relationship applies to surface nucleation during crystal growth. If we view dissolution as essentially the opposite of nucleation and growth (e.g., Kuo and Kirkpatrick 1985), then the activation energy for dissolution should decrease as σ increases. The most irregular and un-facet-like surfaces would have had the highest fraction of unsatisfied bonds, and thus the highest surface energies. Therefore, it is these surfaces that would have been most susceptible to dissolution. Surfaces with facets or low-amplitude roughness would have had substantially lower σ, and thus been less susceptible to dissolution.

During the initial stages of the experiment, where Regime I dissolution was likely, high-energy surfaces underwent dissolution, progressively reducing σ. By the time irregularities had been removed or their amplitudes greatly lessened, dissolution had modified the surrounding melt composition to the point of near-equilibrium with labradorite (Figure 5.11), and Regime II dissolution took over. Dissolution would have slowed by this juncture, because dissolution rate is thought to decrease with increasing thermodynamic stability of the phase (Edwards and Russell

1996). For surfaces that were low-energy to begin with, or reached a low-energy state during Regime I dissolution, little additional dissolution would have taken place during the more prolonged period of Regime II dissolution. The faces of the An_{47} growth tabs are a good example of surfaces with low σ that largely retained their substance. For surfaces that began in a very high-energy state and were unable to reach a sufficiently low-energy state by the end of Regime I dissolution, additional dissolution would have continued for the duration of Regime II, although still at a relatively slow rate. The top right edge of crystal h3.2 (Figure 5.7) is an example of the type of surface that represents a higher energy state. Overall, because the thermodynamic driving force for dissolution was low, the σ of exposed surfaces became the dominant factor in determining which crystals (or parts thereof) were preserved and which were further resorbed into the melt.

We interpret the Mg diffusivities that are < ~1 x 10^{-17} m^2 s^{-1} to reflect relatively large dissolution distances of crystal surfaces with initially high σ. The occurrence of these small D_{Mg}^{plag} values across all crystallographic orientations (Figure 5.12) supports this interpretation; given the random nature of the input plagioclase shapes, an orientation control on surface energy is not expected, and indeed not observed. Interestingly, some anisotropy is preserved in these low-D_{Mg}^{plag} profiles, with the faster D_{Mg}^{plag} values falling in a similar orientation to those in the ellipsoid of D_{Mg}^{plag} > 1 x 10^{-17} m^2 s^{-1} (Figure 5.12). Given a similar enhancement of dissolution due to exposed high-energy surfaces, a profile oriented in the faster diffusion direction would still record faster diffusion than a profile oriented in the slower diffusion direction – but the magnitude of D_{Mg}^{plag} would be smaller than the true magnitude. Additional work is required to refine the cutoff D_{Mg}^{plag} between profiles that are acceptable and those that are too resorbed, but the similar anisotropy in both sets based on a cutoff of 1 x 10^{-17} m^2 s^{-1} indicates that the value is reasonable.

The Mg concentration profiles that reflect higher diffusivity values (i.e., D_{Mg}^{plag} > ~1 x 10^{-17} m^2 s^{-1}) are interpreted as products of crystal surfaces with initially low σ. The low driving force for dissolution of these more energetically favorable surfaces led to little dissolution compared to that experienced by the higher σ surfaces. Therefore, more complete Mg concentration profiles were preserved. There is no anticipated orientation dependence of the low σ initial surfaces, just

as for the high σ initial surfaces. Thus, the anisotropy of D_{Mg}^{plag} evident across the higher-diffusivity profiles likely reflects some intrinsic characteristic of the labradorite crystal lattice, rather than anisotropy of dissolution.

The hypothesis of Regime II dissolution and σ control of Mg profile preservation is based on sound theory, but cannot be explicitly tested with the data available. We lack the direct knowledge of input crystal shape and the evolution of dissolution rate with time for each crystal that would be required to evaluate the hypothesis rigorously. However, as a working hypothesis it explains the morphology of labradorite and low-An growth tabs, the wide range of modeled Mg diffusivities, the lack of compositional boundary layers in the glass, and it agrees with thermodynamic predictions (Figure 5.11).

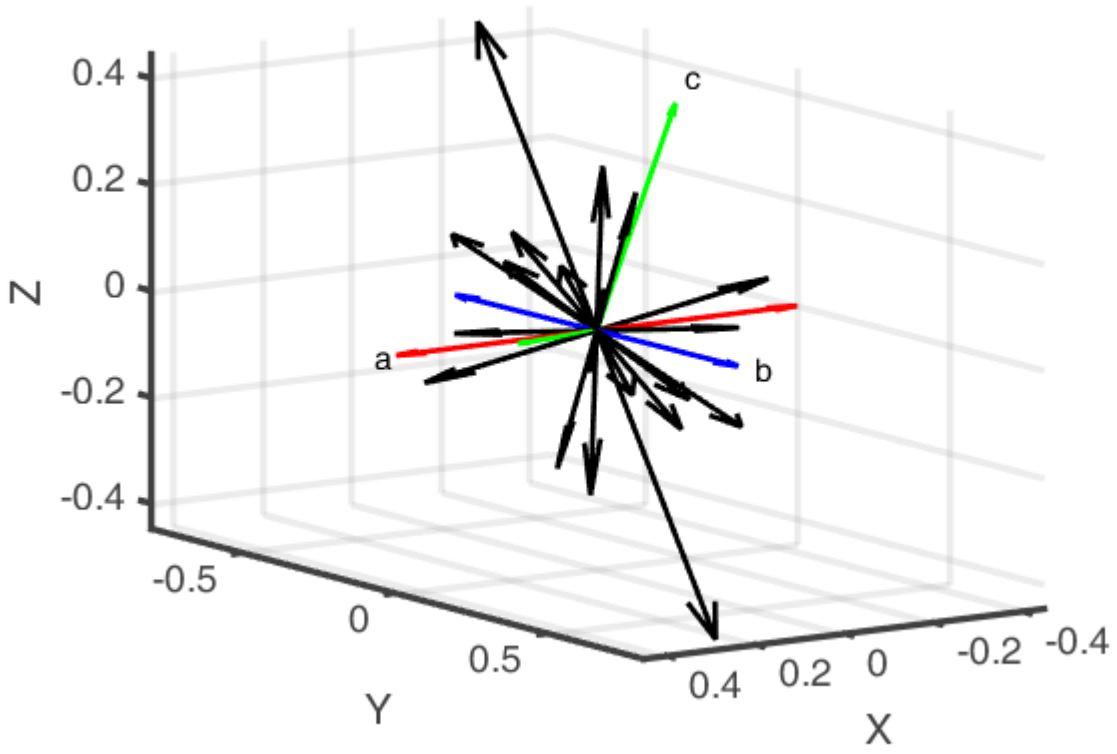

Figure 5.12. Orientation of all model A diffusivity vectors representing $D_{Mg}^{plag} < 1 \times 10^{-17}$ m^2 s^{-1}. As in Figures 5.7 and 5.11, diffusivity vales were scaled by 1×10^{17}. Note that the anisotropy shown in Figure 5.10 is present in approximately the same orientation here. See text for analysis.

5.4.3.3 The means to fast-path diffusion?

While maintaining that D_{Mg}^{plag} anisotropy is related to the inherent crystal lattice, we explore the possibility that dissolution enhanced this anisotropy, and/or is responsible for the large magnitude of D_{Mg}^{plag}. Growth and dissolution are both processes known to alter the crystal lattice via strain and defect formation. Recent evidence suggests that dissolution, more than growth, can result in enhanced strain not only on the surface undergoing dissolution, but within the larger volume of the crystal. A seminal study of calcite growth and dissolution reveals that during crystal growth, surface effects are minimally important in the larger volume of the crystal (Clark et al. 2015). However, during dissolution, an increase in overall strain in the entire crystal is created due to surface defects (e.g., etch pits) that are a direct result of dissolution (Clark et al. 2015). Strain is known to enhance disordering in feldspar (Kramer and Seifert 1991) and is associated with higher mobile dislocation densities, which enhance pipe diffusion, that is, diffusion of atoms through the cores of crystal dislocations (e.g., Kramer and Seifert 1991; Love 1964; Yund et al. 1981). Thus, if dissolution enhances dislocation formation throughout a crystal, this could explain why there is a growing body of evidence for increased cation diffusivity in dissolving crystals (Mg in plagioclase: this study; Fe-Mg in olivine: Tom Shea unpublished data and Chakraborty et al. 2016). If the effects of dissolution extend beyond the macroscopic surface that is dissolving, creating greater strain throughout the volume of the crystal, defect structures within that volume become more prevalent, forming faster pathways for cation diffusion. Of particular importance is that this process does not appear to be as prevalent during crystal growth (Clark et al. 2015), allowing for a crucial difference between what are, for many other purposes, equal-and-opposite phenomena (e.g., Dove and Han 2007).

Although Mg is not known to diffuse by pipe diffusion, no studies have examined concurrent dissolution, so no possibility can be ruled out. Alternatively, it is reasonable that dissolution could enhance the formation of other types of defects, like simple site vacancies. The site preference for Mg (tetrahedral T versus metal M) remains unclear, with partitioning data favoring M-site only in some cases (Sun et al. 2017) and a T-site preference in others (Faak et al. 2013). However, Faak et al. (2013) allow for the possibility that Mg might occur on either site, and advocate for a vacancy-based diffusion mechanism for Mg, tied to excess Si^{4+} in the crystal. Incorporation of non-stoichiometric silica into plagioclase was demonstrated explicitly by

Longhi and Hays (1979), and theoretically results in vacancies on both the M sites and aluminum T sites (Faak et al. 2013). Increased silica content (and associated vacancies) is not sufficient to explain the An-content dependence of D_{Mg}^{plag}, according to Van Orman et al. (2014), but their conclusion does not preclude the mechanism in general.

If dissolution can enhance vacancy formation, or the movement of vacancies through the plagioclase crystal lattice, then it is plausible that Mg diffusion could be enhanced in the presence of dissolution. Mg diffusion would also be enhanced if Mg can diffuse via pipe diffusion. Assuming some degree of initial site ordering for Mg, a simple uptick in disorder with dissolution, allowing Mg to occupy either M or T sites with less preference, would also serve to increase D_{Mg}^{plag}. Order-limited diffusion is invoked by Spander and O'Neill (2010) to explain the slower diffusion of some elements in olivine that occupy multiple sites with a relatively high degree of ordering (e.g., Al, Ca, Ni). Based on the evidence that dissolution can increase disorder and possibly create higher defect densities, we put forth that dissolution of labradorite is one reasonable explanation for the high D_{Mg}^{plag} values determined in our study. On the other hand, except in the case of pipe diffusion, dissolution would not likely be the cause of diffusional anisotropy, because experiments on plagioclase show that dissolution is isotropic (Tsuchiyama 1985; Yu et al. 2016).

Because pipe diffusion does not directly involve lattice site occupancy/vacancy, and the dislocations involved may not exist without dissolution, preferred pathways for dislocation formation might express themselves only during dissolution. For diffusion controlled by other mechanisms, dissolution and associated rapid diffusion may serve to exaggerate lattice anisotropy already present. For example, the enhancement of vacancy formation may not be a linear process, but may itself depend on vacancy concentration. Thus, if more vacancies align in one orientation than another, diffusion along the orientation with greater vacancy density would be even more enhanced during crystal dissolution, resulting in a larger ΔD_{Mg}^{plag} between different crystal orientations.

5.5 CONCLUSIONS

Despite the difficulties in choosing an appropriate melt and addressing problems of crystal growth and/or dissolution, it is necessary to examine systems that are close imitations of nature to ascertain diffusion coefficients relevant to magmatic plumbing systems. Our

experimental setup was the closest to a natural magmatic environment of any Mg-in-plagioclase studies to date, including a water-saturated natural melt, intermediate plagioclase composition, and magmatic temperature, pressure, and fO_2. We acknowledge that starting with crystal fragments is less analogous to many natural systems, but the effect of differential surface energy is interpreted to affect dissolution distance rather than diffusivity itself. Thus, the fast diffusivities derived herein should be applicable to natural systems, and recharge-to-eruption timescales at Santorini (Druitt et al., 2012), Quizapu (Ruprecht and Cooper, 2012), Novarupta (Singer et al., 2016), and other volcanoes may need to be reconsidered.

For a full expression of D_{Mg}^{plag} to be written and applied to volcanic systems, experiments using different plagioclase and melt compositions, temperatures, water contents, and fO_2 are sorely needed. The effect of dissolution on diffusivity is also a topic deserving of much more study, both experimental and theoretical. We cannot draw unqualified conclusions with regard to the current study, but the occurrence of partially resorbed crystals with the highest D_{Mg}^{plag} values yet reported suggests the intriguing possibility that in this case, correlation does equal causation. The anisotropy and/or rapid diffusivity of Mg in labradorite may also be linked to the hydrous nature of our experiment. Whatever the ultimate cause of high D_{Mg}^{plag}, it is clear that diffusion of Mg in labradorite can take place at rates 100+ times faster than previously thought. We have also demonstrated that D_{Mg}^{plag}can be anisotropic. These key conclusions reinforce the need for additional studies using natural melts at hydrous conditions, to isolate the effects of melt composition and water content. Paired experiments that compare diffusion rates during dissolution and growth are also needed, along with nano-scale investigations (e.g., TEM) of crystal defect structures.

Chapter 6. Conclusions

6.1 IMPACTS

In Chapter 2 (*Igneous cooling history of olivine-phyric shergottite Yamato 980459 constrained by dynamic crystallization experiments*), a volcanological context is provided for a meteorite that, until now, has been studied chiefly to gain insight regarding the state of the martian mantle (e.g., Filiberto and Dasgupta 2011; Musselwhite et al. 2006). For meteorites, which have no associated geological context, establishing precise cooling rates for various stages of their igneous history is one of the only ways to gain insight into the history of plutonic or volcanic processes. In addition, the establishment of specific eruption scenarios has the potential to aid in the continuing search for the shergottite source region on Mars. Despite decades of effort, point(s) of ejection from the martian surface have yet to be unequivocally established (e.g., McSween 1985; Ody et al. 2015; Werner et al. 2014). Now knowing that Y-980459 is likely to come from an area characterized by pāhoehoe-type flows, its source region (and that of the near-identical meteorite NWA 5789) can be limited to terrains matching this description. Combining studies like this one with studies dedicated to establishing source regions for the martian meteorites will provide the best idea yet of local geological settings in areas that may eventually be destined for human exploration.

The phase-equilibrium experiments in Chapter 3 (*Experimental constraints on dacite magma storage beneath Volcán Quizapu, Chile*) represent the first experimental petrology study on Quizapu. In the absence of geophysical or melt inclusion data, this work is the best estimate of magma chamber conditions prior to each of its two contrasting eruptions. Should future unrest occur, seismic or geodetic data can be compared to this determination of magma chamber depth, to assess whether the reservoir implicated in the two previous eruptions is the source of unrest, or if the source is rather a less immediately hazardous influx of magma to deeper crustal storage regions. The study also underscores that, for Quizapu and many other predominantly dacite volcanoes, pre-eruptive storage conditions are not good indicators of eruption style. However, the work here is valuable in that it provides more accurate temperature information for use in heating calculations, and provides the key parameters (other than composition) necessary to calculate initial magma viscosity, a key starting point for further modeling of ascent processes and their effects on eruptive style. In addition, the experimental suite and general observations of

the Quizapu system lead to the conclusion that any heating prior to the effusive eruption was extremely heterogeneous, leaving sections of the magma largely unaffected. Although the involvement of mafic magma may be a key component driving effusive silicic eruptions at some volcanoes (Watts et al. 1999 and references therein), alternative hypotheses should be considered for Quizapu. One possibility is that in 1846-7, an eruptive fissure, rather than a point source vent, allowed large volumetric discharge at low ascent rates, while also promoting outgassing via a greater area of melt-wall rock contact. Indeed, this "top-down" conduit geometry control is beginning to be recognized for its potential as a globally significant mechanism for producing effusive silicic eruptions (e.g., Loewen et al. 2017).

Chapter 4 (*Re-equilibration of Fe-Ti oxides: Textural and compositional effects of a single-step reduction*), presents the first detailed textural and compositional analysis of hemoilmenite as it responds to a reduction in fO_2 (in this instance, by ~2 log units). This information is valuable for assessing the history of natural hemoilmenite crystals in magmas that may have undergone reduction, for example due to influx of hotter, more primitive melt. Three higher- fO_2 experiments demonstrate that Fe-Ti oxide textures are sensitive to even a small or transient change in fO_2, making detailed studies of their textural re-equilibration paths all the more important to pursue. A final point of the study is that after 7-14 days at experimentally-imposed conditions, all Fe-Ti oxide crystals from the starting material display highly disequilibrium textures and compositions. These "fast-equilibrating" minerals therefore may not reflect rapidly-changing magmatic conditions as faithfully as often supposed. Compositional changes do occur rapidly, but those changes do not necessarily reflect a new equilibrium state. Continued use of the Fe-Ti oxide oxybarometer will require thorough assurance that the phases used are truly in equilibrium with each other and with the host magma. Given that Mg and Mn appear to diffuse quickly in Fe-Ti oxides (Chapter 3 Discussion), the oft-applied Bacon and Hirschmann (1988) test for equilibrium may not be sufficient. We suggest turning to major-element components and checking for equilibrium based on the intersecting compositional isopleths determined in temperature- fO_2 space by Buddington and Lindsley (1964). Thermodynamic calculation schemes like rhyolite MELTS (Gualda et al. 2012) can provide additional estimates of equilibrium oxide compositions.

The implications of Chapter 5 (*Mg diffusivity in labradorite at hydrous magmatic conditions*) are far-reaching. Mg diffusion in plagioclase has already been used to estimate

magma mixing timescales at volcanoes worldwide, from mid-ocean ridges (e.g., Moore et al. 2014) to caldera complexes (Druitt et al. 2012) to stratovolcanoes (e.g., Sato et al. 2017; Singer et al. 2016), but this work shows that the values of D_{Mg}^{plag} used may have been too low by more than two orders of magnitude. A discrepancy of this amount in D_{Mg}^{plag} would result in timescale estimates that are equally too slow (i.e., more than 100 times slower than their true value), potentially leading to inappropriate hazard assessments. Given that the direction of highest diffusivity in labradorite is not perpendicular to crystal faces or parallel to crystal axes (i.e., the directions frequently measured), it is possible that most measurements in natural samples were made in crystallographic directions in which Mg diffusivity is lower, and closer to previously published values. However, EBSD measurements on the natural samples in question are required to confirm transect orientation and subsequently re-calculate timescales based on new diffusivity data as more work is published. The anisotropy of D_{Mg}^{plag} discovered by the present study also makes a strong argument for analyzing diffusion experiments in a suite of random orientations, rather than just crystallographic axis orientations. Evidently, natural magmatic conditions, imposed in the laboratory, can enhance Mg diffusion in labradorite by mechanisms not yet well understood. These unique results also serve to reinforce the questions that linger regarding Mg diffusivity in plagioclase – does anorthite content affect D_{Mg}^{plag} ? Do natural samples also reflect the anisotropy observed in the experiment presented here?

6.2 FUTURE DIRECTIONS

6.2.1 Toward a deeper understanding of the Y-980459 flow and potential source regions

The excellent match of cooling experiments and the Y-980459 meteorite, both in texture and composition, is more than satisfactory for procuring cooling rate estimates. However, the minutiae of the groundmass olivine and pyroxene populations provide opportunities for additional study. Textural comparison of experimental and natural olivine dendrite populations would be instructive, yielding an additional line of evidence for the Stage 2 cooling rate. The analysis would be difficult, however, given the relative scarcity of the dendrites in experimental samples. This very scarcity inspires another potential study, aimed at further examination of the reasons for the higher glass content of experimental samples relative to the meteorite. Experiments with a t-T path identical to that of the best match established in Chapter 2 could be repeated, but with varying degrees of agitation of the sample during Stage 2 cooling (e.g., Vona

and Romano 2013). Given that physical flow is cited as a potential cause of higher nucleation density in the meteorite, these experiments could confirm or refute this hypothesis, as well as provide material for detailed study of groundmass textures for comparison to that in Chapter 2. The strain rate induced in the proposed experiments could be used to estimate flow velocity in the pāhoehoe breakout that was the likely quenching stage of Y-980459.

On a broader scale, a comprehensive examination of the highest-resolution (~0.5 m) HiRISE imagery of Mars could be undertaken in an attempt to identify potential source regions for Y-980459 and other shergottite meteorites, based on the prevalence of topographical features indicative of low-effusion-rate lavas (e.g., Keszthelyi et al. 2008). A study of this nature would be bolstered by a multidisciplinary approach aimed at linking imagery with spectral and cratering data for identified areas of interest.

6.2.2 Furthering the experimental approach at Volcán Quizapu

The phase equilibrium experiments presented here provide the ideal baseline for further experimental petrology work, this time dedicated to assessing the hypothesis of heating prior to the 1846-7 effusive eruption (e.g., Ruprecht and Bachmann 2010). The study highlights inconsistencies in the hypothesis and underscores that any heating that did occur was localized and extremely heterogeneous. A small suite of experiments aimed at heating the end-member dacite material by 130 °C for various durations could address several important questions: What is the maximum duration of heating (by 130 °C) that allows preservation of euhedral amphibole phenocrysts? Conversely, given the heating timescale estimated by Ruprecht and Cooper (2012), what is the maximum temperature at which euhedral amphibole phenocrysts are preserved? Does orthopyroxene develop reverse zoning upon heating? Do Fe-Ti oxide crystals re-equilibrate without evidence of textural disequilibrium (as they apparently do in the Quizapu lavas)? Why do the natural magnetite crystals not preserve high-Ti rims, a feature noted in other systems that are interpreted to have undergone pre-eruptive heating (e.g., Mount Unzen, Soufrière Hills)?

A second experimental suite of decompression experiments, similar to that of Rutherford and Hill (1993), could be used to estimate ascent rates for the 1846-7 and 1932 eruptions. This work would dovetail well with field work aimed at uncovering evidence for the 1846-7 eruptive vent, which may have been a fissure. Using ascent rates from experiments and field observations of vent geometry, conduit models could corroborate or refute the hypothesis that conduit geometry, rather than reheating, was the more dominant control on eruptive style at Quizapu.

6.2.3 In pursuit of accurate temperatures and timescales

The studies in Chapters 4 and 5 demonstrate that our understanding of the characteristics of relatively short-lived magmatic events (e.g., temperature and duration of transient recharge or pre-eruptive heating) is greatly hampered by a lack of experimental data. At present there are only a handful of experimental studies with any appreciable detail regarding Fe-Ti oxide textures and compositions as they equilibrate at new magmatic conditions. Diffusivities of important minor elements in Fe-Ti oxides (e.g., Mn, Mg, both used to assess equilibrium) remain insufficiently constrained, and experiments on Mg diffusivity in plagioclase are limited and contradictory. There is a wide enough knowledge gap here to fill tens of experimental studies.

Key questions that should guide future research include: In Fe-Ti oxides, what are the textural manifestations of imposed disequilibrium conditions, followed by relaxation to equilibrium? Are re-equilibration mechanisms dependent on the cause and direction of perturbation (i.e., heating versus cooling, versus a change in fO_2)? Are Mg and Mn the most appropriate elements for determining overall equilibrium of coexisting Fe-Ti oxide minerals (i.e., are their diffusivities comparable to those of major elements, or too fast/slow)? How do melt composition, temperature, pressure, fO_2, and volatile content affect the rate and mechanism(s) of Fe-Ti oxide re-equilibration? How do those same variables affect diffusivities of trace species in plagioclase? Is Mg diffusivity in plagioclase dependent on anorthite content? Can the fast diffusivities measured in the study herein be reproduced in the absence of crystal dissolution? Why is Mg diffusivity anisotropic, and what features of the lattice (or its deformation) cause the rapid diffusivity observed? This last question would benefit from an atomic-scale examination of experimental crystal structures, perhaps via TEM. In addition, we stress that plagioclase crystals other than the NMNH standards used in this study should be used in at least some future experiments, to confirm that any anorthite (in)dependence of diffusivity is not unique to this sample set (which was also used by Van Orman et al. (2014) to determine D_{Mg}^{plag}). Extending beyond the specific systems studied here, it may be necessary to re-examine diffusion coefficients not only for other species in plagioclase (e.g., Sr, Fe) and Fe-Ti oxides (e.g., Mg, Al), but for many other systems (e.g., Ti in quartz, Li in olivine) for which current determinations are based on idealized experiments.

6.2.4 Advancing the utility of experimental petrology

Overall, this dissertation highlights the use of micro-scale compositional and textural features to glean information about macro-scale magmatic and volcanic processes. These chapters demonstrate that the accuracy of the micro-macro link rests on the availability and applicability of experimental data, which are used to calibrate thermobarometers, link textures to cooling rates, and establish rate constants for diffusion. To understand any volcanic system fully, it is critical to perform petrological experiments, and that the resulting experimental suite(s) must (1) cover compositional space that includes the system of interest, (2) explore a variety of t-T-P-fO_2 combinations, and (3) occur at conditions relevant to natural settings. Those three criteria may be met separately or all at once, depending on the type of experiment. Advancing the field of experimental petrology necessitates finding a way to marry the clear-cut results of simple-system experiments, which easily isolate individual variables, with the complex findings from experiments on natural systems, which involve multiple variables at once. In turn, this deeper understanding of complex experimental data, when combined with field observations and petrography of natural samples, can shed light on magmatic and volcanic processes that are otherwise inscrutable.

Appendix A

INTRODUCTION

This Appendix contains all of the material made available as the "electronic Supplement" for the published version of Chapter 2. A brief description of each item is below:

Supplement. Additional information about Raman analyses, a description of the method used to determine sample size (n) for S_v^P statistics, and Figures S1-S20.

Table S1. Complete run table of all experiments mentioned in the paper.

Table S2. Microprobe glass analyses, including standards.

Table S3. Microprobe olivine analyses, including standards.

Table S4. Microprobe pyroxene analyses, including standards.

Table S5. Complete surface area per unit volume data.

Table S6. Inputs to the conductive cooling model.

SUPPLEMENT

Supporting material for "Igneous cooling history of olivine-phyric shergottite Yamato 980459 constrained by *dynamic* crystallization experiments" by First and Hammer

Raman

We performed Raman spectroscopy as a check on our visual characterization of the SiO_2 phase present in Y98*-f69 (bead ii). Using the WITec alphaR 300 Raman microscope run by the Hawaii Institute of Geophysics and Planetology (HIGP) at UH Mānoa, a 532 nm laser with a grating of 1800 gratings/mm was set up. Data was gathered on a thin section of the bead for 30 second intervals, with 5 accumulations per point. Optical magnification was 20x. Based on reference spectra taken on quartz, cristobalite, and tridymite with a 532 nm laser, the mineral phase in our experiment is, indeed, cristobalite.

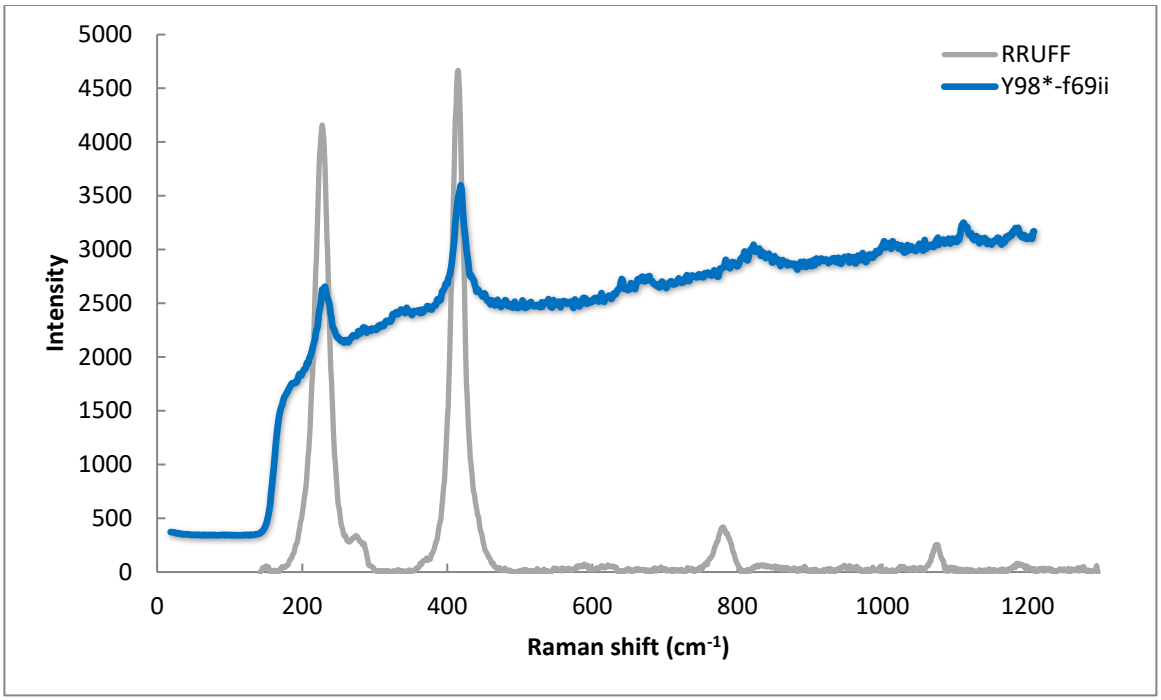

[blue]: cristobalite in Y98*-f69 (bead ii), corrected for offset in the Si peak measured at the beginning of the session [grey]: processed cristobalite spectrum R061107 from RRUFF database (intensity divided by 5)

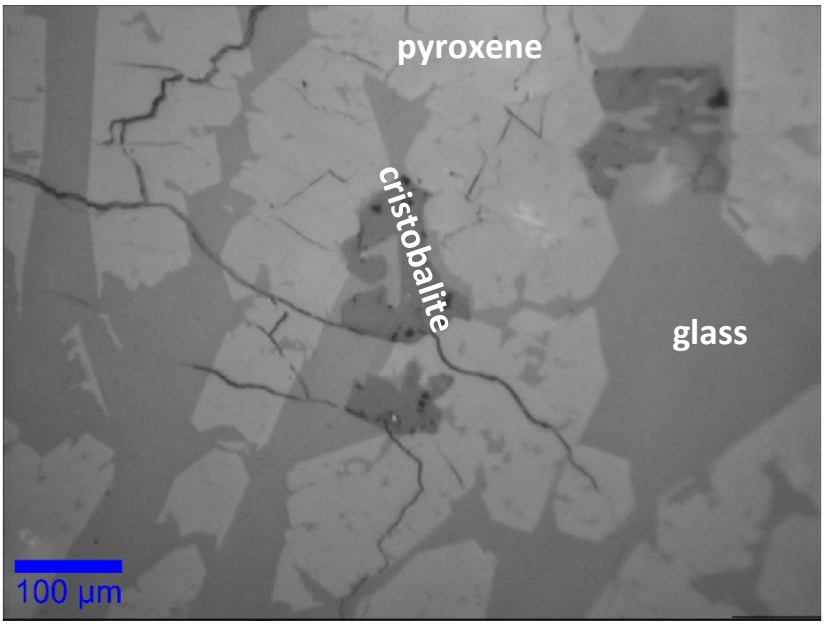

Reflected light image of cristobalite grain used to obtain spectrum shown above (labelled grain).

Test line sample size

To determine a sample size for each circular test line used in surface area per unit volume analyses, we considered the resolution of each image and the length of each test line. For every image, we measured the size of the smallest resolvable gap (e.g. between two crystal protrusions). To be conservative, we multiplied this length by two and considered this to be the "standard" length value for the image. The n value for each test line was calculated by dividing the total length by this image-specific standard value. Then, by using this n value, we were able to calculate statistics that require a sample size.

Supplementary figures

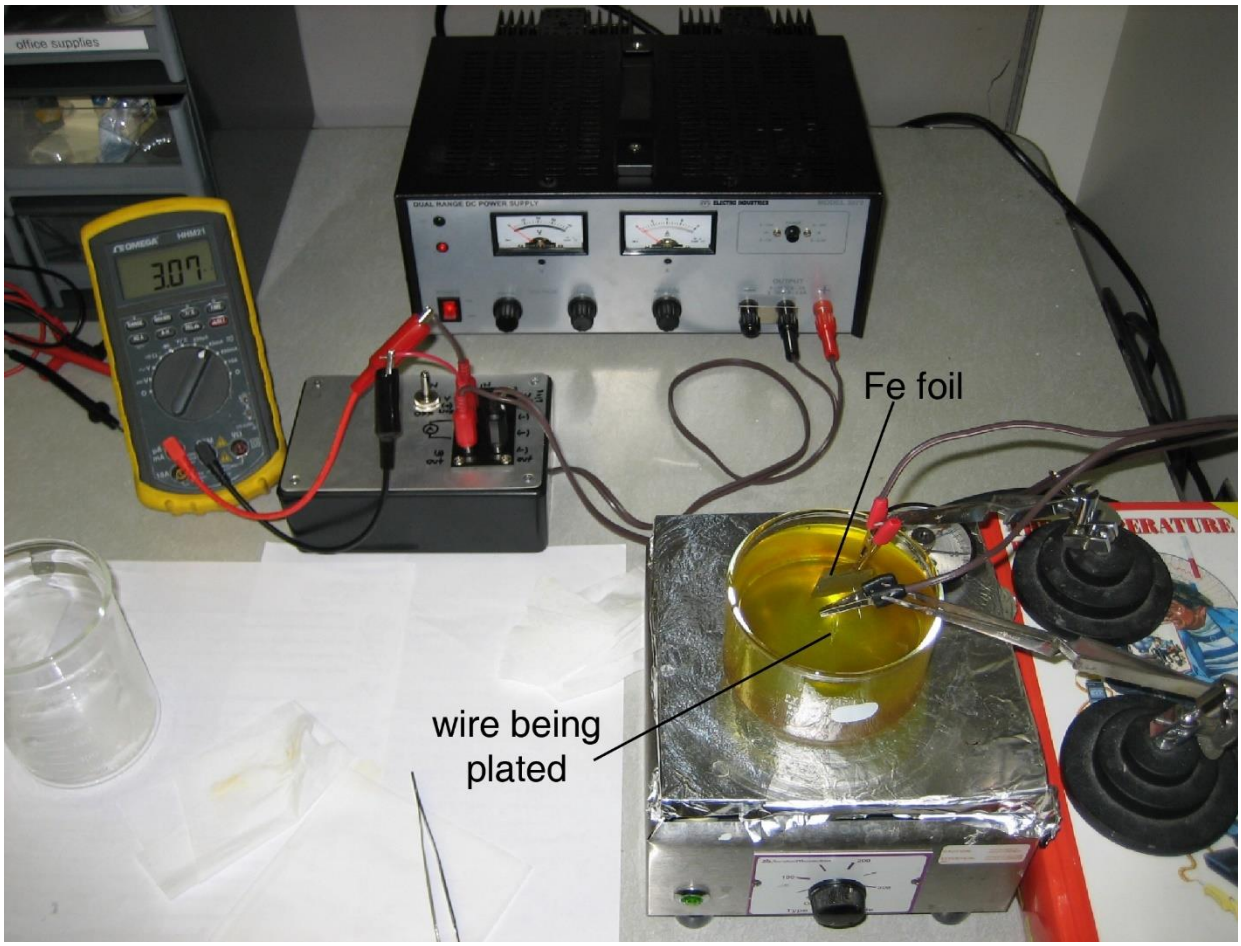

Figure S1. Electroplating configuration. Current reading in the image shown (3.07 mA) is lower than the optimum values determined through trial and error (45-50 mA).

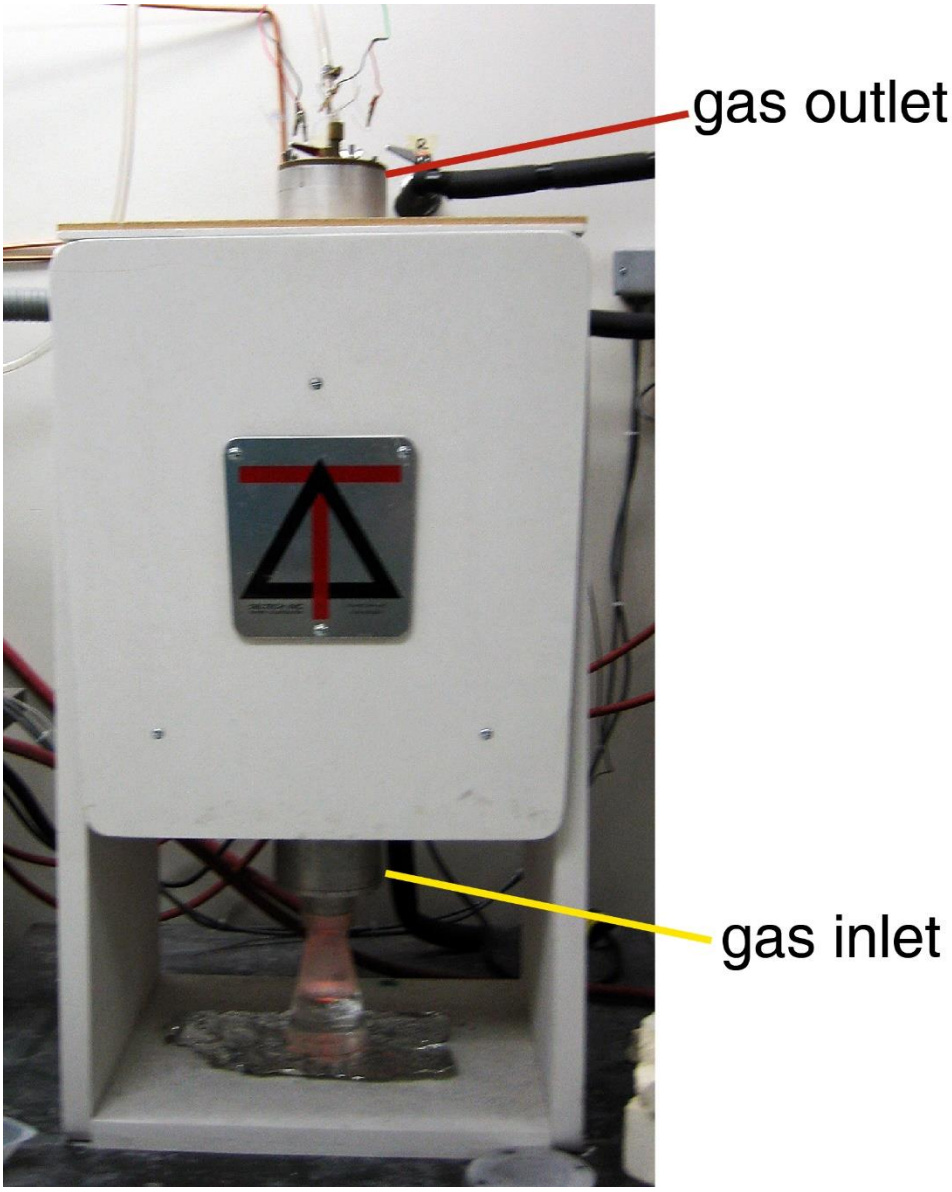

Figure S2. DelTech 1-atm gas mixing furnace at the University of Hawaii, Mānoa.

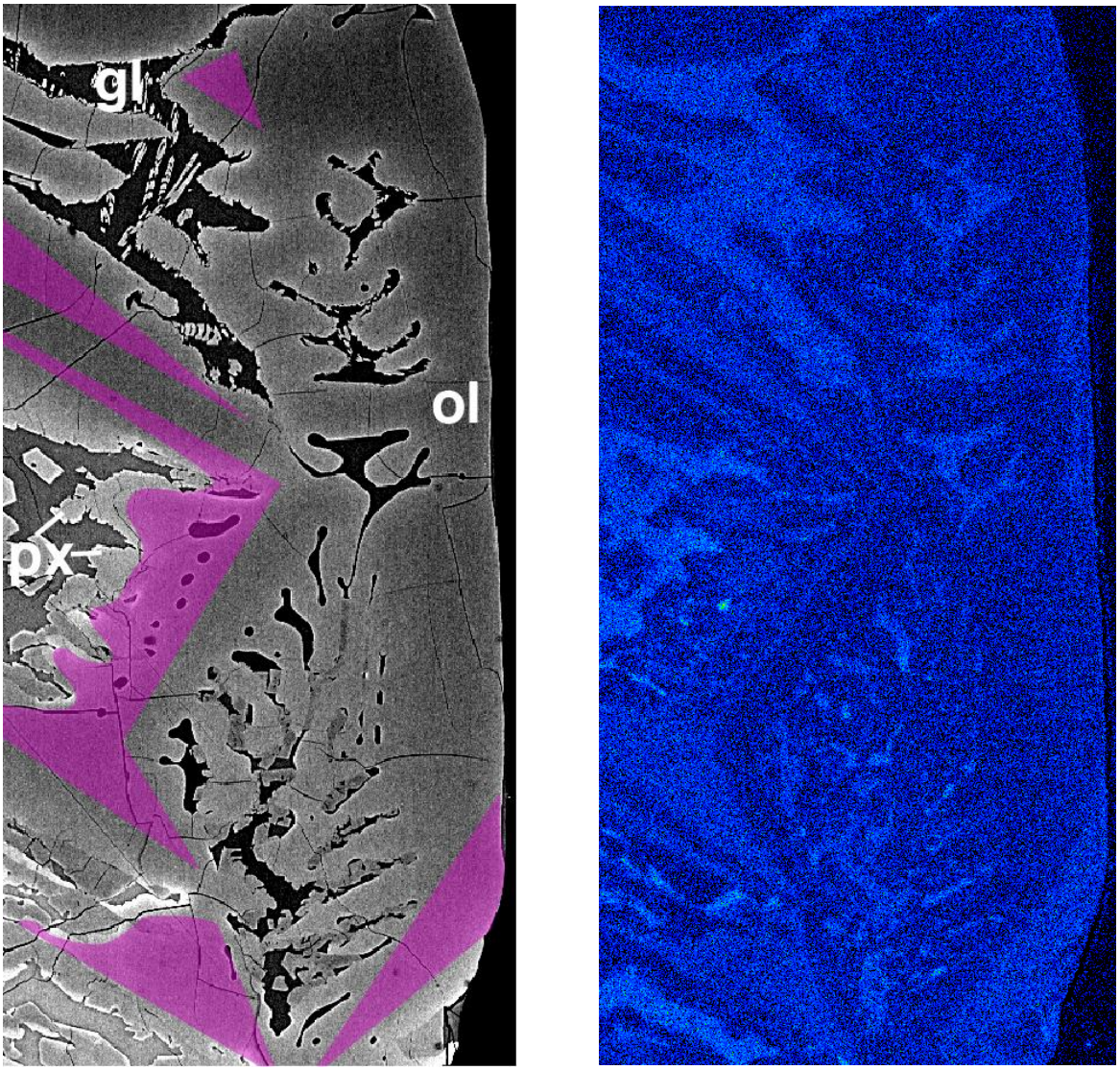

Figure S3. Evidence for P enrichment in Y98*-f18 (6 h at 1198.5 °C, followed by 3 h at 1434 °C, followed by cooling at 72 °C h^{-1} down to 1000 °C). At left, BSE image overlain with semi-transparent pink highlighting, showing areas of P enrichment seen in P X-ray map at right (lighter blue = higher concentration of P). Scale bar in BSE image is approximately 50 μm and applies to P-map as well. ol = olivine, px = pyroxene, gl = glass

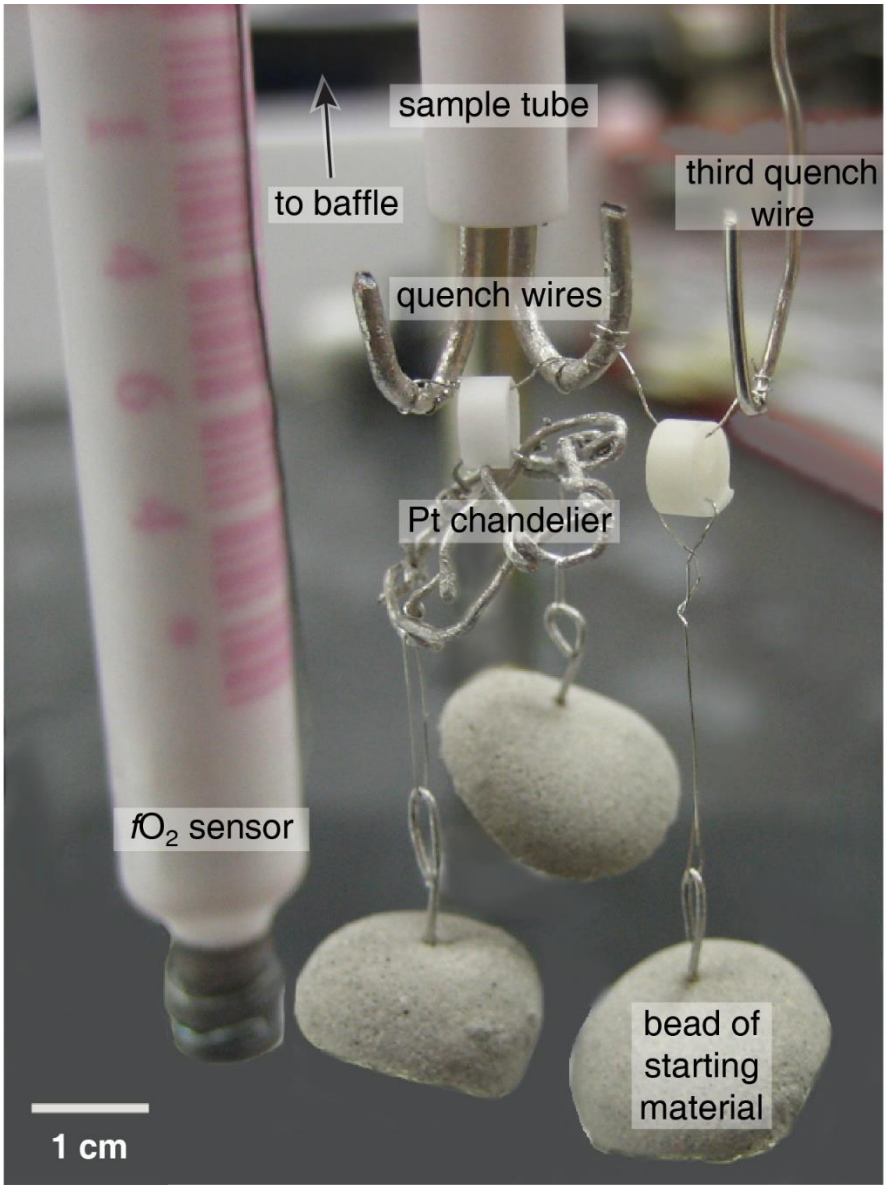

Figure S4. Bottom end of removable sample apparatus, shown after third quench wire was added.

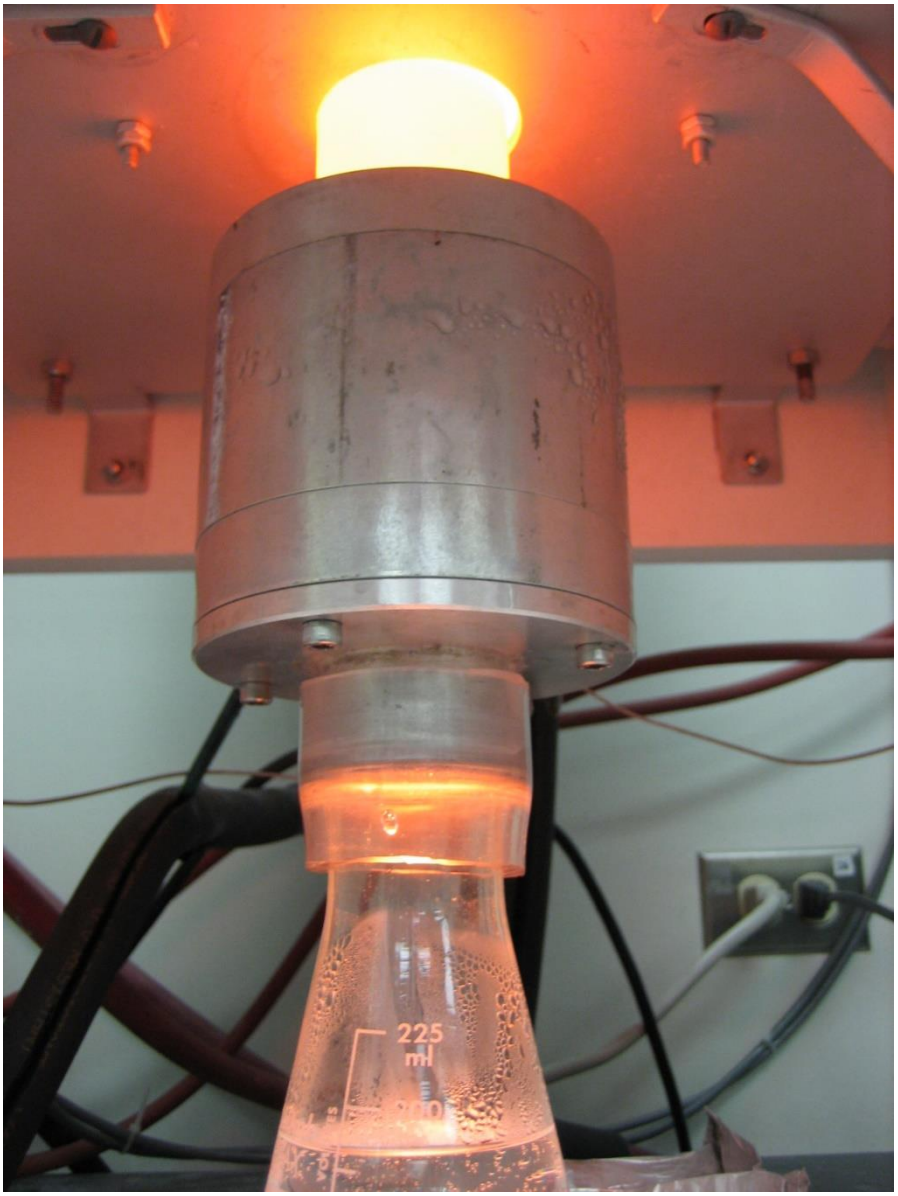

Figure S5. Close-up of quench flask during a high-temperature run.

Figure S6. Backscattered electron (BSE) comparison of experimental run products on pure Pt wire and FePt wire. Both beads were held for 12 h at 1385 °C, cooled to 1113 °C at 28 °C h^{-1}, cooled to 909 °C at 320.6 °C h^{-1}, and quenched. Scale bar applies to A and B. **(A)** Sample Y98*-f35(1) on Pt wire. Offsets in the mosaic are due to slight distortion that prevented perfect image alignment. **(B)** Sample Y98*-f47i on FePt wire.

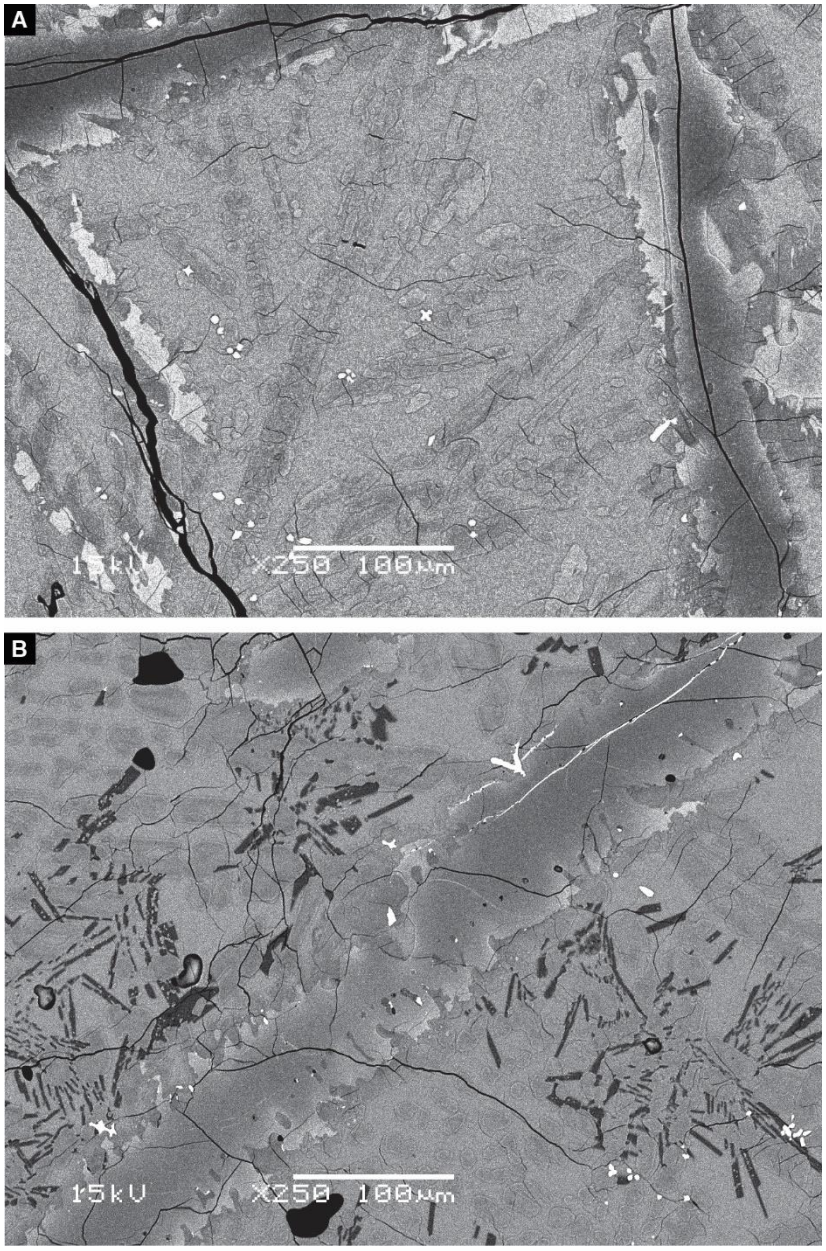

Figure S7. BSE images of isothermal experiments bracketing the plagioclase-in temperature **(A)** Y98*-f60i: held for 12 h at 1432 °C, cooled to 1133 °C at 300 °C h^{-1}, held for 26.47 h, and quenched. No plagioclase crystallized. **(B)** Y98*-f61: began with second bead of Y98*-f60, still intact and on wire, held at 1120 °C for 26.43 h and quenched. Plagioclase crystallized.

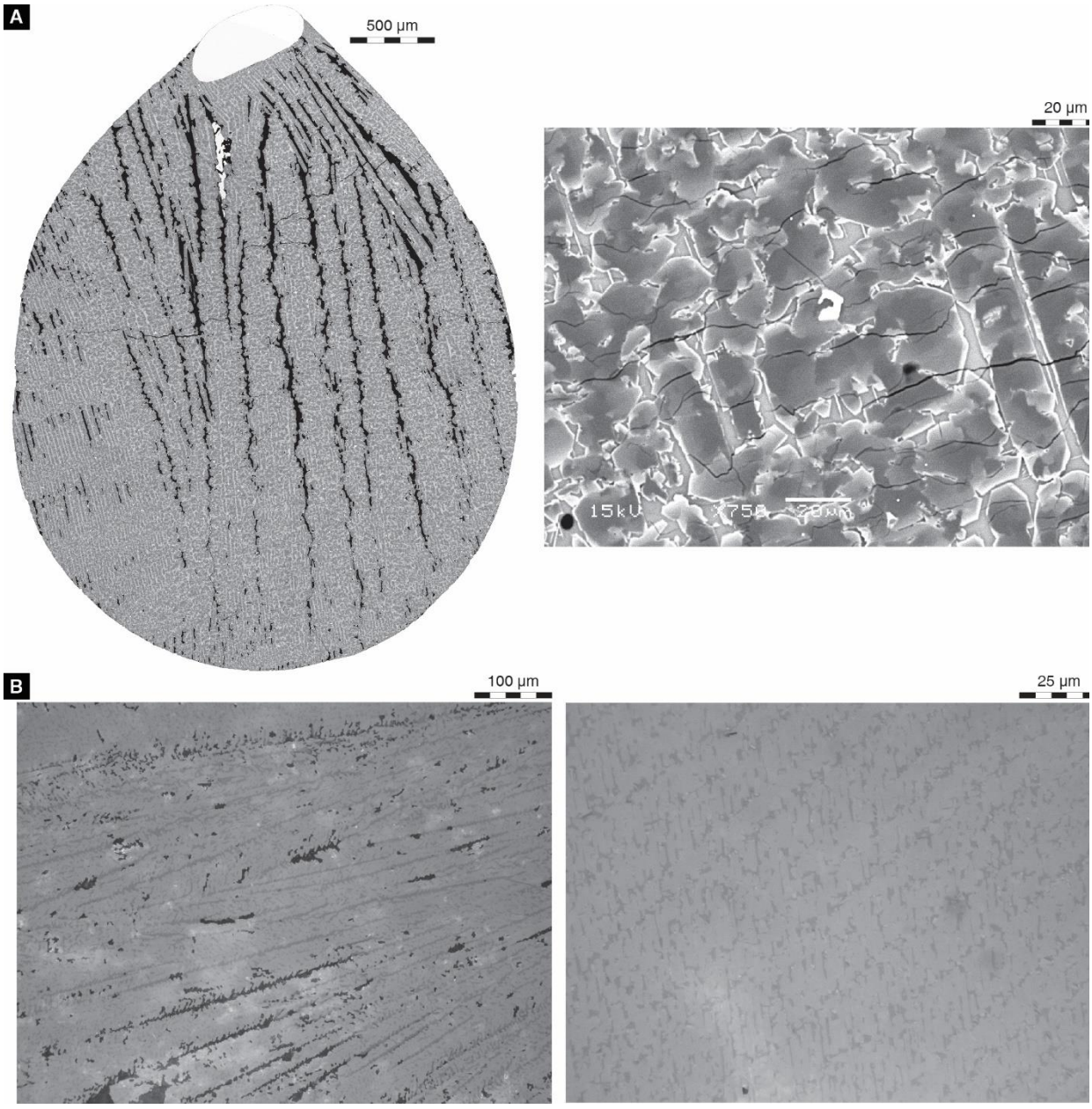

Figure S8. (A) BSE images of Y98*-f55ii, superheated at 1548 °C for 16 h, cooled to 1391.5 °C at 1000 °C h^{-1}, held at 1391.5 °C for 12 h, cooled to 1116 °C at 28 °C h^{-1}, cooled to 909 °C at 320.6 °C h^{-1}, quenched. Black regions are likely glass, either unpolished or plucked during polishing. **(B)** Reflected light images of run Y98*-f37, superheated at 1495 °C for 4 h, cooled to 1000 °C at 72 °C h^{-1}, quenched. Despite their vastly different cooling histories, the samples are very similar, suggesting that crystallization was dominantly controlled by the superheating step(s). In each sample, most of the charge is taken up by one or a few branching crystals of pyroxene, with glass and anhedral Cr-spinel grains filling the interstices.

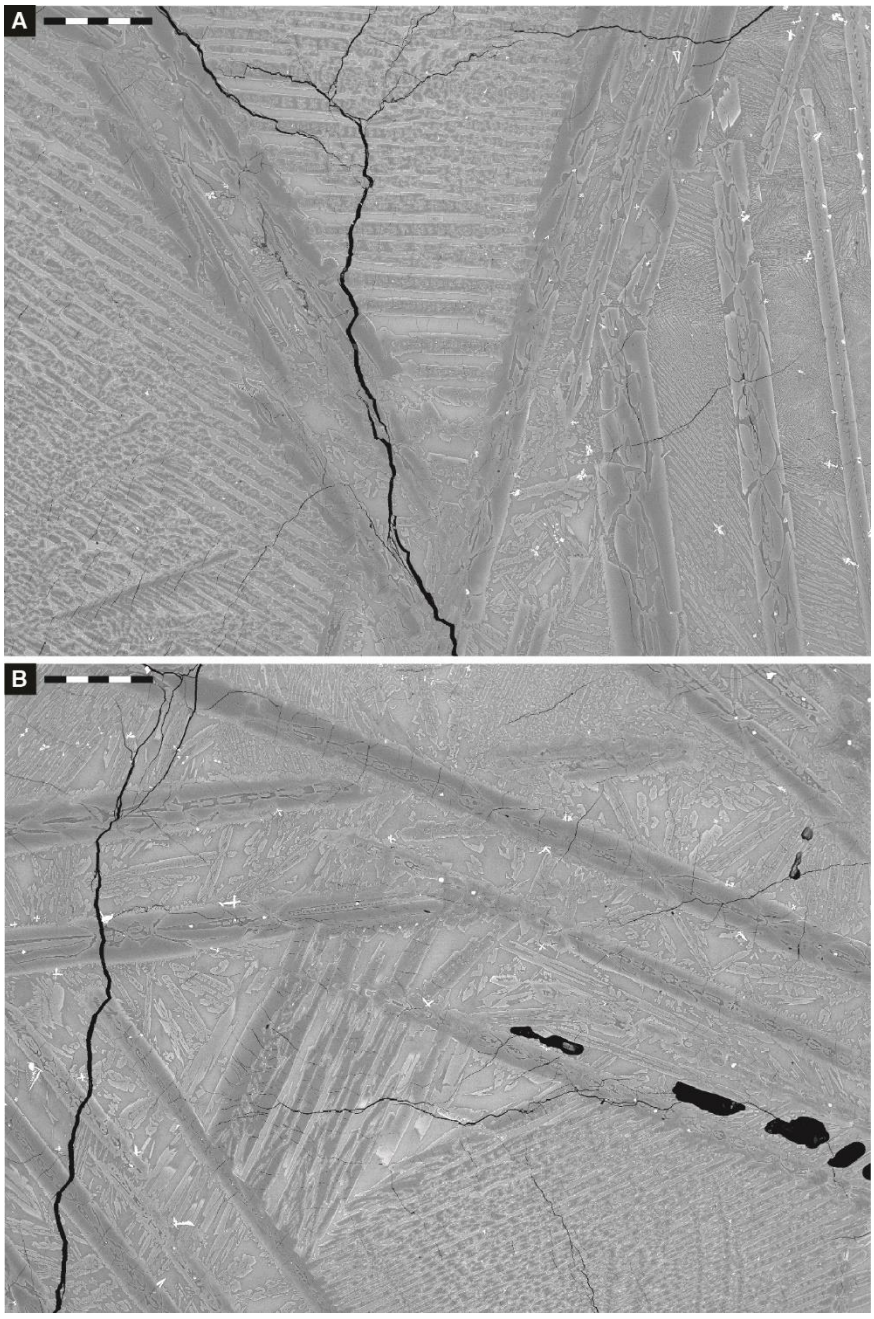

Figure S9. BSE comparison of runs identical other than high temperature dwell time. Time temperature paths were 12/24 h dwell at 1432 °C, cooled to 909 °C at 320.6 °C h^{-1}, quenched. Scale bars are 200 μm. **(A)** Y98*-f58ii, 12 h dwell. **(B)** Y98*-f59ii, 24 h dwell.

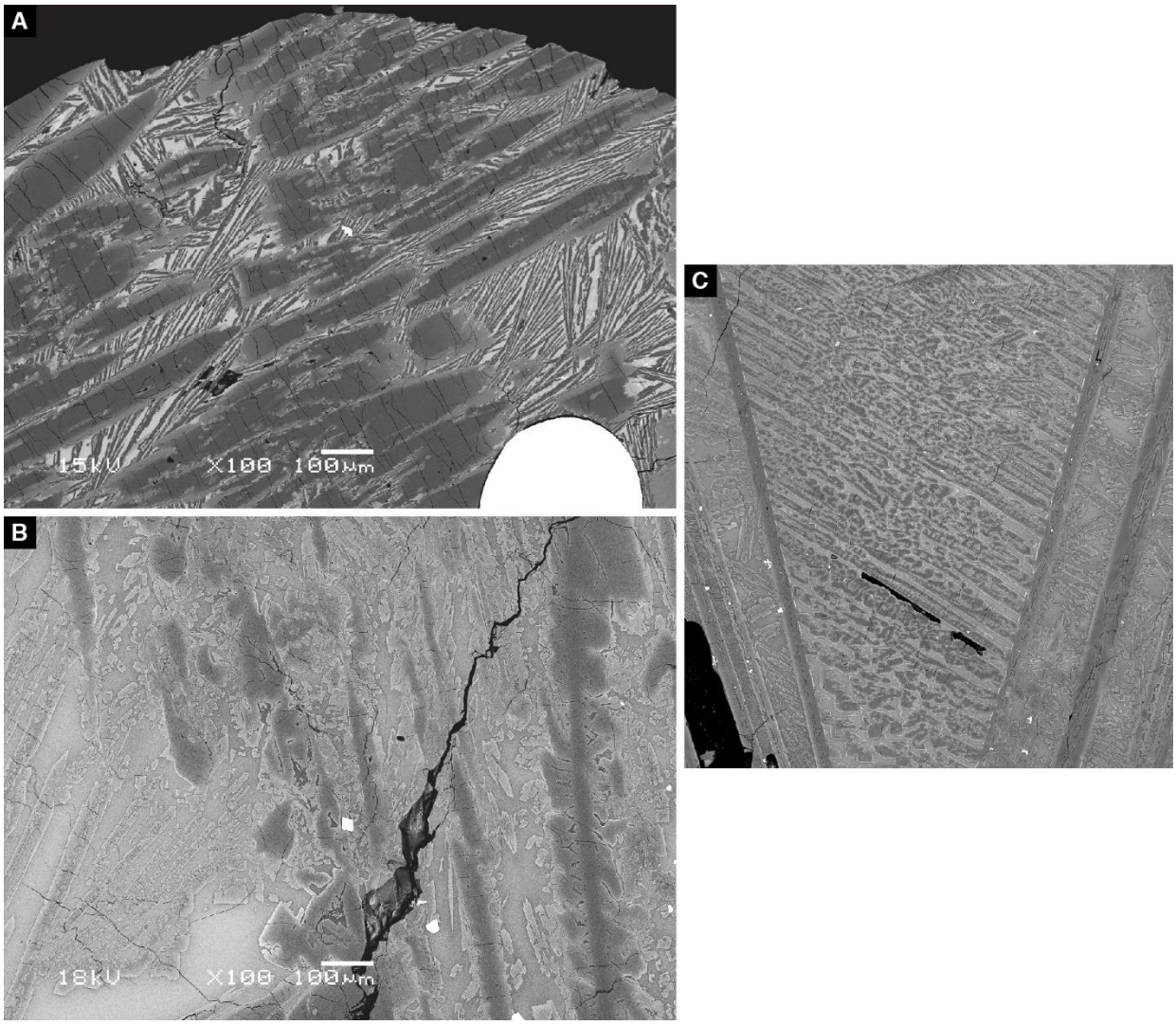

Figure S10. BSE images of runs with a single, linear cooling rate. (A) Y98*-f26a, held for 6 h at 1126.5 °C and 6 h at 1433.5 °C, then cooled to 1000 °C at 36 °C h^{-1}, quenched. Plagioclase is present. (B) Y98*-f18, held for 6 h at 1198.5 °C and 3 h at 1434 °C, then cooled to 1000 °C at 72 °C h^{-1}, quenched. (C) Y98*-f58ii, held 12 h at 1432 °C, then cooled to 909 °C at 320.6 °C h^{-1}, quenched.

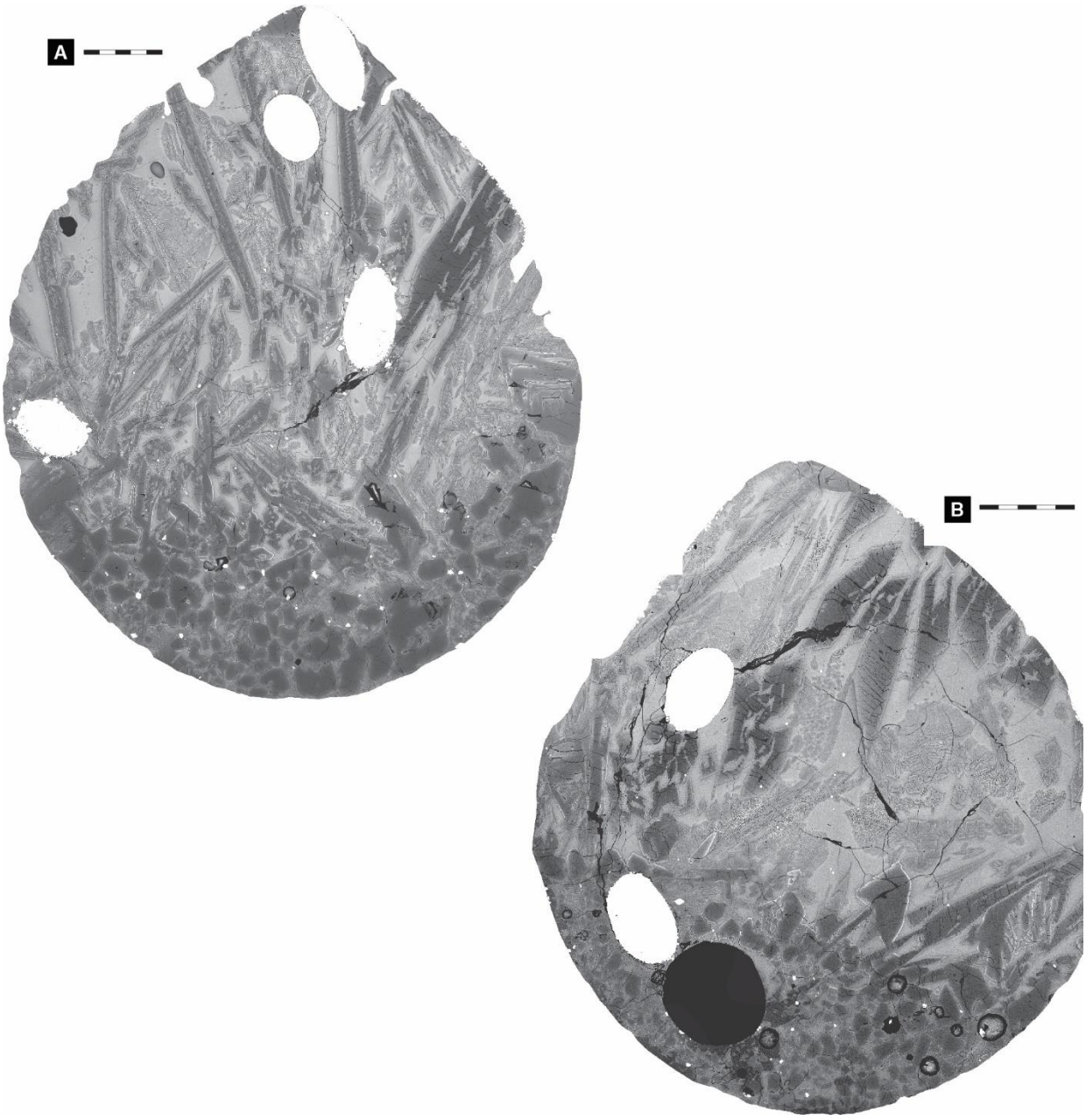

Figure S11. BSE images of runs (A) Y98*-f50i, quenched at 859 °C and (B) Y98*-f48iii, quenched at 909 °C. Time-temperature paths were both as follows: 12 h at 1384.5 °C, cooled to 1113 °C at 28 °C h^{-1}, cooled to 859/909 °C at 320.6 °C h^{-1}, quenched. Scale bars are 500 μm.

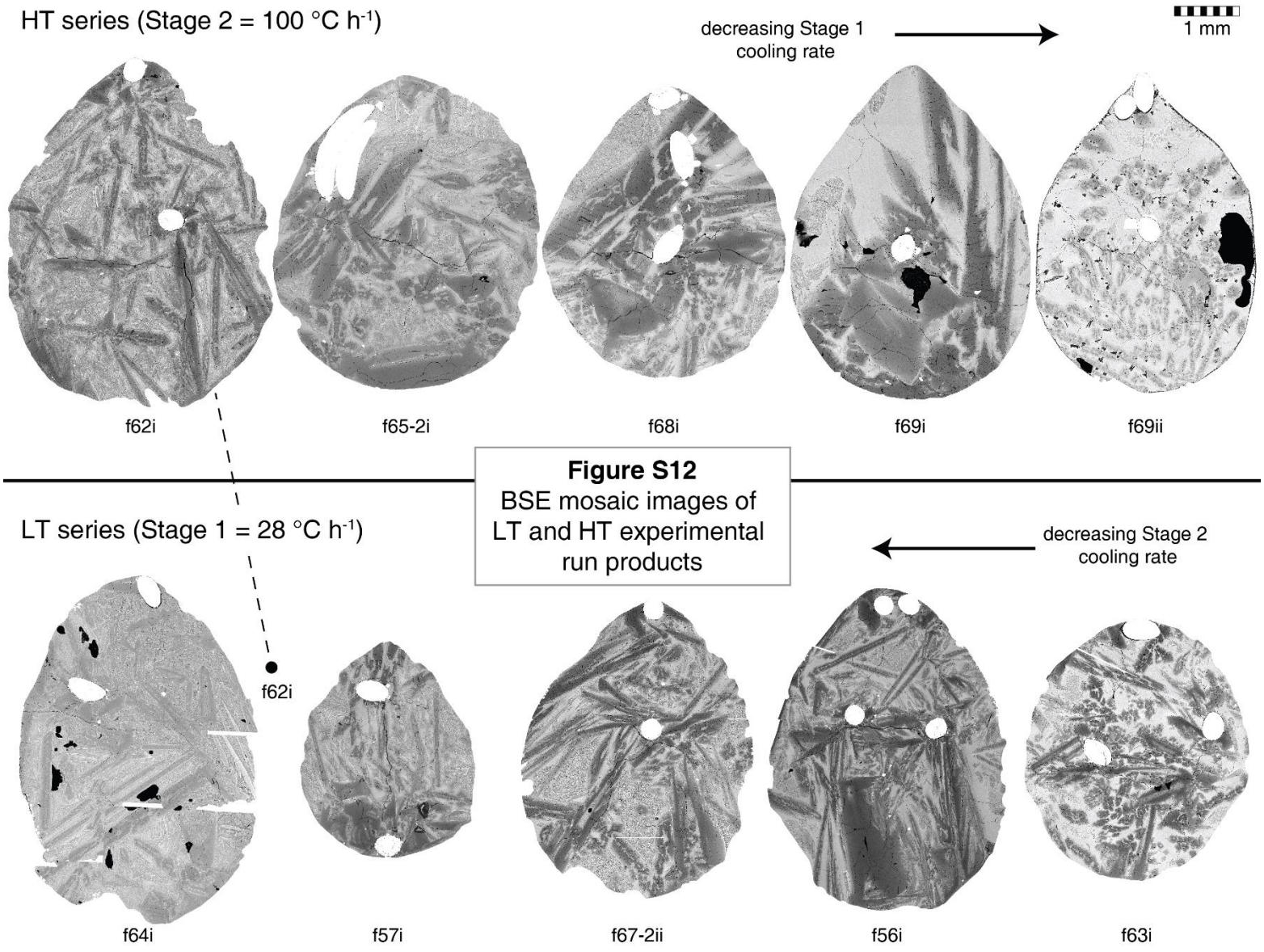

Figure S12
BSE mosaic images of LT and HT experimental run products

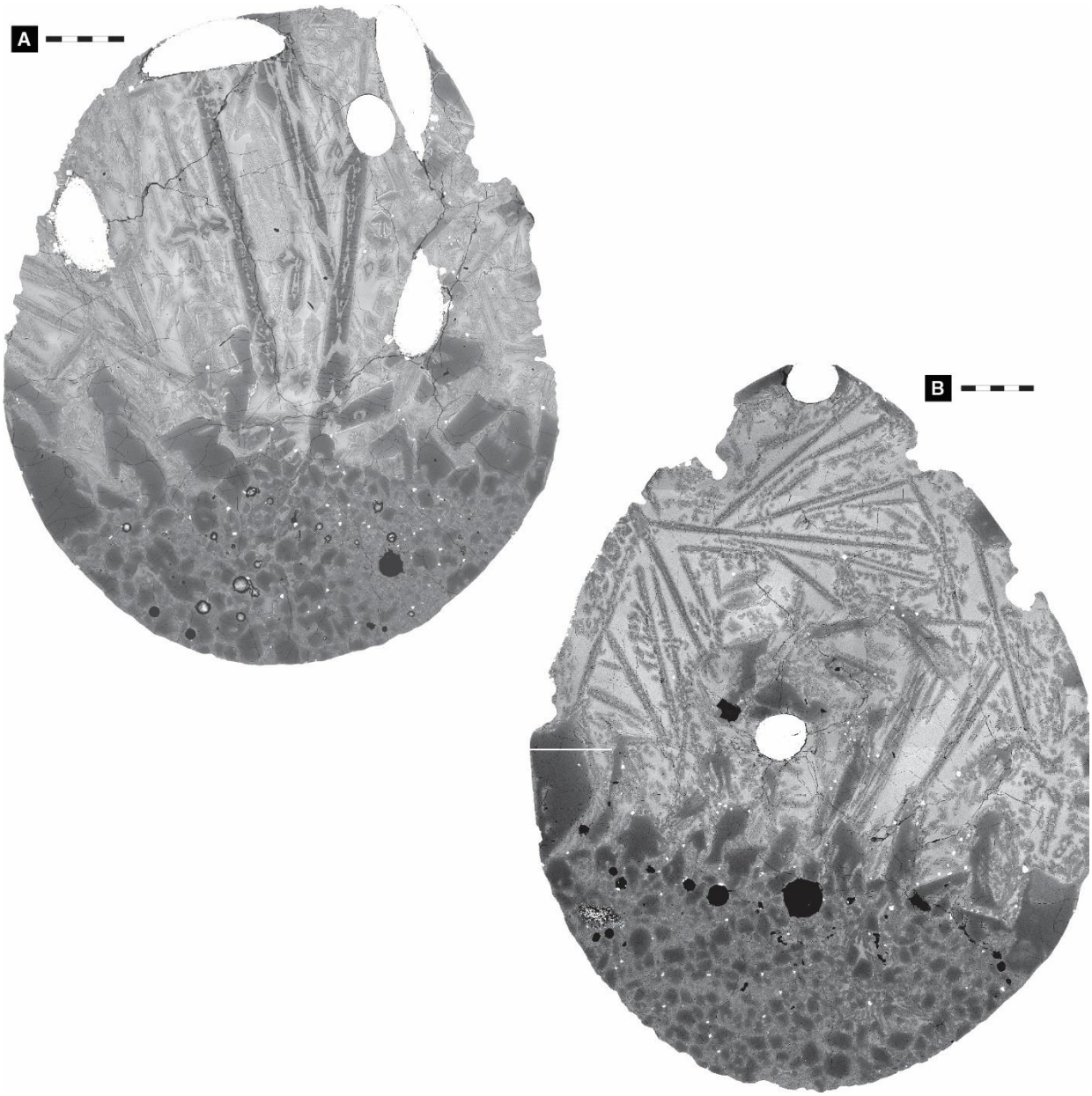

Figure S13. The two beads from the LT and HT series runs that contain many small crystals of olivine, accumulated at the base of the charge, instead of several large ones. Scale bars are 500 μm. **(A)** Y98*-f57 (bead ii). **(B)** Y98*-f63 (bead ii).

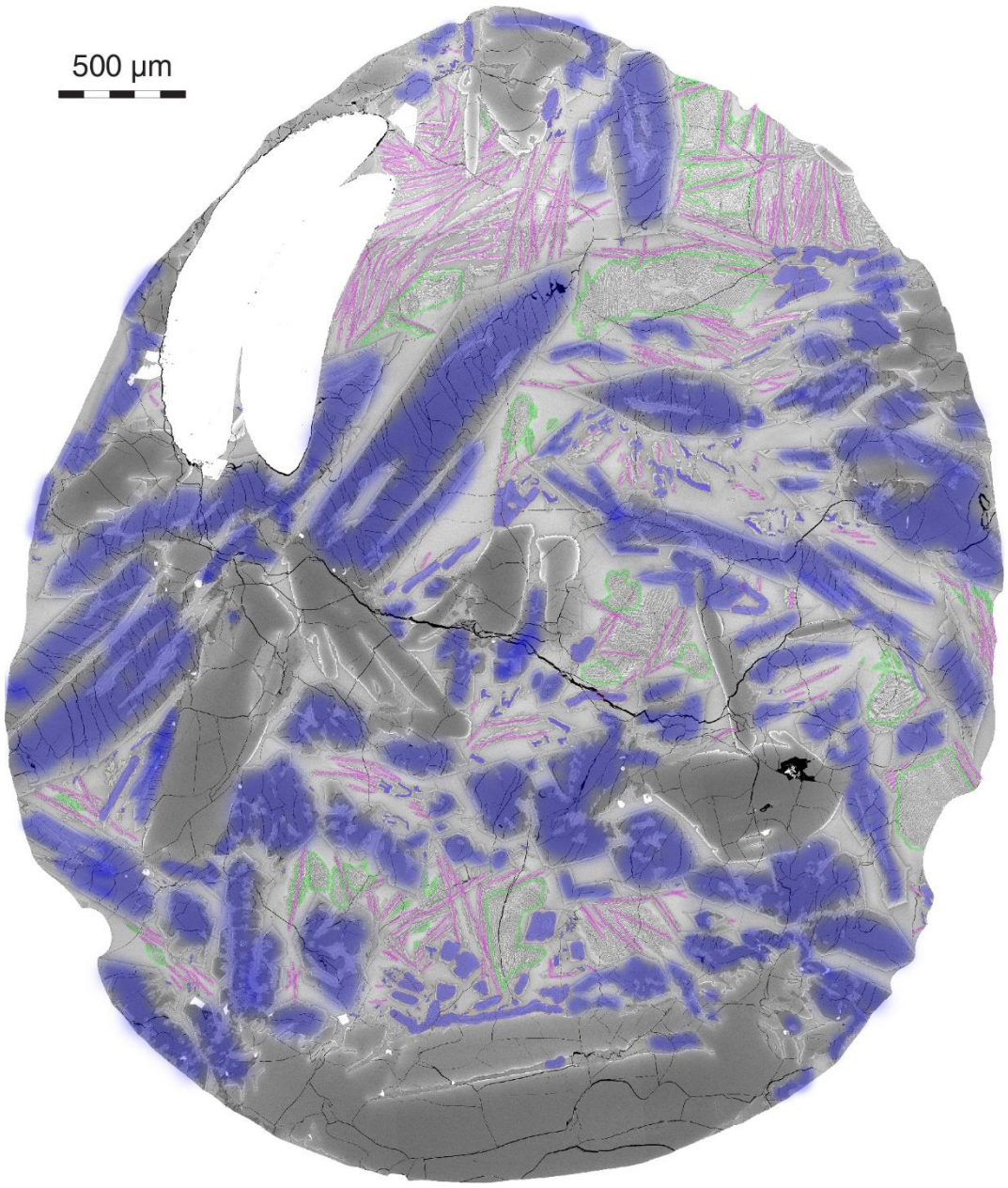

Figure S14. Example of pyroxene populations for one experimental bead (run Y98*-f65, see Table 2 in main text). Background is a BSE mosaic at 100x magnification. Blue highlights population A_e, pink highlights population B_e, and green outlines areas containing population C_e.

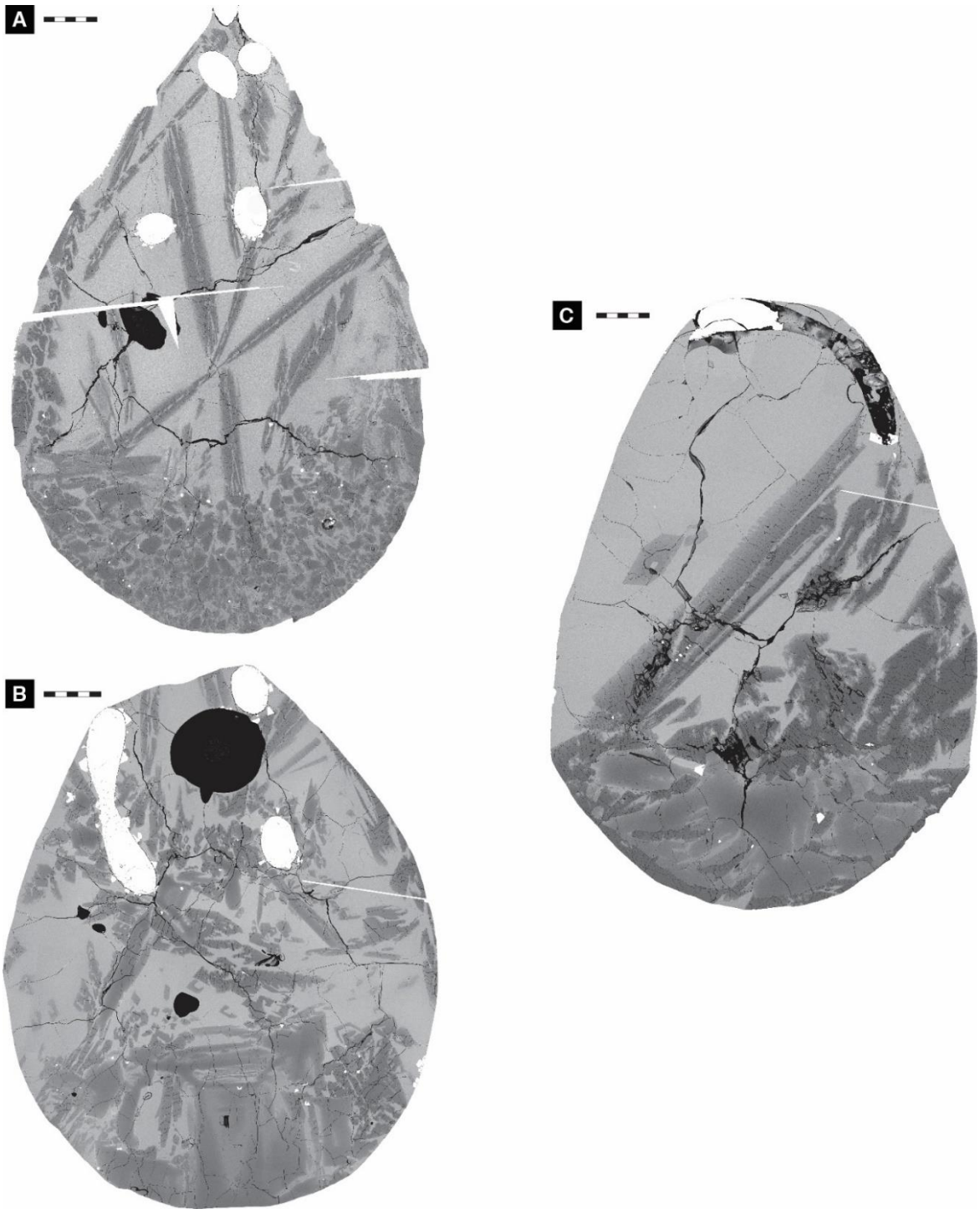

Figure S15. BSE mosaic images of cooling experiments quenched at the end of Stage 1. No pyroxene crystals of populations B_e or C_e are present. Scale bars are 500 μm. (A)Y98*-f51, held 12 h at 1385 °C, cooled to 1113 °C at 28 °C h^{-1}, quenched. (B)Y98*-f65-1, held 12 h at 1433 °C, cooled to 1115.5 °C at 10 °C h^{-1}, quenched. (C)Y98*-f66-1ii, held 12 h at 1433 °C, cooled to 1116.5 °C at 1 °C h^{-1}, quenched.

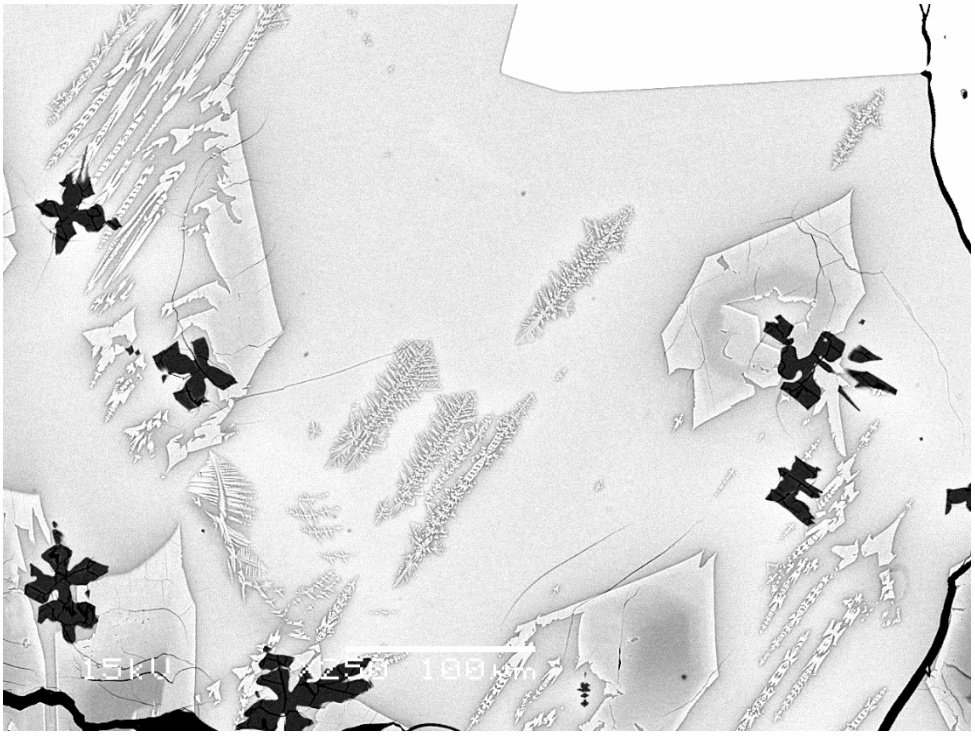

Figure S16. BSE image of experiment Y98*-f69 (bead ii). Black, cross-shaped crystals with interior fracture patterns are cristobalite.

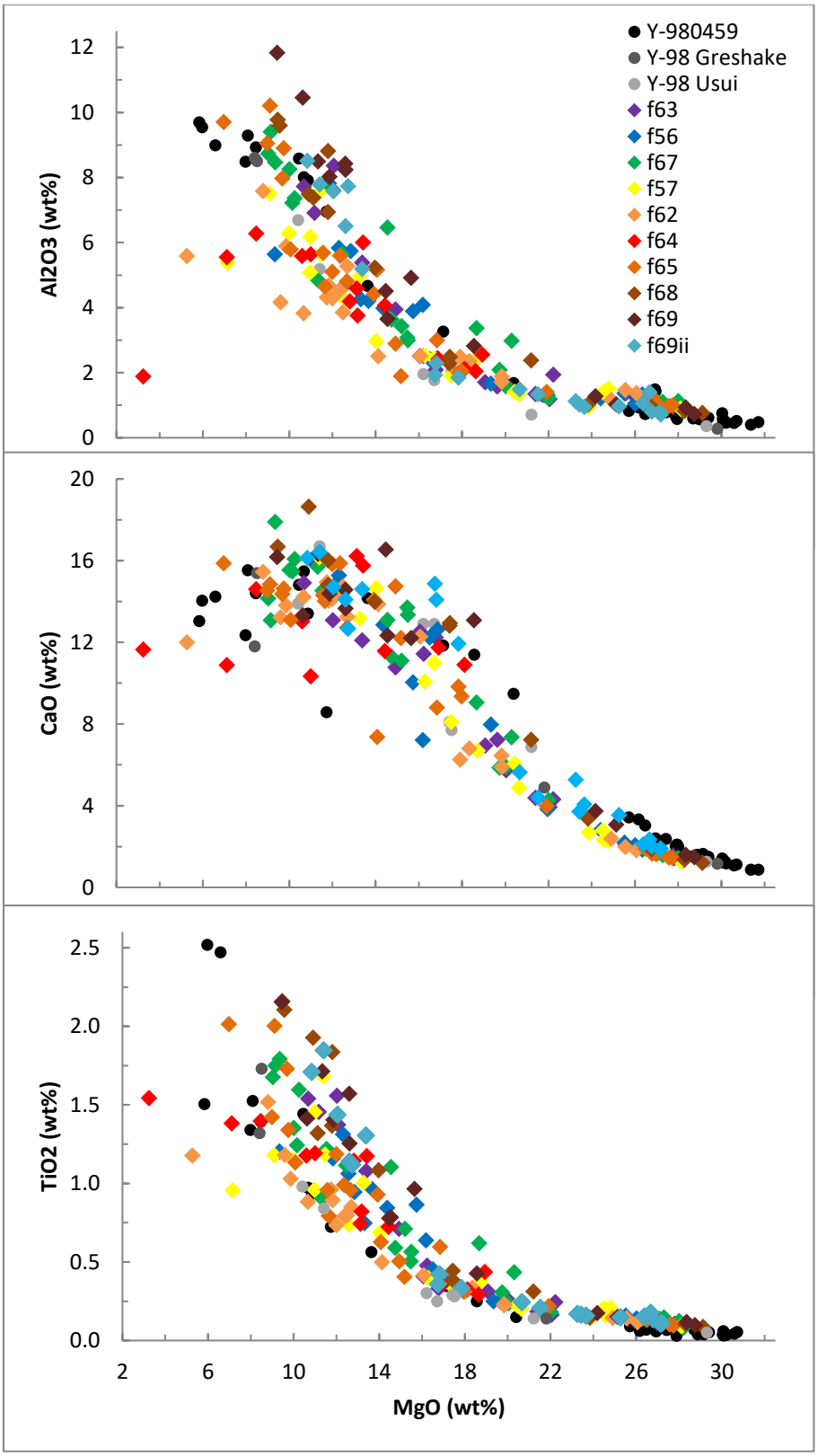

Figure S17. Composition of pyroxene crystals in experiments and Y-980459. Horizontal axis and legend apply to all three plots. No compositional trend with cooling rate is evident.

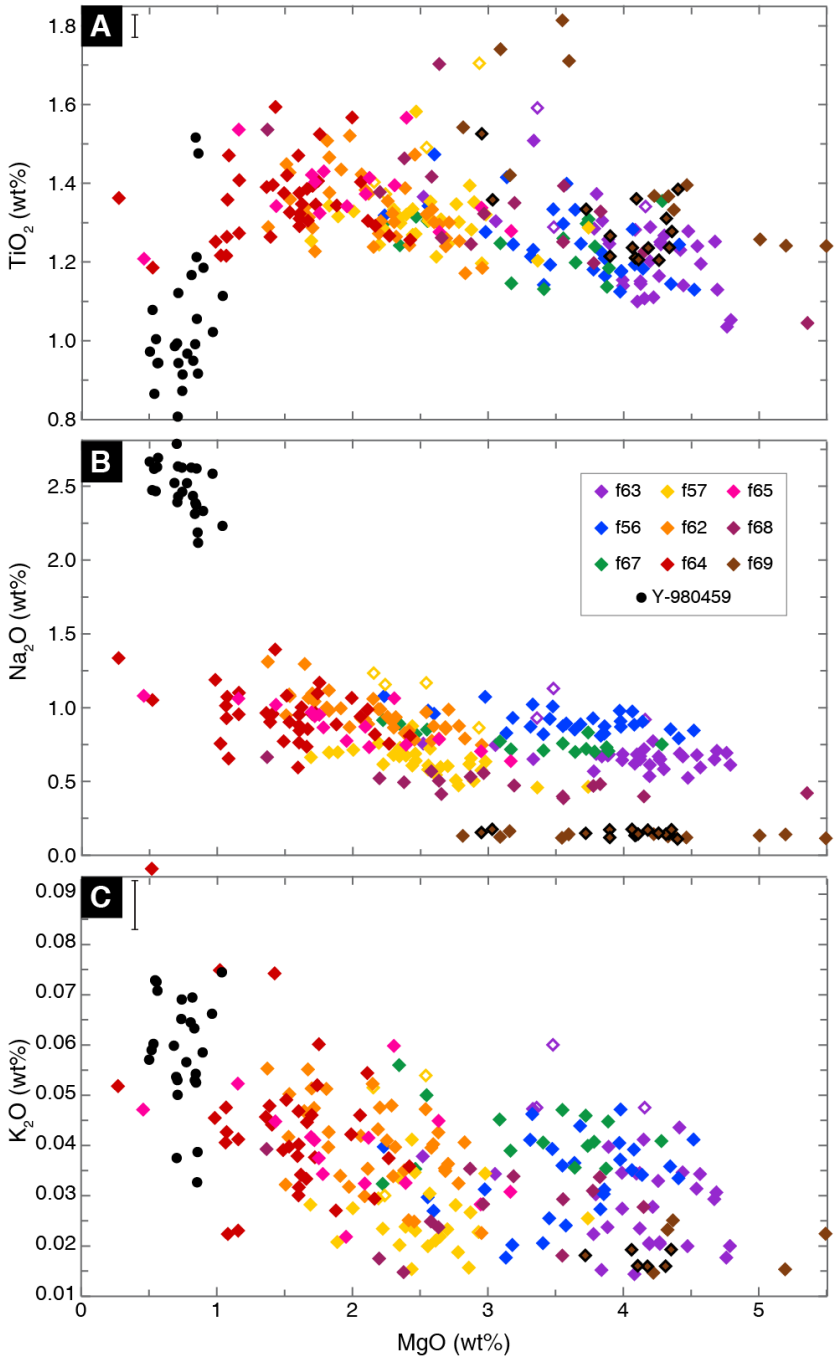

Figure S18. Glass compositions in Y-980459 and experiments. Error bars are shown in the upper left of each plot, when larger than the symbol size. Horizontal axis and legend apply to all three plots. Open symbols indicate "intercumulus" glass; f69 points with black outlines indicate analyses from the cristobalite-bearing bead. Note the low TiO_2 content of the meteorite in (A), the Na_2O depletion of experiments in (B), and the heterogeneous nature of K_2O in (C).

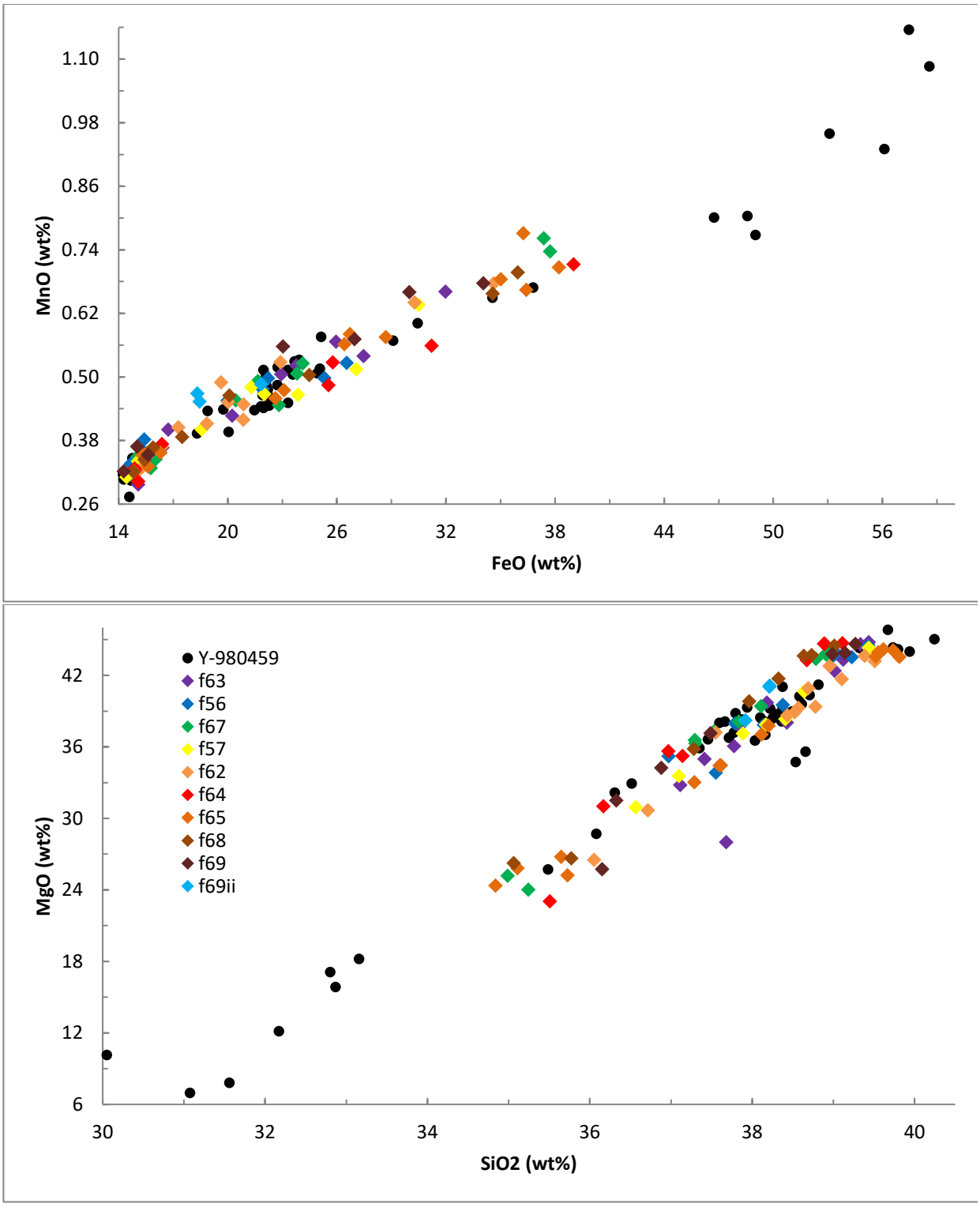

Figure S19. Olivine compositions in experiments and Y-980459. Legend applies to both plots. Note the absence of cooling-rate dependent compositional trends. The high FeO, MnO points correspond to the low MgO, SiO_2 points.

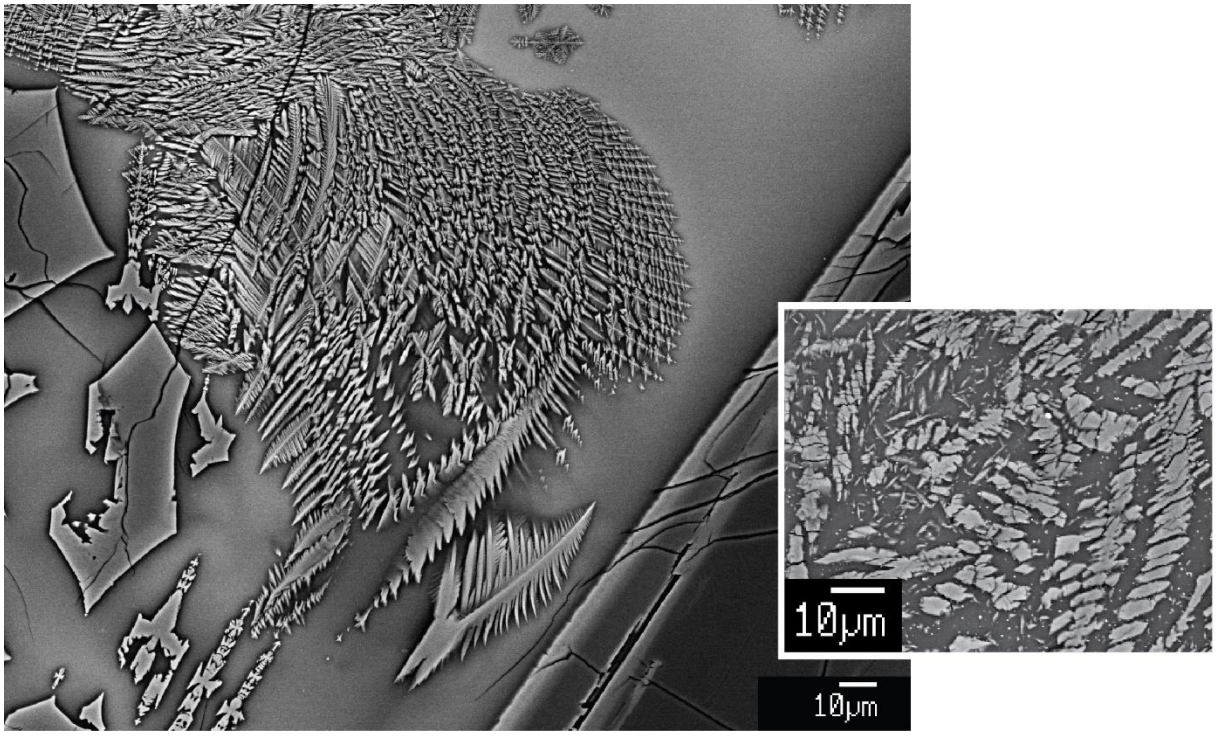

Figure S20. Boundary layers preserved in the quenched glass of experiment Y98*-f67 and more subtly in Y-980459 (inset). Crystals in both images are pyroxene.

Table S1. Complete run table of all experiments mentioned in the paper.

Run (Y98*-f__)	Starting Material	Wire (plated wt% Fe)	Pre-cooling history*	Stage 1 rate (°C h^{-1})	Pivot T (°C)	Stage 2 rate (°C h^{-1})	Quench T (°C)	Duration** (h)	Phases
4^	RM	0	6h at 1453°C	n/a	n/a	n/a	1453	9	gl
5	RM	0	9h at 1200°C, 6h at 1411°C	n/a	n/a	n/a	n/a	18	n/a
6	RM	0	5.2h at 1200°C, 6h at 1424°C	n/a	n/a	n/a	1424	13.5	gl, ol
7	RM	0	6h at 1434°C	n/a	n/a	n/a	1434	8.3	gl, ol
8	RM	0	6h at 1439.5°C	n/a	n/a	n/a	1439.5	9	gl
9	RM	0	6h at 1438.5°C	n/a	n/a	n/a	1436.5	9.1	n.a.
10	RM	0	6h at 1439°C	n/a	n/a	n/a	1438.5	10	gl, ol?
11	RM	0	6h at 1441°C	n/a	n/a	n/a	1441	9.1	gl
12	RM	0	3h at 1434°C	72	n/a	n/a	1000	12.3	gl, px, ol, crsp, plag
13	RM	0	6h at 1335°C	n/a	n/a	n/a	1335	8	gl, ol, crsp
14	FG	0	3h at 1435°C	72	n/a	n/a	1000	12.1	gl, px, ol, crsp
15	RM	0	6h at 1199.5°C	n/a	n/a	n/a	1199.5	7.5	gl, px, ol?, crsp
16	RM	0	6h at 1199.5°C	n/a	n/a	n/a	1199.5	7.5	gl, px?, ol, crsp
17	FG	0	3h at 1435°C	72	n/a	n/a	1000	12.2	gl, px, crsp
18	RM	0	6h at 1198.5°C, 3h at 1434°C	72	n/a	n/a	1000	18.2	gl, px, ol, crsp
19	FG	0	6h at 1198.5°C, 3h at 1434°C	72	n/a	n/a	1000	18.2	
20	RM	0	9h at 1435°C	72	n/a	n/a	1000	18.2	gl, px, crsp
21	RM	0	4h at 1445°C	n/a	n/a	n/a	1445	6.9	gl
22	RM	0	12h at 1435°C	72	n/a	n/a	1000	21.2	gl, px, ol, crsp
23	RM	0	6h at 1435°C	72	n/a	n/a	1000	15.2	gl, px, ol, crsp
24	RM	0	6h at 1197.5°C, 9h at 1434.5°C	72	n/a	n/a	1000	24.2	gl, px, crsp
25a	RM	0	6h at 1126°C, 6h at 1434°C	72	n/a	n/a	1000	21.2	gl, px, crsp
25b	FG	0	6h at 1126°C, 6h at 1434°C	72	n/a	n/a	1000	21.2	gl, px, ol, crsp, plag?
26a	RM	0	6h at 1126.5°C, 6h at 1433.5°C	36	n/a	n/a	1000	27.5	gl, px, crsp, plag

Table S1, *continued*

26b	FG	0	6h at 1126.5°C, 6h at 1433.5°C	36	n/a	n/a	1000	27.5	gl, px, ol, crsp, plag?
27a	RM	0	6h at 1126.5°C	n/a	n/a	n/a	1126.5	7.1	px, ol, crsp, plag
27b	FG	0	6h at 1126.5°C	n/a	n/a	n/a	1126.5	7.1	px, crsp?, plag
28a	RM	0	6h at 1126.5°C, 6h at 1433.5°C	2	n/a	n/a	1409	27.4	gl, ol?
28b	FG	0	6h at 1126.5°C, 6h at 1433.5°C	2	n/a	n/a	1409	27.4	gl
29a	RM	0	6h at 1126°C, 6h at 1433.5°C	28	1113	320.6	909	27.5	gl, px, ol, crsp
29b	FG	0	6h at 1126°C, 6h at 1433.5°C	28	1113	320.6	909	27.5	gl, px, ol, crsp
30	RM	0	3h at 1433.5°C	72	n/a	n/a	1000	12.3	gl, px, ol, crsp
31a[#]	RM	0	6h at 1126.5°C, 6h at 1433.5°C	14	1113	320.6	909	51.5	gl, px, crsp, plag
31b[#]	FG	0	6h at 1126.5°C, 6h at 1433.5°C	14	1113	320.6	909	51.5	px, ol, crsp, plag, SiO_2?
32a	RM	0	12h at 1409.5°C	n/a	n/a	n/a	1409.5	14.7	gl
32b	FG	0	12h at 1409.5°C	n/a	n/a	n/a	1409.5	14.7	gl, ol
33a	RM	0	12h at 1384.5°C	n/a	n/a	n/a	1384.5	14.6	gl, ol, crsp
33b	FG	0	12h at 1384.5°C	n/a	n/a	n/a	1384.5	14.6	gl, ol, crsp
34a	RM	0	12h at 1385°C	28	1113	320.6	909	25.46	gl, px, ol, crsp
34b	FG	0	12h at 1385°C	28	1113	320.6	909	25.46	gl, px, ol, crsp
35 (1)	RM	0	12h at 1385°C	28	1113	320.6	909	25.46	gl, px, ol, crsp
35 (2)	RM	0	12h at 1385°C	28	1113	320.6	909	25.46	gl, px, ol, crsp
36	RM	0	12h at 1385.5°C	28	1274	320.6	909	20	gl, px, ol, crsp
37a	RM	0	4h at 1495°C	72	n/a	n/a	1000	14.4	gl, px?
37b	FG	0	4h at 1495°C	72	n/a	n/a	1000	14.4	gl, px, ol, crsp
38	RM	0	12h at 1385.5°C	28	1113	200	909	25.9	gl, px, ol, crsp (+mgsp?), plag
39a	RM	0	4h at 1495.5°C	72	n/a	n/a	1000	14.4	gl, px, ol?, crsp, plag

Table S1, *continued*

39aa (1)	RMf	0	4h at 1495.5°C	72	n/a	n/a	1000	14.4	gl, px, ol?, crsp
39aa (2)	RMf	0	4h at 1495.5°C	72	n/a	n/a	1000	14.4	gl, px, ol?, crsp
40a	RM	0	12h at 1385.5°C	n/a	n/a	n/a	1385.5	14.6	gl, ol?, crsp?
40b	FG	0	12h at 1385.5°C	n/a	n/a	n/a	1385.5	14.6	gl, ol?, crsp?
40aa	RMf	0	12h at 1385.5°C	n/a	n/a	n/a	1385.5	14.6	gl, ol?, crsp?
f41a	RM	0	4h at 1552.5°C	72	n/a	n/a	1000	15.6	gl, px, ol?, crsp
f41b	FG	0	4h at 1552.5°C	72	n/a	n/a	1000	15.6	gl, px, ol?, crsp
f41aa	RMf	0	4h at 1552.5°C	72	n/a	n/a	1000	15.6	gl, px, ol?, crsp, plag
f42a	RM	0	4h at 1496.5°C	n/a	n/a	n/a	1496.5	7.2	gl
f42b	FG	0	4h at 1496.5°C	n/a	n/a	n/a	1496.5	7.2	gl
f42aa	RMf	0	4h at 1496.5°C	n/a	n/a	n/a	1496.5	7.2	gl
f43a	RM	0	4h at 1553°C	n/a	n/a	n/a	1553	7.6	gl
f43b	FG	0	4h at 1553°C	n/a	n/a	n/a	1553	7.6	gl
f43aa	RMf	0	4h at 1553°C	n/a	n/a	n/a	1553	7.6	gl
f44	RM	0	12h at 1386.5°C	2	n/a	n/a	1175	124.6	gl, px, ol, crsp
f45	RM	27.7	4h at 1495.5°C	n/a	n/a	n/a	1495.5	7.2	gl
f46i	RM	17.13	4h at 1496°C	n/a	n/a	n/a	1496	7.2	gl
f46ii	RM	22.74	4h at 1496°C	n/a	n/a	n/a	1496	7.2	gl
f47i	RM	17.44	12h at 1384.5°C	28	1113	320.6	908	25.46	gl, px, ol, crsp
f47ii	RM	18.13	12h at 1384.5°C	28	1113	320.6	908	25.46	gl, px, ol, crsp
f47iii	RM	18.64	12h at 1384.5°C	28	1113	320.6	908	25.46	gl, px, ol, crsp
f48i	RM	19.38	12h at 1384.5°C	28	1113	320.6	909	25.46	n/a
f48ii	RM	22.23	12h at 1384.5°C	28	1113	320.6	909	25.46	n/a
f48iii	RM	19.96	12h at 1384.5°C	28	1113	320.6	909	25.46	gl, px, ol, crsp
f49i	RM	19.57	12h at 1384.5°C	28	1113	320.6	909	25.46	n/a
f49ii	RM	22.45	12h at 1384.5°C	28	1113	320.6	909	25.46	gl, px, ol, crsp, plag
f49iii	RM	20.06	12h at 1384.5°C	28	1113	320.6	909	25.46	n/a
f50i	RM	21.02	12h at 1384.5°C	28	1113	320.6	859	25.63	gl, px, ol, crsp

Table S1, *continued*

f50ii	RM	19.97	12h at 1384.5°C	28	1113	320.6	859	25.63	gl, px, ol, crsp
f51	RM	20.55	12h at 1385°C	28	n/a	n/a	1113	24.8	gl, px, ol, crsp
f52a/i	RM	17.72†	16h at 1540°C, cool to 1385°C at 999.9°Ch^{-1}, 12h at 1385°C	28	1113	320.6	906	42.53	gl?, px, crsp?
f52b/ii	RM	17.62†	16h at 1540°C, cool to 1385°C at 999.9°Ch^{-1}, 12h at 1385°C	28	1113	320.6	906	42.53	gl, px, ol, crsp
f53i	RM	17.93†	see notes	n/a	n/a	n/a	n/a	n/a	n/a
f53ii	RM	18.13†	see notes	n/a	n/a	n/a	n/a	n/a	n/a
f54i	RM	17.71†	12h at 1433.5°C	28	1116	320.6	909	27.28	gl, px, ol, crsp
f54ii	RM	16.77†	12h at 1433.5°C	28	1116	320.6	909	27.28	gl, px, ol, crsp
f55i	RM	20.9	16h at 1548°C, cool to 1391.5°C at 999.9°Ch^{-1}, 12h at 1391.5°C	28	1116	320.6	909	42.53	gl, px, crsp
f55ii	RM	18.14†	16h at 1548°C, cool to 1391.5°C at 999.9°Ch^{-1}, 12h at 1391.5°C	28	1116	320.6	909	42.53	gl, px, crsp
f56i	RM	20.47	12h at 1433.5°C	28	1116	500	909	27.08	gl, px, ol, crsp
f56ii	RM	19.36	12h at 1433.5°C	28	1116	500	909	27.08	gl, px, ol, crsp
f57i	RM	19.52†	12h at 1433°C	28	1116	150	909	28.13	gl, px, ol, crsp
f57ii	RM	17.58†	12h at 1433°C	28	1116	150	909	28.13	gl, px, ol, crsp
f58i	RM	17.54†	12h at 1432°C	320.6	n/a	n/a	909	16.58	gl, px, ol, crsp
f58ii	RM	17.49†	12h at 1432°C	320.6	n/a	n/a	909	16.58	gl, px, ol, crsp
f59i	RM	16.78†	24h at 1432°C	320.6	n/a	n/a	909	28.58	gl, px, ol, crsp
f59ii	RM	17.03†	24h at 1432°C	320.6	n/a	n/a	909	28.58	gl, px, ol, crsp
f60i%	RM	17.66†	12h at 1432°C	300	1133	n/a	1133	42.25	gl, px, ol, crsp
f60ii%	RM	17.53†	12h at 1432°C	300	1133	n/a	1133	42.25	n/a

Table S1, *continued*

f61	RM	17.53†	26.43h at 1120°C	n/a	n/a	n/a	1120	27.48	gl, px, ol, crsp, plag
f62i	RM	18.02†	12h at 1433°C	28	1116	100	909	28.8	gl, px, ol, crsp
f62ii	RM	16.81†	12h at 1433°C	28	1116	100	909	28.8	gl, px, ol, crsp
f63i	RM	18.15†	12h at 1428°C	28	1111	1000	909	26.93	gl, px, ol, crsp
f63ii	RM	18.37†	12h at 1428°C	28	1111	1000	909	26.93	gl, px, ol, crsp
f64i	RM	17.37†	12h at 1432°C	28	1112	50	909	31.08	gl, px, ol, crsp, plag
f64ii	RM	17.47†	12h at 1432°C	28	1112	50	909	31.08	gl, px, ol, crsp, plag
f65-1	RM	18.85†	12h at 1433°C	10	n/a	n/a	1115.5	48.25	gl, px, ol, crsp
f65-2i	RM	18.90†	12h at 1433°C	10	1115	100	909	50.45	gl, px, ol, crsp
f65-2ii	RM	19.11†	12h at 1433°C	10	1115	100	909	50.45	gl, px, ol, crsp
f66-1i	RM	18.83†	12h at 1433°C	1	n/a	n/a	1116.5	349	n/a
f66-1ii	RM	18.43†	12h at 1433°C	1	n/a	n/a	1116.5	349	gl, px, ol, crsp
f66-2	RM	18.66†	12h at 1433°C	1	1116	100	909	351.23	gl, ox, ol, crsp, cristobalite
f67-2i/i	RM	17.75†	12h at 1435°C	28	1115	350	909	27.5	gl, px, ol, crsp
f67-2ii/ii	RM	18.42†	12h at 1435°C	28	1115	350	909	27.5	gl, px, ol, crsp
f67-2iii/iii	RM	18.13†	12h at 1435°C	28	1115	350	909	27.5	n/a
f68i	RM	16.73†	12h at 1435°C	5	1115	100	909	84.05	gl, ol, px, crsp
f68ii	RM	17.71†	12h at 1435°C	5	1115	100	909	84.05	gl, ol, px, crsp
f69i	RM	16.78†	12h at 1435°C	1	1115	100	909	376.08	gl, ol, px, crsp
f69ii	RM	17.94†	12h at 1435°C	1	1115	100	909	376.08	gl, ol, px, crsp, cristobalite

†post-annealing %Fe; ^fO_2 was closer to IW+2; *when ramp rate is not indicated between steps, it is 180°C h^{-1}

**completed insertion to quench, actual time; n/a=not analyzed; # 12 h hold at pivot T; % 26.5 hour hold at pivot

Starting Materials:

RM = Reagent mix, no pre-experiment fusion

FG = Fused glass: RM that was melted at 1500°C for 2 hours, quenched, crushed (x2)

RMf = RM "fine" that was ground/crushed an extra hour under ethanol is synthetic garnet/corundum-like mortar

Table S2. Microprobe glass analyses, including standards.

Run & Spot ID	SiO2 WT%	TiO2 WT%	Al2O3 WT%	Cr2O3 WT%	FeO WT%	MnO WT%	MgO WT%	CaO WT%	Na2O WT%	K2O WT%	P2O5 WT%	TOTAL
Un 17 Y98_glass_1	50.79	0.94	16.89		17.20	0.31	0.56	8.48	2.63	0.07	1.19	99.07
Un 17 Y98_glass_1	51.30	0.91	17.02		15.90	0.33	0.74	8.85	2.46	0.07	1.23	98.82
Un 18 Y98_glass_2	52.86	1.52	16.93	0.08	12.13	0.38	0.84	11.27	2.38	0.05	1.06	99.50
Un 18 Y98_glass_2	52.87	1.48	16.15	0.04	12.67	0.32	0.86	11.64	2.12	0.04	0.92	99.09
Un 18 Y98_glass_2	51.21	0.92	16.94		13.63	0.32	0.86	11.40	2.19	0.03	1.28	98.78
Un 19 Y98_glass_3	50.00	1.17	17.55		15.94	0.41	0.81	8.96	2.63	0.06	1.36	98.89
Un 19 Y98_glass_3	50.15	1.12	17.41	0.03	16.22	0.40	0.71	8.83	2.63	0.05	1.28	98.84
Un 20 Y98_glass_4	50.97	0.99	16.89	0.05	16.83	0.31	0.84	8.60	2.31	0.06	1.36	99.21
Un 20 Y98_glass_4	51.52	0.87	18.06		14.62	0.32	0.74	8.50	2.63	0.07	1.39	98.72
Un 21 Y98_glass_5	51.20	0.99	17.32		16.10	0.28	0.70	8.43	2.79	0.05	1.33	99.20
Un 21 Y98_glass_5	50.99	0.95	17.99	0.06	15.02	0.39	0.82	8.77	2.43	0.07	1.38	98.87
Un 21 Y98_glass_5	50.00	1.06	16.95		17.13	0.36	0.85	8.56	2.62	0.05	1.24	98.81
Un 22 Y98_glass_6	50.66	0.81	17.29		16.11	0.37	0.71	8.94	2.39	0.04	1.36	98.67
Un 22 Y98_glass_6	51.51	0.94	17.36		15.42	0.25	0.56	8.56	2.69	0.07	1.42	98.79
Un 23 Y98_glass_7	50.20	0.97	17.54		16.04	0.28	0.78	8.71	2.52	0.06	1.41	98.51
Un 24 Y98_glass_8	49.97	0.99	16.99		16.73	0.34	0.68	8.82	2.52	0.06	1.40	98.51
Un 6 Y98_Glass_1	51.08	0.87	18.50		14.03	0.31	0.53	9.63	2.62	0.06	1.57	99.20
Un 7 Y98_Glass_2	51.89	1.11	17.71		12.94	0.29	1.04	10.60	2.23	0.07	1.26	99.14
Un 8 Y98_Glass_3	50.53	1.00	17.95		15.48	0.34	0.55	9.20	2.47	0.07	1.19	98.79
Un 9 Y98_Glass_4	51.46	1.21	16.75		14.27	0.37	0.84	10.08	2.37	0.05	1.10	98.51
Un 10 Y98_Glass_5	51.49	1.19	17.96		13.78	0.32	0.90	9.73	2.33	0.06	1.17	98.93
Un 12 Y98_Glass_7	52.14	1.02	17.59		13.08	0.32	0.97	9.64	2.58	0.07	1.23	98.63
Un 13 Y98_Glass_8	51.52	0.94	17.37		15.48	0.30	0.71	8.87	2.43	0.05	1.28	98.95
Un 14 Y98_Glass_9	52.18	0.97	17.53		14.47	0.28	0.50	8.81	2.67	0.06	1.18	98.65
Un 15 Y98_Glass_10	51.07	1.08	17.53		16.20	0.31	0.52	8.25	2.47	0.06	1.22	98.70
Un 62 Y98-f56i_glass_1_10um	54.31	1.13	11.22	0.08	15.82	0.38	4.52	11.71	0.84	0.04	0.04	100.10
Un 64 Y98-f56i_glass_3_10um	53.65	1.21	11.73	0.04	17.26	0.41	3.31	11.40	0.87	0.04		99.94
Un 65 Y98-f56i_glass_4_10um	53.81	1.14	10.96	0.05	16.52	0.43	4.35	11.63	0.85	0.04		99.78

Table S2, *continued*

Un 66 Y98-f56i_glass_5_10um	52.99	1.19	12.12		16.32	0.45	4.08	11.78	0.88	0.04		99.86
Un 67 Y98-f56i_glass_6_10um	51.87	1.33	13.13		16.48	0.38	3.64	12.26	0.85	0.04	0.07	100.06
Un 68 Y98-f56i_glass_7_10um	51.47	1.41	13.67		16.99	0.40	3.13	11.65	0.83	0.02	0.07	99.64
Un 69 Y98-f56i_glass_8_10um	54.72	1.19	11.70	0.05	15.90	0.39	3.45	11.57	0.92	0.03	0.06	99.99
Un 70 Y98-f56i_glass_9_10um	54.54	1.28	12.42		15.70	0.35	2.98	11.21	1.07	0.03		99.56
Un 71 Y98-f56i_glass_10_10um	53.66	1.23	12.78		15.76	0.41	3.33	11.76	1.02	0.05		100.01
Un 72 Y98-f56i_glass_11_10um	52.15	1.40	13.08	0.04	16.16	0.39	3.58	12.18	0.89	0.02		99.89
Un 75 Y98-f56i_glass_12_10um	54.19	1.21	11.37		16.39	0.36	3.86	11.56	0.82	0.03		99.78
Un 76 Y98-f56i_glass_13_10um	54.01	1.24	11.74	0.05	17.26	0.44	3.18	11.25	0.93	0.02		100.12
Un 78 Y98-f56i_glass_15_10um	52.38	1.30	13.08		16.69	0.34	3.55	11.61	0.87	0.04		99.85
Un 79 Y98-f56i_glass_16_10um	54.18	1.32	14.22	0.04	15.49	0.35	2.23	11.03	1.08	0.04		99.98
Un 44 Y98-f56ii_glass_2_10um	54.19	1.18	11.33	0.06	16.25	0.36	4.14	11.56	0.91	0.03		100.01
Un 45 Y98-f56ii_glass_3_10um	53.51	1.16	11.82	0.04	16.50	0.37	3.86	11.85	0.87	0.03		100.01
Un 46 Y98-f56ii_glass_4_10um	54.05	1.18	11.65	0.07	15.79	0.43	3.77	11.75	0.93	0.03	0.04	99.70
Un 47 Y98-f56ii_glass_5_10um	53.42	1.24	11.23	0.04	16.34	0.40	4.41	12.09	0.79	0.03		100.00
Un 48 Y98-f56ii_glass_6_10um	52.82	1.25	12.49	0.08	16.41	0.44	3.68	12.12	0.89	0.04	0.06	100.28
Un 49 Y98-f56ii_glass_7_10um	53.89	1.18	11.82	0.08	15.84	0.41	3.98	11.60	0.91	0.04	0.04	99.78
Un 50 Y98-f56ii_glass_8_10um	54.19	1.23	11.03	0.10	16.99	0.45	3.83	11.56	0.81	0.03	0.05	100.27
Un 52 Y98-f56ii_glass_10_10um	52.27	1.33	12.94		17.06	0.38	3.48	11.59	1.01	0.04		100.11
Un 53 Y98-f56ii_glass_11_10um	54.26	1.12	11.83		15.55	0.35	3.97	11.58	0.98	0.04		99.68
Un 54 Y98-f56ii_glass_12_10um	53.43	1.28	12.27		15.56	0.34	4.06	11.70	0.97	0.03		99.66
Un 56 Y98-f56ii_glass_14_10um	54.65	1.18	11.11	0.08	16.56	0.41	3.98	11.61	0.87	0.05		100.49
Un 59 Y98-f56ii_glass_15_10um	52.77	1.34	13.85		16.65	0.38	2.56	11.53	0.98	0.03	0.05	100.15

Table S2, *continued*

Un 60 Y98-f56ii_glass_16_10um	52.05	1.47	14.26		16.38	0.35	2.60	11.69	0.96	0.03	0.06	99.85
Un 61 Y98-f56ii_glass_17_10um	52.60	1.14	11.47		17.61	0.49	3.41	11.56	0.82	0.02		99.12
Un 100 Y98-f57i_glass_1_10um	54.72	1.33	13.33		15.73	0.39	2.44	11.47	0.61	0.04		100.06
Un 101 Y98-f57i_glass_2_10um	53.34	1.20	11.30		17.86	0.41	3.36	11.78	0.46			99.71
Un 102 Y98-f57i_glass_3_10um	53.92	1.30	12.00		17.61	0.46	2.56	11.48	0.58			99.91
Un 103 Y98-f57i_glass_4_10um	54.92	1.27	13.21		15.95	0.43	2.46	11.44	0.69	0.03		100.40
Un 104 Y98-f57i_glass_5_10um	53.65	1.20	12.46		17.14	0.49	2.95	11.53	0.58			99.99
Un 105 Y98-f57i_glass_6_10um	53.75	1.21	11.40		19.06	0.38	2.61	11.19	0.54	0.02	0.06	100.24
Un 106 Y98-f57i_glass_7_10um	54.84	1.25	12.19		17.84	0.36	1.69	10.66	0.66	0.03		99.51
Un 107 Y98-f57i_glass_8_10um	53.96	1.32	12.60		17.82	0.36	1.89	11.05	0.70	0.02		99.71
Un 108 Y98-f57i_glass_9_10um	53.79	1.30	13.31	0.05	17.02	0.42	2.35	11.40	0.73	0.02	0.08	100.45
Un 111 Y98-f57i_glass_10_10um	55.20	1.24	13.85		15.41	0.34	2.19	11.30	0.76	0.03		100.33
Un 113 Y98-f57i_glass_12_10um	53.83	1.28	11.84		19.30	0.40	2.23	10.96	0.62	0.02		100.48
Un 115 Y98-f57i_glass_14_10um	51.38	1.58	15.82		15.68	0.31	2.47	12.26	0.64	0.02		100.16
Un 117 Y98-f57i_glass_16_10um	53.59	1.25	11.81		18.59	0.40	2.70	11.46	0.60	0.02		100.43
Un 118 Y98-f57i_glass_17_10um	53.02	1.32	12.87		17.31	0.27	2.98	11.88	0.63	0.03		100.32
Un 119 Y98-f57i_glass_18_10um	53.96	1.31	12.79		17.48	0.38	2.56	11.34	0.61	0.02		100.45
Un 80 Y98-f57ii_glass_1_10um	55.98	1.33	13.18		15.73	0.44	2.00	10.94	0.71	0.03		100.33
Un 81 Y98-f57ii_glass_2_10um	52.23	1.35	12.68		18.08	0.42	2.89	11.51	0.50			99.67
Un 82 Y98-f57ii_glass_3_10um	52.40	1.29	13.58		16.00	0.41	3.74	12.20	0.46	0.03	0.07	100.17
Un 83 Y98-f57ii_glass_4_10um	54.27	1.32	13.12		16.70	0.37	2.39	11.37	0.67	0.02		100.25
Un 84 Y98-f57ii_glass_5_10um	54.66	1.34	14.10		15.51	0.33	1.82	11.39	0.70		0.06	99.92
Un 85 Y98-f57ii_glass_6_10um	53.65	1.30	11.82		18.15	0.37	2.78	11.38	0.47	0.02		99.94
Un 86 Y98-f57ii_glass_7_10um	52.07	1.35	13.47	0.06	17.95	0.43	2.76	11.71	0.51	0.03		100.34
Un 87 Y98-f57ii_glass_8_10um	54.22	1.33	14.12		15.47	0.39	2.30	11.42	0.68		0.04	99.98

Table S2, *continued*

Un 88 Y98-f57ii_glass_9_10um	53.50	1.28	13.86	0.04	15.69	0.39	2.87	11.67	0.66	0.03	0.06	100.05
Un 89 Y98-f57ii_glass_10_10um	54.15	1.39	13.38	0.04	15.74	0.40	2.86	11.88	0.62	0.02		100.49
Un 90 Y98-f57ii_glass_11_10um	55.33	1.35	13.30		14.77	0.42	2.57	11.47	0.72	0.03		99.97
Un 93 Y98-f57ii_glass_12_10um	56.75	1.27	13.84		13.90	0.29	2.44	10.97	0.87	0.02	0.07	100.41
Un 94 Y98-f57ii_glass_13_10um	53.95	1.31	12.88		16.39	0.42	2.65	11.67	0.60	0.02	0.04	99.93
Un 95 Y98-f57ii_glass_14_10um	55.75	1.31	12.76		15.49	0.38	2.34	11.15	0.67	0.03	0.04	99.93
Un 96 Y98-f57ii_glass_15_5um	53.29	1.49	19.49		10.66	0.22	2.54	11.30	1.17	0.05	0.07	100.28
Un 97 Y98-f57ii_glass_16_5um	52.76	1.37	20.41	0.05	10.57	0.23	2.24	11.23	1.16	0.03	0.06	100.10
Un 98 Y98-f57ii_glass_17_5um	53.77	1.40	20.05	0.05	10.01	0.23	2.15	11.50	1.23	0.05		100.45
Un 99 Y98-f57ii_glass_18_5um	51.61	1.70	19.11		11.18	0.29	2.93	12.61	0.86	0.02	0.05	100.36
Un 144 Y98-f62i_glass_1_10um	50.95	1.51	16.41		16.39	0.34	1.81	11.22	1.00	0.05	0.09	99.77
Un 145 Y98-f62i_glass_2_10um	52.04	1.52	14.44		16.91	0.38	1.98	11.56	0.87	0.03		99.72
Un 146 Y98-f62i_glass_3_10um	51.96	1.47	13.06		17.81	0.39	2.46	11.87	0.78	0.02	0.04	99.87
Un 147 Y98-f62i_glass_4_10um	53.71	1.24	12.14		17.34	0.41	2.42	11.08	0.84	0.03	0.06	99.27
Un 148 Y98-f62i_glass_5_10um	54.08	1.24	12.33		16.99	0.38	2.68	11.15	0.87	0.04		99.75
Un 149 Y98-f62i_glass_6_10um	51.91	1.33	12.28		19.20	0.39	2.58	10.97	0.78	0.04		99.50
Un 150 Y98-f62i_glass_7_10um	54.40	1.23	13.18		16.85	0.36	1.72	10.60	1.04	0.05	0.05	99.48
Un 151 Y98-f62i_glass_8_10um	53.50	1.26	12.09		17.88	0.37	2.69	10.84	0.86	0.03		99.52
Un 152 Y98-f62i_glass_9_10um	53.51	1.35	12.83		17.47	0.38	2.26	10.70	0.94	0.04		99.47
Un 153 Y98-f62i_glass_10_10um	52.49	1.42	14.08		17.17	0.40	2.06	11.23	0.93	0.04		99.83
Un 154 Y98-f62i_glass_11_10um	51.65	1.45	14.68		17.44	0.37	1.51	11.13	0.95	0.03	0.06	99.27
Un 155 Y98-f62i_glass_12_10um	51.79	1.39	12.90		18.64	0.43	2.38	11.55	0.83	0.03	0.05	100.00
Un 156 Y98-f62i_glass_13_10um	53.91	1.26	12.85		16.96	0.40	2.32	10.96	0.94	0.04	0.06	99.69
Un 157 Y98-f62i_glass_14_10um	54.30	1.32	13.11		16.19	0.30	2.54	11.21	0.97	0.05		100.00

Table S2, *continued*

Un 158 Y98-f62i_glass_15_10um	54.04	1.38	13.17		17.15	0.34	1.83	10.84	0.98	0.04	0.05	99.81
Un 159 Y98-f62i_glass_16_10um	53.36	1.18	11.66	0.06	18.01	0.35	2.95	11.18	0.75	0.02	0.06	99.59
Un 160 Y98-f62i_glass_17_10um	54.79	1.24	13.21		16.27	0.36	2.15	10.88	1.06	0.05	0.05	100.08
Un 163 Y98-f62i_glass_18_10um	53.51	1.36	14.79		16.39	0.43	1.54	10.81	1.08	0.05	0.05	100.01
Un 124 Y98-f62ii_glass_1_10um	53.86	1.30	13.00		16.49	0.42	2.20	11.13	0.99	0.05		99.45
Un 125 Y98-f62ii_glass_2_10um	54.25	1.31	13.86		15.75	0.34	1.67	10.85	1.07	0.06	0.05	99.21
Un 126 Y98-f62ii_glass_3_10um	53.80	1.30	12.21		16.78	0.40	2.71	11.34	0.99	0.04		99.57
Un 127 Y98-f62ii_glass_4_10um	51.81	1.47	16.04		15.81	0.39	1.82	11.49	1.12	0.04		99.99
Un 128 Y98-f62ii_glass_5_10um	50.67	1.43	17.31		16.10	0.37	1.53	11.09	1.09	0.04	0.08	99.70
Un 129 Y98-f62ii_glass_6_10um	53.00	1.25	12.52		17.14	0.35	2.78	11.23	0.88	0.03	0.06	99.25
Un 130 Y98-f62ii_glass_7_10um	53.47	1.17	11.69		17.42	0.43	2.83	11.31	0.79	0.04	0.04	99.19
Un 131 Y98-f62ii_glass_8_10um	54.59	1.29	13.93		15.71	0.32	1.70	10.67	1.09	0.05	0.04	99.40
Un 132 Y98-f62ii_glass_9_10um	51.91	1.43	15.33		15.89	0.33	1.91	11.84	1.00	0.03	0.05	99.73
Un 133 Y98-f62ii_glass_10_10um	54.10	1.27	12.64		16.82	0.36	2.19	10.77	0.99	0.04		99.19
Un 134 Y98-f62ii_glass_11_10um	52.07	1.37	13.49		17.71	0.42	2.11	11.51	0.89	0.04	0.07	99.68
Un 135 Y98-f62ii_glass_12_10um	52.23	1.30	12.72		18.41	0.50	2.30	11.08	0.86	0.03	0.05	99.48
Un 136 Y98-f62ii_glass_13_10um	52.63	1.30	13.31		16.78	0.36	2.60	11.35	0.87	0.04		99.23
Un 137 Y98-f62ii_glass_14_10um	54.09	1.34	14.51		15.48	0.36	1.65	10.59	1.30	0.05		99.36
Un 138 Y98-f62ii_glass_15_10um	52.25	1.32	13.72		17.11	0.36	2.29	11.07	0.91	0.05	0.05	99.13
Un 139 Y98-f62ii_glass_16_10um	52.64	1.38	13.25		17.69	0.41	2.09	10.96	0.92	0.03	0.05	99.42
Un 140 Y98-f62ii_glass_17_10um	52.41	1.30	12.70	0.04	17.91	0.44	2.64	11.37	0.79	0.04	0.05	99.68
Un 141 Y98-f62ii_glass_18_10um	58.66	1.29	12.93		13.99	0.37	1.37	9.63	1.31	0.06		99.60

Table S2, *continued*

Un 189 Y98-f63i_glass_6_10um	53.08	1.14	12.05		16.77	0.39	4.12	12.10	0.67	0.03		100.36
Un 190 Y98-f63i_glass_7_10um	54.37	1.11	11.00	0.05	16.71	0.40	4.15	11.76	0.72	0.04		100.32
Un 192 Y98-f63i_glass_9_10um	53.30	1.13	11.16	0.07	16.49	0.39	4.69	12.08	0.71	0.03		100.05
Un 193 Y98-f63i_glass_10_10um	51.44	1.24	12.44		16.86	0.39	4.54	12.28	0.68	0.03		99.90
Un 194 Y98-f63i_glass_11_10um	52.54	1.16	12.06	0.09	16.95	0.43	4.26	11.93	0.67	0.03		100.11
Un 195 Y98-f63i_glass_12_10um	54.24	1.14	11.42	0.07	16.33	0.44	3.99	11.55	0.69	0.03	0.04	99.94
Un 196 Y98-f63i_glass_13_10um	50.81	1.25	13.31		16.52	0.38	4.67	12.35	0.65	0.03		99.97
Un 197 Y98-f63i_glass_14_10um	52.24	1.20	12.36	0.06	15.43	0.37	4.57	12.83	0.59	0.03		99.69
Un 200 Y98-f63i_glass_15_10um	52.83	1.14	11.18	0.09	16.85	0.41	4.44	11.96	0.67	0.03		99.61
Un 201 Y98-f63i_glass_16_10um	50.67	1.37	13.21	0.05	17.47	0.47	3.80	12.27	0.69	0.03	0.04	100.08
Un 202 Y98-f63i_glass_17_10um	53.59	1.11	11.75	0.09	15.95	0.35	4.22	12.07	0.77	0.03	0.04	99.96
Un 203 Y98-f63i_glass_18_10um	50.29	1.51	15.62		14.39	0.37	3.33	13.88	0.65	0.05	0.07	100.15
Un 165 Y98-f63ii_glass_2_10um	53.78	1.24	12.19		15.22	0.45	4.27	12.31	0.65	0.02		100.12
Un 166 Y98-f63ii_glass_3_10um	52.58	1.20	11.70		16.62	0.38	4.19	12.31	0.54	0.02		99.54
Un 167 Y98-f63ii_glass_4_10um	53.13	1.29	12.19	0.05	15.83	0.42	4.19	12.34	0.61	0.02	0.04	100.12
Un 168 Y98-f63ii_glass_5_10um	54.23	1.23	11.94		14.97	0.39	4.41	12.01	0.69	0.04	0.06	99.97
Un 169 Y98-f63ii_glass_6_10um	54.20	1.25	12.01	0.07	14.97	0.40	4.27	12.18	0.65	0.02		100.02
Un 170 Y98-f63ii_glass_7_10um	53.64	1.15	11.85	0.07	15.84	0.36	4.12	11.96	0.65	0.02		99.67
Un 171 Y98-f63ii_glass_8_10um	52.56	1.28	12.36		16.00	0.44	3.78	12.09	0.57	0.02		99.11
Un 172 Y98-f63ii_glass_9_10um	52.04	1.28	11.83	0.04	16.97	0.41	4.47	12.19	0.52	0.02		99.79
Un 173 Y98-f63ii_glass_10_10um	55.05	1.25	12.24	0.04	14.39	0.35	3.89	11.79	0.68	0.04		99.72
Un 174 Y98-f63ii_glass_11_10um	52.91	1.28	12.24		16.30	0.34	4.08	12.11	0.62	0.01		99.91
Un 175 Y98-f63ii_glass_12_10um	53.99	1.26	12.78	0.06	15.14	0.37	3.88	11.93	0.68	0.02		100.11

Table S2, *continued*

Un 176 Y98-f63ii_glass_13_10um	54.19	1.30	11.72		16.01	0.42	3.84	11.80	0.67	0.02	0.04	100.02
Un 177 Y98-f63ii_glass_14_10um	52.48	1.27	11.61	0.06	16.73	0.44	4.30	12.25	0.58			99.71
Un 178 Y98-f63ii_glass_15_10um	53.45	1.30	13.69		15.09	0.29	3.05	11.91	0.75	0.03	0.05	99.62
Un 181 Y98-f63ii_glass_16_5um	52.46	1.59	18.76	0.06	10.05	0.30	3.36	12.79	0.93	0.05	0.07	100.42
Un 182 Y98-f63ii_glass_17_5um	56.91	1.29	15.60		9.50	0.23	3.48	11.56	1.13	0.06		99.76
Un 183 Y98-f63ii_glass_18_5um	54.39	1.34	15.18		10.78	0.31	4.16	12.66	0.92	0.05		99.79
Un 229 Y98-f64i_glass_6_10um	54.31	1.41	14.85		16.20	0.38	1.16	10.16	1.10	0.04	0.06	99.68
Un 230 Y98-f64i_glass_7_10um	54.76	1.35	13.90		16.70	0.35	1.62	10.47	1.00	0.03	0.08	100.26
Un 231 Y98-f64i_glass_8_10um	53.18	1.29	13.27		18.34	0.42	2.16	10.64	0.82	0.03	0.06	100.21
Un 232 Y98-f64i_glass_9_10um	54.84	1.36	14.97		15.97	0.38	1.07	10.21	1.07	0.04		99.92
Un 233 Y98-f64i_glass_10_10um	53.19	1.27	13.02		17.90	0.43	2.27	10.76	0.76	0.04	0.05	99.66
Un 234 Y98-f64i_glass_11_10um	53.20	1.29	12.79		18.82	0.47	1.60	10.40	0.88	0.03		99.49
Un 237 Y98-f64i_glass_12_10um	53.91	1.34	13.63	0.04	16.87	0.38	1.88	10.57	0.89	0.03	0.07	99.61
Un 238 Y98-f64i_glass_13_10um	55.45	1.26	15.08		15.30	0.30	1.07	10.10	0.93	0.05	0.06	99.60
Un 239 Y98-f64i_glass_14_10um	54.65	1.27	13.47		17.60	0.40	1.16	10.01	0.95	0.02	0.05	99.59
Un 240 Y98-f64i_glass_15_10um	53.88	1.47	12.65		19.32	0.42	1.08	10.07	0.66	0.02	0.06	99.63
Un 241 Y98-f64i_glass_16_10um	55.32	1.32	13.70		16.48	0.31	1.61	10.29	0.84	0.03		99.90
Un 242 Y98-f64i_glass_17_10um	53.76	1.39	14.61		16.71	0.43	1.70	10.59	0.96	0.05	0.04	100.23
Un 243 Y98-f64i_glass_18_10um	54.34	1.33	13.83		17.33	0.33	1.53	10.33	0.90	0.04		99.98
Un 204 Y98-f64ii_glass_1_10um	55.75	1.22	17.43		12.89	0.28	1.02	10.23	0.76	0.07	0.08	99.73
Un 205 Y98-f64ii_glass_2_10um	55.05	1.39	12.68		17.02	0.37	1.66	10.26	0.74	0.03		99.19
Un 206 Y98-f64ii_glass_3_10um	52.40	1.57	19.16		12.07	0.29	1.99	11.29	1.07	0.04	0.07	99.96
Un 207 Y98-f64ii_glass_4_10um	54.97	1.26	13.01		17.22	0.34	1.39	9.96	0.90	0.05	0.06	99.16

Table S2, *continued*

Un_208_Y98-f64ii_glass_5_10um	55.04	1.40	13.33		17.51	0.33	1.41	10.06	0.96	0.04		100.07
Un_209_Y98-f64ii_glass_6_10um	54.85	1.22	14.37		16.38	0.30	1.06	9.87	1.01	0.04	0.07	99.17
Un_210_Y98-f64ii_glass_7_10um	53.96	1.31	13.95		16.89	0.36	1.61	10.48	0.95	0.04	0.05	99.61
Un_211_Y98-f64ii_glass_8_10um	53.34	1.40	13.28		17.28	0.43	2.06	10.49	0.94	0.05	0.04	99.32
Un_212_Y98-f64ii_glass_9_10um	51.66	1.52	17.42		14.48	0.34	1.75	11.01	1.17	0.06	0.07	99.49
Un_213_Y98-f64ii_glass_10_10um	53.69	1.39	14.00		17.41	0.36	1.36	10.19	0.96	0.05		99.40
Un_214_Y98-f64ii_glass_11_10um	52.59	1.41	15.64		16.17	0.31	1.74	10.61	1.10	0.05	0.06	99.69
Un_215_Y98-f64ii_glass_12_10um	53.30	1.30	14.16		16.39	0.38	2.11	10.69	0.99	0.05	0.07	99.44
Un_218_Y98-f64ii_glass_13_10um	51.93	1.59	19.49		13.30	0.34	1.43	10.19	1.39	0.07	0.07	99.81
Un_219_Y98-f64ii_glass_14_10um	54.06	1.42	13.87		17.09	0.43	1.51	10.36	1.08	0.05	0.05	99.93
Un_220_Y98-f64ii_glass_15_10um	53.83	1.26	13.03		17.32	0.42	2.42	10.61	0.81	0.04		99.73
Un_221_Y98-f64ii_glass_16_5um	57.05	1.36	14.51		15.20	0.32	0.27	9.17	1.34	0.05	0.04	99.30
Un_222_Y98-f64ii_glass_17_5um	56.79	1.19	15.66		13.76	0.28	0.52	9.23	1.05	0.09		98.57
Un_223_Y98-f64ii_glass_18_5um	53.94	1.37	13.92		17.15	0.39	1.49	10.18	0.77	0.04	0.06	99.30
Un_25_Y98-f65-2i_Glass_6	53.39	1.34	13.50		16.19	0.40	2.95	11.35	0.70	0.03		99.84
Un_26_Y98-f65-2i_Glass_7	50.42	1.54	19.68		14.94	0.27	1.16	10.49	1.06	0.05	0.08	99.70
Un_27_Y98-f65-2i_Glass_8	53.25	1.34	13.09		18.22	0.43	1.95	10.82	0.77	0.02		99.91
Un_28_Y98-f65-2i_Glass_9	50.85	1.57	16.14		15.41	0.38	2.39	12.07	0.75	0.03		99.59
Un_29_Y98-f65-2i_Glass_10	51.54	1.41	14.25		18.08	0.41	2.12	10.86	0.73	0.04	0.06	99.51
Un_30_Y98-f65-2i_Glass_11	53.16	1.37	13.40		17.46	0.38	2.09	10.75	0.87	0.03		99.52
Un_31_Y98-f65-2i_Glass_12	53.52	1.43	13.42		17.35	0.40	1.78	10.52	0.87	0.03	0.04	99.36
Un_32_Y98-f65-2i_Glass_13	54.72	1.32	13.31		16.83	0.35	1.75	10.33	0.95	0.04	0.04	99.65
Un_33_Y98-f65-2i_Glass_14	53.58	1.40	15.02		15.90	0.34	1.72	10.55	0.94	0.04		99.50
Un_34_Y98-f65-2i_Glass_15	55.72	1.39	16.69		10.71	0.28	2.31	11.71	1.06	0.06		99.94
Un_54_Y98-f67-2ii_Glass_6	52.72	1.20	12.19	0.04	17.13	0.40	3.64	11.46	0.70	0.04		99.52
Un_55_Y98-f67-2ii_Glass_7	53.65	1.31	12.79		17.08	0.40	2.47	10.97	0.82	0.04		99.52

Table S2, *continued*

Un 56 Y98-f67-2ii_Glass_8	54.01	1.30	13.34		15.94	0.39	2.22	11.16	0.91	0.03	0.04	99.35
Un 57 Y98-f67-2ii_Glass_9	52.46	1.26	12.68		17.14	0.39	3.55	11.65	0.76	0.05	0.04	99.99
Un 58 Y98-f67-2ii_Glass_10	53.86	1.13	11.33	0.06	17.56	0.43	3.41	11.19	0.71	0.04		99.71
Un 59 Y98-f67-2ii_Glass_11	51.56	1.36	14.12		14.59	0.37	4.28	12.56	0.75	0.04		99.63
Un 60 Y98-f67-2ii_Glass_12	53.91	1.15	12.68	0.07	15.93	0.37	3.17	11.25	0.72	0.04	0.04	99.33
Un 61 Y98-f67-2ii_Glass_13	53.12	1.24	12.64	0.08	16.16	0.39	3.79	11.97	0.70	0.04	0.05	100.16
Un 62 Y98-f67-2ii_Glass_14	54.28	1.14	11.32	0.09	16.68	0.45	3.87	11.29	0.73	0.04		99.87
Un 63 Y98-f67-2ii_Glass_15	53.00	1.31	13.33	0.05	14.80	0.38	3.74	12.14	0.83	0.04		99.62
Un 71 Y98-f68i_Glass_6	54.15	1.54	17.22	0.05	13.65	0.38	1.37	10.60	0.66	0.04		99.64
Un 72 Y98-f68i_Glass_7	53.18	1.26	12.81		17.86	0.38	2.65	11.17	0.41			99.73
Un 73 Y98-f68i_Glass_8	52.47	1.46	15.19		16.06	0.37	2.38	11.13	0.49	0.01	0.06	99.62
Un 74 Y98-f68i_Glass_9	54.31	1.25	13.61		15.34	0.40	2.87	11.23	0.53	0.04	0.05	99.62
Un 75 Y98-f68i_Glass_10	59.50	1.05	10.62	0.22	10.13	0.29	5.35	12.26	0.42			99.83
Un 76 Y98-f68i_Glass_11	49.65	1.70	17.09		16.54	0.35	2.64	11.51	0.50	0.02	0.07	100.07
Un 77 Y98-f68i_Glass_12	51.30	1.39	13.63		17.01	0.43	3.56	11.62	0.39	0.03		99.34
Un 78 Y98-f68i_Glass_13	52.11	1.35	13.53		17.09	0.35	3.19	11.38	0.47	0.03	0.04	99.55
Un 79 Y98-f68i_Glass_14	52.34	1.33	13.30		16.42	0.36	3.83	11.43	0.48	0.03	0.06	99.58
Un 80 Y98-f68i_Glass_15	52.89	1.42	14.53		15.88	0.37	2.58	11.32	0.57	0.02		99.59
Un 84 Y98-f69i_Glass_2	52.71	1.24	13.00	0.08	15.29	0.46	5.19	12.37	0.14	0.02		100.50
Un 85 Y98-f69i_Glass_3	52.72	1.24	12.20	0.06	15.84	0.45	5.49	12.19	0.11	0.02	0.05	100.38
Un 86 Y98-f69i_Glass_4	52.38	1.42	15.11		15.39	0.42	3.16	11.80	0.16			99.84
Un 87 Y98-f69i_Glass_5	52.14	1.37	14.14	0.05	15.25	0.43	4.33	12.05	0.13	0.02		99.91
Un 88 Y98-f69i_Glass_6	52.32	1.37	14.12	0.04	15.57	0.42	4.22	11.93	0.14	0.01		100.15
Un 89 Y98-f69i_Glass_7	50.88	1.40	14.48		16.01	0.43	4.46	12.12	0.12		0.06	99.95
Un 90 Y98-f69i_Glass_8	52.09	1.26	13.44	0.09	15.28	0.44	5.00	12.28	0.13			100.00
Un 92 Y98-f69i_Glass_10	51.88	1.33	14.22		15.10	0.43	4.37	12.09	0.14	0.03		99.58
Un 93 Y98-f69i_Glass_11	51.99	1.54	16.38		14.70	0.33	2.81	11.81	0.13		0.04	99.73
Un 94 Y98-f69i_Glass_12	49.78	1.71	17.55		14.34	0.33	3.59	12.61	0.14		0.05	100.09
Un 95 Y98-f69i_Glass_13	48.17	1.81	17.98		15.77	0.40	3.54	12.16	0.12		0.06	100.02

Table S2, *continued*

Un	97	Y98-f69i_Glass_15	51.16	1.74	18.11	0.05	11.56	0.37	3.09	14.10	0.12		0.07	100.38
Un	25	A99_std_1	50.57	4.34	12.44		13.17	0.19	5.13	9.14	2.61	0.89	0.45	98.48
Un	25	A99_std_1	51.01	3.58	12.41		13.40	0.16	5.10	9.25	2.65	0.85	0.50	98.41
Un	25	A99_std_1	50.94	3.97	12.41		13.15	0.17	5.15	9.21	2.66	0.83	0.44	98.48
Un	3	A99_std_1	50.35	4.14	12.29		13.41	0.22	5.08	10.22	2.72	0.87	0.38	99.31
Un	3	A99_std_1	50.57	4.17	12.34		13.17	0.13	5.06	9.95	2.72	0.82	0.46	98.93
Un	3	A99_std_1	50.42	4.19	12.35		13.35	0.15	5.03	9.89	2.73	0.85	0.42	98.96
Un	21	A99_std_2	50.31	4.15	12.34		13.35	0.20	5.05	9.45	2.70	0.83	0.45	98.37
Un	21	A99_std_2	50.59	4.11	12.39		13.34	0.21	5.08	9.42	2.73	0.81	0.41	98.68
Un	21	A99_std_2	50.29	4.14	12.31		13.16	0.18	5.04	9.55	2.70	0.82	0.42	98.18
Un	39	A99_std_3	50.14	4.13	12.57		13.34	0.20	5.11	9.47	2.73	0.82	0.43	98.52
Un	39	A99_std_3	50.51	4.15	12.53		13.33	0.20	5.05	9.34	2.73	0.83	0.47	98.67
Un	39	A99_std_3	50.37	4.17	12.39		13.37	0.18	5.08	9.42	2.68	0.83	0.38	98.49
Un	57	A99_std_4	50.38	4.11	12.50		13.54	0.21	5.18	9.56	2.63	0.85	0.40	98.97
Un	57	A99_std_4	50.87	4.12	12.47		13.29	0.20	5.07	9.51	2.69	0.85	0.44	99.07
Un	57	A99_std_4	50.90	4.07	12.52		13.36	0.15	5.12	9.40	2.70	0.82	0.41	99.04
Un	73	A99_std_5	50.21	4.16	12.53		13.40	0.21	5.12	9.42	2.60	0.83	0.41	98.49
Un	73	A99_std_5	50.32	4.08	12.46		13.57	0.18	5.19	9.40	2.70	0.83	0.44	98.73
Un	73	A99_std_5	50.26	4.11	12.50	0.04	13.27	0.22	5.20	9.40	2.77	0.83	0.43	98.59
Un	91	A99_std_6	51.02	4.19	12.53		13.38	0.16	5.04	9.36	2.74	0.82	0.46	99.24
Un	91	A99_std_6	50.80	4.10	12.55		13.64	0.19	5.14	9.34	2.69	0.82	0.40	99.26
Un	91	A99_std_6	50.71	4.15	12.52		13.58	0.22	5.09	9.40	2.72	0.81	0.40	99.21
Un	109	A99_std_7	50.60	4.08	12.52		13.53	0.18	5.13	9.37	2.70	0.84	0.48	98.96
Un	109	A99_std_7	50.83	4.13	12.53		13.44	0.18	5.10	9.39	2.60	0.83	0.45	99.04
Un	109	A99_std_7	50.70	4.13	12.47		13.33	0.17	5.08	9.41	2.72	0.84	0.42	98.84
Un	120	A99_std_8	51.05	4.12	12.54		13.33	0.19	5.13	9.37	2.72	0.80	0.44	99.26
Un	120	A99_std_8	51.22	4.13	12.63		13.45	0.17	5.11	9.36	2.67	0.82	0.46	99.55
Un	120	A99_std_8	51.24	4.17	12.58		13.41	0.19	5.09	9.32	2.66	0.81	0.40	99.48
Un	122	A99_std_1	50.76	4.14	12.48		13.02	0.19	5.01	10.17	2.79	0.85	0.40	99.41
Un	122	A99_std_1	50.72	4.18	12.35		13.07	0.21	5.11	9.92	2.84	0.85	0.41	99.27

Table S2, *continued*

Un	122	A99_std_1	50.68	4.06	12.37		13.04	0.20	5.08	9.84	2.74	0.79	0.42	98.81
Un	142	A99_std_2	50.77	4.11	12.45		13.34	0.21	5.06	9.45	2.70	0.84	0.41	98.94
Un	142	A99_std_2	50.70	4.23	12.37	0.06	13.05	0.23	5.06	9.48	2.73	0.86	0.40	98.76
Un	142	A99_std_2	50.58	4.19	12.36		13.23	0.22	5.05	9.52	2.76	0.83	0.42	98.73
Un	161	A99_std_3	50.86	4.07	12.49		13.30	0.19	5.13	9.51	2.67	0.84	0.43	99.06
Un	161	A99_std_3	50.88	4.13	12.57		13.37	0.21	5.15	9.55	2.69	0.82	0.40	99.38
Un	161	A99_std_3	50.70	4.15	12.44		13.23	0.19	5.13	9.37	2.70	0.82	0.40	98.72
Un	179	A99_std_4	50.63	4.00	12.46		13.24	0.21	5.10	9.45	2.72	0.81	0.43	98.63
Un	179	A99_std_4	50.81	4.21	12.46		13.39	0.22	5.07	9.35	2.66	0.83	0.39	98.99
Un	179	A99_std_4	50.68	4.12	12.48		13.54	0.20	5.12	9.39	2.69	0.82	0.46	99.05
Un	198	A99_std_5	50.75	4.12	12.61		13.32	0.20	5.14	9.40	2.75	0.81	0.45	99.11
Un	198	A99_std_5	50.91	4.19	12.55		13.34	0.23	5.12	9.29	2.73	0.84	0.42	99.20
Un	198	A99_std_5	51.03	4.11	12.47		13.23	0.17	5.04	9.28	2.76	0.85	0.41	98.95
Un	216	A99_std_6	50.84	4.18	12.52		13.49	0.21	5.13	9.49	2.68	0.83	0.48	99.38
Un	216	A99_std_6	50.74	4.16	12.58		13.51	0.21	5.13	9.48	2.69	0.84	0.45	99.34
Un	216	A99_std_6	50.76	4.12	12.59		13.38	0.24	5.12	9.44	2.74	0.81	0.44	99.20
Un	235	A99_std_7	50.80	4.10	12.46		13.22	0.20	5.14	9.38	2.64	0.85	0.41	98.80
Un	235	A99_std_7	50.88	4.16	12.52		13.29	0.19	5.10	9.44	2.58	0.85	0.40	99.02
Un	235	A99_std_7	50.81	4.20	12.49		13.40	0.23	5.07	9.32	2.70	0.84	0.45	99.06
Un	244	A99_std_8	50.97	4.07	12.49		13.46	0.19	5.13	9.43	2.68	0.81	0.40	99.25
Un	244	A99_std_8	50.88	4.11	12.56		13.46	0.18	5.11	9.33	2.63	0.85	0.42	99.10
Un	244	A99_std_8	50.95	4.12	12.66		13.42	0.24	5.10	9.33	2.67	0.81	0.44	99.29
Un	4	A99_std_1	51.09	4.15	12.46		13.51	0.22	4.95	9.60	2.73	0.88	0.40	99.58
Un	4	A99_std_1	51.17	4.12	12.48		13.37	0.16	4.96	9.47	2.72	0.85	0.36	99.31
Un	4	A99_std_1	50.89	4.09	12.42		13.34	0.18	4.96	9.34	2.74	0.85	0.36	98.83
Un	16	A99_std_2	50.77	4.11	12.37		13.30	0.21	5.03	9.18	2.69	0.84	0.36	98.50
Un	16	A99_std_2	51.05	4.08	12.33		13.30	0.20	4.99	9.17	2.74	0.85	0.40	98.72
Un	16	A99_std_2	51.05	4.09	12.38		13.29	0.19	4.98	9.20	2.72	0.86	0.37	98.75
Un	23	A99_std_3	51.06	4.08	12.27		13.36	0.20	4.94	9.64	2.70	0.84	0.35	99.08
Un	23	A99_std_3	51.06	4.09	12.37		13.28	0.21	4.96	9.45	2.71	0.85	0.42	98.99

Table S2, *continued*

Un	23	A99_std_3	50.82	4.09	12.37		13.31	0.21	4.96	9.35	2.67	0.83	0.42	98.61
Un	35	A99_std_4	50.94	4.00	12.37		13.35	0.19	4.94	9.15	2.75	0.84	0.39	98.52
Un	35	A99_std_4	50.92	4.13	12.40		13.64	0.18	4.95	9.15	2.74	0.80	0.39	98.91
Un	35	A99_std_4	51.17	4.15	12.37		13.32	0.19	5.01	9.22	2.69	0.84	0.39	98.96
Un	47	A99_std_5	51.05	4.22	12.40		13.38	0.20	4.93	9.61	2.66	0.84	0.41	99.30
Un	47	A99_std_5	50.97	4.07	12.30		13.20	0.17	4.90	9.48	2.77	0.82	0.38	98.69
Un	47	A99_std_5	51.01	4.11	12.35		13.31	0.21	4.85	9.27	2.67	0.87	0.37	98.68
Un	64	A99_std_6	51.08	4.05	12.35		13.22	0.19	4.98	9.06	2.71	0.83	0.43	98.47
Un	64	A99_std_6	50.92	4.10	12.41		13.32	0.24	4.97	8.99	2.72	0.86	0.40	98.53
Un	64	A99_std_6	51.12	4.14	12.40		13.25	0.18	4.94	9.07	2.75	0.84	0.38	98.69
Un	81	A99_std_7	50.45	4.10	12.44		13.17	0.22	5.05	9.13	2.75	0.81	0.44	98.12
Un	81	A99_std_7	50.65	4.10	12.53		13.41	0.21	5.06	9.04	2.77	0.81	0.38	98.56
Un	81	A99_std_7	50.75	4.12	12.51		13.41	0.21	5.07	9.08	2.76	0.82	0.43	98.73
Un	98	A99_std_8	50.64	4.03	12.47		13.51	0.22	5.08	8.93	2.70	0.83	0.37	98.42
Un	98	A99_std_8	50.62	4.03	12.49		13.37	0.19	5.09	9.00	2.75	0.86	0.40	98.39
Un	98	A99_std_8	50.55	4.17	12.65		13.61	0.20	5.05	8.98	2.73	0.84	0.40	98.77
Un	115	A99_std_9	51.07	3.99	12.55		13.24	0.21	5.06	8.92	2.62	0.83	0.40	98.50
Un	115	A99_std_9	50.83	4.05	12.46		13.53	0.18	5.08	8.91	2.69	0.83	0.41	98.55
Un	115	A99_std_9	50.79	4.11	12.55		13.41	0.18	4.99	8.84	2.72	0.82	0.41	98.41
Un	26	VG2_std_1	50.42	1.90	13.86		11.59	0.19	6.98	11.08	2.65	0.21	0.20	99.09
Un	26	VG2_std_1	50.65	1.85	13.95		11.81	0.28	6.97	11.04	2.65	0.21	0.22	99.62
Un	26	VG2_std_1	50.43	1.75	13.90		11.58	0.23	7.00	11.13	2.70	0.18	0.21	99.12
Un	4	VG2_std_1	50.04	1.89	13.86		11.54	0.18	6.96	11.70	2.69	0.20	0.23	99.30
Un	4	VG2_std_1	49.93	1.92	13.91		11.56	0.27	6.99	11.78	2.63	0.20	0.19	99.38
Un	4	VG2_std_1	50.18	1.84	13.95		11.73	0.23	6.96	11.62	2.74	0.22	0.19	99.65
Un	22	VG2_std_2	50.02	1.85	13.88	0.05	11.80	0.24	6.98	11.55	2.73	0.19	0.19	99.48
Un	22	VG2_std_2	50.11	1.90	13.89		11.77	0.21	6.97	11.52	2.68	0.18	0.17	99.40
Un	22	VG2_std_2	50.20	1.85	13.97		11.64	0.22	6.95	11.54	2.68	0.18	0.21	99.44
Un	40	VG2_std_3	50.30	1.90	13.98		11.60	0.24	6.99	11.43	2.61	0.18	0.21	99.45
Un	40	VG2_std_3	50.01	1.94	13.91		11.78	0.22	7.01	11.36	2.64	0.18	0.19	99.24

Table S2, *continued*

Un	40	VG2_std_3	50.10	1.89	13.84		11.60	0.27	6.99	11.48	2.61	0.19	0.21	99.18
Un	58	VG2_std_4	50.49	1.83	13.98		11.72	0.19	7.08	11.38	2.69	0.20	0.18	99.74
Un	58	VG2_std_4	50.25	1.90	13.92		11.54	0.24	7.00	11.49	2.60	0.19	0.15	99.27
Un	58	VG2_std_4	50.37	1.86	13.97		11.54	0.16	7.05	11.46	2.63	0.18	0.22	99.43
Un	74	VG2_std_5	50.16	1.87	14.00		11.76	0.17	7.10	11.31	2.59	0.18	0.16	99.31
Un	74	VG2_std_5	50.30	1.79	13.97		11.65	0.19	7.04	11.35	2.72	0.19	0.21	99.41
Un	74	VG2_std_5	50.25	1.82	14.12		11.69	0.18	7.05	11.41	2.62	0.18	0.19	99.52
Un	92	VG2_std_6	50.25	1.85	13.97		11.86	0.12	7.10	11.36	2.66	0.18	0.16	99.51
Un	92	VG2_std_6	50.14	1.87	14.05		11.69	0.18	7.05	11.41	2.61	0.20	0.15	99.34
Un	92	VG2_std_6	50.20	1.89	14.01		11.77	0.20	7.09	11.24	2.70	0.19	0.17	99.46
Un	110	VG2_std_7	50.82	1.88	14.05		11.72	0.23	7.09	11.31	2.62	0.18	0.23	100.14
Un	110	VG2_std_7	50.90	1.84	14.00		11.68	0.21	7.04	11.27	2.61	0.18	0.15	99.88
Un	110	VG2_std_7	50.85	1.88	14.01		11.68	0.16	7.14	11.27	2.59	0.18	0.15	99.88
Un	121	VG2_std_8	50.46	1.86	14.10		11.59	0.18	7.03	11.27	2.66	0.19	0.23	99.57
Un	121	VG2_std_8	50.67	1.86	14.01		11.69	0.23	7.05	11.37	2.64	0.18	0.21	99.90
Un	121	VG2_std_8	50.42	1.85	14.06		11.65	0.18	7.00	11.19	2.63	0.19	0.19	99.35
Un	123	VG2_std_1	50.11	1.86	13.82		11.39	0.19	6.97	11.87	2.74	0.21	0.14	99.28
Un	123	VG2_std_1	50.16	1.97	13.81		11.65	0.23	6.98	11.75	2.71	0.20	0.16	99.62
Un	123	VG2_std_1	50.09	1.86	13.89	0.05	11.80	0.19	6.98	11.73	2.67	0.18	0.17	99.62
Un	143	VG2_std_2	50.22	1.83	13.77		11.68	0.19	7.01	11.43	2.68	0.18	0.18	99.18
Un	143	VG2_std_2	50.00	1.86	13.81		11.56	0.17	6.98	11.49	2.71	0.18	0.19	98.95
Un	143	VG2_std_2	50.18	1.88	13.83		11.82	0.20	6.97	11.38	2.64	0.20	0.17	99.29
Un	162	VG2_std_3	50.50	1.88	13.94		11.60	0.20	7.02	11.38	2.65	0.18	0.16	99.50
Un	162	VG2_std_3	50.36	1.89	13.89		11.73	0.22	6.96	11.39	2.68	0.18	0.18	99.47
Un	162	VG2_std_3	50.53	1.89	13.96		11.47	0.21	7.02	11.29	2.79	0.21	0.16	99.51
Un	180	VG2_std_4	50.26	1.85	14.00		11.47	0.26	7.05	11.32	2.60	0.19	0.18	99.19
Un	180	VG2_std_4	50.25	1.91	13.94	0.07	11.81	0.20	7.02	11.43	2.74	0.20	0.19	99.76
Un	180	VG2_std_4	50.21	1.91	14.03		11.75	0.21	7.00	11.33	2.71	0.17	0.15	99.47
Un	199	VG2_std_5	50.32	1.86	13.92		11.64	0.21	7.14	11.24	2.65	0.18	0.20	99.36
Un	199	VG2_std_5	50.36	1.84	14.00		11.71	0.23	7.08	11.18	2.60	0.19	0.20	99.40

Table S2, *continued*

Un	199	VG2_std_5	50.45	1.88	14.14		11.74	0.19	7.01	11.13	2.62	0.17	0.17	99.51
Un	217	VG2_std_6	50.45	1.87	13.98		11.63	0.21	7.09	11.23	2.73	0.19	0.18	99.56
Un	217	VG2_std_6	50.57	1.86	14.03		11.55	0.19	7.08	11.22	2.67	0.19	0.18	99.55
Un	217	VG2_std_6	50.61	1.88	14.11		11.68	0.21	7.01	11.11	2.66	0.19	0.18	99.63
Un	236	VG2_std_7	50.72	1.80	13.97		11.54	0.25	7.06	11.11	2.67	0.19	0.22	99.54
Un	236	VG2_std_7	50.74	1.87	14.04	0.06	11.80	0.18	7.04	11.11	2.60	0.18	0.19	99.79
Un	236	VG2_std_7	50.74	1.88	13.97		11.74	0.18	6.99	11.10	2.64	0.21	0.19	99.65
Un	245	VG2_std_8	50.83	1.85	14.05		11.62	0.17	6.99	11.21	2.59	0.20	0.20	99.70
Un	245	VG2_std_8	50.63	1.88	13.97		11.68	0.22	7.01	11.07	2.62	0.19	0.23	99.50
Un	245	VG2_std_8	50.58	1.83	14.07	0.04	11.56	0.22	7.01	11.13	2.66	0.19	0.16	99.45
Un	5	VG2_std_1	50.53	1.85	13.85	0.07	11.60	0.19	6.92	11.25	2.69	0.18	0.19	99.32
Un	5	VG2_std_1	50.42	1.82	13.83		11.65	0.21	6.86	11.35	2.69	0.18	0.20	99.22
Un	5	VG2_std_1	50.66	1.90	13.90		11.62	0.22	6.90	11.23	2.65	0.18	0.16	99.42
Un	17	VG2_std_2	50.68	1.86	13.83		11.54	0.22	6.90	10.87	2.70	0.19	0.18	98.96
Un	17	VG2_std_2	50.51	1.85	13.83		11.59	0.19	6.93	10.83	2.68	0.20	0.17	98.78
Un	17	VG2_std_2	50.52	1.83	13.91		11.53	0.19	6.80	10.82	2.67	0.20	0.19	98.66
Un	24	VG2_std_3	50.32	1.81	13.86		11.76	0.19	6.83	11.11	2.62	0.20	0.13	98.83
Un	24	VG2_std_3	50.13	1.86	13.87	0.04	11.63	0.18	6.87	11.04	2.70	0.19	0.19	98.70
Un	36	VG2_std_4	50.36	1.87	13.72		11.55	0.26	6.80	10.93	2.77	0.19	0.17	98.62
Un	36	VG2_std_4	50.47	1.87	13.84		11.66	0.21	6.82	11.04	2.67	0.20	0.18	98.96
Un	36	VG2_std_4	50.26	1.88	13.75		11.80	0.18	6.82	10.97	2.77	0.20	0.18	98.80
Un	48	VG2_std_5	50.53	1.83	13.92		11.58	0.17	6.82	11.20	2.75	0.19	0.18	99.16
Un	48	VG2_std_5	50.46	1.87	13.97		11.56	0.23	6.86	11.25	2.73	0.18	0.16	99.28
Un	48	VG2_std_5	50.40	1.86	13.83		11.43	0.19	6.85	11.23	2.75	0.18	0.20	98.91
Un	65	VG2_std_6	50.78	1.86	13.94		11.57	0.21	6.93	10.94	2.68	0.17	0.18	99.28
Un	65	VG2_std_6	50.39	1.87	13.99		11.62	0.19	6.94	10.92	2.68	0.20	0.17	98.97
Un	65	VG2_std_6	50.35	1.86	13.90		11.46	0.21	6.81	10.90	2.69	0.20	0.16	98.54
Un	82	VG2_std_7	50.27	1.81	13.96	0.06	11.89	0.20	6.93	10.97	2.72	0.20	0.16	99.17
Un	82	VG2_std_7	50.15	1.87	13.99		11.57	0.19	6.96	10.84	2.70	0.20	0.16	98.62
Un	82	VG2_std_7	50.35	1.81	13.97		11.75	0.23	6.95	10.92	2.67	0.20	0.21	99.06

Table S2, *continued*

Un	99	VG2_std_8	50.59	1.87	14.15	11.82	0.24	6.95	10.82	2.73	0.19	0.18	99.54
Un	99	VG2_std_8	50.36	1.86	14.00	11.75	0.20	6.99	10.85	2.72	0.19	0.15	99.08
Un	99	VG2_std_8	50.54	1.81	14.08	11.85	0.22	6.96	10.83	2.70	0.19	0.22	99.38
Un	116	VG2_std_9	50.68	1.82	14.00	11.70	0.21	6.91	10.78	2.66	0.17	0.17	99.11
Un	116	VG2_std_9	50.39	1.82	13.90	11.72	0.23	6.99	10.80	2.69	0.18	0.16	98.88
Un	116	VG2_std_9	50.23	1.83	14.05	11.74	0.19	6.97	10.71	2.64	0.18	0.13	98.67

Notes- Light grey shading indicates intercumulus glass (f57ii, f63ii); Blank cells indicate concentrations below detection limit

Table S3. Microprobe olivine analyses, including standards.

	IDENTIFIER	SiO2 WT%	Al2O3 WT%	Cr2O3 WT%	FeO WT%	MnO WT%	MgO WT%	CaO WT%	TOTAL	Fo
CORES	Un 6 olivine_1	40.25	0.05	0.42	14.28	0.31	45.04	0.17	100.59	84.90
	Un 11 olivine_2_core	39.74	0.05	0.44	14.80	0.34	44.33	0.17	100.02	84.22
	Un 15 olivine_4_core	39.80	0.04	0.43	14.75	0.35	44.19	0.17	99.82	84.23
	Un 16 olivine_5_rim to core	38.10	0.03	0.25	22.26	0.45	38.46	0.26	100.01	75.49
	Un 16 olivine_5_rim to core	37.88	0.22	0.33	22.10	0.50	38.29	0.23	99.97	75.55
	Un 21 olivine_6_core	39.32		0.38	14.66	0.30	44.30	0.18	99.24	84.34
	Un 24 olivine_7_unaltered to fusion crust	38.58	0.04	0.30	19.75	0.44	40.25	0.20	99.65	78.42
	Un 24 olivine_7_unaltered to fusion crust	38.71	0.04	0.32	20.04	0.40	40.34	0.21	100.14	78.21
	Un 34 olivine_5_rim to core2	38.30		0.26	22.08	0.45	38.74	0.26	100.29	75.77
	Un 2 ol_1_core_check	39.67	0.03	0.39	14.24	0.32	45.81	0.16	100.71	85.15
	Un 52 ol_5_traverse_a	37.66	0.03	0.31	22.22	0.47	38.13	0.27	99.36	75.37
	Un 52 ol_5_traverse_a	37.79	0.04	0.33	21.92	0.49	38.82	0.25	99.98	75.94
*	Un 40 olivine_9_core	38.03	0.08	0.20	25.06	0.52	36.53	0.33	100.90	72.21
RIMS	Un 24 olivine_7_unaltered to fusion crust	38.37	0.03	0.26	21.96	0.51	39.35	0.27	100.84	76.16
	Un 24 olivine_7_unaltered to fusion crust	38.37	0.11	0.33	18.30	0.39	41.05	0.25	98.94	79.99
*	Un 13 olivine_3_rim to core	35.48	0.30	0.12	36.79	0.67	25.72	0.35	99.52	55.48
*	Un 13 olivine_3_rim to core	37.72	0.09	0.23	23.57	0.50	36.77	0.28	99.31	73.55
*	Un 16 olivine_5_rim to core	38.36	0.03	0.19	23.31	0.45	38.15	0.29	100.83	74.47
	Un 20 olivine_6_rim	38.61	0.05	0.25	21.47	0.44	39.59	0.26	100.77	76.68
	Un 22 olivine_6_bound_lower	38.82	0.05	0.34	18.90	0.44	41.22	0.19	100.08	79.54
	Un 23 olivine_6_bound_upper	39.94	0.04	0.39	14.58	0.27	43.99	0.19	99.51	84.32
*	Un 31 olivine_8_rim to core	37.35	0.14	0.19	24.92	0.51	35.89	0.33	99.53	71.97
	Un 34 olivine_5_rim to core2	36.08	0.13	0.10	34.55	0.65	28.72	0.40	100.81	59.70
	Un 34 olivine_5_rim to core2	38.16	0.08	0.19	23.92	0.53	37.02	0.31	100.31	73.40
	Un 34 olivine_5_rim to core2	38.25	0.05	0.22	22.73	0.48	38.39	0.29	100.48	75.07
	Un 52 ol_5_traverse_a	36.31	0.13	0.10	30.44	0.60	32.16	0.41	100.18	65.32

Table S3, *continued*

	Un 52 ol_5_traverse_a	37.83	0.13	0.21	22.11	0.48	37.55	0.32	98.71	75.17
	Un 52 ol_5_traverse_a	37.46	0.11	0.16	25.13	0.58	36.64	0.34	100.44	72.22
	Un 52 ol_5_traverse_a	36.52	0.14	0.16	29.10	0.57	32.92	0.35	99.87	66.85
	Un 53 ol_5_traverse_b	38.22	0.03	0.27	21.94	0.47	39.20	0.24	100.51	76.10
	Un 53 ol_5_traverse_b	38.66	0.08	0.30	23.31	0.51	35.61	0.22	99.05	73.14
	Un 53 ol_5_traverse_b	37.59	0.73	0.25	22.07	0.49	38.02	0.23	99.60	75.43
	Un 54 ol_5_traverse_c	37.77	0.12	0.26	22.74	0.52	37.20	0.29	99.10	74.47
	Un 54 ol_5_traverse_c	38.13	0.07	0.27	22.20	0.48	38.21	0.28	99.99	75.42
	Un 54 ol_5_traverse_c	38.53	0.26	0.27	23.67	0.53	34.72	0.31	98.50	72.34
	Un 54 ol_5_traverse_c	37.94	0.05	0.31	21.83	0.44	39.32	0.21	100.34	76.25
	Un 54 ol_5_traverse_c	38.39	0.03	0.31	21.96	0.44	38.83	0.22	100.39	75.91
BRIGHT RIMS	Un 7 ol_1_ol dendrite_b	31.56	0.70		57.46	1.16	7.81	1.04	100.52	19.50
	Un 10 ol_1_ol dendrite_e	32.17	0.38		53.09	0.96	12.15	0.72	100.00	28.97
	Un 18 ol_2_bright rim_a	32.80	0.19		48.58	0.80	17.11	0.40	100.42	38.57
	Un 22 ol_4_ol dendrite_b	31.08	0.93		58.58	1.09	6.98	0.76	100.54	17.52
	Un 26 ol_6_bright rim_a	33.16	0.20		46.74	0.80	18.21	0.46	100.01	40.98
	Un 36 ol_9_bright rim_a	32.87	0.22	0.57	49.02	0.77	15.86	0.54	100.07	36.59
	Un 47 ol_dendrite_5	30.05	0.63	0.04	56.10	0.93	10.14	0.70	99.57	24.38
CORES	Un 116 Y98-f56i_olivine_1_core	39.43	0.04	0.39	14.67	0.34	44.49	0.19	99.54	84.39
	Un 118 Y98-f56i_olivine_2_core	39.01	0.05	0.42	15.16	0.35	44.00	0.19	99.17	83.80
	Un 120 Y98-f56i_olivine_3_core	38.99	0.06	0.45	15.32	0.36	43.59	0.18	98.95	83.53
	Un 122 Y98-f56i_olivine_4_core	39.03	0.04	0.43	15.29	0.33	43.86	0.18	99.17	83.65
	Un 124 Y98-f56i_olivine_5_core	39.23	0.05	0.40	15.40	0.38	43.54	0.18	99.19	83.44
RIMS	Un 117 Y98-f56i_olivine_1_rim	38.14	0.02	0.36	21.92	0.48	37.84	0.24	98.99	75.47
	Un 119 Y98-f56i_olivine_2_rim	37.79	0.05	0.31	22.21	0.50	37.98	0.27	99.11	75.30
	Un 121 Y98-f56i_olivine_3_rim	38.38		0.43	19.99	0.46	39.53	0.22	99.00	77.91
	Un 123 Y98-f56i_olivine_4_rim	36.97	0.04	0.20	25.32	0.50	35.22	0.29	98.53	71.26
BRIGHT RIMS	Un 99 Y98-f56i_olivine_outer_2	37.55	0.06	0.13	26.53	0.53	33.84	0.28	98.93	69.45
CORES	Un 142 Y98-f57i_olivine_1_core	38.64	0.04	0.46	18.56	0.40	40.66	0.19	98.94	79.62

Table S3, *continued*

	Un 144 Y98-f57i_olivine_2_core	39.44	0.05	0.38	14.43	0.31	44.32	0.18	99.10	84.55
	Un 146 Y98-f57i_olivine_3_core	39.46	0.02	0.41	15.05	0.34	44.01	0.19	99.48	83.90
	Un 148 Y98-f57i_olivine_4_core	38.17	0.03	0.38	22.01	0.47	37.86	0.24	99.16	75.41
RIMS	Un 143 Y98-f57i_olivine_1_rim	37.10	0.03	0.27	27.07	0.51	33.55	0.26	98.80	68.84
	Un 145 Y98-f57i_olivine_2_rim	38.41	0.04	0.27	21.30	0.48	38.34	0.24	99.06	76.24
	Un 147 Y98-f57i_olivine_3_rim	37.88	0.05	0.39	23.86	0.47	37.12	0.25	100.02	73.50
	Un 149 Y98-f57i_olivine_4_rim	36.57	0.07	0.22	30.49	0.64	30.92	0.36	99.29	64.38
CORES	Un 2 Y98-f62i_olivine_6_core	38.43	0.05	0.50	20.87	0.45	38.64	0.24	99.18	76.75
	Un 30 Y98-f62i_olivine_2_core	39.51	0.04	0.44	15.53	0.35	43.20	0.17	99.24	83.21
	Un 32 Y98-f62i_olivine_3_core	38.95	0.03	0.47	16.38	0.37	42.80	0.20	99.20	82.32
	Un 34 Y98-f62i_olivine_4_core	39.39	0.02	0.42	15.17	0.33	43.64	0.20	99.17	83.68
	Un 36 Y98-f62i_olivine_5_core	39.10	0.04	0.47	17.29	0.40	41.69	0.21	99.22	81.13
RIMS	Un 3 Y98-f62i_olivine_6_rim	36.71	0.04	0.31	30.27	0.64	30.67	0.33	98.99	64.36
	Un 29 Y98-f62i_olivine_1_rim	38.57	0.03	0.48	20.02	0.45	39.27	0.24	99.06	77.76
	Un 31 Y98-f62i_olivine_2_rim	38.78	0.03	0.27	19.62	0.49	39.38	0.22	98.80	78.15
	Un 33 Y98-f62i_olivine_3_rim	37.55	0.03	0.54	22.90	0.53	37.20	0.26	99.00	74.33
	Un 35 Y98-f62i_olivine_4_rim	38.69	0.02	0.31	18.86	0.41	40.91	0.22	99.45	79.46
	Un 37 Y98-f62i_olivine_5_rim	38.52	0.03	0.45	20.85	0.42	38.91	0.22	99.39	76.89
BRIGHT RIMS	Un 8 Y98-f62i_olivine_near4_outer	36.05	0.05	0.09	34.62	0.68	26.53	0.48	98.53	57.73
CORES	Un 90 Y98-f63i_olivine_1_core	39.42	0.05	0.42	15.07	0.30	44.64	0.17	100.07	84.08
	Un 92 Y98-f63i_olivine_2_core	39.12	0.03	0.46	16.41	0.37	43.32	0.20	99.92	82.48
	Un 94 Y98-f63i_olivine_3_core	39.44	0.05	0.41	14.47	0.31	44.78	0.17	99.63	84.66
	Un 96 Y98-f63i_olivine_4_core	39.02	0.05	0.48	16.72	0.40	42.39	0.19	99.23	81.88
	Un 98 Y98-f63i_olivine_5_core	39.33	0.03	0.42	15.22	0.34	44.61	0.18	100.14	83.93
RIMS	Un 91 Y98-f63i_olivine_1_rim	37.84	0.03	0.29	22.94	0.51	37.72	0.24	99.56	74.56
	Un 93 Y98-f63i_olivine_2_rim	37.41	0.05	0.24	25.95	0.57	34.99	0.32	99.53	70.62
	Un 95 Y98-f63i_olivine_3_rim	38.43	0.04	0.43	21.57	0.49	38.04	0.23	99.24	75.87
	Un 97 Y98-f63i_olivine_4_rim	37.78	0.02	0.33	23.77	0.52	36.06	0.23	98.72	73.01
	Un 99 Y98-f63i_olivine_5_rim	38.18	0.04	0.43	20.24	0.43	39.72	0.23	99.30	77.77

Table S3, *continued*

BRIGHT RIMS	Un 20 Y98-f63i_olivine_3_outer	37.68	0.47	0.11	31.97	0.66	28.00	0.66	99.63	60.96
	Un 21 Y98-f63i_olivine_5_outer	37.11	0.07	0.14	27.47	0.54	32.80	0.36	98.54	68.04
CORES	Un 25 Y98-f64i_Olivine_1_core	39.11	0.03	0.43	15.08	0.30	44.69	0.18	99.82	84.09
	Un 27 Y98-f64i_Olivine_2_core	38.89	0.04	0.38	14.88	0.33	44.66	0.18	99.38	84.25
	Un 29 Y98-f64i_Olivine_3_core	38.89	0.03	0.43	14.90	0.32	44.65	0.17	99.39	84.23
	Un 31 Y98-f64i_Olivine_4_core	38.67	0.03	0.45	16.37	0.37	43.28	0.18	99.35	82.49
RIMS	Un 28 Y98-f64i_Olivine_2_rim	37.14	0.08	0.16	25.77	0.53	35.25	0.30	99.23	70.91
	Un 30 Y98-f64i_Olivine_3_rim	36.17	0.08	0.22	31.20	0.56	31.01	0.36	99.63	63.93
	Un 32 Y98-f64i_Olivine_4_rim	36.97	0.05	0.22	25.54	0.48	35.64	0.30	99.23	71.33
BRIGHT RIMS	Un 37 Y98-f64i_Olivine_7_br_focused	35.51	0.56	0.06	39.01	0.71	23.05	1.01	100.05	51.30
CORES	Un 128 Y98-f65-2i_olivine_1_core	39.81	0.03	0.42	16.30	0.36	43.56	0.19	100.67	82.65
	Un 130 Y98-f65-2i_olivine_2_core	39.55	0.03	0.42	15.31	0.35	43.93	0.18	99.77	83.65
	Un 132 Y98-f65-2i_olivine_3_core	39.62	0.02	0.41	14.83	0.32	44.18	0.17	99.55	84.15
	Un 134 Y98-f65-2i_olivine_4_core	39.52	0.02	0.44	15.61	0.33	43.58	0.18	99.68	83.27
	Un 136 Y98-f65-2i_olivine_5_core	39.74	0.02	0.44	15.54	0.36	44.10	0.18	100.39	83.50
RIMS	Un 129 Y98-f65-2i_olivine_1_rim	37.61	0.04	0.23	26.71	0.58	34.46	0.32	99.98	69.70
	Un 131 Y98-f65-2i_olivine_2_rim	38.12	0.02	0.28	23.09	0.48	37.04	0.23	99.30	74.09
	Un 133 Y98-f65-2i_olivine_3_rim	37.60	0.04	0.20	26.41	0.56	34.43	0.28	99.55	69.91
	Un 135 Y98-f65-2i_olivine_4_rim	37.29	0.05	0.19	28.69	0.58	33.02	0.33	100.15	67.23
	Un 137 Y98-f65-2i_olivine_5_rim	38.20	0.04	0.21	22.62	0.46	37.78	0.21	99.52	74.86
BRIGHT RIMS	Un 124 Y98-f65-2i_olivine_1_outer	35.73	0.05	0.13	36.25	0.77	25.24	0.47	98.64	55.37
	Un 125 Y98-f65-2i_olivine_5_outer	35.65	0.04	0.05	35.02	0.68	26.78	0.45	98.73	57.69
	Un 93 Y98-f65-2i_Olivine_1_focused	35.11	0.19	0.03	36.42	0.66	25.81	0.71	99.04	55.82
	Un 94 Y98-f65-2i_Olivine_2_focused	34.84	0.15	0.05	38.21	0.71	24.37	0.68	99.10	53.20
CORES	Un 59 Y98-f67-2ii_olivine_1_core	38.97	0.02	0.39	15.04	0.35	44.04	0.18	98.99	83.92
	Un 61 Y98-f67-2ii_olivine_2_core	38.93	0.08	0.43	15.77	0.33	43.66	0.19	99.40	83.15
	Un 63 Y98-f67-2ii_olivine_3_core	38.95	0.03	0.41	15.04	0.30	44.23	0.19	99.15	83.98
	Un 65 Y98-f67-2ii_olivine_4_core	38.79	0.03	0.41	16.03	0.34	43.39	0.18	99.18	82.83

Table S3, *continued*

	Un 67 Y98-f67-2ii_olivine_5_core	38.90	0.04	0.40	15.41	0.34	43.78	0.18	99.07	83.51
RIMS	Un 60 Y98-f67-2ii_olivine_1_rim	37.84	0.06	0.33	21.66	0.49	38.13	0.29	98.83	75.83
	Un 62 Y98-f67-2ii_olivine_2_rim	38.11	0.05	0.39	20.44	0.46	39.41	0.23	99.08	77.46
	Un 64 Y98-f67-2ii_olivine_3_rim	37.53	0.05	0.30	22.82	0.45	37.32	0.23	98.70	74.46
	Un 66 Y98-f67-2ii_olivine_4_rim	37.30	0.03	0.41	24.11	0.53	36.30	0.25	98.95	72.85
	Un 68 Y98-f67-2ii_olivine_5_rim	37.29	0.06	0.34	23.82	0.51	36.58	0.25	98.88	73.25
BRIGHT RIMS	Un 14 Y98-f67-2ii_olivine_3_outer	34.99	0.20	0.07	37.72	0.74	25.19	0.76	99.77	54.35
	Un 56 Y98-f67-2ii_Olivine_2_focused	35.24	0.60	0.08	37.37	0.76	24.03	0.78	98.94	53.41
CORES	Un 12 Y98-f68i_olivine_1_core	39.01	0.03	0.40	14.81	0.32	44.49	0.18	99.24	84.26
	Un 14 Y98-f68i_olivine_2_core	38.73	0.02	0.44	15.42	0.34	43.69	0.17	98.81	83.47
	Un 16 Y98-f68i_olivine_3_core	38.64	0.05	0.42	15.89	0.37	43.63	0.19	99.17	83.04
RIMS	Un 17 Y98-f68i_olivine_3_rim	37.28	0.05	0.11	24.48	0.50	35.82	0.30	98.55	72.29
OLIVINE IN PX	Un 18 Y98-f68i_olivine_4	37.96	0.03	0.37	20.09	0.47	39.81	0.19	98.92	77.94
	Un 19 Y98-f68i_olivine_5	38.32	0.04	0.37	17.48	0.39	41.74	0.18	98.51	80.97
BRIGHT RIMS	Un 3 Y98-f68i_olivine_2_outer	35.77	0.35	0.06	34.57	0.66	26.65	0.45	98.55	57.88
	Un 61 Y98-f68i_Olivine_1_focused	35.06	0.23	0.09	35.94	0.70	26.25	0.45	98.77	56.56
CORES	Un 57 Y98-f69i_olivine_1_core_a	39.14	0.02	0.38	15.61	0.35	43.88	0.17	99.56	83.37
	Un 58 Y98-f69i_olivine_1_core_b	39.27	0.03	0.41	14.28	0.32	44.64	0.16	99.14	84.78
	Un 59 Y98-f69i_olivine_1_core_c	38.99	0.02	0.43	15.01	0.37	43.79	0.18	98.79	83.87
RIMS	Un 60 Y98-f69i_olivine_1_rim_a	37.49	0.04	0.11	23.03	0.56	37.14	0.29	98.66	74.20
	Un 61 Y98-f69i_olivine_1_rim_b	36.88	0.03	0.06	26.96	0.57	34.25	0.42	99.23	69.36
	Un 62 Y98-f69i_olivine_1_rim_c	36.33	0.07	0.04	29.98	0.66	31.50	0.48	99.13	65.19
BRIGHT RIMS	Un 39 Y98-f69i_olivine_1_outer_b	36.15	1.01	0.03	34.06	0.68	25.74	1.57	99.45	57.40
CORES	Un 75 Y98-f69ii_olivine_1_core_a	38.21		0.30	18.33	0.47	41.14	0.19	98.66	80.01
	Un 76 Y98-f69ii_olivine_1_core_b	38.21	0.03	0.30	18.45	0.45	41.04	0.19	98.68	79.86
RIMS	Un 78 Y98-f69ii_olivine_1_rim_b	37.92	0.02	0.14	21.84	0.49	38.22	0.25	98.87	75.73
STAND.	Un 17 ol_USNM_std	39.26	0.01	0.02	16.37	0.33	43.47	0.01	99.48	82.56
	Un 17 ol_USNM_std	39.31	0.01	0.02	16.52	0.27	43.65	0.02	99.83	82.49
	Un 17 ol_USNM_std	39.30	0.00	0.01	16.41	0.35	43.66	0.02	99.76	82.58

Table S3, *continued*

Un	42	ol_USNM_std_1	39.24	0.01	0.02	16.51	0.30	43.52	0.01	99.64	82.45
Un	42	ol_USNM_std_1	39.43	0.00	0.04	16.47	0.34	43.55	0.01	99.84	82.50
Un	42	ol_USNM_std_1	39.22	0.00	0.00	16.39	0.26	43.53	0.00	99.41	82.56
Un	50	std_ol_USNM_1	38.95	0.00	0.03	16.48	0.32	43.80	0.01	99.59	82.58
Un	50	std_ol_USNM_1	38.90	0.00	0.04	16.55	0.31	43.99	0.01	99.83	82.58
Un	50	std_ol_USNM_1	38.71	0.00	0.02	16.43	0.36	43.86	0.03	99.42	82.64
Un	4	USNM_ol_std_1	39.13	0.00	0.00	16.31	0.30	43.51	0.02	99.28	82.62
Un	4	USNM_ol_std_1	39.12	0.00	0.02	16.13	0.32	43.45	0.01	99.06	82.77
Un	4	USNM_ol_std_1	39.11	0.00	0.03	16.39	0.33	43.71	0.00	99.57	82.62
Un	57	USNM_ol_std_2	39.17	0.00	0.02	16.08	0.28	43.43	0.01	98.99	82.80
Un	57	USNM_ol_std_2	39.16	0.00	0.02	16.20	0.33	43.41	0.00	99.11	82.69
Un	57	USNM_ol_std_2	39.20	0.00	0.02	16.00	0.31	43.36	0.00	98.93	82.85
Un	88	USNM_ol_std_3	38.95	0.00	0.02	16.34	0.31	44.03	0.02	99.68	82.77
Un	88	USNM_ol_std_3	39.11	0.00	0.02	16.35	0.29	44.22	0.01	100.00	82.82
Un	88	USNM_ol_std_3	39.07	0.00	0.01	16.56	0.31	44.05	0.01	100.01	82.59
Un	116	USNM_ol_std_4	39.00	0.00	0.02	16.43	0.32	43.76	0.00	99.55	82.61
Un	116	USNM_ol_std_4	38.83	0.00	0.01	16.32	0.31	43.75	0.00	99.24	82.69
Un	116	USNM_ol_std_4	38.97	0.00	0.00	16.46	0.30	43.68	0.00	99.42	82.55
Un	126	USNM_ol_std_5	39.55	0.00	0.03	16.31	0.29	43.46	0.01	99.66	82.61
Un	126	USNM_ol_std_5	39.55	0.00	0.03	16.45	0.30	43.50	0.00	99.83	82.50
Un	126	USNM_ol_std_5	39.53	0.00	0.02	16.39	0.29	43.43	0.01	99.70	82.53
Un	159	USNM_ol_std_6	39.10	0.00	0.02	16.47	0.32	43.66	0.01	99.59	82.53
Un	159	USNM_ol_std_6	39.36	0.00	0.03	16.47	0.29	43.55	0.02	99.72	82.50
Un	159	USNM_ol_std_6	39.16	0.00	0.01	16.43	0.33	43.59	0.01	99.53	82.55
Un	10	USNM_ol_std_7	38.85	0.00	0.01	16.17	0.32	43.26	0.01	98.64	82.67
Un	10	USNM_ol_std_7	38.88	0.00	0.02	16.24	0.31	43.42	0.01	98.91	82.66
Un	10	USNM_ol_std_7	38.96	0.00	0.01	16.13	0.32	43.41	0.01	98.86	82.75
Un	36	USNM_ol_std_8	39.13	0.00	0.00	16.15	0.31	43.31	0.02	98.93	82.69
Un	36	USNM_ol_std_8	39.11	0.00	0.02	16.09	0.31	43.35	0.01	98.90	82.77
Un	36	USNM_ol_std_8	39.20	0.00	0.01	16.37	0.32	43.53	0.01	99.45	82.58

Table S3, *continued*

Un	55	USNM_ol_std_9	38.99	0.00	0.02	16.24	0.33	43.74	0.00	99.34	82.77
Un	55	USNM_ol_std_9	38.88	0.00	0.02	16.01	0.32	43.48	0.01	98.73	82.88
Un	55	USNM_ol_std_9	38.85	0.01	0.02	16.15	0.31	43.67	0.01	99.04	82.82
Un	94	USNM_ol_std_10	39.07	0.00	0.03	16.27	0.34	43.61	0.02	99.34	82.69
Un	94	USNM_ol_std_10	39.00	0.00	0.02	16.19	0.30	43.46	0.01	98.99	82.72
Un	94	USNM_ol_std_10	39.08	0.00	0.01	16.29	0.31	43.57	0.01	99.28	82.66
Un	96	USNM_ol_std_11	39.12	0.00	0.02	16.26	0.28	43.52	0.02	99.22	82.67
Un	96	USNM_ol_std_11	39.19	0.00	0.03	16.30	0.29	43.55	0.01	99.38	82.65
Un	96	USNM_ol_std_11	39.25	0.00	0.03	16.34	0.30	43.66	0.01	99.61	82.65
Un	114	USNM_ol_std_12	38.97	0.01	0.02	16.12	0.28	43.49	0.00	98.91	82.78
Un	114	USNM_ol_std_12	38.87	0.00	0.02	16.35	0.30	43.47	0.01	99.03	82.57
Un	114	USNM_ol_std_12	38.92	0.00	0.01	16.17	0.30	43.71	0.01	99.13	82.82
Un	140	USNM_ol_std_13	39.16	0.00	0.02	16.24	0.32	43.41	0.01	99.16	82.65
Un	140	USNM_ol_std_13	39.06	0.00	0.02	16.36	0.32	43.43	0.01	99.21	82.55
Un	140	USNM_ol_std_13	39.13	0.00	0.02	16.34	0.32	43.32	0.01	99.16	82.54
Un	164	USNM_ol_std_14	39.26	0.00	0.03	16.43	0.31	43.37	0.00	99.40	82.47
Un	164	USNM_ol_std_14	39.23	0.00	0.02	16.52	0.33	43.74	0.00	99.86	82.52
Un	164	USNM_ol_std_14	39.11	0.00	0.03	16.47	0.31	43.44	0.00	99.35	82.46
Un	4	SPR_std_1	38.89	0.00	0.03	16.58	0.31	43.72	0.00	99.54	82.46
Un	4	SPR_std_1	38.83	0.00	0.03	16.53	0.32	43.47	0.00	99.19	82.41
Un	4	SPR_std_1	38.71	0.00	0.02	16.57	0.31	43.60	0.00	99.22	82.42
Un	33	SPR_std_2	38.66	0.00	0.02	16.37	0.27	43.58	0.00	98.91	82.60
Un	33	SPR_std_2	38.66	0.01	0.03	16.40	0.29	43.56	0.01	98.97	82.56
Un	33	SPR_std_2	38.64	0.00	0.03	16.42	0.31	43.54	0.01	98.95	82.54
Un	53	SPR_std_3	38.68	0.00	0.04	16.43	0.32	43.57	0.01	99.06	82.54
Un	53	SPR_std_3	38.56	0.00	0.01	16.47	0.34	43.74	0.01	99.13	82.56
Un	53	SPR_std_3	38.69	0.00	0.02	16.39	0.31	43.78	0.00	99.19	82.65
Un	79	SPR_std_4	38.70	0.00	0.04	15.96	0.31	43.50	0.02	98.53	82.93
Un	99	SPR_std_5	38.47	0.00	0.01	16.17	0.30	44.07	0.01	99.04	82.93

Table S3, *continued*

	Un	99	SPR_std_5	38.63	0.01	0.02	16.02	0.30	43.79	0.01	98.79	82.97
	Un	99	SPR_std_5	38.48	0.00	0.00	16.01	0.31	43.89	0.00	98.70	83.02

Notes- Y-98 crystals contain P_2O_5 from non-detectable to 0.46 wt%, as well as NiO typically < 0.1 wt%; TiO_2 is below detection for most analyses; greyscale coding: dark = core, medium = rim, light = outermost bright rim, very dark = olivine inclusions in pyroxene; * = smaller, more Fe-rich crystal; blank cells indicate concentrations below detection limit.

Table S4. Microprobe pyroxene analyses, including standards.

IDENTIFIER	SiO2 WT%	TiO2 WT%	Al2O3 WT%	Cr2O3 WT%	FeO WT%	MnO WT%	MgO WT%	CaO WT%	Na2O WT%	TOT
Un 7 pyroxene_1_opx	54.57	0.06	0.57	0.53	13.35	0.43	28.98	1.54	0.03	100.05
Un 12 pyroxene_2_rim to core	54.67	0.05	0.51	0.62	11.49	0.37	30.70	1.12		99.55
Un 18 pyroxene_3_rim to core	54.79		0.48	0.54	10.44	0.31	31.71	0.87		99.15
Un 19 pyroxene_4_rim to core	53.53	0.07	0.59	0.56	13.48	0.50	28.69	1.54	0.02	98.97
Un 19 pyroxene_4_rim to core	54.34	0.04	0.45	0.61	11.68	0.37	30.58	1.08		99.15
Un 25 pyroxene_5_rim to core	53.60	0.07	0.65	0.53	14.03	0.48	27.92	2.09	0.02	99.40
Un 26 pyroxene_6_tip to core	53.20	0.06	1.49	0.45	14.05	0.46	26.92	2.35	0.08	99.05
Un 26 pyroxene_6_tip to core	53.48	0.06	0.67	0.51	13.91	0.50	27.96	2.07	0.02	99.19
Un 26 pyroxene_6_tip to core	52.65	0.12	1.43	1.05	13.71	0.48	26.95	2.40	0.05	98.86
Un 30 pyroxene_7_rim to core	54.14	0.05	0.61	0.62	12.87	0.48	29.39	1.50	0.03	99.69
Un 30 pyroxene_7_rim to core	54.21	0.03	0.47	0.63	11.90	0.37	30.07	1.22		98.92
Un 30 pyroxene_7_rim to core	54.06	0.04	0.75	0.88	11.92	0.43	30.04	1.41	0.02	99.54
Un 32 pyroxene_8_rim to core	53.03	0.09	0.83	0.55	15.78	0.57	25.70	3.43	0.03	100.02
Un 32 pyroxene_8_rim to core	53.36	0.10	1.08	0.98	13.72	0.47	28.00	2.00		99.70
Un 32 pyroxene_8_rim to core	54.62	0.04	0.50	0.64	11.96	0.39	30.17	1.26	0.03	99.61
Un 35 pyroxene_9_rim to core	53.38	0.03	0.66	0.49	14.10	0.45	27.88	2.02		99.01
Un 35 pyroxene_9_rim to core	54.96		0.40	0.55	10.92	0.36	31.36	0.87		99.41
Un 36 pyroxene_10_rim to core	54.78	0.06	0.58	0.66	12.11	0.45	30.06	1.38		100.08
Un 37 pyroxene_10_fusioncrust	53.10	0.07	0.73	0.51	14.72	0.52	26.47	3.04	0.03	99.19
Un 38 pyroxene_11_rim to core	54.17	0.06	0.64	0.58	13.35	0.45	28.89	1.60	0.04	99.78
Un 38 pyroxene_11_rim to core	54.11	0.04	0.63	0.58	13.05	0.43	29.14	1.64	0.02	99.64
Un 39 pyroxene_11_core	54.75	0.04	0.47	0.54	12.41	0.38	30.22	1.19	0.02	100.00
Un 12 pyroxene_2_rim to core	53.92	0.04	0.64	0.64	13.27	0.43	28.87	1.57		99.38
Un 19 pyroxene_4_rim to core	49.22	0.35	3.27	0.82	15.44	0.54	17.12	11.85	0.12	98.72
Un 35 pyroxene_9_rim to core	53.86	0.07	0.58	0.49	14.05	0.53	27.95	2.09		99.62
Un 38 pyroxene_11_rim to core	53.55	0.07	0.78	0.56	14.09	0.51	27.42	2.38	0.04	99.40
Un 8 pyroxene_1_cpx	46.09	0.93	7.91	0.03	19.64	0.60	10.85	13.41	0.18	99.64
Un 12 pyroxene_2_rim to core	50.57	0.25	2.36	0.87	14.50	0.57	18.55	11.39	0.13	99.19

Table S4, *continued*

Un 18 pyroxene_3_rim to core	48.34	0.56	4.67	0.19	17.04	0.54	13.62	14.17	0.11	99.24
Un 19 pyroxene_4_rim to core	44.60	1.44	8.58		18.10	0.56	10.44	14.81	0.20	98.75
Un 25 pyroxene_5_rim to core	44.24	1.52	9.29		20.11	0.56	8.08	15.53	0.24	99.57
Un 26 pyroxene_6_tip to core	45.66	0.97	8.01	0.03	17.75	0.50	10.67	15.48	0.19	99.27
Un 30 pyroxene_7_rim to core	51.01	0.15	1.69	0.76	14.67	0.61	20.38	9.49	0.10	98.86
Un 36 pyroxene_10_rim to core	52.82	0.06	0.93	0.57	14.22	0.50	26.16	3.33	0.05	98.64
Un 38 pyroxene_11_rim to core	46.11	0.72	6.95	0.03	24.58	0.75	11.72	8.59	0.09	99.56
Un 14 ol_2_px dendrite_b	46.04	1.39	8.92		19.85	0.60	8.45	14.41	0.32	99.99
Un 17 ol_2_px dendrite_e	44.60	1.34	8.48		22.89	0.61	7.97	12.35	0.28	98.53
Un 23 ol_4_px dendrite_a	43.10	2.47	8.99		23.26	0.64	6.58	14.24	0.28	99.56
Un 41 px_dendrite_1	44.13	1.50	9.69		24.21	0.64	5.83	13.04	0.53	99.58
Un 42 px_dendrite_2	42.70	2.52	9.55	0.05	23.30	0.65	5.96	14.05	0.28	99.04
Un 126 Y98-f56i_pyroxene_1_core	53.46	0.16	1.36	1.24	14.71	0.54	25.50	2.20		99.17
Un 130 Y98-f56i_pyroxene_3_core	53.82	0.15	1.33	1.48	13.63	0.53	26.33	1.85		99.11
Un 132 Y98-f56i_pyroxene_4_core	53.63	0.14	1.05	1.25	13.95	0.50	26.01	2.07		98.60
Un 134 Y98-f56i_pyroxene_5_core	53.29	0.19	1.22	1.21	15.26	0.58	24.40	2.81	0.03	98.99
Un 138 Y98-f56i_pyroxene_6	51.33	0.41	2.45	0.96	13.92	0.54	16.86	12.64	0.03	99.14
Un 139 Y98-f56i_pyroxene_7	49.35	0.86	3.90	0.47	18.15	0.56	15.73	10.05		99.06
Un 127 Y98-f56i_pyroxene_1_rim	52.50	0.18	1.31	0.96	17.65	0.67	21.94	3.83		99.05
Un 131 Y98-f56i_pyroxene_3_rim_5um	52.26	0.25	1.66	0.91	15.63	0.61	19.33	7.98	0.04	98.67
Un 133 Y98-f56i_pyroxene_4_rim	48.23	1.31	5.84	0.40	14.62	0.46	12.29	15.28	0.07	98.51
Un 135 Y98-f56i_pyroxene_5_rim_5um	49.64	0.84	3.98	0.84	15.61	0.54	14.36	12.87	0.05	98.73
Un 137 Y98-f56i_pyroxene_pop2_b_5um	51.01	0.45	2.41	0.88	14.63	0.55	16.50	12.24	0.06	98.73
Un 45 Y98-f56i_Pyroxene_2_1um	50.07	0.64	4.09	0.43	20.40	0.68	16.17	7.22	0.05	99.75
Un 100 Y98-f56i_pyroxene_outer_1	49.52	0.75	4.27	0.70	14.53	0.54	13.30	15.26	0.05	98.91
Un 44 Y98-f56i_Pyroxene_1_chain_focused	49.42	1.20	5.64	0.11	22.27	0.62	9.33	12.13	0.15	100.87
Un 101 Y98-f56i_pyroxene_pop3_a_1um	49.68	0.96	4.21	0.63	16.11	0.54	13.66	13.25	0.06	99.09
Un 102 Y98-f56i_pyroxene_pop3_b_1um	48.84	1.06	4.67	0.40	15.98	0.54	12.55	14.58	0.03	98.65
Un 103 Y98-f56i_pyroxene_pop3_c_1um	47.96	1.16	7.82	0.14	18.02	0.54	11.83	11.38	0.07	98.92

Table S4, *continued*

	Un 104 Y98-f56i_pyroxene_pop3_d_1um	48.83	0.94	5.74	0.34	17.41	0.62	12.83	12.29	0.06	99.06
	Un 150 Y98-f57i_pyroxene_1_core	53.22	0.21	1.51	1.48	15.24	0.53	24.78	2.29		99.26
	Un 152 Y98-f57i_pyroxene_2_core	54.72	0.09	0.89	1.12	12.63	0.39	28.11	1.27		99.22
	Un 154 Y98-f57i_pyroxene_3_core	53.43	0.16	1.41	1.37	15.68	0.52	24.55	2.34		99.45
	Un 156 Y98-f57i_pyroxene_4_core	53.52	0.21	1.40	0.84	15.60	0.51	24.51	2.80		99.37
	Un 162 Y98-f57i_pyroxene_5	52.44	0.22	1.41	0.64	17.23	0.54	20.43	6.07	0.02	99.01
	Un 163 Y98-f57i_pyroxene_6	51.36	0.33	1.91	0.98	18.25	0.66	17.49	8.10		99.08
	Un 151 Y98-f57i_pyroxene_1_rim	52.21	0.20	1.34	0.90	18.10	0.64	20.63	4.88		98.91
	Un 153 Y98-f57i_pyroxene_2_rim_5um	53.46	0.14	0.95	0.69	16.76	0.52	23.86	2.69		99.07
	Un 155 Y98-f57i_pyroxene_3_rim_5um	48.64	1.00	4.96	0.55	16.71	0.55	13.26	13.16	0.04	98.87
	Un 157 Y98-f57i_pyroxene_4_rim_5um	46.97	1.68	7.56	0.19	14.70	0.42	11.39	16.17	0.04	99.12
	Un 50 Y98-f57i_Pyroxene_1_5um	51.10	0.40	2.53	1.01	17.87	0.62	16.27	10.08	0.04	99.92
	Un 52 Y98-f57i_Pyroxene_3_5um	51.13	0.37	2.47	1.30	18.53	0.68	18.72	6.70		99.89
	Un 161 Y98-f57i_pyroxene_pop2_b	50.36	0.68	2.97	1.13	14.79	0.55	14.03	14.66	0.02	99.18
	Un 51 Y98-f57i_Pyroxene_2_5um	51.17	0.39	2.43	1.37	16.14	0.60	16.70	11.00	0.03	99.84
	Un 113 Y98-f57i_pyroxene_pop2_a_1um	47.51	1.45	6.18	0.12	18.05	0.54	10.97	14.24	0.06	99.10
	Un 108 Y98-f57i_pyroxene_1_outer	48.00	1.18	5.65	0.08	20.09	0.59	11.47	12.83	0.03	99.91
	Un 110 Y98-f57i_pyroxene_pop4_b_1um	47.73	1.15	6.29	0.31	17.94	0.54	9.97	15.24	0.04	99.21
	Un 111 Y98-f57i_pyroxene_pop4_c_1um	47.83	0.96	5.38	0.18	23.25	0.60	7.13	13.15	0.05	98.53
	Un 112 Y98-f57i_pyroxene_pop4_d_1um	46.99	1.18	7.51	0.15	18.89	0.53	9.08	15.23	0.03	99.58
	Un 159 Y98-f57i_pyroxene_pop3_a_5um	48.37	0.96	5.08	0.28	18.50	0.56	10.96	14.44	0.04	99.19
	Un 160 Y98-f57i_pyroxene_pop3_b_5um	49.14	0.74	4.23	0.68	16.83	0.55	12.59	13.74	0.03	98.53
	Un 38 Y98-f62i_pyroxene_1_core	53.52	0.14	1.47	1.71	14.20	0.55	25.56	1.98		99.14
	Un 40 Y98-f62i_pyroxene_2_core	53.71	0.12	1.38	1.72	13.70	0.46	26.06	1.83	0.02	98.97
	Un 42 Y98-f62i_pyroxene_3_core	53.48	0.14	1.16	1.44	15.03	0.51	24.90	2.39		99.04
	Un 119 Y98-f62i_pyroxene_4_core_1um	52.26	0.22	1.72	1.71	16.45	0.61	19.82	6.46	0.03	99.28
	Un 47 Y98-f62i_pyroxene_6_core	51.70	0.23	1.88	1.73	16.83	0.62	19.83	5.89	0.03	98.75
	Un 46 Y98-f62i_pyroxene_5	51.03	0.42	2.51	1.13	15.19	0.56	16.06	12.28	0.05	99.23
	Un 50 Y98-f62i_pyroxene_8	49.18	0.96	4.31	0.35	16.68	0.50	11.74	14.95	0.03	98.70

Table S4, *continued*

	Un 51 Y98-f62i_pyroxene_9	50.66	0.50	2.51	1.11	15.41	0.56	14.12	13.87	0.03	98.77
	Un 39 Y98-f62i_pyroxene_1_rim	50.77	0.31	2.49	1.13	19.28	0.67	17.90	6.25		98.80
	Un 41 Y98-f62i_pyroxene_2_rim	51.34	0.34	2.36	0.82	18.28	0.64	18.33	6.82	0.03	98.95
	Un 43 Y98-f62i_pyroxene_3_rim	48.42	0.85	5.28	0.43	17.06	0.57	12.68	13.26	0.04	98.59
	Un 48 Y98-f62i_pyroxene_6_rim	49.41	0.80	3.85	0.53	16.37	0.56	12.48	14.74	0.05	98.78
	Un 55 Y98-f62i_pyroxene_13	48.83	0.89	4.69	0.44	17.28	0.56	11.81	14.04	0.05	98.59
	Un 52 Y98-f62i_pyroxene_10	49.21	0.73	4.29	0.56	17.69	0.56	11.98	14.14	0.04	99.21
	Un 53 Y98-f62i_pyroxene_11_5um	48.81	0.88	3.83	0.34	19.26	0.61	10.66	14.22	0.04	98.64
	Un 56 Y98-f62i_pyroxene_14_5um	49.25	0.79	4.54	0.47	16.13	0.54	12.36	14.57	0.04	98.70
	Un 9 Y98-f62i_pyroxene_pop4_a_1um	47.69	1.03	5.89	0.12	20.13	0.60	9.84	13.82	0.04	99.15
	Un 84 Y98-f62i_Pyroxene_1_focused	47.09	1.52	7.58	0.05	18.25	0.57	8.78	15.45	0.07	99.36
	Un 85 Y98-f62i_Pyroxene_2_focused	48.22	1.18	4.17	0.09	21.59	0.64	9.59	13.22	0.04	98.74
	Un 86 Y98-f62i_Pyroxene_3_focused	46.92	1.18	5.59	0.04	27.72	0.70	5.26	12.01	0.13	99.55
	Un 100 Y98-f63i_pyroxene_1_core	54.48	0.10	0.95	1.02	13.43	0.46	27.75	1.56		99.75
	Un 102 Y98-f63i_pyroxene_2_core	54.08	0.13	1.26	1.26	14.36	0.50	26.00	1.95		99.53
	Un 104 Y98-f63i_pyroxene_3_core	54.32	0.11	1.13	1.31	13.61	0.46	26.96	1.67		99.56
	Un 106 Y98-f63i_pyroxene_4_core	54.37	0.10	1.00	1.36	12.87	0.45	27.81	1.43	0.02	99.42
	Un 108 Y98-f63i_pyroxene_5_core	53.79	0.14	1.37	1.70	14.47	0.51	25.57	2.08		99.62
	Un 110 Y98-f63i_pyroxene_6	51.75	0.33	2.09	1.08	14.77	0.56	16.77	12.24	0.02	99.60
	Un 111 Y98-f63i_pyroxene_7	51.77	0.31	1.71	0.98	17.72	0.65	19.06	6.94		99.14
	Un 112 Y98-f63i_pyroxene_8	51.98	0.25	1.58	0.98	17.34	0.69	19.62	7.23		99.68
	Un 113 Y98-f63i_pyroxene_9	50.94	0.48	2.51	0.61	16.57	0.58	16.22	11.45	0.03	99.39
	Un 101 Y98-f63i_pyroxene_1_rim	52.40	0.18	1.35	1.00	17.73	0.63	21.38	4.38		99.06
	Un 103 Y98-f63i_pyroxene_2_rim	52.85	0.16	1.18	0.86	17.52	0.60	22.04	3.94	0.02	99.18
	Un 105 Y98-f63i_pyroxene_3_rim	52.85	0.24	1.94	0.78	16.90	0.55	22.21	4.32		99.79
	Un 107 Y98-f63i_pyroxene_4_rim	51.77	0.25	1.70	0.81	18.16	0.63	19.87	5.90		99.09
	Un 109 Y98-f63i_pyroxene_5_rim	52.31	0.25	1.63	0.99	17.99	0.62	20.03	5.74	0.02	99.58
	Un 114 Y98-f63i_pyroxene_10_5um	48.36	1.37	8.36	0.15	14.70	0.45	12.06	14.77	0.08	100.31
	Un 115 Y98-f63i_pyroxene_11_5um	50.87	0.41	2.51	0.91	15.16	0.56	16.05	12.53	0.02	99.01

Table S4, *continued*

	Un 25 Y98-f63i_pyroxene_2_outer	48.20	1.54	7.73	0.20	15.40	0.47	10.67	14.91	0.07	99.18
	Un 89 Y98-f63i_Pyroxene_1_focused	46.58	1.56	7.62	0.10	18.16	0.55	12.01	13.08	0.04	99.70
	Un 23 Y98-f63i_pyroxene_pop4_b_1um	48.83	1.08	5.38	0.34	17.59	0.58	13.37	12.10	0.03	99.29
	Un 24 Y98-f63i_pyroxene_pop4_c_1um	48.06	1.45	6.91	0.38	15.21	0.51	11.16	15.87	0.06	99.60
	Un 90 Y98-f63i_Pyroxene_2_focused	50.34	0.71	3.95	0.36	18.68	0.63	14.91	10.77	0.04	100.38
	Un 8 Y98-f64i_Pyroxene_2	52.42	0.29	2.04	1.22	16.48	0.59	18.63	9.27	0.04	100.98
	Un 13 Y98-f64i_Pyroxene_5	51.93	0.44	2.56	0.80	14.17	0.50	18.92	11.10	0.04	100.47
	Un 18 Y98-f64i_Pyroxene_8	48.90	1.14	4.19	0.31	18.24	0.55	12.80	13.60	0.06	99.79
	Un 19 Y98-f64i_Pyroxene_9	50.10	0.82	3.75	0.77	15.71	0.54	13.16	15.28	0.05	100.18
	Un 7 Y98-f64i_Pyroxene_1_rim_5um	52.14	0.33	2.12	1.15	15.68	0.54	18.11	10.90	0.03	100.99
	Un 10 Y98-f64i_Pyroxene_3_rim_5um	50.14	0.72	4.07	0.20	18.94	0.60	14.42	11.58	0.06	100.72
	Un 12 Y98-f64i_Pyroxene_4_rim_5um	47.89	1.19	5.64	0.04	22.96	0.67	10.98	10.34	0.05	99.77
	Un 15 Y98-f64i_Pyroxene_6_rim	49.13	1.17	6.00	0.22	14.28	0.48	13.41	15.76	0.05	100.51
	Un 17 Y98-f64i_Pyroxene_7_rim	49.65	0.74	4.59	1.04	14.32	0.48	13.12	16.23	0.06	100.23
	Un 21 Y98-f64i_Pyroxene_10_rim_5um	51.75	0.36	2.42	1.05	15.62	0.56	16.91	11.75	0.05	100.47
	Un 24 Y98-f64i_Pyroxene_13	47.89	1.18	5.59	0.14	21.15	0.66	10.59	13.03	0.03	100.25
	Un 22 Y98-f64i_Pyroxene_11_5um	47.18	1.38	5.55		27.28	0.77	7.10	10.89	0.05	100.21
	Un 23 Y98-f64i_Pyroxene_12_5um	47.25	1.40	6.28	0.02	21.16	0.61	8.46	14.60	0.08	99.86
	Un 38 Y98-f64i_Pyroxene_14_gm_focused	46.21	1.54	1.88	0.02	33.64	0.82	3.24	11.65	0.03	99.04
	Un 138 Y98-f65-2i_pyroxene_1_core	54.70	0.13	1.07	1.21	14.04	0.53	26.48	1.90		100.05
	Un 140 Y98-f65-2i_pyroxene_2_core	54.95	0.10	1.00	1.23	13.14	0.42	27.73	1.45		100.01
	Un 142 Y98-f65-2i_pyroxene_3_core	54.66	0.12	1.08	1.16	13.48	0.45	26.99	1.63		99.57
	Un 144 Y98-f65-2i_pyroxene_4_core	55.05	0.10	0.98	1.27	12.89	0.47	27.57	1.46		99.78
	Un 146 Y98-f65-2i_pyroxene_5_core	54.40	0.14	1.25	1.55	13.36	0.44	26.79	1.66		99.60
	Un 148 Y98-f65-2i_pyroxene_6	51.76	0.33	2.01	0.99	15.67	0.56	17.82	9.84	0.02	99.00
	Un 149 Y98-f65-2i_pyroxene_7	51.82	0.31	2.05	0.91	16.25	0.61	17.97	9.36		99.28
	Un 150 Y98-f65-2i_pyroxene_8	48.83	0.99	5.59	0.33	14.76	0.49	12.34	15.87	0.04	99.24
	Un 151 Y98-f65-2i_pyroxene_9	48.93	0.96	4.81	0.15	18.46	0.60	12.66	12.72	0.02	99.29
	Un 139 Y98-f65-2i_pyroxene_1_rim	49.92	0.93	4.42	0.62	15.51	0.55	13.91	14.09	0.04	99.98

Table S4, *continued*

	Un 141 Y98-f65-2i_pyroxene_2_rim	52.75	0.22	1.41	0.97	17.62	0.64	21.90	3.97	0.02	99.49
	Un 143 Y98-f65-2i_pyroxene_3_rim	51.70	0.41	1.89	0.30	17.25	0.60	15.17	12.21		99.53
	Un 145 Y98-f65-2i_pyroxene_4_rim	51.09	0.59	3.00	0.56	17.86	0.64	16.83	8.81		99.38
	Un 147 Y98-f65-2i_pyroxene_5_rim	50.95	0.50	2.89	0.97	13.91	0.53	14.92	14.74	0.03	99.45
	Un 163 Y98-f65-2i_pyroxene_2_outer	48.62	0.63	5.16	0.21	21.80	0.73	14.07	7.37		98.57
	Un 164 Y98-f65-2i_pyroxene_4_outer	44.77	2.00	10.21	0.11	17.82	0.54	9.10	14.84	0.08	99.46
	Un 152 Y98-f65-2i_pyroxene_10_5um	49.02	1.19	5.10	0.20	15.69	0.55	11.99	15.82	0.04	99.60
	Un 153 Y98-f65-2i_pyroxene_11_5um	46.51	1.73	7.98	0.03	18.45	0.52	9.67	14.36	0.04	99.30
	Un 154 Y98-f65-2i_pyroxene_12_5um	49.14	0.79	4.65	0.34	18.18	0.60	11.63	14.03	0.04	99.40
	Un 156 Y98-f65-2i_pyroxene_14_5um	48.37	0.96	5.69	0.22	17.80	0.60	11.57	14.31	0.04	99.54
	Un 161 Y98-f65-2i_pyroxene_pop4_a_1um	45.63	1.42	9.05	0.04	18.78	0.54	8.97	14.55	0.06	99.04
	Un 165 Y98-f65-2i_pyroxene_pop4_c_1um	45.92	1.34	8.90	0.05	17.98	0.55	9.74	14.63	0.06	99.17
	Un 96 Y98-f65-2i_Pyroxene_1_focused	48.33	1.13	5.79		20.03	0.61	10.06	13.10	0.06	99.11
	Un 97 Y98-f65-2i_Pyroxene_2_focused	45.60	2.01	9.71		18.53	0.51	6.96	15.87	0.09	99.27
	Un 69 Y98-f67-2ii_pyroxene_1_core	54.47	0.08	0.83	1.01	12.53	0.42	28.19	1.33		98.86
	Un 71 Y98-f67-2ii_pyroxene_2_core	53.45	0.14	1.26	1.21	13.88	0.47	26.29	1.96		98.66
	Un 73 Y98-f67-2ii_pyroxene_3_core	53.99	0.14	1.09	1.08	13.72	0.45	27.07	1.70		99.23
	Un 75 Y98-f67-2ii_pyroxene_4_core	54.23	0.15	1.10	1.45	13.01	0.45	27.28	1.59		99.26
	Un 77 Y98-f67-2ii_pyroxene_5_core	54.55	0.12	1.12	1.36	12.37	0.40	28.00	1.45		99.37
	Un 79 Y98-f67-2ii_pyroxene_6	50.26	0.50	3.08	0.99	14.27	0.49	15.45	13.70	0.04	98.79
	Un 80 Y98-f67-2ii_pyroxene_7	50.08	0.56	3.00	0.84	14.81	0.55	15.49	13.35	0.04	98.72
	Un 81 Y98-f67-2ii_pyroxene_8	48.27	1.10	6.46	0.47	14.31	0.52	14.54	13.10	0.04	98.82
	Un 70 Y98-f67-2ii_pyroxene_1_rim	52.42	0.18	1.22	0.80	17.19	0.62	22.00	4.28		98.71
	Un 72 Y98-f67-2ii_pyroxene_2_rim	50.42	0.62	3.37	0.52	16.03	0.52	18.66	9.06	0.02	99.22
	Un 74 Y98-f67-2ii_pyroxene_3_rim	51.92	0.24	1.58	0.81	18.01	0.62	20.02	5.90		99.09
	Un 76 Y98-f67-2ii_pyroxene_4_rim	51.30	0.31	2.09	1.07	17.60	0.64	19.73	5.86	0.02	98.61
	Un 78 Y98-f67-2ii_pyroxene_5_rim	51.14	0.43	2.99	0.97	15.00	0.56	20.29	7.36		98.73
	Un 83 Y98-f67-2ii_pyroxene_10_5um	49.64	0.71	3.43	0.65	17.42	0.57	15.19	11.10	0.02	98.75
	Un 84 Y98-f67-2ii_pyroxene_11_5um	47.63	1.35	8.26	0.26	14.85	0.48	10.00	15.55	0.17	98.55

Table S4, *continued*

	Un 18 Y98-f67-2ii_pyroxene_near5_outer	45.80	1.68	8.73	0.03	19.34	0.59	9.02	14.16	0.07	99.41
	Un 82 Y98-f67-2ii_pyroxene_9_5um	46.93	1.79	8.47	0.07	14.19	0.44	9.34	17.90	0.08	99.21
	Un 17 Y98-f67-2ii_pyroxene_pop4_c_1um	48.40	0.90	4.85	0.27	16.62	0.53	11.31	15.70	0.04	98.63
	Un 85 Y98-f67-2ii_pyroxene_12_5um	46.59	1.60	7.37	0.11	16.33	0.46	10.24	16.09	0.05	98.84
	Un 86 Y98-f67-2ii_pyroxene_13_5um	48.18	1.11	5.65	0.17	16.33	0.52	12.43	14.40	0.05	98.86
	Un 87 Y98-f67-2ii_pyroxene_14_5um	49.95	0.59	3.63	0.80	17.26	0.54	14.73	11.31	0.04	98.84
	Un 58 Y98-f67-2ii_Pyroxene_1_focused	46.01	1.75	9.40	0.04	19.80	0.57	9.13	13.09	0.09	99.90
	Un 59 Y98-f67-2ii_Pyroxene_2_focused	47.46	1.24	7.22	0.12	16.90	0.51	10.14	15.47	0.08	99.14
	Un 60 Y98-f67-2ii_Pyroxene_3_focused	46.94	1.22	7.71	0.27	16.84	0.54	11.53	14.53	0.08	99.66
	Un 20 Y98-f68i_pyroxene_1_core	54.27	0.10	0.83	1.02	12.37	0.40	28.29	1.37		98.66
	Un 22 Y98-f68i_pyroxene_2_core	53.80	0.16	0.95	1.08	13.69	0.51	26.75	1.87		98.82
	Un 24 Y98-f68i_pyroxene_3_core	54.77	0.09	0.76	1.04	11.60	0.41	29.11	1.21		98.99
	Un 63 Y98-f68i_Pyroxene_1_5um	52.03	0.31	2.38	0.66	15.89	0.59	21.19	7.23		100.29
	Un 30 Y98-f68i_pyroxene_6	48.61	1.08	5.22	0.35	14.87	0.48	13.95	13.99	0.03	98.58
	Un 31 Y98-f68i_pyroxene_7	46.14	1.93	7.49	0.13	13.04	0.41	10.89	18.64	0.02	98.70
	Un 21 Y98-f68i_pyroxene_1_rim	52.91	0.14	1.02	0.70	16.28	0.58	23.82	3.37		98.82
	Un 64 Y98-f68i_Pyroxene_2_5um	51.49	0.38	2.28	1.15	14.07	0.58	17.41	12.82		100.19
	Un 65 Y98-f68i_Pyroxene_3_5um	51.09	0.44	2.48	1.10	14.12	0.54	17.42	12.95		100.15
	Un 34 Y98-f68i_pyroxene_10_5um	47.21	1.37	6.94	0.18	14.56	0.49	11.78	16.02	0.04	98.59
	Un 66 Y98-f68i_Pyroxene_4_focused	45.89	1.84	8.81	0.05	15.86	0.55	11.79	14.82	0.04	99.65
	Un 67 Y98-f68i_Pyroxene_5_focused	45.86	2.16	9.77	0.04	15.99	0.47	9.46	16.69	0.06	100.50
	Un 4 Y98-f68i_pyroxene_1_outer	45.55	2.10	9.60	0.05	15.03	0.50	9.55	16.93	0.05	99.36
	Un 8 Y98-f68i_pyroxene_pop4_c_1um	47.10	1.32	7.38	0.13	17.50	0.59	11.11	13.63		98.76
	Un 63 Y98-f69i_pyroxene_1_core	54.88	0.10	0.72	0.74	11.77	0.46	28.74	1.49		98.90
	Un 69 Y98-f69i_pyroxene_3_core	54.82	0.12	0.93	0.85	12.19	0.46	28.35	1.61		99.33
	Un 64 Y98-f69i_pyroxene_1_mid	53.80	0.15	1.03	0.66	15.04	0.56	25.13	3.08		99.44
	Un 70 Y98-f69i_pyroxene_3_mid	53.41	0.17	1.28	0.71	14.94	0.62	24.17	3.74		99.03
	Un 71 Y98-f69i_Pyroxene_2_5um	51.80	0.43	2.82	0.94	12.50	0.53	18.55	13.09		100.65
	Un 65 Y98-f69i_pyroxene_1_rim	49.62	0.78	4.51	0.66	11.80	0.50	14.46	16.55		98.88

Table S4, *continued*

	Un 41 Y98-f69i_pyroxene_2_outer	44.95	2.15	11.83		13.50	0.47	9.43	16.19	0.02	98.55
	Un 71 Y98-f69i_pyroxene_3_rim_5um	49.94	0.78	3.65	0.12	17.28	0.69	14.53	12.35		99.35
	Un 72 Y98-f69i_pyroxene_pop2_a	49.35	0.96	4.92	0.55	14.57	0.55	15.63	12.22		98.76
	Un 73 Y98-f69i_pyroxene_pop2_b	46.12	1.71	8.49	0.17	13.95	0.51	11.32	16.34		98.61
	Un 40 Y98-f69i_pyroxene_1_outer	46.64	1.40	8.03	0.13	15.58	0.56	11.85	14.40		98.58
	Un 42 Y98-f69i_pyroxene_2_pop4_a_1um	46.72	1.57	8.42	0.24	14.10	0.49	12.59	14.58	0.02	98.73
	Un 43 Y98-f69i_pyroxene_2_pop4_b_1um	46.79	1.25	8.24	0.19	15.29	0.55	12.60	13.66	0.02	98.59
	Un 73 Y98-f69i_Pyroxene_4_focused	46.25	1.41	10.45	0.05	17.98	0.67	10.61	13.32		100.75
	Un 79 Y98-f69ii_pyroxene_1_core	53.82	0.15	1.05	0.91	13.63	0.55	26.38	2.11		98.61
	Un 82 Y98-f69ii_pyroxene_2_core	54.13	0.14	0.80	0.79	13.48	0.53	26.77	2.01		98.64
	Un 85 Y98-f69ii_pyroxene_3_core	54.38	0.11	0.71	0.72	13.40	0.51	27.19	1.91		98.93
	Un 88 Y98-f69ii_pyroxene_4_core	54.35	0.11	0.80	0.78	13.41	0.50	27.14	1.88		98.98
	Un 90 Y98-f69ii_pyroxene_5_core	53.86	0.18	1.40	0.63	13.23	0.46	26.67	2.35		98.77
	Un 80 Y98-f69ii_pyroxene_1_mid	53.04	0.16	1.02	0.65	15.90	0.62	23.42	3.71		98.53
	Un 86 Y98-f69ii_pyroxene_3_mid	53.12	0.16	0.95	0.74	15.17	0.66	23.65	4.07		98.51
	Un 77 Y98-f69ii_Pyroxene_3_5um	53.74	0.17	1.13	0.72	15.48	0.64	23.24	5.28		100.40
	Un 78 Y98-f69ii_Pyroxene_4_5um	54.19	0.15	0.97	0.71	15.40	0.64	25.25	3.54		100.84
	Un 81 Y98-f69ii_pyroxene_1_rim	52.24	0.24	1.49	0.56	17.15	0.65	20.66	5.64		98.63
	Un 84 Y98-f69ii_pyroxene_2_rim_5um	51.51	0.33	1.85	0.86	13.61	0.58	17.82	11.93		98.50
	Un 87 Y98-f69ii_pyroxene_3_rim	51.58	0.36	1.93	0.93	11.93	0.54	16.73	14.87		98.87
	Un 89 Y98-f69ii_pyroxene_4_rim	51.20	0.42	2.30	1.03	12.28	0.58	16.80	14.09		98.69
	Un 91 Y98-f69ii_pyroxene_5_rim	52.50	0.21	1.34	0.62	17.34	0.66	21.51	4.40		98.57
	Un 92 Y98-f69ii_pyroxene_6_5um	49.32	1.14	6.51	0.34	14.61	0.56	12.60	14.11	0.02	99.20
	Un 53 Y98-f69ii_pyroxene_pop2_b_1um	46.44	1.85	7.79	0.21	14.17	0.55	11.40	16.43		98.82
	Un 75 Y98-f69ii_Pyroxene_1_focused	48.20	1.71	8.51	0.11	14.15	0.51	10.83	16.13	0.03	100.18
	Un 76 Y98-f69ii_Pyroxene_2_focused	49.22	1.30	5.19	0.20	16.08	0.62	13.36	14.60		100.57
	Un 54 Y98-f69ii_pyroxene_pop4_c_1um	47.60	1.44	7.57	0.34	14.40	0.55	12.04	14.71		98.64
	Un 51 Y98-f69ii_pyroxene_pop4_b_1um	49.33	1.12	7.73	0.36	15.65	0.63	12.72	12.68		100.22
	Un 4 Kakanui-aug-std	49.08	0.78	8.86	0.18	6.20	0.19	16.86	15.51	1.27	99.01

Table S4, *continued*

Un	51	std_aug_kakanui_1	49.96	0.88	8.57	0.14	6.18	0.17	16.60	16.03	1.32	99.90
Un	51	std_aug_kakanui_1	50.45	0.84	8.59	0.19	6.31	0.12	16.61	16.00	1.33	100.50
Un	51	std_aug_kakanui_1	50.56	0.85	8.56	0.17	6.30	0.17	16.57	15.93	1.30	100.46
Un	5	KKN_px_std_1	49.60	0.89	8.67	0.17	6.12	0.12	16.09	16.02	0.92	98.63
Un	5	KKN_px_std_1	49.73	0.88	8.68	0.15	6.06	0.16	16.02	16.12	0.96	98.77
Un	27	KKN_px_std_1a	49.57	0.91	8.72	0.17	6.07	0.14	15.99	16.08	0.96	98.65
Un	89	KKN_px_std_3	49.96	0.88	8.77	0.16	6.06	0.14	16.01	15.99	0.97	98.96
Un	89	KKN_px_std_3	50.05	0.89	8.79	0.15	6.13	0.13	16.15	16.10	0.94	99.36
Un	89	KKN_px_std_3	49.76	0.89	8.71	0.16	6.13	0.13	15.98	15.98	0.93	98.71
Un	117	KKN_px_std_4	49.82	0.89	8.75	0.17	6.16	0.14	16.02	16.09	0.94	99.03
Un	117	KKN_px_std_4	50.05	0.87	8.72	0.15	6.17	0.12	16.11	15.99	0.93	99.17
Un	117	KKN_px_std_4	49.84	0.88	8.71	0.15	6.09	0.13	16.02	16.06	0.95	98.87
Un	127	KKN_px_std_5	49.88	0.87	8.68	0.15	6.25	0.13	16.04	16.05	0.91	99.02
Un	127	KKN_px_std_5	50.15	0.89	8.66	0.15	6.14	0.14	15.95	16.03	0.93	99.07
Un	127	KKN_px_std_5	50.07	0.87	8.75	0.17	6.13	0.14	16.01	15.99	0.96	99.10
Un	160	KKN_px_std_6	49.97	0.88	8.71	0.15	6.08	0.14	16.02	16.01	0.98	98.97
Un	160	KKN_px_std_6	50.10	0.89	8.72	0.16	6.06	0.13	15.91	16.03	0.96	98.98
Un	160	KKN_px_std_6	50.16	0.90	8.75	0.15	6.09	0.14	15.84	15.97	0.95	99.00
Un	11	KKN_px_std_7	49.64	0.87	8.70	0.16	6.14	0.15	16.03	16.15	0.97	98.85
Un	11	KKN_px_std_7	49.84	0.89	8.72	0.17	6.00	0.15	16.02	16.03	0.94	98.80
Un	11	KKN_px_std_7	49.76	0.87	8.70	0.15	6.07	0.13	15.84	16.01	0.94	98.52
Un	37	KKN_px_std_8	49.57	0.88	8.71	0.16	6.08	0.13	16.14	16.16	0.97	98.81
Un	37	KKN_px_std_8	49.63	0.88	8.72	0.15	6.05	0.14	16.02	16.06	0.97	98.67
Un	37	KKN_px_std_8	49.43	0.88	8.68	0.16	6.16	0.14	16.01	16.06	0.96	98.52
Un	95	KKN_px_std_10	49.54	0.89	8.68	0.17	6.18	0.12	16.00	16.05	0.93	98.62
Un	95	KKN_px_std_10	49.50	0.90	8.66	0.14	6.21	0.14	15.96	16.04	0.95	98.56
Un	95	KKN_px_std_10	49.71	0.91	8.70	0.18	6.11	0.15	15.94	16.13	0.92	98.76
Un	97	KKN_px_std_11	49.86	0.90	8.73	0.15	6.09	0.14	16.04	15.95	0.96	98.87
Un	97	KKN_px_std_11	49.98	0.87	8.71	0.15	6.22	0.15	16.11	16.09	0.97	99.29
Un	97	KKN_px_std_11	49.74	0.88	8.74	0.16	6.19	0.14	15.98	16.06	0.96	98.87

Table S4, *continued*

Un	115	KKN_px_std_12	49.46	0.87	8.68	0.16	6.05	0.14	15.99	16.17	0.95	98.50
Un	115	KKN_px_std_12	49.40	0.86	8.65	0.15	6.13	0.15	16.04	16.14	0.97	98.52
Un	141	KKN_px_std_13	49.67	0.88	8.69	0.16	6.14	0.15	16.08	16.08	0.95	98.82
Un	165	KKN_px_std_14	49.95	0.91	8.69	0.16	6.12	0.12	16.03	16.06	0.93	98.98
Un	165	KKN_px_std_14	50.08	0.90	8.71	0.16	6.04	0.16	16.04	16.02	0.94	99.09
Un	165	KKN_px_std_14	49.81	0.89	8.71	0.16	6.07	0.13	15.99	16.05	0.94	98.78
Un	5	KKN_std_1	50.43	0.85	8.70	0.15	6.13	0.14	16.81	15.98	1.26	100.49
Un	34	KKN_std_2	50.54	0.88	8.68	0.16	6.05	0.15	16.85	15.87	1.26	100.48
Un	54	KKN_std_3	50.39	0.85	8.68	0.15	6.08	0.15	16.81	16.04	1.24	100.43
Un	80	KKN_std_4	50.33	0.83	8.69	0.15	6.05	0.12	16.87	16.06	1.27	100.41
Un	80	KKN_std_4	50.32	0.90	8.65	0.13	6.00	0.14	16.74	15.97	1.26	100.15
Un	80	KKN_std_4	50.39	0.89	8.68	0.15	6.05	0.15	16.78	16.00	1.28	100.39
Un	100	KKN_std_5	50.34	0.87	8.65	0.15	6.09	0.14	16.85	15.99	1.28	100.40

	This fill color indicates analyses of the BSE darkest area of the population A_e crystal analyzed (the "core")
	This fill color indicates analyses on A_e crystals without distinctive core/rim, or a point in between the core and rim of a crystal (classified as "core" if division is necessary)
	This fill color indicates analyses of A_e "rims," classified here as the thicker mantles that are distinct from cores but not the outermost 5-10 microns of the crystal; also some of A_e smaller subset
	This fill color indicates analyses from the BSE brightest pyroxene areas: population B_e, bright rims of A_e, smaller subset of A_e (classified as "rim" if division is necessary)

Note - Blank cells indicate concentrations below detection limit.

Table S5-1. Surface area per unit volume data for pyroxene A populations

Sample	Image/Circle Number	Stage 1 (°C h^{-1})	Stage 2 (°C h^{-1})	Magnification	$\mathbf{S}_v^P$ (mm^{-1})	n	Weighted Average	Total n	STDEV.S
Y98-f63i	1	28	1000	100	94.8				
Y98-f56i	1	28	500	75	89.1				
Y98-f67-2ii	1	28	350	100	64.9				
Y98-f57i	1	28	150	75	88.8				
Y98-f62i	mosaic_updated	28	100	80	85.7	740			
Y98-f62i	“ ”_TL_shifted	28	100	80	71.1	740			
Y98-f62i	“ ”_TL_smaller_A	28	100	80	69.5	469			
Y98-f62i	“ ”_TL_smaller_B	28	100	80	104	385	80.8	2334	12.3
Y98-f65-2i	mosaic_updated	10	100	100	48.1	793			
Y98-f65-2i	“ ”_TL_shifted	10	100	100	56.3	793			
Y98-f65-2i	“ ”_TL_smaller_A	10	100	100	45.2	611			
Y98-f65-2i	“ ”_TL_smaller_B	10	100	100	39.9	419	48.6	2616	5.76
Y98-f68i	mosaic_updated	5	100	100	35.4	672			
Y98-f68i	“ ”_TL_shifted	5	100	100	37.4	672			
Y98-f68i	“ ”_TL_smaller_A	5	100	100	50.9	407			
Y98-f68i	“ ”_TL_smaller_B	5	100	100	35.1	407			
Y98-f68i	“ ”_TL_smaller_C	5	100	100	45.6	407	40.0	2564	5.91
Y98-f69i	mosaic_updated	1	100	100	22.8	1013			
Y98-f69i	mosaic_TL_shifted	1	100	100	26.2	1013			
Y98-f69i	mosaic_TL_smaller_A	1	100	100	19.3	397			
Y98-f69i	mosaic_TL_smaller_B	1	100	100	39.0	259	25.1	2683	5.13
Y-980459	1			100	53.5	531			
Y-980459	2			100	48.8	531			
Y-980459	3			100	44.3	531			
Y-980459	4			100	43.9	531			
Y-980459	5			100	43.0	531			
Y-980459	6			100	44.0	531	46.2	3186	3.74
Y-980459	**average**			**100**	**46.2**				
Y-980459	st dev (P)			100	3.7				
Y-980459	st dev (S)			100	4.1				

Table S5-2. Surface area per unit volume data for pyroxene population B

Sample	Stage 1 (°C h^{-1})	Stage 2 (°C h^{-1})	Magnification	Test Line Length (μm)	Sv^P(mm^{-1})	Weighted Average (mm^{-1})
Y98-f63i	28	1000	500	63.1	4236	
Y98-f63i	28	1000	500	72.6	3716	
Y98-f63i	28	1000	500	152.9	978	
Y98-f63i	28	1000	500	282.3	1110	1752
Y98-f56i	28	500	500	293.4	1486	
Y98-f56i	28	500	500	109.7	2130	
Y98-f56i	28	500	500	222.3	2292	
Y98-f56i	28	500	500	127.4	1501	
Y98-f56i	28	500	500	177.8	2256	
Y98-f56i	28	500	500	156.8	2033	1922
Y98-f67-2ii	28	350	500	71.8	3683	
Y98-f67-2ii	28	350	500	146.9	1892	
Y98-f67-2ii	28	350	500	155.6	1718	
Y98-f67-2ii	28	350	500	138.1	2331	
Y98-f67-2ii	28	350	500	190.6	2189	
Y98-f67-2ii	28	350	500	491.6	1208	
Y98-f67-2ii	28	350	500	223.2	1841	1801
Y98-f57i	28	150	250	752.2	639	
Y98-f57i	28	150	250	597.5	1102	
Y98-f57i	28	150	500	260.5	1421	
Y98-f57i	28	150	500	445.0	1460	
Y98-f57i	28	150	500	281.4	2133	1181
Y98-f62i	28	100	500	352.7	1253	
Y98-f62i	28	100	500	334.7	1551	
Y98-f62i	28	100	500	206.9	1339	
Y98-f62i	28	100	500	202.1	1657	
Y98-f62i	28	100	500	423.6	560	
Y98-f62i	28	100	500	487.2	1620	1295
Y98-f65-2i	10	100	500	531.5	1704	
Y98-f65-2i	10	100	500	242.4	923	
Y98-f65-2i	10	100	500	257.7	1458	
Y98-f65-2i	10	100	500	349.7	1804	
Y98-f65-2i	10	100	250	1030.6	584	
Y98-f65-2i	10	100	1000	272.9	1468	1169
Y98-f68i	5	100	500	268.2	1422	
Y98-f68i	5	100	500	400.5	1850	
Y98-f68i	5	100	500	252.9	1748	
Y98-f68i	5	100	1000	159.9	2950	1882
Y98-f69i	1	100	500	271.9	1312	
Y98-f69i	1	100	500	373.1	1350	
Y98-f69i	1	100	1000	100.1	3735	1657

Table S5-3. Surface area per unit volume data for pyroxene C populations

Sample	**Stage 1 (°C h^{-1})**	**Stage 2 (°C h^{-1})**	Magnification	Test Line Length (μm)	Sv^P(mm^{-1})	Weighted Average (mm^{-1})	n	Average, applying n	total n	STDEV.S
Y98-f63i	28	1000	2000	142.4	8487		301.8			
Y98-f63i	28	1000	2000	98.3	10833		208.4			
Y98-f63i	28	1000	2000	68.9	8861		146.0			
Y98-f63i	28	1000	2000	120.6	7840		255.7			
Y98-f63i	28	1000	2000	48.4	9975		102.7			
Y98-f63i	28	1000	2000	48.4	8164		102.7			
Y98-f63i	28	1000	2000	62.2	11253	9178	131.9	9178	1249	1242
Y98-f56i	28	500	2000	146.8	9425		311.2			
Y98-f56i	28	500	2000	90.7	6568		192.3			
Y98-f56i	28	500	2000	87.2	6703		184.9			
Y98-f56i	28	500	2000	148.5	7806		314.8			
Y98-f56i	28	500	2000	145.5	9716		308.5			
Y98-f56i	28	500	2000	146.7	10111	8649	311.0	8649	1623	1351
Y98-f67-2ii	28	350	2000	144.0	6425		305.4			
Y98-f67-2ii	28	350	2000	109.1	5644		231.2			
Y98-f67-2ii	28	350	2000	69.6	5142		147.7			
Y98-f67-2ii	28	350	2000	148.5	5213		314.8			
Y98-f67-2ii	28	350	2000	33.9	6542		71.9			
Y98-f67-2ii	28	350	2000	54.7	9678		115.9			
Y98-f67-2ii	28	350	2000	48.6	10372		103.1			
Y98-f67-2ii	28	350	2000	63.3	10126		134.2			
Y98-f67-2ii	28	350	2000	77.7	9887	7123	164.8	7123	1589	2058
Y98-f57i	28	150	2000	129.5	4977		274.6			
Y98-f57i	28	150	2000	146.7	8281		311.0			
Y98-f57i	28	150	2000	145.6	4365		308.7			
Y98-f57i	28	150	2000	102.9	9776	6672	218.2	6672	1113	2192
Y98-f62i	28	100	2000	119.2	6231		252.8			
Y98-f62i	28	100	2000	20.8	8111		44.1			
Y98-f62i	28	100	2000	91.9	5996		194.8			
Y98-f62i	28	100	2000	53.6	3444		113.7			
Y98-f62i	28	100	2000	123.6	6363		262.0			
Y98-f62i	28	100	2000	66.2	5834		140.3			
Y98-f62i	28	100	2000	102.3	4297	5642	217.0	5642	1225	1094
Y98-f65-2i	10	100	2000	139.4	7986					
Y98-f65-2i	10	100	2000	73.3	4455					

Table S5-3, *continued*

Y98-f65-2i	10	100	2000	85.8	3696					
Y98-f65-2i	10	100	2000	139.3	6873					
Y98-f65-2i	10	100	2000	144.3	8532	6778				
Y98-f68i	5	100	2000	134.5	7752					
Y98-f68i	5	100	2000	47.1	4581					
Y98-f68i	5	100	2000	105.3	4517					
Y98-f68i	5	100	2000	70.8	4726					
Y98-f68i	5	100	2000	147.4	4484	5404				
Y98-f69i	1	100	2000	144.2	4834					
Y98-f69i	1	100	2000	80.9	5803					
Y98-f69i	1	100	2000	80.9	5008					
Y98-f69i	1	100	2000	83.3	6511					
Y98-f69i	1	100	2000	69.8	3649	5159				
Y-980459			2000	122.7	6090		261.2			
Y-980459			2000	104.6	7486		222.7			
Y-980459			2000	116.3	4889		247.6			
Y-980459			2000	49.1	9822		104.6			
Y-980459			2000	91.8	6064	6477	195.4	6477	1032	1425

Table S6. Inputs to cooling model

used in model from Patrick et al. (2004)

***run 1** examined cooling equivalent to Stage 1; **run 2** examined cooling equivalent to Stage 2*

INPUT	RUN	VALUE	UNIT	REFERENCE	NOTES
flow thickness	1, 2	10	m	-	thick enough so that upper reaches of the flow are unaffected by cooling from the base, over the time span of interest
density at 1450 K	1, 2	3000	kg m^{-3}	MELTS [Ghiorso and Sack (1995)]	for fractional crystallization, system is 3000 kg m^{-3} at 1450 K and QFM-3
emissivity	1, 2	0.95	-	Harris (2013)	see p. 83 of Harris (2013); average emissivity of basalt is 0.95, across 2-15 μm waveband range
solidus	1, 2	1182.15	K	experimental quench temperature (this study)	no additional crystallization below that temperature (909 °C); may be a slight underestimate
conductivity at 273 K	1, 2	2	W m^{-1} K^{-1}	Keszthelyi (1994), Schumacher and Breuer (2006)	from curve in Keszthelyi (1994), 2 W m^{-1} K^{-1} is reasonable for conductivity at 273 K; Schumacher and Breuer (2006) use that value as the representative value for basaltic crust on Mars
specific heat	1, 2	1100	J kg^{-1} K^{-1}	Keszthelyi (1994) *fit to data from* Touloukian (1989)	for T > 1010 K, as reported in Patrick et al. (2004)
latent heat of fusion	1, 2	350,000	J kg^{-1}	Harris et al. (2005)	350,000 J kg^{-1} is used in this reference
convective heat transfer coefficient	1, 2	75	W m^{-2} K^{-1}	Patrick et al. (2004) and references therein	appropriate for wind speed ~ 7 m/s (Viking lander measurements for martian surface: 2-7 m/s summer, 5-10 m/s fall *from* NASA Mars Fact Sheet http://nssdc.gsfc.nasa.gov/planetary/factsheet/marsfact.html)
surface temperature	1, 2	243.15	K	NASA REMS (Curiosity)	-30 °C is a reasonable value based on archived martian surface temperature data (http://mars.nasa.gov/msl/mission/instruments/environsensors/rems/)
rain	1, 2	0	cm $year^{-1}$	Gomez-Elvira et al. (2014)	relative humidity at Gale Crater consistently below saturation
vesicle volume fraction	1, 2	0	-	petrographic observation (this study)	no vesicles are present in the thin section of Y-980459
crystal fraction	1	0.71	-	point count (this study)	crystal fraction of phenocrysts in Y-980459 (probably an overestimate, since some phenocryst rim material formed during Stage 2)
	2	0.06	-	point count (this study)	crystal fraction of groundmass in Y-980459 (probably an underestimate, since it doesn't include outer rims on phenocrysts)
time span to analyze	1	10	days	-	adequate to examine the temperature range over which crystallization occurs
	2	1	days	-	adequate to examine the temperature range over which crystallization occurs
time array elements	1	2880	-	-	according to Patrick et al. (2004), to ensure stability $\kappa(\Delta t/\Delta x^2) < 0.25$, where κ is thermal diffusivity, Δt is time step, Δx is element size; in this case, Δt = 300 s, Δx = 0.05 m, and κ assumed ~10^{-6}
	2	4320	-	-	according to Patrick et al. (2004), to ensure stability $\kappa(\Delta t/\Delta x^2) < 0.25$, where κ is thermal diffusivity, Δt is time step, Δx is element size; in this case, Δt = 20 s, Δx = 0.01 m, and κ assumed ~10^{-6}
starting lava temperature	1	1708.15	K	-	1435 °C is the start of experimental Stage 1
	2	1388.15	K	-	1115 °C is the start of experimental Stage 2

Appendix B

INTRODUCTION

This Appendix complements Chapter 3. EPMA data for glass, plagioclase, and amphibole are presented in Tables B1-B4 (1 glass, 2 plagioclase, 3 amphibole wt% analysis, 4 amphibole site occupancy based on Robinson et al., 1982).

Table B1. Glass analyses of Quizapu starting materials and experiments (norm 100% anhydrous)

SAMPLE	Temperature (°C)	Pressure (MPa)	SiO_2	TiO_2	Al_2O_3	FeO	MnO	MgO	CaO	Na_2O	K_2O	P_2O_5	Cl
VQ0606_9_7um	800	120	71.85	0.39	15.48	1.47	b.d.	0.13	0.84	5.08	4.57	b.d.	0.13
VQ-06-06_2_7um	800	120	71.97	0.39	15.11	1.52	0.05	0.15	0.81	5.23	4.58	0.06	0.12
VQ-06-06_6_10um	800	120	72.01	0.29	15.03	1.66	0.05	0.21	0.85	5.30	4.44	b.d.	0.11
VQ0606 AVERAGE	**800**	**120**	**71.94**	**0.36**	**15.21**	**1.55**	**0.05**	**0.16**	**0.84**	**5.20**	**4.53**	**0.06**	**0.12**
			0.09	0.06	0.24	0.10	0.00	0.04	0.02	0.11	0.08	-	0.01
QZ-07-05D_4_5um	805	120	71.74	0.33	15.17	1.66	0.10	0.34	1.14	5.25	4.09	0.05	0.16
QZ-07-05D_9_5um	805	120	71.70	0.34	15.21	1.71	0.05	0.33	1.11	5.24	4.10	0.05	0.16
QZ-07-05D_10_5um	805	120	71.49	0.34	15.16	1.61	0.05	0.34	1.10	5.61	4.06	0.04	0.20
QZ-07-05D_11_5um	805	120	71.56	0.35	15.26	1.61	0.10	0.34	1.12	5.34	4.09	0.06	0.15
QZ-07-05D_17_5um	805	120	71.42	0.36	15.30	1.64	0.06	0.35	1.11	5.44	4.12	0.05	0.16
QZ-07-05D_18_10um	805	120	71.54	0.34	14.90	1.77	0.07	0.34	1.09	5.72	4.01	0.05	0.17
QZ-07-05D_20_5um	805	120	71.20	0.39	15.12	1.82	0.08	0.34	1.12	5.72	3.97	0.07	0.16
QZ-07-05D_23_5um	805	120	71.77	0.32	15.20	1.57	0.07	0.33	1.11	5.31	4.12	b.d.	0.16
QZ-07-05D_26_5um	805	120	71.55	0.37	15.26	1.64	0.07	0.32	1.09	5.33	4.14	0.06	0.16
QZ-07-05D_28_5um	805	120	71.69	0.27	15.24	1.66	0.08	0.33	1.10	5.26	4.10	0.05	0.22
QZ-07-05D_30_5um	805	120	71.52	0.32	15.14	1.67	0.05	0.35	1.16	5.49	4.12	b.d.	0.17
QZ0705D AVERAGE	**805**	**120**	**71.56**	**0.34**	**15.18**	**1.67**	**0.07**	**0.34**	**1.11**	**5.43**	**4.08**	**0.05**	**0.17**
			0.16	0.03	0.11	0.07	0.02	0.01	0.02	0.18	0.05	0.01	0.02
QDeq9A_1	850	175	71.53	0.34	15.41	1.87	0.07	0.32	1.31	5.16	3.84	0.06	0.08
QDeq9A_2	850	175	71.47	0.30	15.54	1.82	0.04	0.30	1.31	5.19	3.89	0.04	0.10
QDeq9A_3	850	175	70.82	0.27	15.68	2.03	b.d.	0.33	1.42	5.37	3.88	0.05	0.10
QDeq9A_4	850	175	71.08	0.27	15.53	2.11	b.d.	0.30	1.37	5.27	3.90	0.05	0.08
QDeq9A_5	850	175	70.56	0.27	15.96	2.16	0.07	0.31	1.46	5.22	3.87	0.04	0.08
QDeq9A_6	850	175	70.25	0.29	16.13	2.12	0.05	0.30	1.53	5.28	3.94	b.d.	0.10
QDeq9A_7	850	175	70.56	0.27	15.87	2.06	0.06	0.30	1.48	5.36	3.85	0.11	0.09
QDeq9A_8	850	175	71.15	0.30	15.54	2.02	0.08	0.29	1.38	5.17	3.92	0.06	0.09
QDeq9A_9	850	175	71.30	0.28	15.59	1.96	b.d.	0.29	1.37	5.19	3.85	0.06	0.08
QDeq9A_10	850	175	71.35	0.29	15.47	1.96	0.07	0.28	1.32	5.17	3.92	0.07	0.10
9A AVERAGE	**850**	**175**	**71.01**	**0.29**	**15.67**	**2.01**	**0.06**	**0.30**	**1.39**	**5.24**	**3.89**	**0.06**	**0.09**

Table B1, *continued*

			0.44	0.02	0.24	0.11	0.01	0.01	0.07	0.08	0.03	0.02	0.01
QD_eq_9B_2	850	175	70.82	0.21	15.55	2.15	0.05	0.31	1.36	5.57	3.88	0.06	0.04
QD_eq_9B_3	850	175	71.49	0.35	15.06	2.02	0.06	0.28	1.27	5.44	3.90	0.07	0.05
QD_eq_9B_4	850	175	70.84	0.29	15.63	1.97	0.05	0.30	1.36	5.51	3.92	0.08	0.05
QD_eq_9B_5	850	175	70.50	0.28	15.64	2.02	0.05	0.29	1.42	5.81	3.88	0.04	0.07
QD_eq_9B_6	850	175	71.58	0.26	15.16	1.93	0.05	0.27	1.33	5.37	3.94	0.06	0.05
QD_eq_9B_7	850	175	70.58	0.25	15.67	1.97	0.04	0.29	1.40	5.76	3.91	0.07	0.06
QD_eq_9B_8	850	175	70.85	0.29	15.59	1.92	b.d.	0.31	1.36	5.60	3.94	0.04	0.07
QD_eq_9B_9	850	175	71.03	0.26	15.46	1.91	0.07	0.28	1.38	5.54	3.94	0.07	0.05
9B AVERAGE	**850**	**175**	**70.96**	**0.27**	**15.47**	**1.99**	**0.05**	**0.29**	**1.36**	**5.58**	**3.91**	**0.06**	**0.06**
			0.39	0.04	0.23	0.08	0.01	0.01	0.04	0.15	0.03	0.02	0.01
QDeq10A_1	875	175	69.77	0.40	16.13	2.42	0.07	0.45	1.82	5.15	3.68	0.04	0.07
QDeq10A_2	875	175	68.98	0.34	16.69	2.42	0.08	0.46	1.92	5.31	3.64	0.08	0.10
QDeq10A_3	875	175	68.60	0.33	16.80	2.51	0.07	0.45	1.90	5.53	3.64	0.07	0.08
QDeq10A_4	875	175	69.59	0.35	16.31	2.30	0.05	0.44	1.86	5.26	3.67	0.06	0.10
QDeq10A_5	875	175	70.08	0.36	15.91	2.30	0.06	0.43	1.70	5.41	3.63	0.04	0.08
QDeq10A_6	875	175	70.72	0.39	15.54	2.25	0.10	0.43	1.62	5.15	3.63	0.07	0.10
QDeq10A_7	875	175	69.44	0.36	16.45	2.32	0.06	0.45	1.82	5.23	3.70	0.06	0.10
QDeq10A_8	875	175	70.49	0.39	15.63	2.24	0.05	0.41	1.61	5.36	3.69	0.05	0.07
QDeq10A_9	875	175	70.65	0.43	15.67	2.23	0.05	0.44	1.62	5.07	3.68	0.08	0.08
QDeq10A_10	875	175	70.70	0.43	15.56	2.21	b.d.	0.44	1.59	5.10	3.78	0.09	0.10
10A AVERAGE	**875**	**175**	**69.90**	**0.38**	**16.07**	**2.32**	**0.07**	**0.44**	**1.75**	**5.26**	**3.67**	**0.06**	**0.09**
			0.75	0.03	0.48	0.10	0.02	0.01	0.13	0.15	0.04	0.02	0.01
QD_eq_10B_1	875	175	70.88	0.31	15.29	2.06	0.05	0.39	1.48	5.67	3.75	0.04	0.06
QD_eq_10B_2	875	175	70.64	0.36	15.29	2.19	0.05	0.41	1.50	5.68	3.77	0.04	0.07
QD_eq_10B_3	875	175	71.05	0.37	15.13	2.17	0.09	0.37	1.46	5.45	3.77	0.06	0.07
QD_eq_10B_4	875	175	70.04	0.39	15.76	2.27	0.06	0.40	1.63	5.60	3.72	0.06	0.06
QD_eq_10B_5	875	175	69.78	0.36	16.04	2.12	0.07	0.39	1.66	5.66	3.78	0.07	0.07
QD_eq_10B_6	875	175	71.09	0.35	15.39	1.94	0.10	0.37	1.49	5.34	3.82	0.05	0.07
QD_eq_10B_7	875	175	70.27	0.36	15.77	2.01	0.05	0.40	1.59	5.71	3.74	0.04	0.06
QD_eq_10B_8	875	175	70.17	0.33	15.80	1.98	0.08	0.40	1.57	5.81	3.74	0.07	0.05
QD_eq_10B_9	875	175	70.38	0.33	15.65	2.25	0.04	0.41	1.64	5.44	3.75	0.05	0.05
QD_eq_10B_10	875	175	68.98	0.33	16.46	2.37	0.08	0.45	1.85	5.60	3.75	0.07	0.07
10B AVERAGE	**875**	**175**	**70.33**	**0.35**	**15.66**	**2.14**	**0.07**	**0.40**	**1.59**	**5.60**	**3.76**	**0.05**	**0.06**
			0.65	0.02	0.40	0.14	0.02	0.02	0.12	0.14	0.03	0.01	0.01
QDeq15A_2	835	150	71.77	0.23	15.41	1.80	0.06	0.23	1.17	5.25	3.98	b.d.	0.10
QDeq15A_3	835	150	71.68	0.26	15.44	1.95	0.07	0.21	1.21	5.04	4.04	b.d.	0.09
QDeq15A_4	835	150	71.45	0.18	15.65	1.87	0.08	0.23	1.22	5.19	4.06	b.d.	0.08
QDeq15A_5	835	150	71.88	0.21	15.45	1.98	0.05	0.23	1.22	4.90	3.97	b.d.	0.10
QDeq15A_6	835	150	71.19	0.24	15.78	2.01	0.05	0.23	1.24	5.10	4.04	b.d.	0.09
QDeq15A_7	835	150	71.52	0.23	15.63	1.82	0.04	0.23	1.20	5.12	4.06	0.04	0.09

Table B1, *continued*

QDeq15A_8	835	150	71.57	0.22	15.27	1.90	0.08	0.22	1.26	5.29	4.01	0.07	0.11
QDeq15A_9	835	150	71.38	0.22	15.79	1.82	0.06	0.24	1.22	5.07	4.03	0.07	0.09
QDeq15A_10	835	150	71.76	0.25	15.52	1.77	0.06	0.24	1.19	5.03	4.04	0.07	0.08
15A AVERAGE	**835**	**150**	**71.58**	**0.23**	**15.55**	**1.88**	**0.06**	**0.23**	**1.21**	**5.11**	**4.03**	**0.06**	**0.09**
			0.22	0.02	0.18	0.08	0.01	0.01	0.03	0.12	0.03	0.01	0.01
QDeq15B_1	835	150	71.67	0.21	15.67	1.73	b.d.	0.21	1.26	5.02	4.08	b.d.	0.09
QDeq15B_2	835	150	71.44	0.20	15.57	1.75	0.07	0.21	1.15	5.41	4.06	0.05	0.08
QDeq15B_3	835	150	71.69	0.20	15.58	1.69	0.07	0.28	1.29	5.03	4.05	0.05	0.07
QDeq15B_4	835	150	71.79	0.21	15.70	1.59	0.04	0.22	1.20	5.11	4.03	0.04	0.07
QDeq15B_5	835	150	71.64	0.23	15.57	1.71	0.05	0.23	1.19	5.21	4.12	b.d.	0.07
QDeq15B_6	835	150	71.72	0.23	15.45	1.74	0.05	0.23	1.24	5.16	4.03	0.04	0.10
QDeq15B_7	835	150	71.79	0.23	15.61	1.79	0.07	0.22	1.20	4.97	4.02	b.d.	0.09
QDeq15B_8	835	150	71.51	0.21	15.61	1.78	0.04	0.21	1.21	5.26	4.04	0.04	0.09
QDeq15B_9	835	150	71.49	0.27	15.52	1.69	0.06	0.21	1.19	5.40	4.05	b.d.	0.09
QDeq15B_10	835	150	71.55	0.23	15.58	1.71	b.d.	0.22	1.19	5.25	4.09	0.08	0.09
15B AVERAGE	**835**	**150**	**71.63**	**0.22**	**15.59**	**1.72**	**0.06**	**0.22**	**1.21**	**5.18**	**4.06**	**0.05**	**0.09**
			0.13	0.02	0.07	0.06	0.01	0.02	0.04	0.15	0.03	0.02	0.01
QDeq17A_1	860	150	69.76	0.34	16.34	2.16	0.09	0.39	1.66	5.31	3.79	0.05	0.10
QDeq17A_2	860	150	70.37	0.30	16.22	2.18	0.10	0.41	1.68	5.22	3.36	0.07	0.09
QDeq17A_3	860	150	70.16	0.37	16.10	2.04	0.05	0.40	1.64	5.28	3.79	0.07	0.10
QDeq17A_4	860	150	69.81	0.34	16.23	2.18	0.04	0.41	1.65	5.39	3.77	0.07	0.11
QDeq17A_5	860	150	70.18	0.37	16.09	2.15	0.09	0.37	1.61	5.22	3.76	0.07	0.09
QDeq17A_6	860	150	69.93	0.31	16.36	2.21	b.d.	0.38	1.69	5.17	3.75	0.09	0.09
QDeq17A_7	860	150	70.21	0.33	16.09	2.07	0.08	0.42	1.61	5.31	3.72	0.06	0.11
QDeq17A_8	860	150	70.16	0.33	16.22	2.13	0.05	0.38	1.60	5.20	3.77	0.05	0.10
QDeq17A_9	860	150	69.93	0.33	16.32	2.18	0.11	0.41	1.66	5.18	3.76	b.d.	0.09
QDeq17A_10	860	150	70.08	0.33	16.15	2.10	0.06	0.39	1.65	5.29	3.81	0.06	0.08
17A AVERAGE	**860**	**150**	**70.06**	**0.34**	**16.21**	**2.14**	**0.08**	**0.39**	**1.65**	**5.26**	**3.73**	**0.07**	**0.10**
			0.19	0.02	0.10	0.05	0.03	0.02	0.03	0.07	0.13	0.01	0.01
QD_eq_17B_1	860	150	69.91	0.29	15.86	2.08	0.07	0.34	1.63	5.81	3.85	0.08	0.08
QD_eq_17B_2	860	150	71.14	0.33	15.29	1.99	0.05	0.31	1.41	5.55	3.80	0.06	0.08
QD_eq_17B_3	860	150	70.52	0.28	15.70	1.96	0.06	0.34	1.52	5.66	3.84	0.05	0.08
QD_eq_17B_5	860	150	70.32	0.30	15.80	2.30	0.10	0.34	1.53	5.40	3.80	0.05	0.06
QD_eq_17B_6	860	150	70.67	0.31	15.66	2.11	b.d.	0.33	1.51	5.44	3.81	0.07	0.08
QD_eq_17B_7	860	150	71.25	0.29	15.02	2.03	0.06	0.31	1.40	5.69	3.84	0.05	0.06
QD_eq_17B_8	860	150	71.15	0.27	15.54	2.26	0.06	0.32	1.49	4.97	3.86	b.d.	0.06
QD_eq_17B_9	860	150	70.23	0.29	15.59	2.32	0.08	0.32	1.51	5.65	3.88	0.07	0.07
QD_eq_17B_10	860	150	70.48	0.29	15.60	2.22	0.05	0.34	1.48	5.60	3.81	0.04	0.08
17B AVERAGE	**860**	**150**	**70.63**	**0.29**	**15.56**	**2.14**	**0.07**	**0.33**	**1.50**	**5.53**	**3.83**	**0.06**	**0.07**
			0.47	0.02	0.26	0.14	0.02	0.01	0.07	0.25	0.03	0.01	0.01
QDeq18A_2	875	150	70.72	0.42	15.54	2.30	0.08	0.44	1.59	5.06	3.72	b.d.	0.09

Table B1, *continued*

QDeq18A_3	875	150	70.43	0.35	15.75	2.32	0.08	0.42	1.58	5.18	3.70	0.09	0.10
QDeq18A_4	875	150	69.50	0.32	16.50	2.33	0.06	0.45	1.80	5.21	3.72	b.d.	0.09
QDeq18A_5	875	150	70.58	0.35	15.67	2.25	0.05	0.41	1.60	5.29	3.67	b.d.	0.11
QDeq18A_6	875	150	70.50	0.38	15.64	2.32	0.06	0.40	1.57	5.30	3.69	0.07	0.08
QDeq18A_7	875	150	71.12	0.40	15.28	2.46	0.06	0.40	1.52	5.01	3.63	b.d.	0.09
QDeq18A_8	875	150	70.65	0.37	15.59	2.42	0.09	0.43	1.61	5.05	3.63	0.06	0.10
QDeq18A_9	875	150	71.10	0.37	15.27	2.32	0.08	0.40	1.54	5.13	3.63	0.06	0.10
QDeq18A_10	875	150	70.96	0.34	15.51	2.28	0.08	0.44	1.53	4.94	3.75	0.06	0.09
18A AVERGE	**875**	**150**	**70.62**	**0.37**	**15.64**	**2.33**	**0.07**	**0.42**	**1.59**	**5.13**	**3.68**	**0.07**	**0.10**
			0.49	0.03	0.36	0.07	0.01	0.02	0.08	0.12	0.05	0.01	0.01
QD_eq_18B_1	875	150	69.62	0.37	16.22	2.25	0.08	0.42	1.67	5.46	3.75	0.08	0.08
QD_eq_18B_2	875	150	69.94	0.35	15.98	2.11	0.08	0.40	1.65	5.56	3.81	0.05	0.07
QD_eq_18B_3	875	150	69.61	0.31	16.19	2.24	0.06	0.44	1.70	5.58	3.75	0.05	0.07
QD_eq_18B_4	875	150	70.01	0.32	15.93	2.17	0.07	0.42	1.60	5.60	3.77	0.04	0.09
QD_eq_18B_5	875	150	69.99	0.30	15.78	2.03	0.08	0.39	1.59	5.93	3.78	0.07	0.08
QD_eq_18B_6	875	150	69.64	0.33	16.35	1.87	0.08	0.42	1.69	5.72	3.77	0.05	0.08
QD_eq_18B_7	875	150	70.24	0.34	16.00	1.93	0.07	0.39	1.67	5.48	3.79	b.d.	0.06
QD_eq_18B_8	875	150	69.92	0.32	16.02	2.00	b.d.	0.42	1.64	5.78	3.77	b.d.	0.08
QD_eq_18B_9	875	150	69.95	0.35	15.92	2.10	0.06	0.43	1.66	5.61	3.80	0.05	0.08
QD_eq_18B_10	875	150	70.52	0.34	15.48	2.10	0.07	0.39	1.56	5.66	3.77	0.06	0.07
18B AVERAGE	**875**	**150**	**69.94**	**0.33**	**15.99**	**2.08**	**0.07**	**0.41**	**1.64**	**5.64**	**3.78**	**0.05**	**0.08**
			0.29	0.02	0.25	0.13	0.01	0.02	0.05	0.14	0.02	0.01	0.01
QD_eq_20A_1	860	125	71.51	0.35	15.15	1.64	b.d.	0.32	1.17	5.58	4.13	b.d.	0.10
QD_eq_20A_2	860	125	71.11	0.32	15.22	1.94	0.07	0.30	1.21	5.61	4.08	0.05	0.09
QD_eq_20A_3	860	125	71.37	0.36	15.21	1.91	0.06	0.32	1.18	5.31	4.15	0.04	0.10
QD_eq_20A_4	860	125	71.30	0.35	15.12	1.96	0.06	0.31	1.20	5.48	4.11	b.d.	0.10
QD_eq_20A_5	860	125	71.03	0.35	15.33	1.90	0.08	0.30	1.28	5.52	4.08	0.04	0.09
QD_eq_20A_6	860	125	71.52	0.31	15.10	1.94	0.05	0.28	1.17	5.42	4.07	0.05	0.09
QD_eq_20A_7	860	125	71.24	0.33	15.25	1.90	0.06	0.28	1.20	5.57	4.06	b.d.	0.09
QD_eq_20A_8	860	125	70.96	0.28	15.37	2.02	0.06	0.28	1.20	5.58	4.09	0.05	0.10
QD_eq_20A_9	860	125	71.12	0.31	15.23	1.99	0.06	0.29	1.23	5.53	4.10	0.06	0.08
QD_eq_20A_10	860	125	70.97	0.30	15.32	2.06	0.05	0.28	1.24	5.66	3.99	0.04	0.09
20A AVERAGE	**860**	**125**	**71.21**	**0.32**	**15.23**	**1.93**	**0.06**	**0.30**	**1.21**	**5.53**	**4.09**	**0.05**	**0.09**
			0.21	0.02	0.09	0.11	0.01	0.02	0.03	0.10	0.04	0.01	0.01
QD_eq_20B_1	860	125	71.44	0.32	14.94	2.06	b.d.	0.29	1.21	5.48	4.06	0.07	0.09
QD_eq_20B_2	860	125	71.36	0.29	15.16	1.83	0.05	0.29	1.19	5.55	4.12	0.05	0.09
QD_eq_20B_3	860	125	71.46	0.30	15.18	1.99	0.05	0.28	1.15	5.39	4.07	0.06	0.08
QD_eq_20B_4	860	125	71.46	0.30	15.22	1.89	0.07	0.28	1.16	5.40	4.10	0.05	0.09
QD_eq_20B_5	860	125	71.27	0.30	15.11	2.13	0.07	0.26	1.16	5.46	4.09	0.05	0.11
QD_eq_20B_6	860	125	71.18	0.31	15.25	1.92	0.06	0.27	1.18	5.60	4.13	0.03	0.06
QD_eq_20B_7	860	125	71.54	0.30	15.17	1.84	0.08	0.26	1.12	5.45	4.08	0.09	0.06

Table B1, *continued*

QD_eq_20B_8	860	125	71.59	0.30	15.09	1.86	0.08	0.27	1.16	5.48	4.08	0.04	0.05
QD_eq_20B_9	860	125	71.67	0.31	15.08	1.94	b.d.	0.27	1.21	5.29	4.11	0.04	0.06
QD_eq_20B_10	860	125	71.50	0.27	15.30	1.97	0.05	0.26	1.21	5.25	4.07	0.05	0.07
20B AVERAGE	**860**	**125**	**71.45**	**0.30**	**15.15**	**1.94**	**0.06**	**0.27**	**1.18**	**5.44**	**4.09**	**0.05**	**0.08**
			0.15	0.01	0.10	0.10	0.01	0.01	0.03	0.11	0.02	0.02	0.02
QDeq21A_1	850	125	71.38	0.27	15.49	1.99	b.d.	0.23	1.16	5.24	4.09	b.d.	0.11
QDeq21A_2	850	125	71.83	0.22	15.44	1.75	0.04	0.26	1.15	5.01	4.14	0.06	0.11
QDeq21A_3	850	125	71.57	0.26	15.48	1.86	b.d.	0.25	1.17	5.17	4.09	b.d.	0.10
QDeq21A_4	850	125	71.36	0.28	15.45	1.92	0.06	0.23	1.21	5.18	4.11	0.07	0.12
QDeq21A_5	850	125	71.51	0.22	15.51	1.96	0.09	0.23	1.15	5.04	4.13	0.04	0.12
QDeq21A_6	850	125	71.43	0.25	15.51	1.78	0.05	0.25	1.15	5.27	4.12	0.08	0.10
QDeq21A_7	850	125	71.53	0.25	15.60	1.71	0.07	0.23	1.14	5.12	4.17	0.09	0.09
QDeq21A_8	850	125	71.38	0.28	15.59	1.87	0.07	0.24	1.16	5.13	4.12	0.06	0.09
QDeq21A_9	850	125	71.75	0.24	15.37	1.90	0.09	0.22	1.16	5.04	4.09	0.04	0.10
QDeq21A_10	850	125	71.49	0.24	15.44	1.93	0.07	0.25	1.21	5.06	4.14	0.07	0.10
21A AVERAGE	**850**	**125**	**71.52**	**0.25**	**15.49**	**1.87**	**0.07**	**0.24**	**1.17**	**5.12**	**4.12**	**0.06**	**0.10**
			0.16	0.02	0.07	0.09	0.02	0.01	0.03	0.09	0.03	0.02	0.01
QD_eq_21B_1	850	125	71.86	0.24	15.14	1.83	b.d.	0.22	1.11	5.22	4.23	0.04	0.07
QD_eq_21B_2	850	125	71.42	0.25	15.19	1.86	b.d.	0.24	1.11	5.65	4.15	b.d.	0.08
QD_eq_21B_3	850	125	71.41	0.19	15.17	1.95	0.05	0.22	1.12	5.67	4.15	b.d.	0.05
QD_eq_21B_4	850	125	71.31	0.23	15.28	1.94	0.07	0.22	1.13	5.55	4.16	b.d.	0.08
QD_eq_21B_5	850	125	71.52	0.23	15.26	1.79	b.d.	0.21	1.08	5.61	4.17	b.d.	0.07
QD_eq_21B_6	850	125	71.63	0.20	15.19	1.87	0.06	0.22	1.14	5.43	4.16	0.04	0.06
QD_eq_21B_7	850	125	71.47	0.24	15.30	1.68	0.06	0.23	1.10	5.64	4.14	0.07	0.07
QD_eq_21B_8	850	125	71.50	0.32	15.15	1.89	0.10	0.21	1.09	5.44	4.13	0.11	0.06
QD_eq_21B_9	850	125	71.33	0.22	15.15	1.82	0.06	0.23	1.14	5.77	4.19	0.05	0.05
QD_eq_21B_10	850	125	71.52	0.23	15.21	1.88	b.d.	0.23	1.13	5.51	4.17	b.d.	0.05
21B AVERAGE	**850**	**125**	**71.50**	**0.23**	**15.20**	**1.85**	**0.07**	**0.22**	**1.11**	**5.55**	**4.17**	**0.06**	**0.06**
			0.16	0.04	0.06	0.08	0.02	0.01	0.02	0.15	0.03	0.03	0.01
QDeq22A_1_7um	835	125	72.27	0.23	15.26	1.72	0.04	0.20	0.93	4.96	4.26	b.d.	0.12
QDeq22A_5_10um	835	125	72.09	0.26	15.13	1.94	0.08	0.18	1.00	4.96	4.24	b.d.	0.09
QDeq22A_6_10um	835	125	71.93	0.29	15.17	1.77	0.05	0.19	1.04	5.05	4.33	0.09	0.09
QDeq22A_7_7um	835	125	72.15	0.22	15.21	1.70	0.06	0.19	0.94	5.04	4.35	0.05	0.09
QDeq22A_8_10um	835	125	72.48	0.15	15.16	1.73	0.04	0.18	0.96	4.82	4.29	0.08	0.09
QDeq22A_9_7um	835	125	72.11	0.22	15.26	1.75	0.09	0.19	0.93	5.00	4.30	0.04	0.11
QDeq22A_10_7um	835	125	72.26	0.24	15.19	1.62	0.05	0.19	0.96	5.04	4.27	0.05	0.12
22A AVERAGE	**835**	**125**	**72.19**	**0.23**	**15.20**	**1.75**	**0.06**	**0.19**	**0.97**	**4.98**	**4.29**	**0.06**	**0.10**
			0.18	0.04	0.05	0.10	0.02	0.01	0.04	0.08	0.04	0.02	0.01
QDeq22B_2_5um	835	125	72.58	0.19	15.33	1.59	b.d.	0.18	0.95	4.76	4.32	b.d.	0.05
QDeq22B_3_10um	835	125	72.51	0.18	15.18	1.58	0.05	0.18	0.91	4.92	4.38	b.d.	0.08
QDeq22B_4_5um	835	125	72.28	0.23	15.38	1.67	0.06	0.17	0.93	4.80	4.33	0.06	0.09

Table B1, *continued*

QDeq22B_5_7um	835	125	72.60	0.20	15.21	1.62	0.04	0.17	0.91	4.69	4.42	b.d.	0.10
QDeq22B_6_7um	835	125	72.47	0.22	15.25	1.58	0.07	0.19	0.91	4.87	4.33	0.04	0.08
QDeq22B_7_10um	835	125	72.57	0.21	15.17	1.49	0.04	0.20	0.90	4.77	4.49	0.08	0.10
QDeq22B_8_7um	835	125	72.61	0.21	15.27	1.46	0.06	0.18	0.87	4.82	4.42	b.d.	0.09
QDeq22B_9_5um	835	125	72.43	0.22	15.33	1.34	0.06	0.20	0.89	5.08	4.32	0.05	0.09
QDeq22B_10_5um	835	125	72.58	0.24	15.38	1.40	0.05	0.18	0.90	4.82	4.31	0.05	0.09
22B AVERAGE	**835**	**125**	**72.51**	**0.21**	**15.28**	**1.52**	**0.05**	**0.18**	**0.91**	**4.84**	**4.37**	**0.05**	**0.09**
			0.11	0.02	0.08	0.11	0.01	0.01	0.02	0.11	0.06	0.01	0.01
QD_eq_24A_6	850	150	72.41	0.29	14.86	1.63	b.d.	0.24	1.05	5.33	4.10	b.d.	0.05
QD_eq_24A_8	850	150	71.89	0.26	15.09	1.72	0.06	0.24	1.07	5.43	4.16	0.06	0.03
24A AVERAGE	**850**	**150**	**72.15**	**0.28**	**14.97**	**1.67**	**0.06**	**0.24**	**1.06**	**5.38**	**4.13**	**0.06**	**0.04**
			0.37	0.01	0.16	0.06	-	0.00	0.01	0.07	0.04	-	0.01
QD_eq_24B_1	850	150	71.76	0.20	15.16	1.84	0.06	0.25	1.15	5.42	4.03	0.05	0.07
QD_eq_24B_2	850	150	71.84	0.23	15.10	1.86	0.06	0.25	1.17	5.34	4.03	b.d.	0.07
QD_eq_24B_3	850	150	71.21	0.21	15.33	2.00	0.05	0.26	1.21	5.55	4.05	0.04	0.09
QD_eq_24B_4	850	150	71.85	0.26	15.11	1.88	0.08	0.26	1.14	5.34	3.99	b.d.	0.06
QD_eq_24B_5	850	150	71.96	0.23	15.04	1.81	0.04	0.25	1.15	5.35	4.07	0.06	0.05
QD_eq_24B_6	850	150	70.80	0.28	15.55	2.01	0.08	0.26	1.25	5.64	4.00	0.03	0.10
QD_eq_24B_7	850	150	72.07	0.24	15.01	1.68	0.10	0.25	1.13	5.35	4.06	0.06	0.05
QD_eq_24B_8	850	150	70.99	0.22	15.53	1.98	0.07	0.27	1.25	5.63	3.93	0.04	0.09
QD_eq_24B_9	850	150	71.33	0.22	15.34	2.01	0.08	0.27	1.28	5.43	3.95	b.d.	0.08
QD_eq_24B_10	850	150	70.78	0.23	15.65	2.01	0.07	0.26	1.33	5.54	3.96	0.08	0.10
24B AVERAGE	**850**	**150**	**71.46**	**0.23**	**15.28**	**1.91**	**0.07**	**0.26**	**1.21**	**5.46**	**4.01**	**0.05**	**0.08**
			0.50	0.02	0.23	0.11	0.02	0.01	0.07	0.12	0.05	0.02	0.02
QD_eq_25A_1	835	175	71.33	0.24	15.42	1.94	0.06	0.28	1.43	5.40	3.71	0.08	0.11
QD_eq_25A_2	835	175	71.42	0.24	15.30	1.90	0.07	0.28	1.39	5.54	3.74	b.d.	0.09
QD_eq_25A_3	835	175	70.99	0.20	15.64	1.85	0.05	0.28	1.46	5.62	3.79	b.d.	0.10
QD_eq_25A_4	835	175	70.54	0.22	15.83	1.90	b.d.	0.29	1.51	5.72	3.80	0.06	0.10
QD_eq_25A_4	835	175	71.21	0.22	15.38	2.00	0.05	0.25	1.33	5.50	3.89	0.06	0.10
QD_eq_25A_5	835	175	70.65	0.18	15.79	1.88	0.09	0.29	1.47	5.64	3.83	0.07	0.09
QD_eq_25A_6	835	175	70.77	0.20	15.70	2.16	0.08	0.27	1.43	5.45	3.76	0.04	0.12
QD_eq_25A_7	835	175	70.82	0.18	15.76	2.07	0.06	0.28	1.43	5.52	3.78	b.d.	0.09
QD_eq_25A_8	835	175	70.45	0.19	15.80	2.11	0.08	0.29	1.47	5.68	3.76	0.06	0.11
QD_eq_25A_9	835	175	70.90	0.24	15.62	2.06	0.09	0.26	1.45	5.42	3.79	0.08	0.08
QD_eq_25A_10	835	175	70.57	0.23	15.83	2.09	0.05	0.28	1.47	5.51	3.82	0.04	0.10
25A AVERAGE	**835**	**175**	**70.88**	**0.21**	**15.64**	**2.00**	**0.07**	**0.28**	**1.44**	**5.55**	**3.79**	**0.06**	**0.10**
			0.33	0.02	0.19	0.11	0.02	0.01	0.05	0.11	0.05	0.02	0.01
QD_eq_25B_1	835	175	73.25	0.22	15.72	2.00	b.d.	0.25	1.39	3.15	3.84	0.06	0.10
QD_eq_25B_2	835	175	71.52	0.22	15.36	1.90	b.d.	0.27	1.32	5.38	3.87	0.05	0.10
QD_eq_25B_3	835	175	71.01	0.20	15.50	1.84	0.06	0.26	1.33	5.72	3.95	0.04	0.09
QD_eq_25B_4	835	175	71.26	0.19	15.29	1.90	0.07	0.26	1.30	5.68	3.88	0.07	0.09

Table B1, *continued*

QD_eq_25B_5	835	175	71.09	0.20	15.67	1.79	0.05	0.29	1.40	5.39	3.92	0.11	0.10
QD_eq_25B_6	835	175	71.06	0.26	15.55	1.91	0.08	0.26	1.41	5.40	3.89	0.07	0.11
QD_eq_25B_7	835	175	71.04	0.22	15.58	1.90	0.05	0.26	1.38	5.55	3.90	b.d.	0.10
QD_eq_25B_8	835	175	71.21	0.24	15.45	1.95	0.07	0.26	1.30	5.54	3.87	b.d.	0.09
QD_eq_25B_9	835	175	71.08	0.27	15.64	1.86	0.06	0.25	1.39	5.38	3.94	0.05	0.09
QD_eq_25B_10	835	175	71.19	0.23	15.44	1.97	0.06	0.27	1.32	5.51	3.85	0.05	0.11
25B AVERAGE	**835**	**175**	**71.37**	**0.22**	**15.52**	**1.90**	**0.06**	**0.26**	**1.35**	**5.27**	**3.89**	**0.06**	**0.10**
			0.68	0.03	0.14	0.06	0.01	0.01	0.04	0.76	0.04	0.02	0.01
QD_eq_27_1	810	175	72.30	0.10	15.08	1.65	0.06	0.15	0.99	5.45	4.07	b.d.	0.11
QD_eq_27_2	810	175	72.24	0.17	15.00	1.80	b.d.	0.14	1.00	5.42	4.10	b.d.	0.10
QD_eq_27_3	810	175	72.30	0.13	14.93	1.71	0.06	0.12	0.97	5.63	4.05	b.d.	0.08
QD_eq_27_4	810	175	72.17	0.14	15.08	1.90	0.05	0.15	1.06	5.33	4.03	b.d.	0.08
QD_eq_27_5	810	175	72.43	0.15	15.00	1.62	0.05	0.12	1.00	5.44	4.06	0.04	0.09
QD_eq_27_6	810	175	72.38	0.17	14.91	1.72	0.06	0.14	0.99	5.31	4.18	0.04	0.10
QD_eq_27_7	810	175	72.44	0.11	14.95	1.68	b.d.	0.14	0.96	5.46	4.11	0.05	0.08
QD_eq_27_8	810	175	72.44	0.18	14.85	1.58	0.07	0.16	0.98	5.50	4.09	b.d.	0.13
QD_eq_27_9	810	175	72.42	0.13	14.84	1.66	0.08	0.12	0.99	5.52	4.11	b.d.	0.10
QD_eq_27_10	810	175	72.68	0.12	14.91	1.46	0.07	0.14	0.99	5.39	4.10	b.d.	0.10
27 AVERAGE	**810**	**175**	**72.38**	**0.14**	**14.95**	**1.68**	**0.06**	**0.14**	**0.99**	**5.44**	**4.09**	**0.04**	**0.10**
			0.14	0.03	0.08	0.12	0.01	0.01	0.03	0.09	0.04	0.00	0.02
QD_eq_28A_1_10um	810	125	73.82	0.13	14.29	1.30	0.07	0.14	0.72	5.07	4.37	b.d.	0.08
QD_eq_28A_2_7um	810	125	73.85	0.15	14.33	1.35	0.05	0.12	0.76	4.94	4.36	b.d.	0.06
QD_eq_28A_3_5um	810	125	73.82	0.14	14.45	1.28	0.06	0.14	0.72	4.96	4.37	b.d.	0.05
QD_eq_28A_4_5um	810	125	73.80	0.08	14.72	1.23	0.12	0.10	0.67	4.81	4.43	b.d.	b.d.
QD_eq_28A_5_5um	810	125	72.64	0.25	14.60	1.94	0.06	0.46	0.71	4.72	4.47	0.05	0.09
QD_eq_28A_6_7um	810	125	73.61	0.19	14.29	1.43	0.06	0.12	0.75	5.16	4.29	b.d.	0.09
QD_eq_28A_7_10um	810	125	73.78	0.13	14.36	1.38	0.08	0.11	0.74	4.96	4.34	0.04	0.08
QD_eq_28A_8_7um	810	125	73.71	0.16	14.45	1.27	0.07	0.12	0.76	5.04	4.32	0.04	0.07
QD_eq_28A_9_5um	810	125	73.68	0.17	14.53	1.31	0.11	0.12	0.75	4.91	4.33	b.d.	0.08
QD_eq_28A_10_5um	810	125	73.47	0.17	14.53	1.29	0.09	0.12	0.77	5.17	4.31	b.d.	0.07
28A AVERAGE	**810**	**125**	**73.62**	**0.16**	**14.45**	**1.38**	**0.07**	**0.16**	**0.74**	**4.98**	**4.36**	**0.04**	**0.07**
			0.36	0.05	0.14	0.21	0.02	0.11	0.03	0.14	0.06	0.01	0.01
QD_eq_28B_1_10um	810	125	73.69	0.12	14.18	1.38	0.07	0.19	0.71	5.14	4.45	b.d.	0.06
QD_eq_28B_2_5um	810	125	73.90	0.13	14.47	1.29	0.04	0.12	0.76	4.77	4.39	b.d.	0.09
QD_eq_28B_3_7um	810	125	73.81	0.15	14.28	1.35	0.07	0.13	0.76	4.97	4.40	b.d.	0.08
QD_eq_28B_4_5um	810	125	73.81	0.18	14.49	1.33	0.08	0.11	0.76	4.71	4.39	0.04	0.09
QD_eq_28B_5_7um	810	125	73.58	0.17	14.31	1.36	0.05	0.13	0.81	5.03	4.40	0.07	0.08
QD_eq_28B_6_10um	810	125	73.90	0.14	14.29	1.25	0.05	0.12	0.73	5.03	4.43	b.d.	0.03
QD_eq_28B_7_10um	810	125	73.72	0.19	14.13	1.25	0.07	0.13	0.72	5.20	4.48	0.05	0.07
QD_eq_28B_8_5um	810	125	73.39	0.17	14.71	1.37	0.06	0.14	0.90	4.77	4.35	0.06	0.09
QD_eq_28B_9_10um	810	125	73.85	0.17	14.12	1.30	b.d.	0.13	0.73	5.06	4.51	b.d.	0.09

Table B1, *continued*

QD_eq_28B_10_10um	810	125	73.65	0.15	14.15	1.36	0.05	0.13	0.77	5.15	4.50	0.04	0.06
28B AVERAGE	**810**	**125**	**73.73**	**0.16**	**14.31**	**1.32**	**0.06**	**0.13**	**0.76**	**4.98**	**4.43**	**0.05**	**0.07**
			0.16	0.02	0.19	0.05	0.01	0.02	0.06	0.17	0.05	0.02	0.02
QD_eq_29_1	810	150	72.42	0.15	14.89	1.57	0.06	0.13	0.96	5.52	4.18	b.d.	0.11
QD_eq_29_2	810	150	72.28	0.15	14.92	1.64	0.06	0.14	0.99	5.44	4.24	0.04	0.11
QD_eq_29_3	810	150	72.60	0.13	14.67	1.60	0.09	0.16	0.94	5.50	4.17	b.d.	0.10
QD_eq_29_4	810	150	72.76	0.18	14.69	1.59	0.04	0.13	0.93	5.38	4.17	b.d.	0.12
QD_eq_29_5	810	150	72.70	0.09	14.82	1.58	0.07	0.15	0.92	5.38	4.17	b.d.	0.12
QD_eq_29_6	810	150	72.32	0.17	14.71	1.76	b.d.	0.14	0.99	5.47	4.23	0.06	0.11
QD_eq_29_7	810	150	72.44	0.14	14.79	1.73	0.04	0.14	0.99	5.38	4.18	0.04	0.12
QD_eq_29_8	810	150	72.20	0.15	14.85	1.67	b.d.	0.15	0.99	5.58	4.20	0.06	0.12
QD_eq_29_9	810	150	72.46	0.17	14.84	1.68	0.06	0.15	0.99	5.35	4.20	b.d.	0.10
QD_eq_29_10	810	150	72.47	0.18	14.80	1.65	0.06	0.15	0.98	5.32	4.21	0.06	0.12
29 AVERAGE	**810**	**150**	**72.47**	**0.15**	**14.80**	**1.65**	**0.06**	**0.14**	**0.97**	**5.43**	**4.20**	**0.05**	**0.11**
			0.18	0.03	0.08	0.06	0.02	0.01	0.03	0.08	0.03	0.01	0.01
QD_eq_30A_1	890	175	70.11	0.35	15.59	2.17	0.07	0.49	1.70	5.71	3.68	b.d.	0.11
QD_eq_30A_2	890	175	69.86	0.34	15.79	2.21	b.d.	0.48	1.81	5.62	3.75	b.d.	0.09
QD_eq_30A_3	890	175	69.16	0.30	16.24	2.31	0.09	0.51	1.89	5.68	3.67	0.06	0.08
QD_eq_30A_4	890	175	69.59	0.32	16.01	2.14	0.07	0.49	1.87	5.65	3.69	0.08	0.09
QD_eq_30A_5	890	175	69.89	0.36	15.68	2.13	b.d.	0.50	1.76	5.72	3.75	0.07	0.11
QD_eq_30A_6	890	175	69.79	0.36	15.73	2.34	b.d.	0.48	1.74	5.68	3.70	0.04	0.11
QD_eq_30A_7	890	175	69.65	0.33	15.98	2.33	0.04	0.48	1.82	5.52	3.68	0.07	0.10
QD_eq_30A_8	890	175	69.85	0.28	15.95	2.15	0.10	0.48	1.84	5.47	3.74	0.05	0.10
QD_eq_30A_9	890	175	70.04	0.31	15.69	2.23	0.08	0.48	1.79	5.51	3.70	0.05	0.11
QD_eq_30A_10	890	175	69.84	0.32	15.63	2.36	0.12	0.51	1.80	5.61	3.66	0.05	0.10
30A AVERAGE	**890**	**175**	**69.78**	**0.33**	**15.83**	**2.24**	**0.08**	**0.49**	**1.80**	**5.62**	**3.70**	**0.06**	**0.10**
			0.26	0.03	0.21	0.09	0.03	0.01	0.06	0.09	0.03	0.01	0.01
QD_eq_30B_1	890	175	69.07	0.36	16.23	2.38	0.07	0.51	1.86	5.64	3.72	0.08	0.08
QD_eq_30B_2	890	175	70.34	0.34	15.46	2.26	0.07	0.45	1.66	5.64	3.65	0.06	0.08
QD_eq_30B_3	890	175	70.09	0.34	15.45	2.59	0.05	0.49	1.78	5.46	3.60	0.07	0.07
QD_eq_30B_4	890	175	70.32	0.43	15.31	2.38	0.08	0.45	1.64	5.57	3.65	0.09	0.08
QD_eq_30B_5	890	175	69.46	0.32	16.07	2.41	0.04	0.45	1.80	5.54	3.76	0.08	0.08
QD_eq_30B_6	890	175	68.13	0.31	16.31	3.24	0.09	0.53	2.04	5.61	3.59	0.06	0.09
QD_eq_30B_7	890	175	67.89	0.32	16.46	3.09	0.09	0.53	2.14	5.71	3.59	0.09	0.08
QD_eq_30B_8	890	175	67.86	0.41	16.53	3.00	0.05	0.56	2.12	5.72	3.58	0.11	0.06
QD_eq_30B_9	890	175	68.11	0.34	16.52	2.82	0.07	0.57	2.09	5.76	3.58	0.08	0.08
QD_eq_30B_10	890	175	68.67	0.34	16.53	2.58	0.10	0.47	2.01	5.50	3.62	0.11	0.05
30B AVERAGE	**890**	**175**	**68.99**	**0.35**	**16.09**	**2.67**	**0.07**	**0.50**	**1.91**	**5.62**	**3.64**	**0.08**	**0.07**
			1.01	0.04	0.50	0.34	0.02	0.05	0.19	0.10	0.06	0.02	0.01
QD_eq_31_1	810	200	71.69	0.16	15.42	1.67	0.10	0.17	1.28	5.58	3.83	b.d.	0.08

Table B1, *continued*

QD_eq_31_2	810	200	71.79	0.22	15.42	1.61	0.07	0.18	1.28	5.51	3.82	b.d.	0.08
QD_eq_31_3	810	200	71.40	0.12	15.52	1.71	0.09	0.18	1.27	5.73	3.84	0.06	0.09
QD_eq_31_4	810	200	71.59	0.15	15.33	1.77	0.10	0.18	1.24	5.73	3.82	b.d.	0.07
QD_eq_31_5	810	200	71.21	0.20	15.51	1.76	0.07	0.23	1.26	5.69	3.94	0.05	0.09
QD_eq_31_6	810	200	71.53	0.21	15.37	1.72	0.05	0.19	1.30	5.66	3.87	b.d.	0.10
QD_eq_31_7	810	200	71.70	0.14	15.43	1.81	0.07	0.19	1.29	5.34	3.90	0.05	0.09
QD_eq_31_8	810	200	71.56	0.17	15.49	1.71	0.09	0.18	1.32	5.43	3.92	b.d.	0.11
QD_eq_31_9	810	200	71.50	0.10	15.53	1.81	0.06	0.17	1.24	5.52	3.93	0.03	0.10
QD_eq_31_10	810	200	71.72	0.19	15.36	1.86	0.07	0.17	1.22	5.45	3.89	b.d.	0.07
31 AVERAGE	**810**	**200**	**71.57**	**0.17**	**15.44**	**1.74**	**0.08**	**0.18**	**1.27**	**5.56**	**3.88**	**0.05**	**0.09**
			0.17	0.04	0.07	0.07	0.02	0.02	0.03	0.14	0.05	0.01	0.01
QD_eq_32_1	835	200	69.99	0.21	16.09	2.07	0.06	0.27	1.65	5.76	3.78	b.d.	0.10
QD_eq_32_2	835	200	70.53	0.22	15.89	2.00	0.05	0.28	1.60	5.55	3.73	0.06	0.10
QD_eq_32_3	835	200	70.48	0.26	15.91	2.10	0.04	0.26	1.58	5.49	3.72	0.04	0.11
QD_eq_32_4	835	200	69.89	0.23	16.12	2.11	0.10	0.28	1.65	5.71	3.75	0.06	0.10
QD_eq_32_5	835	200	69.73	0.26	16.10	2.34	0.08	0.27	1.71	5.68	3.72	b.d.	0.08
QD_eq_32_6	835	200	70.64	0.23	15.71	2.01	0.10	0.25	1.58	5.58	3.75	b.d.	0.11
QD_eq_32_7	835	200	71.11	0.23	15.59	1.89	b.d.	0.25	1.52	5.54	3.70	0.05	0.08
QD_eq_32_8	835	200	70.97	0.25	15.62	1.88	b.d.	0.26	1.58	5.58	3.69	0.04	0.10
QD_eq_32_9	835	200	70.86	0.22	15.79	1.85	0.05	0.25	1.57	5.45	3.76	0.08	0.11
QD_eq_32_10	835	200	70.34	0.23	16.03	1.82	0.07	0.27	1.58	5.72	3.80	0.04	0.10
32 AVERAGE	**835**	**200**	**70.45**	**0.23**	**15.89**	**2.01**	**0.07**	**0.26**	**1.60**	**5.61**	**3.74**	**0.05**	**0.10**
			0.47	0.02	0.20	0.16	0.02	0.01	0.05	0.11	0.04	0.01	0.01
QD_eq_33_1	850	200	70.65	0.28	15.80	1.80	0.05	0.29	1.53	5.58	3.88	0.05	0.09
QD_eq_33_2	850	200	70.59	0.30	15.82	1.86	0.07	0.27	1.46	5.67	3.83	b.d.	0.11
QD_eq_33_3	850	200	71.23	0.41	15.32	1.90	0.09	0.28	1.41	5.39	3.87	b.d.	0.08
QD_eq_33_4	850	200	71.15	0.21	15.41	1.87	b.d.	0.27	1.39	5.69	3.86	0.05	0.09
QD_eq_33_5	850	200	70.29	0.25	15.96	1.65	0.08	0.27	1.50	5.96	3.90	b.d.	0.11
QD_eq_33_6	850	200	70.97	0.26	15.74	1.93	b.d.	0.27	1.50	5.29	3.88	b.d.	0.10
QD_eq_33_7	850	200	70.96	0.19	15.64	1.87	0.07	0.27	1.55	5.52	3.83	b.d.	0.10
QD_eq_33_8	850	200	71.53	0.22	15.31	1.73	0.09	0.26	1.39	5.49	3.84	b.d.	0.11
QD_eq_33_9	850	200	70.85	0.24	15.85	1.86	0.04	0.26	1.54	5.27	3.92	0.04	0.11
QD_eq_33_10	850	200	71.71	0.30	15.15	1.70	0.09	0.26	1.34	5.52	3.83	b.d.	0.10
33 AVERAGE	**850**	**200**	**70.99**	**0.27**	**15.60**	**1.82**	**0.07**	**0.27**	**1.46**	**5.54**	**3.86**	**0.04**	**0.10**
			0.43	0.06	0.28	0.09	0.02	0.01	0.08	0.20	0.03	0.01	0.01
QDeq34_gl_1	860	125	70.97	0.29	15.76	1.82	0.10	0.33	1.33	5.15	4.06	0.07	0.13
QDeq34_gl_2	860	125	71.47	0.33	15.56	1.82	0.09	0.35	1.39	4.87	3.95	0.05	0.11
QDeq34_gl_3	860	125	70.90	0.31	15.68	2.02	0.06	0.36	1.38	5.08	4.05	0.05	0.11
QDeq34_gl_4	860	125	71.09	0.32	15.68	1.89	0.06	0.34	1.38	5.08	4.00	0.06	0.11
QDeq34_gl_5	860	125	71.23	0.28	15.59	1.84	0.09	0.34	1.35	5.03	4.06	0.05	0.14
QDeq34_gl_7	860	125	71.31	0.30	15.56	1.83	0.06	0.29	1.26	5.17	4.05	0.06	0.12

Table B1, *continued*

QDeq34_gl_8	860	125	71.27	0.31	15.62	1.76	0.09	0.33	1.29	5.13	4.05	0.04	0.12
QDeq34_gl_10	860	125	71.50	0.33	15.58	1.77	0.07	0.31	1.31	4.97	3.99	0.04	0.13
34 AVERAGE	**860**	**125**	**71.22**	**0.31**	**15.63**	**1.84**	**0.08**	**0.33**	**1.34**	**5.06**	**4.02**	**0.05**	**0.12**
			0.22	0.02	0.07	0.08	0.02	0.02	0.05	0.10	0.04	0.01	0.01
QDeq35_gl_1	835	150	72.58	0.26	14.89	1.52	0.05	0.23	0.95	5.13	4.26	b.d.	0.13
QDeq35_gl_2	835	150	72.69	0.25	14.90	1.43	0.07	0.21	0.92	5.08	4.24	0.07	0.14
QDeq35_gl_4	835	150	72.68	0.19	14.96	1.44	0.09	0.21	0.94	5.10	4.24	b.d.	0.13
QDeq35_gl_5	835	150	72.34	0.25	15.11	1.55	0.09	0.20	0.95	5.04	4.28	0.05	0.13
QDeq35_gl_6	835	150	72.67	0.28	14.86	1.42	0.06	0.21	0.94	5.12	4.26	b.d.	0.14
QDeq35_gl_7	835	150	72.87	0.23	14.91	1.43	0.07	0.19	0.94	4.91	4.29	b.d.	0.13
QDeq35_gl_8	835	150	72.78	0.23	14.92	1.48	0.04	0.22	0.92	5.01	4.26	b.d.	0.14
QDeq35_gl_9	835	150	72.77	b.d.	15.00	1.54	0.08	0.21	0.95	5.01	4.29	b.d.	0.14
QDeq35_gl_10	835	150	72.34	0.27	14.86	1.46	0.11	0.24	0.99	5.27	4.26	0.07	0.12
35 AVERAGE	**835**	**150**	**72.64**	**0.24**	**14.93**	**1.48**	**0.07**	**0.21**	**0.95**	**5.08**	**4.26**	**0.06**	**0.13**
			0.19	0.03	0.08	0.05	0.02	0.02	0.02	0.10	0.02	0.01	0.01
QDeq36_gl_1	810	175	71.97	0.22	15.60	1.26	0.07	0.25	1.21	5.20	4.07	0.04	0.11
QDeq36_gl_2	810	175	71.98	0.24	15.53	1.26	0.07	0.24	1.26	5.17	4.10	0.05	0.10
QDeq36_gl_3	810	175	72.22	0.24	15.58	1.35	0.09	0.24	1.18	4.90	4.08	b.d.	0.10
QDeq36_gl_4	810	175	72.14	0.27	15.55	1.23	0.07	0.22	1.18	5.13	4.07	b.d.	0.10
QDeq36_gl_5	810	175	71.99	0.26	15.50	1.28	0.04	0.28	1.17	5.31	4.07	b.d.	0.09
QDeq36_gl_6	810	175	71.85	0.25	15.66	1.24	0.09	0.24	1.17	5.31	4.06	0.04	0.10
QDeq36_gl_7	810	175	71.87	0.28	15.59	1.25	0.08	0.24	1.19	5.34	4.02	0.04	0.10
QDeq36_gl_8	810	175	71.97	0.27	15.53	1.29	0.07	0.25	1.17	5.30	4.03	b.d.	0.10
QDeq36_gl_9	810	175	72.29	0.26	15.55	1.19	0.06	0.23	1.19	4.99	4.09	0.05	0.10
QDeq36_gl_10	810	175	72.01	0.27	15.59	1.31	0.07	0.23	1.22	5.07	4.10	b.d.	0.10
36 AVERAGE	**810**	**175**	**72.03**	**0.26**	**15.57**	**1.26**	**0.07**	**0.24**	**1.19**	**5.17**	**4.07**	**0.04**	**0.10**
			0.14	0.02	0.05	0.05	0.02	0.02	0.03	0.15	0.03	0.00	0.00

Sample **averages in bold** at the end of the individual analyses; next line down, *in italics, is standard deviation*

Table B2. Plagioclase compositions of Quizapu starting materials and experiments.

SAMPLE	Temp (°C)	Pres (MPa)	SiO_2	Al_2O_3	FeO	MgO	CaO	Na_2O	K_2O	Total	Ab	An	Or
VQ0606_plagmicro_1	800	120	62.55	23.38	0.40	b.d.	4.99	7.84	0.64	99.81	71	25	4
VQ0606_plagmicro_2	800	120	65.32	21.77	0.56	0.02	3.87	7.51	1.13	100.20	72	21	7
VQ0606_plagmicro_3	800	120	66.33	21.52	0.55	b.d.	3.67	8.42	0.82	101.31	77	18	5
VQ0606_plagmicro_4	800	120	65.28	21.43	0.73	0.03	3.94	8.02	0.89	100.33	74	20	5
VQ0606_plagmicro_5	800	120	65.24	22.22	0.44	b.d.	4.04	8.30	0.73	100.97	75	20	4
VQ0606_plagmicro_6	800	120	58.32	26.11	0.50	b.d.	8.19	6.32	0.41	99.85	57	41	2
VQ0606_plagmicro_7	800	120	57.74	26.34	0.68	0.04	8.64	5.97	0.38	99.78	54	43	2
QZ0705D_plag_2	805	121	58.73	26.16	0.35	b.d.	7.92	6.49	0.41	100.05	58	39	2
QZ0705D_plag_3	805	121	56.83	27.42	0.40	b.d.	9.32	5.72	0.32	100.00	52	47	2
QZ0705D_plag_4	805	121	59.96	25.40	0.33	b.d.	7.10	6.79	0.50	100.09	61	36	3
QZ0705D_plag_5	805	121	59.27	26.02	0.30	b.d.	7.62	6.77	0.45	100.43	60	37	3
QZ0705D_plag_6	805	121	59.81	25.64	0.31	b.d.	7.32	6.81	0.48	100.36	61	36	3
QZ0705D_plag_7	805	121	60.18	25.15	0.28	b.d.	6.78	7.00	0.53	99.93	63	34	3
QZ0705D_plag_8	805	121	60.17	25.38	0.32	b.d.	6.89	6.99	0.53	100.28	63	34	3
QDeq7_plagmicro_7	850	100	64.82	22.02	0.49	b.d.	3.41	8.28	1.34	100.36	75	17	8
QDeq7_plagmicro_8	850	100	64.54	22.42	0.40	b.d.	3.68	7.99	1.28	100.30	74	19	8
QDeq7_plagmicro_9	850	100	63.13	23.21	0.43	b.d.	4.64	7.79	0.96	100.16	71	23	6
QDeq12A_plagmicro_1	875	75	63.52	23.05	0.46	b.d.	4.59	7.81	1.05	100.48	71	23	6
QDeq12A_plagmicro_2	875	75	63.79	22.68	0.39	b.d.	4.24	7.90	1.08	100.09	72	21	6
QDeq12A_plagmicro_3	875	75	64.13	22.51	0.42	b.d.	3.99	7.71	1.12	99.87	72	21	7
QDeq12A_plagmicro_4	875	75	64.67	22.25	0.43	b.d.	4.03	7.66	1.24	100.29	72	21	8
QDeq12A_plagmicro_5	875	75	63.54	23.37	0.28	b.d.	4.71	7.54	1.02	100.46	70	24	6
QDeq12A_plagmicro_6	875	75	65.29	22.22	0.38	0.02	3.55	8.07	1.31	100.84	74	18	8
QDeq12A_plagmicro_7	875	75	64.84	22.21	0.47	b.d.	3.72	8.09	1.24	100.56	74	19	7
QDeq12A_plagmicro_8	875	75	63.61	23.58	0.35	b.d.	4.77	7.83	0.99	101.12	70	24	6
QDeq9A_plagmicro_1	850	175	59.47	26.26	0.41	b.d.	7.86	6.34	0.50	100.85	58	39	3

Table B2, *continued*

QDeq9A_plagmicro_2	850	175	60.59	25.54	0.29	b.d.	7.00	6.88	0.51	100.80	62	35	3
QDeq9A_plagmicro_3	850	175	58.85	26.41	0.41	b.d.	8.44	5.78	0.57	100.47	53	43	3
QDeq9A_plagmicro_4	850	175	61.83	24.29	0.32	b.d.	6.11	6.79	0.70	100.04	64	32	4
QDeq9A_plagmicro_5	850	175	61.04	24.99	0.24	b.d.	6.38	7.10	0.59	100.34	64	32	4
QDeq9A_plagmicro_7	850	175	62.05	24.85	0.33	b.d.	6.36	7.03	0.64	101.25	64	32	4
QDeq9A_plagmicro_8	850	175	61.38	24.99	0.35	b.d.	6.36	7.11	0.58	100.76	65	32	3
QDeq10A_plagrim_1	875	175	62.17	24.34	0.35	b.d.	5.73	7.43	0.71	100.73	67	29	4
QDeq10A_plagrim_2	875	175	61.66	24.97	0.35	b.d.	6.33	7.15	0.64	101.11	65	32	4
QDeq10A_plagrim_3	875	175	61.82	24.56	0.36	b.d.	6.31	7.00	0.70	100.76	64	32	4
QDeq10A_plagrim_6	875	175	59.06	26.04	0.36	0.07	8.24	5.11	0.65	99.54	51	45	4
QDeq10A_plagmicro_7	875	175	54.76	29.46	0.62	b.d.	11.49	4.57	0.26	101.17	41	57	2
QDeq10A_plagmicro_8	875	175	54.91	28.62	0.88	0.06	11.09	4.74	0.26	100.57	43	56	2
QDeq10A_plagmicro_9	875	175	53.74	29.98	0.75	0.04	12.36	4.12	0.23	101.22	37	62	1
QDeq22A_plagmicro_1	835	125	62.92	23.88	0.21	b.d.	5.14	7.79	0.84	100.79	70	25	5
QDeq22A_plagmicro_2	835	125	66.43	21.60	0.42	b.d.	3.45	7.87	1.40	101.19	74	18	9
QDeq22A_plagmicro_3	835	125	62.90	23.53	0.21	b.d.	5.01	7.54	0.95	100.13	69	25	6
QDeq22A_plagmicro_4	835	125	62.85	23.16	0.39	b.d.	4.58	7.88	0.89	99.76	72	23	5
QDeq22A_plagmicro_6	835	125	62.02	24.17	0.17	b.d.	5.33	7.64	0.79	100.13	69	27	5
QDeq22A_plagmicro_7	835	125	64.37	22.39	0.59	b.d.	3.95	7.86	1.11	100.27	73	20	7
QDeq22A_plagmicro_8	835	125	60.90	24.60	0.48	b.d.	6.32	7.17	0.62	100.09	65	32	4
QDeq22A_plagmicro_9	835	125	64.99	21.92	0.48	b.d.	3.23	8.38	1.23	100.22	76	16	7
QDeq21A_plagmicro_1	850	125	59.91	25.51	0.39	b.d.	7.20	6.74	0.53	100.29	61	36	3
QDeq21A_plagmicro_2	850	125	57.49	27.42	0.41	b.d.	9.57	5.31	0.45	100.65	49	49	3
QDeq21A_plagrim_3	850	125	60.27	25.72	0.39	b.d.	7.49	6.55	0.54	100.96	59	37	3
QDeq21A_plagmicro_4	850	125	61.19	24.67	0.36	b.d.	6.55	6.95	0.67	100.40	63	33	4
QDeq21A_plagrim_5	850	125	62.74	24.54	0.23	b.d.	6.05	6.96	0.73	101.25	65	31	4
QDeq21A_plagmicro_6	850	125	61.64	24.58	0.46	b.d.	6.19	7.16	0.67	100.71	65	31	4

Table B2, *continued*

QDeq21A_plagmicro_7	850	125	62.98	23.19	0.46	b.d.	5.18	7.26	0.89	99.95	68	27	5
QDeq21A_plagrim_8	850	125	59.32	25.73	0.42	b.d.	7.44	6.49	0.51	99.91	59	38	3
QDeq21A_plagmicro_10	850	125	62.11	24.31	0.54	b.d.	5.85	7.20	0.69	100.69	66	30	4
QDeq25A_plag_1	835	175	59.89	25.76	0.24	b.d.	7.55	6.13	0.59	100.16	57	39	4
QDeq25A_plag_2	835	175	58.94	25.65	0.25	b.d.	7.72	5.98	0.59	99.13	56	40	4
QDeq25A_plag_3	835	175	61.12	24.13	0.33	b.d.	5.91	7.17	0.71	99.37	66	30	4
QDeq25A_plag_4	835	175	60.50	24.66	0.28	b.d.	6.54	6.89	0.59	99.45	63	33	4
QDeq25A_plag_5	835	175	59.64	25.32	0.40	b.d.	7.13	6.09	0.62	99.20	58	38	4
QDeq25A_plag_6	835	175	60.17	25.25	0.33	b.d.	6.84	6.85	0.54	99.99	62	34	3
QDeq25A_plag_7	835	175	60.08	25.44	0.34	b.d.	7.22	6.66	0.51	100.25	61	36	3
QDeq25A_plag_8	835	175	58.62	26.02	0.17	b.d.	7.78	6.49	0.46	99.53	58	39	3
QDeq25B_plag_1	835	175	60.18	25.41	0.24	b.d.	6.86	6.96	0.53	100.18	63	34	3
QDeq25B_plag_2	835	175	60.64	25.06	0.32	b.d.	6.63	6.98	0.55	100.18	63	33	3
QDeq25B_plag_3	835	175	57.46	26.39	0.55	0.04	9.51	4.44	0.66	99.05	44	52	4
QDeq25B_plag_4	835	175	59.79	25.43	0.33	b.d.	6.96	6.64	0.51	99.66	61	36	3
QDeq28A_plag_2	810	125	63.68	23.52	0.18	b.d.	4.58	8.10	0.82	100.88	73	23	5
QDeq28A_plag_4	810	125	64.40	22.76	0.39	b.d.	3.97	7.62	1.04	100.18	73	21	6
QDeq28A_plag_5	810	125	63.63	23.35	0.28	b.d.	4.43	8.18	0.97	100.84	73	22	6
QDeq28A_plag_6	810	125	65.77	21.60	0.39	b.d.	3.51	7.64	1.30	100.21	73	19	8
QDeq28A_plag_7	810	125	63.56	23.43	0.40	b.d.	4.74	8.24	0.99	101.35	72	23	6
QDeq28A_plag_8	810	125	63.38	23.41	0.33	b.d.	4.80	8.04	0.86	100.83	71	24	5
QDeq28B_plag_2	810	125	63.74	22.73	0.48	b.d.	4.30	7.96	0.89	100.11	73	22	5
QDeq28B_plag_4	810	125	64.35	22.48	0.37	b.d.	3.79	8.36	1.12	100.48	75	19	7
QDeq27_plag_1	810	175	61.72	24.57	0.15	b.d.	5.73	7.73	0.58	100.48	69	28	3
QDeq27_plag_2	810	175	61.23	24.73	0.17	b.d.	5.84	7.54	0.58	100.07	68	29	3
QDeq27_plag_3	810	175	61.38	25.24	0.37	b.d.	6.46	7.06	0.60	101.12	64	32	4
QDeq27_plag_5	810	175	61.57	22.98	0.28	b.d.	5.81	7.06	0.81	98.51	65	30	5

Table B2, *continued*

QDeq27_plag_6	810	175	62.54	24.39	0.26	b.d.	5.71	7.51	0.67	101.10	68	28	4
QDeq27_plag_7	810	175	61.84	24.56	0.16	b.d.	5.53	7.58	0.61	100.28	69	28	4
QDeq27_plag_8	810	175	61.15	24.50	0.34	b.d.	5.97	7.23	0.62	99.82	66	30	4

Table B3. Amphibole analyses (wt%) for Quizapu experiments and lava

SAMPLE	T (C)	P (MPa)	Rim?*	SiO2	TiO2	Al2O3	Fe2O3	FeO	MnO	MgO	CaO	Na2O	K2O	Cl	O=Cl	TOTAL
Un 173 VQ0606_amph1_a			4	44.72	2.59	8.09	4.96	8.87	0.40	13.70	10.86	2.19	0.66	0.09	0.02	97.13
Un 174 VQ0606_amph1_b			3	44.56	2.83	8.39	5.27	9.00	0.38	13.63	10.83	2.35	0.70	0.08	0.02	97.99
Un 175 VQ0606_amph1_c			4	44.92	2.73	8.13	4.92	9.16	0.44	13.73	10.90	2.27	0.71	0.08	0.02	97.97
Un 176 VQ0606_amph2			3	44.69	2.80	8.25	5.28	8.82	0.43	13.73	10.86	2.25	0.71	0.06	0.01	97.86
Un 177 VQ0606_amph3_a			3	45.45	2.65	8.11	5.16	7.85	0.41	14.48	10.90	2.24	0.68	0.08	0.02	98.00
Un 178 VQ0606_amph3_b_1um			4	44.19	3.08	9.16	4.49	8.39	0.35	13.99	10.94	2.39	0.70	0.07	0.02	97.74
Un 179 VQ0606_amph4_a			3	44.84	2.68	8.28	5.36	8.90	0.40	13.66	10.83	2.27	0.68	0.09	0.02	97.98
Un 180 VQ0606_amph4_b			3	44.70	2.68	8.16	5.50	8.90	0.43	13.62	10.82	2.28	0.67	0.07	0.02	97.81
Un 181 VQ0606_amph5_a			3	44.70	2.90	8.46	5.67	8.04	0.38	14.11	10.91	2.28	0.69	0.06	0.01	98.19
Un 182 VQ0606_amph5_b			3	44.41	2.83	8.41	4.86	8.98	0.40	13.75	10.87	2.39	0.71	0.06	0.01	97.65
Un 183 VQ0606_amph5_c			3	44.84	2.84	8.22	4.88	9.07	0.40	13.75	10.86	2.32	0.68	0.06	0.01	97.91
Un 184 VQ0606_amph6			3	44.72	2.72	8.13	4.66	9.20	0.43	13.61	10.79	2.29	0.68	0.08	0.02	97.29
Un 185 VQ0606_amph7_a			3	43.25	3.14	10.19	4.54	7.36	0.33	14.22	11.15	2.39	0.60	0.04	0.01	97.20
Un 186 VQ0606_amph7_b			3	43.09	3.06	10.39	5.95	6.37	0.32	14.49	11.14	2.52	0.53	0.04	0.01	97.89
Un 187 VQ0606_amph7_c_1um			3	44.06	3.01	9.34	5.36	7.44	0.36	14.27	10.89	2.44	0.68	0.06	0.01	97.90
Un 25 QDeq10A_amph1_d	875	175	1	44.73	2.70	8.35	5.50	8.75	0.44	13.60	10.71	2.32	0.68	0.07	0.02	97.83
Un 26 QDeq10A_amph2	875	175	3	44.38	2.66	8.78	5.58	7.11	0.41	14.54	10.99	2.31	0.62	0.05	0.01	97.43
Un 27 QDeq10A_amph3_a	875	175	3	43.97	2.78	8.35	4.49	9.02	0.44	13.61	10.83	2.30	0.71	0.08	0.02	96.56
Un 28 QDeq10A_amph3_b_5um	875	175	3	44.40	2.75	8.33	4.86	8.90	0.38	13.77	10.88	2.33	0.73	0.07	0.02	97.38
Un 31 QDeq10A_amph4	875	175	3	44.80	2.64	8.27	5.33	8.60	0.43	13.73	10.80	2.21	0.68	0.08	0.02	97.54
Un 32 QDeq10A_amph5	875	175	3	42.20	3.21	10.87	5.27	7.86	0.30	13.40	10.90	2.67	0.54	0.04	0.01	97.25
Un 33 QDeq15A_amph1_a	835	150	1	42.95	2.83	10.17	6.34	6.47	0.34	14.22	11.01	2.48	0.55	0.05	0.01	97.39
Un 34 QDeq15A_amph1_b_1um	835	150	2	46.06	2.59	8.43	3.60	11.76	0.41	12.01	10.27	2.22	0.73	0.04	0.01	98.12
Un 35 QDeq15A_amph2	835	150	1	43.63	2.85	9.69	5.12	7.83	0.36	13.88	10.96	2.39	0.65	0.04	0.01	97.39
Un 36 QDeq15A_amph3_a	835	150	1	44.08	3.00	9.01	4.62	8.96	0.41	13.61	10.87	2.40	0.71	0.08	0.02	97.73
Un 37 QDeq15A_amph3_b_1um	835	150	2	44.94	2.60	8.43	6.92	10.32	0.39	11.73	10.05	2.21	0.62	0.03	0.01	98.23
Un 38 QDeq15A_amph4_a	835	150	1	44.53	2.89	8.71	5.09	8.60	0.38	13.79	10.87	2.29	0.71	0.06	0.01	97.90
Un 39 QDeq15A_amph4_b_1um	835	150	2	45.89	2.54	7.73	6.27	10.19	0.42	12.30	10.16	2.11	0.58	0.04	0.01	98.23
Un 40 QDeq15A_amph5_a	835	150	1	44.81	2.66	8.30	5.13	8.81	0.44	13.57	10.69	2.23	0.70	0.06	0.01	97.38
Un 41 QDeq15A_amph5_b_1um	835	150	2	45.65	2.65	8.81	3.73	12.52	0.34	11.52	10.29	2.40	0.69	0.05	0.01	98.64

Table B3, *continued*

Un 43 QDeq15A_amph5_d	835	150	1	45.38	2.53	7.96	4.96	8.35	0.45	14.08	10.76	2.21	0.66	0.06	0.01	97.37
Un 44 QDeq15B_amph1_a_5um	835	150	1	44.15	2.79	8.60	4.84	9.10	0.45	13.52	10.85	2.36	0.69	0.08	0.02	97.41
Un 45 QDeq15B_amph1_b_1um	835	150	2	45.38	2.54	8.19	4.55	11.16	0.37	12.20	10.48	2.17	0.63	0.05	0.01	97.70
Un 46 QDeq15B_amph1_c_5um	835	150	1	44.37	2.87	8.61	5.07	8.67	0.36	13.73	10.81	2.38	0.67	0.06	0.01	97.59
Un 55 QDeq17A_amph1_a	860	150	1	42.84	3.52	10.47	5.01	7.21	0.28	14.28	11.22	2.52	0.55	0.03	0.01	97.92
Un 56 QDeq17A_amph1_b_1um	860	150	2	44.83	3.44	8.63	3.33	10.47	0.31	13.00	10.78	2.19	0.64	0.03	0.01	97.66
Un 57 QDeq17A_amph2_a_5um	860	150	1	42.71	3.33	10.42	4.75	7.20	0.28	14.25	11.19	2.49	0.60	0.04	0.01	97.24
Un 58 QDeq17A_amph2_c_1um	860	150	2	46.02	2.99	10.46	1.55	12.28	0.30	12.33	10.84	2.47	0.78	0.03	0.01	100.05
Un 59 QDeq17A_amph3_a_5um	860	150	1	42.33	3.24	11.23	5.62	6.04	0.20	14.46	11.22	2.56	0.49	0.02	0.00	97.42
Un 60 QDeq17A_amph3_b_1um	860	150	2	44.16	2.91	9.05	3.67	10.77	0.32	12.35	10.64	2.25	0.60	0.03	0.01	96.75
Un 61 QDeq17A_amph3_c_1um	860	150	2	43.30	3.28	9.37	2.90	11.51	0.29	12.00	10.76	2.27	0.63	0.03	0.01	96.35
Un 65 QDeq17A_amph5_a	860	150	1	42.78	3.40	9.82	4.11	8.46	0.34	13.85	11.21	2.47	0.59	0.06	0.01	97.08
Un 67 QDeq17A_amph5_c_1um	860	150	2	44.09	3.17	8.91	3.29	10.92	0.32	12.48	10.71	2.26	0.63	0.07	0.02	96.85
Un 68 QDeq18A_amph1_a	875	150	1	43.05	2.60	10.69	7.50	4.36	0.25	15.09	11.06	2.52	0.50	0.02	0.01	97.62
Un 69 QDeq18A_amph1_b_5um	875	150	2	43.97	3.20	9.38	4.99	10.09	0.33	12.42	10.54	2.37	0.62	0.04	0.01	97.93
Un 70 QDeq18A_amph1_c_1um	875	150	2	43.83	3.17	9.05	4.24	10.41	0.29	12.39	10.57	2.28	0.64	0.03	0.01	96.90
Un 72 QDeq18A_amph2_a	875	150	3	43.81	2.99	9.01	4.47	8.57	0.41	13.81	10.90	2.38	0.72	0.06	0.01	97.12
Un 74 QDeq18A_amph2_c_1um	875	150	3	44.40	2.83	8.53	1.80	10.60	0.34	13.98	11.76	2.22	0.63	0.07	0.02	97.14
Un 75 QDeq18A_amph3	875	150	4	44.45	2.91	8.77	4.93	8.05	0.35	14.20	10.97	2.35	0.66	0.07	0.02	97.69
Un 78 QDeq18A_amph4_a	875	150	3	44.64	2.79	8.42	5.77	8.64	0.43	13.73	10.77	2.41	0.70	0.08	0.02	98.37
Un 79 QDeq18A_amph4_b	875	150	3	44.54	2.68	8.36	5.16	9.07	0.43	13.48	10.70	2.36	0.70	0.07	0.02	97.52
Un 82 QDeq22A_amph1_a_5um	835	125	1	44.13	2.68	8.82	5.20	8.27	0.42	13.84	10.89	2.28	0.73	0.09	0.02	97.33
Un 83 QDeq22A_amph1_b_1um	835	125	2	45.27	2.92	7.73	4.18	11.41	0.43	12.11	10.23	2.24	0.63	0.04	0.01	97.18
Un 84 QDeq22A_amph1_c_2um	835	125	1	42.16	3.04	9.88	13.84	2.16	0.28	13.70	9.43	2.37	0.58	0.03	0.01	97.46
Un 85 QDeq22A_amph2_a_5um	835	125	1	44.58	2.90	8.52	5.25	8.28	0.40	14.05	10.93	2.32	0.65	0.06	0.01	97.93

Table B3, *continued*

Un 86 QDeq22A_amph2_b_1um	835	125	2	45.64	2.50	7.17	10.02	8.60	0.48	11.87	9.33	2.18	0.50	0.05	0.01	98.32
Un 87 QDeq22A_amph2_c	835	125	1	44.98	2.72	8.18	6.02	7.98	0.39	14.03	10.79	2.20	0.70	0.11	0.02	98.08
Un 88 QDeq22A_amph2_d_1um	835	125	2	44.40	3.02	8.50	5.25	12.30	0.41	11.07	10.07	2.39	0.70	0.07	0.02	98.16
Un 89 QDeq22A_amph3_a	835	125	3	44.40	2.88	8.47	6.03	8.28	0.41	13.72	10.73	2.31	0.69	0.07	0.02	97.97
Un 90 QDeq22A_amph3_b_2um	835	125	4	44.87	2.79	8.33	4.69	7.82	0.37	14.41	10.85	2.28	0.69	0.08	0.02	97.17
Un 91 QDeq22A_amph4_a_5um	835	125	3	42.34	3.59	10.89	5.00	7.13	0.25	13.98	11.04	2.58	0.53	0.03	0.01	97.36
Un 92 QDeq22A_amph4_b_1um	835	125	4	44.83	3.21	8.88	3.35	11.88	0.36	11.76	10.22	2.38	0.69	0.04	0.01	97.59
Un 93 QDeq22A_amph5_5um	835	125	1	43.12	3.00	10.23	6.31	5.92	0.30	14.56	11.07	2.35	0.61	0.04	0.01	97.49
Un 94 QDeq22A_amph6_a	835	125	3	45.23	2.51	7.93	5.35	8.89	0.42	13.69	10.72	2.26	0.67	0.09	0.02	97.74
Un 96 QDeq22A_amph6_c_1um	835	125	4	45.80	2.96	8.61	2.37	12.87	0.36	11.53	10.06	2.32	0.87	0.04	0.01	97.80
Un 97 QDeq22B_amph1_a_1um	835	125	2	45.28	2.88	7.77	4.13	11.97	0.39	12.03	10.50	2.22	0.66	0.04	0.01	97.85
Un 98 QDeq22B_amph1_b_2um	835	125	1	44.21	2.77	8.44	5.47	8.49	0.40	13.74	10.81	2.30	0.72	0.08	0.02	97.41
Un 99 QDeq22B_amph2_a_1um	835	125	1	42.03	2.94	11.02	5.26	8.93	0.39	12.98	11.15	2.64	0.67	0.03	0.01	98.02
Un 100 QDeq22B_amph2_b_1um	835	125	4	41.64	3.09	10.81	5.74	8.99	0.43	12.53	10.79	2.63	0.69	0.08	0.02	97.41
Un 105 QDeq21A_amph1_a	850	125	1	44.50	2.81	8.42	4.69	9.43	0.40	13.25	10.69	2.27	0.68	0.07	0.02	97.20
Un 106 QDeq21A_amph1_b_1um	850	125	1	44.82	2.76	8.13	4.47	9.66	0.43	13.12	10.52	2.21	0.74	0.07	0.02	96.91
Un 107 QDeq21A_amph1_c_1um	850	125	4	44.67	2.70	8.36	4.31	9.51	0.42	13.30	10.64	2.27	0.75	0.07	0.01	96.99
Un 108 QDeq21A_amph2_a_1um	850	125	1	43.43	2.73	9.76	5.35	7.27	0.31	14.13	11.02	2.36	0.67	0.02	0.01	97.05
Un 109 QDeq21A_amph2_b_1um	850	125	4	43.50	2.71	9.76	4.51	8.19	0.29	13.80	11.04	2.41	0.64	0.04	0.01	96.89
Un 110 QDeq21A_amph2_c_5um	850	125	1	43.66	2.98	9.45	4.10	8.38	0.31	13.66	10.74	2.35	0.75	0.06	0.01	96.42
Un 111 QDeq21A_amph3_a_1um	850	125	3	44.21	3.30	9.32	4.63	8.05	0.37	14.13	10.87	2.44	0.70	0.06	0.01	98.06
Un 112 QDeq21A_amph3_b_1um	850	125	4	44.56	2.95	8.40	3.66	10.12	0.38	13.03	10.72	2.17	0.67	0.07	0.02	96.72
Un 113 QDeq21A_amph3_c_5um	850	125	3	45.20	2.63	8.04	4.61	8.95	0.43	13.75	10.74	2.18	0.72	0.06	0.01	97.30
Un 114 QDeq21A_amph4_a_1um	850	125	1	43.73	2.95	8.94	4.51	8.05	0.36	14.03	10.90	2.34	0.67	0.07	0.02	96.53

Table B3, *continued*

Un_115 QDeq21A_amph4_b_1um	850	125	2	46.91	3.03	9.32	2.59	12.53	0.39	11.54	9.73	2.51	0.82	0.04	0.01	99.41
Un_116 QDeq21A_amph4_c_3um	850	125	1	41.28	3.15	10.59	3.61	10.01	0.36	12.56	11.12	2.53	0.71	0.07	0.02	95.98
Un_117 QDeq21A_amph5_2um	850	125	1	42.86	3.04	9.93	3.91	9.00	0.35	13.37	10.96	2.52	0.68	0.05	0.01	96.67
Un_118 QDeq20A_amph1_a_1um	860	125	2	45.00	2.87	8.35	5.07	9.84	0.39	13.01	10.55	2.31	0.71	0.08	0.02	98.16
Un_119 QDeq20A_amph1_b_2um	860	125	3	45.29	2.53	8.10	4.98	8.95	0.40	13.75	10.74	2.25	0.75	0.09	0.02	97.81
Un_120 QDeq20A_amph1_c_2um	860	125	1	44.74	2.73	8.45	5.59	8.78	0.45	13.48	10.63	2.31	0.70	0.06	0.01	97.90
Un_121 QDeq20A_amph2_a	860	125	3	42.57	3.63	10.58	5.88	6.75	0.28	14.11	10.94	2.58	0.56	0.03	0.01	97.91
Un_122 QDeq20A_amph2_b_1um	860	125	4	42.99	3.47	10.28	4.27	8.72	0.33	13.53	11.02	2.60	0.58	0.05	0.01	97.85
Un_125 QDeq20A_amph3_a_1um	860	125	1	44.93	2.75	8.48	4.78	8.12	0.37	14.35	10.93	2.37	0.70	0.06	0.01	97.82
Un_126 QDeq20A_amph3_b_3um	860	125	1	44.60	2.87	8.65	4.64	8.48	0.38	13.86	10.77	2.31	0.67	0.05	0.01	97.27
Un_127 QDeq20A_amph4_a_1um	860	125	4	43.87	3.27	9.39	4.33	8.84	0.37	13.78	10.98	2.49	0.67	0.04	0.01	98.03
Un_128 QDeq20A_amph4_b_6um	860	125	3	43.67	3.24	9.29	3.97	9.16	0.34	13.70	11.07	2.48	0.64	0.07	0.02	97.61
Un_129 QDeq20A_amph5_a_2um	860	125	3	44.72	2.73	8.25	4.17	9.75	0.43	13.34	10.76	2.24	0.76	0.08	0.02	97.22
Un_130 QDeq20A_amph5_b_2um	860	125	4	44.02	2.94	9.37	4.88	8.36	0.39	13.71	10.79	2.43	0.67	0.05	0.01	97.60
Un_131 QDeq1_amph1_a_5um	875	125	1	44.60	2.78	8.42	4.32	9.45	0.41	13.44	10.72	2.34	0.72	0.07	0.02	97.24
Un_133 QDeq1_amph2_a_2um	875	125	4	44.82	2.72	8.45	4.59	9.10	0.39	13.63	10.70	2.37	0.75	0.06	0.01	97.57
Un_134 QDeq1_amph2_b_6um	875	125	3	44.52	2.97	8.96	3.95	9.20	0.39	13.77	10.89	2.50	0.67	0.07	0.02	97.89
Un_135 QDeq1_amph3_a_3um	875	125	3	44.53	2.81	8.43	5.33	8.97	0.39	13.51	10.77	2.30	0.70	0.08	0.02	97.79
Un_136 QDeq1_amph3_b_1um	875	125	4	46.40	2.79	9.43	2.72	10.75	0.38	13.00	10.45	2.44	0.91	0.06	0.01	99.31
Un_137 QDeq1_amph4_a_2um	875	125	4	44.12	2.90	9.11	4.65	8.01	0.37	14.01	10.78	2.38	0.74	0.05	0.01	97.12
Un_138 QDeq1_amph4_b_7um	875	125	3	44.07	3.02	8.94	4.78	8.06	0.36	14.08	10.94	2.32	0.66	0.05	0.01	97.27
Un_139 QDeq1_amph5_a	875	125	1	42.96	3.27	10.79	4.55	7.42	0.26	14.19	11.20	2.63	0.53	0.04	0.01	97.83
Un_141 QDeq1_amph5_c_1um	875	125	4	44.34	3.08	10.94	2.78	8.70	0.27	13.45	10.50	2.61	0.75	0.03	0.01	97.46
Un_146 QDeq8A_amph1_a_5um	875	100	3	42.34	3.36	10.80	5.17	7.37	0.33	13.93	11.05	2.72	0.51	0.04	0.01	97.61
Un_147 QDeq8A_amph1_b_1um	875	100	4	44.24	2.75	9.43	5.74	6.64	0.55	14.55	10.87	2.47	0.52	0.04	0.01	97.80
Un_148 QDeq8A_amph1_c_1um	875	100	4	42.12	2.98	11.05	6.50	7.05	0.37	13.45	10.80	2.70	0.50	0.04	0.01	97.55
Un_149 QDeq8A_amph2_a	875	100	3	43.76	2.73	9.84	6.44	6.16	0.56	14.57	10.86	2.59	0.50	0.04	0.01	98.04

Table B3, *continued*

Un_150 QDeq8A_amph2_b	875	100	3	42.09	2.68	11.42	6.54	6.88	0.29	13.61	11.18	2.57	0.47	0.05	0.01	97.78
Un_151 QDeq8A_amph2_c_2um	875	100	4	44.74	3.04	9.46	4.61	8.26	0.36	14.10	10.95	2.40	0.73	0.09	0.02	98.71
Un_152 QDeq8A_amph3_a	875	100	3	43.23	3.31	9.36	4.51	8.86	0.38	13.58	10.95	2.52	0.62	0.04	0.01	97.34
Un_153 QDeq8A_amph3_b_1um	875	100	4	43.92	2.90	8.76	5.45	7.76	0.39	14.05	10.80	2.37	0.70	0.07	0.01	97.15
Un_154 QDeq8A_amph4_a_1um	875	100	4	43.16	2.98	8.86	5.77	7.83	0.40	13.73	10.78	2.34	0.68	0.06	0.01	96.58
Un_155 QDeq8A_amph4_b	875	100	3	42.84	3.25	9.36	4.64	8.65	0.34	13.55	10.92	2.51	0.62	0.05	0.01	96.72
Un_156 QDeq8A_amph5_a	875	100	3	41.42	3.34	11.62	4.24	8.33	0.21	13.50	11.48	2.72	0.45	0.01	0.00	97.32
Un_157 QDeq8A_amph5_b_2um	875	100	4	43.77	3.15	9.09	4.07	8.48	0.38	13.89	10.91	2.35	0.70	0.08	0.02	96.86
Un_158 QDeq8A_amph5_c_1um	875	100	4	41.66	3.15	11.77	5.93	7.03	0.25	13.76	11.28	2.71	0.54	0.03	0.01	98.11
Un_159 QDeq23A_amph1_a	875	100	3	43.02	3.58	10.04	4.71	7.66	0.30	14.14	11.09	2.53	0.57	0.02	0.00	97.67
Un_160 QDeq23A_amph1_b_2um	875	100	4	43.12	3.42	9.68	4.50	8.56	0.36	13.79	11.06	2.52	0.66	0.07	0.02	97.72
Un_161 QDeq23A_amph2_a_2um	875	100	4	43.65	3.05	9.18	4.99	8.10	0.32	13.90	10.88	2.40	0.71	0.07	0.02	97.25
Un_162 QDeq23A_amph2_b	875	100	3	41.61	3.25	11.64	4.97	7.48	0.22	13.75	11.36	2.69	0.48	0.00	0.00	97.44
Un_163 QDeq23A_amph3_1um	875	100	3	41.50	3.17	11.28	5.99	7.72	0.30	13.15	11.03	2.59	0.57	0.03	0.01	97.32
Un_164 QDeq23A_amph4_a_5um	875	100	3	44.82	2.63	8.33	5.83	7.77	0.42	14.14	10.74	2.33	0.67	0.06	0.01	97.74
Un_168 QDeq23A_amph5_a	875	100	3	44.52	2.80	8.21	5.29	9.11	0.45	13.56	10.80	2.34	0.69	0.09	0.02	97.84
Un_169 QDeq23A_amph5_b	875	100	4	43.09	3.09	10.34	5.52	6.42	0.32	14.58	11.17	2.50	0.54	0.05	0.01	97.59
Un_170 QDeq23A_amph5_c_5um	875	100	4	43.37	3.07	10.25	5.33	6.62	0.34	14.48	11.13	2.44	0.52	0.03	0.01	97.58
Un_171 QDeq23A_amph6_a_1um	875	100	4	43.36	3.17	9.01	5.45	8.08	0.36	13.69	10.73	2.45	0.63	0.09	0.02	96.98
Un_172 QDeq23A_amph6_b	875	100	3	43.75	3.13	9.02	4.83	8.75	0.38	13.61	10.83	2.46	0.65	0.06	0.01	97.47

*1 = core, 2 = rim, 3 = central but no BSE difference, 4 = edge but no BSE difference
See Table B4 for site occupancy

Table B4. Amphibole site occupancy (formulated based on Robinson et al., 1982)

	T Sites			C sites						B sites			A site			volatile site (V)		useful numbers		
SAMPLE	Si	^{IV}Al	Fe 3+	^{VI}Al	Ti	Fe 3+	Mg	Fe 2+	Mn	Mn	Ca	Na	Na	K	Vac.	Cl	F+OH	Mg#	total Al	total Fe
Un 173 VQ0606_amph1_a	6.61	1.39	0.00	0.02	0.29	0.55	3.02	1.10	0.03	0.03	1.72	0.25	0.37	0.12	0.50	0.023	1.98	0.73	1.41	1.65
Un 174 VQ0606_amph1_b	6.54	1.45	0.01	0.00	0.31	0.58	2.98	1.10	0.02	0.02	1.70	0.27	0.40	0.13	0.47	0.020	1.98	0.73	1.45	1.69
Un 175 VQ0606_amph1_c	6.59	1.41	0.00	0.00	0.30	0.54	3.00	1.12	0.03	0.03	1.71	0.26	0.39	0.13	0.48	0.021	1.98	0.73	1.41	1.67
Un 176 VQ0606_amph2	6.56	1.43	0.01	0.00	0.31	0.57	3.01	1.08	0.03	0.03	1.71	0.26	0.38	0.13	0.49	0.015	1.99	0.74	1.43	1.67
Un 177 VQ0606_amph3_a	6.62	1.38	0.00	0.02	0.29	0.57	3.15	0.96	0.03	0.03	1.70	0.27	0.36	0.13	0.51	0.021	1.98	0.77	1.39	1.52
Un 178 VQ0606_amph3_b_1um	6.48	1.52	0.00	0.06	0.34	0.49	3.06	1.03	0.02	0.02	1.72	0.26	0.42	0.13	0.45	0.017	1.98	0.75	1.58	1.52
Un 179 VQ0606_amph4_a	6.58	1.42	0.00	0.01	0.30	0.59	2.99	1.09	0.03	0.03	1.70	0.27	0.37	0.13	0.50	0.023	1.98	0.73	1.43	1.68
Un 180 VQ0606_amph4_b	6.57	1.41	0.01	0.00	0.30	0.60	2.99	1.09	0.03	0.03	1.71	0.27	0.38	0.13	0.49	0.018	1.98	0.73	1.41	1.70
Un 181 VQ0606_amph5_a	6.53	1.46	0.02	0.00	0.32	0.61	3.07	0.98	0.02	0.02	1.71	0.27	0.37	0.13	0.50	0.015	1.99	0.76	1.46	1.61
Un 182 VQ0606_amph5_b	6.54	1.46	0.00	0.00	0.31	0.54	3.02	1.11	0.02	0.02	1.72	0.26	0.42	0.13	0.44	0.016	1.98	0.73	1.46	1.64
Un 183 VQ0606_amph5_c	6.58	1.42	0.00	0.00	0.31	0.54	3.01	1.11	0.02	0.03	1.71	0.27	0.39	0.13	0.48	0.016	1.98	0.73	1.42	1.65
Un 184 VQ0606_amph6	6.60	1.40	0.00	0.02	0.30	0.52	3.00	1.14	0.03	0.03	1.71	0.27	0.39	0.13	0.48	0.020	1.98	0.73	1.42	1.65
Un 185 VQ0606_amph7_a	6.35	1.65	0.00	0.11	0.35	0.50	3.11	0.90	0.02	0.02	1.75	0.23	0.45	0.11	0.43	0.009	1.99	0.78	1.76	1.41
Un 186 VQ0606_amph7_b	6.28	1.72	0.00	0.07	0.34	0.65	3.15	0.78	0.02	0.02	1.74	0.24	0.47	0.10	0.43	0.009	1.99	0.80	1.79	1.43
Un 187 VQ0606_amph7_c_1um	6.44	1.56	0.00	0.04	0.33	0.59	3.11	0.91	0.02	0.02	1.70	0.27	0.42	0.13	0.45	0.015	1.98	0.77	1.61	1.50
Un 25 QDeq10A_amph1_d	6.57	1.43	0.00	0.01	0.30	0.61	2.98	1.07	0.03	0.03	1.68	0.29	0.37	0.13	0.50	0.018	1.98	0.73	1.44	1.68
Un 26 QDeq10A_amph2	6.50	1.50	0.00	0.02	0.29	0.62	3.17	0.87	0.03	0.03	1.73	0.25	0.41	0.12	0.47	0.014	1.99	0.78	1.52	1.49
Un 27 QDeq10A_amph3_a	6.55	1.45	0.00	0.01	0.31	0.50	3.02	1.12	0.03	0.03	1.73	0.24	0.42	0.14	0.44	0.020	1.98	0.73	1.47	1.63
Un 28 QDeq10A_amph3_b_5um	6.55	1.45	0.00	0.00	0.31	0.54	3.03	1.10	0.02	0.02	1.72	0.26	0.41	0.14	0.45	0.018	1.98	0.73	1.45	1.64
Un 31 QDeq10A_amph4	6.59	1.41	0.00	0.02	0.29	0.59	3.01	1.06	0.03	0.03	1.70	0.27	0.36	0.13	0.51	0.019	1.98	0.74	1.43	1.65
Un 32 QDeq10A_amph5	6.23	1.77	0.00	0.12	0.36	0.59	2.95	0.97	0.02	0.02	1.72	0.26	0.51	0.10	0.39	0.010	1.99	0.75	1.89	1.56
Un 33 QDeq15A_amph1_a	6.30	1.70	0.00	0.06	0.31	0.70	3.11	0.79	0.02	0.02	1.73	0.25	0.46	0.10	0.44	0.012	1.99	0.80	1.76	1.49
Un 34 QDeq15A_amph1_b_1um	6.76	1.24	0.00	0.22	0.29	0.40	2.63	1.44	0.03	0.03	1.61	0.36	0.27	0.14	0.59	0.011	1.99	0.65	1.46	1.84
Un 35 QDeq15A_amph2	6.41	1.59	0.00	0.09	0.31	0.57	3.04	0.96	0.02	0.02	1.73	0.25	0.43	0.12	0.45	0.010	1.99	0.76	1.68	1.53
Un 36 QDeq15A_amph3_a	6.48	1.52	0.00	0.05	0.33	0.51	2.98	1.10	0.03	0.03	1.71	0.26	0.42	0.13	0.44	0.020	1.98	0.73	1.56	1.61
Un 37 QDeq15A_amph3_b_1um	6.61	1.39	0.00	0.08	0.29	0.77	2.57	1.27	0.02	0.02	1.59	0.39	0.24	0.12	0.64	0.008	1.99	0.67	1.46	2.04
Un 38 QDeq15A_amph4_a	6.53	1.47	0.00	0.03	0.32	0.56	3.01	1.05	0.02	0.02	1.71	0.27	0.38	0.13	0.49	0.014	1.99	0.74	1.51	1.62
Un 39 QDeq15A_amph4_b_1um	6.73	1.27	0.00	0.06	0.28	0.69	2.69	1.25	0.03	0.03	1.60	0.38	0.22	0.11	0.67	0.011	1.99	0.68	1.34	1.94
Un 40 QDeq15A_amph5_a	6.60	1.40	0.00	0.04	0.29	0.57	2.98	1.09	0.03	0.03	1.69	0.29	0.35	0.13	0.52	0.016	1.98	0.73	1.44	1.65
Un 41 QDeq15A_amph5_b_1um	6.70	1.30	0.00	0.22	0.29	0.41	2.52	1.54	0.02	0.02	1.62	0.36	0.32	0.13	0.55	0.012	1.99	0.62	1.52	1.95
Un 43 QDeq15A_amph5_d	6.66	1.34	0.00	0.04	0.28	0.55	3.08	1.03	0.03	0.03	1.69	0.28	0.35	0.12	0.53	0.016	1.98	0.75	1.38	1.57
Un 44 QDeq15B_amph1_a_5um	6.52	1.48	0.00	0.02	0.31	0.54	2.98	1.13	0.03	0.03	1.72	0.25	0.42	0.13	0.45	0.021	1.98	0.73	1.50	1.66
Un 45 QDeq15B_amph1_b_1um	6.70	1.30	0.00	0.13	0.28	0.51	2.68	1.38	0.02	0.02	1.66	0.32	0.30	0.12	0.58	0.013	1.99	0.66	1.43	1.88

Table B4, *continued*

Un 46 QDeq15B_amph1_c_5um	6.53	1.47	0.00	0.02	0.32	0.56	3.01	1.07	0.02	0.02	1.70	0.27	0.40	0.13	0.47	0.016	1.98	0.74	1.49	1.63
Un 55 QDeq17A_amph1_a	6.26	1.74	0.00	0.06	0.39	0.55	3.11	0.88	0.02	0.02	1.76	0.23	0.49	0.10	0.41	0.008	1.99	0.78	1.80	1.43
Un 56 QDeq17A_amph1_b_1um	6.59	1.41	0.00	0.09	0.38	0.37	2.85	1.29	0.02	0.02	1.70	0.28	0.34	0.12	0.53	0.007	1.99	0.69	1.50	1.66
Un 57 QDeq17A_amph2_a_5um	6.28	1.72	0.00	0.08	0.37	0.52	3.12	0.89	0.02	0.02	1.76	0.22	0.49	0.11	0.40	0.009	1.99	0.78	1.81	1.41
Un 58 QDeq17A_amph2_c_1um	6.61	1.39	0.00	0.38	0.32	0.17	2.64	1.47	0.02	0.02	1.67	0.31	0.37	0.14	0.48	0.008	1.99	0.64	1.77	1.64
Un 59 QDeq17A_amph3_a_5um	6.19	1.81	0.00	0.12	0.36	0.62	3.15	0.74	0.01	0.01	1.76	0.23	0.50	0.09	0.41	0.005	1.99	0.81	1.93	1.36
Un 60 QDeq17A_amph3_b_1um	6.57	1.43	0.00	0.16	0.33	0.41	2.74	1.34	0.02	0.02	1.70	0.28	0.37	0.11	0.52	0.007	1.99	0.67	1.59	1.75
Un 61 QDeq17A_amph3_c_1um	6.50	1.50	0.00	0.15	0.37	0.33	2.68	1.44	0.02	0.02	1.73	0.25	0.41	0.12	0.47	0.008	1.99	0.65	1.66	1.77
Un 65 QDeq17A_amph5_a	6.33	1.67	0.00	0.04	0.38	0.46	3.05	1.05	0.02	0.02	1.78	0.20	0.51	0.11	0.38	0.016	1.98	0.74	1.71	1.50
Un 67 QDeq17A_amph5_c_1um	6.56	1.44	0.00	0.13	0.35	0.37	2.77	1.36	0.02	0.02	1.71	0.27	0.38	0.12	0.50	0.017	1.98	0.67	1.56	1.73
Un 68 QDeq18A_amph1_a	6.25	1.75	0.00	0.08	0.28	0.82	3.27	0.53	0.02	0.02	1.72	0.26	0.45	0.09	0.46	0.006	1.99	0.86	1.83	1.35
Un 69 QDeq18A_amph1_b_5um	6.48	1.52	0.00	0.10	0.35	0.55	2.73	1.24	0.02	0.02	1.66	0.32	0.36	0.12	0.52	0.009	1.99	0.69	1.63	1.80
Un 70 QDeq18A_amph1_c_1um	6.52	1.48	0.00	0.11	0.35	0.47	2.75	1.30	0.02	0.02	1.68	0.30	0.36	0.12	0.52	0.007	1.99	0.68	1.59	1.77
Un 72 QDeq18A_amph2_a	6.47	1.53	0.00	0.04	0.33	0.50	3.04	1.06	0.03	0.03	1.73	0.25	0.43	0.14	0.43	0.016	1.98	0.74	1.57	1.56
Un 74 QDeq18A_amph2_c_1um	6.57	1.43	0.00	0.06	0.32	0.20	3.09	1.31	0.02	0.02	1.87	0.11	0.52	0.12	0.36	0.018	1.98	0.70	1.49	1.51
Un 75 QDeq18A_amph3	6.51	1.49	0.00	0.03	0.32	0.54	3.10	0.99	0.02	0.02	1.72	0.26	0.41	0.12	0.47	0.018	1.98	0.76	1.51	1.53
Un 78 QDeq18A_amph4_a	6.53	1.45	0.02	0.00	0.31	0.62	2.99	1.06	0.03	0.03	1.69	0.29	0.40	0.13	0.47	0.020	1.98	0.74	1.45	1.69
Un 79 QDeq18A_amph4_b	6.57	1.43	0.00	0.02	0.30	0.57	2.96	1.12	0.03	0.03	1.69	0.28	0.39	0.13	0.47	0.018	1.98	0.73	1.45	1.69
Un 82 QDeq22A_amph1_a_5um	6.51	1.49	0.00	0.04	0.30	0.58	3.04	1.02	0.03	0.03	1.72	0.25	0.40	0.14	0.46	0.022	1.98	0.75	1.53	1.60
Un 83 QDeq22A_amph1_b_1um	6.73	1.27	0.00	0.08	0.33	0.47	2.68	1.42	0.03	0.03	1.63	0.34	0.30	0.12	0.58	0.011	1.99	0.65	1.35	1.88
Un 84 QDeq22A_amph1_c_2um	6.17	1.70	0.13	0.00	0.33	1.40	2.99	0.26	0.02	0.02	1.48	0.51	0.17	0.11	0.73	0.008	1.99	0.92	1.70	1.79
Un 85 QDeq22A_amph2_a_5um	6.53	1.47	0.00	0.00	0.32	0.58	3.07	1.01	0.03	0.03	1.71	0.26	0.40	0.12	0.48	0.015	1.98	0.75	1.47	1.59
Un 86 QDeq22A_amph2_b_1um	6.70	1.24	0.06	0.00	0.28	1.04	2.60	1.05	0.03	0.03	1.47	0.50	0.12	0.09	0.79	0.012	1.99	0.71	1.24	2.16
Un 87 QDeq22A_amph2_c	6.57	1.41	0.02	0.00	0.30	0.65	3.06	0.97	0.02	0.02	1.69	0.29	0.34	0.13	0.53	0.028	1.97	0.76	1.41	1.64
Un 88 QDeq22A_amph2_d_1um	6.59	1.41	0.00	0.08	0.34	0.59	2.45	1.53	0.03	0.03	1.60	0.37	0.32	0.13	0.55	0.017	1.98	0.62	1.49	2.11
Un 89 QDeq22A_amph3_a	6.51	1.46	0.02	0.00	0.32	0.64	3.00	1.02	0.03	0.03	1.69	0.29	0.37	0.13	0.50	0.019	1.98	0.75	1.46	1.68
Un 90 QDeq22A_amph3_b_2um	6.59	1.41	0.00	0.03	0.31	0.52	3.16	0.96	0.02	0.02	1.71	0.27	0.38	0.13	0.49	0.020	1.98	0.77	1.44	1.48
Un 91 QDeq22A_amph4_a_5um	6.22	1.78	0.00	0.10	0.40	0.55	3.06	0.88	0.02	0.02	1.74	0.25	0.49	0.10	0.41	0.009	1.99	0.78	1.88	1.43

Table B4, *continued*

Un_92 QDeq22A_amph4_b_1um	6.63	1.37	0.00	0.18	0.36	0.37	2.59	1.47	0.02	0.02	1.62	0.36	0.33	0.13	0.54	0.010	1.99	0.64	1.55	1.84
Un_93 QDeq22A_amph5_5um	6.30	1.70	0.00	0.06	0.33	0.69	3.17	0.72	0.02	0.02	1.73	0.25	0.42	0.11	0.47	0.011	1.99	0.81	1.76	1.42
Un_94 QDeq22A_amph6_a	6.64	1.36	0.00	0.02	0.28	0.59	3.00	1.09	0.03	0.03	1.69	0.29	0.36	0.13	0.52	0.022	1.98	0.73	1.37	1.68
Un_96 QDeq22A_amph6_c_1um	6.76	1.24	0.00	0.26	0.33	0.26	2.54	1.59	0.02	0.02	1.59	0.39	0.28	0.16	0.56	0.010	1.99	0.61	1.50	1.85
Un_97 QDeq22B_amph1_a_1um	6.70	1.30	0.00	0.06	0.32	0.46	2.66	1.48	0.02	0.02	1.66	0.31	0.33	0.12	0.55	0.009	1.99	0.64	1.36	1.94
Un_98 QDeq22B_amph1_b_2um	6.52	1.47	0.01	0.00	0.31	0.60	3.02	1.05	0.02	0.02	1.71	0.27	0.39	0.14	0.47	0.020	1.98	0.74	1.47	1.65
Un_99 QDeq22B_amph2_a_1um	6.20	1.80	0.00	0.11	0.33	0.58	2.85	1.10	0.02	0.02	1.76	0.21	0.54	0.13	0.33	0.007	1.99	0.72	1.91	1.68
Un_100 QDeq22B_amph2_b_1um	6.19	1.81	0.00	0.09	0.35	0.64	2.78	1.12	0.03	0.03	1.72	0.25	0.51	0.13	0.36	0.021	1.98	0.71	1.89	1.76
Un_105 QDeq21A_amph1_a	6.58	1.42	0.00	0.05	0.31	0.52	2.92	1.17	0.02	0.02	1.69	0.28	0.37	0.13	0.50	0.019	1.98	0.71	1.47	1.69
Un_106 QDeq21A_amph1_b_1um	6.65	1.35	0.00	0.07	0.31	0.50	2.90	1.20	0.03	0.03	1.67	0.30	0.33	0.14	0.53	0.018	1.98	0.71	1.42	1.70
Un_107 QDeq21A_amph1_c_1um	6.62	1.38	0.00	0.08	0.30	0.48	2.94	1.18	0.03	0.03	1.69	0.29	0.37	0.14	0.49	0.017	1.98	0.71	1.46	1.66
Un_108 QDeq21A_amph2_a_1um	6.40	1.60	0.00	0.09	0.30	0.59	3.10	0.89	0.02	0.02	1.74	0.24	0.43	0.13	0.44	0.006	1.99	0.78	1.69	1.49
Un_109 QDeq21A_amph2_b_1um	6.43	1.57	0.00	0.13	0.30	0.50	3.04	1.01	0.02	0.02	1.75	0.23	0.46	0.12	0.42	0.009	1.99	0.75	1.70	1.51
Un_110 QDeq21A_amph2_c_5um	6.48	1.52	0.00	0.13	0.33	0.46	3.02	1.04	0.02	0.02	1.71	0.27	0.40	0.14	0.46	0.016	1.98	0.74	1.65	1.50
Un_111 QDeq21A_amph3_a_1um	6.45	1.55	0.00	0.05	0.36	0.51	3.07	0.98	0.02	0.02	1.70	0.28	0.41	0.13	0.46	0.015	1.99	0.76	1.60	1.49
Un_112 QDeq21A_amph3_b_1um	6.62	1.38	0.00	0.09	0.33	0.41	2.89	1.26	0.02	0.02	1.71	0.27	0.36	0.13	0.51	0.017	1.98	0.70	1.47	1.67
Un_113 QDeq21A_amph3_c_5um	6.66	1.34	0.00	0.05	0.29	0.51	3.02	1.10	0.03	0.03	1.69	0.28	0.34	0.13	0.52	0.016	1.98	0.73	1.40	1.61
Un_114 QDeq21A_amph4_a_1um	6.48	1.52	0.00	0.05	0.33	0.50	3.10	1.00	0.02	0.02	1.73	0.25	0.43	0.13	0.45	0.017	1.98	0.76	1.56	1.50
Un_115 QDeq21A_amph4_b_1um	6.78	1.22	0.00	0.37	0.33	0.28	2.48	1.51	0.02	0.02	1.51	0.47	0.23	0.15	0.62	0.010	1.99	0.62	1.59	1.80
Un_116 QDeq21A_amph4_c_3um	6.23	1.77	0.00	0.12	0.36	0.41	2.83	1.26	0.02	0.02	1.80	0.18	0.56	0.14	0.30	0.018	1.98	0.69	1.88	1.67
Un_117 QDeq21A_amph5_2um	6.37	1.63	0.00	0.12	0.34	0.44	2.96	1.12	0.02	0.02	1.75	0.23	0.49	0.13	0.38	0.013	1.99	0.73	1.74	1.56
Un_118 QDeq20A_amph1_a_1um	6.60	1.40	0.00	0.05	0.32	0.56	2.85	1.21	0.02	0.02	1.66	0.32	0.34	0.13	0.53	0.019	1.98	0.70	1.44	1.77
Un_119 QDeq20A_amph1_b_2um	6.64	1.36	0.00	0.04	0.28	0.55	3.01	1.10	0.02	0.02	1.69	0.29	0.35	0.14	0.51	0.022	1.98	0.73	1.40	1.65
Un_120 QDeq20A_amph1_c_2um	6.57	1.43	0.00	0.03	0.30	0.62	2.95	1.08	0.03	0.03	1.67	0.30	0.36	0.13	0.51	0.015	1.98	0.73	1.46	1.69
Un_121 QDeq20A_amph2_a	6.22	1.78	0.00	0.04	0.40	0.65	3.07	0.82	0.02	0.02	1.71	0.27	0.46	0.10	0.43	0.008	1.99	0.79	1.82	1.47
Un_122 QDeq20A_amph2_b_1um	6.31	1.69	0.00	0.09	0.38	0.47	2.96	1.07	0.02	0.02	1.73	0.25	0.49	0.11	0.40	0.012	1.99	0.73	1.78	1.54
Un_125 QDeq20A_amph3_a_1um	6.57	1.43	0.00	0.03	0.30	0.53	3.13	0.99	0.02	0.02	1.71	0.27	0.41	0.13	0.46	0.015	1.99	0.76	1.46	1.52

Table B4, *continued*

Un_126 QDeq20A_amph3_b_3um	6.56	1.44	0.00	0.06	0.32	0.51	3.04	1.04	0.02	0.02	1.70	0.28	0.38	0.13	0.49	0.012	1.99	0.74	1.50	1.56
Un_127 QDeq20A_amph4_a_1um	6.43	1.57	0.00	0.05	0.36	0.48	3.01	1.08	0.02	0.02	1.72	0.25	0.45	0.13	0.42	0.010	1.99	0.74	1.62	1.56
Un_128 QDeq20A_amph4_b_6um	6.43	1.57	0.00	0.04	0.36	0.44	3.01	1.13	0.02	0.02	1.75	0.23	0.48	0.12	0.40	0.017	1.98	0.73	1.61	1.57
Un_129 QDeq20A_amph5_a_2um	6.62	1.38	0.00	0.06	0.30	0.46	2.94	1.21	0.03	0.03	1.71	0.27	0.38	0.14	0.48	0.021	1.98	0.71	1.44	1.67
Un_130 QDeq20A_amph5_b_2um	6.46	1.54	0.00	0.09	0.32	0.54	3.00	1.03	0.02	0.02	1.70	0.28	0.41	0.13	0.46	0.012	1.99	0.74	1.62	1.57
Un_131 QDeq1_amph1_a_5um	6.59	1.41	0.00	0.06	0.31	0.48	2.96	1.17	0.03	0.03	1.70	0.28	0.40	0.13	0.47	0.019	1.98	0.72	1.47	1.65
Un_133 QDeq1_amph2_a_2um	6.59	1.41	0.00	0.06	0.30	0.51	2.99	1.12	0.02	0.02	1.69	0.29	0.39	0.14	0.47	0.016	1.98	0.73	1.47	1.63
Un_134 QDeq1_amph2_b_6um	6.53	1.47	0.00	0.07	0.33	0.44	3.01	1.13	0.02	0.02	1.71	0.26	0.45	0.13	0.43	0.018	1.98	0.73	1.55	1.56
Un_135 QDeq1_amph3_a_3um	6.55	1.45	0.00	0.01	0.31	0.59	2.96	1.10	0.02	0.02	1.70	0.28	0.38	0.13	0.49	0.019	1.98	0.73	1.46	1.69
Un_136 QDeq1_amph3_b_1um	6.69	1.31	0.00	0.29	0.30	0.30	2.79	1.30	0.02	0.02	1.61	0.36	0.32	0.17	0.51	0.014	1.99	0.68	1.60	1.59
Un_137 QDeq1_amph4_a_2um	6.50	1.50	0.00	0.08	0.32	0.52	3.08	0.99	0.02	0.02	1.70	0.28	0.40	0.14	0.46	0.014	1.99	0.76	1.58	1.50
Un_138 QDeq1_amph4_b_7um	6.48	1.52	0.00	0.03	0.33	0.53	3.09	0.99	0.02	0.02	1.73	0.25	0.41	0.12	0.47	0.013	1.99	0.76	1.55	1.52
Un_139 QDeq1_amph5_a	6.27	1.73	0.00	0.13	0.36	0.50	3.09	0.91	0.02	0.02	1.75	0.23	0.51	0.10	0.39	0.009	1.99	0.77	1.86	1.41
Un_141 QDeq1_amph5_c_1um	6.47	1.53	0.00	0.35	0.34	0.31	2.93	1.06	0.02	0.02	1.64	0.34	0.40	0.14	0.46	0.008	1.99	0.73	1.88	1.37
Un_146 QDeq8A_amph1_a_5um	6.22	1.78	0.00	0.08	0.37	0.57	3.05	0.91	0.02	0.02	1.74	0.24	0.53	0.10	0.37	0.011	1.99	0.77	1.87	1.48
Un_147 QDeq8A_amph1_b_1um	6.45	1.55	0.00	0.07	0.30	0.63	3.16	0.81	0.03	0.03	1.70	0.27	0.43	0.10	0.47	0.010	1.99	0.80	1.62	1.44
Un_148 QDeq8A_amph1_c_1um	6.20	1.80	0.00	0.11	0.33	0.72	2.95	0.87	0.02	0.02	1.70	0.27	0.49	0.09	0.41	0.010	1.99	0.77	1.92	1.59
Un_149 QDeq8A_amph2_a	6.37	1.63	0.00	0.05	0.30	0.70	3.16	0.75	0.03	0.03	1.69	0.27	0.46	0.09	0.45	0.009	1.99	0.81	1.69	1.45
Un_150 QDeq8A_amph2_b	6.17	1.83	0.00	0.15	0.30	0.72	2.98	0.84	0.02	0.02	1.76	0.23	0.51	0.09	0.41	0.013	1.99	0.78	1.97	1.56
Un_151 QDeq8A_amph2_c_2um	6.48	1.52	0.00	0.10	0.33	0.50	3.05	1.00	0.02	0.02	1.70	0.28	0.40	0.13	0.47	0.022	1.98	0.75	1.62	1.50
Un_152 QDeq8A_amph3_a	6.39	1.61	0.00	0.02	0.37	0.50	2.99	1.10	0.02	0.02	1.73	0.24	0.48	0.12	0.40	0.010	1.99	0.73	1.63	1.60
Un_153 QDeq8A_amph3_b_1um	6.48	1.52	0.00	0.00	0.32	0.61	3.09	0.96	0.02	0.02	1.71	0.27	0.41	0.13	0.46	0.017	1.98	0.76	1.52	1.56
Un_154 QDeq8A_amph4_a_1um	6.42	1.55	0.02	0.00	0.33	0.62	3.05	0.97	0.03	0.03	1.72	0.26	0.42	0.13	0.45	0.016	1.98	0.76	1.55	1.62
Un_155 QDeq8A_amph4_b	6.37	1.63	0.00	0.01	0.36	0.52	3.00	1.08	0.02	0.02	1.74	0.24	0.49	0.12	0.40	0.012	1.99	0.74	1.64	1.60
Un_156 QDeq8A_amph5_a	6.12	1.88	0.00	0.14	0.37	0.47	2.97	1.03	0.01	0.01	1.82	0.17	0.61	0.09	0.31	0.002	2.00	0.74	2.02	1.50
Un_157 QDeq8A_amph5_b_2um	6.47	1.53	0.00	0.06	0.35	0.45	3.06	1.05	0.02	0.02	1.73	0.25	0.43	0.13	0.44	0.019	1.98	0.74	1.59	1.50
Un_158 QDeq8A_amph5_c_1um	6.09	1.91	0.00	0.12	0.35	0.65	3.00	0.86	0.02	0.02	1.77	0.22	0.55	0.10	0.35	0.009	1.99	0.78	2.03	1.51
Un_159 QDeq23A_amph1_a	6.30	1.70	0.00	0.04	0.39	0.52	3.09	0.94	0.02	0.02	1.74	0.24	0.48	0.11	0.41	0.004	2.00	0.77	1.74	1.46
Un_160 QDeq23A_amph1_b_2um	6.34	1.66	0.00	0.02	0.38	0.50	3.02	1.05	0.02	0.02	1.74	0.23	0.49	0.12	0.39	0.018	1.98	0.74	1.68	1.55
Un_161 QDeq23A_amph2_a_2um	6.44	1.56	0.00	0.03	0.34	0.55	3.06	1.00	0.02	0.02	1.72	0.26	0.43	0.13	0.44	0.019	1.98	0.75	1.60	1.55
Un_162 QDeq23A_amph2_b	6.12	1.88	0.00	0.14	0.36	0.55	3.02	0.92	0.01	0.01	1.79	0.19	0.57	0.09	0.34	0.000	2.00	0.77	2.02	1.47
Un_163 QDeq23A_amph3_1um	6.14	1.86	0.00	0.11	0.35	0.67	2.90	0.96	0.02	0.02	1.75	0.23	0.51	0.11	0.38	0.008	1.99	0.75	1.97	1.62
Un_164 QDeq23A_amph4_a_5um	6.56	1.44	0.00	0.00	0.29	0.64	3.09	0.95	0.03	0.03	1.69	0.29	0.37	0.13	0.50	0.016	1.98	0.76	1.44	1.59
Un_168 QDeq23A_amph5_a	6.55	1.42	0.02	0.00	0.31	0.56	2.98	1.12	0.03	0.03	1.70	0.27	0.40	0.13	0.47	0.022	1.98	0.73	1.42	1.71

Table B4, *continued*

Un_169_QDeq23A_amph5_b	6.29	1.71	0.00	0.08	0.34	0.61	3.17	0.78	0.02	0.02	1.75	0.23	0.48	0.10	0.42	0.012	1.99	0.80	1.78	1.39
Un_170_QDeq23A_amph5_c_5um	6.33	1.67	0.00	0.10	0.34	0.59	3.15	0.81	0.02	0.02	1.74	0.24	0.45	0.10	0.45	0.007	1.99	0.80	1.76	1.39
Un_171_QDeq23A_amph6_a_1um	6.42	1.57	0.01	0.00	0.35	0.60	3.02	1.00	0.02	0.02	1.70	0.28	0.43	0.12	0.45	0.022	1.98	0.75	1.57	1.61
Un_172_QDeq23A_amph6_b	6.45	1.55	0.00	0.02	0.35	0.54	2.99	1.08	0.02	0.02	1.71	0.26	0.44	0.12	0.44	0.015	1.98	0.73	1.57	1.62

For temperature, pressure, and spatial context, see Table B3, which contains additional information about the same analyses.

Appendix C

INTRODUCTION

This Appendix provides EPMA data for natural and experimental Quizapu Fe-Ti oxides (Chapter 4). Hemoilmenite is shown in Table C1, and titanomagnetite is shown in Table C2.

Table C1. Hemoilmenite compositions (wt%)

SAMPLE	T (C)	P (MPa)	SiO_2	TiO_2	Al_2O_3	V2O3	Cr2O3	Fe2O3	FeO	MnO	MgO	Total
VQ0606_oxide_3_a			0.00	45.22	0.20	0.08	0.02	16.09	33.96	0.89	3.26	99.73
VQ0606_oxide_10_a			0.00	46.94	0.17	0.09	0.00	12.87	35.85	0.91	3.06	99.88
VQ0606_ox7a_1um			0.00	45.48	0.05	0.10	0.00	13.85	34.83	0.91	2.90	98.12
VQ0606_ox7b_1um			0.02	45.29	0.04	0.11	0.00	13.80	34.72	0.89	2.88	97.74
VQ0606_ox7c_1um			0.05	45.45	0.06	0.11	0.00	14.10	34.91	0.89	2.87	98.44
VQ0606_ox9a_1um			0.13	45.02	0.05	0.06	0.00	13.99	34.48	0.89	2.96	97.58
VQ0606_ox9b_1um			0.08	45.17	0.05	0.09	0.00	14.28	34.47	0.92	3.00	98.05
VQ0606_ox11a_foc			0.19	44.85	0.10	0.10	0.00	14.25	34.35	0.90	2.98	97.73
QZ0705D_ox5a_1um			0.00	45.79	0.20	0.12	0.00	14.02	35.12	1.06	2.80	99.11
QZ0705D_ox5b_foc			0.10	45.25	0.21	0.08	0.00	14.07	34.61	1.07	2.88	98.27
QZ0705D_ox5c_1um			0.00	45.75	0.20	0.09	0.00	14.10	35.00	1.06	2.85	99.05
QZ0705D_ox8a_1um			0.00	45.64	0.19	0.08	0.00	13.88	34.91	1.05	2.85	98.60
QZ0705D_ox8b_foc			0.14	44.80	0.20	0.08	0.00	13.93	34.48	1.02	2.78	97.43
QZ0705D_ox11a_1um			0.02	45.34	0.17	0.09	0.00	13.63	34.58	1.07	2.89	97.77
QZ0705D_ox11b_foc			0.17	44.88	0.21	0.14	0.00	13.96	34.28	1.04	2.94	97.61
QZ0705D_ox11c_1um			0.00	45.33	0.18	0.07	0.02	13.92	34.55	1.05	2.89	98.01
QDeq1_oxide_3_a_1um	875	125	0.00	53.83	0.21	0.11	0.00	0.00	42.83	0.86	2.26	100.09
QDeq1_oxide_3_b_focused	875	125	0.31	52.86	0.24	0.10	0.00	0.34	42.60	0.85	2.50	99.81
QDeq1_oxide_4_a_1um	875	125	0.14	54.01	0.18	0.14	0.00	0.00	41.17	0.92	2.44	98.99
QDeq1_oxide_4_b_1um	875	125	0.00	53.86	0.12	0.19	0.00	0.00	41.75	0.94	2.43	99.29
QDeq8A_oxide_1_a_focused	875	100	0.00	52.86	0.12	0.04	0.00	0.98	43.09	0.95	1.96	100.00
QDeq8A_oxide_5_a_focused	875	100	0.00	48.03	0.40	0.12	0.00	10.42	38.00	0.91	2.40	100.29
QDeq9A_oxide_4_a_focused	850	175	0.09	47.74	0.99	0.50	0.04	8.05	38.79	0.85	1.91	98.96
QDeq9A_oxide_6_a_3um	850	175	0.00	44.53	0.22	0.11	0.00	16.24	36.36	0.63	1.72	99.80
QDeq9A_oxide_6_b_focused	850	175	0.00	45.81	0.16	0.11	0.00	14.35	36.42	0.69	2.29	99.84
QD_eq_9A_ox2c_focused	850	175	0.87	50.97	0.34	1.05	0.06	0.00	42.14	0.86	1.58	97.88
QD_eq_9A_ox7a_focused	850	175	0.95	52.88	0.29	0.20	0.00	0.00	40.09	1.00	2.23	97.63
QDeq10A_oxide_4_a_1um	875	175	0.00	53.09	0.13	0.34	0.03	0.00	43.63	0.78	1.85	99.84
QDeq10A_oxide_4_b_1um	875	175	0.05	52.85	0.13	0.80	0.05	0.00	42.77	0.77	2.17	99.61
QDeq10A_oxide_6_a_focused	875	175	0.65	52.73	0.15	0.08	0.00	0.00	41.62	0.91	2.90	99.04

Table C1, *continued*

QDeq10A_oxide_8_a_1um	875	175	0.06	53.16	0.08	1.10	0.05	0.00	41.79	0.88	2.81	99.93
QDeq10A_ox3a_1um	875	175	0.69	53.40	0.15	0.91	0.05	0.00	39.60	0.89	2.76	98.44
QDeq10A_ox4a_foc	875	175	0.75	52.34	0.19	0.40	0.03	0.00	41.88	0.80	1.85	98.24
QDeq15A_oxide_1_b_focused	835	150	0.23	51.91	0.19	0.22	0.02	0.86	44.95	0.76	0.70	99.84
QDeq15A_oxide_6_a_focused	835	150	0.16	45.85	0.45	0.37	0.00	11.94	38.47	0.68	1.28	99.19
QDeq15A_oxide_6_b_focused	835	150	0.12	44.44	0.48	0.20	0.00	14.19	37.30	0.65	1.21	98.58
QDeq15A_oxide_6_c_focused	835	150	0.21	46.35	0.49	0.13	0.00	11.46	38.41	0.82	1.51	99.38
QDeq17A_oxide_2_a_1um	860	150	0.13	46.51	0.53	0.07	0.00	11.51	37.94	0.62	1.92	99.22
QDeq17A_oxide_3_c_1um	860	150	0.16	51.96	0.13	0.36	0.04	1.04	43.13	0.74	1.71	99.26
QDeq17A_oxide_5_a_1um	860	150	0.05	46.07	0.56	0.13	0.00	12.07	37.21	0.66	2.03	98.79
QDeq17A_oxide_6_a_1um	860	150	0.07	47.25	0.52	0.34	0.02	9.01	38.29	0.68	2.02	98.19
QDeq17A_ox2a_1um	860	150	0.35	50.81	0.22	0.13	0.00	1.12	41.77	0.79	1.99	97.19
QDeq17A_ox4c_foc	860	150	0.31	51.94	0.07	0.19	0.02	0.00	43.41	0.71	1.20	97.87
QDeq18A_oxide_4_a_1um	875	150	0.19	54.78	0.14	0.12	0.00	0.00	41.89	0.88	2.75	100.76
QDeq18A_ox1a_1um	875	150	0.39	53.24	0.08	0.94	0.08	0.00	39.37	0.88	2.37	97.34
QDeq20A_oxide_1_a_1um	860	125	0.00	44.25	0.35	0.07	0.00	15.98	36.29	0.58	1.64	99.16
QDeq20A_oxide_4_a_1um	860	125	0.00	44.96	0.81	0.17	0.00	13.95	36.79	0.62	1.70	98.99
QDeq20A_oxide_7_a_1um	860	125	0.00	53.81	0.14	0.10	0.00	0.00	43.32	0.87	1.94	100.18
QDeq21A_oxide_2_a_focused	850	125	0.84	51.91	0.36	1.10	0.06	0.00	41.75	0.98	2.21	99.22
QDeq21A_oxide_2_b_focused	850	125	0.62	51.97	0.45	0.91	0.05	0.00	41.86	1.02	2.34	99.22
QDeq21A_oxide_3_a_1um	850	125	0.00	44.23	0.31	0.07	0.03	15.94	36.57	0.60	1.47	99.21
QDeq21A_oxide_3_b_1um	850	125	0.00	44.23	0.56	0.28	0.00	13.89	36.58	0.65	1.43	97.61
QDeq21A_oxide_5_a_1um	850	125	0.00	43.86	0.50	0.12	0.00	15.58	36.39	0.59	1.38	98.42
QDeq21A_oxide_5_b_1um	850	125	0.00	43.78	0.41	0.12	0.00	15.97	36.34	0.58	1.37	98.57
QDeq21A_ox5a_1um	850	125	0.00	52.58	0.00	0.69	0.04	0.00	41.86	0.97	1.63	97.77
QDeq22A_oxide_2_a_1um	835	125	0.16	44.68	0.45	0.12	0.00	14.83	37.65	0.59	1.20	99.68
QDeq22A_oxide_3_a_7um	835	125	0.00	45.43	0.21	0.13	0.00	16.15	34.17	0.91	3.24	100.24
QDeq22B_oxide_3_a_focused	835	125	0.11	53.50	0.12	0.10	0.00	0.00	42.10	1.27	2.18	99.39
QDeq23A_oxide_1_a_1um	875	100	0.00	52.64	0.12	1.06	0.29	0.00	41.64	0.72	2.69	99.16
QDeq23A_oxide_1_b_focused	875	100	0.00	52.56	0.14	1.38	0.22	0.00	41.41	0.72	2.69	99.12
QDeq23A_oxide_2_a_1um	875	100	0.00	54.84	0.12	0.12	0.02	0.00	41.53	0.86	3.02	100.52
QDeq23A_oxide_2_b_focused	875	100	0.00	54.12	0.12	0.13	0.02	0.00	41.35	0.86	3.13	99.73
QDeq23A_oxide_6_b_1um	875	100	0.00	52.97	0.17	0.44	0.03	0.04	44.08	0.67	1.62	100.02
QDeq24A_ox3b_foc	850	150	0.36	49.20	0.22	0.14	0.03	4.47	39.78	1.20	2.07	97.47
QDeq24B_ox1a_foc	850	150	0.51	48.35	0.22	0.15	0.00	5.76	39.77	1.03	1.84	97.63
QDeq24B_ox6a_foc	850	150	0.14	49.61	0.14	0.29	0.05	4.96	39.77	1.08	2.20	98.24
QDeq24B_ox6b_foc	850	150	0.35	49.27	0.16	0.27	0.07	4.45	39.55	1.07	2.30	97.49

Table C1, *continued*

QDeq25A_ox1a_1um	835	175	0.00	45.36	0.17	0.10	0.00	13.58	37.14	0.76	1.62	98.74
QDeq25A_ox1b_foc	835	175	0.12	47.83	0.14	0.07	0.00	8.57	39.43	0.93	1.57	98.66
QDeq25A_ox5a_1um	835	175	0.18	50.09	0.14	0.13	0.00	3.05	41.17	1.06	1.70	97.53
QDeq25A_ox6a_foc	835	175	0.22	50.38	0.14	0.46	0.00	2.60	40.75	1.07	2.10	97.72
QDeq25B_ox1b_1um	835	175	0.02	44.63	0.20	0.11	0.00	14.50	36.36	0.75	1.71	98.30
QDeq25B_ox1c_foc	835	175	0.11	46.67	0.15	0.05	0.00	10.81	38.07	0.78	1.82	98.46
QDeq25B_ox2a_1um	835	175	0.00	45.70	0.19	0.13	0.00	14.24	34.88	0.82	3.02	98.98
QDeq25B_ox3a_1um	835	175	0.18	51.07	0.12	0.27	0.03	2.46	41.33	1.16	2.05	98.66
QDeq25B_ox6a_foc	835	175	0.36	49.19	0.20	0.14	0.00	4.30	40.04	1.06	2.00	97.29
QDeq27_ox1a_5um	810	175	0.39	45.70	0.17	0.11	0.00	13.55	35.56	1.04	2.78	99.30
QDeq27_ox1b_1um	810	175	0.56	44.07	0.28	0.10	0.00	13.01	38.16	0.80	0.75	97.74
QDeq27_ox1c_1um	810	175	0.55	44.29	0.31	0.13	0.00	12.08	38.30	0.76	0.80	97.22
QDeq27_ox3a_foc	810	175	0.66	51.45	0.14	0.23	0.03	0.00	43.38	1.06	0.61	97.55
QDeq27_ox4b_1um	810	175	0.58	52.21	0.08	0.55	0.04	0.00	44.06	1.04	0.50	99.07
QDeq27_ox5c_foc	810	175	0.62	51.91	0.08	0.16	0.02	0.00	44.19	1.05	0.42	98.44
QDeq27_ox6a_1um	810	175	0.66	44.27	0.24	0.11	0.00	12.19	38.20	0.82	0.89	97.38
QDeq28A_ox6a_1um	810	125	0.71	44.80	0.17	0.08	0.00	12.09	37.66	1.32	1.20	98.03
QDeq28A_ox6b_1um	810	125	0.69	45.03	0.19	0.11	0.00	12.31	37.68	1.25	1.34	98.60
QDeq28A_ox6c_1um	810	125	0.71	44.45	0.14	0.07	0.00	12.41	37.19	1.37	1.26	97.60
QDeq28A_ox6d_5um	810	125	0.61	45.70	0.20	0.08	0.00	12.70	36.96	1.10	2.11	99.46
QDeq28B_ox4b_foc	810	125	0.68	43.71	0.15	0.07	0.00	13.74	36.92	1.16	1.14	97.59
QDeq28B_ox4c_1um	810	125	0.64	44.16	0.17	0.08	0.00	13.04	37.24	1.14	1.17	97.65
QDeq28B_ox6a_foc	810	125	0.74	44.86	0.18	0.09	0.00	11.72	37.26	1.47	1.39	97.71
QDeq28B_ox6c_1um	810	125	0.73	43.98	0.16	0.12	0.00	13.01	37.06	1.21	1.20	97.47
QDeq28B_ox4d_1um	810	125	0.60	44.65	0.20	0.11	0.00	12.99	37.80	1.12	1.09	98.55
QDeq29_ox2a_foc	810	150	0.75	45.52	0.34	0.20	0.00	9.86	39.44	0.89	0.84	97.84
QDeq29_ox2b_foc	810	150	0.71	49.11	0.19	0.11	0.00	2.87	42.06	1.11	1.03	97.18
QDeq29_ox3a_1um	810	150	0.68	44.69	0.39	0.13	0.00	10.93	39.09	0.82	0.61	97.36
QDeq29_ox3b_1um	810	150	0.52	45.83	0.18	0.13	0.00	11.54	37.14	0.95	2.10	98.38
QDeq29_ox3c_foc	810	150	0.71	48.51	0.22	0.10	0.00	4.30	41.92	1.03	0.85	97.64
QDeq29_ox5b_1um	810	150	0.61	51.97	0.07	0.32	0.02	0.00	43.36	1.19	0.60	98.14
QDeq29_ox6a_1um	810	150	0.61	44.56	0.32	0.10	0.00	11.52	38.73	0.79	0.72	97.36
QDeq29_ox7b_foc	810	150	0.55	51.69	0.08	0.20	0.00	0.00	44.17	1.10	0.39	98.16
QDeq30B_ox1e_foc	890	175	0.51	51.45	0.18	0.80	0.07	0.00	41.30	0.82	2.32	97.45
QDeq30B_ox3c_1um	890	175	0.45	51.84	0.17	0.41	0.02	0.00	42.48	0.74	2.11	98.23
QDeq30B_ox3e_foc	890	175	0.48	51.85	0.14	0.55	0.04	0.00	42.24	0.78	2.19	98.27
QDeq31_ox1d_foc	810	200	0.26	50.88	0.08	0.15	0.00	1.11	43.89	1.08	0.61	98.07
QDeq31_ox1e_foc	810	200	0.17	51.69	0.14	0.18	0.00	0.06	43.74	1.20	0.98	98.16
QDeq31_ox2a_1um	810	200	0.00	45.50	0.21	0.13	0.00	14.53	35.98	0.93	2.24	99.53
QDeq31_ox2b_foc	810	200	0.28	44.81	0.42	0.12	0.02	11.81	38.73	0.77	0.63	97.57

Table C1, *continued*

QDeq31_ox2c_foc	810	200	0.11	44.50	0.39	0.11	0.00	12.74	38.35	0.74	0.59	97.54
QDeq31_ox2d_foc	810	200	0.07	50.12	0.17	0.08	0.00	4.44	42.07	1.05	1.14	99.14
QDeq31_ox3a_1um	810	200	0.00	45.79	0.19	0.08	0.00	14.49	35.21	1.03	2.77	99.55
QDeq31_ox3b_foc	810	200	0.04	43.85	0.38	0.09	0.00	14.11	37.52	0.78	0.66	97.42
QDeq31_ox4a_foc	810	200	0.13	52.97	0.12	0.13	0.00	0.00	43.07	1.23	1.03	98.67
QDeq31_ox4b_foc	810	200	0.14	52.87	0.11	0.19	0.00	0.00	42.89	1.24	1.02	98.45
QDeq31_ox5a_foc	810	200	0.65	51.55	0.22	0.05	0.00	0.00	42.45	1.22	1.23	97.36
QDeq31_ox6a_1um	810	200	0.00	45.80	0.20	0.08	0.00	14.54	35.21	1.04	2.77	99.63
QDeq31_ox6b_foc	810	200	0.14	44.31	0.37	0.11	0.00	13.14	38.09	0.74	0.67	97.58
QDeq31_ox7a_1um	810	200	0.12	52.69	0.08	0.28	0.00	0.00	43.54	1.17	0.90	98.77
QDeq32_ox1a_1um	835	200	0.15	44.75	0.35	0.06	0.00	13.63	37.98	0.66	1.00	98.60
QDeq32_ox1b_foc	835	200	0.14	51.77	0.19	0.07	0.00	1.13	43.35	0.96	1.35	98.97
QDeq32_ox2a_1um	835	200	0.08	51.79	0.09	0.14	0.00	0.78	44.43	0.88	0.76	98.96
QDeq32_ox3a_foc	835	200	0.54	52.09	0.21	0.12	0.00	0.00	41.96	1.09	1.80	97.81
QDeq32_ox4a_foc	835	200	0.18	45.13	0.39	0.10	0.00	13.01	38.14	0.67	1.12	98.74
QDeq32_ox4b_foc	835	200	0.13	52.30	0.17	0.08	0.00	0.97	43.36	0.98	1.59	99.58
QDeq32_ox5a_foc	835	200	0.22	46.73	0.45	0.16	0.00	9.46	39.29	0.76	1.26	98.32
QDeq32_ox6a_foc	835	200	0.28	52.73	0.13	0.28	0.03	0.00	41.17	1.12	1.66	97.40

Medium grey shading represents analyses of small, euhedral (hemo)ilmenite

Very light shading represents analyses of rounded, relict blebs

Table C2. Titanomagnetite compositions (wt%)

SAMPLE	Rim?*	T (C)	Pres (MPa)	SiO_2	TiO_2	Al2O3	V2O3	Cr2O3	Fe2O3	FeO	MnO	MgO	Total
VQ0606_oxide_1_a#	1			0.00	10.32	1.96	0.26	0.03	47.96	37.46	0.75	1.93	100.66
VQ0606_oxide_1_b_1um#	2			0.00	9.93	2.12	0.29	0.00	48.02	36.80	0.72	2.00	99.88
VQ0606_oxide_2_a_5um#	1			0.00	6.74	1.52	0.29	0.08	54.29	34.35	0.76	1.51	99.54
VQ0606_oxide_4_a_5um#	1			0.00	10.27	2.01	0.26	0.00	47.95	37.28	0.77	1.98	100.51
VQ0606_oxide_5_a#	1			0.00	10.29	1.98	0.29	0.02	47.65	37.41	0.76	1.86	100.26
VQ0606_oxide_5_b_1um#	2			0.00	9.76	2.22	0.22	0.00	47.65	36.32	0.74	2.01	98.92
VQ0606_oxide_6_a_1um	1			0.00	10.08	1.98	0.30	0.00	47.99	37.16	0.76	1.87	100.15
VQ0606_oxide_6_b_1um	2			0.00	10.30	2.06	0.30	0.03	46.38	36.87	0.76	1.88	98.57
VQ0606_oxide_9_a_5um#	1			0.00	10.25	1.99	0.30	0.03	47.61	37.20	0.74	1.94	100.06
VQ0606_oxide_9_b_focused#	2			0.00	9.76	2.09	0.24	0.00	47.82	36.35	0.75	2.00	99.00
VQ0606_ox1a_1um	2			0.00	9.82	1.83	0.33	0.00	48.60	37.17	0.76	1.71	100.23
VQ0606_ox1b_1um	2			0.00	9.76	1.92	0.34	0.00	48.00	36.69	0.78	1.79	99.26
VQ0606_ox1c_1um	1			0.00	9.91	1.73	0.32	0.02	47.96	37.12	0.73	1.65	99.44
VQ0606_ox2a_foc	2			0.00	9.80	1.91	0.29	0.00	48.16	36.92	0.78	1.72	99.58
VQ0606_ox2b_1um	1			0.00	9.97	1.73	0.30	0.02	47.78	37.06	0.73	1.69	99.27
VQ0606_ox3a_1um	2			0.00	10.04	1.77	0.28	0.02	47.90	37.19	0.75	1.72	99.67
VQ0606_ox3b_1um	1			0.00	10.08	1.73	0.29	0.00	47.21	37.07	0.76	1.63	98.78
VQ0606_ox3c_1um	1			0.00	10.04	1.74	0.29	0.02	48.05	37.29	0.74	1.69	99.87
VQ0606_ox3d_1um	3			0.00	10.21	1.79	0.27	0.02	46.85	37.03	0.77	1.70	98.64
VQ0606_ox5a_1um	2			0.00	9.95	1.82	0.31	0.03	48.14	37.23	0.73	1.70	99.92
VQ0606_ox5b_1um	1			0.00	9.88	1.84	0.28	0.00	47.73	37.18	0.76	1.53	99.20
VQ0606_ox5c_1um	3			0.00	10.22	1.93	0.32	0.02	46.04	36.91	0.77	1.65	97.87
VQ0606_ox10a_1um	2			0.21	9.77	2.09	0.25	0.00	46.87	36.83	0.77	1.77	98.55
VQ0606_ox10b_1um	2			0.20	9.89	1.91	0.23	0.00	47.02	37.12	0.77	1.67	98.81
VQ0606_ox12a_1um	2			0.30	9.28	1.96	0.24	0.00	47.91	36.94	0.75	1.55	98.93
VQ0606_ox12b_1um	1			0.22	9.73	2.02	0.29	0.02	47.00	36.96	0.75	1.70	98.70
QZ0705D_ox2a_1um#	1			0.00	10.18	1.86	0.25	0.00	47.26	37.49	0.83	1.50	99.37
QZ0705D_ox2b_1um#	2			0.54	9.68	2.02	0.24	0.02	46.37	37.54	0.86	1.52	98.78
QZ0705D_ox3a_1um	1			0.05	10.21	1.83	0.26	0.03	47.20	37.62	0.84	1.51	99.55
QZ0705D_ox4a_1um#	1			0.05	10.16	1.87	0.27	0.02	46.92	37.40	0.82	1.53	99.03
QZ0705D_ox4b_1um#	2			0.07	10.04	1.86	0.24	0.03	46.21	36.84	0.85	1.55	97.70
QZ0705D_ox6a_1um#	2			0.06	11.30	1.89	0.26	0.02	45.11	38.67	0.83	1.53	99.68
QZ0705D_ox6b_foc#	2			0.07	11.26	2.02	0.29	0.02	44.65	38.40	0.82	1.60	99.11
QZ0705D_ox6c_1um#	3			0.07	10.55	1.89	0.25	0.02	44.83	37.52	0.77	1.39	97.30
QZ0705D_ox7a_1um#	1			0.11	9.88	1.84	0.25	0.02	46.56	36.89	0.84	1.51	97.90
QZ0705D_ox9a_1um#	1			0.07	10.01	1.89	0.30	0.00	46.57	37.05	0.85	1.52	98.26

Table C2, *continued*

QZ0705D_ox9b_foc[#]	2			0.15	9.81	1.88	0.24	0.00	46.64	36.88	0.84	1.53	97.98
QZ0705D_ox10a_1um[#]	1			0.04	10.19	1.90	0.27	0.00	46.74	37.33	0.84	1.53	98.84
QZ0705D_ox10b_1um[#]	2			0.11	9.93	1.84	0.25	0.03	46.86	36.93	0.82	1.61	98.38
QDeq1_oxide_1_a_5um	1	875	125	0.00	8.11	1.77	0.37	0.02	51.31	38.17	0.37	0.32	100.44
QDeq1_oxide_1_b_2um	2	875	125	0.00	19.47	4.33	0.43	0.04	26.09	48.45	0.50	0.61	99.91
QDeq1_oxide_1_c_1um	2	875	125	0.00	13.01	3.75	0.35	0.06	38.48	42.45	0.43	0.38	98.91
QDeq1_oxide_2_a_5um	1	875	125	0.00	10.20	1.98	0.29	0.02	47.58	38.36	0.60	1.31	100.33
QDeq1_oxide_2_b_1um	2	875	125	0.00	23.51	4.22	0.64	0.04	18.10	51.56	0.69	0.82	99.58
QDeq1_oxide_5_a_5um	1	875	125	0.00	10.37	1.97	0.28	0.00	46.66	39.86	0.36	0.53	100.04
QDeq1_oxide_5_b_1um	2	875	125	0.00	22.28	4.13	0.54	0.02	21.12	51.00	0.60	0.65	100.35
QDeq8A_oxide_2_a_1um	2	875	100	0.00	23.64	6.91	0.74	0.11	14.03	51.87	0.74	0.84	98.90
QDeq8A_oxide_2_b_1um	1	875	100	0.00	13.75	4.04	0.59	0.05	36.53	42.96	0.40	0.54	98.87
QDeq8A_oxide_3_a_5um	1	875	100	0.00	10.24	1.98	0.30	0.03	47.37	38.71	0.61	1.10	100.34
QDeq8A_oxide_3_b_5um	1	875	100	0.00	10.33	1.96	0.28	0.02	47.54	38.45	0.61	1.36	100.55
QDeq8A_oxide_4_a_5um	1	875	100	0.00	10.27	2.02	0.33	0.02	47.16	39.71	0.52	0.59	100.61
QDeq8A_oxide_6_a_5um	1	875	100	0.00	10.26	1.99	0.32	0.00	47.24	38.65	0.56	1.14	100.15
QDeq8A_oxide_6_b_focused	2	875	100	0.00	15.86	3.66	0.34	0.02	33.24	44.41	0.75	0.61	98.89
QDeq9A_oxide_1_a	1	850	175	0.00	10.30	1.91	0.29	0.02	47.52	39.50	0.45	0.82	100.80
QDeq9A_oxide_1_b_1um	2	850	175	0.38	21.86	4.42	0.46	0.03	20.36	51.59	0.56	0.34	99.99
QDeq9A_oxide_7_b_1um	2	850	175	0.01	21.49	4.14	0.68	0.03	22.02	50.69	0.53	0.35	99.94
QD_eq_9A_ox2_1um	2	850	175	0.40	23.23	3.22	0.58	0.04	18.40	52.38	0.58	0.35	99.17
QD_eq_9A_ox2b_1um	2	850	175	0.33	17.88	3.87	0.37	0.03	28.25	47.70	0.49	0.21	99.14
QD_eq_9A_ox5a_1um	2	850	175	0.56	23.80	3.54	1.15	0.05	16.26	52.95	0.64	0.52	99.46
QD_eq_9A_ox5b_focused	2	850	175	0.51	24.57	3.22	1.01	0.04	15.04	53.36	0.63	0.54	98.90
QD_eq_9A_ox6b_focused	2	850	175	0.63	12.85	5.09	0.35	0.02	35.94	43.40	0.47	0.38	99.13
QDeq10A_oxide_1_a	1	875	175	0.00	10.26	1.96	0.29	0.00	48.03	37.95	0.69	1.65	100.84
QDeq10A_oxide_1_b_1um	2	875	175	0.01	22.54	4.03	0.53	0.02	21.07	51.41	0.55	0.66	100.83
QDeq10A_ox4b_1um	2	875	175	0.69	24.51	2.93	0.65	0.03	15.54	53.48	0.60	0.58	99.02
QDeq10A_ox4c_foc	2	875	175	0.63	19.86	3.03	0.38	0.03	24.53	49.12	0.48	0.56	98.63
QDeq10A_ox4e_1um	2	875	175	0.71	25.34	2.91	1.02	0.04	14.04	53.92	0.62	0.90	99.49
QDeq15A_oxide_1_a_focused	1.5	835	150	0.06	10.99	2.08	0.29	0.02	45.45	41.24	0.39	0.20	100.73
QDeq15A_oxide_3_a_1um	1	835	150	0.04	6.47	1.65	0.37	0.04	53.85	36.86	0.36	0.05	99.68
QDeq15A_oxide_4_a_5um	1	835	150	0.00	10.33	1.94	0.27	0.00	47.79	37.82	0.70	1.71	100.57
QDeq15A_oxide_4_b_5um	1.5	835	150	0.02	10.80	2.09	0.24	0.02	46.06	39.98	0.56	0.70	100.47

Table C2, *continued*

QDeq15A_oxide_5_a_3um	1	835	150	0.01	10.25	1.94	0.26	0.02	47.73	38.36	0.59	1.39	100.55
QDeq15A_oxide_5_b_focused	2	835	150	0.18	23.67	2.92	0.77	0.02	18.56	52.54	0.65	0.34	99.65
QDeq15A_ox1_1um	2	835	150	0.82	18.58	3.09	0.40	0.00	26.64	48.58	0.58	0.32	99.02
QDeq15A_ox1b_foc	2	835	150	0.88	22.93	2.66	0.81	0.03	17.92	52.43	0.66	0.34	98.65
QDeq15A_ox3a_foc	2	835	150	0.79	18.30	3.28	0.41	0.03	26.97	48.06	0.60	0.44	98.88
QDeq15A_ox3b_foc	2	835	150	0.84	20.03	3.20	0.44	0.00	23.50	49.84	0.64	0.33	98.83
QDeq15B_oxide_1_a_1um	1	835	150	0.06	9.03	2.16	0.33	0.03	48.12	38.97	0.33	0.24	99.26
QDeq17A_oxide_3_a_3um	1	860	150	0.04	10.65	1.89	0.31	0.02	46.56	40.23	0.38	0.61	100.70
QDeq17A_oxide_3_b_1um	1.5	860	150	0.04	22.25	3.02	0.76	0.04	22.22	50.33	0.61	0.95	100.20
QDeq17A_ox1a_1um[#]	2	860	150	0.52	13.35	5.35	0.60	0.02	34.62	43.04	0.44	0.80	98.74
QDeq17A_ox4a_1um	1.5	860	150	0.42	23.90	3.25	1.07	0.04	16.00	52.18	0.61	0.68	98.15
QDeq17A_ox4b_foc	2	860	150	0.36	23.44	3.17	1.10	0.06	17.82	52.05	0.60	0.65	99.25
QDeq17A_ox5a_1um	2	860	150	0.34	22.00	3.14	0.77	0.04	20.80	50.36	0.60	0.77	98.82
QDeq17A_ox5b_1um	2	860	150	0.38	23.52	3.04	1.52	0.05	16.79	51.56	0.63	0.82	98.31
QDeq18A_oxide_1_a_5um	1	875	150	0.02	10.49	1.96	0.30	0.00	46.64	39.36	0.42	0.92	100.10
QDeq18A_oxide_1_b_1um	2	875	150	0.05	21.74	4.18	0.61	0.04	20.84	50.61	0.56	0.38	99.01
QDeq18A_oxide_5_a_3um	1.5	875	150	0.00	24.36	3.80	0.55	0.03	17.40	52.62	0.57	0.79	100.10
QDeq18A_oxide_6_a_3um	1	875	150	0.00	10.24	1.95	0.27	0.03	46.90	40.30	0.33	0.23	100.26
QDeq18A_oxide_7_a_3um	1	875	150	0.00	11.72	1.81	0.29	0.03	43.64	41.28	0.43	0.24	99.44
QDeq18A_ox3a_1um	2	875	150	0.30	20.44	4.85	0.50	0.03	21.92	50.02	0.46	0.29	98.79
QDeq18A_ox3b_foc	2	875	150	0.32	19.80	4.25	0.46	0.02	24.29	49.48	0.47	0.32	99.40
QDeq18A_ox4a_foc	2	875	150	0.29	15.75	3.76	0.39	0.03	31.85	45.33	0.43	0.25	98.10
QDeq18A_ox5a_1um	2	875	150	0.28	13.82	4.24	0.38	0.04	34.96	43.77	0.49	0.10	98.08
QDeq18A_ox7a_1um	2	875	150	0.27	19.70	3.88	0.39	0.00	24.64	49.42	0.46	0.11	98.86
QDeq20A_oxide_2_a_5um	1	860	125	0.00	10.32	1.98	0.32	0.01	47.51	37.52	0.69	1.85	100.19
QDeq20A_oxide_2_b_1um	2	860	125	0.00	23.18	4.03	0.60	0.03	19.42	51.33	0.68	0.88	100.15
QDeq20A_oxide_2_c_focused	3	860	125	0.00	9.00	1.75	0.28	0.00	48.64	36.46	0.55	1.36	98.02
QDeq20A_oxide_5_a_3um	1	860	125	0.00	17.81	3.29	0.36	0.03	30.12	46.44	0.53	0.63	99.19
QDeq20A_oxide_6_a	1	860	125	0.00	9.98	2.06	0.26	0.00	47.87	37.43	0.64	1.68	99.92
QDeq20A_ox1a_1um	2	860	125	0.25	21.25	4.04	0.42	0.03	21.81	50.06	0.65	0.55	99.06
QDeq20A_ox1b_foc	2	860	125	0.49	22.40	4.26	0.61	0.03	19.09	51.59	0.69	0.59	99.76
QDeq20A_ox3a_foc	2	860	125	0.29	20.28	4.81	0.57	0.04	21.50	49.71	0.54	0.15	97.88
QDeq20A_ox3b_1um	2	860	125	0.24	20.88	4.30	0.53	0.03	21.76	50.35	0.54	0.19	98.83
QDeq20A_ox4a_foc[#]	2	860	125	0.63	22.57	4.27	0.70	0.05	17.07	51.48	0.65	0.57	97.97
QDeq20A_ox4b_1um[#]	2	860	125	0.25	23.67	2.87	0.60	0.04	17.36	51.73	0.63	0.53	97.67

Table C2, *continued*

QDeq21A_oxide_1_a_5 um	1	850	125	0.00	10.29	1.88	0.31	0.03	47.32	39.14	0.42	0.96	100.36
QDeq21A_oxide_1_b_1 um	2	850	125	0.00	22.89	3.43	0.48	0.02	20.16	51.18	0.63	0.61	99.41
QDeq21A_oxide_4_a_2 um	1	850	125	0.00	10.31	1.93	0.27	0.04	46.77	40.04	0.34	0.40	100.11
QDeq21A_oxide_4_b_fo cused	2	850	125	0.00	23.67	3.16	0.61	0.05	19.03	51.86	0.65	0.66	99.69
QDeq21A_oxide_4_c_fo cused	2	850	125	0.00	24.56	2.63	0.82	0.07	17.29	52.69	0.62	0.52	99.20
QDeq21A_oxide_6_a_1 um	2	850	125	0.00	20.35	3.30	0.45	0.02	25.58	48.96	0.57	0.63	99.86
QDeq21A_ox1_1um	2	850	125	0.00	22.37	3.25	0.54	0.03	20.70	50.81	0.61	0.39	98.69
QDeq21A_ox1b_foc	2	850	125	0.00	20.35	3.88	0.42	0.00	23.68	49.03	0.59	0.32	98.26
QDeq21A_ox3a_1um	2	850	125	0.00	20.47	3.12	0.49	0.00	24.27	49.36	0.56	0.14	98.42
QDeq21A_ox3b_1um	2	850	125	0.00	20.63	3.10	0.53	0.03	24.85	49.85	0.58	0.17	99.74
QDeq21A_ox6a_foc	2	850	125	0.00	23.20	2.97	0.66	0.02	18.95	51.36	0.64	0.38	98.17
QDeq22A_oxide_1_a_5 um	1	835	125	0.00	10.29	1.96	0.28	0.02	47.91	37.80	0.67	1.75	100.68
QDeq22A_oxide_1_b_5 um	1.5	835	125	0.00	10.15	1.95	0.28	0.02	48.12	38.02	0.59	1.58	100.70
QDeq22A_oxide_4_a_5 um	1	835	125	0.00	10.30	1.95	0.27	0.00	47.58	38.24	0.57	1.47	100.38
QDeq22A_oxide_4_b_1 um	2	835	125	0.01	22.10	2.76	0.59	0.04	22.00	50.70	0.61	0.35	99.15
QDeq22A_oxide_5_a_5 um	1	835	125	0.00	10.30	2.02	0.29	0.00	47.36	39.09	0.47	1.03	100.55
QDeq22A_oxide_6_a_5 um	1	835	125	0.00	10.27	1.97	0.31	0.02	47.19	37.19	0.75	1.86	99.56
QDeq22A_ox1a_foc	2	835	125	0.00	20.80	3.56	0.47	0.03	23.82	49.34	0.68	0.48	99.18
QDeq22A_ox1b_foc	2	835	125	0.00	18.53	3.78	0.42	0.00	27.89	47.41	0.61	0.40	99.04
QDeq22A_ox2a_1um[#]	1	835	125	0.00	22.28	3.59	0.46	0.04	21.07	51.27	0.65	0.22	99.57
QDeq22A_ox3a_foc	2	835	125	0.00	20.74	3.59	0.75	0.03	23.56	49.67	0.59	0.30	99.23
QDeq22A_ox3b_1um	2	835	125	0.00	20.50	3.91	0.67	0.04	24.07	49.69	0.58	0.29	99.76
QDeq22A_ox4a_foc	2	835	125	0.00	20.05	3.84	0.49	0.02	24.39	48.73	0.67	0.33	98.54
QDeq22A_ox5a_foc	2	835	125	0.00	21.14	3.91	0.62	0.03	22.39	49.84	0.66	0.37	98.97
QDeq22B_oxide_2_a_5 um	1	835	125	0.00	10.20	1.97	0.28	0.02	47.14	39.19	0.52	0.77	100.09
QDeq22B_oxide_2_b_1 um	2	835	125	0.00	20.66	4.52	0.51	0.02	23.05	49.34	0.66	0.55	99.30
QDeq22B_oxide_4_a-_2um	2	835	125	0.00	18.93	3.21	0.41	0.02	27.99	48.11	0.53	0.26	99.46
QDeq23A_oxide_3_a_1 um	1	875	100	0.00	10.33	1.99	0.28	0.07	47.58	38.15	0.57	1.59	100.54
QDeq23A_oxide_3_b_fo cused	2	875	100	0.00	23.74	2.98	0.85	0.08	19.21	51.90	0.51	0.83	100.10
QDeq23A_oxide_4_a_5 um	1	875	100	0.00	10.33	1.99	0.29	0.00	47.66	38.25	0.60	1.52	100.65
QDeq23A_oxide_4_b_1 um	2	875	100	0.00	22.44	3.61	0.52	0.03	21.54	51.05	0.52	0.73	100.43
QDeq23A_oxide_6_a_1 um	1	875	100	0.00	23.63	3.62	1.06	0.04	18.70	51.71	0.51	1.00	100.27
QDeq24A_ox2a_foc[#]	2	850	150	0.43	15.29	1.99	0.55	0.04	34.95	43.49	0.83	0.91	98.48

Table C2, *continued*

QDeq24A_ox2b_foc#	1.5	850	150	0.22	15.58	1.81	0.56	0.04	34.76	43.19	0.87	0.94	97.97
QDeq24A_ox2c_1um#	1	850	150	0.16	16.19	1.81	0.51	0.02	34.34	43.83	0.86	1.00	98.72
QDeq24A_ox4a_1um#	2	850	150	0.12	15.48	1.59	0.40	0.00	35.90	42.90	0.84	1.04	98.28
QDeq24A_ox4b_foc#	2	850	150	0.14	14.56	1.60	0.73	0.02	36.97	42.02	0.85	1.00	97.90
QDeq24A_ox6a_1um#	1	850	150	0.16	13.14	2.71	0.29	0.02	38.50	41.42	0.65	0.75	97.64
QDeq24B_ox2a_foc#	2	850	150	0.14	14.52	1.94	0.49	0.02	36.55	42.21	0.72	0.88	97.48
QDeq24B_ox2b_1um#	2	850	150	0.15	14.19	1.80	0.57	0.03	37.54	42.25	0.69	0.78	98.02
QDeq24B_ox5a_foc#	1.5	850	150	0.21	13.43	2.05	1.73	0.38	36.94	41.26	0.69	1.00	97.68
QDeq25B_ox5a_foc#	2	835	175	0.08	14.28	1.77	0.45	0.03	38.16	42.17	0.71	0.92	98.57
QDeq25B_ox5b_1um#	1	835	175	0.06	10.32	2.02	0.28	0.00	46.15	38.40	0.62	1.12	98.96
QDeq25B_ox5c_1um#	2	835	175	0.43	14.15	1.78	0.89	0.06	36.86	42.47	0.73	0.88	98.26
QDeq25B_ox5d_foc#	2	835	175	0.10	14.07	1.87	0.41	0.03	38.60	42.15	0.69	0.89	98.80
QDeq27_ox3c_foc	2	810	175	0.62	15.92	2.85	0.37	0.02	32.09	46.17	0.59	0.00	98.62
QDeq27_ox3d_1um	1	810	175	0.62	20.96	3.16	0.51	0.03	22.07	50.61	0.73	0.14	98.83
QDeq27_ox4a_foc	1	810	175	0.79	24.49	2.03	2.59	0.12	13.92	53.82	0.84	0.16	98.77
QDeq27_ox5a_foc#	2	810	175	0.74	22.06	2.46	0.84	0.03	19.85	51.40	0.80	0.18	98.36
QDeq27_ox5b_1um#	1	810	175	0.62	21.39	2.46	0.75	0.02	22.40	51.13	0.78	0.12	99.66
QDeq27_ox7a_1um	2	810	175	0.71	23.95	2.38	1.40	0.06	16.25	53.28	0.85	0.19	99.06
QDeq27_ox7b_foc	2	810	175	0.65	20.09	2.78	0.59	0.02	24.73	50.01	0.76	0.17	99.79
QDeq27_ox7c_1um	1	810	175	0.62	10.13	1.87	0.26	0.00	46.04	38.56	0.75	1.43	99.67
QDeq28A_ox1a_foc	2	810	125	0.82	9.78	1.94	0.27	0.00	45.37	38.33	0.86	1.27	98.64
QDeq28A_ox1b_1um	2	810	125	0.85	9.64	1.52	0.24	0.02	45.67	39.07	0.97	0.60	98.58
QDeq28A_ox2b_1um#	1	810	125	0.88	10.56	1.39	0.33	0.02	43.30	39.58	1.06	0.61	97.72
QDeq28A_ox4a_1um#	1	810	125	0.91	8.21	1.44	0.21	0.00	47.88	37.86	0.92	0.46	97.88
QDeq28A_ox5a_1um#	2	810	125	0.75	10.65	1.57	0.25	0.02	44.29	39.86	1.00	0.69	99.07
QDeq28A_ox6e_foc#	1	810	125	0.78	10.79	1.31	0.07	0.00	43.65	39.94	0.99	0.52	98.04
QDeq28B_ox1a_foc#	2	810	125	0.71	10.41	1.68	0.28	0.02	44.07	39.48	0.86	0.68	98.19
QDeq28B_ox1b_5um#	1	810	125	0.61	10.29	1.96	0.30	0.02	45.90	38.42	0.74	1.68	99.92
QDeq28B_ox2c_foc#	2	810	125	0.83	10.39	1.29	0.29	0.02	43.64	39.42	0.98	0.54	97.40
QDeq28B_ox4a_foc#	1	810	125	0.81	10.38	1.28	0.10	0.00	44.04	39.64	0.88	0.47	97.59
QDeq28B_ox6b_foc#	2	810	125	0.79	11.52	1.27	0.10	0.00	42.55	40.91	0.95	0.46	98.54
QDeq29_ox4a_1um	2	810	150	0.57	18.69	2.55	0.44	0.00	27.29	48.41	0.73	0.07	98.74
QDeq29_ox4b_1um	2	810	150	0.57	18.73	2.47	0.52	0.03	27.35	48.39	0.71	0.14	98.89
QDeq29_ox4c_1um	1	810	150	0.55	10.15	1.90	0.25	0.00	45.02	39.82	0.57	0.51	98.77
QDeq29_ox5a_1um#	1	810	150	0.66	22.97	2.00	1.49	0.05	17.88	52.03	0.89	0.08	98.06
QDeq29_ox7a_foc	2	810	150	0.57	20.89	2.73	0.57	0.02	22.04	50.23	0.76	0.04	97.84
QDeq29_ox7c_1um	2	810	150	0.56	19.24	2.24	0.49	0.03	26.22	48.67	0.74	0.08	98.27
QDeq29_ox8a_1um	2	810	150	0.55	18.64	2.79	0.37	0.02	27.52	48.70	0.66	0.00	99.24
QDeq29_ox8b_foc	2	810	150	0.58	18.49	2.52	0.44	0.02	27.14	48.24	0.62	0.00	98.06
QDeq30B_ox3a_1um	1	890	175	0.49	11.19	2.13	0.30	0.00	42.93	41.09	0.35	0.46	98.95

Table C2, *continued*

QDeq30B_ox3b_foc	2	890	175	0.51	21.70	2.52	0.70	0.04	21.35	49.28	0.61	1.19	97.89
QDeq30B_ox4a_5um	1	890	175	0.39	10.23	2.02	0.27	0.02	45.79	38.26	0.67	1.44	99.08
QDeq30B_ox4b_1um	2	890	175	0.47	18.56	3.01	0.55	0.04	27.53	47.38	0.56	0.76	98.86
QDeq30B_ox4c_1um	2	890	175	0.49	18.03	2.77	0.48	0.04	28.76	46.94	0.56	0.69	98.75
QDeq31_ox1a_1um	1	810	200	0.00	10.19	1.91	0.26	0.00	47.63	37.96	0.82	1.37	100.15
QDeq31_ox1b_foc	2	810	200	0.01	21.86	2.62	0.78	0.05	22.08	50.78	0.73	0.00	98.92
QDeq31_ox1c_foc	2	810	200	0.04	20.26	2.89	0.55	0.03	25.17	49.40	0.71	0.03	99.09
QDeq32_ox2b_1um	2	835	200	0.14	21.48	2.55	0.76	0.04	22.92	50.08	0.68	0.39	99.04
QDeq32_ox2c_1um	2	835	200	0.14	19.34	3.14	0.56	0.04	26.64	48.51	0.67	0.24	99.29
QDeq32_ox2d_1um	1	835	200	0.10	10.21	1.87	0.26	0.00	47.22	37.72	0.86	1.51	99.76

*core=1, "rim"=2, other/no difference = 3; # samples do not display core-rim zoning

Appendix D

INTRODUCTION

This Appendix is associated with Chapter 5. Example MATLAB scripts are provided, for coordinate transformation and diffusion modeling. Model parameters and best fit outcomes (with error bars) are provided as Tables D1-D4.

TRANSFORMING DIFFUSIVITY VECTORS INTO CARTESIAN TRIPLETS

```
%transforming from triclinic to orthonormal coordinate system
%convention: x is in the same direction as a ; y is in the ab plane; z is
%perpendicular to x and y

clear variables
close all
clc

% [data,datatxt,dataraw] = xlsread('EPMA Transect Angles.xlsx','downD erfc3
SunRim','B6:AC57')
% [data,datatxt,dataraw] = xlsread('EPMA Transect Angles.xlsx','downD erfc3
Rimoferfc','B6:AC57')
% [data,datatxt,dataraw] = xlsread('EPMA Transect Angles.xlsx','angles + DMg
models downdif erf','B6:AC57')
%load a file containing the diffusivity and angle data for each transect
load('erfc.mat')
%% Transformation Matrix

%assume a, b, and c are all unit vectors (don't need lattice
%parameter lengths, for now)

%expressions of the unit vectors in crystallographic space
%if you input lattice parameter lengths (a=8.18;b=12.87c=14.17), the length
of the resultant
%vectors is different, but the directions are the same
a = [1 0 0];
b = [0 1 0];
c = [0 0 1];

%There's uncertainty in the data set!
%I used Stereonet9.5, marking the center of a cloud of points for a,
%b, and c axes, even though those center points aren't exactly alpha, beta,
%and gamma angles from each other. No Stereonet measurements are more than
%one degree different from the match unit alpha, beta, or gamma, but in
%order to have the calculations work out exactly, use those slightly-off
%measured angles, instead of the match unit parameters

%match unit angles between crystallographic axes are expressed in the first
%row of data.mat (alpha = 93.1, beta = 115.9, gamma = 91.2)
alpha = round(data(:,4),1);
```

```
beta = round(data(:,5),1);
gamma = round(data(:,6),1);

%volume of the unit cell %but it's not really the crystal unit cell, because
%I'm using unit vectors for a, b, and c...more like the volume of the a-b-c
%parallelepiped;

%a(1).*b(2).*c(3) should come in front of sqrt, generally (but here they're
%all = 1 so I've left it out, b/c I leave out length in T also)
V = sqrt(1-cosd(alpha).^2-cosd(beta).^2-
cosd(gamma).^2+2.*cosd(alpha).*cosd(beta).*cosd(gamma));

%get set up for a loop with transformation matrix
T = zeros(3*size(data,1),3);
a_cc = zeros(size(data,1),3);
b_cc = zeros(size(data,1),3);
c_cc = zeros(size(data,1),3);
alpha_cc = zeros(size(data,1),1);
beta_cc = zeros(size(data,1),1);
gamma_cc = zeros(size(data,1),1);

for n = 1:size(data,1)

%transformation matrix (crystal space to cartesian space)%vlength only
%works for a, b, and c here B/C they are unit vectors (generally, you
%cannot use the sqrt(elements squared) formula to obtain vector magnitude
%in a non-orthogonal system %actually, a, b, and c are all mag = 1, so I
%left those parts out

%see "Mathematical Techniques in Crystallography and Material Science" by
%Edward Prince (2nd ed., 1994) for the T matrix below (transposed)

T_n = [1                  0
0
      cosd(gamma(n))      sind(gamma(n))
0
      cosd(beta(n))      (cosd(alpha(n))-
cosd(beta(n)).*cosd(gamma(n))./sind(gamma(n))     V(n)./sind(gamma(n))];

T(n+2*(n-1):3*n,:) = T_n;

%cartesian coordinates of a, b, and c
a_cc_n = a*T_n;
b_cc_n = b*T_n;
c_cc_n = c*T_n;

a_cc(n,:) = a_cc_n;
b_cc(n,:) = b_cc_n;
c_cc(n,:) = c_cc_n;

%angles between _cc axes, using dot product and magnitudes
alpha_cc_n =
acosd(dot(b_cc(n,:),c_cc(n,:))./(vlength(b_cc(n,:)).*vlength(c_cc(n,:))));
```

```
beta_cc_n =
acosd(dot(a_cc(n,:),c_cc(n,:))./(vlength(a_cc(n,:)).*vlength(c_cc(n,:))));
gamma_cc_n =
acosd(dot(a_cc(n,:),b_cc(n,:))./(vlength(a_cc(n,:)).*vlength(b_cc(n,:))));

alpha_cc(n) = alpha_cc_n;
beta_cc(n) = beta_cc_n;
gamma_cc(n) = gamma_cc_n;

end

%axes to plot on 3D graph (using match unit angles only)
axes_cc = [a_cc(1,:);b_cc(1,:);c_cc(1,:)];
axes = axes_cc';

%verfiy that the angles between a_cc, b_cc, and c_cc are equal to alpha,
%beta, and gamma %the output here should be all zeros, if everything's good
alpha_ok = alpha-round(alpha_cc,10)
beta_ok = beta-round(beta_cc,10)
gamma_ok = gamma-round(gamma_cc,10)

%% Solution of Vector Coordinates

%solve for endpoint coordinates of vectors in the direction of EPMA
%transects, scaled by diffusivity

%magnitude of the vector of interest (d): diffusivity in m2/s
d_mag = data(:,18)*1e17; %numbers are in the realm of roundoff errors, so I'm
multiplying everything by a large coefficient

%these variables come into play in the equation of the plane perpendicular
%to each axis; should use the unit vectors for a, b, and c directions
a1=a_cc(:,1); a2=a_cc(:,2); a3=a_cc(:,3);
b1=b_cc(:,1); b2=b_cc(:,2); b3=b_cc(:,3);
c1=c_cc(:,1); c2=c_cc(:,2); c3=c_cc(:,3);

%angles between d and the positive crystal axes
theta_a = round(data(:,7),1);
theta_b = round(data(:,8),1);
theta_c = round(data(:,9),1);

%center points of the circles/cone bases, plus circle (and sphere) radius;
%a plane perpendicular to the a axis passes through (xa,ya,za), etc.
xa = a1.*d_mag.*cosd(theta_a);
ya = repelem(0,size(data,1))';
za = repelem(0,size(data,1))';
ra = d_mag.*sind(theta_a);

xb = b1.*d_mag.*cosd(theta_b);
yb = b2.*d_mag.*cosd(theta_b);
zb = repelem(0,size(data,1))';
rb = d_mag.*sind(theta_b);

xc = c1.*d_mag.*cosd(theta_c);
```

```
yc = c2.*d_mag.*cosd(theta_c);
zc = c3.*d_mag.*cosd(theta_c);
rc = d_mag.*sind(theta_c);

%solving for x, y, and z coordinates of the intersection of the three
%planes perpendicular to the a, b, and c axes (respectively) that pass
%through center points given above

%the expressions for x, y, and z come from hand solving; for the actual
%equations of the planes and spheres, see section "Double Check"

x = xa; %because one circle of interest is in the y-z plane at x = xa, the x
coordinate of d must also have x = xa

y = (b1./b2).*(((b1.*xb+b2.*yb)./b1)-x); %using x knowledge, plus plane
equation Pb, solve for y

z = ((c1.*(x-xc)+c2.*(y-yc))./(-c3))+zc; %use plane equation Pc to solve for
z (now that we know x and y)

%this is it! the endpoint of the vector in Cartesian coordinates!
d_cc = [x y z]
Dvectors = d_cc(2:end,:); %use this as the variable in ellipsoid fit to the
data (separate script)

%make variable of [x,y,z] triples for only d_mag > 1, for ellipsoid fitting
ind = d_mag >= 1;
% ind = d_mag >=3; %use this for rimSun_top8 (will give the same 8 profiles
used in rimerfc and erfc)
d_cc_eigfit = d_cc(ind,:);

%everything less than 1, to show non-directionality of small D
ind_small = d_mag < 1;
d_cc_small = d_cc(ind_small,:);

%% Double Check

%some checks on the math, to make sure it all "adds up"

%equations of the planes perpendicular to each crystal axis should equal zero
Pa = round(a1.*(x-xa),10)

Pb = round(b1.*(x-xb)+b2.*(y-yb),10)

Pc = round(c1.*(x-xc)+c2.*(y-yc)+c3.*(z-zc),10)

%equations of the spheres that intersect those planes to form the circles
%of interest should equal the square of the sphere's radius

Sa = (x-xa).^2+y.^2+z.^2;
Sa_ok = round(Sa-ra.^2,10)

Sb = (x-xb).^2+(y-yb).^2+z.^2;
```

```
Sb_ok = round(Sb-rb.^2,10)

Sc = (x-xc).^2+(y-yc).^2+(z-zc).^2;
Sc_ok = round(Sc-rc.^2,10)

%transform cartesian d vector back to d in abc space
d = zeros(size(data,1),3);

for m = 1:size(data,1)

d_m=d_cc(m,:)*inv(T(m+2*(m-1):3*m,:));

d(m,:) = d_m;

end

%a-b-c space coordinates for d; where input theta angles are obtuse, expect
%negative values
d
```

MODEL B/C FITTING

```
%Mg Diffusion in Plagioclase
%complementary error function solution, as in Faak et al. (2013) p.204

%Here, the solution is obtained by minimizing misfit, allowing three
%parameters (diffusivity, Mg rim value, Mg core value) to vary independently,
plus considering dissolution and variability of core plateau distance

%h3x2 profile 1

clear variables
close all
clc

%% Load EPMA data

%load data
load('h3x2pr1.mat'); h3x2pr1_edit = [h3x2pr1(1:28,:);h3x2pr1(37:end,:)]; %dip
removed

%% Set up variables

%set initial Mg wt%
MgRIM = 0.003035012; %predicted by Sun et al. (2017)
% MgRIM = 0.0632;
% MgRIMmin = 0.003035012; %predicted by Sun et al. (2017)
% MgRIMmax = 0.07; %max rim to test should be just larger than best fit
predicted by erfc.m codes
% dMgRIM = 0.005; %step size
% MgRIMstep = ceil((MgRIMmax-MgRIMmin)/dMgRIM); %number of steps
MgCOREmin = 0.081;
```

```
MgCOREmax = 0.085;
dMgCORE = 0.0002; %step size
MgCOREstep = ceil((MgCOREmax - MgCOREmin)/dMgCORE); %number of steps
MgCORE = [MgCOREmin:dMgCORE:MgCOREmax]';

%create the data variables
x_data = h3x2pr1_edit(:,1);
x_data_all = h3x2pr1(:,1); %distance from crystal rim, in microns
Mg_data = h3x2pr1_edit(:,3);
Mg_data_all = h3x2pr1(:,3); %Mg wt%
t = 1010.5*60*60; %total experimental duration, in seconds

%set up the x data to shift around in distance
%set up Mg data to have one fabricated anchor point at various distances
%away from end of real data
disMIN = 0; %minimum dissolution distance
disMAX = 100; %maximum dissolution distance
ddis = 10; %step size (microns) for dissolution
dis = [disMIN:ddis:disMAX]';
disstep = ceil((disMAX-disMIN)/ddis)+1; %number of iterations of different
dissolution distances
extMIN = 0;  %minumum core extenstion distance
extMAX = 100; %maximum core extenstion distance
dext = 10; %step size (microns) for core extenstion distance
ext = [extMIN:dext:extMAX]';
extstep = ceil((extMAX-extMIN)/dext)+1; %number of iterations of different
core distances
Dmin = 1e-5;  %minimum diffusivity to test, in microns squared per second
Dmax = 1e-3; %maximum diffusivity to test, in microns squared per second
dD = 1e-6; %choose the magnitude of each diffusivity step
D = [Dmin:dD:Dmax]';
Dstep = ceil((Dmax-Dmin)/dD); %number of steps in diffusivity

%%%consider adding more fabricated plateau points, instead of just one
Mg1 = zeros([size(Mg_data,1)+1,MgCOREstep]);  %zeros matrix that will be
populated with all the different Mg data values

for z = 1:MgCOREstep
    Mg_var1 = [Mg_data;MgCORE(z)];
    Mg1(:,z) = Mg_var1;
end

X1 = zeros(size(Mg1,1),size(Mg1,2),size(ext,1)); %zeros matrix that will be
populated with all the different x data values
% x_data_new = [x_data;max(x_data)+1]; %add a row to x_data, to align with Mg
variable created above

for q = 1:size(ext,1)
    X_var1 = [x_data;max(x_data)+ext(q)];
    X1(:,:,q) = repmat(X_var1,1,size(Mg1,2));
end

X2 = zeros(size(Mg1,1),size(Mg1,2),size(ext,1),size(dis,1));
```

```
for v = 1:size(dis,1)
    X_var2 = X1+dis(v);
    X2(:,:,:,v) = X_var2;
end

% X3 = zeros(size(X2,1),size(X2,2),size(X2,3),size(X2,4),size(D,1));
X3 = repmat(X2,1,1,1,1,size(D,1));

% Mg2 = repmat(Mg1,1,1,size(ext,1),size(dis,1)); %now Mg1 is copied into the
same number of pages that X2 has

MgRIM2 =
repmat(MgRIM,size(X3,1),size(X3,2),size(X3,3),size(X3,4),size(X3,5)); %matrix
of rim values same size as X2

MgCORE1 = Mg1(end,:);

MgCORE2 = repmat(MgCORE1,size(X3,1),1,size(X3,3),size(X3,4),size(X3,5));

D1 = zeros(size(X3,1),size(X3,2),size(X3,3),size(X3,4),size(X3,5));

for n = 1:size(D,1)
    D1_var = Dmin + (n-1)*dD;
    D1(:,:,:,:,n) = D1_var;
end

t1 = repmat(t,size(X3,1),size(X3,2),size(X3,3),size(X3,4),size(X3,5));

iter = size(X3,2)*size(X3,3)*size(X3,4)*size(X3,5);

%% Calculate the model Mg concentrations

%set up the model concentration grid: x changes down each column, MgCORE
%changes across each row, x location of core changes in dim3, dissolution
%distance changes in dim4, D changes in dim5
CMg = zeros(size(X2,1),size(X2,2),size(X2,3),size(X2,4),size(D,1));

%use vbls: MgCORE2, MgRIM2, X3, D1, t1
CMg = MgCORE2 + (MgRIM2-MgCORE2).*erfc(X3./(2.*sqrt(D1.*t1))); %complementary
error function solution

%% Assess the model outputs

%repeat Mg data variable in order to get residuals (but use Mg1, which
%includes fake core point)
Mg1_rep = repmat(Mg1,1,1,size(X3,3),size(X3,4),size(X3,5));

%compare calculated Mg concentration to measured Mg concentration
resid = Mg1_rep - CMg; %each value individually compared
residsqr = resid.^2; %each residual individually squared
residss = sum(residsqr,1); %sum down each column to get one value for each
profile
```

```
%calculate the misfit for each concentration profile
%should have iter number of values
misfit = (1/size(X3,1)).*sqrt(residss);

%input the error bars
%option 1
std = 0.002; %standard deviation (1 sigma) of repeated analyses of EPMA Lake
Co standard...seems too large...
%option 2
anaERR = (h3x2pr1_edit(:,5)./100).*Mg_data; %one sigma analytical error from
probe printout (%ERR), converted to Mg wt% for each point
anaERR2 = [anaERR;mean(anaERR)]; %create a fake error bar for fake core data
point
anaERR_all = (h3x2pr1(:,5)./100).*Mg_data_all;
anaERR_all2 = [anaERR_all;mean(anaERR_all)]; %includes fake error bar for
fake core data point
%create the appropriate 5-D array filled with repeating columns of
%analytical error on the Mg measurements
error = zeros(size(anaERR2,1),size(X3,2),size(X3,3),size(X3,4),size(X3,5));
error = repmat(anaERR2,1,size(X3,2),size(X3,3),size(X3,4),size(X3,5));
error_all =
zeros(size(anaERR_all2,1),size(X3,2),size(X3,3),size(X3,4),size(X3,5));
error_all =
repmat(anaERR_all2,1,size(X3,2),size(X3,3),size(X3,4),size(X3,5));
%create low and high limits for Mg, based on the error determined above
Mg_low = Mg1_rep - error;
Mg_high = Mg1_rep + error;
%evaluate the number of model points that fall outside analytical error
disc = sum(CMg<Mg_low,1)+sum(CMg>Mg_high,1); % "discrepancy" (a la Girona and
Costa 2013)
discpct = 100*(disc./size(Mg1,1));

%%%%%%%%%%%%%%%%%%%%%%%%%%%%%%%%%%%%%%%%%%%%%%%%%%%%%%%%%%%%%%%%%%%%%%%%%%%%

[misfitmin indmm]= min(misfit(:)); %value and linear index of minimum misfit
[I1 I2 I3 I4 I5] = ind2sub(size(misfit),indmm); %subscript index of minimum
misfit

Dbest = D1(I1,I2,I3,I4,I5); %diffusivity associated with minimum misfit
(microns^2/s)
Dbest_m = Dbest*1e-12; %best fit diffusivity in meters squared per second

MgCOREbest = MgCORE2(I1,I2,I3,I4,I5); %best fit core value

extbest = dext*(I3-1); %make sure that extMIN = 0 for this to work

disbest = ddis*(I4-1); %make sure that disMIN = 0 for this to work

xbest = X3(:,I2,I3,I4,I5);

discbest = disc(I1,I2,I3,I4,I5);    %discrepancy for best fit solution
discpctbest = discpct(I1,I2,I3,I4,I5);  %pct of points outside of stated
error, for best fit solution
```

```
%% Plot the best fit solution
%calculated solution as blue line
%measured Mg as black points (with x shifted according to model)

figure('Name','Best Fit DMg','NumberTitle','off')
plot(X3(:,I2,I3,I4,I5),CMg(:,I2,I3,I4,I5))
xlabel('Distance from rim (microns)')
ylabel('wt% Mg')
title('h3.2.1')
hold on
plot(X3(:,I2,I3,I4,I5),Mg1_rep(:,I2,I3,I4,I5),'ko','MarkerSize',5,'MarkerFace
Color','k');
hold on
str = sprintf('D = %g m^2 s^{-1}',Dbest_m);
text(0.7,0.4,str,'Units','Normalized','HorizontalAlignment','right','FontSize
',14)
hold on

%double check that the correct solution is being plotted (need to use the
%vbls for best core and best x values)
CMgbest = MgCOREbest + (MgRIM-
MgCOREbest).*erfc(X3(:,I2,I3,I4,I5)./(2.*sqrt(Dbest.*t))); %double check the
right curve was plotted above
plot(X3(:,I2,I3,I4,I5),CMgbest,'m.')

%% Error assessment, based on discrepancy

%for D, based on discrepancy, and holding the rest at the best fit values
indDerr = disc(:,I2,I3,I4,:) <= discbest; %find the index for best core and x
values, where discrepancy is better than or equal the disc for best misfit
Derr = D1(:,I2,I3,I4,indDerr); %values of D where disc <= discbest
CMgbest_err = CMg(:,I2,I3,I4,indDerr); %grab all the CMg fits where core and
x are best and disc is <= best fit disc value

indCMgbest_err_high = Derr(:,:,:,:,:) == max(Derr(:));
indCMgbest_err_low = Derr(:,:,:,:,:) == min(Derr(:));
CMgbest_err_high = CMgbest_err(indCMgbest_err_high);
CMgbest_err_low = CMgbest_err(indCMgbest_err_low);
Derr_high = max(Derr(:)); Derr_high_m = Derr_high*1e-12;
Derr_low = min(Derr(:)); Derr_low_m = Derr_low*1e-12;

figure('Name','Range of D holding other vbls as best fits; disc
criterion','NumberTitle','off')
plot(X3(:,I2,I3,I4,I5),CMgbest_err_high,'r-')
hold on
plot(X3(:,I2,I3,I4,I5),CMgbest_err_low,'b-')
hold on
plot(X3(:,I2,I3,I4,I5),CMgbest,'k-')
xlabel('Distance from rim (microns)')
ylabel('wt% Mg')
title('h3.2.1')
hold on
plot(X3(:,I2,I3,I4,I5),Mg1_rep(:,I2,I3,I4,I5),'ko','MarkerSize',5,'MarkerFace
Color','k');
hold on
```

```
errorbar(X3(:,I2,I3,I4,I5),Mg1_rep(:,I2,I3,I4,I5),anaERR2,'ko','MarkerSize',4
,'MarkerFaceColor','k');
str = sprintf('Dbest = %g m^2 s^{-1}',Dbest_m)
text(0.4,0.4,str,'Units','Normalized','HorizontalAlignment','left','FontSize'
,14)
hold on
str2 = sprintf('Dmax = %g m^2 s^{-1}',Derr_high_m)
text(0.4,0.5,str2,'Units','Normalized','HorizontalAlignment','left','FontSize
',12)
hold on
str3 = sprintf('Dmin = %g m^2 s^{-1}',Derr_low_m)
text(0.4,0.3,str3,'Units','Normalized','HorizontalAlignment','left','FontSize
',12)

%% Error assessment 2, based on misfit

%for D, based on misfit, and holding the rest at the best fit values
mfpct = 50; %percent of minimum misfit to add to minimum misfit to obtain
error bars on D
indDerr2 = misfit(:,I2,I3,I4,:) <= misfitmin+((mfpct/100)*misfitmin); %find
the index for best core and x values, where misfit is within mfpct% of
minimum misfit
Derr2 = D1(:,I2,I3,I4,indDerr2); %values of D where misfit within mfpct% of
minimum
CMgbest_err2 = CMg(:,I2,I3,I4,indDerr2); %grab all the CMg fits where core
and x are best and misfit is within mfpct% of minimum

indCMgbest_err_high2 = Derr2(:,:,:,:,:) == max(Derr2(:));
indCMgbest_err_low2 = Derr2(:,:,:,:,:) == min(Derr2(:));
CMgbest_err_high2 = CMgbest_err2(indCMgbest_err_high2);
CMgbest_err_low2 = CMgbest_err2(indCMgbest_err_low2);
Derr_high2 = max(Derr2(:)); Derr_high_m2 = Derr_high2*1e-12;
Derr_low2 = min(Derr2(:)); Derr_low_m2 = Derr_low2*1e-12;

figure('Name','Range of D holding other vbls as best fits; misfit
criterion','NumberTitle','off')
plot(X3(:,I2,I3,I4,I5),CMgbest_err_high2,'r-')
hold on
plot(X3(:,I2,I3,I4,I5),CMgbest_err_low2,'b-')
hold on
plot(X3(:,I2,I3,I4,I5),CMgbest,'k-')
xlabel('Distance from rim (microns)')
ylabel('wt% Mg')
title('h3.2.1')
hold on
plot(X3(:,I2,I3,I4,I5),Mg1_rep(:,I2,I3,I4,I5),'ko','MarkerSize',5,'MarkerFace
Color','k');
hold on
errorbar(X3(:,I2,I3,I4,I5),Mg1_rep(:,I2,I3,I4,I5),anaERR2,'ko','MarkerSize',4
,'MarkerFaceColor','k');
str = sprintf('Dbest = %g m^2 s^{-1}',Dbest_m)
text(0.4,0.4,str,'Units','Normalized','HorizontalAlignment','left','FontSize'
,14)
hold on
str2 = sprintf('Dmax = %g m^2 s^{-1}',Derr_high_m2)
```

```
text(0.4,0.5,str2,'Units','Normalized','HorizontalAlignment','left','FontSize
',12)
hold on
str3 = sprintf('Dmin = %g m^2 s^{-1}',Derr_low_m2)
text(0.4,0.3,str3,'Units','Normalized','HorizontalAlignment','left','FontSize
',12)

%% Final plot (smoother curve) with disc-based error

x = 0:0.1:max(xbest)+2
CMgB = MgCOREbest + (MgRIM-MgCOREbest).*erfc(x./(2.*sqrt(Dbest.*t))); %best
fit
CMgH = MgCOREbest + (MgRIM-MgCOREbest).*erfc(x./(2.*sqrt(Derr_high.*t)));
%high D error
CMgL = MgCOREbest + (MgRIM-MgCOREbest).*erfc(x./(2.*sqrt(Derr_low.*t))); %low
D error

figure('Name','Final Plot, disc-based error','NumberTitle','off')
plot(x,CMgB,'k-','LineWidth',1.25)
hold on
plot(x,CMgH,'k--')
hold on
plot(x,CMgL,'k--')
xlabel('Distance from rim (\mum)')
ylabel('Mg (wt%)')
title('profile h3.2.1')
hold on
errorbar(x_data_all+disbest,Mg_data_all,anaERR_all,'ko','MarkerSize',4,'Marke
rFaceColor','k');
hold on
str = sprintf('Dbest = %g m^2 s^{-1}',Dbest_m)
text(0.4,0.4,str,'Units','Normalized','HorizontalAlignment','left','FontSize'
,14)
hold on
str2 = sprintf('Dmax = %g m^2 s^{-1}',Derr_high_m)
text(0.4,0.5,str2,'Units','Normalized','HorizontalAlignment','left','FontSize
',12)
hold on
str3 = sprintf('Dmin = %g m^2 s^{-1}',Derr_low_m)
text(0.4,0.3,str3,'Units','Normalized','HorizontalAlignment','left','FontSize
',12)
axis square

%% Final plot (smoother curve) with misfit-based error

CMgH2 = MgCOREbest + (MgRIM-MgCOREbest).*erfc(x./(2.*sqrt(Derr_high2.*t)));
%high D error
CMgL2 = MgCOREbest + (MgRIM-MgCOREbest).*erfc(x./(2.*sqrt(Derr_low2.*t)));
%low D error

figure('Name','Final Plot, misfit-based error','NumberTitle','off')
plot(x,CMgB,'k-','LineWidth',1.25)
hold on
plot(x,CMgH2,'k--')
hold on
```

```
plot(x,CMgL2,'k--')
xlabel('Distance from rim (\mum)')
ylabel('Mg (wt%)')
title('profile h3.2.1')
hold on
errorbar(x_data_all+disbest,Mg_data_all,anaERR_all,'ko','MarkerSize',4,'Marke
rFaceColor','k');
hold on
str = sprintf('Dbest = %g m^2 s^{-1}',Dbest_m)
text(0.4,0.4,str,'Units','Normalized','HorizontalAlignment','left','FontSize'
,14)
hold on
str2 = sprintf('Dmax = %g m^2 s^{-1}',Derr_high_m2)
text(0.4,0.5,str2,'Units','Normalized','HorizontalAlignment','left','FontSize
',12)
hold on
str3 = sprintf('Dmin = %g m^2 s^{-1}',Derr_low_m2)
text(0.4,0.3,str3,'Units','Normalized','HorizontalAlignment','left','FontSize
',12)
axis square

%% Output results to file

output = [MgRIM MgCOREmin MgCOREmax dMgCORE MgCOREstep disMIN disMAX ddis
disstep extMIN extMAX dext extstep Dmin Dmax dD Dstep iter MgCOREbest disbest
extbest Dbest Dbest_m misfitmin mfpct Derr_low_m2 Derr_high_m2 discbest
discpctbest Derr_low_m Derr_high_m];

csvwrite('results.csv',output)
```

MODEL INPUT AND OUTPUT

Table D1. Inputs to model A

	Mg rim				Mg core				DMg (um2/s)				TOTAL
profile	min	max	interval	steps	min	max	interval	steps	min	max	interval	steps	combinations tried
h3.1.1	0.068	0.073	1E-04	50	0.08	0.085	1E-04	51	5E-05	5E-04	1E-06	450	1E+06
Bt.1.2	0.04	0.055	1E-04	150	0.079	0.083	1E-04	41	7E-05	7E-04	2E-06	315	2E+06
h3.2.1	0.05	0.068	1E-04	180	0.078	0.083	1E-04	51	5E-05	5E-04	1E-06	450	4E+06
C5.1.1	0.06	0.074	1E-04	140	0.079	0.083	1E-04	41	1E-05	5E-04	2E-07	2450	1E+07
Bb.1.1	0.055	0.07	1E-04	151	0.081	0.085	1E-04	41	1E-05	9E-05	2E-07	401	2E+06
Ab.1.1&3	0.065	0.075	1E-04	100	0.08	0.084	1E-04	41	5E-07	6E-05	1E-07	595	2E+06
Bt.1.1	0.06	0.07	1E-04	101	0.08	0.085	1E-04	51	5E-07	6E-05	1E-07	595	3E+06
h6.1.1	0.06	0.072	1E-04	120	0.082	0.085	1E-04	31	5E-07	5E-05	1E-07	496	2E+06
h3.3.1	0.06	0.075	1E-04	150	0.079	0.083	1E-04	41	5E-07	5E-05	1E-07	496	3E+06
C3.2.1	0.065	0.073	1E-04	80	0.079	0.082	1E-04	31	5E-07	5E-05	1E-07	496	1E+06
h1.2.2	0.065	0.073	1E-04	80	0.08	0.084	1E-04	41	1E-07	5E-05	2E-08	2495	8E+06
C5.2.1	0.06	0.07	1E-04	101	0.081	0.084	1E-04	31	1E-07	5E-05	2E-08	2495	8E+06
C3.1.1	0.06	0.071	1E-04	110	0.079	0.083	1E-04	41	1E-07	5E-05	2E-08	2495	1E+07
C3.1.2	0.063	0.073	1E-04	100	0.081	0.084	1E-04	31	1E-07	5E-05	2E-08	2495	8E+06
C3.4.1	0.065	0.075	1E-04	100	0.081	0.084	1E-04	31	1E-07	5E-05	1E-08	4990	2E+07
h3.3.2	0.06	0.073	1E-04	130	0.08	0.083	1E-04	31	1E-07	1E-05	2E-08	495	2E+06
h1.2.1	0.064	0.0785	1E-04	145	0.0805	0.0825	1E-04	21	1E-08	6E-06	1E-08	599	2E+06
h3.2.2	0.06	0.074	1E-04	140	0.079	0.083	1E-04	41	2E-07	7E-05	2E-07	349	2E+06
h3.2.2	0.06	0.074	1E-04	140	0.079	0.083	1E-04	41	2E-07	7E-05	2E-07	349	2E+06
Bb.2.1	0.045	0.061	1E-04	160	0.065	0.068	1E-04	31	1E-06	1E-05	2E-08	450	2E+06
h1.1.1&2	0.05	0.068	1E-04	180	0.078	0.081	1E-04	31	5E-06	1E-04	1E-06	96	5E+05

Notes- “v” downdrop removed for modeling h3.2.2 and Bb.2.1; anomalous points removed from h1.1.1&2

Table D2. Outputs of model A

	best fit values				misfit-based error analysis				discrepancy-based error analysis			
profile	rim	core	D (um2/s)	D (m2/s)	misfit	misfit%	Dmin	Dmax	disc	disc%best	Dmin	Dmax
h3.1.1	0.0704	0.0834	2.8E-04	2.8E-16	1.9E-04	50	1.6E-16	4.7E-16	10	33	2.7E-16	3.7E-16
Bt.1.2	0.0506	0.0812	2.8E-04	2.8E-16	2.0E-04	50	1.9E-16	3.9E-16	26	53	2.7E-16	3.2E-16
h3.2.1	0.0632	0.0803	2.6E-04	2.6E-16	1.4E-04	50	1.7E-16	3.8E-16	16	38	2.0E-16	3.0E-16
C5.1.1	0.0707	0.0811	6.9E-05	6.9E-17	2.0E-04	50	2.8E-17	1.4E-16	7	28	6.7E-17	7.0E-17
Bb.1.1	0.0679	0.0831	4.5E-05	4.5E-17	2.1E-04	50	2.2E-17	8.1E-17	10	40	2.3E-17	7.1E-17
Ab.1.1&3	0.0719	0.0826	1.9E-05	1.9E-17	1.0E-04	50	4.3E-18	5.6E-17	28	33	1.9E-17	2.9E-17
Bt.1.1	0.0651	0.0833	1.6E-05	1.6E-17	1.7E-04	50	5.3E-18	3.7E-17	14	34	1.5E-17	1.7E-17
h6.1.1	0.0706	0.0831	9.8E-06	9.8E-18	2.2E-04	50	4.1E-18	2.0E-17	6	32	7.7E-18	1.3E-17
h3.3.1	0.0722	0.0817	9.3E-06	9.3E-18	1.4E-04	50	3.4E-18	2.1E-17	5	20	7.6E-18	1.6E-17
C3.2.1	0.0705	0.0805	5.1E-06	5.1E-18	1.7E-04	50	2.5E-18	9.6E-18	4	27	4.0E-18	6.5E-18
h1.2.2	0.0704	0.0817	5.0E-06	5.0E-18	1.9E-04	50	8.0E-19	2.0E-17	8	30	3.7E-18	6.3E-18
C5.2.1	0.07	0.0831	2.9E-06	2.9E-18	1.6E-04	50	3.6E-19	1.1E-17	12	34	2.5E-18	3.5E-18
C3.1.1	0.0655	0.0807	3.6E-06	3.6E-18	1.7E-04	50	9.4E-19	9.2E-18	14	41	1.0E-19	5.4E-18
C3.1.2	0.0662	0.0826	3.5E-06	3.5E-18	2.1E-04	50	8.4E-19	1.2E-17	19	61	1.0E-19	4.0E-17
C3.4.1	0.0721	0.0824	3.1E-06	3.1E-18	1.8E-04	50	3.6E-19	1.1E-17	11	42	2.0E-18	5.5E-18
h3.3.2	0.0705	0.0815	3.0E-06	3.0E-18	1.9E-04	50	5.6E-19	9.1E-18	8	36	2.0E-18	4.1E-18
h1.2.1	0.0763	0.0813	8.7E-07	8.7E-19	1.5E-04	50	6.0E-20	5.2E-18	2	12	3.1E-19	2.0E-18
h3.2.2	0.0679	0.079	1.5E-05	1.5E-17	5.1E-04	50	1.8E-18	6.3E-17	9	56	1.0E-17	1.6E-17
h3.2.2	0.0685	0.0804	2.4E-05	2.4E-17	2.7E-04	50	1.4E-17	3.9E-17	2	18	2.4E-17	2.4E-17
Bb.2.1	0.0526	0.0659	3.8E-06	3.8E-18	2.3E-04	50	1.2E-18	9.3E-18	5	26	3.1E-18	4.3E-18
h1.1.1&2	0.0671	0.0796	3.5E-05	3.5E-17	1.6E-04	50	2.2E-17	6.0E-17	0	0	3.2E-17	3.8E-17

Notes – for profiles C3.1.1 and C3.1.2, the discrepancy-based Dmin is essentially infinitely small (step function)

Table D3. Inputs to models B, C, and D

			Core (wt% Mg)				Dissolution distance (μm)				Core extension distance (μm)				Diffusivity ($\mu m^2\ s^{-1}$)				total
	Profile	Rim (wt% Mg)	min	max	step size	# steps	min	max	step size	# steps	min	max	step size	# steps	min	max	step size	# steps	# combo
C	h3.2.1	0.0030	0.081	0.085	2E-04	21	0	100	10	11	0	100	10	11	1E-05	1E-03	1E-06	990	3E+06
B	h3.2.1	0.0632	0.081	0.085	2E-04	21	0	100	10	11	0	100	10	11	1E-05	1E-03	1E-06	990	3E+06
C	h3.1.1	0.0030	0.081	0.085	2E-04	21	0	100	10	11	0	100	10	11	1E-05	1E-03	1E-06	990	3E+06
B	h3.1.1	0.0704	0.081	0.085	2E-04	21	0	100	10	11	0	100	10	11	1E-05	1E-03	1E-06	990	3E+06
D	Bt.1.2	0.0030	0.081	0.085	2E-04	21	0	0		2	0	100	10	11	1E-06	1E-04	1E-07	991	5E+05
C	Bt.1.2	0.0030	0.081	0.085	2E-04	21	0	100	10	11	0	100	10	11	1E-05	1E-03	1E-06	990	3E+06
B	Bt.1.2	0.0506	0.081	0.085	2E-04	21	0	100	10	11	0	100	10	11	1E-05	1E-03	1E-06	990	3E+06
D	C5.1.1	0.0030	0.081	0.085	2E-04	21	0	0		2	0	100	10	11	1E-08	1E-06	1E-09	990	5E+05
C	C5.1.1	0.0030	0.081	0.085	2E-04	21	0	100	10	11	0	100	10	11	1E-05	1E-03	1E-06	990	3E+06
B	C5.1.1	0.0707	0.081	0.085	2E-04	21	0	100	10	11	0	100	10	11	1E-05	1E-03	1E-06	990	3E+06
C	Bb.1.1	0.0030	0.081	0.085	2E-04	21	0	100	10	11	0	100	10	11	1E-06	1E-04	1E-07	991	3E+06
B	Bb.1.1	0.0679	0.081	0.085	2E-04	21	0	100	10	11	0	100	10	11	1E-06	1E-04	1E-07	991	3E+06
C	Ab.1.1&3	0.0030	0.081	0.085	2E-04	21	0	100	10	11	0	100	10	11	5E-06	5E-04	1E-06	495	1E+06
B	Ab.1.1&3	0.0719	0.081	0.085	2E-04	21	0	100	10	11	0	100	10	11	1E-06	1E-04	1E-07	991	3E+06
C	Bt.1.1	0.0030	0.081	0.085	2E-04	21	0	100	10	11	0	100	10	11	1E-06	1E-04	1E-07	991	3E+06
B	Bt.1.1	0.0651	0.081	0.085	2E-04	21	0	100	10	11	0	100	10	11	1E-06	1E-04	1E-07	991	3E+06
C	h6.1.1	0.0030	0.081	0.085	2E-04	21	0	100	10	11	0	100	10	11	1E-06	1E-04	1E-07	991	3E+06
B	h6.1.1	0.0706	0.081	0.085	2E-04	21	0	100	10	11	0	100	10	11	1E-06	1E-04	1E-07	991	3E+06
C	h3.3.1	0.0030	0.081	0.085	2E-04	21	0	100	10	11	0	100	10	11	1E-07	5E-05	1E-08	4990	1E+07
B	h3.3.1	0.0722	0.081	0.085	2E-04	21	0	100	10	11	0	100	10	11	5E-07	5E-05	1E-07	496	1E+06
C	C3.2.1	0.0030	0.081	0.085	2E-04	21	0	100	10	11	0	100	10	11	5E-07	5E-05	1E-07	496	1E+06
B	C3.2.1	0.0705	0.081	0.085	2E-04	21	0	100	10	11	0	100	10	11	5E-07	5E-05	1E-07	496	1E+06
C	h1.2.2	0.0030	0.081	0.085	2E-04	21	0	100	10	11	0	100	10	11	5E-07	5E-05	1E-07	496	1E+06
B	h1.2.2	0.0704	0.081	0.085	2E-04	21	0	100	10	11	0	100	10	11	5E-07	5E-05	1E-07	496	1E+06
C	C5.2.1	0.0030	0.081	0.085	2E-04	21	0	100	10	11	0	100	10	11	5E-07	5E-05	1E-07	496	1E+06
B	C5.2.1	0.0724	0.081	0.085	2E-04	21	0	100	10	11	0	100	10	11	5E-07	5E-05	1E-07	496	1E+06
C	C3.1.1	0.0030	0.081	0.085	2E-04	21	0	100	10	11	0	100	10	11	1E-07	5E-05	1E-07	499	1E+06
B	C3.1.1	0.0655	0.081	0.085	2E-04	21	0	100	10	11	0	100	10	11	5E-07	5E-05	1E-07	496	1E+06
C	C3.1.2	0.0030	0.081	0.085	2E-04	21	0	100	10	11	0	100	10	11	1E-07	5E-05	1E-07	499	1E+06

Table D3, *continued*

B	C3.1.2	0.0662	0.081	0.085	2E-04	21	0	100	10	11	0	100	10	11	1E-07	5E-05	1E-07	499	1E+06
C	C3.4.1	0.0030	0.081	0.085	2E-04	21	0	100	10	11	0	100	10	11	1E-07	5E-05	1E-07	499	1E+06
B	C3.4.1	0.0721	0.081	0.085	2E-04	21	0	100	10	11	0	100	10	11	1E-07	5E-05	1E-07	499	1E+06
D	h3.3.2	0.0030	0.081	0.085	2E-04	21	0	0		2	0	100	10	11	1E-08	1E-06	1E-08	99	5E+04
C	h3.3.2	0.0030	0.081	0.085	2E-04	21	0	100	10	11	0	100	10	11	1E-07	5E-05	1E-07	499	1E+06
B	h3.3.2	0.0705	0.081	0.085	2E-04	21	0	100	10	11	0	100	10	11	1E-07	5E-05	1E-07	499	1E+06
C	h1.2.1	0.0030	0.081	0.085	2E-04	21	0	100	10	11	0	100	10	11	5E-08	8E-06	1E-08	795	2E+06
B	h1.2.1	0.0763	0.081	0.085	2E-04	21	0	100	10	11	0	100	10	11	5E-08	8E-06	1E-08	795	2E+06
C	h3.2.2	0.0030	0.081	0.085	2E-04	21	0	100	10	11	0	100	10	11	1E-06	1E-04	1E-06	100	3E+05
B	h3.2.2	0.0685	0.081	0.085	2E-04	21	0	100	10	11	0	100	10	11	1E-06	1E-04	1E-06	100	3E+05

Notes – for h3.2.1, the dipping “v” of points was excluded; for Bb.1.1, three points at profile ends were excluded

Table D4. Outputs of models B, C, and D

	Best values				Error analysis (misfit-based)				Error analysis (discrepancy-based)			
Profile	Core (wt% Mg)	Dissol'n (μm)	Core dist. (μm)	D (m^2 s^{-1})	misfit	misfit% error envelope	Dmin (m^2 s^{-1})	Dmax (m^2 s^{-1})	Disc	Disc%	Dmin (m^2 s^{-1})	Dmax (m^2 s^{-1})
h3.2.1	0.081	90	100	7.9E-16	1.3E-04	50	7.2E-16	8.7E-16	11	26	7.9E-16	8.1E-16
h3.2.1	0.081	0	100	3.0E-16	1.5E-04	50	1.9E-16	4.5E-16	14	33	2.6E-16	3.2E-16
h3.1.1	0.0834	100	100	7.5E-16	1.9E-04	50	6.5E-16	8.5E-16	13	42	7.1E-16	8.1E-16
h3.1.1	0.0834	0	100	2.8E-16	1.9E-04	50	1.6E-16	4.7E-16	10	32	2.7E-16	3.7E-16
Bt.1.2	0.081	0	0	1.4E-17	1.3E-03	50	1.0E-22	1.3E-16	39	78	1.0E-22	2.7E-16
Bt.1.2	0.0814	50	100	5.2E-16	1.7E-04	50	4.6E-16	5.8E-16	23	46	5.0E-16	5.5E-16
Bt.1.2	0.0812	0	90	2.8E-16	2.0E-04	50	1.9E-16	3.9E-16	26	52	2.6E-16	3.3E-16
C5.1.1	0.081	0	0	2.0E-19	5.9E-04	50	1.0E-22	5.2E-19	15	58	1.9E-19	4.5E-17
C5.1.1	0.0812	60	70	2.3E-16	1.8E-04	50	2.0E-16	2.6E-16	7	27	2.1E-16	2.3E-16
C5.1.1	0.0812	0	10	7.2E-17	1.9E-04	50	3.0E-17	1.5E-16	8	31	4.7E-17	8.1E-17
Bb.1.1	0.083	30	10	8.5E-17	1.9E-04	50	7.1E-17	9.9E-17	11	42	7.1E-17	1.0E-16
Bb.1.1	0.0832	0	0	4.6E-17	2.0E-04	50	2.3E-17	8.3E-17	10	38	2.3E-17	7.4E-17
Ab.1.1&3	0.0826	30	0	5.8E-17	9.8E-05	50	4.3E-17	7.2E-17	29	33	5.7E-17	6.4E-17
Ab.1.1&3	0.0826	0	0	1.9E-17	9.9E-05	50	4.3E-18	5.6E-17	28	32	1.9E-17	2.9E-17
Bt.1.1	0.0834	20	0	4.0E-17	1.7E-04	50	3.0E-17	5.0E-17	14	33	3.9E-17	4.1E-17
Bt.1.1	0.0834	0	0	1.6E-17	1.7E-04	50	5.4E-18	3.8E-17	14	33	1.5E-17	1.7E-17
h6.1.1	0.0832	20	30	2.9E-17	2.1E-04	50	2.4E-17	3.4E-17	6	30	2.7E-17	3.1E-17
h6.1.1	0.083	0	10	9.4E-18	2.1E-04	50	3.9E-18	1.9E-17	6	30	7.5E-18	1.2E-17
h3.3.1	0.0816	20	0	2.5E-17	1.3E-04	50	1.9E-17	3.0E-17	4	15	2.4E-17	2.6E-17
h3.3.1	0.0816	0	0	8.9E-18	1.3E-04	50	3.2E-18	2.0E-17	4	15	7.4E-18	1.2E-17
C3.2.1	0.081	20	20	2.4E-17	1.9E-04	50	2.0E-17	2.8E-17	4	25	2.3E-17	2.5E-17
C3.2.1	0.081	0	0	6.1E-18	1.8E-04	50	2.8E-18	1.2E-17	4	25	4.8E-18	7.8E-18
h1.2.2	0.0818	20	0	2.5E-17	1.9E-04	50	1.8E-17	3.2E-17	9	32	2.4E-17	2.5E-17
h1.2.2	0.0818	0	0	5.1E-18	1.8E-04	50	9.0E-19	2.1E-17	8	29	3.9E-18	6.5E-18
C5.2.1	0.083	10	0	7.4E-18	1.6E-04	50	4.4E-18	1.0E-17	12	33	7.2E-18	7.7E-18

Table D4, *continued*

C5.2.1	0.0832	0	0	4.6E-18	1.6E-04	50	6.0E-19	1.8E-17	12	33	4.1E-18	4.8E-18
C3.1.1	0.081	10	0	9.1E-18	1.7E-04	50	6.1E-18	1.2E-17	15	43	1.0E-19	9.6E-18
C3.1.1	0.081	0	0	3.8E-18	1.7E-04	50	1.0E-18	1.0E-17	13	37	2.7E-18	4.0E-18
C3.1.2	0.0826	10	0	9.2E-18	2.1E-04	50	5.7E-18	1.3E-17	18	56	8.5E-18	2.6E-17
C3.1.2	0.0826	0	0	3.5E-18	2.1E-04	50	9.0E-19	1.2E-17	19	59	1.0E-19	4.0E-17
C3.4.1	0.0824	10	0	6.4E-18	1.8E-04	50	4.7E-18	8.1E-18	11	41	5.9E-18	8.4E-18
C3.4.1	0.0824	0	0	3.1E-18	1.8E-04	50	4.0E-19	1.1E-17	11	41	2.0E-18	5.5E-18
h3.3.2	0.0812	0	0	7.0E-20	2.6E-04	50	4.0E-20	1.0E-19	10	43	6.1E-20	6.4E-18
h3.3.2	0.0816	10	0	7.0E-18	1.9E-04	50	5.1E-18	8.9E-18	8	35	6.6E-18	7.2E-18
h3.3.2	0.0816	0	0	3.1E-18	1.8E-04	50	6.0E-19	9.3E-18	8	35	2.2E-18	4.1E-18
h1.2.1	0.0814	10	0	4.1E-18	1.4E-04	50	2.4E-18	5.3E-18	4	22	3.7E-18	4.6E-18
h1.2.1	0.0814	0	0	9.4E-19	1.4E-04	50	7.0E-20	5.5E-18	4	22	3.3E-19	2.2E-18
h3.2.2	0.081	30	50	6.9E-17	2.7E-04	50	6.1E-17	7.7E-17	5	42	6.4E-17	7.3E-17
h3.2.2	0.081	0	30	2.9E-17	2.6E-04	50	1.7E-17	4.6E-17	5	42	1.8E-17	4.9E-17

Notes – for Bt.1.2 and C5.1.1, the Dmin values based on discrepancy are essentially infinite (step function)

References

Adams N. K., Houghton B. F., Fagents S. A., Hildreth W. 2006. The transition from explosive to effusive eruptive regime: the example of the 1912 Novarupta eruption, Alaska. *Geological Society of America Bulletin* 118:620–634.

Adams N. K., Houghton B. F., Hildreth W. 2006. Abrupt transitions during sustained explosive eruptions: examples from the 1912 eruption of Novarupta, Alaska. *Bulletin of Volcanology* 69:189-206.

Aggarwal S., and Dieckmann R. 2002. Point defects and cation tracer diffusion in $(Ti_x Fe_{1-x})_{3-\delta}O_4$. II. Cation tracer diffusion. *Physics and Chemistry of Minerals* 29:707–718.

Albarede F. and Bottinga Y. 1972. Kinetic disequilibrium in trace element partitioning between phenocrysts and host lava. *Geochimica et Cosmochimica Acta* 36:141–156.

Allmendinger R. W., Cardozo N. C., and Fisher D. 2013. *Structural Geology Algorithms: Vectors and Tensors*, Cambridge, England: Cambridge University Press.

Andersen D. J. and Lindsley D. H. 1988. Internally consistent solution models for Fe-Mg-Mn-Ti oxides: Fe-Ti oxides. *American Mineralogist* 73:714–726.

Anderson J. L., and Smith D. R. 1995. The effects of temperature and fO_2 on the Al-in-hornblende barometer. *American Mineralogist* 80:549–559.

Andújar J., and Scaillet B. 2012. Relationships between pre-eruptive conditions and eruptive styles of phonolite–trachyte magmas. *Lithos* 152:122–131.

Angel R. J., Carpenter M. A., and Finger L. W. 1990. Structural variation associated with compositional variation and order-disorder behavior in anorthite-rich feldspars. *American Mineralogist* 75:150–162.

Annen C. 2009. From plutons to magma chambers: Thermal constraints on the accumulation of eruptible silicic magma in the upper crust. *Earth and Planetary Science Letters* 284:409–416.

Aragon R., McCallister R. H., and Harrison H. R. 1984. Cation diffusion in titanomagnetites. *Contributions to Mineralogy and Petrology* 85:174–185.

Armstrong J. T. 1988. Quantitative analysis of silicate and oxide materials: Comparison of Monte Carlo, ZAF, and $\phi(\rho z)$ procedures. In *Microbeam Analysis 1988: Proceedings of*

the 23rd Annual Conference of the Microbeam Analysis Society, Milwaukee, Wisconsin, 8-12 August 1988, edited by Newbury D. E. San Francisco: San Francisco Press. p. 527.

Bachmann O., and Dungan M. A. 2002. Temperature-induced Al-zoning in hornblendes of the Fish Canyon magma, Colorado. *American Mineralogist* 87:1062–1076.

Bacon C. R., and Hirschmann M. M. 1988. Mg/Mn partitioning as a test for equilibrium between coexisting Fe-Ti oxides. *American Mineralogist* 73:57–61.

Ball M., Pinkerton H., and Harris A. J. L. 2008. Surface cooling, advection and the development of different surface textures on active lavas on Kilauea, Hawai'i. *Journal of Volcanology and Geothermal Research* 173:148–156.

Balta J. B., Sanborn M. E., Udry A., Wadhwa M., and McSween H. Y. 2015. Petrology and trace element geochemistry of Tissint, the newest shergottite fall. *Meteoritics & Planetary Science* 50:63–85.

Balta J. B., Sanborn M., McSween H. Y., and Wadhwa M. 2013. Magmatic history and parental melt composition of olivine-phyric shergottite LAR 06319: Importance of magmatic degassing and olivine antecrysts in Martian magmatism. *Meteoritics & Planetary Science* 48:1359–1382.

Barrat J. A., Gillet P., Sautter V., Jambon A., Javoy M., Göpel C., Lesourd M., Keller F., and Petit E. 2002. Petrology and chemistry of the basaltic shergottite North West Africa 480. *Meteoritics & Planetary Science* 37:487–499.

Barrat J. A., Jambon A., Bohn M., Gillet P., Sautter V., Göpel C., Lesourd M., and Keller F. 2002. Petrology and chemistry of the picritic shergottite North West Africa 1068 (NWA 1068). *Geochimica et Cosmochimica Acta* 66:3505–3518.

Baschek G., and Johannes W. 1995. The estimation of NaSi-CaAl interdiffusion rates in peristerite by homogenization experiments. *European Journal of Mineralogy* 7:295–307.

Behrens H., Johannes W., and Schmalzried H. 1990. On the mechanisms of cation diffusion processes in ternary feldspars. *Physics and Chemistry of Minerals* 17:62–78.

Bindeman I. N., Davis A. M., and Drake M. J. 1998. Ion microprobe study of plagioclase-basalt partition experiments at natural concentration levels of trace elements. *Geochimica et Cosmochimica Acta* 62:1175–1193.

Bish D. L. et al. 2013. X-ray Diffraction Results from Mars Science Laboratory: Mineralogy of Rocknest at Gale Crater. *Science* 341:1238932.

Blinova A. and Herd C. D. K. 2009. Experimental study of polybaric REE partitioning between olivine, pyroxene and melt of the Yamato 980459 composition: Insights into the petrogenesis of depleted shergottites. *Geochimica et Cosmochimica Acta* 73:3471–3492.

Bowen N. L. 1928. *The Evolution of the Igneous Rocks*, Princeton University Press.

Bowen N. L., and Tuttle O. F. 1949. The System MgO—SiO_2—H_2O. *GSA Bulletin* 60:439–460.

Brachfeld S., Shah D., First E., Hammer J., and Bowles J. 2015. Influence of redox conditions on the intensity of Mars crustal magnetic anomalies. *Meteoritics & Planetary Science* 50:1703–1717, doi:10.1111/maps.12505.

Browne B., and Gardner J. 2006. The influence of magma ascent path on the texture, mineralogy, and formation of hornblende reaction rims. *Earth and Planetary Science Letters* 246:161–176.

Brugger C. R., and Hammer J. E. 2010. Crystallization Kinetics in Continuous Decompression Experiments: Implications for Interpreting Natural Magma Ascent Processes. *Journal of Petrology* 51:1941–1965.

Bryan W. B. 1972. Morphology of quench crystals in submarine basalts. *Journal of Geophysical Research* 77:5812–5819.

Buddington A. F., and Lindsley D. H. 1964. Iron-Titanium Oxide Minerals and Synthetic Equivalents. *Journal of Petrology* 5:310–357.

Bullard F. M. 1984. *Volcanoes of the Earth*, Second Revised. Austin: University of Texas Press.

Burgess K. D., and Cooper R. F. 2013. Extended planar defects and the rapid incorporation of Ti^{4+} into olivine. *Contributions to Mineralogy and Petrology* 166:1223–1233.

Cabrera A., Weinberg R. F., and Wright H. M. N. 2015. Magma Fracturing and Degassing Associated with Obsidian Formation: The Explosive-Effusive Transition. *Journal of Volcanology and Geothermal Research* 298:71–84.

Cardozo N., and Allmendinger R. W. 2013. Spherical Projections with OSXStereonet. *Comput. Geosci.* 51:193–205.

Caricchi L., Pommier A., Pistone M., Castro J., Burgisser A., and Perugini D. 2011. Strain-induced magma degassing: insights from simple-shear experiments on bubble bearing melts. *Bulletin of Volcanology* 73:1245–1257.

Cashman K. V., Thornber C., and Kauahikaua J. P. 1999. Cooling and crystallization of lava in open channels, and the transition of pāhoehoe lava to'a'ā. *Bulletin of Volcanology* 61:306–323.

Cashman K., Pinkerton H., and Stephenson J. 1998. Introduction to Special Section: Long Lava Flows. *Journal of Geophysical Research: Solid Earth* 103:27281–27289.

Cembrano J., and Lara L. 2009. The link between volcanism and tectonics in the southern volcanic zone of the Chilean Andes: A review. *Tectonophysics* 471:96–113.

Chakraborty S., Marquardt K., and Bobrowski H. 2016. The connection between diffusion, dissolution, deformation and evaportation: The role of mobile dislocations (abstract #MR42A-05). AGU Fall Meeting.

Charilaou M., Löffler J. F., and Gehring A. U. 2011. Fe-Ti-O exchange at high temperature and thermal hysteresis. *Geophysical Journal International* 185:647–652.

Cherniak D. J., and Watson E. B. 2011. Helium diffusion in rutile and titanite, and consideration of the origin and implications of diffusional anisotropy. *Chemical Geology* 288:149–161.

Clark J. N., Ihli J., Schenk A. S., Kim Y.-Y., Kulak A. N., Campbell J. M., Nisbet G., Meldrum F. C., and Robinson I. K. 2015. Three-dimensional imaging of dislocation propagation during crystal growth and dissolution. *Nature Materials* 14:780–784.

Coombs M., and Gardner J. 2001. Shallow-storage conditions for the rhyolite of the 1912 eruption at Novarupta, Alaska. *Geology* 29:775-778.

Coppola D., Staudacher T., and Cigolini C. 2007. Field thermal monitoring during the August 2003 eruption at Piton de la Fournaise (La Réunion). *Journal of Geophysical Research: Solid Earth* 112:B05215.

Costa F., and Chakraborty S. 2004. Decadal time gaps between mafic intrusion and silicic eruption obtained from chemical zoning patterns in olivine. *Earth and Planetary Science Letters* 227:517–530.

Costa F., Chakraborty S., and Dohmen R. 2003. Diffusion coupling between trace and major elements and a model for calculation of magma residence times using plagioclase. *Geochimica et Cosmochimica Acta* 67:2189–2200.

Costa F., Coogan L. A., and Chakraborty S. 2010. The time scales of magma mixing and mingling involving primitive melts and melt–mush interaction at mid-ocean ridges. *Contributions to Mineralogy and Petrology* 159:371–387.

Costa F., Dohmen R., and Chakraborty S. 2008. Time Scales of Magmatic Processes from Modeling the Zoning Patterns of Crystals. *ResearchGate* 69:545–594.

Costa F., Scaillet B., and Pichavant M. 2004. Petrological and Experimental Constraints on the Pre-eruption Conditions of Holocene Dacite from Volcan San Pedro (36 S, Chilean Andes) and the Importance of Sulphur in Silicic Subduction-related Magmas. *Journal of Petrology* 45:855–881.

Crank J. 1975. *The Mathematics of Diffusion*, Second. Oxford: Clarendon Press.

Dall'Agnol R., Scaillet B., and Pichavant M. 1999. An Experimental Study of a Lower Proterozoic A-type Granite from theEastern Amazonian Craton, Brazil. *Journal of Petrology* 40:1673–1698.

De Angelis S. H., Larsen J., Coombs M., Dunn A., and Hayden L. 2015. Amphibole reaction rims as a record of pre-eruptive magmatic heating: An experimental approach. *Earth and Planetary Science Letters* 426:235–245.

Del Bello E., Lane S. J., James M. R., Llewellin E. W., Taddeucci J., Scarlato P., and Capponi A. 2015. Viscous plugging can enhance and modulate explosivity of strombolian eruptions. *Earth and Planetary Science Letters* 423:210–218.

Devine J. D., Rutherford M. J., Norton G. E., and Young S. R. 2003. Magma Storage Region Processes Inferred from Geochemistry of Fe–Ti Oxides in Andesitic Magma, Soufrière Hills Volcano, Montserrat, W.I. *Journal of Petrology* 44:1375–1400.

Dieckmann R., Hilton M. R., and Mason T. O. 1987. Defects and Cation Diffusion in Magnetite (VIII): Migration Enthalpies for Iron and Impurity Cations. *Berichte der Bunsengesellschaft für physikalische Chemie* 91:59–66.

Dohmen R., and Blundy J. 2014. A predictive thermodynamic model for element partitioning between plagioclase and melt as a function of pressure, temperature and composition. *American Journal of Science* 314:1319–1372.

Dohmen R., and Chakraborty S. 2007. Fe–Mg diffusion in olivine II: point defect chemistry, change of diffusion mechanisms and a model for calculation of diffusion coefficients in natural olivine. *Physics and Chemistry of Minerals* 34:409–430.

Dohmen R., Faak K., and Blundy J. D. 2017. Chronometry and speedometry of magmatic processes using chemical diffusion in olivine, plagioclase and pyroxenes. *Reviews in Mineralogy and Geochemistry* 83:535–575.

Dohmen R., Kasemann S. A., Coogan L., and Chakraborty S. 2010. Diffusion of Li in olivine. Part I: Experimental observations and a multi species diffusion model. *Geochimica et Cosmochimica Acta* 74:274–292.

Donaldson C. H. 1976. An experimental investigation of olivine morphology. *Contributions to Mineralogy and Petrology* 57:187–213.

Donaldson C. H. 1979. An experimental investigation of the delay in nucleation of olivine in mafic magmas. *Contributions to Mineralogy and Petrology* 69:21–32.

Donaldson C. H. 1990. Forsterite dissolution in superheated basaltic, andesitic and rhyolitic melts. *Mineral. Mag* 54:67–74.

Donaldson C. H., Usselman T. M., Williams R. J., and Lofgren G. E. 1975. Experimental modeling of the cooling history of Apollo 12 olivine basalts. *Proceedings of the 6th Lunar Science Conference* 843–869.

Donaldson C. H., Williams R. J., and Lofgren G. 1975. A sample holding technique for study of crystal growth in silicate melts. *American Mineralogist* 60:324–326.

Donnelly-Nolan J. M., Champion D. E., and Grove T. L. 2016. Late Holocene volcanism at Medicine Lake volcano, northern California Cascades: U.S. Geological Survey Professional Paper 1822, 59 p., http://dx.doi.org/10.3133/pp1822.

Donovan J. J. and Tingle T. N. 1996. An Improved Mean Atomic Number Background Correction for Quantitative Microanalysis. *Microscopy and Microanalysis* 2:1–7.

Donovan J. J., Lowers H. A., and Rusk B. G. 2011. Improved electron probe microanalysis of trace elements in quartz. *American Mineralogist* 96:274–282.

Donovan J. J., Snyder D. A., and Rivers M. L. 1993. An improved interference correction for trace element analysis. *Microbeam Analysis* 2:23–28.

Dove P. M., and Han N. 2007. Kinetics of Mineral Dissolution and Growth as Reciprocal Microscopic Surface Processes Across Chemical Driving Force. In *Perspectives on Inorganic, Organic, and Biological Crystal Growth: From Fundamentals to Applications*, edited by Skowronski M., DeYoreo J. J., and Wang C.A. Melville, NY: American Institute of Physics. pp. 215–234.

Dowty E. 1980. Crystal growth and nucleation theory and the numerical simulation of igneous crystallization. In *Physics of Magmatic Processes*, edited by Hargraves R. B. Princeton, NJ: Princeton University Press. pp. 419–486.

Drake R. E. 1976. Chronology of Cenozoic igneous and tectonic events in the central Chilean Andes- Latitudes 35o30' to 36oS. *Journal of Volcanology and Geothermal Research* 1:265–284.

Droop G. T. R. 1987. A general equation for estimating Fe3+ concentrations in ferromagnesian silicates and oxides from microprobe analyses, using stoichiometric criteria. *Mineralogical Magazine* 51:431–435.

Druitt T. H., Costa F., Deloule E., Dungan M., and Scaillet B. 2012. Decadal to monthly timescales of magma transfer and reservoir growth at a caldera volcano. *Nature* 482:77–80.

Dvorak J. J., and Dzurisin D. 1997. Volcano geodesy: The search for magma reservoirs and the formation of eruptive vents. *Reviews of Geophysics* 35:343–384.

Edgar A. D. 1973. *Experimental petrology: basic principles and techniques*. Oxford: Clarendon Press.

Edwards B. R., and Russell J. K. 1996. A review and analysis of silicate mineral dissolution experiments in natural silicate melts. *Chemical Geology* 130:233–245.

Eggler D. H., and Burnham C. W. 1973. Crystallization and Fractionation Trends in the System Andesite-H_2O-CO_2-O_2 at Pressures to 10 Kb. *GSA Bulletin* 84:2517–2532.

Eichelberger J. C. 1995. Silicic volcanism: ascent of viscous magmas from crustal reservoirs. *Annual Review of Earth and Planetary Sciences* 23:41–63.

Eichelberger J. C., Carrigan C. R., Westrich H. R., and Price R. H. 1986. Non-explosive silicic volcanism. *Nature* 323:598–602.

Eugster H. P., and Skippen B. 1967. Igneous and metamorphic reactions involving gas equilibria. In *Researches in Geochemistry*, edited by Ableson P. H. New York: John Wiley and Sons. pp. 492–520.

Evans B. W., and Bachmann O. 2013. Implications of equilibrium and disequilibrium among crystal phases in the Bishop Tuff. *American Mineralogist* 98:271–274.

Evans B. W., and Scaillet B. 1997. The redox state of Pinatubo dacite and the ilmenite-hematite solvus. *American Mineralogist* 82:625–629.

Evans B. W., Hildreth W., Bachmann O., and Scaillet B. 2016. In defense of magnetite-ilmenite thermometry in the Bishop Tuff and its implication for gradients in silicic magma reservoirs. *American Mineralogist* 101:469–482.

Faak K., Chakraborty S., and Coogan L. A. 2013. Mg in plagioclase: Experimental calibration of a new geothermometer and diffusion coefficients. *Geochimica et Cosmochimica Acta* 123:195–217.

Faak K., Coogan L. A., and Chakraborty S. 2014. A new Mg-in-plagioclase geospeedometer for the determination of cooling rates of mafic rocks. *Geochimica et Cosmochimica Acta* 140:691–707.

Faure F. and Schiano P. 2005. Experimental investigation of equilibrium conditions during forsterite growth and melt inclusion formation. *Earth and Planetary Science Letters* 236: 882–898.

Faure F., Schiano P., Trolliard G., Nicollet C., and Soulestin B. 2007. Textural evolution of polyhedral olivine experiencing rapid cooling rates. *Contributions to Mineralogy and Petrology* 153:405–416.

Faure F., Trolliard G., Nicollet C., and Montel J.-M. 2003. A developmental model of olivine morphology as a function of the cooling rate and the degree of undercooling. *Contributions to Mineralogy and Petrology* 145:251–263.

Fick A. 1855. Ueber Diffusion. *Annalen der Physik* 170:59–86.

Fiege A., Ruprecht P., and Simon A. 2017. A magma mixing redox trap that moderates mass transfer of sulphur and metals. *Geochemical Perspectives Letters* 190–199.

Filiberto J. and Dasgupta R. 2011. Fe^{2+}–Mg partitioning between olivine and basaltic melts: Applications to genesis of olivine-phyric shergottites and conditions of melting in the Martian interior. *Earth and Planetary Science Letters* 304:527–537.

Filiberto J., Musselwhite D. S., Gross J., Burgess K., Le L., and Treiman A. H. 2010. Experimental petrology, crystallization history, and parental magma characteristics of olivine-phyric shergottite NWA 1068: Implications for the petrogenesis of “enriched” olivine-phyric shergottites. *Meteoritics & Planetary Science* 45:1258–1270.

First E., and Hammer J. 2016. Igneous cooling history of olivine-phyric shergottite Yamato 980459 constrained by dynamic crystallization experiments. *Meteoritics & Planetary Science* 51:1233–1255.

Flynn L. P., and Mouginis-Mark P. J. 1992. Cooling rate of an active Hawaiian lava flow from nighttime spectroradiometer measurements. *Geophysical research letters* 19:1783–1786.

Freer R., and Hauptman Z. 1978. An experimental study of magnetite-titanomagnetite interdiffusion. *Physics of the Earth and Planetary Interiors* 16:223–231.

Frey H. M. and Lange R. A. 2011. Phenocryst complexity in andesites and dacites from the Tequila volcanic field, Mexico: Resolving the effects of degassing vs. magma mixing. *Contributions to Mineralogy and Petrology* 162:415-445.

Frost R. B. 1991. Magnetic petrology: Factors that control the occurrence of magnetite in crustal rocks. In *Oxide Minerals: Petrologic and Magnetic Significance*. Mineralogical Society of America. pp. 489–509.

Fuenzalida H. 1942. El Volcan Descabezado Grande. *Boletin del Museo Nacional de Historia Natural* 21:37–53.

Ganguly J., Dasgupta S., Cheng W., and Neogi S. 2000. Exhumation history of a section of the Sikkim Himalayas, India: records in the metamorphic mineral equilibria and compositional zoning of garnet. *Earth and Planetary Science Letters* 183:471–486.

Gardner J. E., Carey S., Rutherford M. J., and Sigurdsson H. 1995b. Petrologic diversity in Mount St. Helens dacites during the last 4,000 years: implications for magma mixing. *Contributions to Mineralogy and Petrology* 119:224–238.

Gardner J. E., Rutherford M., Carey S., and Sigurdsson H. 1995a. Experimental constraints on pre-eruptive water contents and changing magma storage prior to explosive eruptions of Mount St Helens volcano. *Bulletin of Volcanology* 57:1–17.

Gerlach D. C., and Grove T. L. 1982. Petrology of Medicine Lake Highland volcanics: Characterization of endmembers of magma mixing. *Contributions to Mineralogy and Petrology* 80:147–159.

Geschwind C.-H., and Rutherford M. J. 1992. Cummingtonite and the evolution of the Mount St. Helens (Washington) magma system: an experimental study. *Geology* 20:1011–1014.

Ghiorso M. S., and Evans B. W. 2008. Thermodynamics of rhombohedral oxide solid solutions and a revision of the Fe-Ti two-oxide geothermometer and oxygen-barometer. *American Journal of science* 308:957–1039.

Ghiorso M. S., and Sack O. 1991. Fe-Ti oxide geothermometry: thermodynamic formulation and the estimation of intensive variables in silicic magmas. *Contributions to Mineralogy and Petrology* 108:485–510.

Ghiorso M. S., and Sack R. O. 1995. Chemical mass transfer in magmatic processes IV. A revised and internally consistent thermodynamic model for the interpolation and extrapolation of liquid-solid equilibria in magmatic systems at elevated temperatures and pressures. *Contributions to Mineralogy and Petrology* 119:197–212.

Gibb F. G. 1974. Supercooling and the crystallization of plagioclase from a basaltic magma. *Mineral. Mag* 39:641–653.

Giletti B. J. 1991. Rb and Sr diffusion in alkali feldspars, with implications for cooling histories of rocks. *Geochimica et Cosmochimica Acta* 55:1331–1343.

Giletti B. J., and Casserly J. E. D. 1994. Strontium diffusion kinetics in plagioclase feldspars. *Geochimica et Cosmochimica Acta* 58:3785–3793.

Giletti B. J., and Shanahan T. M. 1997. Alkali diffusion in plagioclase feldspar. *Chemical Geology* 139:3–20.

Gillis-Davis J. J., Lucey P. G., Bradley J. P., Ishii H. A., Kaluna H. M., Misra A., and Connolly Jr. H. C. 2017. Incremental laser space weathering of Allende reveals non-lunar like space weathering effects. *Icarus* 286:1–14.

Giordano D., Russell J. K., and Dingwell D. B. 2008. Viscosity of magmatic liquids: A model. *Earth and Planetary Science Letters* 271:123–134.

Girona T., and Costa F. 2013. DIPRA: A user-friendly program to model multi-element diffusion in olivine with applications to timescales of magmatic processes: DIPRA diffusion code. *Geochemistry, Geophysics, Geosystems* 14:422–431.

Gómez-Elvira J. et al. 2014. Curiosity's rover environmental monitoring station: Overview of the first 100 sols. *Journal of Geophysical Research: Planets* 119: 1680–1688.

Gonnermann H. M., and Manga M. 2003. Explosive volcanism may not be an inevitable consequence of magma fragmentation. *Nature* 426:432–435.

Gonnermann H. M., and Manga M. 2012. Dynamics of magma ascent in the volcanic conduit. In *Modeling Volcanic Processes: The Physics and Mathematics of Volcanism*, edited by Fagents S. A., Gregg T. K. P., and Lopes R. M. C. Cambridge: Cambridge University Press. pp. 55–84.

Greenberg M. D. 1998. *Advanced Engineering Mathematics*, Second. Upper Sadle River, NJ: Prentice Hall.

Greshake A., Fritz J., and Stöffler D. 2004. Petrology and shock metamorphism of the olivine-phyric shergottite Yamato 980459. *Geochimica et Cosmochimica Acta* 68:2359–2377.

Gross J., Treiman A. H., Filiberto J., and Herd C. D. K. 2011. Primitive olivine-phyric shergottite NWA 5789: Petrography, mineral chemistry, and cooling history imply a magma similar to Yamato-980459. *Meteoritics & Planetary Science* 46:116–133.

Grove T. L. 1981. Use of FePt alloys to eliminate the iron loss problem in 1 atmosphere gas mixing experiments: Theoretical and practical considerations. *Contributions to Mineralogy and Petrology* 78:298–304.

Grove T. L., Baker M. B., and Kinzler R. J. 1984. Coupled CaAl-NaSi diffusion in plagioclase feldspar: Experiments and applications to cooling rate speedometry. *Geochimica et Cosmochimica Acta* 48:2113–2121.

Grunder A., and Mahood G. 1988. Physical and Chemical-Models of Zoned Silicic Magmas - the Loma Seca Tuff and Calabozos Caldera, Southern Andes. *Journal of Petrology* 29:831–867.

Gualda G. A. R., Ghiorso M. S., Lemons R. V., and Carley T. L. 2012. Rhyolite-MELTS: A Modified Calibration of MELTS Optimized for Silica-rich, Fluid-bearing Magmatic Systems. *Journal of Petrology* 53:875–890.

Hammer J. E. 2006. Influence of fO_2 and cooling rate on the kinetics and energetics of Fe-rich basalt crystallization. *Earth and Planetary Science Letters* 248:618–637.

Hammer J. E. 2008. Experimental Studies of the Kinetics and Energetics of Magma Crystallization. *Reviews in Mineralogy and Geochemistry* 69:9–59.

Hammer J. E. 2009. Application of a textural geospeedometer to the late-stage magmatic history of MIL 03346. *Meteoritics & Planetary Science* 44:141–154.

Hammer J. E., and Rutherford M. J. 2002. An experimental study of the kinetics of decompression-induced crystallization in silicic melt. *Journal of Geophysical Research: Solid Earth* 107:ECV 8-1-ECV 8-24.

Hammer J. E., and Rutherford M. J. 2003. Petrologic indicators of preeruption magma dynamics. *Geology* 31:79–82.

Hammer J. E., Rutherford M. J., and Hildreth W. 2002. Magma storage prior to the 1912 eruption at Novarupta, Alaska. *Contributions to Mineralogy and Petrology* 144:144–162.

Hammer J., Jacob S., Welsch B., Hellebrand E., and Sinton J. 2016. Clinopyroxene in postshield Haleakala ankaramite: 1. Efficacy of thermobarometry. *Contributions to Mineralogy and Petrology* 171:7.

Hammond P. A., and Taylor L. A. 1982. The ilmenite/titano-magnetite assemblage: kinetics of re-equilibration. *Earth and Planetary Science Letters* 61:143–149.

Harris A. 2013. *Thermal Remote Sensing of Active Volcanoes: A User's Manual*. New York: Cambridge University Press.

Harris A. J. L., Dehn J., James M. R., Hamilton C., Herd R., Lodato L., and Steffke A. 2007. Pāhoehoe flow cooling, discharge, and coverage rates from thermal image chronometry. *Geophysical Research Letters* 34:L19303.

Harris A., Bailey J., Calvari S., and Dehn J. 2005. Heat loss measured at a lava channel and its implications for down-channel cooling and rheology. In *Special Paper 396: Kinematics and dynamics of lava flows*. Geological Society of America. pp. 125–146.

Hartley M. E., Morgan D. J., Maclennan J., Edmonds M., and Thordarson T. 2016. Tracking timescales of short-term precursors to large basaltic fissure eruptions through Fe–Mg diffusion in olivine. *Earth and Planetary Science Letters* 439:58–70.

Hauber E., Bleacher J., Gwinner K., Williams D., and Greeley R. 2009. The topography and morphology of low shields and associated landforms of plains volcanism in the Tharsis region of Mars. *Journal of Volcanology and Geothermal Research* 185:69–95.

Higgins M. D., Voos S., and Vander Auwera J. 2015. Magmatic processes under Quizapu volcano, Chile, identified from geochemical and textural studies. *Contributions to Mineralogy and Petrology* 170:51.

Hildreth W. and Fierstein J. 2012. The Novarupta-Katmai eruption of 1912—largest eruption of the twentieth century; centennial perspectives: U.S. Geological Survey Professional Paper 1791.

Hildreth W., and Drake R. E. 1992. Volcán Quizapu, Chilean Andes. *Bulletin of Volcanology* 54:93–125.

Hildreth W., and Wilson C. J. N. 2007. Compositional Zoning of the Bishop Tuff. *Journal of Petrology* 48:951–999.

Hildreth W., Grunder A., and Drake R. 1984. The Loma Seca Tuff and the Calabozos caldera: A major ash-flow and caldera complex in the southern Andes of central Chile. *Geological Society of America Bulletin* 95:45–54.

Hilliard J. E. 1968. Measurement of Volume in Volume. In *Quantitative Microscopy*, edited by DeHoff R. T. and Rhines F. N. New York: McGraw-Hill. pp. 45-76.

Ho A. M. and Cashman K. V. 1997. Temperature constraints on the Ginkgo flow of the Columbia River Basalt Group. *Geology* 25:403–406.

Hoblitt R. P., Orr T. R., Heliker C., Denlinger R. P., Hon K., and Cervelli P. F. 2012. Inflation rates, rifts, and bands in a pāhoehoe sheet flow. *Geosphere* 8:179–195.

Holtz F. 2005. Experimental Petrology of the 1991-1995 Unzen Dacite, Japan. Part I: Phase relations, phase composition and pre-eruptive conditions. *Journal of Petrology* 46:319–337.

Holzapfel C., Chakraborty S., Rubie D. C., and Frost D. J. 2007. Effect of pressure on Fe–Mg, Ni and Mn diffusion in $(Fe_xMg_{1-x})_2SiO_4$ olivine. *Physics of the Earth and Planetary Interiors* 162:186–198.

Hon K., Gansecki C., and Kauahikaua J. 2003. The transition from ʻaʻā to pāhoehoe crust on flows emplaced during the Puʻu ʻŌʻō-Kūpaianaha eruption. *USGS Professional Paper* 1676:89–104.

Hon K., Kauahikaua J. P., and Mackay K. 1993. Inflation and cooling data from pahoehoe sheet flows on Kilauea volcano. USGS Open-File Report 93-342-A.

Hon K., Kauahikaua J., Denlinger R., and Mackay K. 1994. Emplacement and inflation of pahoehoe sheet flows: Observations and measurements of active lava flows on Kilauea Volcano, Hawaii. *Geological Society of America Bulletin* 106:351–370.

Hoppa G., Tufts B. R., Greenberg R., and Geissler P. 1999. Strike–Slip Faults on Europa: Global Shear Patterns Driven by Tidal Stress. *Icarus* 141:287–298.

Hort M., Marsh B. D., Resmini R. G., and Smith M. K. 1999. Convection and Crystallization in a Liquid Cooled from above: An Experimental and Theoretical Study. *Journal of Petrology* 40:1271–1300.

Houghton B. F., Carey R. J., Cashman K. V., Wilson C. J. N., Hobden B. J., and Hammer J. E. 2010. Diverse patterns of ascent, degassing, and eruption of rhyolite magma during the 1.8 ka Taupo eruption, New Zealand: Evidence from clast vesicularity. *Journal of Volcanology and Geothermal Research* 195:31–47.

Ikeda Y. 2004. Petrology of the Yamato 980459 shergottite. *Antarctic Meteorite Research* 17:35–54.

Jakobsson S., and Oskarsson N. 1994. The system C-O in equilibrium with graphite at high pressure and temperature: An experimental study. *Geochimica et Cosmochimica Acta* 58:9–17.

Jarosewich E., Nelen J. A., and Norberg J. A. 1980. Reference samples for electron microprobe analysis. *Geostandards Newsletter* IV:43–47.

Johnson E. A., and Rossman G. R. 2013. The diffusion behavior of hydrogen in plagioclase feldspar at 800-1000 C: Implications for re-equilibration of hydroxyl in volcanic phenocrysts. *American Mineralogist* 98:1779–1787.

Johnson M. C., and Rutherford M. J. 1989. Experimental calibration of the aluminum-in-hornblende geobarometer with application to Long Valley caldera (California) volcanic rocks. *Geology* 17:837–841.

Johnson M. C., Anderson A. T., and Rutherford M. J. 1994. Pre-eruptive volatile contents of magmas. *Reviews in Mineralogy and Geochemistry* 30:281–330.

Jolles J., and Lange R. 2017. A re-examination of temperature and mineral-melt equilibrium across Early to Late Bishop Tuff: Insights from all possible pairs of Fe-Ti oxides per pumice clast.

Jurado-Chichay Z. and Rowland S. K. 1995. Channel overflows of the Pōhue Bay flow, Mauna Loa, Hawai'i: examples of the contrast between surface and interior lava. *Bulletin of Volcanology* 57:117–126.

Kessel R., Beckett J. R., and Stolper E. M. 2001. Thermodynamic properties of the Pt-Fe system. *American Mineralogist* 86:1003–1014.

Keszthelyi L. 1994. Calculated Effect of Vesicles on the Thermal-Properties of Cooling Basaltic Lava Flows. *Journal of Volcanology and Geothermal Research* 63: 257–266.

Keszthelyi L. and Self S. 1998. Some physical requirements for the emplacement of long basaltic lava flows. *Journal of Geophysical Research: Solid Earth* 103:27447–27464.

Keszthelyi L., Jaeger W., McEwen A., Tornabene L., Beyer R. A., Dundas C., and Milazzo M. 2008. High Resolution Imaging Science Experiment (HiRISE) images of volcanic terrains from the first 6 months of the Mars Reconnaissance Orbiter Primary Science Phase. *Journal of Geophysical Research: Planets* 113:E04005.

Keszthelyi L., Thordarson T., McEwen A., Haack H., Guilbaud M.-N., Self S., and Rossi M. J. 2004. Icelandic analogs to Martian flood lavas. *Geochemistry, Geophysics, Geosystems* 5:Q11014, doi:10.1029/2004GC000758.

Kirkpatrick J. R. 1975. Crystal Growth from the Melt: A Review. *American Mineralogist* 60:798–814.

Kirkpatrick R. J. 1974. Kinetics of crystal growth in the system $CaMgSi_2O_6$ -$CaAl_2SiO_6$. *American Journal of Science* 274:215–242.

Kirkpatrick R. J. 1981. Kinetics of crystallization in igneous rocks. In *Kinetics of Geochemical Processes,* edited by Lasaga A. C., and Kirkpatrick R. J. Chantilly, Virginia: Mineralogical Society of America. pp. 321–398.

Kirkpatrick R. J., Klein L., Uhlmann D. R., and Hays J. F. 1979. Rates and processes of crystal growth in the system anorthite-albite. *Journal of Geophysical Research: Solid Earth* 84:3671–3676.

Kohlstedt D. L., and Mackwell S. J. 2008. The role of protons in ionic diffusion in (Mg, Fe)O and $(Mg, Fe)_2SiO_4$. *Journal of Materials Science* 43:4693–4700.

Kondepudi D., and Prigogine I. 2014. *Modern Thermodynamics: From Heat Engines to Dissipative Structures,* John Wiley & Sons.

Korotev R. L. 2005. Lunar geochemistry as told by lunar meteorites. *Chemie der Erde - Geochemistry* 65:297–346.

Kouchi A., Tsuchiyama A., and Sunagawa I. 1986. Effect of stirring on crystallization kinetics of basalt: texture and element partitioning. *Contributions to Mineralogy and Petrology* 93:429–438.

Kramer M. J., and Seifert K. E. 1991. Strain Enhanced Diffusion in Feldspars. In *Diffusion, Atomic Ordering, and Mass Transport*, edited by Ganguly J. New York: Springer. pp. 286–303.

Kuo L.-C., and Kirkpatrick J. R. 1985. Kinetics of crystal dissolution in the system diopside-forsterite-silica. *American Journal of Science* 285:51–90.

Lange R. A., Frey H. M., and Hector J. 2009. A thermodynamic model for the plagioclase-liquid hygrometer/thermometer. *American Mineralogist* 94:494–506.

Larsen J. F. 2006. Rhyodacite magma storage conditions prior to the 3430 yBP caldera-forming eruption of Aniakchak volcano, Alaska. *Contributions to Mineralogy and Petrology* 152:523–540.

Lasaga A. C. 1982. Toward a master equation in crystal growth. *American Journal of Science* 282:1264–1288.

Lasaga A. C. 1998. *Kinetic Theory in the Earth Sciences*, Princeton, NJ: Princeton University Press.

LaTourrette T., and Wasserburg G. J. 1998. Mg diffusion in anorthite: implications for the formation of early solar system planetesimals. *Earth and Planetary Science Letters* 158:91–108.

Lattard D., Sauerzapf U., and Kontny A. 2012. Rapid surficial oxidation of synthetic Fe-Ti oxides at high temperature: Observations and consequences for magnetic measurements. *Geochemistry, Geophysics, Geosystems* 13:Q08Z46.

Leake B. E. 1978. Nomenclature of amphiboles. *American Mineralogist* 63:1023–1052.

Lentz R. C. F. and McSween H. Y. Jr. 2005. A textural examination of the Yamato 980459 and Los Angeles shergottites using crystal size distribution analysis. *Antarctic Meteorite Research* 18:66–82.

Leroux H. and Cordier P. 2006. Magmatic cristobalite and quartz in the NWA 856 Martian meteorite. *Meteoritics & Planetary Science* 41:913–923.

Lessel J. and Putirka K. 2015. New thermobarometers for martian igneous rocks, and some implications for secular cooling on Mars. *American Mineralogist* 100:2163–2171, doi:10.2138/am-2015-4732.

Liang Y. 1999. Diffusive dissolution in ternary systems: analysis with applications to quartz and quartzite dissolution in molten silicates. *Geochimica et Cosmochimica Acta* 63:3983–3995.

Liang Y. 2000. Dissolution in molten silicates: effects of solid solution. *Geochimica et Cosmochimica Acta* 64:1617–1627.

Liang Y. 2003. Kinetics of crystal-melt reaction in partially molten silicates: 1. Grain scale processes. *Geochemistry, Geophysics, Geosystems* 4:1045.

Lipman P. W., and Mullineaux D. R., eds. 1985. The 1980 Eruptions of Mount St. Helens, Washington. *USGS Professional Paper* 1250.

Liu M., and Yund R. 1992. Nasi-Caal Interdiffusion in Plagioclase. *American Mineralogist* 77:275–283.

Lloyd A. S., Plank T., Ruprecht P., Hauri E. H., and Rose W. 2013. Volatile loss from melt inclusions in pyroclasts of differing sizes. *Contributions to Mineralogy and Petrology* 165:129–153.

Loewen M. W., Bindeman I. N., and Melnik O. E. 2017. Eruption mechanisms and short duration of large rhyolitic lava flows of Yellowstone. *Earth and Planetary Science Letters* 458:80–91.

Lofgren G. 1980. Experimental studies on the dynamic crystallization of silicate melts. In *Physics of Magmatic Processes*, edited by Hargraves R. B. Princeton, New Jersey: Princeton University Press. pp. 487–551.

Lofgren G. E. 1983. Effect of heterogeneous nucleation on basaltic textures: a dynamic crystallization study. *Journal of Petrology* 24:229–255.

Lofgren G., Williams R. J., Usselman T. M., Donaldson C. H., and Mullins O. Jr. 1974. Experimentally reproduced textures and mineral chemistry of Apollo 15 quartz normative basalts. Proceedings, Fifth Lunar Science Conference. pp. 549–567.

Longhi J., and Hays J. F. 1979. Phase equilibria and solid solution along the join $CaAl_2Si_2O_8$-SiO_2. *American Journal of Science* 279:876–890.

Love G. R. 1964. Dislocation pipe diffusion. *Acta Metallurgica* 12:731–737.

Lowrie W. 2007. *Fundamentals of Geophysics*, Cambridge: Cambridge University Press.

Lu Z., Masterlark T., and Dzurisin D. 2005. Interferometric synthetic aperture radar study of Okmok volcano, Alaska, 1992–2003: Magma supply dynamics and postemplacement lava flow deformation. *Journal of Geophysical Research: Solid Earth* 110:B02403.

Lucey P. G., Taylor G. J., and Malaret E. 1995. Abundance and Distribution of Iron on the Moon. *Science* 268:1150–1153.

Lunar Sample Preliminary Examination Team 1. 1969. Preliminary Examination of Lunar Samples from Apollo 11. *Science* 165:1211–1227.

Lynn K. J., Garcia M. O., Shea T., Costa F., and Swanson D. A. 2017. Timescales of mixing and storage for Keanakāko‘i Tephra magmas (1500–1820 C.E.), Kīlauea Volcano, Hawai‘i. *Contributions to Mineralogy and Petrology* 172:76.

Macdonald G. A. 1953. Pahoehoe, aa, and block lava. *American Journal of Science* 251:169–191.

Mader H. M., Brodsky E. E., Howard D., and Sturtevant B. 1997. Laboratory simulations of sustained volcanic eruptions. *Nature* 388:462–464.

Martel C., Pichavant M., Holtz F., Scaillet B., Bourdier J.-L., and Traineau H. 1999. Effects of fO_2 and H_2O on andesite phase relations between 2 and 4 kbar. *Journal of Geophysical Research* 104:29453–29470.

Mastin L. G. 2002. Insights into volcanic conduit flow from an open-source numerical model. *Geochemistry, Geophysics, Geosystems* 3:1–18.

Mastin L. G. et al. 2009. A multidisciplinary effort to assign realistic source parameters to models of volcanic ash-cloud transport and dispersion during eruptions. *Journal of Volcanology and Geothermal Research* 186:10–21.

Mathieu R., Libourel G., Deloule E., Tissandier L., Rapin C., and Podor R. 2011. Na_2O solubility in CaO–MgO–SiO_2 melts. *Geochimica et Cosmochimica Acta* 75:608–628.

McBirney A. R. 1993. *Igneous Petrology*, Second. Boston: Jones and Bartlett Publishers.

McCanta M. C., Beckett J. R., and Stolper E. M. 2016. Correlations and zoning patterns of phosphorus and chromium in olivine from H chondrites and the LL chondrite Semarkona. *Meteoritics & Planetary Science*, doi:10.1111/maps.12604.

McCoy T. J., and Lofgren G. E. 1999. Crystallization of the Zagami shergottite: An experimental study. *Earth and Planetary Science Letters* 173:397–411.

McCoy T., Taylor G., and Keil K. 1992. Zagami: Product of a 2-Stage Magmatic History. *Geochimica Et Cosmochimica Acta* 56:3571–3582.

McEwen A. S. et al. 1998. Active Volcanism on Io as Seen by Galileo SSI. *Icarus* 135:181–219.

Mcsween H. 1985. Snc Meteorites - Clues to Martian Petrologic Evolution. *Reviews of Geophysics* 23:391–416.

McSween H. Y. 2002. The rocks of Mars, from far and near. *Meteoritics & Planetary Science* 37:7–25.

McSween H. Y. et al. 2006. Characterization and petrologic interpretation of olivine-rich basalts at Gusev Crater, Mars. *Journal of Geophysical Research: Planets* 111:E02S10.

Médard E., and Grove T. L. 2008. The effect of H2O on the olivine liquidus of basaltic melts: experiments and thermodynamic models. *Contributions to Mineralogy and Petrology* 155:417–432.

Merzbacher C., and Eggler D. H. 1984. A magmatic geohygrometer: application to Mount St. Helens and other dacitic magmas. *Geology* 12:587–590.

Mikouchi T., Koizumi E., McKay G., Monkawa A., Ueda Y., Chokai J., and Miyamoto M. 2004. Yamato 980459: Mineralogy and petrology of a new shergottite-related rock from Antarctica. *Antarctic Meteorite Research* 17:13–34.

Mikouchi T., Miyamoto M., and McKay G. A. 1998. Mineralogy of Antarctic basaltic shergottite Queen Alexandra Range 94201: Similarities to Elephant Moraine A79001 (lithology B) martian meteorite. *Meteoritics & Planetary Science* 33:181–189.

Milman-Barris M. S., Beckett J. R., Baker M. B., Hofmann A. E., Morgan Z., Crowley M. R., Vielzeuf D., and Stolper E. 2008. Zoning of phosphorus in igneous olivine. *Contributions to Mineralogy and Petrology* 155:739–765.

Misawa K. 2003. The Yamato 980459 shergottite consortium (abstract). International symposium: Evolution of solar system materials. pp. 84–85.

Misawa K. 2004. The Yamato 980459 olivine-phyric shergottite consortium. *Antarctic Meteorite Research* 17:1–12.

Miyamoto M., Koizumi E., and Mikouchi T. 2009a. Cooling rates of Y980459 and DaG476 shergottites on the basis of Fe-Mg zoning of olivine (abstract #1143). 40th Lunar and Planetary Science Conference.

Miyamoto M., McKay D. S., McKay G. A., and Duke M. B. 1986. Chemical zoning and homogenization of olivines in ordinary chondrites and implications for thermal histories of chondrules. *Journal of Geophysical Research: Solid Earth* 91:12804–12816.

Miyamoto M., Mikouchi T., and Jones R. H. 2009b. Cooling rates of porphyritic olivine chondrules in the Semarkona (LL3. 00) ordinary chondrite: A model for diffusional equilibration of olivine during fractional crystallization. *Meteoritics & Planetary Science* 44:521–530.

Mokhtari A., and Velde D. 1987. Sector-zoned kaersutite in camptonites from Morocco. *Mineralogical Magazine* 51:151–156.

Mollo S., Del Gaudio P., Ventura G., Iezzi G., and Scarlato P. 2010. Dependence of clinopyroxene composition on cooling rate in basaltic magmas: Implications for thermobarometry. *Lithos* 118:302–312.

Moore A., Coogan L. A., Costa F., and Perfit M. R. 2014. Primitive melt replenishment and crystal-mush disaggregation in the weeks preceding the 2005–2006 eruption, EPR. *Earth and Planetary Science Letters* 403:15–26.

Moore G., Vennemann T., and Carmichael I. S. E. 1998. An empirical model for the solubility of H2O in magmas to 3 kilobars. *American Mineralogist* 83:36–42.

Moore J. M. et al. 2016. The geology of Pluto and Charon through the eyes of New Horizons. *Science* 351:1284–1293.

Muir D. D., Blundy J. D., Rust A. C., and Hickey J. 2014. Experimental constraints on dacite pre-eruptive magma storage conditions beneath Uturuncu volcano. *Journal of Petrology* 55:749–767.

Mungall J. E., Dingwell D. B., and Chaussidon M. 1999. Chemical diffusivities of 18 trace elements in granitoid melts. *Geochimica et Cosmochimica Acta* 63:2599–2610.

Musselwhite D. S., Dalton H. A., Kiefer W. S., and Treiman A. H. 2006. Experimental petrology of the basaltic shergottite Yamato-980459: Implications for the thermal structure of the Martian mantle. *Meteoritics & Planetary Science* 41:1271–1290.

Nakada S., Shimizu H., and Ohta K. 1999. Overview of the 1990 1995 eruption at Unzen Volcano. *Journal of Volcanology and Geothermal Research* 89:1–22.

Nakamura M. 1995. Continuous mixing of crystal mush and replenished magma in the ongoing Unzen eruption. *Geology* 23:807–810.

Nakamura Y. 1973. Origin of sector-zoning in igneous clinopyroxenes. *American Mineralogist* 58:986–990.

Nekvasil H., Dondolini A., Horn J., Filiberto J., Long H., and Lindsley D. H. 2004. The Origin and Evolution of Silica-saturated Alkalic Suites: An Experimental Study. *Journal of Petrology* 45:693–721.

Newhall C. G., and Punongbayan R. S., eds. 1996. *Fire and Mud: Eruptions and Lahars of Mount Pinatubo, Philippines*, Seattle: University of Washington Press.

Nielsen R. L., Ustunisik G., Weinsteiger A. B., Tepley F. J., Johnston A. D., and Kent A. J. R. 2017. Trace element partitioning between plagioclase and Melt: An investigation of the impact of experimental and analytical procedures. *Geochemistry, Geophysics, Geosystems* 18:3359-3384.

O'Neill H. S. C., Pownceby M. I., and McCammon C. A. 2003. The magnesiowüstite: iron equilibrium and its implications for the activity-composition relations of $(Mg,Fe)_2SiO_4$ olivine solid solutions. *Contributions to Mineralogy and Petrology* 146:308–325.

Ody A., Poulet F., Quantin C., Bibring J.-P., Bishop J. L., and Dyar M. D. 2015. Candidates source regions of martian meteorites as identified by OMEGA/MEx. *Icarus* 258:366–383.

Ohashi Y., and Finger L. W. 1974. Diffusion anisotropy in olivine - model calculation. In *Year book*. Washington, DC: Carnegie Institute of Washington pp. 403-405.

Orr T. R., and Hoblitt R. P. 2008. A versatile time-lapse camera system developed by the Hawaiian Volcano Observatory for use at Kilauea Volcano, Hawai'i. USGS Scientific Investigations Report 2008-5117.

Patrick M. R., Dehn J., and Dean K. 2004. Numerical modeling of lava flow cooling applied to the 1997 Okmok eruption: Approach and analysis. *Journal of Geophysical Research* 109.

Patrick M. R., Dehn J., and Dean K. 2004. Numerical modeling of lava flow cooling applied to the 1997 Okmok eruption: Approach and analysis. *Journal of Geophysical Research* 109:B03202, doi:10.1029/2003JB002537.

Pichavant M., Costa F., Burgisser A., Scaillet B., Martel C., and Poussineau S. 2007. Equilibration Scales in Silicic to Intermediate Magmas Implications for Experimental Studies. *Journal of Petrology* 48:1955–1972.

Presnall D. C. and Brenner N. L. 1974. A method for studying iron silicate liquids under reducing conditions with negligible iron loss. *Geochimica et Cosmochimica Acta* 38:1785–1788.

Prince E. 1994. *Mathematical techniques in crystallography and materials science*, Springer-Verlag.

Putirka K. D. 2008. Thermometers and Barometers for Volcanic Systems. *Reviews in Mineralogy and Geochemistry* 69:61–120.

Putirka K., Johnson M., Kinzler R., Longhi J., and Walker D. 1996. Thermobarometry of mafic igneous rocks based on clinopyroxene-liquid equilibria, 0–30 kbar. *Contributions to Mineralogy and Petrology* 123:92–108.

Pyle D. M. 1989. The thickness, volume and grainsize of tephra fall deposits. *Bulletin of Volcanology* 51:1–15.

Radomsky P. M., and Hewins R. H. 1990. Formation conditions of pyroxene-olivine and magnesian olivine chondrules. *Geochimica et Cosmochimica Acta* 54:3475–3490.

Ridolfi F., and Renzulli A. 2012. Calcic amphiboles in calc-alkaline and alkaline magmas: thermobarometric and chemometric empirical equations valid up to 1,130°C and 2.2 GPa. *Contributions to Mineralogy and Petrology* 163:877–895.

Ridolfi F., Renzulli A., and Puerini M. 2010. Stability and chemical equilibrium of amphibole in calc-alkaline magmas: an overview, new thermobarometric formulations and application to subduction-related volcanoes. *Contributions to Mineralogy and Petrology* 160:45–66.

Riker J. M., Blundy J. D., Rust A. C., Botcharnikov R. E., and Humphreys M. C. S. 2015. Experimental phase equilibria of a Mount St. Helens rhyodacite: A framework for interpreting crystallization paths in degassing silicic magmas. *Contributions to Mineralogy and Petrology* 170:6.

Robinson P., Spear F. S., Schumacher J. C., Laird J., Klein C., Evans B. W., and Doolan B. L. 1982. Phase relations of metamorphic amphiboles: Natural occurrence and theory. *Reviews in Mineralogy* 9B:1-227.

Roy R., and Tuttle O. F. 1956. Investigations under hydrothermal conditions. *Physics and Chemistry of the Earth* 1:138–180.

Rubin A. E., Warren P. H., Greenwood J. P., Verish R. S., Leshin L. A., Hervig R. L., Clayton R. N., and Mayeda T. K. 2000. Los Angeles: The most differentiated basaltic Martian meteorite. *Geology* 28: 1011–1014.

Ruprecht P., and Bachmann O. 2010. Pre-eruptive reheating during magma mixing at Quizapu volcano and the implications for the explosiveness of silicic arc volcanoes. *Geology* 38:919–922.

Ruprecht P., and Cooper K. M. 2012. Integrating the Uranium-Series and Elemental Diffusion Geochronometers in Mixed Magmas from Volcan Quizapu, Central Chile. *Journal of Petrology* 53:841–871.

Ruprecht P., Bergantz G. W., Cooper K. M., and Hildreth W. 2012. The Crustal Magma Storage System of Volcan Quizapu, Chile, and the Effects of Magma Mixing on Magma Diversity. *Journal of Petrology* 53:801–840.

Rutherford M. J. 1969. An Experimental Determination of Iron Biotite-Alkali Feldspar Equilibria. *Journal of Petrology* 10:381–408.

Rutherford M. J. 2008. Magma Ascent Rates. *Reviews in Mineralogy and Geochemistry* 69:241–271.

Rutherford M. J., and Devine J. D. 1996. Pre-eruption pressure-temperaure conditions and volatiles in the 1991 dacitic magma of Mount Pinatubo. In *Fire and Mud: Eruptions and Lahars of Mount Pinatubo, Philippines*, edited by Newhall C. G., and Punongbayan R. S. Seattle: University of Washington Press. pp. 751–766.

Rutherford M. J., and Devine J. D. 2003. Magmatic conditions and magma ascent as indicated by hornblende phase equilibria and reactions in the 1995-2002 Soufriere Hills magma. *Journal of Petrology* 44:1433–1454.

Rutherford M. J., and Devine J. D. 2008. Magmatic conditions and processes in the storage zone of the 2004–2006 Mount St. Helens dacite. *A volcano rekindled: the renewed eruption of Mount St. Helens* 1750:703–725.

Rutherford M. J., Hess P. C., and Daniel G. H. 1974. Experimental liquid line of descent and liquid immiscibility for basalt 70017. *Proceedings, Fifth Lunar Science Conference* 569–583.

Rutherford M. J., Sigurdsson H., Carey S., and Davis A. 1985. The May 18, 1980, Eruption of Mount St. Helens 1. Melt Composition and Experimental Phase Equilibria. *Journal of Geophysical Research* 90:2929–2947.

Rutherford M., and Devine J. 1988. The May 18, 1980, Eruption of Mount-St-Helens .3. Stability and Chemistry of Amphibole in the Magma Chamber. *Journal of Geophysical Research-Solid Earth and Planets* 93:11949–11959.

Rutherford M., and Hill P. 1993. Magma Ascent Rates from Amphibole Breakdown - an Experimental-Study Applied to the 1980-1986 Mount St-Helens Eruptions. *Journal of Geophysical Research-Solid Earth* 98:19667–19685.

Ruzicka A., Snyder G. A., and Taylor L. A. 1997. Vesta as the howardite, eucrite and diogenite parent body: Implications for the size of a core and for large-scale differentiation. *Meteoritics & Planetary Science* 32:825–840.

Salas P. A., Rabbia O. M., Hernández L. B., and Ruprecht P. 2017. Mafic monogenetic vents at the Descabezado Grande volcanic field (35.5°S–70.8°W): the northernmost evidence of regional primitive volcanism in the Southern Volcanic Zone of Chile. *International Journal of Earth Sciences* 106:1107–1121.

Sato H., Holtz F., Botcharnikov R. E., and Nakada S. 2017. Intermittent generation of mafic enclaves in the 1991-1995 dacite of Unzen Volcano recorded in mineral chemistry. *Contributions to Mineralogy and Petrology* 172:22.

Sato H., Nakada S., Fujii T., Nakamura M., and Suzuki-Kamata K. 1999. Groundmass pargasite in the 1991–1995 dacite of Unzen volcano: phase stability experiments and volcanological implications. *Journal of Volcanology and Geothermal Research* 89:197–212.

Scaillet B., and Evans B. W. 1999. The 15 June 1991 eruption of Mount Pinatubo. I. Phase equilibria and pre-eruption P–T–fO_2–fH_2O conditions of the dacite magma. *Journal of Petrology* 40:381–411.

Schmincke H.-U. 1973. Magmatic Evolution and Tectonic Regime in the Canary, Madeira, and Azores Island Groups. *GSA Bulletin* 84:633–648.

Schneider C. A., Rasband W. S., and Eliceiri K. W. 2012. NIH Image to ImageJ: 25 years of image analysis. *Nature Methods* 9:671–675.

Schumacher S., and Breuer D. 2006. Influence of a variable thermal conductivity on the thermochemical evolution of Mars. *Journal of Geophysical Research* 111.

Self S., Keszthelyi L., and Thordarson T. 1998. The importance of pāhoehoe. *Annual Review of Earth and Planetary Sciences* 26:81–110.

Self S., Thordarson T., Keszthelyi L., Walker G. P. L., Hon K., Murphy M. T., Long P., and Finnemore S. 1996. A new model for the emplacement of Columbia River basalts as large, inflated pahoehoe lava flow fields. *Geophysical Research Letters* 23:2689–2692.

Seyfried R., and Freundt A. 2000. Experiments on conduit flow and eruption behavior of basaltic volcanic eruptions. *Journal of Geophysical Research: Solid Earth* 105:23727–23740.

Shaw H. R. and Swanson D. A. 1970. Eruption and flow rates of flood basalts. *Proceedings, Second Columbia River Basalt Symposium* 271–299.

Shea T., and Hammer J. E. 2013. Kinetics of cooling- and decompression-induced crystallization in hydrous mafic-intermediate magmas. *Journal of Volcanology and Geothermal Research* 260:127–145.

Shea T., Costa F., Krimer D., and Hammer J. E. 2015b. Accuracy of timescales retrieved from diffusion modeling in olivine: A. *American Mineralogist* 100:2026–2042.

Shea T., Leonhardi T., Giachetti T., Lindoo A., Larsen J., Sinton J., and Parsons E. 2017. Dynamics of an unusual cone-building trachyte eruption at Puʻu Waʻawaʻa, Hualālai volcano, Hawaiʻi. *Bulletin of Volcanology* 79:26.

Shea T., Lynn K. J., and Garcia M. O. 2015a. Cracking the olivine zoning code: Distinguishing between crystal growth and diffusion. *Geology* 43:935–938.

Shearer C. K., Aaron P. M., Burger P. V., Guan Y., Bell A. S., and Papike J. J. 2013. Petrogenetic linkages among fO_2, isotopic enrichments-depletions and crystallization history in Martian basalts. Evidence from the distribution of phosphorus in olivine megacrysts. *Geochimica et Cosmochimica Acta* 120:17–38.

Shearer C. K., McKay G., Papike J. J., and Karner J. M. 2006. Valence state partitioning of vanadium between olivine-liquid: Estimates of the oxygen fugacity of Y980459 and application to other olivine-phyric martian basalts. *American Mineralogist* 91:1657–1663.

Simons M., Solomon S. C., and Hager B. H. 1997. Localization of gravity and topography: constraints on the tectonics and mantle dynamics of Venus. *Geophysical Journal International* 131:24–44.

Singer B. S., Costa F., Herrin J. S., Hildreth W., and Fierstein J. 2016. The timing of compositionally-zoned magma reservoirs and mafic "priming" weeks before the 1912 Novarupta-Katmai rhyolite eruption. *Earth and Planetary Science Letters* 451:125–137.

Spandler C., and O'Neill H. S. C. 2010. Diffusion and partition coefficients of minor and trace elements in San Carlos olivine at 1,300°C with some geochemical implications. *Contributions to Mineralogy and Petrology* 159:791–818.

Sparks R. S. J. 1986. The dimensions and dynamics of volcanic eruption columns. *Bulletin of Volcanology* 48:3–15.

Sparks R., Folkes C., Humphreys M., Barfod D., Clavero J., Sunagua M., McNutt S., and Pritchard M. 2008. Uturuncu volcano, Bolivia: volcanic unrest due to mid-crustal magma intrusion. *American Journal of Science* 308:727-769.

Spear F. S. 1981. An experimental study of hornblende stability and compositional variability in amphibole. *American Journal of Science* 281:697–734.

Spencer K. J., and Lindsley D. H. 1981. A solution model for coexisting iron-titanium oxides. *American Mineralogist* 66:1189–1201.

Stenhouse I., O'Neill H., and Lister G. 2010. Diffusion in natural ilmenite (abstract). EGU General Assembly. p. 343.

Stewart D. B., Walker G. W., Wright T. L., and Fahey J. J. 1966. Physical properties of calcic labradorite from Lake County, Oregon. *American Mineralogist* 51:177–197.

Sun C., Graff M., and Liang Y. 2017. Trace element partitioning between plagioclase and silicate melt: The importance of temperature and plagioclase composition, with implications for terrestrial and lunar magmatism. *Geochimica et Cosmochimica Acta* 206:273–295.

Taddeucci J., Scarlato P., Capponi A., Del Bello E., Cimarelli C., Palladino D. M., and Kueppers U. 2012. High-speed imaging of Strombolian explosions: The ejection velocity of pyroclasts. *Geophysical Research Letters* 39:L02301.

Taylor J. R., Wall V. J., and Pownceby M. I. 1992. The calibration and application of accurate redox sensors. *American Mineralogist* 77:284–295.

Thomas M. E., and Neuberg J. W. 2014. Understanding which parameters control shallow ascent of silicic effusive magma. *Geochemistry, Geophysics, Geosystems* 15:4481–4506.

Thordarson T. and Self S. 1998. The Roza Member, Columbia River Basalt Group: A gigantic pahoehoe lava flow field formed by endogenous processes? *Journal of Geophysical Research-Solid Earth* 103:27411–27445.

Touloukian Y. S., Judd W. R., and Roy R. F. 1981. *Physical properties of rocks and minerals*. New YorK: McGraw-Hill.

Treiman A. and Sutton S. 1992. Petrogenesis of the Zagami meteorite: Inferences from synchrotron X-Ray (SXRF) microprobe and electron microprobe analyses of pyroxenes. *Geochimica Et Cosmochimica Acta* 56:4059–4074.

Tsuchiyama A. 1985. Dissolution kinetics of plagioclase in the melt of the system diopside-albite-anorthite, and origin of dusty plagioclase in andesites. *Contributions to Mineralogy and Petrology* 89:1–16.

Underwood E. E. 1968. Surface Area and Length in Volume. In *Quantitative Microscopy*, edited by DeHoff R. T. and Rhines F. N. New York: McGraw-Hill. pp. 77-127.

Usselman T. M., and Lofgren G. E. 1976. The phase relations, textures, and mienral chemistries of high-titanium mare basalts as a function of oxygen fugacity and cooling rate. *Proceedings of the 7th Lunar Science Conference* 1345–1363.

Usui T., Alexander C. M. O., Wang J., Simon J. I., and Jones J. H. 2012. Origin of water and mantle–crust interactions on Mars inferred from hydrogen isotopes and volatile element abundances of olivine-hosted melt inclusions of primitive shergottites. *Earth and Planetary Science Letters* 357-358:119–129.

Usui T., McSween H. Y., and Floss C. 2008. Petrogenesis of olivine-phyric shergottite Yamato 980459, revisited. *Geochimica et Cosmochimica Acta* 72:1711–1730.

Van Orman J. A. V., and Crispin K. L. 2010. Diffusion in Oxides. *Reviews in Mineralogy and Geochemistry* 72:757–825.

Van Orman J. A., Cherniak D. J., and Kita N. T. 2014. Magnesium diffusion in plagioclase: Dependence on composition, and implications for thermal resetting of the 26Al–26Mg early solar system chronometer. *Earth and Planetary Science Letters* 385:79–88.

Van Orman J. A., Grove T. L., and Shimizu N. 2001. Rare earth element diffusion in diopside: influence of temperature, pressure, and ionic radius, and an elastic model for diffusion in silicates. *Contributions to Mineralogy and Petrology* 141:687–703.

Venezky D. Y., and Rutherford M. J. 1997. Preeruption conditions and timing of dacite-andesite magma mixing in the 2.2 ka eruption at Mount Rainier. *Journal of Geophysical Research* 102:20069–20086.

Venezky D. Y., and Rutherford M. J. 1999. Petrology and Fe Ti oxide reequilibration of the 1991 Mount Unzen mixed magma. *Journal of Volcanology and Geothermal Research* 89:213–230.

Vona A. and Romano C. 2013. The effects of undercooling and deformation rates on the crystallization kinetics of Stromboli and Etna basalts. *Contributions to Mineralogy and Petrology* 166:491–509.

Vye-Brown C., Self S., and Barry T. L. 2013. Architecture and emplacement of flood basalt flow fields: Case studies from the Columbia River Basalt Group, NW USA. *Bulletin of Volcanology* 75:3, doi:10.1007/s00445-013-0697-2.

Walker D., Powell M. A., Hays J. F., and Lofgren G. E. 1978. Dynamic crystallization of a eucrite basalt. *Proceedings, 9th Lunar and Planetary Science Conference* 1369–1391.

Walker G. P. L. 1971. Compound and simple lava flows and flood basalts. *Bulletin Volcanologique* 35:579–590.

Walker G. P. L. 1974. Eruptive Mechanisms in Iceland. In *Geodynamics of Iceland and the North Atlantic Area*, edited by Kristjansson L. Dordrecht: D. Reidel Publishing Company pp. 189–201.

Waters L. E., and Andrews B. J. 2016. The role of superheating in the formation of Glass Mountain obsidians (Long Valley, CA) inferred through crystallization of sanidine. *Contributions to Mineralogy and Petrology* 171:79.

Waters L. E., and Lange R. A. 2015. An updated calibration of the plagioclase-liquid hygrometer-thermometer applicable to basalts through rhyolites. *American Mineralogist* 100:2172–2184.

Watters T. R., McGovern P. J., and III R. P. I. 2007. Hemispheres Apart: The Crustal Dichotomy on Mars. *Annual Review of Earth and Planetary Sciences* 35:621–652.

Watts R. B., de Silva S. L., de Rios G. J., and Croudace I. 1999. Effusive eruption of viscous silicic magma triggered and driven by recharge: a case study of the Cerro Chascon-Runtu Jarita Dome Complex in Southwest Bolivia. *Bulletin of Volcanology* 61:241–264.

Welsch B., Faure F., Famin V., Baronnet A., and Bachelery P. 2013. Dendritic Crystallization: A Single Process for all the Textures of Olivine in Basalts? *Journal of Petrology* 54:539–574.

Welsch B., Hammer J., and Hellebrand E. 2014. Phosphorus zoning reveals dendritic architecture of olivine. *Geology* 42:867–870.

Welsch B., Hammer J., Baronnet A., Jacob S., Hellebrand E., and Sinton J. 2016. Clinopyroxene in postshield Haleakala ankaramite: 2. Texture, compositional zoning and supersaturation in the magma. *Contributions to Mineralogy and Petrology* 171:6.

Werner S. C., Ody A., and Poulet F. 2014. The Source Crater of Martian Shergottite Meteorites. *Science* 343:1343–1346.

Wieczorek M. A. et al. 2013. The Crust of the Moon as Seen by GRAIL. *Science* 339:671–675.

Wilson L., Sparks R. S. J., Huang T. C., and Watkins N. D. 1978. The control of volcanic column heights by eruption energetics and dynamics. *Journal of Geophysical Research: Solid Earth* 83:1829–1836.

Wright T. L. and Okamura R. T. 1977. Cooling and crystallization of tholeiitic basalt, 1965 Makaopuhi Lava Lake, Hawaii. *USGS Professional Paper* 1004.

Wyllie P. J., Donaldson C. H., Irving A. J., Kesson S. E., Merrill R. B., Presnall D. C., Stolper E. M., Usselman T. M., and Walker D. 1981. Experimental petrology of basalts and their source rocks. In *Basaltic Volcanism on the Terrestrial Planets*. New York: Pergamon Press. pp. 493–630.

Yamada M., Sasaki S., Nagahara H., Fujiwara A., Hasegawa S., Yano H., Hiroi T., Ohashi H., and Otake H. 1999. Simulation of space weathering of planet-forming materials: Nanosecond pulse laser irradiation and proton implantation on olivine and pyroxene samples. *Earth, Planets and Space* 51:1255–1265.

Yoder H. S., and Tilley C. E. 1962. Origin of basalt magmas: An experimental study of natural and synthetic rock systems. *Journal of Petrology* 3:342–532.

Yu Y., Zhang Y., Chen Y., and Xu Z. 2016. Kinetics of anorthite dissolution in basaltic melt. *Geochimica et Cosmochimica Acta* 179:257–274.

Yund R. A., Smith B. M., and Tullis J. 1981. Dislocation-assisted diffusion of oxygen in albite. *Physics and Chemistry of Minerals* 7:185–189.

Zellmer G. F., Blake S., Vance D., Hawkesworth C., and Turner S. 1999. Plagioclase residence times at two island arc volcanoes (Kameni Islands, Santorini, and Soufriere, St. Vincent) determined by Sr diffusion systematics. *Contributions to Mineralogy and Petrology* 136:345–357.

Zhang B., Shan S., and Wu X. 2016. Modeling H, Na, and K diffusion in plagioclase feldspar by relating point defect parameters to bulk properties. *Physics and Chemistry of Minerals* 43:151–159.

Zhang Y. 2010. Diffusion in Minerals and Melts: Theoretical Background. *Reviews in Mineralogy and Geochemistry* 72:5–59.

Zhang Y., Ni H., and Chen Y. 2010. Diffusion Data in Silicate Melts. *Reviews in Mineralogy and Geochemistry* 72:311–408.

Zhang Y., Xu Z., Zhu M., and Wang H. 2007. Silicate melt properties and volcanic eruptions. *Reviews of Geophysics* 45:RG4004.